

BARC NEWSLETTER

FOUNDER'S DAY

**SPECIAL
ISSUE
OCTOBER
2013**

भाभा परमाणु अनुसंधान केंद्र
BHABHA ATOMIC RESEARCH CENTRE



भारत सरकार
Government of India

BARC NEWSLETTER
FOUNDER'S DAY SPECIAL ISSUE

OCTOBER 2013



भारत सरकार
Government of India



भाभा परमाणु अनुसंधान केंद्र
Bhabha Atomic Research Centre

BARC NEWSLETTER

Editorial Committee

Chairman

Dr. S.K. Apte,
Associate Director, BMG

Edited by

Dr. K. Bhanumurthy
Head, SIRD

Associate Editors for this issue

Dr. K. Bhanumurthy, SIRD
Dr. S.C. Deokathey, SIRD

Members

Dr. S.K. Apte, BMG
Dr. R.C. Hubli, MPD
Dr. D.N. Badodkar, DRHR
Dr. K.T. Shenoy, ChED
Dr. K. Bhanumurthy, SIRD
Dr. S. Kannan, FCD
Dr. A.P. Tiwari, RCnD
Dr. A.K. Tyagi, ChD
Mr. G. Venugopala Rao, APPD
Dr. C. Srinivas, PsDD
Dr. G. Rami Reddy, RSD
Dr. A.K. Nayak, RED
Dr. S.M. Yusuf, SSPD
Dr. S.K. Sandur, RB&HSD
Dr. S.C. Deokathey, SIRD

From the Editor's Desk...

At the outset, let me thank you all for your enthusiastic response to this issue. As you may see from the Contents Page, 88 Award winning papers were uploaded through the SIRD portal for this year's Special Issue. This is the fourth consecutive year that we have been publishing the Founder's Day Special Issue in CD form. It has facilitated and speeded up the pre publication work along with substantial reduction in printing costs.

The online SIRD portal which was activated in May this year is fully operational now. Through this portal you may upload full length articles, Brief Communications, News & Events and Awards details for publication in the BARC Newsletter. Apart from this, you may also upload manuscripts to be published as BARC External and Internal Reports.

I take this opportunity to invite you all to contribute information on your R&D efforts for publication in the BARC Newsletter sooner rather than later.

I look forward to your continued cooperation.



Dr. K. Bhanumurthy

On behalf of the Editorial Committee

BARC NEWSLETTER

CONTENTS

DAE (Excellence in Science, Engineering & Technology) Awards-2011

DAE Homi Bhabha Science & Technology Award

- 1. Indigenous Research and Development for Reactor Safety Assessment under Extreme Events and Strategic Applications** 1
Ram Kumar Singh
Reactor Safety Division
Dr. Ram Kumar Singh is the recipient of the Award
- 2. Applications of D-T/D-D neutron Generator for the investigation of ADS neutronics, Fissile Material Detection and Neutron Imaging** 10
Amar Sinha
Neutron & X-Ray Physics Division
Dr. Amar Sinha is the recipient of the Award
- 3. Synthetic and Structural Chemistry of Actinide Complexes** 17
S. Kannan
Fuel Chemistry Division
Dr. S. Kannan is the recipient of the Award
- 4. Thermal Plasma Technology for Specialized DAE Applications** 22
P.V. Ananthpadmanabhan
Laser & Plasma Technology Division
Dr. P.V. Ananthpadmanabhan is the recipient of the Award
- 5. Technology Development Programme in Pulse Electron Accelerators and Utilisation in Compact HPM Sources** 31
Archana Sharma
Accelerator and Pulse Power Division
Dr. Archana Sharma is the recipient of the Award

BARC NEWSLETTER

6. **Anomalous Energy Absorption by Atomic and Molecular Clusters Interacting with Laser Radiation: Experiments Leading to Theoretical Advances** 36
R.K. Vatsa
Chemistry Division
Dr. R.K. Vatsa is the recipient of the Award
7. **Development of Digital Radiotherapy Simulator: "IMAGIN"** 43
D.C. Kar, R. Sahu, K. Jayarajan, R.V. Sakrikar and Manjit Singh
Division of Remote Handling and Robotics
Dr. D.C. Kar is the recipient of the Award
- DAE Scientific & Technical Excellence Award**
8. **Thioflavin T: An Efficient Fluorescent Probe for Exploring Protein Fibrils and G-Quadruplex DNA** 49
Jyotirmayee Mohanty
Radiation & Photochemistry Division
Dr. Smt. Jyotirmayee Mohanty is the recipient of the Award
9. **Structural Investigations on some Functional Materials** 53
S.N. Achary
Chemistry Division
Dr. S.N. Achary is the recipient of the Award
10. **Machining and Inspection of Fine Reference Notches for Defect Evaluation by Non-Destructive Testing Methods** 57
S.P. Srivastava, T.L. Govindankutty, R.K. Gupta and S.B. Jawale
Centre for Design and Manufacture
and
Manjit Singh
Division of Remote Handling and Robotics
Shri S.P. Srivastava is the recipient of the Award

BARC NEWSLETTER

- 11. Crystal structure of Prostate Secretory Protein PSP94** 61
Mukesh Kumar
Solid State Physics Division
and
Ashwani Kumar
High Pressure & Synchrotron Radiation Physics Division
Dr. Mukesh Kumar is the recipient of the Award
- 12. A novel Method using Pulsed Eddy Current for detection of Spacers in Coolant Channel of Pressurised Heavy Water Reactor** 65
T.V. Shyam
Reactor Engineering Division
Shri T.V. Shyam is the recipient of the Award
- 13. Photophysical Studies of Amyloid Fibril Sensor** 70
Sukhendu Nath
Radiation & Photochemistry Division
Dr. Sukhendu Nath is the recipient of the Award
- 14. Indigenous Development of a Spot Picker Robot for Proteomics Applications** 73
Ratnesh Singh Sengar, A.K. Upadhyay, D.N. Badodkar, R.K. Puri and Manjit Singh
Division of Remote Handling & Robotics
and
M.G.R. Rajan
Radiation Medicine Centre
and
V.M. Gadre
Department of Electrical Engineering, Indian Institute of Technology (Bombay), Mumbai
Shri Ratnesh Singh Sengar is the recipient of the Award

BARC NEWSLETTER

- 15. The Child-Langmuir Law - from Quantum to Classical Physics** 79
Debabrata Biswas
Theoretical Physics Division
Dr. Debabrata Biswas is the recipient of the Award
- 16. First Principles Studies on High Pressure Equation of State and Phase Stability of Solids** 83
P. Modak and Ashok K. Verma
High Pressure and Synchrotron Radiation Physics Division
Dr. P. Modak is the recipient of the Award
- 17. Resistive Plate Chambers for the RE4 Upgrade of the CMS experiment at the Large Hadron Collider facility at CERN** 88
L.M. Pant
Nuclear Physics Division
Dr. L.M. Pant is the recipient of the Award
- 18. Enhancement of Charge Carrier Mobility of organic Semiconductor Thin Films** 99
A.K. Debnath, Soumen Samanta, Ajay Singh, D.K. Aswal and S.K.Gupta
Technical Physics Division
Dr. A.K. Debnath is the recipient of the Award
- 19. Photodissociation Dynamic Studies Using Laser Induced Fluorescence and Resonance Enhanced Multiphoton Ionization–Time of Flight Technique** 103
Hari P. Upadhyaya
Radiation & Photochemistry Division
Dr. Hari P. Upadhyaya is the recipient of the Award

BARC NEWSLETTER

DAE Young Applied Scientist / Technologist Award

- 20. Design, Development and Deployment of Inside Diameter Measurement Tool for 220 MWe PHWRs** 106
G. Sharma, S. Bhattacharyya, V.P. Bodile and R.J. Patel
Refuelling Technology Division
Shri G. Sharma is the recipient of the Award
- 21. AnuVi - Development of In-house Scientific Visualization Framework** 110
P.P.K. Venkata, S.K. Bose, Dinesh M. Sarode, Pritam P. Shete, Mohini M. Laghate and R.S. Mundada
Computer Division
Shri P.P.K. Venkata is the recipient of the Award
- 22. Development of a Novel Variable Dispersion Zoom Optics for Magnetic Sector Mass Spectrometer** 113
Rajender K. Bhatia, Varun K. Yadav, Vilas M. Mahadeshwar, Milind M. Gulhane, E. Ravisankar, T.K. Saha, V. Nataraju and S.K. Gupta
Technical Physics Division
Shri Rajender K. Bhatia is the recipient of the Award
- 23. Development & Application of an Eulerian Radiation Magneto-Hydrodynamics (RMHD) Code** 117
C.D. Sijoy and S. Chaturvedi
Computational Analysis Division, BARC, Visakhapatnam
Shri C.D. Sijoy is the recipient of the Award
- 24. Development of Phase contrast Imaging Techniques** 120
Yogesh S. Kashyap and Amar Sinha
Neutron and X-ray Physics Division
Shri Yogesh S. Kashyap is the recipient of the Award

BARC NEWSLETTER

25. Design and Manufacture of Prototype 400 KeV RFQ Accelerator 124

Abhay Kumar, S. Guha, R.S. Vohra, S.B. Jawale and R.L. Suthar

Centre for Design and Manufacture
and

Rajesh Kumar, Pitambar Singh and R.K. Choudhury
Nuclear Physics Division

Shri Abhay Kumar is the joint recipient of the Award

26. Microwave Power Sources for S-Band Electron Linacs 129

Shiv Chandan, A.R. Tillu, V.Yadav, R.B. Chavan,
D. Bhattacharjee, K.P. Dixit, K.C. Mittal and L.M. Gantayet

Accelerator & Pulse Power Division, Beam Technology
Development Group

Shri Shiv Chandan is the recipient of the Award

DAE Young Engineer Award

27. Design, Upgrade, Installation, Commissioning and Maintenance of Process Instrumentation for Research Reactors 133

Kaustubh Gadgil, Prashant Awale, C. Sengupta,
R. Bharathan, G. Bharadhwaj

Research Reactor Maintenance Division

Shri Kaustubh Gadgil is the recipient of the Award

28. Design and Development of Double Actuator Controller with Dual CAN Bus Interface (DACCI) for 6 DOF Shake Table 137

Shiju Varghese, Jay Shah, P. Ramakrishna, N.L. Soni and R.J. Patel

Refuelling Technology Division

Shri Shiju Varghese is the recipient of the Award

BARC NEWSLETTER

- 29. Risk Monitor—A PSA Based Operator Support System for IPHWR** 142
M. Hari Prasad, Gopika Vinod, V.V.S. Sanyasi Rao and R. K. Singh
Reactor Safety Division
Shri M. Hari Prasad is the recipient of the Award
- 30. Development of Low energy Deuteron Accelerator based DC and Pulsed Neutron Generators** 146
Tarun Patel and Amar Sinha
Neutron & X-ray Physics Division
Shri Tarun Patel is the recipient of the Award
- 31. Design, Development, Maintenance, Refurbishing, Installation and Commissioning of Control & Instrumentation for Research Reactors** 150
Parag Puneekar, N. Ramkumar, Kallol Roy, M.D. Darbhe and G. Bharadhwaj
Research Reactor Maintenance Division
Shri Parag Puneekar is the recipient of the Award
- 32. Rare Earth Borides Synthesis by Reduction Distillation** 155
Abhishek Mukherjee, Uttam Jain, Sanjay Kumar and Nagaiyar Krishnamurthy
Fusion Reactor Materials Section, Materials Group
Dr. Abhishek Mukherjee is the recipient of the Award
- 33. Mathematical modeling of Nuclear Systems** 159
Raj Kumar Singh, A. Rama Rao
Reactor Engineering Division
Shri Raj Kumar Singh is the recipient of the Award

BARC NEWSLETTER

- 34. Crystal growth and Morphological study of ADU and its Calcined Product** 162
Subhankar Manna and Saswati B. Roy
Uranium Extraction Division
and
Jyeshtharaj B. Joshi
Homi Bhabha National Institute
Shri Subhankar Manna is the recipient of the Award
- 35. Compact Inductive Energy Storage Pulse Power System** 167
Senthil K.
Accelerator and Pulse Power Division
Shri K. Senthil is the recipient of the Award
- 36. Fluidized Bed Synthesis of Carbon Nanotubes** 170
Kinshuk Dasgupta
Rare Earths Development Section, Materials Group
Shri Kinshuk Dasgupta is the recipient of the Award
- 37. Indigenization in Design and Development of High Precision instruments for synchrotron beam-lines at INDUS-II, RRCAT, Indore** 173
A.D. Patil
Centre for Design & Manufacture
Shri A.D. Patil is the recipient of the Award
- DAE Young Scientist Award**
- 38. Photophysical Studies in Supramolecular Systems** 176
Sharmistha Dutta Choudhury
Radiation & Photochemistry Division
Dr. Kum. Sharmistha Dutta Choudhury is the recipient of the Award

BARC NEWSLETTER

39. **Characterization of DNA Processing Multiprotein Complex reveals the role of its Components in Radioresistance of *Deinococcus radiodurans*** 179
Swathi Kota and H.S. Misra
Molecular Biology Division
Dr. Smt. Swathi Kota is the recipient of the Award
40. **Application of Immobilized Enzyme and Cells in Biosensors for the Detection of Glucose and Methyl parathion** 185
Jitendra Kumar
Nuclear Agriculture & Biotechnology Division
Shri Jitendra Kumar is the recipient of the Award
41. **Tunable structural and Magnetic correlations in Multifunctional Hexacyanometallate Compounds with Possible Technological Applications** 190
Amit Kumar
Solid State Physics Division
Dr. Amit Kumar is the recipient of the Award
42. **Advanced Laser Spectroscopy at Bulk and Interfaces** 194
Jahur Alam Mondal and Dipak K. Palit
Radiation & Photochemistry Division
Dr. Jahur Alam Mondal is the recipient of the Award

DAE Group Achievement Award

43. **Thermal hydraulic Design Validation of Steam Drum Internals, Moderator and Liquid Poison Injection Systems for AHWR** 198
D.S. Pilkhwal, N.K. Maheshwari, R.K. Bagul, A.M. Vaidya, A. Kansal and P.K. Vijayan
Reactor Engineering Division
Shri D.S. Pilkhwal and his team received the Award

BARC NEWSLETTER

- 44. Design, Development, Commissioning and Capacity Demonstration of 6000 Amp Electrolytic Fluorine Generation Cell** 203
C.S.R. Prasad, S. Sarkar, T.M. Sudhakar, S.V.G. Rao and V.K. Misra
Chemical Technology Group
Shri C.S.R. Prasad and his team received the Award
- 45. Development of a TB-PCR Kit for the Diagnosis of Tuberculosis** 207
Savita Kulkarni and M.G.R. Rajan
Radiation Medicine Centre
and
Papia Hazra, A. Islam, R. Seshadri
JONAKI, BRIT, CCMB campus, Hyderabad
Dr. Smt. Savita Kulkarni and her team received the Award
- 46. Development of Fluidized Bed Thermal Denitration technology for Ammonium Nitrate bearing waste streams of Back End of the Nuclear Fuel Cycle** 210
Hanmanth Rao
Chemical Engineering Group
Shri Hanmanth Rao and his team received the Award
- 47. Development of Heavy Liquid Metal technology for Fusion Reactor technology for Fusion Reactor Material Characterization** 213
R.K. Fotedar, N. Krishnamurthy, S. Kumar and P. Chakraborty
Fusion Reactor Materials Section, Materials Group
and
P.K. Pradhan and B. Paul
Materials Processing Division
and

BARC NEWSLETTER

S. Malhotra

Control and Instrumentation Division

Shri R.K. Fotedar and his team received the Award

48. O&M of Heat Treatment Vacuum Furnaces and their Life 217

Enhancement by Innovative Maintenance Techniques

**M. James Jacob, P. Shanmugavelu, C. Eswaramoorthy and
K. Vaiyapuri**

Chemical Technology Group

Shri M. James Jacob and his team received the Award

49. Synthesis of Dicyclohexano 18 Crown 6 Ligand on Bench 223

**Scale and Development and Demonstration of Selective
Recovery of Strontium from Thorium Lean Raffinate (TLR)
waste in the Back End of Nuclear Fuel Cycle using the Ligand**

K.T. Shenoy

Chemical Engineering Division

and

C.P. Kaushik

Waste Management Division

Dr. K.T. Shenoy and his team received the Award

50. Process development for Plasma Spray Deposition of 226

Yttrium oxide Coatings for Containment of Molten Uranium

A.K. Das, P.V.A. Padmanabhan, Jaya Mukherjee,

T.K. Thiyagarajan, S. Sethi, Anupama Prabhala, A. Nagaraj,

Y. Chakravarthy, R.U. Satpute, M.K. Verma, N.V. Patil,

S.L. Songire, A.J. Almeida, S.S. Dehade and S.B. Gaikwad

Laser & Plasma Technology Division, Beam Technology

Development Group

Dr. A.K. Das and his team received the Award

BARC NEWSLETTER

- 51. Development of Three Tank Plating Cycle (TTPC) for Electroless Nickel Plating** 233
V. Ramprasad and K.P. Dinesh
Rare Materials Project, BARC, Mysore
Shri V. Ramprasad and his team received the Award
- 52. 1 Kilo Joule Compact Marx Source and Reflex Triode Based Repetitive High Power Microwave Generator** 238
Archana Sharma, A. Roy, S. Mitra, S.K. Singh, V.K. Sharma, A.S. Patel, Rakhee Menon, K. Senthil, Ritu Agarwal, K.C. Mittal, K.V. Nagesh, D.P. Chakravarthy and A.K. Ray
Accelerator and Pulse Power Division, Beam Technology Development Group
Shri D.P. Chakravarthy and his team received the Award
- 53. Development and Successful Deployment of Weld Inspection Manipulator (WIM) in Reactor Pressure Vessel of TAPS-1** 241
H. Chatterjee, J.P. Singh, R. Ranjon, M.P. Kulkarni and R.J. Patel
Refuelling Technology Division
Shri R.J. Patel and his team received the Award
- 54. Process for Retaining Pericarp Color and Extending Shelf Life of Litchi** 245
S. Gautam, B.B. Mishra, S.N. Hajare, S. Kumar, S. Saxena, V.S. More, S. Wadhawan, N. Bandyopadhyay and A. Sharma
Food Technology Division
Dr. S. Gautam and his team received the Award
- 55. Indigenous Development of a 10 meter Optical Periscope for Prototype Fast Breeder Reactor (PFBR)** 250
D.V. Udupa, Sanjiva K. and N.K. Sahoo
Applied Spectroscopy Division
and

BARC NEWSLETTER

R.V. Sakrikar, A. Kadu and M. Singh

Division of Remote Handling & Robotics

and

S.S. Bhavsar and R.K. Garg

Technical Services Division

and

V. Rajan Babu and V. Balasubramanian

Reactor Component Systems Division, IGCAR

and

R.L. Suthar

Ex-Head, Centre for Design & Manufacture

and

G.P. Kothiyal

Ex-Head, Glass & Advanced Ceramic Division

Shri R.L. Suthar and his team received the Award

56. Design and Development of Explosively driven Helical Flux Compression Generators 256

Anurag Shyam, Partha Banerjee, Rohit Shukla and Rishi Verma

Energetics and Electromagnetics Division, BARC, Visakhapatnam

Dr. Anurag Shyam and his team received the Award

BARC NEWSLETTER

Merit Awards

- 57 Room Temperature operated Flexible Ammonia Sensor** 258
Ajay Singh, Soumen Samanta, A.K. Debnath,
D.K. Aswal and S.K. Gupta
Technical Physics Division
Shri Ajay Singh received the INSA Medal for Young Scientist for the year 2012
- 58. Investigation of Structural and Magnetic Properties of spin-chain oxides** 261
Anil Jain
Solid State Physics Division
This Paper received "IPA's Anil K. and Bharati Bhatnagar Best Ph.D. Thesis Award" at the 57th DAE Solid State Physics Symposium held at IIT Bombay, during December 3–7, 2012
- 59. ^{177}Lu in Targeted Radiotherapy: a Transition from Bench to Bed** 264
Sudipta Chakraborty
Isotope Applications & Radiopharmaceuticals Division
This Paper received the IANCAS Dr. Tarun Datta Mamorial Award 2012, at the Nuclear & Radiochemistry Symposium 2013 (NUCAR 2013), held at Jabalpur between 18-23rd February, 2013
- 60. Effect of Surface Finishing Operations on High Temperature Oxidation Behaviour of Alloy 800** 268
Geogy J. Abraham, Kushal Singla, B. Sunil Kumar and Vivekanand Kain
Materials Science Division
This Paper received the Best Oral Paper Award at the East Asia Pacific Area Corrosion Conference (CORCON 2012), held at Goa, from 26-29th September, 2012

BARC NEWSLETTER

- 61. Marine Cyanobacteria as suitable candidates for Uranium Recovery from Aquatic Environment** 272
Celin Acharya and Shree Kumar Apte
Molecular Biology Division, Bio-Medical Group
This Paper received the Best Oral Paper Presentation Award at the Indo-US Workshop on Cyanobacteria, held at Lonavala, from Dec. 16-20, 2012
- 62. Determination of vapor pressure of H₂O over LaCl₃.7H₂O and the Intermediate Compounds by Dynamic Transpiration Method** 276
D.K. Sahoo
Rare Earths Development Section, Materials Group
and
R. Mishra and D. Das
Chemistry Division
and
N. Krishnamurthy
Fusion Reactor Materials Section, Materials Group
This Paper received the Best Oral Presentation Award (First Prize) at the 18th DAE-BRNS International Symposium on Thermal Analysis, held at Mumbai from 31st January to 2nd February, 2012
- 63. Magnetic Nanoparticles for Targeted-Drug Delivery: A Combinatorial approach of Hyperthermia and Radiation for improvement of Cancer Therapy** 279
Neena V. Jadhav, Amit Kumar and Badri N. Pandey
Radiation Biology and Health Sciences Division
and
R.S. Ningthoujam and R.K. Vatsa
Chemistry Division
This Paper received the 'Best Idea Award' at the International Conference on Radiation Biology (ICRB-2012) and 11th

BARC NEWSLETTER

Biennial Meeting of the Indian Society for Radiation Biology, held at Navi Mumbai, from November 22-24, 2012

- 64. Integrated approach for Enzyme Purification from Non-clarified Crude Homogenate using Macroporous Cryogel Matrix** **284**

Anuj Tripathi

Nuclear Agriculture and Biotechnology Division
and

Ashok Kumar

Department of Biological Sciences and Bioengineering,
Indian Institute of Technology, Kanpur

This Paper received the Best Paper Award at the DAE-BRNS Biennial Symposium Separation Science & Technology 2012, (SESTEC 2012), held at Mumbai, from February 27 - March 1, 2012

- 65. Simultaneous Observation of Laser-induced Photoionization and Fluorescence Signals in Atomic Uranium** **287**

M.L. Shah, G.P. Gupta, Vas Dev, B. Dikshit, M.S. Bhatia and B.M. Suri

Laser and Plasma Technology Division

This Paper received the Best Paper Award at the DAE-BRNS National Laser Symposium, (NLS 20), held at Chennai, from 9-12th January 2012

- 66. Status Review on Spent Desalination Membrane Management** **291**

T.L. Prasad D. Goswami and P.K. Tewari

Desalination Division

This Paper received the 2nd Best Technical Paper Award at the National Symposium, WAVE 2012, held at Mumbai on 27th & 28th September, 2012

BARC NEWSLETTER

- 67. Hydrogen Sorption-desorption Studies on ZrCo-Hydrogen System** 295
Ram Avtar Jat, S.C. Parida, Renu Agarwal and S.G. Kulkarni
Product Development Division
This Paper received the Mettler Toledo Best Poster Award at the 18th DAE-BRNS International Symposium on Thermal Analysis, held at Mumbai from 31st January to 2nd February, 2012
- 68. Detection of 4He Generated during the Reaction of $3\text{He}(3\text{He},2p)4\text{He}$ in a Plasma Focus Device using Lexan Solid State Nuclear Track Detector** 300
Ram Niranjana, R.K. Rout, Rohit Srivastava and Satish C. Gupta
Applied Physics Division
and
R.V. Kolekar
Radiation Safety Systems Division
This Paper received the Z.H. Solapurwala Award for Fusion Research 2012 (Best Poster), at the 27th PSSI National Symposium on Plasma Science & Technology (PLASMA 2012), held at Puducherry, from December 10-13, 2012
- 69. Combined Radiation and Biological Treatment for the Decolouration of Reactive Red-120 dye** 303
Jhimli Paul and Lalit Varshney
Radiation Technology Development Division
and
A.A. Kadam and S.P. Govindwar
Department of Biochemistry, Shivaji University, Kolhapur
and
Pranaw Kumar
Fuel Chemistry Division

BARC NEWSLETTER

This Paper received the Dr. Hari Mohan Memorial Award for Best Poster at the DAE-BRNS 11th Biennial Trombay Symposium on Radiation & Photochemistry (TSRP 2012), held at Mumbai, from 4th-7th January, 2012

- 70. Carboxymethyl Cellulose-polyvinyl Alcohol-clove oil Active Films for Meat Preservation** 307
Shobita Rao Muppalla, Sweetie R. Kanatt, S.P. Chawla, Arun Sharma
Food Technology Division
This Paper received the First Prize for Poster at the Innovations in Food Science and Technology to fuel the growth of the Indian food industry, (XXI ICFOST), held at Pune, on 20th & 21st January, 2012
- 71. Gamma-Tocotrienol Induced Apoptosis in Tumor Cells through Activation of Intrinsic and Extrinsic Pathways** 311
Chandan Wilankar, Nazir M. Khan, Rahul Checker, Deepak Sharma, R. S. Patwardhan, Santosh. K. Sandur and T.P.A. Devasagayam
Radiation Biology & Health Sciences Division
and
Vikram Gota
Clinical Pharmacology, ACTREC, Tata Memorial Centre, Kharghar, Navi Mumbai
This Paper received the Best Poster Award at the International Conference on Free Radicals, Antioxidants and Nutraceuticals in Health, Disease & Radiation Biology, held at Kolkata, from 12-14 January, 2012
- 72. Contribution of ERK & Nrf-2-ARE Pathway to Constitutive and Inducible Radioresistance of Tumor Cells vis a vis Normal cells** 315
Raghavendra S. Patwardhan, Rahul Checker, Deepak Sharma, Santosh Kumar Sandur and Krishna B. Sainis
Radiation Biology & Health Sciences Division

BARC NEWSLETTER

This Paper received the Best Poster Award at the International Conference on Free Radicals, Antioxidants and Nutraceuticals in Health, Disease & Radiation Biology, held at Kolkata, from 12-14 January, 2012

73. **Sintering Kinetics Study of the Nano-Crystalline 3-mol% Yttria-Samarium Codoped Tetragonal Zirconia Polycrystal Ceramics** 319
Soumyajit Koley, A.K. Sahu, A. Ghosh, S. Ramanathan and G.P. Kothiyal
Glass & Advanced Materials Division
This Paper received the Best Poster Award at the 18th DAE-BRNS International Symposium on Thermal Analysis, held at Mumbai from 31st January to 2nd February, 2012
74. **Influence of Ragi-soybean Combination on the Viability of Probiotic Organisms during Storage and under Simulated Gastrointestinal Conditions** 322
Minelly Rodrigues and Subhadra Mandalika
College of Home Science, Mumbai
and
Sahayog Jamdar and Arun Sharma
Food Technology Division
This Paper received the Best Poster Award at the International Conference and Exhibition on Food Processing and Technology, 2012, held at Hyderabad, from 22-24 November, 2012
75. **Suppression of Radiation Induced DNA Damage and Apoptosis in Haematopoietic Cells of Mice by Umbelliferone** 327
S. Jayakumar, Hari N. Bhilwade and Ramesh C. Chaubey
Radiation Biology and Health Sciences Division
This Paper received the Best Poster Award at the International Conference on Emerging Frontiers and Challenges in Radiation Biology, held at Bikaner, on 24th & 25th January, 2012

BARC NEWSLETTER

- 76. Characterisation of Three Single-stranded DNA binding (SSB)-like Proteins from the Nitrogen-fixing cyanobacterium *Anabaena PCC7120*** 332
Anurag Kirti, Hema Rajaram and Shree Kumar Apte
Molecular Biology Division, Bio Medical Group
This Paper received the Best Poster Presentation Award at the Indo-US Workshop on Cyanobacteria, held at Lonavala, from Dec. 16-20, 2012
- 77. Synthesis and Hydrogen Absorption Kinetics of V₄Cr₄Ti alloy** 336
Sanjay Kumar, Sagar Sonak, Uttam Jain and Nagaiyar Krishnamurthy
Fusion Reactor Materials Section, Materials Group
This Paper received the Best Poster Award at the 18th DAE-BRNS International Symposium on Thermal Analysis, held at Mumbai from 31st January to 2nd February, 2012
- 78. Beta-cyclodextrin Functionalized CdSe Quantum Dots synthesized via Electron Beam Irradiation** 339
A. Guleria, S. Singh, M. C. Rath, A. K. Singh, S. Adhikari and S. K. Sarkar
Radiation & Photochemistry Division
This Paper received the Best Poster Award at the DAE-BRNS 11th Biennial Trombay Symposium on Radiation & Photochemistry (TSRP 2012), held at Mumbai, from 4th-7th January, 2012
- 79. Honey: A natural Functional Food having broad-spectrum Antimutagenic and Anti-proliferative Characteristics** 342
S. Saxena, S. Gautam and A. Sharma
Food Technology Division
and
D.K. Maurya
Radiation Biology and Health Sciences Division
and

BARC NEWSLETTER

G. Maru

Advanced Centre for Treatment, Research and Education in Cancer (ACTREC)

This Paper received the Best Poster Award at the Innovations in Food Science and Technology to fuel the growth of the Indian food industry, (XXI ICFOST), held at Pune, on 20th & 21st January, 2012

80. Radiation Induced Cell Death in Bacteria is Partially Programmed 348

S. Wadhawan, S. Gautam, and A. Sharma

Food Technology Division

This Paper received the Best Poster Award at the XXXVI All India Cell Biology Conference and International Symposium on Stress Adaptive Response and Genome Integrity (SARGI), held at Mumbai, from Oct. 17-19, 2012

81. Silver Nanoparticles based Optical Biosensors for Estimation of Uric Acid 355

Nilanjali Misra, Virendra Kumar, Lalit Varshney

Radiation Technology Development Division

This Paper received the Best Poster Presentation Award at the Interdisciplinary Symposium on Materials Chemistry (ISMC-2012), held at Mumbai, from 11th-15th December, 2012

82. Thermal Analysis of Polyethersulfone based Composite Beads Encapsulated with di-2-ethyl hexyl phosphoric acid 358

Kartikey Kumar Yadav, D.K.Singh and H. Singh

Rare Earths Development Section, Materials Group
and

S. Francis and L. Varshney

Radiation Technology Development Division

This Paper received the Best Poster Award (Third Prize) at the 18th DAE-BRNS International Symposium on Thermal Analysis, held at Mumbai from 31st January to 2nd February, 2012

BARC NEWSLETTER

- 83. Studies on CNT doped D2EHPA impregnated Polymeric Beads for Yttrium Extraction** 361
Kartikey Kumar Yadav, Kinshuk Dasgupta, Dhruva Kumar Singh, Mallavarapu Anitha and Harvinderpal Singh
Rare Earths Development Section, Materials Group
and
Lalit Varshney
Radiation Technology Development Division
This Paper received the Best Poster Award (Third Prize) at the Interdisciplinary Symposium on Materials Chemistry (ISMC-2012), held at Mumbai, from 11th-15th December, 2012
- 84. Compatibility of Silicon Carbide with Lead-Bismuth Eutectic- the effect of Oxygen Ingress** 364
P. Chakraborty, R.K. Fotedar and N. Krishnamurthy
Fusion Reactor Materials Section, Materials Group
and
P.K. Pradhan
Materials Processing Division
This Paper received the Best Poster Award at the National Symposium on Materials and Processing, (MAT 2012), held at Mumbai, from 10th-12th October, 2012
- 85. Characterization of Polyphenol oxidase (PPO) from Brinjal (Eggplant; Solanum melongena)** 367
Bibhuti B. Mishra, Satyendra Gautam and Arun Sharma
Food Technology Division
This Paper received the Best Poster Award at the DAE-BRNS Life Sciences Symposium (LSS-2012) on Trends in Plant, Agriculture and Food Sciences, held at Mumbai, from 17th-19th December, 2012
- 86. Characterization and Property Evaluation of U-15wt%Pu alloy for Fast Breeder Reactor** 372

BARC NEWSLETTER

Santu Kaity, Joydipta Banerjee, K. Ravi and Arun Kumar

Radiometallurgy Division

and

R. Keswani

Metallic Fuels Division

and

G.J. Prasad

Nuclear Fuels Group

This Paper received the Best Poster Award at the Interdisciplinary Symposium on Materials Chemistry (ISMC-2012), held at Mumbai, from 11th-15th December, 2012

- 87. Studies on MusaWRKY71, a Multiple Stress Inducible Transcription Factor Gene from Banana which is involved in Diverse Stress Responses** **376**

Upendra K.S. Shekhawat and Thumballi R. Ganapathi

Nuclear Agriculture and Biotechnology Division

This Paper received the Best Poster Award at the DAE-BRNS Life Sciences Symposium (LSS-2012) on Trends in Plant, Agriculture and Food Sciences, held at Mumbai, from 17th-19th December, 2012

- 88. Fuel Cell Fabrication and Characterization of Single Cell of Proton Conducting SOFC** **379**

Pooja Sawant, S. Varma, B.N. Wani and S.R. Bharadwaj

Chemistry Division

and

D. Prakash

Energy Conversion Materials Section, Materials Group

This Paper received the 3rd Best Poster Presentation Award at the Interdisciplinary Symposium on Materials Chemistry (ISMC-2012), held at Mumbai, from 11th-15th December, 2012

- Author Index** **382**

BARC NEWSLETTER

INDIGENOUS RESEARCH AND DEVELOPMENT FOR REACTOR SAFETY ASSESSMENT UNDER EXTREME EVENTS AND STRATEGIC APPLICATIONS

Ram Kumar Singh
Reactor Safety Division

Dr. Ram Kumar Singh is the recipient of the DAE Homi Bhabha Science & Technology Award for the year 2011

Introduction

The relevant areas of nuclear reactor design and development, reactor safety assessment and strategic applications have been enabled through a systematic indigenous research and development program over the years. With focus on computational and experimental structural mechanics, wave propagation in solid and fluid media, fluid-structure interaction, computational fluid dynamics and heat transfer various thrust areas for the closed nuclear fuel cycle have been addressed. Specific case studies of coupled fluid-structure interaction analysis for TAPS-BWR core shroud in case of the recirculation break and PWR HDR-v32 blowdown, shock / seismic wave propagation in solid media for underground nuclear explosion events, assessment of Indian nuclear power plants for extreme events of tsunami and earthquakes and PHWR / AHWR containment structural and thermal hydraulic safety evaluation are presented in this article.

All the above identified problems involve multi-physics coupling and multi-scale modeling and have been addressed due to the rapid growth and development in computer hardware and massive parallel high-performance computers. The novel concepts of computational mechanics and associated algorithms in computational mathematics have enabled to explore multi-physics problems that were earlier not conceivable. A few examples under this category are tracing the evolution of discontinuities in heterogeneous materials, which may evolve at solid-fluid and solid-solid boundaries, problems of phase

change and crack propagation and erosion in solid structures due to hyper velocity impact. This development has been further supplemented with improvements in the experimental techniques with measurement and verification of relevant parameters at different length scales. A few examples in this category are optical crack profiling, digital image correlation and the acoustic emission techniques in addition to the conventional sensors and instrumentation. For large scale problems related to weather forecasting, tsunami, earthquakes and environmental modeling; the satellite imaging, Airborne Lidar Terrain Mapper (ALTM) and GPS systems have helped to improve the modeling capabilities, which has provided the requisite support for tsunami warning system.

Fluid-Structure Interaction Studies for Reactor Components and Wave Propagation in Two Phase Media

The fluid-structure interaction problems are important for various reactor safety issues with regard to PWR core-barrel, BWR core shroud and PHWR core internal safety evaluation resulting from internal postulated blowdown events. Potential safety concerns were raised by regulatory bodies regarding the 360 degrees circumferential separation of TAPS-BWR core shroud following LOCA. The material degradation accelerated by crevices, residual stress, cold work, sensitisation, and corrosive environment could be detrimental for impulsive acoustic load due to pipe break. This might either prevent full insertion of the control rods or open

BARC NEWSLETTER

a gap in the shroud large enough to preclude adequate core cooling. Validation of in-house 3D finite element code **FLUSHEL** for coupled fluid-structure interaction transient analysis of light water reactor components in case of sub-cooled and saturated blowdown accidents has been carried out. Simulation of German HDR (Heiss-Dampf Reaktor) v.32 LOCA experiment on a full scale PWR model for single and two phase blowdown problems were carried out with the implementation of unified sub cooled and saturated critical flow models. With the due considerations to the non-equilibrium effects due to flashing for the rarefaction wave propagation, acoustic load evaluation and structural safety assessment of TAPS-BWR core shroud for postulated Recirculation Line Break (RLB) were carried out. This in-house code has also been used for the evaluation of PHWR internal core components for the postulated calandria tube / pressure tube failure accidents.

For the acoustic wave propagation problems, the code FLUSHEL accounts for the spatial and temporal variation of acoustic speed in the dispersive two-phase media of the light water coolant generated due to the postulated blowdown. The in-house code has been coupled with standard water steam property code WASP to compute the acoustic speed in the two phase fluid domain during the passage of rarefaction wave. The critical discharge and pressure are computed by the unified Leung model for both sub-cooled and saturated blowdowns. It has been shown that for the case of stratified flow in a vertical channel, the liquid gas plug behaves as gas from compressibility point of view, and its mass is close to that of the liquid, which could lead to excitation of coupled fluid acoustic and core internal shell modes. Normally the associated frequencies of acoustic cavity and the submerged shell frequencies of interest are far below compared to the resonance frequency due to the oscillation occurring in the bubble which are in kHz range. Thus only the total gas content per unit volume of the fluid medium is important and not the distribution of this gas content over bubbles of specific size. So a typical density wave oscillation equation of the form:

$$\left(\frac{\partial^2 \Delta \rho}{\partial t^2}\right) - C^2(\nabla^2 \Delta \rho) - \frac{C^2}{\omega_B^2} \left(\frac{\partial^2 (\nabla^2 \Delta \rho)}{\partial t^2}\right) = 0 \quad (1)$$

can be simplified to acoustic wave equation of small amplitude. This assumption is valid for the region within the reactor vessel and the downcomer annulus where bubbles of very small sizes compared to the characteristic dimension of the reactor vessel and core shroud may be present. The bubble oscillation

$$\text{frequency is } \omega_B = \sqrt{\frac{3p_o}{\rho_f R_o^2}} \quad (2)$$

In case of a one-dimensional vapour liquid plug the oscillation frequency of the cavity is:

$$\omega_o = \sqrt{\frac{\gamma p_o}{\rho_f l^2 \alpha (1-\alpha)}} \quad (3)$$

Where p_o is the stagnation pressure, ρ_f is liquid density, R_o is the bubble size, γ is ratio of specific heats for vapour, α is the void fraction of liquid vapour system and l is the characteristic dimension of the acoustic cavity. Normally R_o is of micron size for small vapour nucleation sites. Thus $l \gg R_o$ and the pressure oscillation frequency within the bubble is very large ($\omega_B \gg \omega_o$). The stratified sound speed is given as

$$C_{st} = \sqrt{\frac{\rho_f \alpha + \rho_g (1-\alpha)}{\left\{ \frac{(1-\alpha)\rho_g}{C_f^2} + \frac{\alpha \rho_f}{C_g^2} \right\}}} \quad (4)$$

With the above classical expression for the sound speed in the two-phase medium, the acoustic wave propagation can be described. If the interaction of individual bubbles with the fluid and mutually through the fluid has to be considered, the medium becomes dispersive. The propagation of acoustic wave becomes frequency dependant. However with vapour density being very small compared to the liquid density ($\rho_g \ll \rho_f$), the sound speed in the two-phase medium approaches the sound speed in vapour medium ($C_{st} \approx C_g$). This is based on the assumption of no inter-phase mass or momentum transfer at the gas bubble liquid interface. Thus within the reactor vessel and core shroud downcomer annulus region, homogeneous medium assumption is made after the passage of elastic wave of amplitude ($p_o - p_{so}$) at sonic speed in liquid medium which is typically ~ 1000 m/s. Subsequently after the passage of this elastic wave, the second wave

BARC NEWSLETTER

travels at a speed, which is two to three times less than the elastic wave speed due to high compressibility of the medium. Sudden density changes in case of cavitations and resultant formation of bubbles calls for non-linear analysis and has been implemented using a bilinear fluid model with tension cut-off, which depends on the saturation pressure.

The estimation of the critical flow for blow down due to LOCA was carried out with systematic review of Burnell's model, Moody's homogeneous equilibrium model and Leung's generalised equilibrium model. The adequacy of Leung's generalised model was established for the prediction of sub-cooled and two-phase blow down induced critical discharge for HDR-PWR and TAPS-BWR problems respectively. It has been demonstrated that the acoustic Helmholtz modes of the downcomer annulus and the core shroud shell multi-lobe modes of TAPS-BWR are well separated (Fig. 1). The transient dynamic response of the core shroud shows that the acoustic load induced stresses are within service level D limits of Section III NB of ASME Boiler and Pressure vessel Code.

Wave Propagation in Geogological Media

The indigenous development of in-house finite element code **SHOCK-3D**, with strong capabilities for the three-dimensional simulation of shock wave propagation and coupled fluid-structure interaction analysis of underground explosion induced gas cavity growth and the resulting spall, fracture and crater simulation has helped to strengthen Indian strategic programs. This code has been used to simulate the near field hydrodynamic and anelastic / inelastic features around underground sources using equation of states in different regimes. The study has been useful for wave propagation and seismic signal analysis in rock/soil media for near and far field regions. The work on US Baneberry-1970 nuclear test 3D simulation could successful explain the reported venting due to explosion induced fault movement in the complex geological strata. This 3D code development and subsequent analysis gave requisite confidence for the Indian nuclear test programme. These studies have been useful to explain the effect of local geological formations on the

observations made during the tests and have been cited for resolving critical national security issues.

Constitutive Models in Code SHOCK-3D

The fluid-structure interaction code **SHOCK-3D** with explicit transient formulation is finite element based, where in the two field problem of the rock media and explosion induced gas cavity are coupled to analyze the underground explosion problems. For the explosion induced gas cavity non-viscous hydrodynamic formulation based fluid elements with limited overburden pressure are used to correlate the pressure (p) with volumetric strain (ϵ_v) and specific energy (E).

The constitutive model for the geological medium due to Hoek and Brown (Int. J. Rock Mech. Min. Sci, 34, 1998) for the different rock strata accounts for the confinement effect on the rock strength.

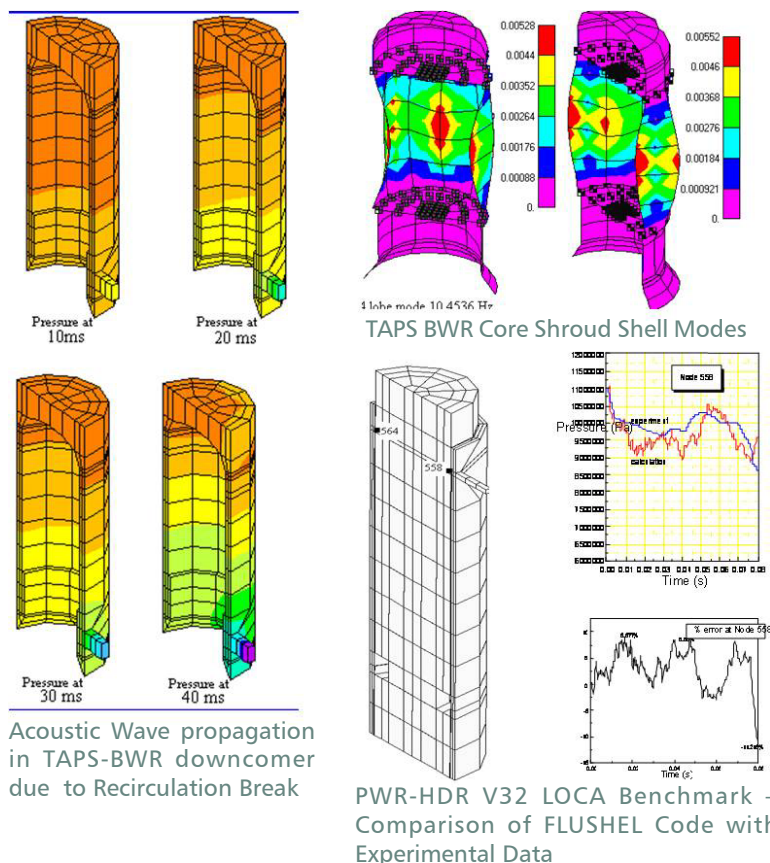


Fig. 1: Coupled Two Phase Fluid-Structure Interaction for TAPS-BWR Core Shroud and HDR-v.32 Core Barrel for Blowdown Problems

BARC NEWSLETTER

Damage mechanics based failure models are used depending on the strain levels for quasi-brittle and ductile failures. The Hugoniot equation of state at high shock pressures and hydrostatic data for different rock media has been used in the present code. The loading and unloading bulk moduli in the different regimes such as the mean pressures corresponding to the maximum tensile and compressive stresses of the rock medium at zero confinement describing the Hugoniot elastic limits, hydrostatic pressure range and high pressure shock range are evaluated for different rock media. The equation of state for the rock media is represented as

$$p = K(\epsilon_v) + \Gamma(\epsilon_v)E \quad (5)$$

Where p is the hydrodynamic pressure, the local bulk modulus $K(\epsilon_v)$, is obtained from Hugoniot equation of state depending on the loading or unloading condition, ϵ_v is the volumetric strain, E is the specific energy and Γ is the Gruneisen parameter which allows dissipation of energy and is a function of volumetric strain.

The strain rate dependent model of the code SHOCK-3D has been formulated with the modified form of classical elasto-viscoplastic constitutive theory, which accounts for strain-rate sensitivity with allowance for progressive degradation of strength. In view of the limitations of the classical elasto-plastic and elasto-viscoplastic models to deal with rate and history dependent problems for transient shock and dynamic loadings, the visco-plastic strain rate is defined as a function of elastic strain /stress rate. In addition the damage due to the viscoplastic flow is monitored with the help of a variable strength limit surface. The yield surface defines the onset of viscoplastic flow and the strength limit surface defines the initiation of material degradation and these are represented with the help of first and second stress invariants of deviatoric stresses. A constant failure strain based criteria is used in this model irrespective of the strain rate. Thus the present viscoplastic constitutive model of the code SHOCK-3D retains all the important features of rate dependent inelastic behavior along with the equation of state which characterize the rock behavior in the different regimes of shock loading,

The overburden simulation is important for the accurate simulation of transient problem of underground explosion event since the rising mound is finally settled due to fall back induced by gravity forces. This feature is accounted with the simulation of the initial stress field due to the overburden. Sommerfeld radiation condition is used to simulate a non-reflecting boundary to avoid any spurious reflection from the model boundary with normal and tangential directions as n and t respectively as follows.

$$\sigma_n = \rho c_b v_n \quad (6)$$

$$\sigma_t = \rho c_s v_t \quad (7)$$

Here σ_n and σ_t are normal and tangential stresses, v_n and v_t are the normal and tangential components of the particle velocity at the mesh boundary, ρ is the medium density and c_b and c_s are the body wave and shear wave velocities for the medium. These conditions are applied sufficiently away from the source where plane elastic wave conditions exist, in which case the wave speeds are constant.

Venting Concept and Baneberry-1970 Event Phenomenology Simulation

The US Baneberry-1970 event with a shot depth of 278 m, yield of 10 kT vented due to the establishment of a fracture path owing to the presence of pre-existing Baneberry fault and unfavorable combination of local geological strata near the source. The classic example with all the complex geological features has been successfully simulated by three-dimensional finite element code SHOCK-3D in the present work. All the undesirable features namely the closeness of the fault with the emplacement point, proximity of the hard Paleozoic layer underneath the source near the fault region on the west end and clay rich tuff layer on the east end (Fig. 2) of the source formed the worst combination leading to venting which is not expected at such large scaled depth of burst $\sim 129.3m/kT^{1/3}$. Here, the shock-induced slip along the pre-existing fault plane has an important bearing on the containment efficiency of this event. None of the earlier reported 2D simulations (UCRL-52365-1977 &

BARC NEWSLETTER

Nuc. Tech. 46, Nov.1979) addressed the slip phenomenon and the influence of variation in geological strata in presence of the pre-existing fault in a three dimensional framework. The Indian simulation work despite the uncertainty of detail data on the local geology demonstrated with precise modeling of the composite geological strata and fault system that a dip slip mechanism developed for Baneberry event leading to final venting. This

was the first 3D simulation of Baneberry event (Fig. 3) and it created a renewed interest among the international community in such development. The vent location prediction of 97 m south-west of source in the simulation compared well with 90 m as noticed at test site. Further the subsidence crater of 200 m dia and 25-26 m depth also compared well with the observed crater of 128 m dia and 24 m depth for this event.

BANEBERRY-1970 EVENT

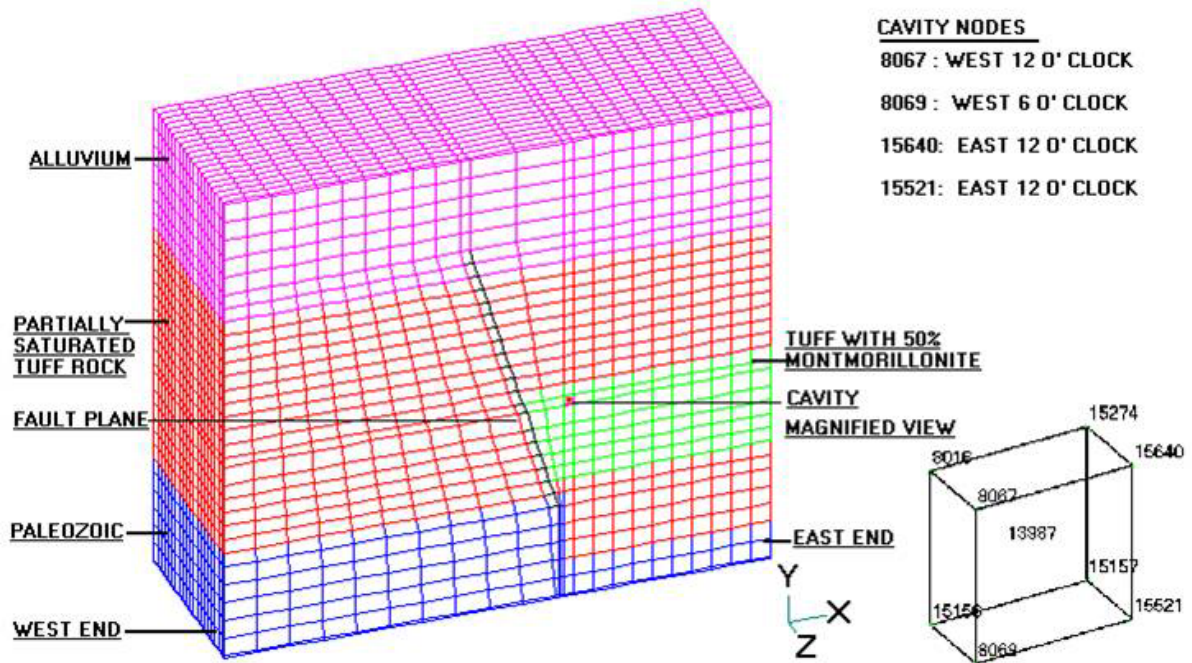


Fig. 2: Three-Dimensional Model with Layered rock Media, Fault, Source Location for 10kT Baneberry-1970 Event

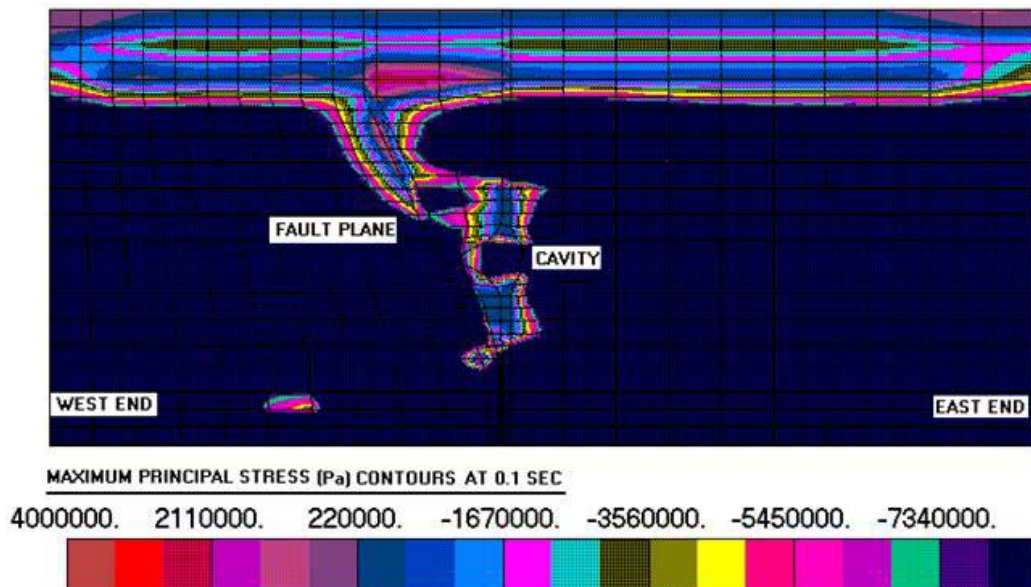


Fig. 3: Maximum Principal Stress (N/m²) at 0.1 sec and Resulting Vent Path for 10kT Baneberry Event

BARC NEWSLETTER

Tsunami Wave Propagation and Run-up Evaluation for Indian Coastal Nuclear Power Plants

The simulation of tsunami events with the indigenous finite element code *Tsunami Solution* (TSUSOL) developed immediately after the Sumatra-2004 tsunami event has been used extensively for the study of Sumatra-2004 and Makran-1945 events and other subsequent events of tsunami wave generation, its propagation and near shore wave run-up evaluation. The predictions of the code for the tsunami wave arrival time and the wave run up heights were noted to be in good agreement with the post tsunami survey observations reported for the different coastal regions of the Indian Ocean for Dec 26 Sumatra earthquake event.

Tsunami In-house Code TSUSOL

In-house finite element code TSUSOL is a compressible wave propagation code with due consideration to free surface shallow water theory and acoustic wave propagation below the free surface. The continuity and momentum equations with velocity components v_i are expressed as

$$\partial \rho / \partial t + \nabla (\rho v_i) = 0 \quad (8)$$

$$\rho Dv_i / Dt = \sigma_{ij,j} - \rho g_i \quad (9)$$

For the tsunami wave propagation throughout the whole 2D surface the normal surface tractions gradient with surface normal n is defined as

$$\partial \rho / \partial n = -1/g \partial^2 p / \partial t^2 \quad (10)$$

The Sommerfeld radiation boundary condition at the non-reflecting boundary is

$$\partial \rho / \partial n = -1/c \partial p / \partial t \quad (11)$$

For computation of fluid continuum coupling to the seabed is obtained from

$$\partial \rho / \partial n = -\rho \partial v_n / \partial t, \quad (12)$$

v_n is the normal velocity at the seabed due to the earthquake/subduction motion

The in-house studies have been effectively utilized for design and implementation of early warning system for coastal region of the country in addition to the site evaluation of Indian nuclear coastal installations. The in-house finite element code TSUSOL predictions of wave arrival time, reflections from coastal regions and run up were later confirmed by Jason satellite data. (Fig. 4) The time signal analysis of the wave time history (Fig. 5) from in-house finite element code TSUSOL confirmed the reflections from Sri Lanka and various other Indian islands. The reflected wave periods from Sri Lanka computed as 4096 sec, 2560 sec and 1280 sec compare well with the spectral periods of 4380 sec, 2580 sec and 1320 sec respectively from the deduced data of National Institute of Oceanography (NIO) tide gauge records for 2004 tsunami event.

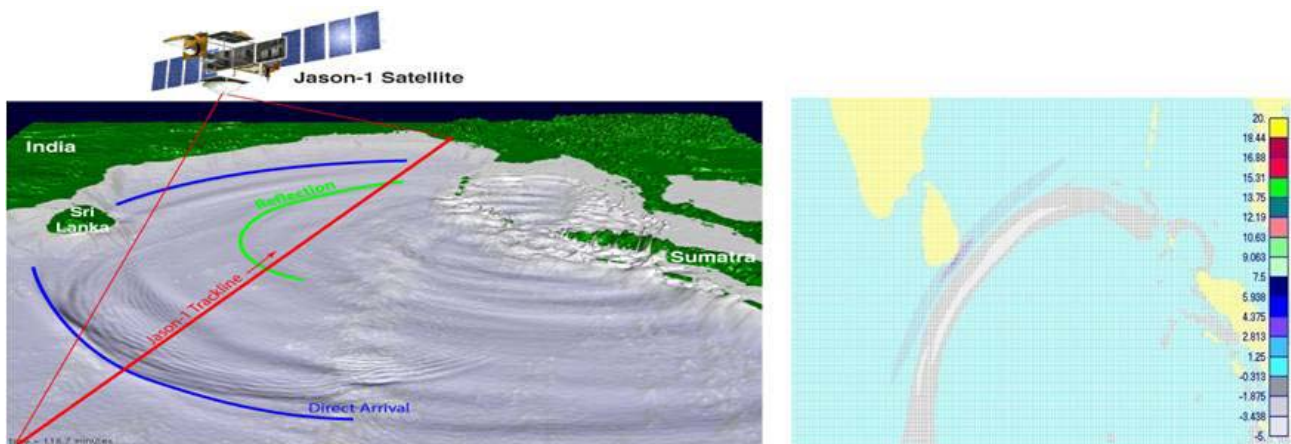
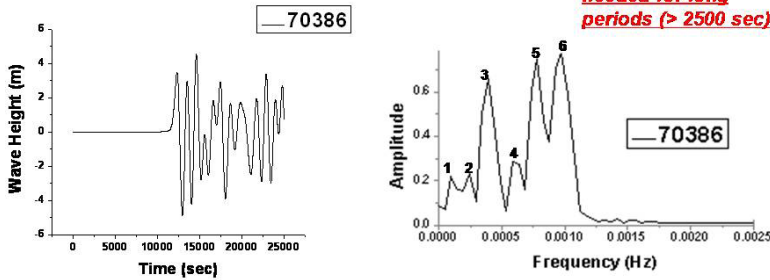


Fig. 4: JASON-1 Track 109 Satellite (altitude 1300 km) Record and TSUSOL Predictions for 2004 Java Sumatra Tsunami Event

BARC NEWSLETTER

TSUSOL-2005 predictions

Peak Wave Height ~ 4.4 m
At 14655 sec



Spectral periods (sec)
4380, 2580 &
1320 (NIO de-tided gauge data Rabinovich (2007))

Wave Periods(sec)
1 - 10240
2 - 4096 (Sri Lanka)
3 - 2560 (Nicobar)
4 - 1707
5 - 1280 (Sri Lanka)
6 - 1024
✓ **Coupled system needed for long periods (> 2500 sec)**

Typical Time Signal at **South Indian Coast** Multiple Wave Periods due to Wave Scattering and Reflections from **Sri Lanka Sumatra event was a far field event and hence decoupled analysis justified with static boottom displacement model as evident here**
Dr R K Singh BARC INDIA

82

Fig. 5: Spectral Analysis of Tsunami Waves from TSUSOL Predictions for Sumatra-2004 Event and Comparison with NIO Tide Gauge Data

For Kalpakkam, Tarapur and Vizag sites tsunami evaluation, coordination with national agencies was carried to obtain bathymetric and land morphology data and source term evaluation was made for accurate inundation and wave run-up modeling. Tsunami effects for these specific nuclear power plant sites in terms of wave height, run-up and the resulting inundation were studied and confirmed with on-site observations of Kalpakkam (Fig. 6) and Vizag sites in a National Round Robin Analysis coordinated for site evaluation. The tsunami height data has been generated for the present and future prospective nuclear coastal facilities, which

is extremely useful for the site evaluation and for evolving necessary up-gradation measures.

Indian PHWR Nuclear Containment Safety Assessment

The beyond design basis accidents of Three Mile Island (1979) and Chernobyl (1986) created interest among the nuclear community for the safety assessment studies related to the ultimate load capacity of the nuclear containment structures in addition to the release of radioactivity to the environment due to over-pressurization. The progression of the severe accident recently at Fukushima (2011) multiple nuclear plants has further emphasized the need for the containment

integrity evaluation. For the containment structural safety evaluation, BARC Containment (BARCOM) the 1:4 size Test Model of 540 MWe PHWR pre-stressed concrete inner containment (Fig. 7) has been constructed and commissioned at Tarapur. The Control & Instrumentation building equipped with modern data logging systems along with 1200 embedded and surface type sensors, process parameter sensors and camera systems have been integrated with BARCOM for the mega size experiment. An International Round Robin Analysis with eighteen participants during the pre-test and post-test phases has been coordinated to

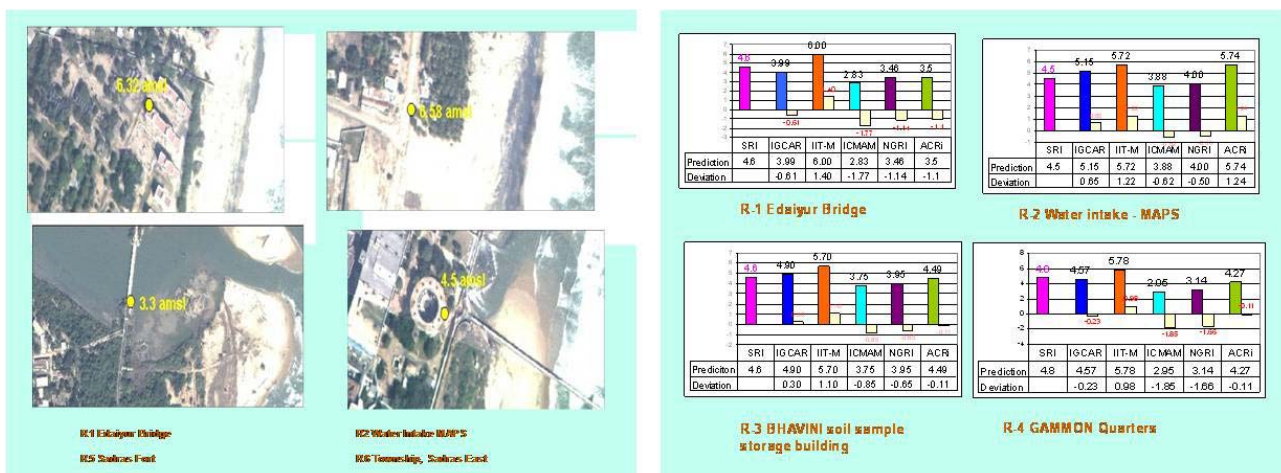


Fig. 6: Kalpakkam Site Tsunami Run up Measurement at Standard Locations and Inter-code Comparison

BARC NEWSLETTER



Fig. 7: BARCOM Test Model and Longitudinal & Shear Cracks around MAL & Embedded Sensor Response during Over-Pressure Tests on July 23-24, 2011 (1.78 Pd) & Oct 02 2011 (1.68 Pd) and Numerical Simulation Results

study the various failure modes of the model and the evaluation of the ultimate load capacity have been completed in different phases of the experiments to benchmark the inelastic computer codes, constitutive models and fracture mechanics models for the design

have been evaluated to address the related modelling issues for inelastic code benchmarking for local and global failure modes, which have been backed up with extensive data collected during the Phase-III experiments.

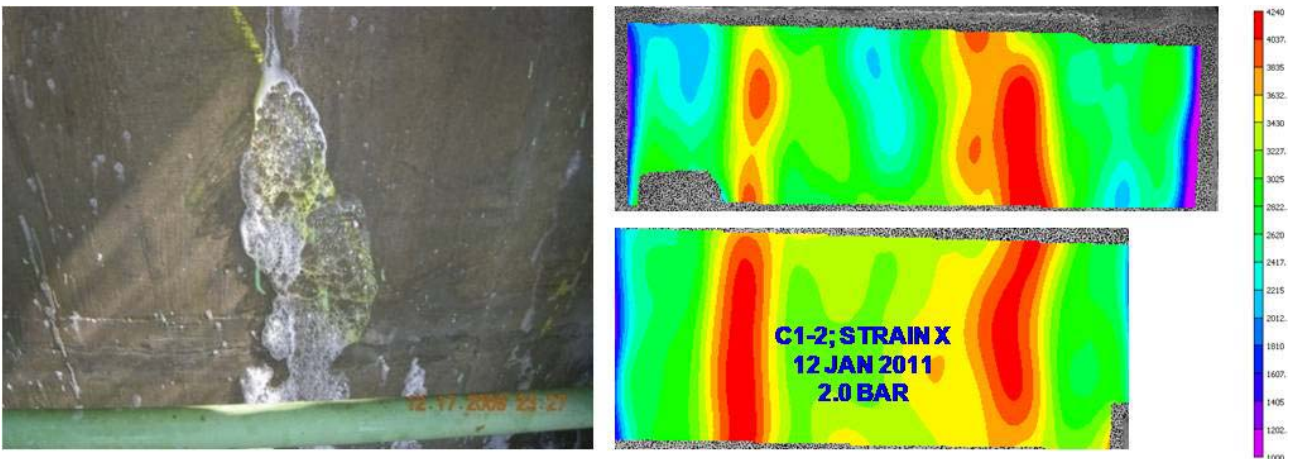


Fig. 8: First Appearance of Crack in BARCOM Test Model during Over-Pressure Test Phase-III Experiment and verification with Soap Bubble Test & Optical Crack Profiling to identify Fracture Process Zone

basis and severe accident scenarios. This research project with academic orientation is very relevant in the present day context for country's nuclear power programme in the aftermath of Chernobyl-1986 and recent Fukushima-2011 severe accident events.

BARCOM experimental program has achieved the desired objectives to obtain the functional failure mode through a systematic test program and has given the requisite confidence for the Indian PHWR containment integrity as demonstrated in this project. The results from the various international round robin participants

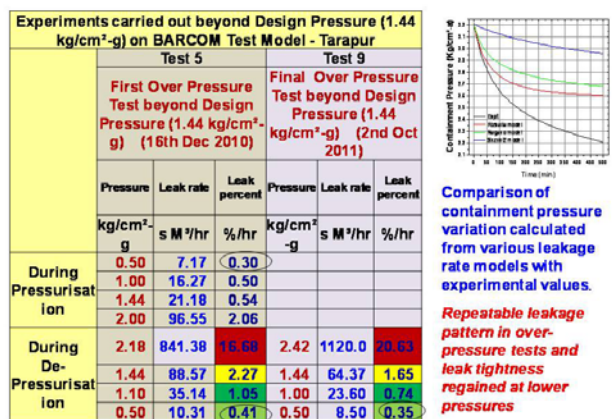


Fig. 9: Leakage Observed in BARCOM Over-Pressure Test

BARC NEWSLETTER

The experiment demonstrated that even after functional failure of primary containment, the leakage rates through with tight cracks (Fig. 8) due to residual prestresses are within controllable and manageable limits and shielding cover is retained. Double containment and related Engineered Safety Features further assist in controlling the ground leakage and releases to the environment. Margin against over-pressurization of BARCOM has addressed important issues with regard to containment safety and the resulting leakages due to over-pressure (Fig. 9) under extreme events.

Conclusions

The indigeneous efforts to address multi-disiplinary coupled problems relevant for various thrust areas of reactor safety and strategic applications enabled through in-house code development and experimental programs have been presented in this article. Our future

endeavours will be directed and focused towards development of robust codes and its validation through various standard problem and round robin exercises for concurrent problems of multi-physics nature, which will be addressed through in-house experimental programs with improved instrumentation techniques.

I sincerely acknowledge with thanks the significant contributions made by a large number of colleagues in Reactor Safety Division, collaborators from BARC, AERB and NPCIL and other academic institutes along with the participants of international / national round robin exercises who have not only supported these in-house efforts with their scientific and technical inputs but also have been along with us to evolve these technologies through a collective thinking process.

BARC NEWSLETTER

APPLICATIONS OF D-T/D-D NEUTRON GENERATOR FOR THE INVESTIGATION OF ADS NEUTRONICS, FISSILE MATERIAL DETECTION AND NEUTRON IMAGING

Amar Sinha

Neutron & X-Ray Physics Division

Dr. Amar Sinha is the recipient of the DAE Homi Bhabha Science & Technology Award for the year 2011

Abstract

D-T/D-D neutron generators have been used for several applications such as neutron driver for a zero power accelerator driven subcritical system (ADS), fissile material detection, explosive detection, neutron imaging etc. We have been working on the development and applications of D-T/D-D neutron generator. In this paper, we discuss three important applications which have been carried out using such generators.

D-T/D-D neutron generator driven ADS

Accelerator driven subcritical systems are increasingly attracting worldwide attention due to their superior safety characteristics and their potential for burning actinide and fission product-wastes and energy production. Indian interest in ADS has an additional dimension, which is related to the planned utilization of our large thorium reserves for future nuclear energy generation. In ADS, the high energy accelerator would accelerate a beam of protons to GeV energy before impinging them into a lead target inside the subcritical reactor core. The bombardment induces the target to release large number of neutrons by spallation which then induces neutron multiplication and fission reaction in a surrounding subcritical reactor producing power. The system shuts off once the accelerator beam is switched off.

There are many challenges both related to technology and physics of ADS which needs to be solved before such a system becomes reality. There are new physics issues which are specific to subcritical reactor and not encountered with critical reactors. For example, the power in subcritical system depends inversely on sub-criticality and directly proportional to external neutron

source strength. The spatial and energy distribution of flux is quite different from critical reactor due to effect of centrally peaked external source neutrons whose energy spectrum is different from that of fission neutrons. This leads to new concept called source importance k_s instead of k_{eff} which affects neutron multiplication and power in the system. Measurement of source importance, injected neutron source strength and most important online criticality monitoring become an important issue in ADS as final output power depends critically on these parameters. The reactor kinetics of ADS is quite different from the critical reactors. New measurement techniques need to be developed especially for ADS applications as the flux in ADS is a combination of fundamental and higher modes.

Before a full fledged ADS using spallation neutrons becomes a reality, many countries have initiated extensive program to study these physics issues of ADS using low power subcritical assemblies driven by neutrons generated using D-T, D-D, photonuclear reactions as spallation sources meeting the requirement of commercial ADS are yet to be developed. Some of these programmes include YALINA in Russia, MUSE in France, RACE in USA, VENUS-1 in China and GUINEVERE

BARC NEWSLETTER

in Belgium. These low power ADS could serve as a useful surrogate for investigating many of the physical characteristics and potential applications of high-power, full-scale ADS systems that are under design but remain to be built. With this in mind, a low power subcritical system **BRAHMMA** (**BeO Reflected And HDPE Moderated Multiplying Assembly**) has been designed and installed at Purnima Laboratory. The subcritical core is coupled to an indigenously developed deuteron accelerator producing D-D and D-T neutrons. This is a first step within the country to develop experimental ADS. The development of such a zero power facility will enable study of various physics parameters related to neutronics, reactor physics and dynamic characteristics of ADS, validating codes and nuclear data as well as development of new but important techniques of a subcriticality measurement. There are several novel features in the design of both subcritical assembly and deuteron accelerator based neutron generator developed by BARC. These two components

of zero power ADS (a) Subcritical assembly and (b) neutron generator are described below.

BRAHMMA Subcritical Core

The subcritical core is designed using metallic natural uranium as fuel, high density polyethylene (HDPE) as moderator and beryllium oxide (BeO) as reflector. Polyethylene has better moderating ratio and moderating power compared to light water. The use of polyethylene sheets makes the system modular. As a reflector material, BeO has excellent neutron reflecting properties and has helped to make the system compact. The core consists of 160 fuel rods in a 13 X 13 square lattice and embedded in HDPE with a pitch of 4.8cm. The central 3 X 3 positions of the lattice are vacant and serve as the central cavity for inserting the neutron source. The target is located at the centre of the core. Behind the target, lead block is used. The purpose of using lead is to soften the energy spectrum of the monoenergetic D-T neutrons.

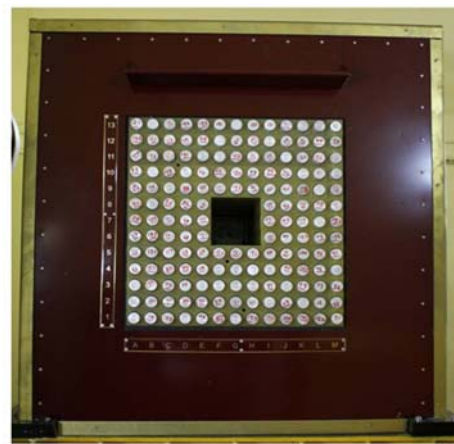
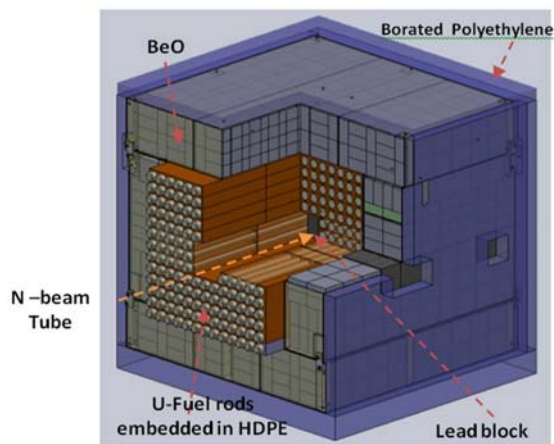


Fig.1: (a) 3D model (b) Photograph of BRAHMMA subcritical core

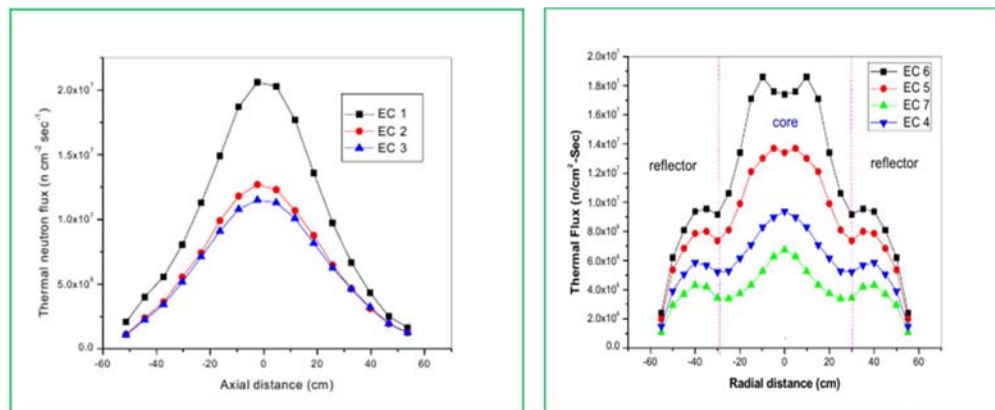


Fig.2: Simulated flux profiles in BRAHMMA (Left) Axial flux profile (Right) Radial flux profile in different experimental channels (EC1-7)

BARC NEWSLETTER

The core is surrounded by beryllium oxide (BeO) reflector of thickness 20cm. The whole assembly is finally surrounded by borated polyethylene and cadmium for neutron shielding. This is important for preventing back reflected neutrons from the walls of the room interfering with effect due to source neutrons.

The assembly has several unique features such as polyethylene as moderator and BeO as reflector and due to these it has become modular and compact. The estimated theoretical k_{eff} value is 0.889 with 2.8 tonnes of fuel. Due to its modular nature, there is a provision for replacing about 25% fuel rods with 1.3% SEU at later stage to achieve a k_{eff} value of 0.95.

PURNIMA Neutron Generator

The coupling of the external source to the subcritical system is provided by the Purnima deuteron accelerator (Fig.3). This indigenously developed neutron generator is presently the most powerful non-reactor neutron source within the country. It is a Cockcroft-Walton type accelerator in which D^+ ions are accelerated to impinge either on Ti-D and Ti-T target. It can produce both D-D (2.45 MeV) and D-T (14.1 MeV) neutrons depending upon the target used. To make this generator suitable for ADS physics study, several new features have been introduced in the system such as both DC mode and pulsed mode generation of neutrons, programmable interruption of generator, provision for online neutron yield measurement using "neutron tagging" technique wherein neutrons are monitored using associated alpha in the nuclear reaction $d(T,\alpha)n$. Several novel miniature neutron detectors have been developed for the first time to measure neutron flux online and thus enabling study of both static and dynamic characteristics of ADS. These detectors include a miniature fibre optic scintillator detector (1 mm) wherein a neutron sensitive scintillator is coupled to a long optical fibre which is then coupled to a photomultiplier tube. This enables online measurement of flux in the narrow experimental channels of subcritical assembly. A trial coupling of accelerator with subcritical was done and some preliminary neutronics experiment with D-D neutrons were carried out. Further validation with D-T neutrons are being planned.



Fig.3: PURNIMA Neutron Generator

Experimental Results

BRAHMMA subcritical core has been coupled to Purnima Neutron Generator (Fig.4). Results of preliminary experiments with D-D neutrons are being reported here.



Fig.4: BRAHMMA with neutron generator

Flux measurement

The axial flux profile (Fig.5) inside the subcritical core was measured with a miniature ^3He detector (Active

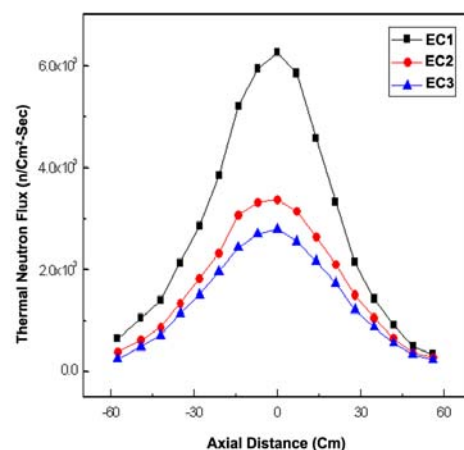


Fig.5: Experimental Axial flux profile with D-D neutron

BARC NEWSLETTER

length: 70mm; diameter: 6.5mm). D-D neutron source was used for flux profile measurement. Figure 5 shows the flux profile along the axial direction inside the core at the experimental channels EC1, EC2 and EC3. The axial profile is peaked at the center of the core. Similarly the flux is maximum at EC1, which is nearest to the core.

Reactivity measurement

The reactivity was measured using pulsed neutron techniques - Source Jerk method, Area Ratio method and Slope Fit method. A brief description of the three methods is described.

Area Method & Slope-Fit method

Reactivity (ρ) is determined by investigating the neutron flux decay during repeated injection of neutron pulses at constant frequency. After large number of neutron puls, equilibrium level of delayed neutron precursors is obtained. These delayed neutron precursors will decay at a constant rate which will cause constant delayed neutron background, but prompt neutron shows very fast time dependent behavior. By operating the neutron generator in pulse mode and registering the detector signals after each pulse, a pulse response of the system can be obtained. For the Area Ratio method, the reactivity is given by the ratio of the prompt and delayed areas. In the slope-fit method, the slope of the prompt decay part gives α which is used to determine reactivity.

$$\rho/\beta_{\text{eff}} = -A_p/A_d \quad (\text{for area ratio method})$$

and

$$\alpha = (\rho - \beta_{\text{eff}})/\Lambda \quad (\text{for slope-fit method})$$

where A_p is the prompt area and A_d is the delayed area, β_{eff} is the delayed neutron fraction, Λ - mean generation time and α is the prompt decay constant. The experimentally measured k_{eff} values are 0.886 ± 0.005 and 0.887 ± 0.003 for Area Ratio and Slope Fit method respectively. It has been observed that the experimental k_{eff} values are in good agreement with the theoretical estimate.

Source-Jerk Method

The idea behind the Source Jerk method is to operate the subcritical system at a steady flux level n_0 and then suddenly switch off the neutron source. The neutron population inside the core will jump to a lower neutron level n_1 . This quasi static level will decay according to the decay rate of delayed neutron background. From the point kinetic equation the reactivity of the subcritical core is given by:

$$\rho/\beta_{\text{eff}} = (n_1 - n_0)/n_1$$

Fig. 6(a) shows the decay of neutron flux. This plot is used for estimating the reactivity using area-ratio and slope-fit method. Fig. 6(b) shows the plot of neutron flux during beam ON and OFF times. This plot is used

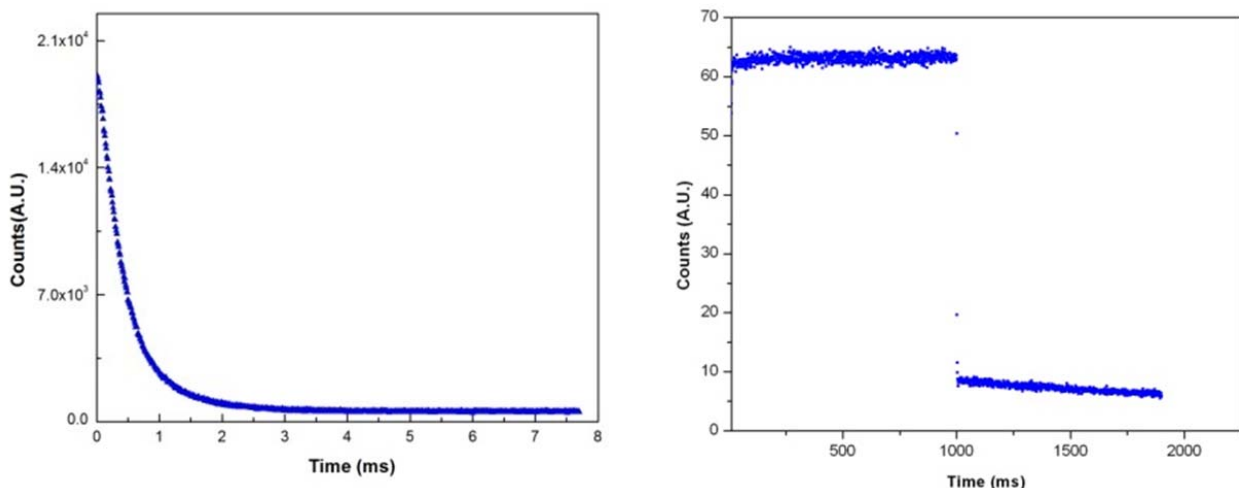


Fig.6: Experimental plots for (a) Area-Ratio and Slope-Fit method (b) Source-Jerk Method

BARC NEWSLETTER

for estimating the reactivity using Source-Jerk method. The experimental result using this method is presently being analyzed.

Fissile material detection using active neutron interrogation (D-T/D-D)

Active neutron interrogation technique is another application using pulsed neutron generator which has been developed at Purnima Labs. This technique is being used world-wide for improving sensitivity of fissile material detection for security as well as in nuclear waste assay for nuclear material accounting. The advantage of this method is that it can detect very small quantities of fissile materials even in presence of high neutron and gamma background and it is much more sensitive compared to passive neutron or gamma techniques. This technique is based on differential die-away analysis^[2] and works by exposing a medium to pulses of neutrons. An external fast neutron detector measures the time-dependent fast neutron flux resulting from the irradiation. When no fissile material is present in the inspected medium (e.g. waste drum, hull, a truck or cargo container being inspected for nuclear material, etc.) the detector should only measure a signal representing the diffusion of the thermalized neutrons in the detector body (detector neutron "die-away" time). If fissile material is present, the detector will show, in addition to a signal decaying with the detector die-away time, an additional signal decaying with the die-away time of the inspected medium (Fig.7). If the latter

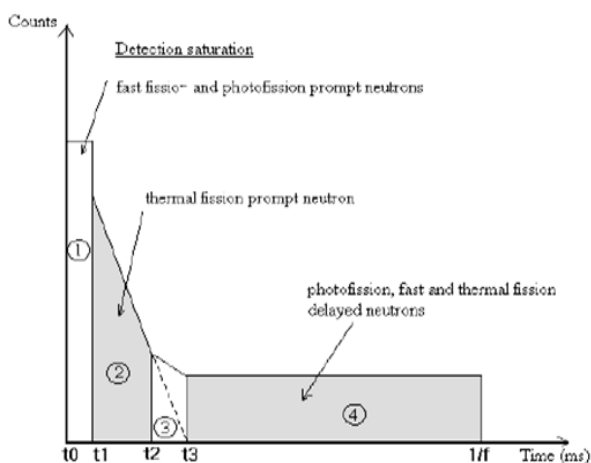


Fig.7: Basic principle of Differential Die away technique for fissile material detection

is significantly longer than the former, it will dominate the decay curve at later times and unequivocally establish the presence of fissile material in the inspected object. The amplitude of the signal and its time constant is determined by several factors, among them the quantity and location of fissile material present in the inspected medium. We have carried out laboratory based studies using this technique and initial results are reported.

Experimental Results

An experimental facility comprising of pulsed D-T neutron generator and He-3 detectors has been set-up to verify the detection limits using this approach especially for the case of leached hull-monitoring. Dry pieces of zircaloy weighing approximately 150kg was used simulated the dry hull (Fig. 8). Experiments were carried by placing 1gm-to-50gm of U-235 (in the matrix of natural metallic uranium) at the centre of the hull matrix (Figs. 9 & 10). Active neutron (10^4 n/s), gamma



Fig.8: Simulated Hull Matrix

background (20mR/hr) and moisture conditions were simulated by keeping 5mCi Am-Be neutron source, 100mCi Cs-137 gamma source and water (60gm), which represent the background radiation and moisture levels typically encountered in hulls. The data was acquired and it was proved that even under these stringent conditions, up to 1gm of U-235 could be easily detected. Experiments are underway to test for lower limits of ^{235}U .

BARC NEWSLETTER

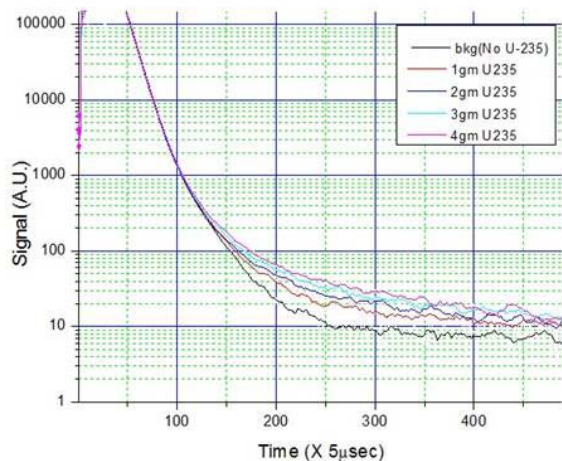


Fig.9: Detector signal as function of time for various quantities of ^{235}U in absence of external neutron and gamma source

Thermal Neutron Imaging using D-T Neutron Generator

Thermal Neutron imaging is a well known non-destructive technique commonly applied to the inspection of nuclear fuel, turbine blades, pyrotechnic devices, etc. Till now, this technique has been mostly used with reactor neutrons which provide a high neutron flux. However, there are many situations such as inspection of pyrotechnic devices used in defence and space applications which require detection of small quantity of explosive charge inside a metal matrix. Detection of these are crucial for qualification of components being used in space flights or missile component. Such a small amount of explosive material cannot be clearly discerned using X-ray and neutron imaging is the only solution. Due to the nature of sample and explosive charge within, such material have problems being taken near reactors. This demands neutron imaging to be carried out at the site. There are many other such applications. Such a situation demands that neutron generators be used for neutron imaging. The problem in this approach is that the neutron sources based on commonly available neutron generators can provide collimated fluxes which are one to two orders of magnitude less compared to those obtained using reactors. Also the sample has to be kept close to generator otherwise the flux will further decrease. This affects the sharpness of the image. Thus the problem of using neutron generator based imaging is to optimize the neutron flux and collimation ratio

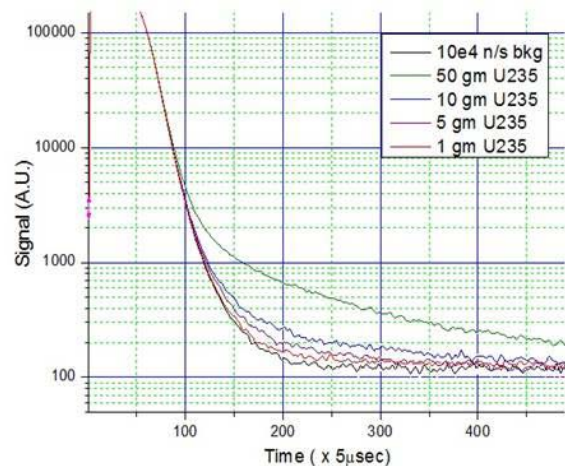


Fig.10: Detector signal as function of time for various quantities of ^{235}U in presence of external neutron (10^4 n/s) and gamma source (100mCi)

with limited source strength. This requires very careful design of moderator collimator assembly in order to get maximum possible neutron flux at the sample with reasonable collimation. Added with this, a sensitive imaging system⁽³⁾ has to be designed which form images even with low neutron flux. Even though image quality at these low flux and collimation ratio is not expected to be as good as those obtained using reactors, nevertheless it has its utility in providing qualitative radiography where presence or absence of some neutron attenuating material is to be detected.

We have tested this concept using Purnima neutron generator in D-T mode. As the D-T neutron produces 14 MeV neutrons, the first challenge has been to effectively thermalize these neutrons in a small volume by using suitable moderators. This required very careful design of layered hybrid moderator. Another criterion which defines the imaging quality is the collimation of the beam which is determined by the L/D of the collimator (where L is the length of the collimator and D is the diameter of the collimator inlet opening). Large L/D improves the quality of the image albeit at the cost of thermal flux. Hence, a tradeoff between the thermal flux and the L/D is required.

A prototype thermal neutron radiography assembly was designed at Purnima lab using a 14 MeV D-T neutron generator in order to test the feasibility of this concept. We tested various designs of neutron moderator

BARC NEWSLETTER

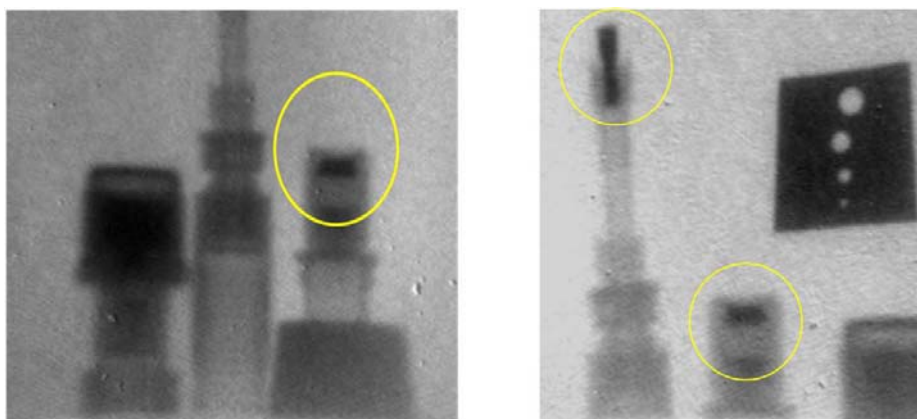


Fig.11: Qualitative neutron radiography images of dummy pyrotechnic devices obtained at a neutron flux of 2×10^3 n/cm²/s at the sample position. Circled area shows the location of explosive charge (in this case wax was used as simulant)

assembly which produces an optimum thermal neutron flux at various L/D ratios. A highly sensitive electronic imaging system was especially developed for obtaining images at low flux level. We tested this system with some dummy pyrotechnic devices which contained wax instead of explosive charge. Fig.11 shows initial radiography images of dummy pyrotechnic devices using this assembly at D-T neutron source strength of $\sim 10^9$ n/s which gave a collimated thermal flux of about 2×10^3 n/cm²/s at the sample with a collimation ratio defined by L/D = 10.

Development of such a technique has several immediate applications in nuclear, space and defence as neutron imaging can be carried out at the site using neutron generators of limited strength rather than only at high flux reactors. The image quality though not as good as reactor, can be improved by using more powerful neutron generator which is under development at our laboratory.

Acknowledgements

The work of this magnitude would not have been possible without the cooperation of several individuals. The author would like to acknowledge the contributions of several of his colleagues from various divisions such as NXP, AFD, RED, RRS, CDM, ThPD, SSPD & NRG of BARC.

References

1. C. Rubbia, S. Buonolil, E Gonzalez, Y. Kadi and A. Rubio, CERN / AT/ 95-53 (ET)
2. K.A. Jordan and T.Gozani, SORMA Conference, University of Michigan, May 2005
3. A.Sinha et al. Nuclear Instrument and Method. A 377(1996)

BARC NEWSLETTER

SYNTHETIC AND STRUCTURAL CHEMISTRY OF ACTINIDE COMPLEXES

S. Kannan

Fuel Chemistry Division

Dr. S. Kannan is the recipient of the DAE Homi Bhabha Science & Technology Award for the year 2011

Abstract

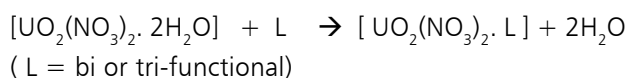
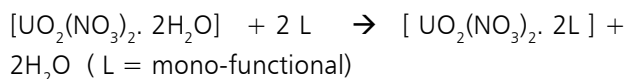
Complex chemistry of mono-functional to multi-functional extractants such as: phosphine oxides, sulfoxides, N-oxides, carbamoyl methyl sulfoxide, carbamoyl methyl pyrazole, diglycolamide, thiodiglycolamide and crown ether with uranyl nitrate, uranyl bis(β -diketonates) and lanthanide nitrates was studied by using IR, NMR spectroscopy, elemental analysis and single crystal x-ray diffraction methods. The structures of most of the isolated complexes of uranyl nitrate with the ligands show that the uranyl group is surrounded by two nitrate groups and one or two ligand(s) in a hexagonal bi-pyramidal geometry. The structures of uranyl bis (β -diketonate), mono-functional ligand complexes show that the uranyl group is surrounded by seven oxygen atoms in a pentagonal bi-pyramidal geometry. The structures of lanthanide nitrate complexes show that the metal ion has either a bi-capped square prismatic or tri-capped trigonal prismatic coordination geometry, depending upon the ligands used.

Introduction

The synthetic and structural chemistry of actinide and lanthanide ions are well studied in last two decades due to the interesting properties such as: selective ion-exchange, mixed valence, ionic conductivity, enhanced fluorescence, photoluminescence, magnetic ordering and nonlinear optical properties exhibited by their complexes [1-5]. The basic understanding of the coordination chemistry of these ions is very important for the selective complexation and separation of these ions from the acid medium during reprocessing of irradiated nuclear fuel and also for the safe disposal of HLW solutions. Various new extractants were developed in last two decades for the above mentioned purposes and their extraction and coordination chemistry are well studied. The trivalent lanthanide ions are used as model compounds for analogous trivalent actinide ions, due to their similarity in both coordination and structural chemistry. This article will give a brief summary of work reported on the synthetic and structural chemistry of uranyl and lanthanide ions with neutral ligands.

Synthetic and structural studies of uranyl nitrate, neutral extractant complexes.

Mono-functional tri-n-butyl phosphate is used as an extractant for the separation of uranium and plutonium from the irradiated nuclear fuel in PUREX process. The bi-functional CMPO and malonamides are used as extractants in TRUEX and DIAMEX processes. In all these processes, the extraction mechanism could be written as follows.



These reactions are basically an inorganic substitution reaction, in which the water molecules from the primary coordination sphere are replaced by the neutral donor ligands. New amide based mono, bi and tri-functional ligands such as: isobutyramide, carbamoyl methyl sulfoxide (CMSO), carbamoyl methyl pyrazole (CMPz),

BARC NEWSLETTER

carbamoyl pyrazole (CPz), diglycolamide(DGA) and thio-diglycolamide(TDGA) were synthesized and their complexation and extraction chemistry with uranyl nitrate were studied. For many of the extraction processes, the species responsible for the same are isolated in the solid state and characterized by using IR, ^1H NMR spectroscopy, elemental analysis and for some of the compounds by using the single crystal x-ray diffraction methods.

The IR spectra of the isolated complexes show that the disappearance of ν_{OH} peak around 3000- 3500 cm^{-1} due to the presence of the coordinated water molecules in the starting complex $[\text{UO}_2(\text{NO}_3)_2 \cdot 2\text{H}_2\text{O}]$. The spectra further show that the ligands are bonded through the functional groups such as, P=O, S=O or C=O groups to the metal center. The elemental analysis revealed that the uranyl nitrate forms 1:2 complex with all mono-functional ligands and 1:1 complex with all bi and tri-functional ligands.

The structures for number of complexes were determined by using the single crystal x-ray diffraction methods to confirm the spectral and elemental analysis data. The structure of complex $[\text{UO}_2(\text{NO}_3)_2 \cdot (\text{Amide})_2]$ [Fig. 1a] [6] shows that the metal is surrounded by two nitrates and two amides in a hexagonal bi-pyramidal geometry, in which the amide acts as a monodentate ligand. The structures of $[\text{UO}_2(\text{NO}_3)_2 \cdot \text{CMSO}]$ [7], $[\text{UO}_2(\text{NO}_3)_2 \cdot \text{CMPz}]$, [8] $[\text{UO}_2(\text{NO}_3)_2 \cdot \text{TDGA}]$ [9] and $[\text{UO}_2(\text{NO}_3)_2 \cdot \text{CPz}]$ [10] show that the metal is surrounded by two nitrates and one bi-functional ligand in a hexagonal bi-pyramidal geometry, in which the ligand acts as a bidentate chelating ligand [Fig. 1 b]. The structure of $[\text{UO}_2(\text{NO}_3)_2 \cdot \text{DGA}]$ [11] shows that the uranyl group is

surrounded by three oxygen atoms from DGA ligand and three oxygen atoms from two nitrate groups in a hexagonal bi-pyramidal geometry, in which the ligand acts as a tridentate chelating ligand. [Fig 1c].

Synthetic and structural studies of neutral ligand, uranyl bis(β -diketonates) complexes.

The synergistic extraction of uranyl ion from the acid media by using the mixture of β -diketones and neutral ligands is a well established method. The increase in extraction during this process is due to the formation of a more organic soluble complex of uranyl ion with both the β -diketones and neutral ligands. In all cases, the neutral ligand replaces the water molecule from the primary coordination sphere to give more organic soluble adduct compound as shown in equation 1. However, in crown ethers, due to their poor donating ability, they form second sphere coordination complexes as given in equation 2.



(Where L = diketonate anion ; A = neutral ligand ; CE = Crown ether)

The complexes responsible for the extraction were synthesized and characterized by IR, NMR spectroscopy and elemental analysis methods. The IR spectra of all neutral ligand, uranyl bis(β -diketonates) compounds show that the water molecule from the starting compound is replaced completely by the ligand. However, this is not true in crown ether complexes, as it forms second sphere complexes. The structures for many of the compounds were characterized by single

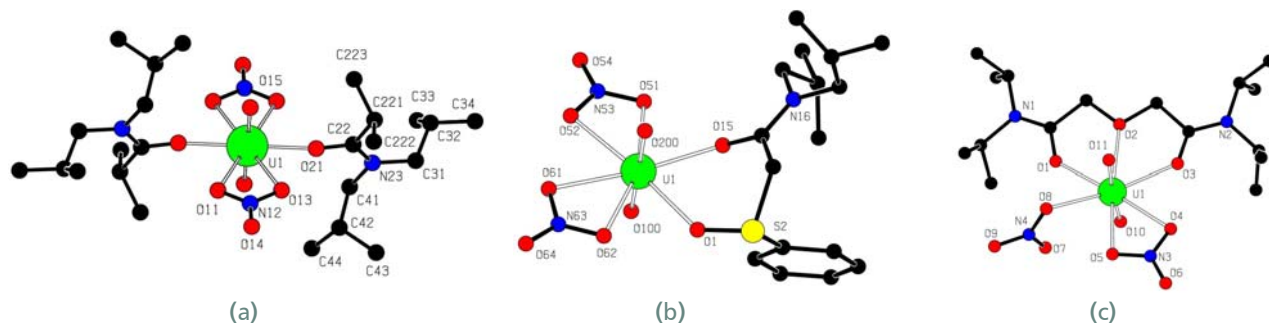


Fig. 1: Structure of : (a) $[\text{UO}_2(\text{NO}_3)_2 \cdot (\text{Amide})_2]$; (b) $[\text{UO}_2(\text{NO}_3)_2 \cdot \text{CMSO}]$; (c) $[\text{UO}_2(\text{NO}_3)_2 \cdot \text{DGA}]$

BARC NEWSLETTER

crystal diffraction method and show that the uranyl group is bonded to two β -diketonate anions and one neutral ligand in the primary coordination sphere. The coordination number and geometry around the uranyl group is seven and pentagonal bi-pyramidal respectively [Fig 2 a]. However, in crown ether complexes the uranyl group is surrounded by two β -diketonate anions and a water molecule in the primary coordination sphere. In all compounds, the crown ether forms invariably a second sphere coordination complex and hydrogen bonded to water molecule via ethereal oxygen atoms [Fig 2 b].

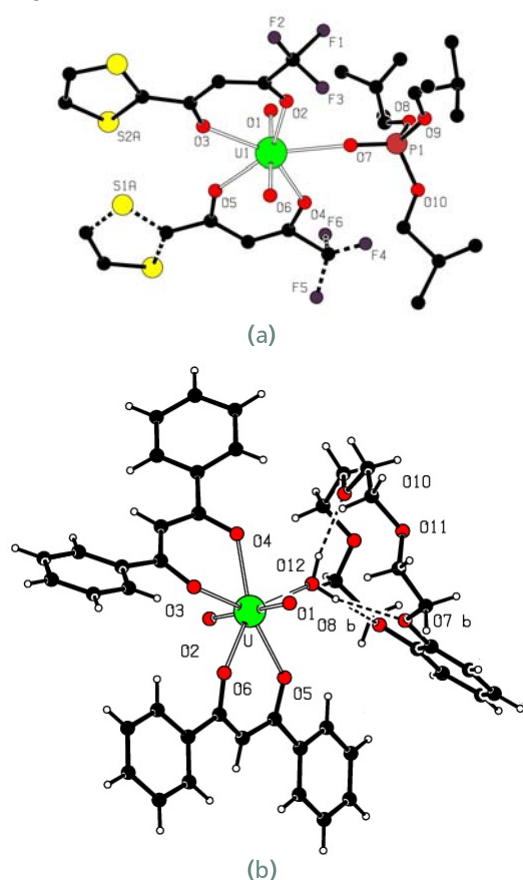


Fig 2.(a) Structure of $[UO_2(TTA)_2.TBP]$;
(b) $[UO_2(DBM)_2.H_2O.B15C5]$

Synthetic and structural studies of neutral ligand, lanthanide nitrate complexes

Bi-functional ligand-lanthanide (III) nitrate complexes

The extraction properties of many bi-functional extractants, such as carbamoyl methyl phosphonates (CMP), carbamoyl methyl phosphine oxides (CMPO), malonamides and bis(dialkyl phosphino methane)

dioxides with the trivalent actinide ion Am(III) from the nitric acid medium have been studied extensively. The species responsible for these extractions were determined using solvent extraction methods. The mechanism for this extraction process can be written as.



Analogous lanthanide (III) ion complexes were prepared by reacting the respective nitrates with the bi-functional ligands in a required ratio and the final products were characterized by using the IR, ¹H, NMR spectroscopy, elemental analysis and single crystal x-ray diffraction methods. These compounds are proposed as model compounds for the analogous trivalent actinide complexes due to their similarity in coordination chemistry.

New bi-functional ligands such as : carbamoyl methyl sulfoxides (CMSO) and carbamoyl methyl pyrazole (CMPz), were prepared and their extraction and coordination chemistry with Am(III) and lanthanide (III) ions are studied. The IR spectra of all compounds show that the water molecules from the starting compound are completely replaced by the ligand. They show further that the ligands are bonded through the SO, CO or both the groups to the metal centre. The ¹H NMR spectra show that all protons are deshielded with respect to free ligand in the complexes and in particular CH₂ protons (CH₂ bridging the SO and CO in CMSO and Pz and CO in CMPz,) are more deshielded compare to other protons.

The structures for number of complexes were determined by using the single crystal x-ray diffraction methods to confirm the spectral and elemental analysis data. The structures of complexes $[La(NO_3)_3 \cdot 2CMSO]$ [7] and $[Ce(NO_3)_3 \cdot 2CMPz]$, [8] show that the lanthanide ion is bonded to three nitrates and two neutral bi-functional ligands to give a bi-capped square antiprismatic geometry around Ln(III) ion [Fig 3]. Both the ligands are acting in a bidentate chelating fashion and bonded through both the sulfoxo or pyrazoly and carbamoyl groups to metal ion. These structure are

very similar to those reported for the complexes of lanthanide nitrates with analogous CMPO, CMP or malonamide types of ligands.

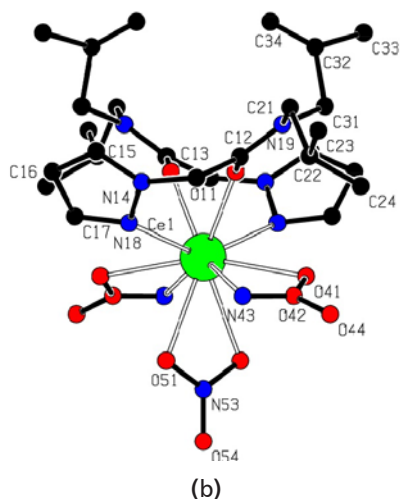
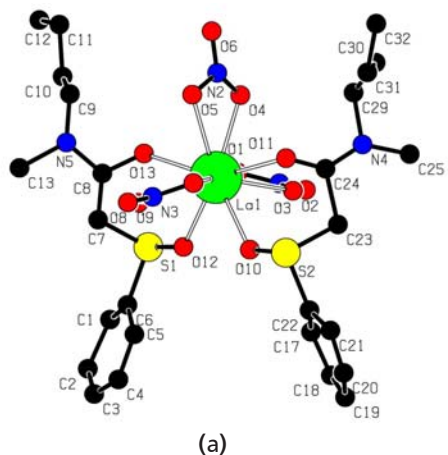


Fig 3 : Structure of : (a) $[La(NO_3)_2 \cdot 2CMSO]$; (b) $[Ce(NO_3)_3 \cdot 2CMPz]$.

Tri-functional ligand, lanthanide (III) nitrate complexes

New tri-functional ligands such as: tetraalkyl diglycolamide and tetraalkyl thio-diglycolamide were synthesized and their complex chemistry with lanthanide (III) ions was studied by using IR, NMR spectroscopy and elemental analysis. The IR spectra of all complexes show that the water molecules from the primary coordination sphere are replaced by the ligands. They show further that the ligands are bonded through the carbamoyl group to the metal centre. The elemental analysis results revealed that the diglycolamide ligands form 3:1 complexes with the lanthanide nitrates, whereas the thio-diglycolamide ligands form 2:1 complexes. The structure of lanthanum nitrate, di-

glycolamide complex shows that the lanthanum ion is surrounded by three diglycolamide ligands in a tri-capped trigonal prismatic geometry to give a cationic compound of the formula $[LaL_3]^{3+}$. The positive charge on the complex is neutralized by the counter ion complex $[La(NO_3)_6]^{3-}$. The La(III) ion in $[La(NO_3)_6]^{3-}$ complex is surrounded by twelve oxygen atoms in a hexagonal anti-prismatic geometry. In $[LaL_3]^{3+}$, all the three ligands act as tridentate chelating ligands and bond through both the carbamoyl and ethereal oxygen atoms to metal center [11] (Fig 4a).

However, the structure of thio-diglycolamide compound of lanthanum nitrate shows that the ligand bonds through both the carbamoyl groups to lanthanum ion in a bidentate chelating fashion, leaving uncoordinated thioether group. The eight membered metallocyclic ring formed between ligand and metal ion has a twist boat conformation [9] (Fig 4b).

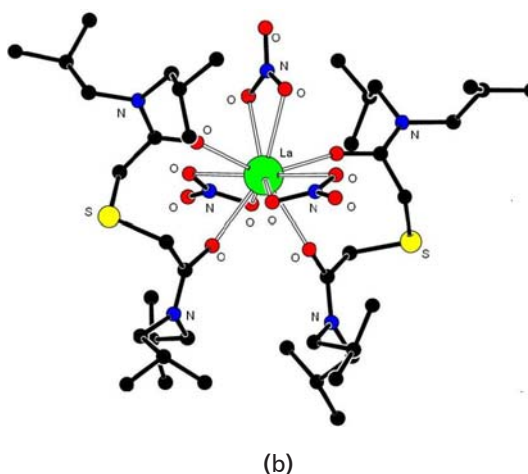
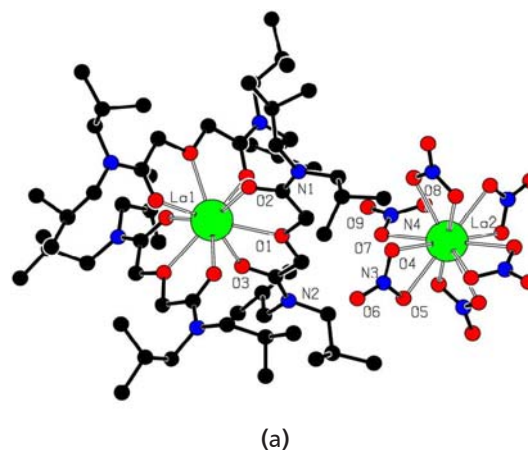


Fig 4. Structure of (a) $[La(NO_3)_3(TBDGA)_3]$ $[La(NO_3)_6]$; (b) $[La(NO_3)_3(TBDTGA)_2]$

BARC NEWSLETTER

Conclusions

Structural studies on the complexes of uranyl nitrate with neutral ligands revealed that the uranyl ion adopts hexagonal bi-pyramidal geometry around the metal center. The structures of uranyl bis(β -diketonates), neutral ligand complexes show that the uranyl group adopts a pentagonal bi-pyramidal geometry. The structures of crown ether, uranyl bis(β -diketonates) complexes show that the crown ethers form invariably a second sphere complex with metal center. The coordination chemistry of trivalent lanthanides with bifunctional CMSO and CMPz and trifunctional thio-diglycolamide ligands shows that the ligands act as bidentate chelating ligand and bond through both the carbamoyl or carbamoyl and sulfoxo or pyrazolyl groups to the metal centre. The structure of diglycolamide, lanthanide nitrate complex shows that the ligand forms a cationic compound, and acts in a tridentate chelating fashion.

Acknowledgements

The author wishes to thank Dr. S.K. Aggarwal, Head, Fuel Chemistry Division and AD, RC&I Group and Dr. K.L. Ramakumar, Director, RC&I Group for their encouragements and supports.

References

1. T. Y. Shvareva, T. A. Sullens, T. C. Schehee, T. E. Albercht-Schmitt, *Inorg. Chem.* 44 (2005) 300 - 305.
2. T. Y. Shvareva, S. Skanthakumar, L. Soderholm, A. Clearfield, T. E. Albercht-Schmitt, *Chem. Matter.* 19 (2007) 132- 134.
3. C. S. Lee, S. I. Wang, K. H. Lii, *J. Am. Chem. Soc.* 131 (2009) 15116. C. H. Lin, K. H. Lii, *Angew. Chem. Int. Ed.* 47 (2008) 8711 -8713.
4. C. L. Cahill, D. T. de Lill, M. Frisch, *Cryst. Eng. Comm.* 9 (2007) 15- 26.
5. S. Wang, E. V. Alekseev, J. Ling, G. Liu, W. Depmeier, T. E. Albercht-Schmitt, *Chem. Matter.* 22(2010) 2155 - 2163.
6. S. Kannan, S. B. Deb, J. S. Gamare, M.G.B. Drew, *Polyhedron*, 27 (2008) 2557-2562.
7. S. Kannan, K. V. Chetty, V. Venugopal, M. G. B. Drew, *Dalton Trans.* (2004) 3604-3610.
8. S. Kannan, K. V. Chetty, M. G. B. Drew, *Polyhedron*, 26, (2007) 3810 -3816.
9. S. B. Deb, S. Kannan, J. S. Gamare, M.G. B. Drew, *Polyhedron*, 27(2009) 2673-2678.
10. D. Das, S. Kannan, D. K. Maity, M. G. B. Drew, *Inorg. Chem.* 51 (2012) 4869-4876.
11. S. Kannan, M. A. Moody, C. L. Barnes, P.B. Duval, *Inorg. Chem.* 47 (2008) 4691-4695.

BARC NEWSLETTER

THERMAL PLASMA TECHNOLOGY FOR SPECIALIZED DAE APPLICATIONS

P.V.Ananthapadmanabhan
L&PT Division

Dr. P.V. Ananthapadmanabhan is the recipient of the DAE Homi Bhabha Science & Technology Award for the year 2011

Abstract

Thermal plasma is a source of high temperature, reactive species such as radicals and ions and intense radiation. These unique properties of the plasma can be utilized to effect a variety of chemical reactions and metallurgical processes of industrial importance. Thermal plasma devices are widely employed for development of thermal and corrosion barrier coatings of aero-engine components and critical components for Nuclear and other advanced technological applications, synthesis of advanced materials and processing of minerals. The Laser & Plasma Technology Division has developed a complete R&D programme to meet the specialized requirements of the Indian nuclear fuel cycle requirements. This paper will cover some of the specific applications, where the process/product has been successfully deployed.

Introduction

Thermal plasma technology utilizes the high temperature and high enthalpy available in the plasma medium to effect a variety of chemical reactions and metallurgical processes of industrial importance. Thermal plasma technology has the capability to transcend the thermodynamic and kinetic barriers by opening up new reaction paths inconceivable in the conventional sense. This technology, which was until recently confined to the realms of the laboratory, is fast emerging as a major technique not only to provide surface engineering solutions to critical problems but also to synthesize novel materials and devise new processing routes.

Advantages of Plasma Processing

The high temperature, high enthalpy and fast quench rate that are characteristic of the process offer unlimited scope to synthesize new materials with improved properties. Temperature encountered in thermal plasma medium is 10,000-15,000 K compared to the maximum temperature of 3000K available in conventional

furnaces. This enables adoption of novel approaches to accomplish chemical reactions and metallurgical processes. The high temperature gas phase chemistry in the plasma promotes various chemical reactions at much faster rates than those possible by conventional means. The high quench rates, typically of the order of 10^5 - 10^7 K/s prevents recombination of the products and favours homogeneous nucleation leading to nano-sized products. Plasma processes are usually one-step processes capable of handling large throughputs.

A comprehensive programme on thermal plasma technology has been developed in our laboratory exclusively dedicated to meet the departmental requirements. This includes the development of plasma devices, development of ceramic and alloy coatings for DAE's strategic applications, plasma aerosol generation, reactive plasma processing for nano-synthesis and mineral processing. Some of these developmental studies and results will be focussed in this paper.

Thermal plasma generation

Thermal plasmas are partially ionized gases consisting of electrons, ions and neutral species. Plasma retains many of the properties of gases and behaves in conformance with the physical laws valid for gases; however, the specific properties of plasma that distinguish it from a hot gas become apparent in presence of a magnetic field, when the plasma acquires non-isotropic characteristics. The electrically charged particles present in the plasma are affected by externally applied electric and magnetic forces.

Thermal plasmas for laboratory and industrial applications are generated in plasmatrons or plasma torches, which are electro-thermal devices that convert electrical energy to thermal energy. Depending on the primary source, the device is classified as DC, AC or RF torch. The DC plasma sources are by far, the most extensively used plasma devices for technological and industrial applications.

A 40 kW DC arc plasma torch, schematic of which is shown in Fig. 1, has been developed in-house for surface engineering and material processing applications. It consists of a rod type cathode, made of thoriated tungsten and a copper nozzle-shaped anode that are water-cooled. The plasma gas is injected tangentially through a gas entry port located in the

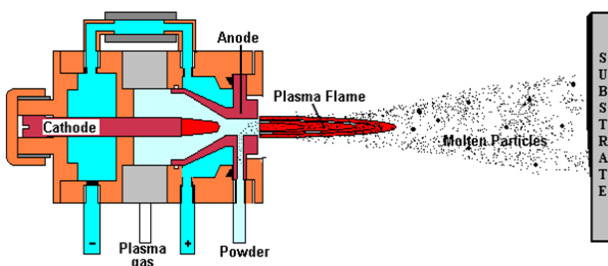


Fig. 1: Schematic of DC arc plasma torch

inter-electrode insulator module. When a gas is injected into the electrode gap and a DC arc is established between the electrodes, the plasma gas extracts energy from the arc and emerges out of the nozzle as a high temperature, high velocity jet. The temperature at the core of the plasma jet ranges between 10,000 K and 15,000 K. A thermal pinch effect is produced by the

joint action of the cold wall arc channel and the cold gas sheath around a very high-temperature conducting core (the arc column). This results in the thermal energy being highly concentrated with improved torch stability and efficiency. The high temperature high velocity plasma jet can be used for various applications including plasma spray deposition of alloys and ceramics, synthesis of nano-materials and conversion of minerals and industrial wastes to value-added products.

Corrosion and Thermal Barrier Coatings for Strategic DAE Applications

Plasma spray deposition

Plasma spray deposition is a surface engineering process that utilizes the high temperature and high enthalpy available in the thermal plasma jet for depositing metals, alloys and ceramics. Plasma spray deposition combines particle heating, melting and quenching in one single operation. The metal or ceramic powder to be deposited is injected into the plasma jet emerging out of a DC plasma torch. The powder particles, as they enter the plasma jet, are heated and melted and the molten droplets are accelerated to very high velocities¹ (exceeding 100 m/s). As these molten droplets strike the substrate surface, they flatten and get anchored to the surface irregularities to form an adherent coating. The coating builds up layer by layer. Compared to other surface engineering technique, the coating process is fast and the thickness can go from a few tens of microns to a few mm. Besides, the spraying technique does not impose any restriction on the work piece dimensions and large samples can be coated with minimum distortion of the substrate.

Simulation studies

In order to achieve high-quality deposits, it is imperative that a large fraction of the injected powder particles melt in the plasma jet and remain in the molten state at the instant they strike the substrate surface. This is decided by the dwelling time of the particle in the plasma and heat transfer from the plasma to the particle. These, in turn, depend on the temperature

BARC NEWSLETTER

and velocity profiles of the plasma gas, plasma gas properties such as thermal conductivity, density, viscosity, thermo-physical properties of the material to be coated, its particle size, etc. The relevant experimental factors that need to be optimized in order to achieve the above goal include the input power to the plasma, electro-thermal efficiency of the plasma torch, plasma gas flow rate, material feed rate, and torch-to-substrate distance.

Numerical process simulation has been carried out using two-dimensional and three-dimensional models to study plasma-particle interaction and its significance on plasma spray deposition. Simulations of plasma jet were carried out using in-house developed code and the temperature and the velocity distribution for the plasma jet obtained from this model were used to analyze the heat transfer and momentum transfer from the plasma to the particle. Fig. 2 shows the temperature and velocity profile in the plasma jet.

In thermal plasma spray, the velocity and the trajectory of an injected particle are mainly affected by viscous

drag force and the governing equation for momentum transfer between single spherical particle of mass m_p and the plasma gas can be written as

$$\frac{du_p}{dt} = \frac{3C_D\rho_g}{4\rho_p D_p} |u_g - u_p|^2 \quad (1)$$

In the above equation, u_p is the velocity of particle, C_D is the drag coefficient, D_p is the particle diameter, ρ_g is the plasma gas density and u_g is the plasma velocity. The equation describing the instantaneous rise in particle temperature is given by:

$$\frac{dT_p}{dt} = \frac{6(2+0.66Re^{0.5}Pr^{0.33})\bar{k}}{\rho_p C_p D_p^2} (T_g - T_p) \quad (2)$$

Equation (2) is solved to get the particle temperature profile in the plasma jet. In Equation (2), C_p is the specific heat of the material of the particle, T_p and T_g are the particle and plasma temperature respectively, \bar{k} is the thermal conductivity of the plasma, Re is the Reynolds number and Pr is the Prandtl Number. Reynolds number and Prandtl number are defined by equations (3) and (4).

$$Re = \frac{\bar{\rho}_g D_p |u_g - u_p|}{\bar{\eta}_g} \quad (3)$$

$$Pr = \frac{\bar{\eta}_g \bar{c}_{pg}}{k} \quad (4)$$

Simulation studies² were carried out to get the temperature and velocity profiles of the plasma jet to study the thermal behaviour of aluminium oxide, yttrium oxide and other ceramic materials with a view to optimize the deposition process. Results of simulation studies on the behaviour of yttrium oxide particles injected into the thermal plasma jet are summarized in Figs. 3. It is evident from the results that the plasma power, gas flow rate and particle size are the significant parameters that affect the particle temperature and velocity. Particle evaporation/dissociation is seen to be significant with increase in plasma power and decrease in the particle size. It is seen from Fig. 3 that at 30 kW and 42 SLPM of total argon flow, particles of 40 micron size or less reach the dissociation temperature of 4573K

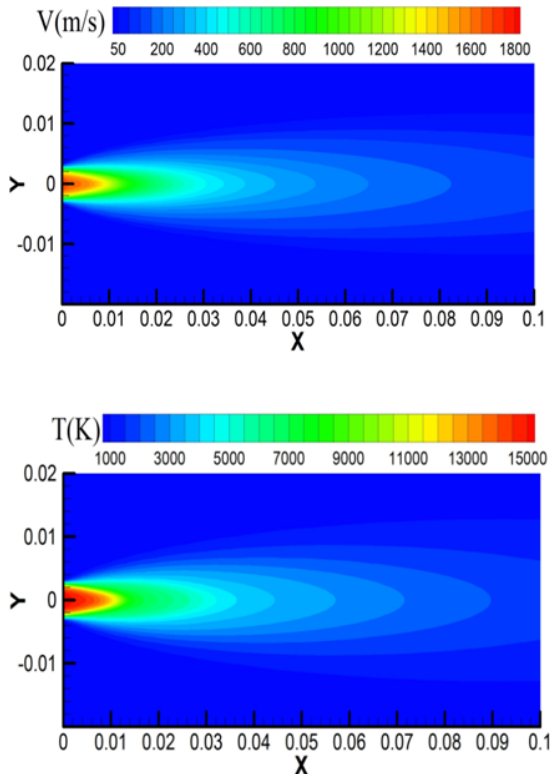
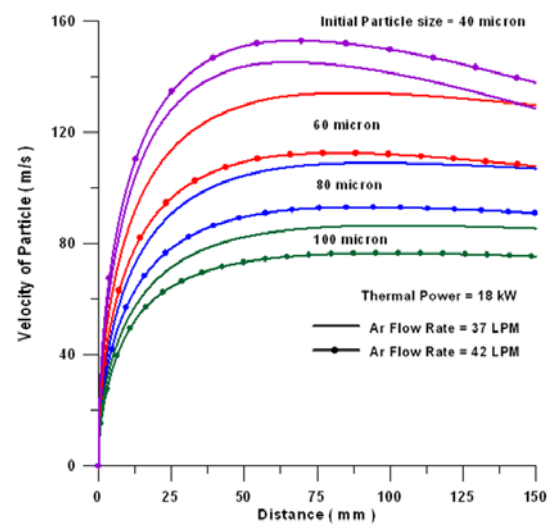
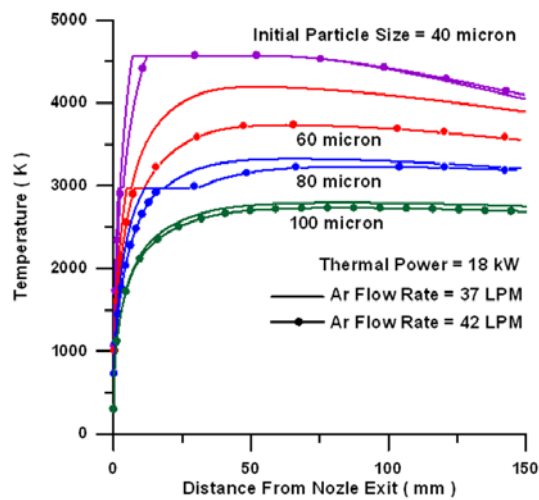


Fig.2: Velocity (left) and temperature (right) distribution in the plasma jet (30 kW, 42 LPM Ar + 3 LPM N₂)

BARC NEWSLETTER



and dissociate into yttrium and oxygen atoms. This problem becomes more severe at higher power levels and lower particle sizes. Particle temperature and velocity at various operating parameters obtained from simulation studies provided a window of parameters for process optimization. Experimental studies were then limited to the range of parameters within this window to optimize the process. Coating adhesion strength was used as the response parameter for process optimization, which was done by maximizing coating-substrate adhesion. For an average particle size of 60 micron, 25 kW input power is seen to be the optimum to get adherent yttrium oxide coatings with adhesion strength of about 8 MPa.

Aluminium oxide coatings

Plasma sprayed aluminium oxide coatings are extensively used for wear resistant and corrosion barrier applications. Plasma spray deposition of alumina on different substrates has been carried out and the coatings have been characterized for phase, microstructure, coating adhesion and thermal stability. The spray process was optimized by simulation as well as experimental studies to maximise coating adhesion. The major use of plasma spray-deposited alumina in DAE is as corrosion barrier on crucibles and moulds that handle molten uranium and other reactive metals. The developmental studies on alumina coatings have led to successful replacement of conventionally used high density imported graphite moulds used to cast uranium. The major drawbacks of the conventional

process included limited life of the moulds, carbon pick-up in the end product, high cost and reduced functional efficiency. These shortcomings could be overcome by providing a corrosion barrier coating of alumina on mild steel split moulds for casting uranium.

Mild steel split moulds of 75 mm internal diameter and 600 mm length, plasma spray-coated with aluminium oxide top coat and molybdenum undercoat, were used for casting uranium. The coatings were found adherent to the moulds even after repeated cyclic uranium casting operations clearly demonstrating the technological superiority as well as cost-effectiveness of the coatings over the conventional process. Fig. 4 shows aluminium oxide coated mild steel split moulds after 10 cycles of uranium-casting experiments. Subsequently, alumina coatings were used with nichrome bond coat as corrosion barrier on special moulds and related components used for casting

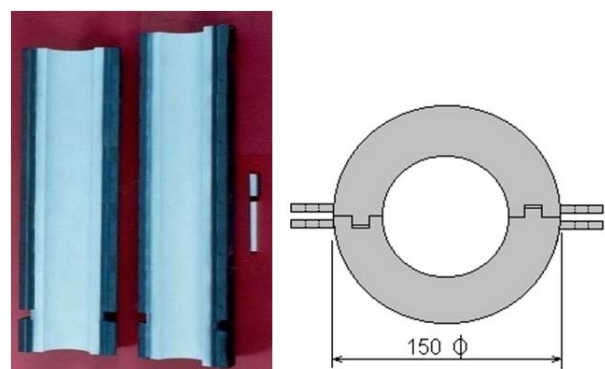


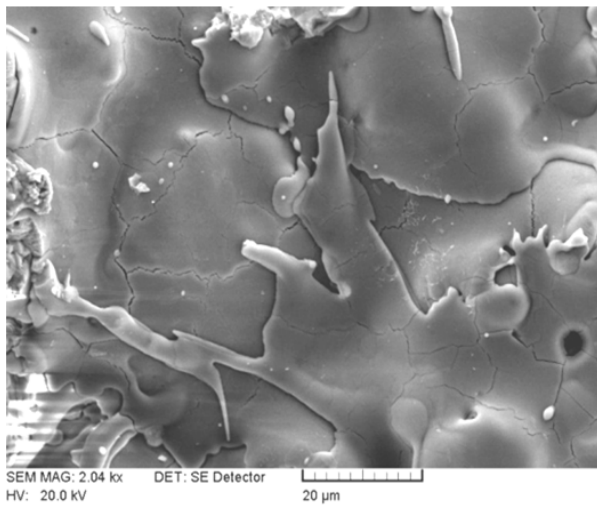
Fig. 4: Cross section of mild steel split mould and alumina-coated mould (75 mm dia x 600 mm long) after 10 U-castings

BARC NEWSLETTER

uranium and plutonium-bearing alloy shells for strategic applications.

Yttrium oxide and Rare earth phosphates

Yttrium oxide and rare earth phosphates coatings capable of handling molten actinides and their alloys for long duration containment have been developed and successfully deployed for corrosion barrier applications. The coating process was optimized based on simulation studies (discussed above) as well as experimental studies. Fig. 5 shows the SEM photographs depicting the morphological features and interface of samples deposited at different power levels. The microstructures of the coatings showed molten lamellae with micro-pores ranging from 1 micron to about 10 microns size. Increase in the plasma power resulted in decreased number of un-melted grains and



uranium. Yttria-coated graphite sample sandwiched between uranium pellets was used for DTA investigations. The DTA curve of the sample was recorded from 300K to 1473K in helium atmosphere. The DTA curve, depicted in Fig. 6, from room temperature to 1473K showed only DTA peaks characteristic of the phase changes in uranium metal indicating that the metal did not penetrate the coating and attacked the graphite substrate. It was also observed that molten uranium did not stick to the coating. The coated substrate was then subject to SEM/EDX analysis, which showed no detectable amount of uranium on the sample surface. The results clearly indicated that the coating offered effective protection to the substrate against corrosion by molten uranium. Long duration corrosion experiments were carried out at the UCUF facility of L&PT Division. Coupons with yttrium oxide coating on tantalum substrates without

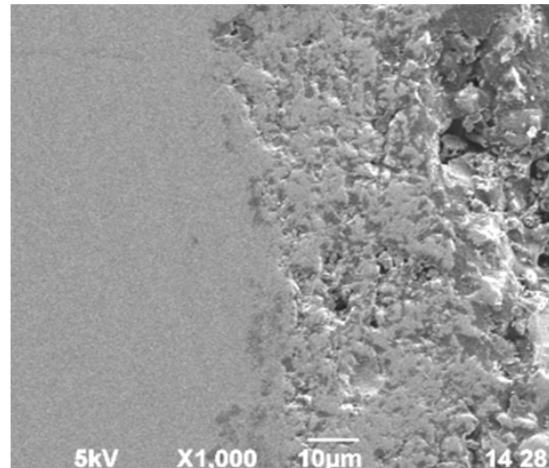


Fig. 5: SEM photograph of surface morphology and cross section of yttrium oxide deposited at 24 kW

reduced porosity level. The microstructure of the coatings deposited under optimized conditions showed fully molten grains having about 10% porosity and coating-interface adhesion strength of about 8 MPa. Thermal shock resistance of the coated samples was studied by quenching the heated samples from 1450 K to room temperature repeatedly. The samples showed excellent thermal stability withstanding more than 50 thermal cycles from 1450K to room temperature.

Differential thermal analysis (DTA) was used to assess the short-term resistance to corrosion by molten

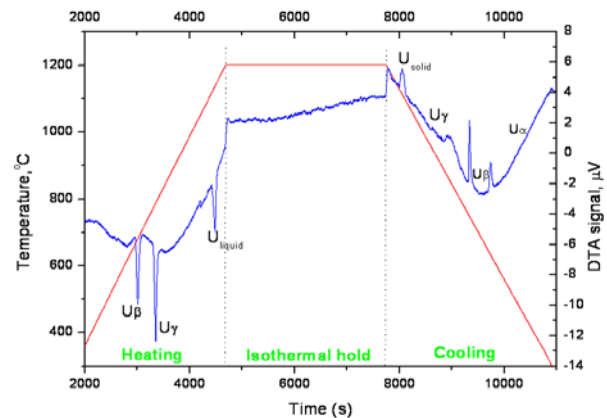


Fig. 6: DTA curve of Yttria-coated graphite-U reaction couple

BARC NEWSLETTER

bond coat were tested for compatibility against liquid uranium at 1573 K up to 800 h in vacuum. Yttrium oxide was deposited on tantalum coupons of 40 mmX 8 mmX 2mm dimension and used for the long-duration corrosion experiments. The coated specimens were partially immersed in a molten pool of uranium at 1573K and the coupons were analyzed after periodic time intervals. Optical microscopy and SEM/EDX investigations were done to evaluate the micro structural features of the coating after exposure to molten uranium. Experimental results showed that yttrium oxide coating exhibits excellent corrosion resistance against liquid uranium at 1573 K.

The process has been extended to coat molybdenum trays with yttrium oxide used to process U-Si alloys at MFD, BARC. The yttrium oxide coatings not only provided excellent protection to the molybdenum substrate but also ensured better purity of the product.

Plasma synthesis of nano-crystalline ceramic oxides

The high temperature vapour phase chemistry in the thermal plasma medium offers an attractive route for synthesis of nano-materials. The process offers flexibility in the choice of the reactants, which can be solids, liquids or gases. The plasma process has been successfully adapted to synthesize nano-crystalline aluminium oxide, titanium oxide and zirconium oxide by 'inflight' oxidation of the respective metal, or the hydride in the plasma jet. The process has also been extended to generate aerosols in large concentration.

In-flight Plasma reactor

Fig. 7 shows the schematic of the plasma reactor used for processing nano-crystalline oxide ceramics. The main components of the plasma reactor include a DC plasma generator, water-cooled reactor segment, product collection facility, DC power supply, cooling water system and exhaust gas vent. The anode and cathode of the plasma torch and the reactor are cooled by water. Powder injection into the plasma jet is facilitated through a side port provided at the anode of the plasma torch. There is provision to inject oxygen or any desired reactive gas downstream the plasma jet, 10 mm down

the nozzle, by means of a gas injector ring fitted on the torch head section. A mixture of argon and nitrogen was used as the plasma-forming gas. The powder feed rate and carrier gas flow rate were monitored and controlled. The experimental run consisted in establishing a stable arc between the electrodes. The plasma was initiated by striking a DC arc between the cathode and anode of the plasma torch. The plasma gas (Ar-N₂ mixture), injected in the inter-electrode region, extracts the energy from the DC arc and emerges out of the torch as a high temperature high velocity jet. Desired power level was maintained by controlling the flow rates of the plasma gases and arc current.



Fig. 7: 40 kW plasma reactor for nano-material synthesis

Synthesis of nano-crystalline aluminium oxide

Aluminium metal powder (40-100 micron) was used as the starting material to synthesize alumina powder. The powder was injected into the plasma jet by using argon as the carrier gas. Oxygen gas was introduced 10 mm downstream of the exit of the plasma torch. Aluminium metal melts in the plasma jet and reacts with oxygen gas downstream to form the oxide. Oxidation of aluminium to alumina is highly exothermic, the standard enthalpy of formation of aluminium oxide from the elements being $-1675.7 \pm 1.2 \text{ KJ mol}^{-1}$. The enthalpy of formation increases with temperature and is $-2243.73 \text{ kJ mol}^{-1}$ at 3000 K. The heat released during oxidation, coupled with the high temperature in the plasma medium leads to the dissociation of aluminium oxide to gaseous sub-oxides of aluminium, aluminium

vapor and oxygen, which recombine (below 3000K) to form nano-sized clusters of the meta-stable phase of alumina³. X-ray diffraction of the synthesized nano powders confirmed the presence of the meta-stable γ -phase. The thermodynamically stable α -phase of Al_2O_3 was not present. The TEM images of aluminium oxide showed that the particle size ranges from a few nanometers to 30 nm.

Synthesis of nano-crystalline titanium oxide

TiH_2 powder and ZrH_2 powder of 99.8% pure were used as the precursor materials to synthesize titania and zirconia respectively. The mechanism of formation of nano-titania and nano-zirconia is also similar to that of alumina. TiH_2 and ZrH_2 dissociate to form the metal particles and hydrogen gas in the plasma jet that are subsequently converted to the oxide and water vapour, which escapes along with the exhaust gas stream. The energy released during the oxidation of the metal heats up the oxide to temperatures above their dissociation temperatures to form the gaseous sub-oxides, metal vapour and oxygen, which recombine further down the reactor to form nano-clusters consisting predominantly of the meta-stable phase.

The nano-titania powder was seen to consist predominantly of the anatase phase admixed with minor amount of the rutile phase. Fig. 8 shows the photograph of nano-sized titanium powder on the reactor walls and its TEM image. Spherical morphology with the particles distributed in the range of a few nanometers to about 30 nm is evident from the figure. It was also observed that the particles collected from the reactor regions near the plasma source were coarser than those collected from regions farther from the torch head section. The phase composition of powder

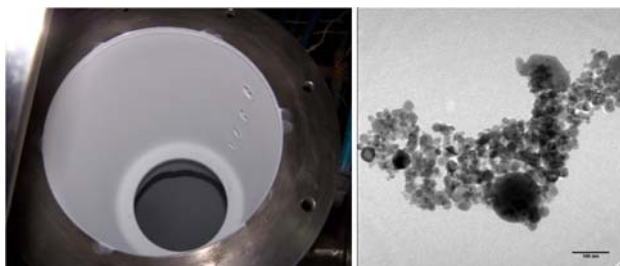


Fig. 8: Nano-crystalline titanium oxide on the reactor wall and TEM of the powder

fractions collected from different regions showed that the anatase phase is favoured as the particle size decreased below 20 microns.

Investigations on the photocatalytic properties of the plasma-synthesized nano-titania powder were followed by studying the degradation of methylene blue under ultraviolet (UV) radiation. The synthesized titania powder was dispersed in aqueous solution of methylene blue dye and was irradiated with UV light in a chamber while the suspension was kept under stirring. The degradation of the dye was monitored at different time intervals using UV-visible spectrophotometer. Concentration of residual methylene blue after irradiation is shown in Fig. 9, which indicates the reduction of methylene blue with respect to time of

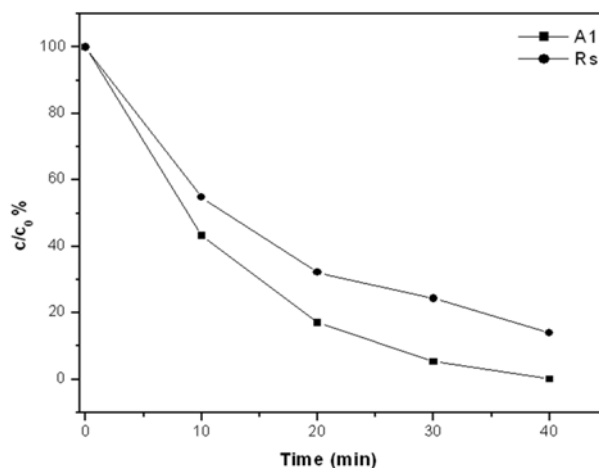


Fig. 9: Kinetics of photo-degradation of methylene blue A1: plasma-synthesized and R_s standard photo-catalytic titania powder

exposure. The photocatalytic activity of the plasma synthesized powder was compared with that of commercially available standard titanium oxide powder. It is observed that the photocatalytic activity of the plasma-synthesized nano-titania is superior to that of commercially available photocatalytic titania powder⁴. Although the phase structure and particle size of the plasma synthesized powder and the standard titania powder were similar, the superior catalytic activity of the former is attributed to larger number of surface Ti^{+3} sites, which are introduced by virtue of the reducing atmosphere in the plasma jet.

Research activities on plasma synthesis of nano-materials have led to the development of a prototype

BARC NEWSLETTER

plasma aerosol generator for generation and study of aerosols of various materials of relevance in the nuclear industry. High levels of aerosol generation rate and output concentration suitable for nuclear simulation studies could be obtained by the plasma aerosol generator.

Plasma processing of zircon

The application of reactive plasma synthesis to processing of minerals is exemplified by plasma dissociation of zircon to zirconium oxide and silicon dioxide. Plasma dissociation of zircon to zirconia offers certain unique advantages compared to conventional processing. Conventionally, zircon sand is mixed with sodium hydroxide and heated to about 1273K to convert zircon to sodium silicate and zirconia, followed by separating the zirconium oxide and drying. However, the process yields a product admixed with un-reacted zircon. Further, the secondary chemical treatment involves large quantities of effluent waste.

The plasma method, on the other hand, offers a convenient one-step process to produce zirconium oxide by in-flight dissociation of zircon with simultaneous removal of silica. The principle involves heating zircon sand in the plasma jet to a temperature above 1900 K, when it spontaneously dissociates into zirconium oxide and silicon dioxide. As the plasma dissociated product exits the plasma jet, it is rapidly

quenched ($\sim 10^5$ K/S), preventing recombination of the oxides to the form zircon.

The experimental system consists of a central hollow graphite cathode, (15 mm OD and 70 mm long) and a graphite anode, 20 mm ID and 100 mm long. Zircon sand is fed centrally through the cathode. The unique feature of the process is that it uses air as the working gas to generate the thermal plasma. Dissociation was carried out over 10-25 kW power range. X-ray powder diffraction, scanning electron microscope and wet chemical analysis were used to characterize the product and determine the extent of dissociation. X-ray diffraction patterns of plasma-dissociated zircon in air plasma medium at different input power levels are shown in Fig. 10. It is seen from the figure that the percentage of dissociation increases with increasing torch power. Complete dissociation could be achieved at 25 Kw⁵. Increasing torch power increases the plasma temperature leading to increased heat transfer from the plasma to the particles, thus leading to higher degree of dissociation.

Degree of dissociation was estimated by chemical method by treating the dissociated zircon with 50% solution of sodium hydroxide to leach out free silica. Results showed that at 25 kW, more than 90% of zircon could be dissociated with more than 60 % removal of silica as SiO gas. Experiments carried out with a mixture of carbon and zircon sand resulted in zirconium dioxide

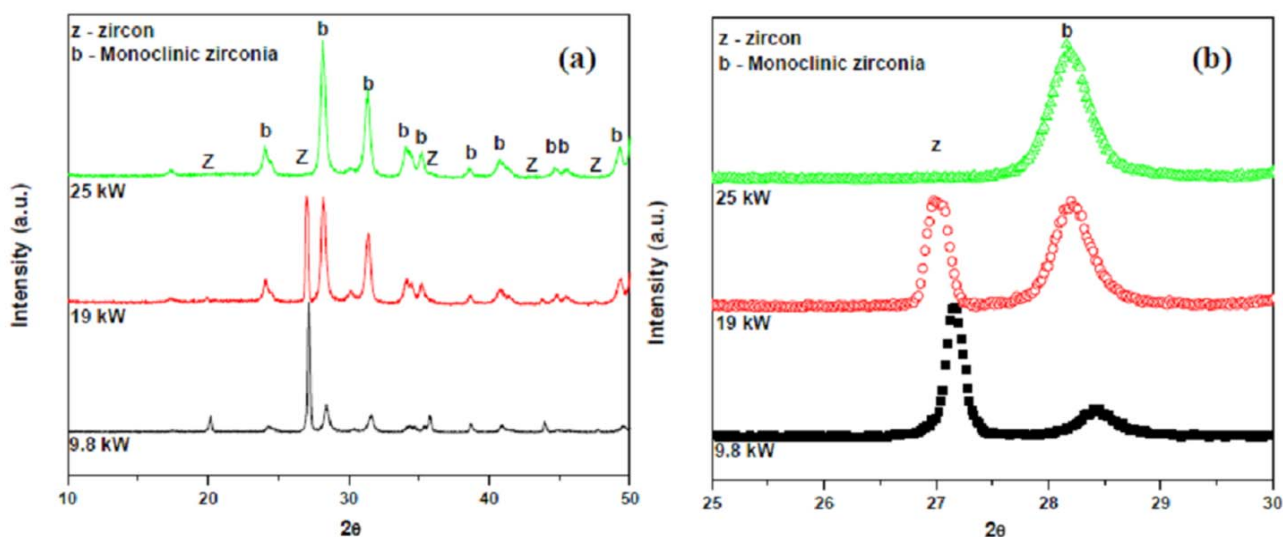


Fig. 10: X-ray diffraction results of plasma dissociated zircon (Power: 9.8, 19 and 25 kW Air flow:12 LPM)

BARC NEWSLETTER

free of silica. The addition of carbon helps in the reduction of SiO_2 by carbon to gaseous SiO which escapes with the exhaust stream. The addition of carbon enhances the dissociation reaction due to favourable thermo-chemical effect, involving the formation of CO , CO_2 and SiO . By adding the appropriate amount of carbon to zircon, complete removal of silica as SiO gas was possible at 20 kW.

The present studies have considerable technological implications. The use of air as the plasma-forming processing gas would lead to significant cost savings. Further, the possibility to remove silica in-flight is an added benefit, leading to additional cost benefits.

Conclusion

A summary of research activities on thermal plasma science and technology directed towards the Indian Nuclear fuel cycle applications has been presented in this article. The ceramic coatings developed could be successfully deployed for strategic DAE applications. Research developments on innovative nano-synthesis culminated in the development of plasma aerosol generator and studies on plasma processing of minerals resulted in a lab-scale one-step process for producing zirconium oxide.

Acknowledgements

I thank Dr. L.M. Gantayet, Director, BTDG, BARC and Dr. A.K. Das, Head L&PTD, BARC for their

encouragement and support. I sincerely thank all my colleagues associated in this work, in particular, Dr.T.K. Thiyagarajan, Mr.Y. Chakravarthy and Mr. A. Nagaraj.

References

1. R.B. Heimann, Plasma-Spray Coating-Principles and Applications, New York, VCH Publishers Inc. 1996.
2. T.K. Thiyagarajan, P. V. Ananthapadmanabhan, K. P. Sreekumar, Y. Chakravarthy, A.K. Das, L.M. Gantayet, B. Selvan and K. Ramachandran, Experimental and simulation approach to plasma spray deposition of yttrium oxide, *Surface Engineering*, 28(9), (2012):646-56.
3. P.V. Ananthapadmanabhan, T.K. Thiyagarajan, K.P. Sreekumar, N. Venkatramani, Formation of nano-sized alumina by in-flight oxidation of aluminium powder in a thermal plasma reactor, *Scripta Materialia*, 50 (2004): 143–147.
4. M. Vijay, V.Selvarajan, K.P. Sreekumar, JiaguoYu, ShengweiLiu, P.V. Ananthapadmanabhan, Characterization and visible light photocatalytic properties of nanocrystalline TiO_2 synthesized by reactive plasma processing, *Solar Energy Materials & Solar Cells*, 93, (2009):1540-49.
5. S. Yugeswaran, P.V. Ananthapadmanabhan, T.K. Thiyagarajan, V. Selvarajan, and Janardhanan Nair, Inflight dissociation of zircon in air plasma, *IOP Journal of Physics: Conference Series* 208 (2010): 012122.

BARC NEWSLETTER

TECHNOLOGY DEVELOPMENT PROGRAMME IN PULSE ELECTRON ACCELERATORS AND UTILISATION IN COMPACT HPM SOURCES

Archana Sharma

Accelerator and Pulse Power Division, Beam Technology Development Group

Dr. Archana Sharma is the recipient of the DAE Homi Bhabha Science & Technology Award for the year 2011

Abstract

This work involves the design and development of high intensity pulsed power systems from multi MW to GW capacity, single shot to repetitive shots and devices for high power microwave (HPM) generation. These systems are ready for deployment to various users in defence, electronic industries and test laboratories. The techniques of generating high pulsed power needs a critical optimization of high voltage and low inductance, fast switching and fast recovery, efficient conversion from electrical power to electron beam pulsed power. It is also critical to match the frequency and power of microwave pulses to get coupled effectively with electronics circuitry and create temporal/operational or permanent damage depending on their circuit configuration frequency and threshold electric field. Keeping these strategic and industrial applications as target, a variety of pulsed power systems have been developed viz. KALI series, LIA series and UWB sources.

Introduction

The pulsed power program has been started in BARC since 1970s, it was developed for fusion related research (till 1980s) and then focus was shifted to NEMP (nuclear electro- magnetic pulse) simulation, hardening and surge suppression. Pulse power systems were developed for generation of high power microwave and Flash X-rays for strategic applications. Power capability was increased from 0.5GW in KALI-75 to 30GW in KALI-30GW systems where KALI stands for Kilo Ampere

Linear Injector. During 1990s, in association with DRDO development of compact and mobile system with repetitive pulsed output and systems like Linear Induction Accelerator (LIA-200) was taken up. Later Pulsed power developments include repetitive 1kJ Marx system and LIA-400 were also developed.

In last four decades various technologies and high energy pulsed power systems have been developed indigenously. It includes design and development of marx generator, tesla transformer, pulse forming line,

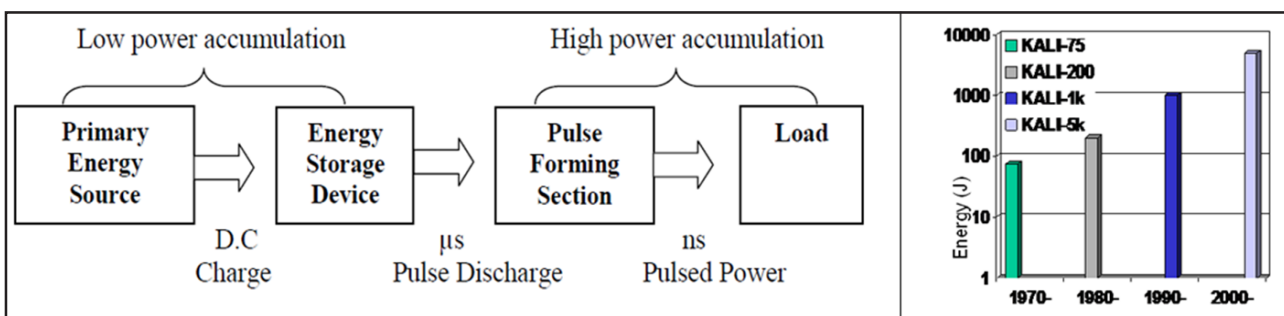


Fig.1: Block Diagram of Pulsed power Systems and year wise growth

BARC NEWSLETTER

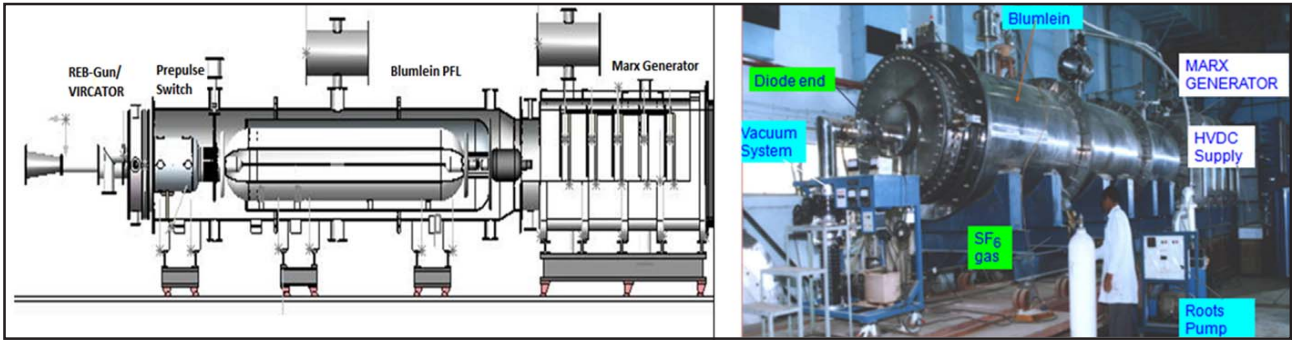


Fig.2: Schematic and Photograph of KALI-5000

blumlein, fast acting sparkgap switches, magnetic pulse compression, solid state modulators and relativistic electron beam diodes. These systems have been demonstrated to its full capacity from single shot to repetitive operation and utilized for the generation of high power microwaves (HPM) and flash X-rays. In this paper a few developed systems are described based on different topology for compact HPM sources successfully and operational as milestones of this long and uninterrupted technical path of achievements.

The essence of pulsed power system is to convert slow charging pulse into fast discharging pulse such that peak power increases manifold. This can be achieved using various techniques of energy storage and power transition switches.

A few Marx based systems were developed as described below:

KALI-5000

For multi gigawatt peak output power, Marx generator based systems are developed, where capacitors are charged in parallel and discharged in series for single shot system operation it can be resistive charging but for repetitive pulsed power system it is inductive charging based system. To reduce the no. of charging stages and sparkgap switches, bipolar charging is utilized. To have control of different operating output

parameters, pressurised sparkgaps are used to vary its breakdown voltage in the sparkgap switches, by changing gas pressure. Thus KALI-5000 system was developed using hybrid insulated Marx generator (gas in the switches and transformer oil for the rest assembly) was developed. It has castor oil filled Blumlein type pulse forming line with prepulse switch along with charging inductor and REB gun. Typical output and photograph of the system is shown in Fig. 2.

It was used for generating high power microwaves (HPM), and Flash X-rays generations with suitable diagnostics. Experiments were conducted with 300-600kV designed Axial and Coaxial vircators (Virtual Cathode Oscillators) using this system as shown in Fig.3, and HPM signals were measured and characterised.

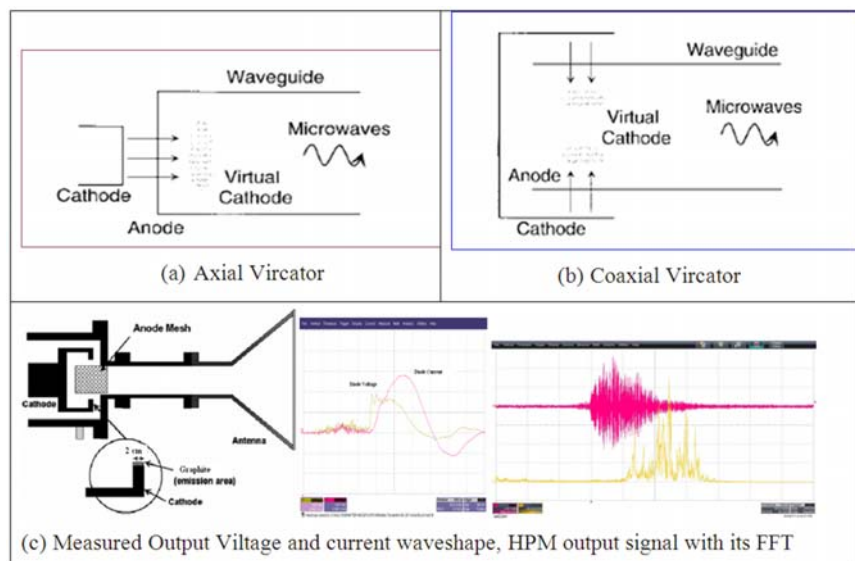


Fig.3: Typical Vircator assembly and Pulsed output signals with KALI-5000

BARC NEWSLETTER

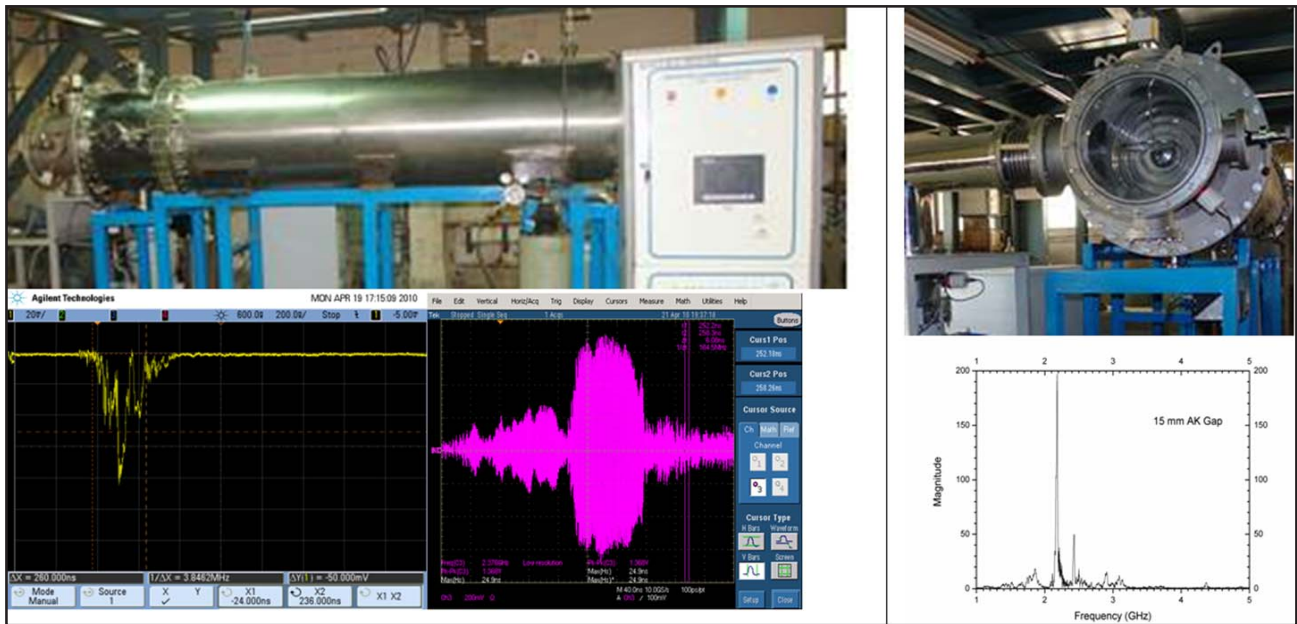


Fig. 4: (a) Photograph of the 1kJ Marx system (b) with Reflex triode assembly (c) and output waveshapes of HPM power (d), filed and frequency

At this output power capacity (>10GW), weight, size and replate are limited to make it a static system for hardening and development of diagnostics etc.

Replate 1kJ Marx System

In order to make the Marx based system compact and repeatable, high pressure gas filled repetitive marx generator was developed using inductive charging viz. 1kJ Replate Marx generator has characteristic impedance of ~ 25 ohms. Instead of using axial or coaxial vircators in this system, a new type of HPM device namely reflex triode was designed and developed for HPM generation directly fed by Marx source. There was no PFL used in this system except a peaking gap after the Marx generator to make the system compact. This system has positive output for anode mesh and cathode is at ground potential. Typical results and system details are given in Fig.4.

This system is quite user friendly due to gaseous insulation and compact assembly it is mobile also. The system was used for HPM characterisation and Intentional Electromagnetic Interference (EMI) studies on Electronics circuitry viz. Susceptibility threshold, hardening techniques etc.

Linear Induction Accelerator (LIA)

In order to make the high voltage pulsed power system operation at higher repetition rate, switching is performed by magnetic pulse compression switches and no sparkgaps are used. This switches are made with special toroidal cores having square B-H characteristics with large permeability and low coercive force at high pulse frequency. APPD, BTDG has developed two such systems as described below.

LIA-200 is a repetitive pulsed power system rated for 200kV, 5kA, 100ns, 100Hz. A solid state modulator was used to charge this system and circuit schematic and photograph of this system is shown in Fig.5. Here, 3-stage Induction cavities are used in Linear Inductive Adder configuration using DM-water capacitors (10nF, 200kV) and water PFL. Russian cores were procured for 2-pulse transformers, 4-magnetic switches and 3-stage induction cavities. This system was developed for the technology demonstration of new replate techniques based on magnetic elements and operated to full rated capacity (LIA-200) as shown in Fig.5.

Challenges involved in this development program was to make magnetic cores saturate at desired volt-time

BARC NEWSLETTER

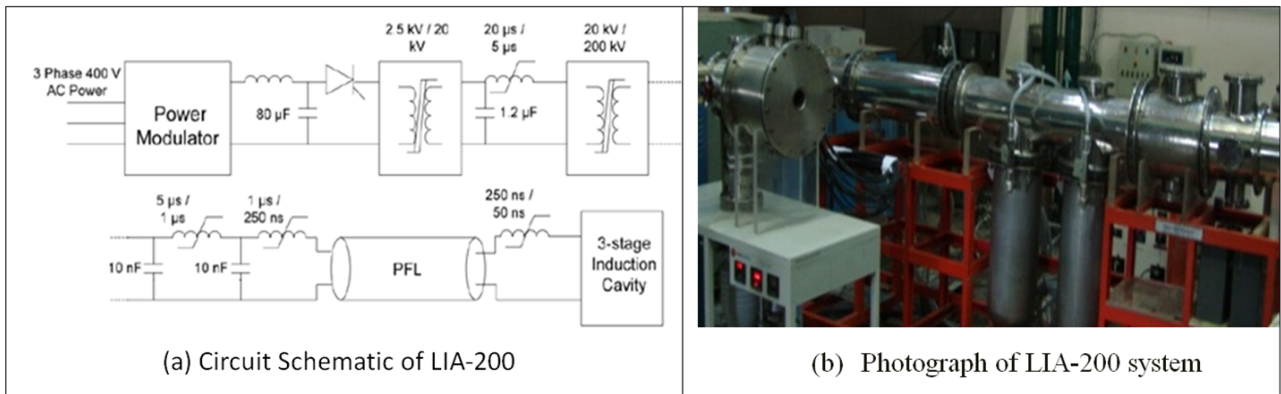


Fig.5: Electrical Circuit (a) and Photograph (b) of LIA-200(200kV,5kA,100ns,100Hz)

level, reset them before the arrival of next pulse, thermal management over 100Hz. The amorphous cores were tested for its characteristic parameters under pulse excitation such as core loss, change in permeability and total flux swing. The size and shape of the oil/vacuum

interface insulators was optimised between core based induction cavities to mitigate any flashover under 100ns pulses in 100Hz replate. Water capacitors were designed for the first time to store energy at 200kV with low inductance at 10nF capacity. Water PFL was

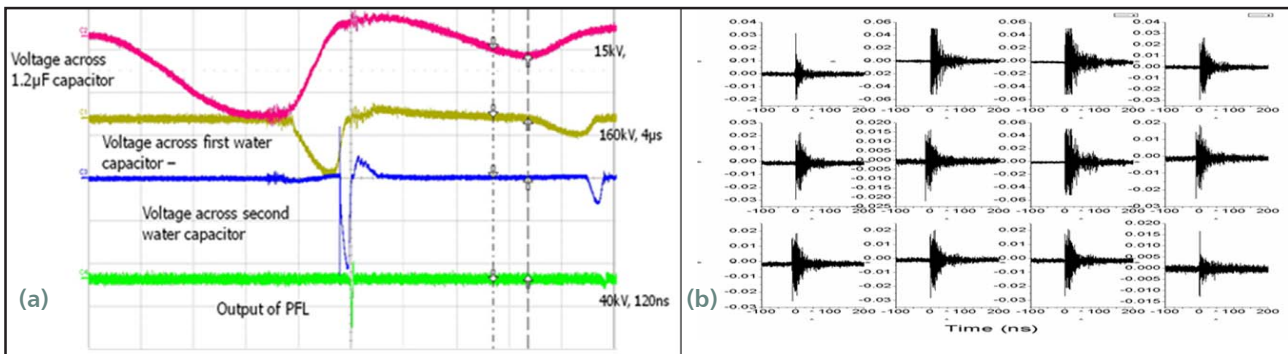


Fig.6: Typical output of LIA-200 at various MPC stages (a) and HPM output @30Hz, 160kV, 12 shots (b) from B-dot probe

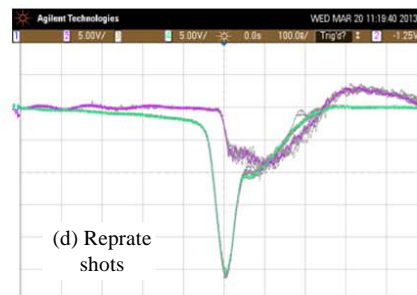
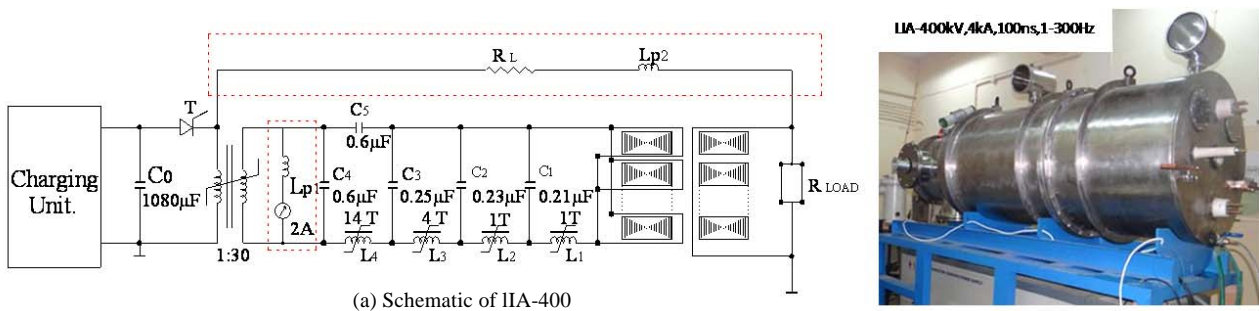


Fig. 7: Schematic (a) and Photograph (b) of LIA-400 with output waveshape in single shot (c) and 100Hz operation (d) for REB generation

BARC NEWSLETTER

Pulse Power System	Diode Voltage (kV)	Diode Current (kA)	A-K Gap (mm)	HPM Device	Microwave Peak power @window (MW)	E-field @10m from window	HPM frequency (GHz)
KALI-1k	250	12	6	Axial Vircator	87	5.1	4-6.6
KALI-5k	300	20	12.5	Coaxial Vircator	26	2.8	2.8
KALI-5k	300	15	12	Reflex Triode	43	3.6	6.5
1kJ Marx	200	4	15	Reflex Triode	100	5.3	2.2-4
IES-1	300	10	15	Reflex Triode	—	7@3m	0.9 & 2.6

also used to shape the output pulse followed by a core based sharpening switch. The typical output of this system is shown in Fig.6 at various stages of pulse compression by magnetic switching. Pulse compression gain (T_2/T_1) was maintained at 3-4 to optimise the core volume (core volume \propto gain²).

The enabling technology with this systems (LIA-200) were magnetic switching, reset techniques, induction cavities adder configuration, fast charging CCPS, core characterisation, surface flashover phenomenon in oil/vacuum interface and toroidal pulse transformer. Based on these experience another system was designed (LIA-400) and successfully developed. Core based elements in this system were jointly developed under BARC-Russia Collaboration. It is also completed in stipulated time period as shown in Fig.7.

Overall systems developed in APPD, BTDG are deployable for various HPM and UWB irradiation to see the effect of high frequency impulse electric and magnetic field coupling with sensitive electronics circuitry, their susceptibility level and hardening techniques

Acknowledgement

I extend heartfelt gratefulness to Dr.P.H.Ron, pioneer of this programme. I also want to acknowledge the encouragement and support given by Dr.L.M.Gantayet, Director, BTDG. My sincere thanks to Dr.K.C.Mittal, Head, APPD, Shri. D.P.Chakravarthy, Dr.K.V.Nagesh and Dr. A.K.Ray for valuable guidance. Lastly all APPD colleagues are gratefully acknowledged for their cooperation.

BARC NEWSLETTER

ANOMALOUS ENERGY ABSORPTION BY ATOMIC AND MOLECULAR CLUSTERS INTERACTING WITH LASER RADIATION: EXPERIMENTS LEADING TO THEORETICAL ADVANCES

R.K. Vatsa
Chemistry Division

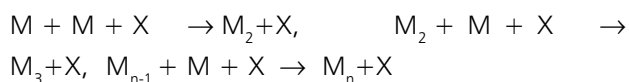
Dr. R.K. Vatsa is the recipient of the DAE Homi Bhabha Science & Technology Award for the year 2011

Starting from the discovery of photo-electric effect by Heinrich Hertz in 1887, interaction of radiation with matter continues to be a topic of research for the last 125 years. The invention of coherent, high intensity laser radiation by Theodore Maiman on May 16th, 1960 [1] provided a very powerful tool in the hands of researchers to study the matter in greater depth and advance their understanding about the optical properties and hence electronic structure. The interaction of laser pulses with isolated atoms/molecules is well understood now [2]. Another form of matter is clusters where a certain number of atoms or molecules are weakly attached to each other. Clusters can be defined as a collection of finite number of atoms or molecules ranging from dimer (consisting of only two atoms) to large clusters made of thousands of atoms. Atomic and molecular clusters are of great interest in physics and chemistry [3], since they exhibit properties intermediate between gas phase and condensed phase (high density of particles). Essentially clusters represent a bridge between isolated atoms and infinite solid. In addition, clusters in gas phase provide nano environment for investigating phenomena in which collective processes or interactions with neighbours begin to play a relevant role which are absent in isolated atoms/molecules.

Generation of Clusters

Neutral clusters in gas phase are generally not available in equilibrium systems and need to be prepared *in-situ*. The expansion of gases through a small nozzle into

vacuum provides a very convenient and often used method for generating neutral clusters of atoms and molecules in the gas phase. The basic process involves adiabatic expansion of a gas (or a gas mixture) at high stagnation pressure (P_0) through a small orifice of diameter D into an evacuated volume having pressure in the range of 10^{-6} – 10^{-5} Torr. In such a system, the gas flow is continuous and particles undergo a large number of collisions while passing through the small orifice during the flow period. Expansion converts random motion into directed flow, thus reducing translation, rotational and vibrational temperature to few Kelvin. Extremely low temperatures coupled with high number density lead to nucleation and condensation. During their initial growth, the dimer and trimer are formed via a third body assisted exoergic association reaction as shown below.



The excess energy is removed by the third body in the form of kinetic energy. Dimer acts as site of further growth and condensation. For the later growth steps, leading to formation of tetramer onwards, need for the third body is less since the exoergic energy can be soaked up by the cluster itself particularly so when many vibrational degrees of freedom are available to act as the sink. Under such conditions, it is difficult to define and measure temperature for an individual cluster. If the clustering is negligible, temperature is generally low. But since cluster formation is exothermic, it causes an

BARC NEWSLETTER

increase in temperature. As a result of this, internal energy increases with each subsequent added atom. The nascent clusters could be very hot in heavily clustered systems.

The degree of cluster formation can be controlled by changing the nozzle diameter, stagnation pressure and initial gas temperature. Condensation evolves through statistical process and the size of clusters is distributed around a mean value for a given set of experimental conditions. It is therefore difficult to obtain narrow size cluster distribution unless some specifically devised conditions are employed. This type of setup, employing supersonic expansion, allows production and study of rare gas clusters (Ar_n , Kr_n , Xe_n) as well as molecular clusters ($(\text{H}_2\text{O})_n$, $(\text{CH}_3\text{I})_n$ etc). Depending on whether a pure gas or a gas mixture is expanded, one may get pure or mixed clusters. In the case of pure rare gases, average cluster size can be estimated using the empirical formula of Hagena [4,5]. The dimensionless Hagena parameter (Γ^*), which gives an idea about the rate of condensation, is expressed as-

$$\Gamma^* = k \frac{(d / \tan \alpha)^{0.85}}{T_0^{2.29}} P_0 \quad (1)$$

where d is the nozzle diameter (mm), α the expansion half angle ($\alpha=45^\circ$ for sonic nozzles, $\alpha < 45^\circ$ for supersonic nozzles), P_0 the stagnation pressure (mbar), T_0 the pre-expansion temperature (Kelvin) and k a constant related to the bond formation. The k values for some inert and common gases are given below. The table simply shows that higher the k value, easier is for the gas to form clusters. Thus, Xe will form clusters $(\text{Xe})_n$ even at low P_0 value as compared to Ne for the same value of P_0 .

The average size of the cluster in terms of the number of atoms per cluster can be written as

$$N_c \cong 33 \left[\frac{\Gamma^*}{1000} \right]^{2.35} \quad (\Gamma^* \leq 10^4) \quad (2)$$

Gas	He	H ₂	N ₂	O ₂	Ne	Ar	Kr	Xe
K	3.9	184	528	1400	185	1650	2890	5500

$$N_c \cong 100 \left[\frac{\Gamma^*}{1000} \right]^{1.8} \quad (\Gamma^* > 10^4) \quad (3)$$

Interaction of a cluster with laser radiation

Interaction of intense laser pulses (intensity $\sim 10^{15}$ Watts/cm²) with atoms and molecules has led to discovery of several interesting phenomena like production of multiply charged atomic ions, generation of extreme UV and X-ray radiations and above-threshold ionization [6-10]. These studies are motivated by the desire to generate particles (photons, electrons and ions) with energies much larger than the energy of single laser photon. As mentioned earlier, clusters due to their intermediate size, between individual molecule and bulk solid, possess advantages of both these media and hence are ideal targets for high intensity laser studies. Clusters when exposed to intense laser pulses lead to several interesting phenomenon including Coulomb explosion which is nothing but fast explosion of matter/plasma due to enormous Coulombic repulsive forces. Coulomb explosion process in clusters is initiated by photoionization of cluster by the early portion of the laser pulse. The resultant electrons, produced by photoionisation of cluster, are collisionally heated by the remaining portion of the pulse, which in turn further ionize the atoms of the cluster through electron impact ionization causing the components of the cluster to become highly charged. The highly charged cluster then experiences Coulomb repulsion. During repeated ionization, a stage comes when the Coulomb repulsive forces between highly charged constituents exceed the total cohesive energy of the cluster, at this stage the cluster explodes. As a result, multiply charged atomic ions with substantial kinetic energy are ejected following Coulomb explosion of clusters. Change of ionization wavelength in the high intensity experiments did not change the results much. Thus, observation of multiply charged species in these high intensity experiments was rationalized based on optical field

BARC NEWSLETTER

ionization mechanism. The electric field associated with the high intensity optical pulse is given by the equation

$$E \text{ (V/cm)} = 27.5 (I)^{1/2} \quad (4)$$

where I is intensity of the laser pulse (in Watts/cm²) at the point of interaction. For an intensity of $\sim 10^{15}$ Watts/cm², the electric field is (10^9 V/cm) which is very large. This high field pulls several electrons from the molecule/cluster and causes multiple ionization which then leads to Coulomb explosion of the system being studied.

Till recently, Coulomb explosion was reported at laser intensities of $>10^{13}$ W/cm² irrespective of the wavelength used. Few years ago, our group at BARC as well as a group from abroad reported Coulomb explosion phenomenon in clusters using laser pulses of intensity $\sim 10^9$ W/cm² (million times less than previously reported) and convincingly demonstrated that it is not necessary to use very high intensities for generation of highly charged energetic ions and electrons [11-13]. The electric field associated with gigawatt laser pulse is almost three orders of magnitude lower (10^6 V/cm) than that required for ionization of atoms/molecules. Therefore, possibility of field ionization can be excluded at such low intensity and multiphoton ionization of cluster following coherent

absorption of 4-5 photons is the most obvious mechanism. Based on the energy conservation, the coherent absorption of 4-5 photons will give rise to singly ionized species. However, generation of highly charged species with large kinetic energies (as reported in ref. 11-13) requires simultaneous absorption of large number of photons (100-1000), which is not possible at an intensity of $\sim 10^9$ W/cm². Therefore, any mechanism entirely based on multiphoton ionization process can't explain generation of multiply charged atomic ions at such low intensity. To unravel the mechanism which leads to generation of multiply charged atomic ions, different atomic and molecular cluster systems were studied. Important results of these investigations are given below. In our experiments, clusters were generated via supersonic expansion of pure gases or by flushing Argon at high pressure (1-6 bar) through the liquid sample (CH_3I , CH_3COCH_3 , $\text{C}_2\text{H}_5\text{Br}$). A pulse valve with 800 μm nozzle diameter and 350 μs pulse duration was used for generation of cluster in the expansion chamber. The supersonic jet produced in this way was skimmed at a distance of 5 cm from the nozzle and allowed to enter into ionization chamber where clusters were ionized by 266, 355 or 532 nm radiation of a pulsed Nd:YAG nanosecond laser. The ions generated were accelerated by applying electrostatic fields and guided into a 100 cm field-free



Fig. 1: Experimental setup for in-situ generation and photoionisation studies of cluster (indigenously designed and fabricated at BARC)

BARC NEWSLETTER

region of home built time-of-flight mass spectrometer based on Wiley–McLaren ion optics and detected using a Channel Electron Multiplier (CEM). The mass resolution of the instrument is ~ 300 . A photograph of the experimental setup indigenously designed and fabricated at BARC is shown below [14].

Generation of Xe^{+10} in photoionisation of Xenon clusters (Xe_n) by nanosecond laser pulses

Fig. 2 (a) represents time-of-flight mass spectrum (after converting into m/z) of xenon clusters photo-ionized with 266 nm laser pulses (intensity $\sim 5 \times 10^9$ W/cm²). The spectrum depicts generation of multiply charged atomic ions of xenon up to +3 state at 266 nm. Under similar experimental conditions, on changing the photoionisation wavelength to 355 nm, the highest observed charge state of xenon ions increased to +6. (Fig. 2 b), while for the case of 532 nm, generation of multiply charged xenon ions up to +10 (Fig. 2 c) was observed. As far as extent of multiple charge state formation is concerned, from these studies it can be concluded that for a given intensity, the laser-cluster interaction is most efficient at 532 nm.

In order to understand the generation of multiply charged ions at low laser intensity, a qualitative model based on the three-stage cluster ionization mechanism has been proposed [15,16]. This mechanism assumes that the primary step for generation of multiply charged atomic ions is the multiphoton ionization of the cluster constituents. Under our laser intensity conditions, Keldysh parameter ($\gamma = (I.E/2U_p)^{0.5}$ I.E: ionization energy, U_p : ponderomotive energy) was found to be ~ 300 which suggests that multiphoton ionization mechanism will be the sole primary ionization mechanism. Multiphoton ionization of xenon cluster results in generation of singly charged xenon ions, Xe^+ and electrons. The electrons generated on the surface of the cluster escape leaving behind a net positive charge on the cluster, which then acts as a potential barrier for subsequent escape of electrons from the cluster.

Thus, the remaining electrons which have left the parent xenon atom, but cannot leave the cluster become quasi free in the Coulomb field of ions. Since ionisation is a femtosecond phenomenon and the laser pulse is 10 ns long, these quasi free electrons are forced to interact with the laser pulse which is still on. These quasi-free electrons, being under the influence of Coulomb field within the cluster and driven by electromagnetic field, keep extracting energy from the laser pulse presumably via inverse Bremsstrahlung (IBS) process, through electron-ion and electron-neutral collisions. Once the electron energy exceeds the ionization energy of singly charged ion, further ionization can occur leading to generation of higher charge state by electron impact ionization, resulting in augmentation of net charge on the cluster. In spite of increasing energy of the electrons due to IBS process, electrons are retained within the cluster because of increasing Coulomb potential which arises due to the small but finite escape probability of energetic electrons. This sequence of events continues until a stage comes when Coulombic repulsive energy overcomes the total cohesive energy of the cluster and the multiply charged cluster violently explodes resulting in formation of multiply charged atomic ions. The huge potential energy of the highly charged cluster before disintegration is converted into large kinetic energy of ions after Coulomb explosion. The higher the charge state of the ion, higher is its kinetic energy [17] as shown below.

The overall energy gained by the caged electrons in the total time span starting from initial ionization till the disintegration of cluster is dictated by the product of ponderomotive energy and the total number of effective electron-ion/neutral collision frequency and can be written as

$$\frac{dE}{dt} = U_p \times \nu \quad (5)$$

Here ν is the collision frequency of the inner ionized electrons and is of the order of $\sim 10^{14}$ - 10^{15} Hz and U_p

Charge State	Xe^{+2}	Xe^{+3}	Xe^{+4}	Xe^{+5}	Xe^{+6}	Xe^{+7}	Xe^{+8}	Xe^{+9}
Kinetic Energy (keV)	0.4	1.2	3.2	6.0	9.6	11.2	12.8	14.4

is ponderomotive energy of electrons given by the equation-

$$U_p \text{ (eV)} = 9.33 \times 10^{-14} I(W/cm^2) \lambda^2 (\mu m^2) \quad (6)$$

From equation 6, it is clear that as wavelength (λ) increases, ponderomotive energy (U_p) of electrons increases quadratically for a given laser intensity. As a result, the extent of energy extraction by the electron from the optical field is higher at longer wavelength. Thus higher level of ionization and charging is expected at longer wavelength, which is qualitatively in agreement with the present experimental observations.

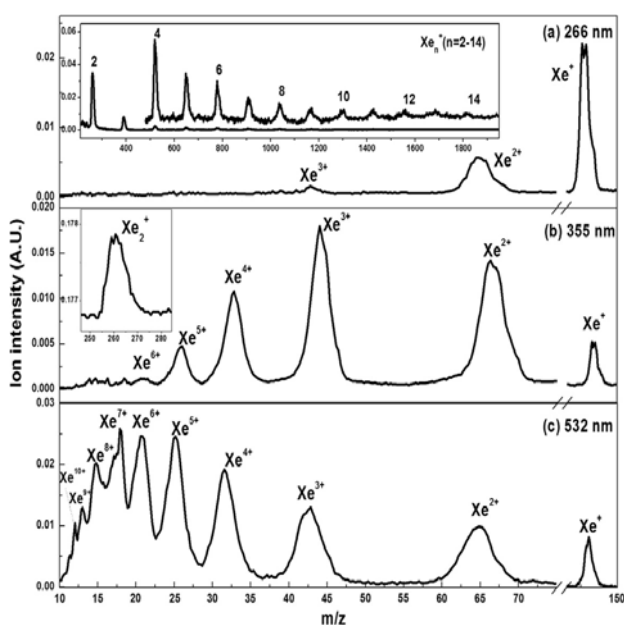


Fig. 2: Mass spectra of Xenon clusters ionized with different wavelength (a) 266 nm (b) 355 nm and (c) 532 nm. Note that 266 nm ionization shows presence of clusters (see inset) and the highest charge state (Xe^{+10}) is in case of 532 nm ionisation.

Effect of cluster size on formation of multiply charged ions

Out of the three wavelengths that were used for photoionisation, 532 nm was found to produce maximum charge state of the xenon ions, hence this wavelength was employed for subsequent studies in which size of the cluster was varied by changing experimental parameter (nozzle diameter and stagnation pressure). Ionisation of clusters of average size $\langle Xe_{17} \rangle$, generated singly charged cluster ions (up

to Xe_4^+) and there was no signal corresponding to a multiply charged xenon ion. However, when $\langle Xe_{50} \rangle$ were photoionised at 532 nm, multiply charged xenon ions could be readily detected in the mass spectrum. Therefore, the minimum cluster size for observation of multiply charged xenon ions under gigawatt laser intensity lies between $17 < n < 50$ where n is number of atoms in the xenon cluster. This observation can be rationalized on the basis of three stage model discussed earlier. $\langle Xe_{17} \rangle$ clusters undergo multiphoton ionization leading to generation of cluster fragments in the mass spectra, since the overall size of $\langle Xe_{17} \rangle$ (radius $\sim 7 \text{ \AA}$) is not enough to trap the electrons within the cluster for sufficient time duration which are essential for further ionization via electron ionization. In contrast, $\langle Xe_{50} \rangle$ with just an extra shell of xenon atoms (radius $\sim 10 \text{ \AA}$) is large enough to cage the quasi free electrons within the cluster and cause further ionization after energization via inverse Brems-strahlung process.

Multiple Ionisation: Property of absorbing molecules or property of cluster

To cross check the applicability of electron heating mechanism for other kind of cluster systems, additional experiments were carried out using water doped methyl iodide clusters. Multiple ionization was earlier observed in methyl iodide clusters and it was to see whether the dopant which does not absorb directly the laser radiation undergoes multiple ionization or not. In these studies, water was chosen as the dopant due to its higher ionization potential (12.62 eV) as compared to that of methyl iodide (9.54 eV). Further, water has much lower vapour pressure as compared to that of methyl iodide. Hence on co-expansion, the methyl iodide clusters have minor contribution from dopant water molecules. As another requirement from experimental point of view, the multiply charged ions of dopant should be different from carbon and iodine and should be unambiguously assignable. Water meets all these criteria as well as it is easily available in the pure form, so water was chosen as dopant. No ion signal arising due to interaction of water clusters with laser pulse could be observed under our experimental conditions when pure H_2O clusters were subjected to laser pulses. However, when water doped methyl iodide clusters

BARC NEWSLETTER

(10% Water : 90% CH₃I v/v) were subjected to laser radiation, these doped clusters were found to generate multiply charged atomic ions of oxygen (up to O⁺⁴) along with other multiply charged atomic ions of carbon and iodine. These results showed that multiple ionization and Coulomb explosion is a collective property of the cluster as a whole and individual molecular properties do not play significant role. Further the secondary ionization mechanism is such that it does not discriminate between the constituents of the cluster. As stated above, this could be the electron heating mechanism.

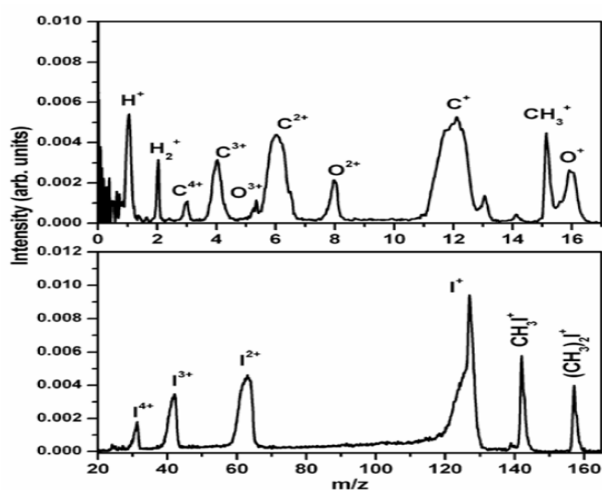


Fig. 3: Mass spectra of H₂O doped CH₃I clusters ionized by 532 nm laser radiation

Laser heating of electrons in a Coulomb field inside a cluster is further supported by measurement of kinetic energy of electrons liberated during the course of Coulomb explosion. Using retarding field analyzer, in our earlier study at 5×10^9 W/cm² intensity [11] we reported detection of electrons with most probable and maximum kinetic energy of ~ 5 and 25 eV liberated during the course of Coulomb explosion of methyl iodide clusters at 532 nm. Recently, Zhang et al. [15] have also reported detection of electrons with mean and maximum kinetic energy of ~ 17 and 30 eV upon Coulomb explosion, when benzene clusters were irradiated with 532 nm laser pulse having intensity $\sim 9 \times 10^9$ W/cm².

Total charge measurement

Although mass spectrometry is a very sensitive method for the detection of ions, it is difficult to comment on

the efficiency of laser-cluster interaction at different wavelengths merely on the basis of the observation of multiply charged ions. In a certain situation, it may be possible that the total yield of ions (including multiply charged ions) generated in the ionization volume at 355 and 532nm might be less than the total yield of singly charged ions generated at 266 nm. To throw more light on the interaction of laser radiation with clusters at different wavelengths, the total charge density of ions generated upon the ionization of clusters (in this case ethyl bromide) at 266, 355 and 532nm was quantified using the parallel plate method and found to be 1.5×10^9 , 5.7×10^9 and 2×10^{11} charges/cm³ respectively. It is worth mentioning that the lower energy visible photons (532 nm) produce more number of charges than the high energy UV photons (266 nm). It is clear that as the wavelength of ionization increases, the charge density also increases. These studies reveal that significantly higher charge (~ 100 times) is generated under Coulomb explosion conditions as compared to studies where no Coulomb explosion occurred. Both, the multiplicity of the charge states (in mass spectrum) and total charge density increase with increasing wavelength [18]. This proves enhanced ionization yield under clustered condition using 532 nm laser pulses.

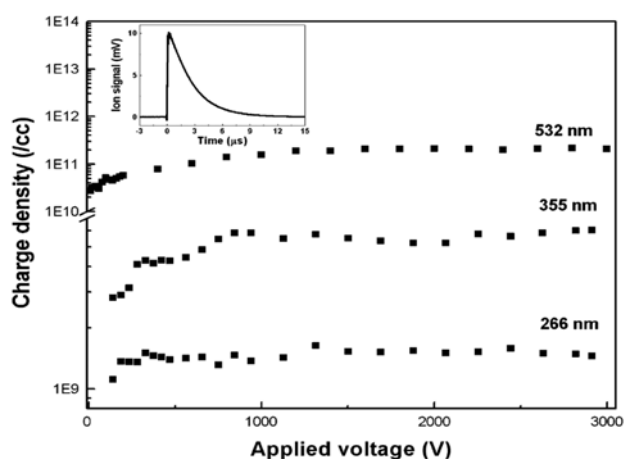


Fig. 4: Total measured charge density as a function of applied voltage between parallel plates at 532, 355 and 266 nm for ethyl bromide cluster photoionisation. A representative oscilloscope trace for ion signal as a function of time is shown in inset. The signal was obtained from the collector plate across a 10K Ω resistance, the applied electric field is 1500 Volts/cm which repels the positively charged ions to collector.

BARC NEWSLETTER

Experiments leading to theoretical advances

Interaction of radiation with matter is a field where experimental observations precede theoretical advances i.e the effects are experimentally observed first and based on the results, theoretical explanation are put forward. It has often given rise to completely new ideas about matter and radiation both. The photoelectric effect, observed in 1887 by Hertz and explained in 1905 by Einstein, is a classic example of this which introduced the important concept of quantization of energy. As far as the present experimental observations are concerned, so far, no theoretical explanation is available and it is very surprising that highly charged atomic ions are generated with such low intensity laser pulses. We believe that the present experimental results will guide the theoreticians to look for new/plausible ways of describing radiation- matter interaction in a partially ionized multi component system.

Applications and Conclusions

The above described experimental observations have shown that the total ionization yield can be enhanced by a factor of 100 to 1000 if clustered media and appropriate ionizing wavelength is used. Further, using this simple approach one can generate copious quantities of multiply charged atomic ions to study their spectroscopy as well as other properties which would otherwise require very costly and huge size apparatus. A wonderful aspect of this phenomenon is its universal applicability to any atomic/molecular system as a result of which the system can be ionized without bothering about the absorption characteristic and nature of atoms/molecules.

In conclusion, photoionisation of clusters investigated at an intensity of 10^9 W/cm², using time-of-flight mass spectrometer, throws unusual surprises. Highly charged ions were generated under these conditions which were earlier thought to be highly improbable. The efficiency of laser-cluster interaction was found to increase with increasing laser wavelength resulting in generation of multiply charged atomic ions (such as Xe¹⁰⁺) with large kinetic energy at 532 nm. Generation of multiply

charged atomic ions has been explained on the basis of efficient heating of quasi free electrons by the laser radiation in a Coulomb field inside a cluster.

References

1. T. Maiman, *Nature* **187** (1960) 493.
2. D. Mathur, *Phys. Rep.* **391** (2004) 1.
3. H. Haberland, "*Clusters of Atoms and Molecules*" Springer Verlag, 1994.
4. O. F. Hagen, *Z. Phys. D*, **4** (1987) 291.
5. F. Dorchies, F. Blasco, T. Caillaud, J. Stevefelt, C. Stenz, A. S. Boldarev and V. A. Gasilov, *Phys. Rev. A* **68** (2003) 023201.
6. V. Kumarappan, M. Krishnamurthy and D. Mathur, *Phys. Rev. A* **67** (2003), 043204.
7. V. P. Krainov and M. B. Smirnov, *Phys. Rep.* **370** (2002) 237.
8. J. V. Ford, Q. Zhong, L. Poth and A. W. Castleman Jr, *J. Chem. Phys.* **110** (1999) 6257
9. J. V. Ford, L. Poth, Q. Zhong and A. W. Castleman Jr, *Int. J. Mass Spectrom.* **192** (1999) 327.
10. H. Thomas, C. Bostedt, M. Hoener, E. Eremina, H. Wabnitz, T. Laarmann, E. Plonjes, R. Treusch, A. R. B. de Castro and T. Moller, *J. Phys. B: At. Mol. Opt. Phys.* **42** (2009) 134018.
11. P. Sharma, R. K. Vatsa, S. K. Kulshreshtha, J. Jha, D. Mathur and M. Krishnamurthy, *J. Chem. Phys.* **125** (2006) 034304.
12. X. Luo, D. Niu, X. Kong, L. Wen, F. Liang, K. Pei, B. Wang and H. Li, *Chem. Phys.* **310** (2005) 17.
13. P. Sharma and R. K. Vatsa, *Rapid Commun. Mass Spectrom.* **21** (2007) 2663.
14. C. Majumder, O.D. Jayakumar, R.K. Vatsa, S.K. Kulshreshtha, J.P. Mittal, *Chem.Phys. Letters*, **304** (1999) 51.
15. N. Zhang, W. Wang, H. Cang, H. Wang and H. Li, *Chem. Phys. Letters*. **469** (2009) 14.
16. W. Wang, H. Li, D. Niu, L. Wen and N. Zhang, *Chem. Phys.* **352** (2008) 111.
17. S. Das, P.M. Badani, P. Sharma, R.K. Vatsa, *Chem.Phys. Letters*, **552** (2012) 13.
18. S. Das, P. M. Badani, P. Sharma, R. K. Vatsa, D. Das, A. Majumder and A. K. Das, *Rapid Commun. Mass Spectrom.* **25** (2011) 1028.

DEVELOPMENT OF DIGITAL RADIOTHERAPY SIMULATOR: "IMAGIN"

D.C. Kar, R. Sahu, K. Jayarajan and R.V. Sakrikar

Division of Remote Handling and Robotics

and

Manjit Singh

DM&A Group

Dr. D.C. Kar is the recipient of the DAE Homi Bhabha Science & Technology Award for the year 2011

Abstract

Cancer is a major health concern in our country, and majority of the patients require radiotherapy during the course of treatment. Radiotherapy simulator is a machine that helps in radiotherapy planning, prior to the radiotherapy treatment. It helps to diagnose the physical extent of the tumour and its relation to the surrounding tissues for selecting the size and orientation of the radiotherapy beams. It also helps to plan the treatment and to protect the critical organs adjacent to the tumour to be treated. The capability of a simulator for real-time review and analyses of the images helps in accurate planning and verification in a short time.

Although, radiotherapy simulator is an essential tool for improving the quality of teletherapy, there is acute shortage of such machines in our country due to the high cost of the imported units and the lack of indigenous technology. Bhabha Atomic Research Centre (BARC), Mumbai has recently developed a Digital Radiotherapy Simulator. In this article, important features of this indigenous machine are discussed in brief.

Introduction

Radiation therapy is one of the established modes of cancer treatment. For the safe and effective radiation therapy, it is necessary to ensure that the whole target is exposed to the prescribed dose of radiation while limiting the exposure to surrounding healthy tissues. This necessitates proper planning through delineation of the tumour and identification of the organs at risk for accurate delivery of the planned radiation dose. The performance of radiotherapy depends mostly upon the precision with which the tumour can be located and the accuracy with which the radiation field is applied. Radiotherapy simulation is a process to determine the shape, size and orientation of the high-energy radiation field(s) to which the patient will be exposed later during

the radiation therapy treatment. It is performed using a machine called radiotherapy simulator, which is a combination of a diagnostic x-ray machine and an external beam radiation therapy machine. In the conventional form [1], it is similar to an isocentric external beam therapy machine. It can reproduce the geometric movements of (external beam) radiotherapy machines. However, unlike a teletherapy machine that delivers high-energy radiation beams for treatment, a radiotherapy simulator uses diagnostic X-ray beams for imaging, either in radiography or fluoroscopy mode. It has two roles: as a tumour localization tool; and as a treatment plan verification tool adapting the same treatment parameters, patient localization, immobilization etc. in a manner similar to a treatment machine.

BARC NEWSLETTER



Fig. 1: Indigenous Radiotherapy Simulator at Tata Memorial Centre, Parel, Mumbai

Unlike the complex CT-Simulators, which performs virtual simulations, radiotherapy simulators are less expensive, easy to operate and easy to maintain [2]. The conventional design of Radiotherapy Simulator does not pose any restriction on the size of the patient. Moreover, the patient dose can be significantly less in conventional simulator compared to that in CT-Simulators. For moving tumours or tumours close to organs moving due to breathing, fluoroscopy mode of conventional simulators can detect the extent of the movement and help in limiting the exposure to normal tissues. Visualization of actual radiation field on the patient's skin is another important feature which helps to avoid accidental exposure.

In India, there is wide gap between the demand and availability of radiotherapy facilities [3]. Most of the centres with teletherapy facilities do not have radiotherapy simulator. They generally depend on conventional radiography units for tumour localization. Considering the growing requirement for such machines in our country, BARC has initiated and successfully developed the technology. So far, three machines are operational including one at Tata Memorial Centre, Parel, Mumbai (Fig. 1). This article describes the development in brief.

Brief Description of the Unit

Major sub-systems in the radiotherapy simulator are *gantry, collimator, x-ray tube, imaging unit, and patient*

support/positioning system [4]. The schematic layout of the machine is shown in Fig. 2.

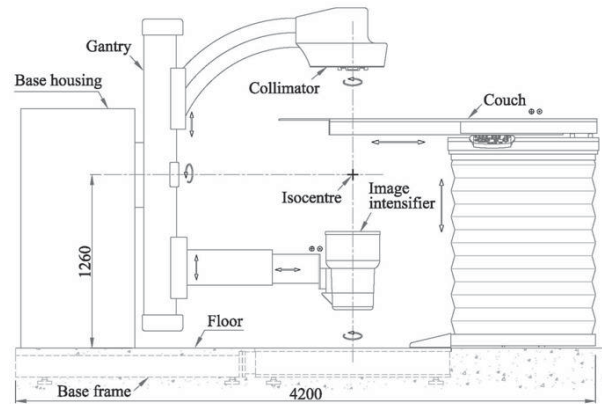


Fig. 2: Schematic layout of the Radiotherapy Simulator

Control Console

The patient setup is generally performed through the local console mounted on the patient positioning couch. Various machine parameters are displayed on the wall-mounted display inside the simulator room.

Another control console is located at outside the simulator room. After immobilizing the patient on the simulator couch, the operator leaves the room, and operates the machine from this console. The console consists of a desktop computer, a mouse, a physical key switch, and two buttons for activating the X-ray beam. One more desktop computer is used for display and storage of the acquired images.

The user can control all unit motions, *viz.* gantry, collimator, imaging arm and the couch, through the graphical user interface as shown in Figure 3. The digital readouts of all the motions are displayed on the console. For imaging, the operator can select one of the two modes: *fluoroscopy* or *radiography*. In fluoroscopy mode, the live images of any moving organ can be viewed continuously. This mode can also be used while one or more unit motions are active, for determining appropriate beam (for therapy) directions. Static anatomical images can be captured in the radiography mode. For either of these modes, the operator can select the exposure parameters, such as tube voltage, tube current and time.

BARC NEWSLETTER

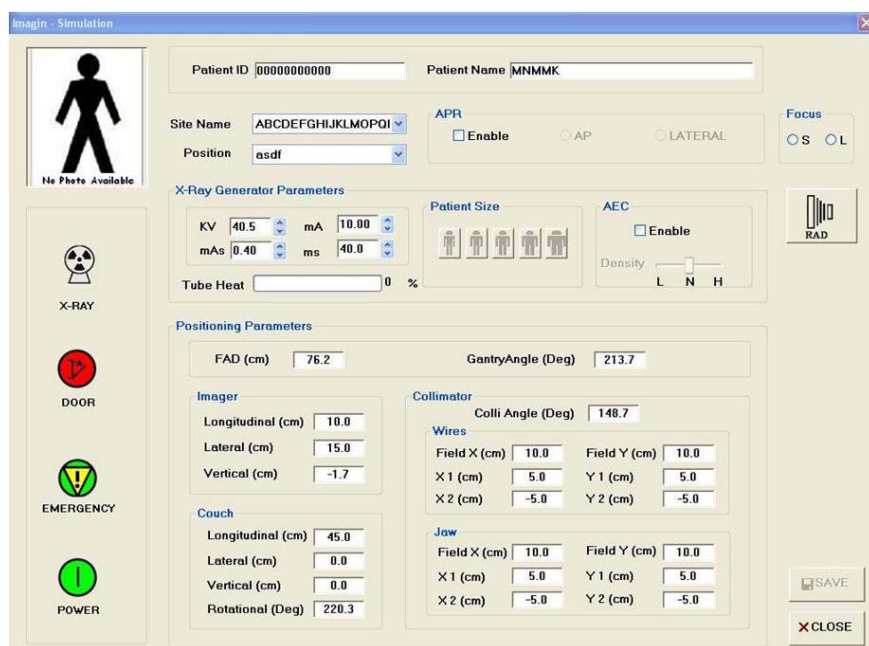
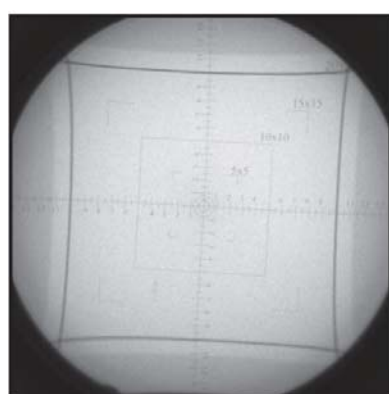
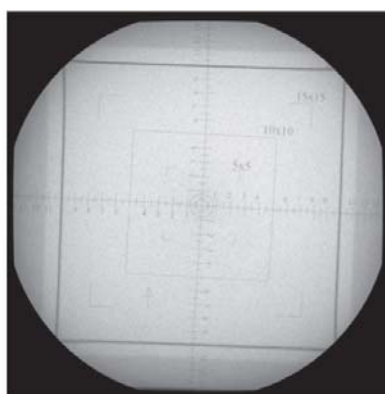


Fig. 3: Graphical user interface at the remote control console



Raw Image



Distortion Corrected

Fig. 4: Correction of Geometrical Distortions

Image intensifiers are widely being used in medical imaging due to cost-effectiveness and significantly low patient radiation dose. However, image distortions introduced by an Image Intensifier are unavoidable. Here, the distortions of the raw image are corrected [5] automatically (Fig. 4) through software without any operator intervention. Important features *viz.* last image hold, MLC (multi leaf collimator) overlay, DICOM (Digital Imaging and COmmunication in Medicine) compatibility, storage and management of acquired images, annotations, image processing and viewing tools, printing etc. are implemented for the convenience of the user.

Auxiliary sub-systems

Anti-Collision Systems

During patient setup, various motions of the machine have to be performed while the patient remains immobilized on the couch. The control software avoids collision between various subsystems *viz.* the couch and the C-arm. Additionally, to ensure any accidental collision between any subsystem of the machine and the patient, the collimator and the image intensifier are equipped with sensors to detect such instances. Whenever the system detects any collision, the motions stop immediately and the operator is intimated by audible beeps.

Patient Positioning Lasers

Accurate patient positioning is essential for effective treatment simulation. The laser system consists of three linear red diode lasers: two in cross planes and one in sagittal plane. The projections of these lasers mark the isocentre, which

serves as the reference for various setup parameters in order to reproduce exact positions on treatment machines.

Safety Interlocks and Emergency Stop Buttons

Many safety interlocks are provided to protect the patient and the operators from unwanted exposure to radiation. These include door interlock of the treatment room (to prevent exposure by accidental opening of door), external mains power supply interlock and emergency interlock (due to fault in any of the unit motions). Emergency stop buttons are installed in the base housing, couch, door, control console and on the passage wall inside the room.

BARC NEWSLETTER

Wall Mounted Display

A monitor in the treatment room displays important parameters related to the machine. Whenever an authorized user logs into the system, system parameters like FAD; image intensifier distance; gantry rotation angle; collimator rotation angle; and positions of the collimator blades, delineator wires, couch longitudinal, lateral, vertical and isocentric rotation are displayed in the monitor.

Connectivity to Hospital Network

After simulation, the patient details, acquired x-ray images and the parameters finalized for the radiotherapy treatment have to be made accessible to the Hospital network through which other systems like Treatment Planning Systems (TPS), treatment machines (medical LINAC, Telecobalt, brachytherapy etc.) can utilize the simulation details. For interoperability, the simulation results are stored/managed and made accessible conforming to the DICOM Standards which is used in virtually all hospitals worldwide.

Patient Simulation

Radiotherapy Simulation is performed prior to the radiation therapy treatment. The purpose is to localize the extent of the tumour so that the whole of the affected region can be exposed to treatment beams while limiting exposure to the adjacent healthy tissues/organs. Once the patient lies down on the patient positioning table, the operator positions the suspected region closer to the isocentre by actuating various motions through the keypads. Focus to axis distance (FAD) is set as the same as the treatment machine in which the patient will be treated. Depending on the affected organ/region, the C-arm is rotated to a suitable angle. Imager, collimating jaws, delineating wires, collimator angles are set for relatively larger x-ray fields. Patient positioning lasers, optical distance indicator, in-room wall-mounted display, field light projections etc are used for accurate and repeatable positioning of the patient. The patient is instructed not to move and all the staffs leave the room.



Fig. 5: Delineated image of the target



Fig. 6: Immobilization mask

At the remote console, patient and treatment related data are entered by authorized operator. Depending on the location of the suspected region and the size/built of the patient, x-ray parameters like kV, mA and time are set. The operator fires the x-ray in appropriate mode, and the raw image appears on the adjacent monitor almost instantly. After couple of seconds, the distortion-corrected image is displayed on the screen. Based on the instruction by the radiation oncologist, the operator needs to repeat after changing some of the machine/ x-ray parameters for better visualization and delineation of the target region (Fig. 5). Processing of the acquired image can also be performed. For multiple fields (if any), the whole process has to be repeated. In some cases, patient-specific immobilization masks (Fig. 6) using perforated thermoplastic sheets are made to ensure repeatable positioning for each radiation therapy treatment. Finally, the set of parameters recommended by the doctor and corresponding images are stored and/or printed.

BARC NEWSLETTER

Quality Assurances and Regulatory Compliances

Radiotherapy simulator has major influence on the overall performance of the radiation therapy process. Although not used directly for the dose delivery, its role is important in determining the target location, treatment planning and spatial accuracy in dose delivery. As the simulator has many features of therapy machine and diagnostic radiology unit, it has to conform to requirements of both the applications. The unit is tested and conforming to the International Electrotechnical Commission (IEC) Standards [6]. The machine is cleared by Atomic Energy Regulatory Board (AERB) for clinical use.

Performance

One unit has been installed at Tata Memorial Centre (TMC), Parel, Mumbai for thorough performance evaluation in the clinical environment. It is inaugurated in March 2013, remotely from Trombay, by H.E. Mr. Yukiya Amano, Director General, IAEA. 10-15 patients are being simulated on this machine daily. Another unit is being commissioned at Saroj Gupta Cancer Centre & Research Institute, Kolkata for the same purpose.

Technology Transfer

Radiotherapy simulator is an essential tool for improving the performance of the radiotherapy treatment. However, in our country, many cancer hospitals with teletherapy units do not have any radiotherapy simulator. The cost of the indigenous Simulator is significantly less compared to the similar imported units. To make the machine available commercially, the technology is transferred to a M/s. Panacea Medical Technologies Pvt. Ltd., Bangalore.

Conclusion

The technology for our indigenous radiotherapy simulator is developed successfully. So far, three units are operational. Based on the operational feedbacks, suggestions and recommendations by the experts and users, the unit is being continuously improved. This computer-controlled machine is simple and user-friendly. Other features of the machine, such as filmless operations and ease of transfer and storage of digital images can streamline the workflow and improve overall performances of the department. The indigenous machine is less expensive, compared to



Fig. 7: Technology Transferred for Commercialization

BARC NEWSLETTER

imported simulators. Therefore, smaller radiotherapy centres, especially those at remote places, will be able to afford this simulator, leading to better accessibility to the common people of the society.

References

1. Cho, P. S., Lindsley, K. L., Douglas, J. G., Stelzer, K. J., and Griffin, T. W. (1998), Digital Radiotherapy Simulator, *Computerized Medical Imaging and Graphics*, Volume 22, pp.1-7.
2. Suhag V., Kaushal, V., Yadav, R., and Das, B. P. (2006), Comparison of Simulator- CT versus simulator fluoroscopy versus surface marking based radiation treatment planning: A prospective study by three-dimensional evaluation, *Radiotherapy and Oncology*, Volume 78, pp.84-90.
3. Jayarajan K., Kar D.C., Sahu R and Singh Manjit, Bhabhatron: An Indigenous Telecobalt Machine for Cancer Treatment, *BARC Newsletter, Founder's Day Special Issue*, Issue No 297, October 2008, page 27-34.
4. Kar D. C., Sahu R., Jayarajan K., Ray D. D. and Singh Manjit (2011), Development of Digital Radiotherapy Simulator: A Device for Tumor Localization, Radiotherapy Planning and verification. *BARC Newsletter*, No.318, January-February, pp.63-69.
5. Chakraborty D.P. (1987), Image Intensifier Distortion Correction. *Medical Physics*, Vol.14(2), pp.249-252.
6. IEC 60601-2-29 - Medical Electrical Equipment- Part 2: Particular Requirements for the Safety of Radiotherapy Simulators, Edition 2, 1999, *International Electrotechnical Commission*, Geneva.

THIOFLAVIN T: AN EFFICIENT FLUORESCENT PROBE FOR EXPLORING PROTEIN FIBRILS AND G-QUADRUPLEX DNA

Jyotirmayee Mohanty
Radiation & Photochemistry Division

Dr. Smt. Jyotirmayee Mohanty is the recipient of the DAE Scientific & Technical Excellence Award for the year 2011

Abstract

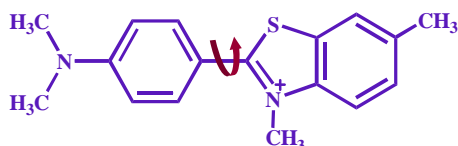
This article discusses the utility of a fluorogenic dye Thioflavin T (ThT) for the early detection of protein fibrillation and also serves as a selective and sensitive fluorescent reporter for the G-quadruplex DNA. In the first case, using human insulin, we report the assessment of fluorescence lifetime of the extrinsically added ThT dye in relation with the incubation time, as a sensitive and convenient therapeutic approach for the early detection of the fibrillation process. We also demonstrate the use of ThT, in a dual role of exclusively inducing quadruplex folding in the 22AG human telomeric DNA, and sensing the same through its fluorescence *light-up* having emission enhancement of the order of 2100- fold in the visible region.

Key Words: Biomolecular assembly, Fluorescence, Thioflavin T, Protein fibril, G-quadruplex.

Introduction

Thioflavin T (ThT)

Noncovalent, extrinsic fluorescent probes find extensive usage as local reporters in many biological applications, especially in various fields of protein/DNA analysis, e.g., for the sensitive and selective detection of assemblies from proteins and DNA. Here, the specific interaction with the protein/DNA environment introduces considerable change in the photophysical characteristics of the dye, projecting the details of its local microenvironment. One of such probes, Thioflavin T, (ThT), is a benzthiazolium dye that has been used quite extensively to detect the presence of amyloid fibrils. The extrinsic detection usually employs fluorescence emission from the added dyes like ThT which is found to be exceptionally specific to the binding on the cavities



Thioflavin T (ThT)

or channels of fibrils and brings out dramatic fluorescence enhancement of the order of ~ 1000 fold.¹ Among various noncanonical nucleic acid structures, the G-quadruplex motifs have attracted immense research attention as prospective targets for chemical intervention of biological functions. There are a limited number of dyes that display a strong modulation in fluorescence behavior when bound to DNAs; however, by and large, none of them exhibits a marked structural selectivity toward quadruplex DNAs, which is a challenge to engineer structure-specific G-quadruplex inducing/stabilizing agents for targeted therapeutic and diagnostic applications. In this article, we propose the use of ThT as an extrinsic fluorescent probe to establish a method for the early detection of amyloid fibrils in fluorescence-based lifetime measurements and for the selective detection of G-quadruplex motif through its fluorescence light-up in the visible region.

Thioflavin T-based Fluorescence Lifetime Assay

Protein misfolding and anomalous aggregation into amyloid fibrils is a complex and intriguing phenomenon

BARC NEWSLETTER

responsible for several neurodegenerative diseases like Alzheimer's disease, Parkinson's disease, Prion diseases, etc.² Along with several ongoing attempts to elucidate an apt molecular mechanism for fibrillation, efforts are also on to establish a sensitive detection method at its early stage, which is utmost important in the development of diagnostic and therapeutic strategies for various fibril affiliated diseases. Among several protein fibrillation cases studied, fibrillation of insulin protein has received much attention over the years. In solution it exists as monomer, dimer or hexamer, depending on the conditions, but its unsolicited conversion to an amyloid fibrillar form raises major concern. Insulin forms amyloid fibrils in *in vitro* conditions on incubation of the acidic solution (pH < 2) at elevated temperatures, ~60 °C, for about 150–180 min, which largely vary depending upon the protein concentration. In 1.5 mg ml⁻¹ insulin solution at pH 1.8, from the onset of incubation at 60 °C, we followed the changes at regular time intervals by monitoring the absorption and emission spectra (Fig. 1A) of the added dye, ThT. The absorption spectrum of ThT shows a maximum at 412 nm. Upon incubation the ThT absorption remained unchanged till ~145 min and, thereafter, gradually shifted by ~32 nm bathochromically to 445 nm with significant decrease in the absorptivity, both indicative of considerable changes in the protein microenvironment experienced by the dye.³ Concomitantly, the emission intensity increased on lapse of time, retaining the emission maximum at 490 nm. A plot of emission enhancement with respect to that of dye alone in water, (I/I_0), at 490 nm with incubation time displayed a sigmoidal increase

(Fig. 1Ba) with an overall fluorescence enhancement of ~2400 fold. Such a remarkable enhancement in the steady-state (time-integrated) emission intensity is highly desirable for a trace level detection of mature fibrils; however, the notable response starts only after ~75 min of incubation and does not provide much information on the early time events in the fibril formation. In other words, from the present perspective of an early stage of fibril detection, the low response of the ThT emission in the initial region (<100 fold) is much disappointing.

On the other hand, as the rigidity of the micro-environment around the dye radically changes en route to the fibril formation, we expected dynamic changes in the photophysics of ThT, which will get reflected in its fluorescence lifetime. The plot of average lifetime (τ_{av}) obtained from the fluorescence lifetime decay traces *versus* incubation time as shown in Fig. 1Bb presented a steadily increasing curve, which reached saturation in τ_{av} (~1.75 ns) at a time lapse of ~70 min. Strikingly, the conveniently detectable changes in ThT lifetime are recognized in the region where the steady-state intensity response is largely missing, and is highly prospective for the early detection of fibrillation. Thus the subtle changes seen in the lifetime patterns at a much earlier time certainly would indicate the presence of precursors, even to the protofibrils, having a rigid micro-environment for binding ThT. In reference to the ThT lifetime changes, it is convincing that while the steady-state absorption/emission changes in ThT were ineffective in reporting the early fibrillation changes (region indicated by the dotted line in

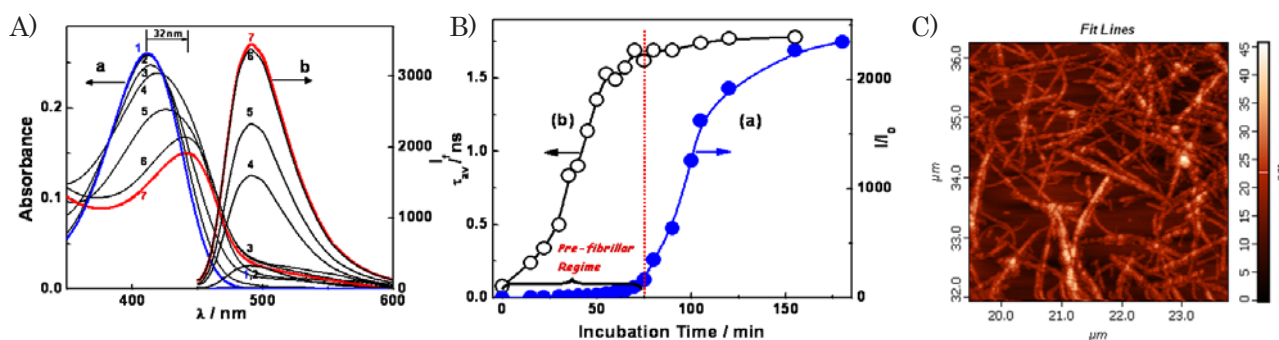


Fig. 1: (A) Absorption (a) and fluorescence (b) spectra and (B) fluorescence intensity (a) and average fluorescence lifetime (b) of ThT (10 μM) in insulin solution at pH 1.8 and 60 °C at different time intervals plotted with respect to that of ThT in water (I/I_0). $\lambda_{ex} = 440$ nm and $\lambda_{mon} = 490$ nm. Time/min: 0 (1); 110 (2); 145 (3); 160 (4); 165 (5); 180 (6) and 195 (7). (C) AFM image of matured fibril.

Fig. 1B), the fluorescence lifetime method discussed here explicitly manifests the early time aggregation changes *en route* to fibril formation.³ The demonstrated lifetime assay of ThT in human insulin can be used as a sensitive and convenient method for the early detection of the fibrillation process and hence, will be a handy tool to explore diagnostic and therapeutic strategies for various fibril affiliated diseases as early as in the pre-fibrillar regime.

Thioflavin T as an Selective Fluorescent Sensor for the Human Telomeric GQuadruplex DNA

The quest for a G-quadruplex specific fluorescent sensor amongst other DNA forms under physiological salt conditions has been addressed in this article. G-quadruplexes are four stranded nucleic acid structures formed by stacking of Hoogsteen base paired G-quartets, which are prevalent in G-rich sequences. The stabilization of different quadruplex foldings by extrinsic molecular ligands can be used as potential therapeutic agents for anticancer treatment.⁴ Gradual addition of 22AG DNA (upto $\sim 5 \mu\text{M}$) to the ThT solution shifted the absorption band of ThT bathochromically to 432 nm with a neat isosbestic point at 425 nm, indicating a strong interaction of dye with the 22AG strand. Concomitantly, the fluorescence spectrum displayed remarkable increase in the emission intensity, and the enhancement (I/I_0) at 490 nm is found to be as large as ~ 1700 -fold (Fig. 2A).⁵

Since the 22AG DNA strand is prone to fold into quadruplex structures in presence of metal ions, it is

quite likely that in the presence of ThT and notably in the absence of any metal ions, the fluorescence enhancement in ThT could originate from its interaction with a quadruplex structure induced by the cationic ThT itself. To explore this, the measurements in presence of K^+ ions displayed remarkable changes as the titration of pre-folded 22AG quadruplexes (both parallel and antiparallel) with ThT (50 mM KCl, 50 mM Tris, pH 7.2), displayed huge enhancement in the emission intensity to ~ 2100 fold. In other words, the good agreement among the spectral features of 22AG-ThT system seen both in the presence of K^+ or in the absence of metal ions, explicitly highlights role of ThT in inducing quadruplex folding in the 22AG sequence, particularly in the absence of salt. The resulting fluorescence 'light-up' in ThT to ~ 2100 - 1700 fold, in the presence and absence of K^+ , respectively, illustrates that ThT acts as an efficient *inducer* of quadruplex DNA.

To recognize the selectivity of ThT towards the quadruplex DNA, similar experiments have been carried out with DNAs of nonspecific sequences, as single strands (ss-) and duplex (ds-) DNAs. In both the cases, the fluorescence enhancements were found to be only in the range of 180-220 fold. Particularly, the double stranded calf thymus DNA (ct-DNA) too afforded emission enhancement in ThT ~ 250 fold, which further decreased in presence of salt. Fig.2B shows a comparison of the overall emission intensity enhancement monitored at 490 nm for different DNA forms with that of 22AG in the absence and presence of salt. Clearly, the striking dominance of emission enhancement in the 22AG DNA in the absence or

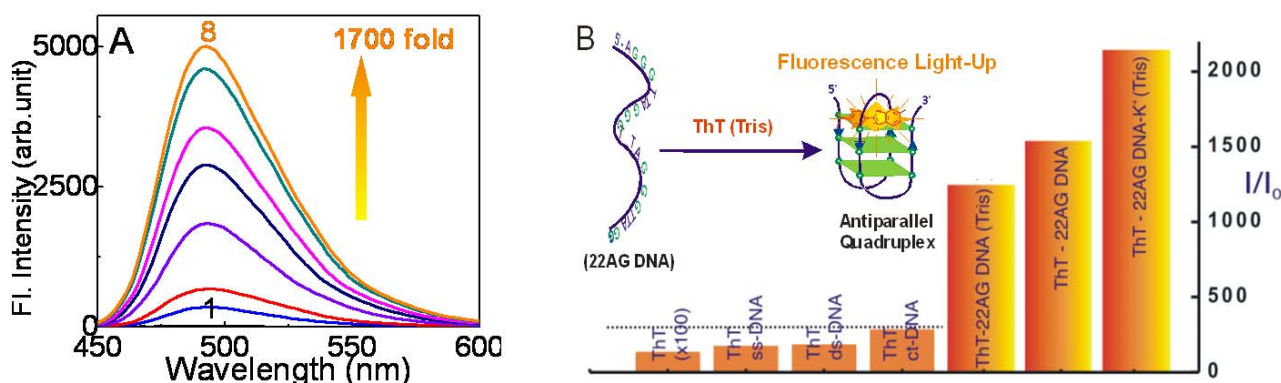


Fig. 2: (A) Fluorescence spectra of ThT solution ($\sim 3 \mu\text{M}$) containing 5 mM Tris (pH 7.2) with [22AG]/ μM : (1) 0, (2) 0.12, (3) 0.25, (4) 0.75, (5) 1.5, (6) 2.5, (7) 4.0, (8) 5.0. (B) Comparison of emission intensity enhancement of ThT in various DNAs and the schematic presentation of 22AG DNA to quadruplex formation with ThT.

BARC NEWSLETTER

presence of salt (especially K⁺) vs other DNA strands, unambiguously establishes the highly selective fluorescence *light-up* of ThT on the quadruplex DNA.⁵ This work opens up avenues to explore new dyes based on ThT scaffold, which have the potential to emerge as highly specific quadruplex sensing agents for diagnostic and therapeutic applications.

Acknowledgements

I acknowledge all my collaborators and co-authors of our published works. I also thank the colleagues in RPCD and CG, BARC for their constant encouragement and support.

References

1. LeVine III, H. *Methods Enzymol.* 309, (1999): 274–284.
2. Woods, I. A., Platt, G. W., Hellewell, . L., Hewitt, E. W., Homans, S. W., Ashcroft, A. E., Radford, S. *Nat. Chem. Biol.* 7, (2011): 730–739.
3. Mohanty, J., Dutta Choudhury, S., Pal, H., Bhasikuttan, A. C. *Chem. Commun.*48, (2012): 2403-2405.
4. Kim, N. W., Piatyszek, M. A., Prowse, K. R., Harley, C. B., West, M. D., Ho, P. L. C., Coviello, G. M., Wright, W. E., Weinrich, S. L., Shay, J. W. *Science* 266, (1994): 2011-2015.
5. Mohanty, J., Barooah, N., Dhamodharan, V., Harikrishna, S, Pradeepkumar, P. I., Bhasikuttan, A. C. *J. Am. Chem. Soc.* 135, (2013): 367-376.

BARC NEWSLETTER

STRUCTURAL INVESTIGATIONS ON SOME FUNCTIONAL MATERIALS

S.N. Achary
Chemistry Division

Dr. S.N. Achary is the recipient of the DAE Scientific & Technical Excellence Award for the year 2011

Abstract

Crystal structure and crystal chemistry of materials have been often used as a guide to explain the properties of materials or to design of novel materials with desired properties. Several important physical properties, like ionic or electronic conductivity, ferroelectricity or dielectric, ferromagnetic or antiferromagnetic etc., mechanical properties like, thermal expansion, compressibility etc. and structural or chemical stabilities of materials are related to their crystal structures. Thus determination of crystal structure is an important step for the characterization of any material. In this article crystal structure of some of the functional materials are presented.

Compositional and structural characterizations are the primary studies carried out for any solid state materials. The compositional characterization of a material is aimed at the qualitative and quantitative estimation of chemical species while the structural characterization deals with an additional feature like spatial arrangement of the chemical species. Thus the structural details of a material are more useful to explain its properties. Several of the technologically important properties like phase transitions, diffusion, ferroelectric, thermal expansion, compressibility are related to the arrangements of chemical species, which may be ions or group of ions together or molecules. In non-molecular solid, as in the case of inorganic crystalline materials, the arrangement of ions and their oxidation states are of interest. Being they are being periodic systems, diffraction techniques like x-ray and/or neutron diffraction are more commonly used for analyses of their crystal structures. Crystal structure and phase transition behavior of some of the investigated systems are presented below.

AX₂O₈ type compounds

Structural studies on such compounds draw significant attention after the discovery of relation of negative

thermal expansion and crystal structure of ZrW₂O₈ and HfW₂O₈. Following these, a large number of such AX₂O₈ and AX₂O₇ (where A = tetravalent; X = hexa- or pentavalent cations) type materials have been investigated to understand their thermal expansion behavior. In order to investigate thermal expansion and crystallographic stabilities, trigonal ZrMo₂O₈ and HfMo₂O₈ have been investigated in detail by powder x-ray diffraction method. The unit cell parameters of trigonal HfMo₂O₈ and ZrMo₂O₈ (space group: *P*-31*c*) are: $a = 10.1086(3)$, $c = 11.7509(4)$ Å and $V = 1039.89(5)$ Å³; $a = 10.1084(3)$, $c = 11.7377(6)$ Å and $V = 1044.83(7)$ Å³, respectively. Both trigonal HfMo₂O₈ and ZrMo₂O₈ have identical structures which are formed by octahedral AO₆ (A = Hf or Zr) and tetrahedral MoO₄ groups. Three corner oxygen atoms of tetrahedral MoO₄ group are shared with octahedral AO₆ groups forming a layer with composition AMo₂O₈. The fourth oxygen atom in the MO₄ tetrahedra is non-bridged and points to the interlayer region. Thus, the trigonal AMo₂O₈ produces a layered structure and enables large amplitude rocking motion of MoO₄ tetrahedra and non-bridged oxygen atoms. A denser monoclinic polymorph of HfMo₂O₈ has been prepared by heating the trigonal phase at around 560°C under pressure of about 2.15 GPa. The unit cell parameters of the monoclinic

HfMo₂O₈ are: $a = 11.4264(8)$, $b = 7.9095(6)$, $c = 7.4461(5)$ Å and $\beta = 122.368(5)^\circ$, $V = 568.4(1)$ Å³. Space group: C2/c. The analyses of the structure parent trigonal phase and the transformed monoclinic phase indicate that the structural transformation occurs with increase in coordination numbers of Hf from six to eight and Mo from four to five. Further, the MoO₅ units are condensed by sharing edges to form Mo₂O₁₀ dimers in monoclinic phase. The close packed condensed structural arrangement lead to about 20 % increase in density. The crystal structures of trigonal and monoclinic polymorphs HfMo₂O₈ are shown in Fig. 1. This structural differences are reflected in their thermal expansion behavior, viz. trigonal HfMo₂O₈ shows negative expansion along a- and b-axes, whereas a significant positive expansion along c-axis ($\alpha_a = \alpha_b = -6.42 \times 10^{-6}$ /°C, $\alpha_c = 56.6 \times 10^{-6}$ /°C, in 25-700 °C) while positive thermal expansion along all the axes in monoclinic HfMo₂O₈ ($\alpha_a = 1.3 \times 10^{-6}$, $\alpha_b = 15.6 \times 10^{-6}$, $\alpha_c = 10.7 \times 10^{-6}$ /°C).

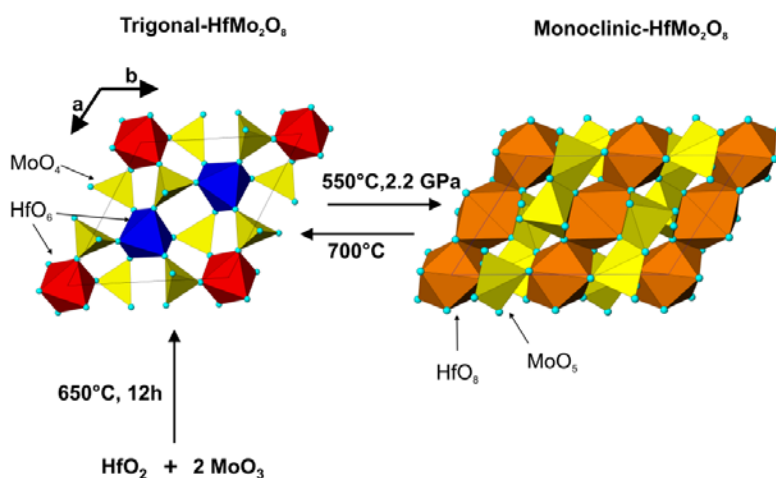


Fig.1: Crystal structures of trigonal and monoclinic polymorphs HfMo₂O₈.

Zircon, scheelite and fergusonite type ThGeO₄

Zircon and scheelite type compounds have been of interest for several technological important properties like laser host materials to high energy particle detectors as well as in mineralogy to understand the geochemistry. Besides, the zircon type compounds are well known for the low thermal expansion and low compressible behavior. However, the analogous

scheelite type compounds show larger thermal expansion coefficients. The scheelite type compounds have higher density compared to zircon type phase and are usually observed as high pressure phases for most of the zircon type materials. ThGeO₄ is one such material which can be prepared as both zircon and scheelite type structures by controlling the syntheses procedures.

The structural details, thermal stability, thermal expansion of the scheelite and zircon type ThGeO₄ have been investigated by powder neutron diffraction and x-ray diffraction methods. Both scheelite and zircon lattices of ThGeO₄ have tetragonal unit cells (space group: $I4_1/a$ and $I4_1/amd$, respectively) and built from the ThO₈ polyhedra (bisdisphenoid) and GeO₄ (tetrahedra). However, the typical connections of the polyhedra are different in these two structures. In the scheelite type structure, ThO₈ polyhedra polyhedra share with eight GeO₄ tetrahedra though its corner oxygen atoms while in zircon type structure ThO₈ units share

four GeO₄ units through corners and two additional GeO₄ units by sharing two opposite edges. In addition it is observed that the Ge–O bond lengths of GeO₄ tetrahedra in scheelite phase (1.764(2) Å) are relatively longer than those in zircon type phase (1.748(2) Å). Similarly, the Th–O bonds of the ThO₈ polyhedron in scheelite phase (2.426(1) Å) are longer compared to zircon type phase (2.422(1) Å). Despite larger inter-atomic distances, the scheelite phase is denser compared to zircon phase due to close packing arrangements of ions leading to shorter cation-cation and anion-anion distances.

The phase transition and thermal expansion behavior have been investigated by in situ high temperature XRD studies. The metastable nature and larger thermal expansion coefficients for scheelite type ThGeO₄ are related to the shorter cation-cation and anion-anion distances. The lattice thermal expansion coefficients measured in between 25-1100 °C are: $\alpha_a = 2.84 \times 10^{-6}$ /°C and $\alpha_c = 6.21 \times 10^{-6}$ /°C (for Zircon type); $\alpha_a = 4.2 \times 10^{-6}$ /°C and $\alpha_c = 9.20 \times 10^{-6}$ /°C (for scheelite type).

In addition to these two phases, a high pressure phase has been observed by in situ high pressure XRD studies. A monoclinic fergusonite type (Space group: $I2/a$) structure has been assigned to this high pressure phase. The fergusonite type phase of ThGeO_4 is closely similar to the scheelite type phase except the lattice distorted feebly ($\beta \sim 90$) and the $16f(u,v,w)$ anion sites of scheelite split into two groups of $8f(x,y,z)$. The structural details of the three different phases are depicted in Fig. 2.

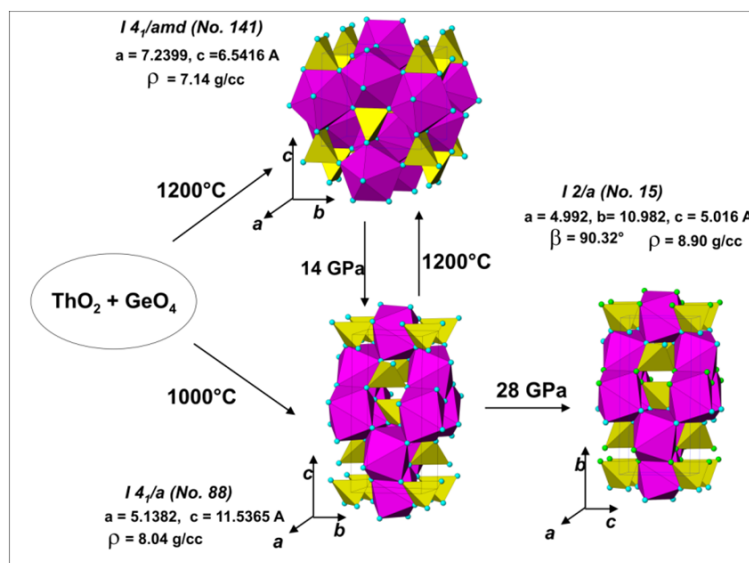


Fig.2: Crystal structures and phase transition sequences in ThGeO_4 .

Pyrochlore type $\text{Ce}_2\text{Zr}_2\text{O}_{7+x}$ ($x = 0.0, 0.5$ and 1.0)

Pyrochlore type ($\text{A}_2\text{B}_2\text{X}_6\text{Y}$, where A is cubically coordinated cation, B is octahedrally coordinated cation, and X and Y are anions) compounds exhibit several important physical properties like high oxygen ion mobilities and catalytic properties. In addition these lattices are promising host lattice for nuclear waste immobilization and inert matrix fuel due to their structural stability under high radiation field and capability of accommodating various radioactive lanthanide and actinide ions. Among the rare-earth zirconates, pyrochlore type $\text{Ce}_2\text{Zr}_2\text{O}_7$ has several additional interests like, efficient catalyst for water gas shift, oxidation of CO and hydrocarbons, dissociation of methane and oxygen storage capacitors. The oxygen stoichiometry between CeO_2 and Ce_2O_3 of the cerium zirconate plays a vital role for such applications. In order to understand crystal chemistry and mechanism of

redox catalytic processes of cerium zirconate, systematic structural studies on $\text{Ce}_2\text{Zr}_2\text{O}_{7+x}$ have been carried out by powder neutron diffraction.

The Rietveld refinement of the observed powder neutron diffraction data of $\text{Ce}_2\text{Zr}_2\text{O}_{7+x}$ for $x = 0.0, 0.5$ and 1.0 revealed all the three have cubic lattices and the unit cell parameters 10.6924(3), 10.6199(2) and 10.5443(2) Å, respectively. The cubic lattice of $\text{Ce}_2\text{Zr}_2\text{O}_7$

has space group $Fd3m$ where Ce^{3+} and Zr^{4+} are occupied in $16c$ and $16d$ sites. The anions are distributed in two symmetrically distinct sites, namely $48f$ and $8b$. It is known that the pyrochlore and fluorite differed by $1/8$ of anions positions, which are vacant in former ($8a$ sites) while occupied in later structure. The anion vacancy are systematically distributed such a manner that the coordination polyhedra of one set of cations (Zr in such case) transforms from eight coordinated polyhedra to six coordinated octahedral configuration. However, often the $8a$ vacant sites are occupied by some oxygen ions liberated from $8b$ and/or $48f$ sites. In the present case no such liberated oxygen atoms are observed from the structural studies. As

the oxygen content increases from 7.0 to 7.5, the vacant sites corresponding to the $8a$ sites are filled by O^{2-} ions and appropriate charge balance is achieved by increasing oxidation state of cerium from 3 to 4. The analyses of structure of the $\text{Ce}_2\text{Zr}_2\text{O}_{7.5}$ indicate that the symmetry is lowered from $Fd3m$ to $F-43m$ and the three anion sites (including vacant $8a$ sites) of the $\text{Ce}_2\text{Zr}_2\text{O}_7$ lattice split into six sites, as O1 ($24f$), O2 ($24g$), O3 ($4a$), O4 ($4b$), O5 ($4c$) and O6 ($4d$). All anions sites show partial vacancy in this structure. Similar analyses of the $\text{Ce}_2\text{Zr}_2\text{O}_8$ structure indicate a further lowering of symmetry (space group $P2_13$) due to incorporation of more O^{2-} ions. The Ce^{4+} and Zr^{4+} sites of the parent pyrochlore lattice split into two different sites ($4a$ and $12b$). The anions are occupied in eight crystallographically distinct sites as: O1 to O4 in $4a$ sites and O5 to O8 in $12b$ sites. Each of the anions is tetrahedrally coordinated like normal fluorite or pyrochlore lattice. Both Ce and Zr atoms form eight coordinated polyhedra with O^{2-} ions similar to the

fluorite structure. In all the three cases the cation ordered structure similar to pyrochlore are retained. The overall arrangement of the various atoms in these two does not show appreciable difference except shift in positions due to extra interstitial anions. The interaction of oxide ions oxidizes an equivalent amount of Ce^{3+} to Ce^{4+} for charge balance reason. The smaller ionic radius of Ce^{4+} is reflected in the contraction of unit cell parameter and hence increasing density of the lattice. Thus, the crystal structure of $\text{Ce}_2\text{Zr}_2\text{O}_{7.5}$ and $\text{Ce}_2\text{Zr}_2\text{O}_8$ can be explained as partially or fully filled variant of the $\text{Ce}_2\text{Zr}_2\text{O}_7$ structure. It is observed that the pyrochlore type structural arrangement is preserved due to the gentle intercalation of oxide ions and becomes fully chemically stable structure in air or oxidizing atmosphere.

Further to investigate the thermal and pressure stability, $\text{Ce}_2\text{Zr}_2\text{O}_8$ has been studied at higher temperature and pressure. It is observed that the structure is stable in air

up to 1200°C and decomposes around 1400°C to two solid solution phases due to cation migrations. Pressure dependent structural studies indicate reversible structural transition around 5 GPa. The structure of high pressure phase is obtained from the powder XRD data recorded at 12 GPa. A rhombohedral lattice with unit cell parameters as: $a_h = 14.6791(3)$, $c_h = 17.9421(5)$ Å, $V = 3348.1(1)$ Å³ (space group: $P3_2$) is assigned to this high pressure phase and the structure is closely related to that of cubic $\text{Ce}_2\text{Zr}_2\text{O}_8$. The unit cell has 16 Ce atoms, 16 Zr atoms and 64 oxygen atoms all occupied in the general (3a) sites. The typical structural arrangements of the investigated $\text{Ce}_2\text{Zr}_2\text{O}_{7+x}$ phases are shown in Fig. 3.

Besides, these structural studies on a number of complex crystalline functional materials, namely tetragonal NbOPO_4 , Monazite and scheelite type LnVO_4 , $\text{Cr}_2\text{V}_4\text{O}_{13}$, ZrU_2O_7 , $\text{Th}(\text{VO}_3)_4$, $\text{Pu}(\text{VO}_3)_4$, UF_4 and a number of ordered fluorides in alkaline-earth and rare-earth

fluoride systems have been carried out. The structural studies under non ambient conditions have also been carried out to understand their structural chemistry and these have been used to prepare several metastable phases.

Acknowledgements

Author thanks Dr. A. K. Tyagi, Head Solid State Chemistry Section, Chemistry Division, Dr. V. K. Jain, Head Chemistry Division and Dr. D. Das, former Head Chemistry Division for their supports to these studies. Also, author thanks all the colleagues and collaborators in these studies.

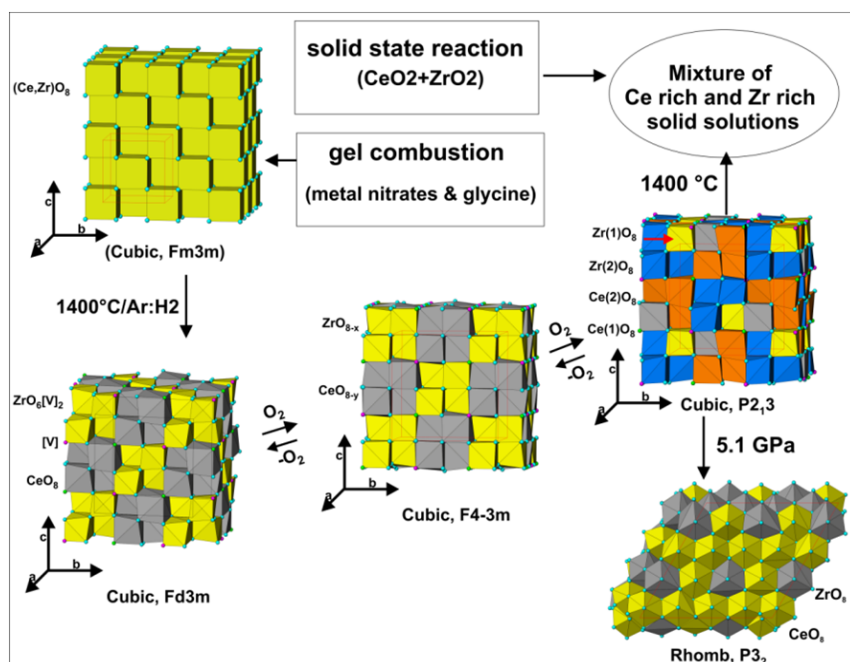


Fig. 3: Crystal structure and phase transition sequences in $\text{Ce}_2\text{Zr}_2\text{O}_{7+x}$.

BARC NEWSLETTER

MACHINING AND INSPECTION OF FINE REFERENCE NOTCHES FOR DEFECT EVALUATION BY NON-DESTRUCTIVE TESTING METHODS

S.P. Srivastava, T.L. Govindankutty, R.K. Gupta and S.B. Jawale

Centre for Design and Manufacture

and

Manjit Singh

Division for Remote Handling and Robotics

Shri S.P. Srivastava is the recipient of the DAE Scientific & Technical Excellence Award for the year 2011

Abstract

In ultrasonic testing and eddy current testing, acceptance or rejection of flaws in the test specimen is determined by comparing their signal to that from an artificial flaw in the reference block, preferably made from the cut piece of the actual product. However, in case of 540 MWe PHWR, to meet the regulatory requirement during in-service inspection of coolant channel, it was desirable to have full size reference block. It was a challenging task to inspect as well as machine, 0.150 mm wide and 0.086 mm deep notches with close tolerances, especially on inner surface of 6.332 m long Zirconium – Nb 2.5% pressure tube having 103.4 mm ID and 4.3 mm wall thickness. A special micro scribing technique was developed for machining longitudinal and circumferential notches and their dimensions were certified using replica method.

Introduction

Presently, in-service inspection of coolant channels of each 235 MWe Pressurised Heavy Water Reactors (PHWRs) is being done by remotely operated channel inspection system known as BARCIS (Bhabha Atomic Research Centre Channel Inspection System). Design of a new system for in-service inspection of 540 MWe PHWR coolant channels is under progress. The BARCIS inspection head contains various Ultrasonic Testing (UT) and Eddy Current Testing (ET) transducers, enabling it to perform wall thickness measurement and flaw detection besides other activities.

Since UT is a comparative method, in order to ascertain the shape, size and type of discontinuity, the signal must be compared with that of known flaws in a representative part. In the absence of natural flaw of similar type, it is a standard practice to machine artificial flaws of acceptable size in acoustically similar material.

The three most common types of artificial discontinuities are Flat Bottom Holes (FBH), Side Drilled Holes (SDH) and notches. FBHs are representative of embedded flaws like inclusions, lamination etc. whereas linear flaws inside the materials are represented by SDH. Notches, representing the most severe type of surface breaking flaws such as cracks, are difficult to machine even on a flat surface having proper access. Generally, to facilitate the insertion of a cutting tool, a sectorial opening is provided on the opposite side of the notch. However, it becomes extremely difficult to machine precision notch deep inside a tube or pipe without any cutout for tool insertion.

In case of Indian 540 MWe PHWR, to meet the regulatory requirement it was desirable to have reference tube of circular cross section without any cutout, so that calibration could be carried out during mock up, simulating the pressure and flow of the coolant at the time of actual inspection. It was required

BARC NEWSLETTER

to make different types of notches on 6.332 m long tube in circumferential and axial directions on inner and outer surfaces. It was a challenging task to machine 0.150 mm wide and 0.086 mm deep (2% of wall thickness) with a tolerance of 5 micron, square notches on the inner surface of 103.4 mm diameter tube at 300 mm from one end. Not only machining but inspection was also difficult for such type of notches due to limited access for inserting any measuring instrument.

Review of the Machining Processes

Machining processes, such as Electro-Discharge Machining (EDM) and Milling on CNC lathe machine were not suitable due to either length of the job or access to the inner surface. In the EDM process electrode of required shape and size with proper tolerance is machined and used as formed tool. In this, size of the job is controlled by the size of the Kerosene tank. Another associated problem is difficulty in maintaining the exact profile of the notch at microscopic level due to continuous erosion of the form tool through which arc is generated. Further, if the thickness of the form tool is very less, as in the present case it was 0.150 mm, erosion of the tool is very fast. Considering above difficulties, a machining process known as micro scribing was developed for making fine notches on both outer and inner surfaces. Several trials were made to establish the process and it was observed that based on the accuracy and repeatability of the notch dimensions, result of micro scribing was far better than that of micro EDM. Measurement of notch dimensions was done by replica method and same was validated by other direct measurement technique.

Review of the Inspection Techniques

Because of the limited access, direct measurement of the notch dimensions particularly on inner surface of a pipe or tube is very difficult. Following methods were explored for measurement and qualification:

Direct measurement on microscope

Microscope is used for direct measurement of notch dimensions on a cut out of a small size specimen. It

has different magnifications for different purpose. In this measuring machine, the magnified image of the component is obtained which is seen through eyepiece. The measurement is taken using a dedicated PC and software. This measurement, being a direct method, was used for machining process qualification.

Replica Method

In this method an impression of the notch is taken and the impression is measured at high magnification on a microscope or a profile projector. Care is taken that the impression material should fill up to the bottom of the notch so that correct impression could be obtained. Since it was possible to prepare replica of notches located up to 300 mm distance from one end on the ID side, replica technique was considered suitable for measurement. The technique was qualified by comparing its result with that of direct measurement on a small test piece.

Development of Micro Scribing Technique

Considering the softness of the material (Hardness BHN 205-215) scribing technique was considered feasible, as this technique can be used on a hollow spindle lathe machine which can accommodate large job. In this method a micro scribing tool was employed for notch machining. Since standard scribing tool is not available, a micro scribing tool of the required dimensions was developed using tool and cutter grinder. The micro scribing tool was made using a High Speed Steel (HSS) single point cutting tool (Fig. 1). Since notch width is same as the width of cutting edge, it was very critical



Fig. 1: Micro scribing tool

BARC NEWSLETTER

to maintain the width of the small edge and therefore high skill was required to perform the tool grinding operation. Before using, each tool was checked for its all dimensions and geometrical features and tools with proper geometry were used for trial and final machining.

Notch machining was carried out on hollow spindle lathe machine. For longitudinal notch, tool was given reciprocating motion manually, against the stationary job, held in the chuck. Marking was done on the tool holding bar for the length of the notch. For making circumferential notch, tool was kept fixed and job was given rotational movement manually (Fig. 2). Marking corresponding to the length of the notch was done on the head stock and a pointer was fixed to the chuck for setting the length of the notch. Control of depth in case of ID notch was very difficult due to boring bar deflection. Numbers of trials were made to establish a relation between feed depth and actual depth obtained by measurement. Actual machining was carried out in number of stages. After each stage depth was measured and then depending upon the requirement, final cut was given. This ensured that depth was within the specified tolerance.

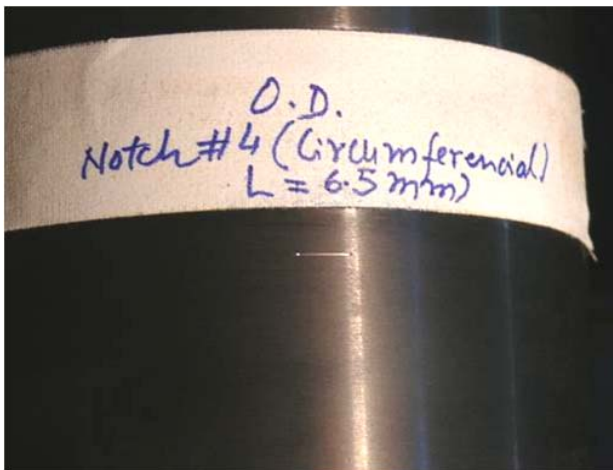


Fig. 2: Circumferential notch

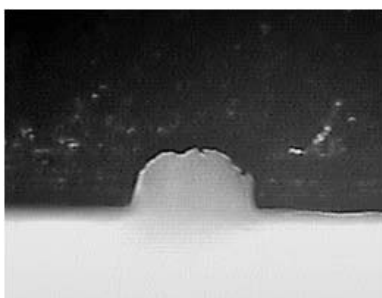


Fig. 3: Cross section of notch by micro EDM (left), slot milling cutter (center) and micro scribing technique (right)

Cross sectional images of notch made by micro EDM, slot milling cutter and micro scribing tool on a coolant tube cut piece are shown in Fig. 3.

Results And Discussions

Using the scribing technique in total eight notches, four at each end, were machined on the pressure tube of 540MWe. Out of four notches two were on OD and two were on ID. All these notches were measured by replica method using 50 X magnifications on the Profile Projector. The dimensions actually obtained were well within the tolerance specified. The geometrical requirements of notches i.e. flat bottom and square sides were also achieved. Similarly for 220 MWe PHWR, sixteen notches, eight circumferential and eight axial were made on coolant channel of size OD 89.1 x ID 82.55 x Length 1500 mm. Out of forty eight dimensions only two depth dimensions were out of tolerances. Therefore, the procedure developed for notch machining and measurement is capable of producing the specified quality notches required for carrying out the Non Destructive Examination (NDE) of pressure tube.

Present and Future Development

Successful trials have been made to machine circumferential as well as longitudinal notches on the outer surface of hard material 17-4 PH Stainless Steel having diameter of 49.5 mm and length of 62 mm (Hardness HR_c 42 or HVN 425). Special scribing tool with carbide tip brazed on shank of EN 29 Alloy Steel (Hardness HR_c 45) was used for the purpose (Fig. 4a). Carbide tip was ground to obtain end clearance of 14° and end relief of 23° (Fig. 4b). Results are very

BARC NEWSLETTER



Fig. 4a: Tool for 17-4-PH Steel; Carbide insert brazed in SS EN29 shank.

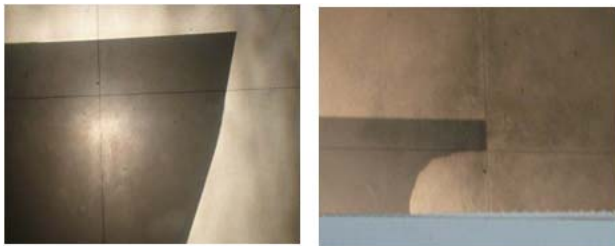
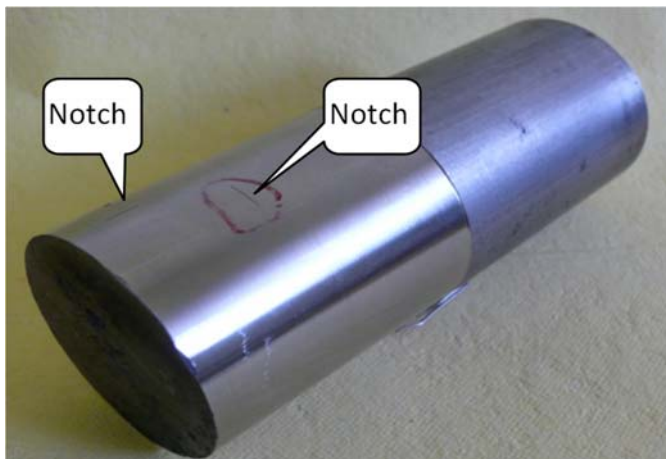


Fig. 4b: Enlarged views (in two directions) of the cutting edge

encouraging as it can be seen (Figs. 5 a, b, c) that shape of the cross section of the notch is better than that obtained for Zr Nb 2.5% material, because of stability of the material due to high hardness. However, carbide tips are prone to breakage because of its very high hardness HVN 1366, hence after each operation tool tip is inspected for its integrity. Further development includes trial for making internal notches on hard material such as 17-4-PH Stainless Steel.

Future scope of work includes machining of fine notches on external and internal surfaces of small diameter tubes. For an example, Incoloy tube of diameter 16 mm and wall thickness 1 mm, used in steam generator



(a) Circumferential and longitudinal notches on 17-4-PH Stainless Steel Rod

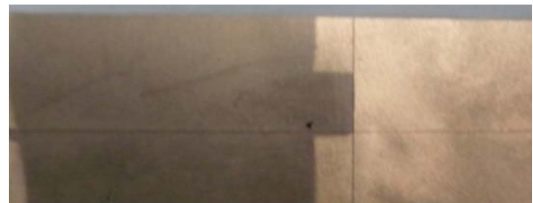
and heat exchanger for passage of high temperature fluid, needs pre-service and in-service inspection either by UT or ET for which reference notches are essential.

Conclusion

Micro scribing technique using HSS tool, is very much suitable for machining very fine external and internal notches of the order of 0.086mm deep and 0.150mm wide, either on 6.3 m long pressure tube for 540 MWe PHWR or 1.5 m long pressure tube for 220 MWe PHWR. The critical requirement of dimensions and geometry of the notches could be achieved by using micro scribing technique. Measurement of the notch dimensions by preparing its replica is validated by direct measurement of notch using microscope. Notch on hard material can be done by using special tool made of carbide material.

References

1. S. P. Srivastava, et al, "Machining and Inspection of Fine Reference Notches on Ultrasonic Calibration Block for the Inspection of Coolant Channels using BARCIS" *proceeding of National Seminar NDE 2011, ISNT*, pp 432-436, December 8-10, 2011.
2. Manjit Singh, BARCIS (BARC Channel Inspection System) *BARC Newsletter*, 189, pp. 39-49 (1999).
3. Placid Rodriguez and Baldev Raj, "Development of In-service Inspection techniques for nuclear power plants in India" *Int. J. Pres. Ves. & Piping* 73, pp. 59-68 (1997).



(b) Cross section of longitudinal notch
Width-0.160mm, Depth-0.087mm



(c) Cross section of circumferential notch
Width-0.153mm, Depth-0.086mm

Fig. 5: External notches on 17-4-PH Stainless Steel Rod

BARC NEWSLETTER

CRYSTAL STRUCTURE OF PROSTATE SECRETORY PROTEIN PSP94

Mukesh Kumar

Solid State Physics Division

and

Ashwani Kumar

High Pressure & Synchrotron Radiation Physics Division

Dr. Mukesh Kumar is the recipient of the DAE Scientific & Technical Excellence Award for the year 2011

Abstract

Prostate Secretory Protein of 94 amino acids (PSP94) has been attracting interest since last three decades due to its abundant presence (~1 mg/ml) in human semen. Several biological roles of PSP94 have been proposed since then, including the recently discovered fungicidal activity, but the exact function still remains elusive. To get better insight, crystal structure of human PSP94 has been determined here to 2.3 Å resolutions. During the course of this investigation, it was found that PSP94 undergoes a pH dependent monomer/dimer transition, which has a significant biological implication. The molecular mechanism of such transitions has been proposed based on our crystal structure.

Introduction

Prostate Secretory Protein of 94 amino acids (PSP94), also known as beta-microseminoprotein (β -MSP) is one of the three most abundant proteins in the human seminal plasma. PSP94 binds to human immunoglobulin G (IgG) and it was suggested that it may be involved in regulation of immune response in the female reproductive tract against the allogeneic sperm⁷⁻⁹. PSP94 also binds to cysteine rich secretory proteins (CRISPs) with high affinity but the biological significance of such binding is not clear. Recently, it has been demonstrated that PSP94 possesses fungicidal activity in the acidic environment of vagina and it has been hypothesized then that an unknown infectious agent, which is a target for PSP94, might be responsible for the onset of different prostatic diseases in men¹. The hypothesis is consistent with the fact that the expression of PSP94 progressively decreases during the development of prostate cancer⁵.

The structure of PSP94 has been reported earlier using NMR by two laboratories^{2-3,25,26}. In these two structures,

secondary structure elements are similar, but the overall shape of the protein is very different (globular vs elongated). As no crystal structures for any member of this family of proteins are known, independent confirmation of the overall shape of the molecule was not available. The crystal structure of PSP94 was, therefore, determined to establish the overall shape (elongated) of the molecule. The structure further gave insight into a pH driven monomer/dimer transition of PSP94, which has a significant biological implications.

Results & Discussion

PSP94 was purified from human seminal plasma and crystallized in tetragonal space group $P4_12_12$ with unit cell dimensions $a=b=107.9$ Å, $c=82.1$ Å²⁷. There are four molecules per asymmetric unit. The structure was determined from diffraction data extending to 2.3 Å resolution. Experimental phases were obtained from single isomorphous replacement with anomalous scattering (SIRAS) using crystals soaked in uranyl nitrate. Experimental electron density maps, improved by density modification, allowed unambiguous placement

BARC NEWSLETTER

of most of the residues. The final refined atomic model contains 2941 non-hydrogen atoms in four polypeptide chains. The atomic coordinates have been deposited in the Protein Data Bank (PDB) with the accession code 3IX0.

Overall structure of PSP94 monomer

PSP94 monomer has a long extended structure, rich in β -sheets (Fig. 1a). There are two distinct domains: an N-terminal domain from residues 1-52 and a C-terminal domain from residues 53-94. The two domains are held together by a disulfide bond (^{37}Cys - ^{73}Cys). The N-terminal domain has four antiparallel β -strands ($\beta 1$: 1-6, $\beta 4$: 30-34, $\beta 5$: 38-42 and $\beta 6$: 46-51) arranged in the form of Greek-key motif and two small antiparallel β -strands ($\beta 2$: 18-21 and $\beta 3$: 23-27) forming a flap on top of the Greek key motif. There are three disulfide bonds in the N-terminal domain. The disulfides ^{2}Cys - ^{50}Cys between strands $\beta 1$ and $\beta 6$ and ^{40}Cys - ^{49}Cys between strands $\beta 5$ and $\beta 6$ make the Greek key structure rigid while the third disulfide ^{18}Cys - ^{42}Cys between $\beta 2$ and $\beta 5$ orients the flap onto the Greek key motif. The C-terminal domain has two double-stranded antiparallel β -sheets. The strand $\beta 7$: 55-58, which is an extension of the N-terminal strand $\beta 6$, is associated with the C-terminal β -strand $\beta 10$: 90-94. Interestingly, $\beta 10$ seems to get extended further by the first strand $\beta 1$ of the N-terminal domain. The other two β -strands in the C-terminal domain $\beta 8$: 64-70 and $\beta 9$: 74-79 are longer and separated from the first pair. The arrangement of these four β -strands in the C-terminal domain is unusual and gives rise to a unique fold. The lone disulfide ^{64}Cys - ^{87}Cys in the C-terminal domain brings rigidity to the loop structure. One of the remarkable features of PSP94 monomer is the close proximity of the amino and carboxyl ends of the polypeptide chain, which are facing each other with a strong hydrogen bond

between main chain nitrogen atom of the first residue and one of the carboxyl oxygen atoms of the last residue (N-O distances 2.45-2.66 Å). The significance of this hydrogen bond in pH induced monomer/dimer transition is discussed in subsequent section.

Structural similarity search

The structural similarity search for PSP94 shows that the C-terminal domain has no structural similarity with any known proteins, but the residues 15 to 52 in the N-terminal domain have a fold similar to the fibronectin type I module (FnI) (Fig. 1b). The structure based

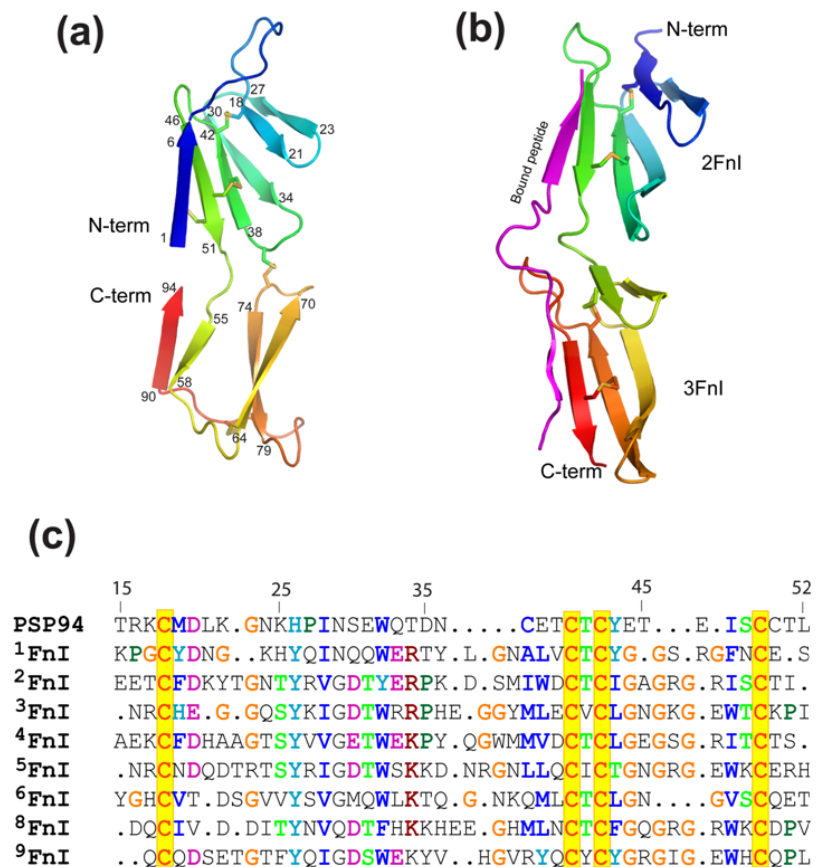


Fig. 1: PSP94 monomer and its comparison with fibronectin type I (FnI) modules. (a) Cartoon representation of PSP94 with polypeptide chain in rainbow color from blue (N-terminus) to red (C-terminus). Five disulfides are shown in stick representation (b) Cartoon representation of fibronectin module pair (^2FnI / ^3FnI from pdb id 2rkz) with polypeptide chain in rainbow color and a bound peptide, making an antiparallel β -strand, in magenta color. (c) Structure based sequence alignment of PSP94 with different fibronectin FnI modules. The pdb files used for structural superposition of different fibronectin modules are: 1o9a, 3cal, 2rky, 1e8b, 3ejh for ^1FnI , ^2FnI & ^3FnI , ^4FnI & ^5FnI , ^6FnI and ^8FnI & ^9FnI respectively. The completely conserved cysteine residues making disulfides are highlighted in yellow color and the other partially conserved residues are shown in different colors. The residue numbering indicated at the top is with respect to PSP94 sequence.

sequence alignment further shows that the four conserved cysteine residues in the Fnl structures, which make two disulfide bonds and hold the β -strands together, is present at the corresponding positions even in PSP94 structure (Fig. 1c). PSP94, however, has two extra cysteine residues (^{37}Cys and ^{50}Cys) in this region of the sequence which make additional disulfide bonds.

PSP94 dimer

The arrangement of four molecules of PSP94 in the crystallographic asymmetric unit suggests that they form two dimers. Within a dimer, there is a non-

crystallographic dyad axis that orients the N-terminal domain of one monomer adjacent to the C-terminal domain of the other monomer (Fig. 2a). In this arrangement, β -sheet of the N-terminal Greek key motif in each monomer gets extended across the dimer interface by the C-terminal strands β_{10} and β_7 of the adjacent monomer. This leads to the formation of two six-stranded β -sheets in the PSP94 dimer (Fig. 2b). The dimeric interaction further brings the two N- and two C-terminal ends of the monomers in close proximity to each other (Fig. 2a, 3a).

pH driven monomer/dimer transition

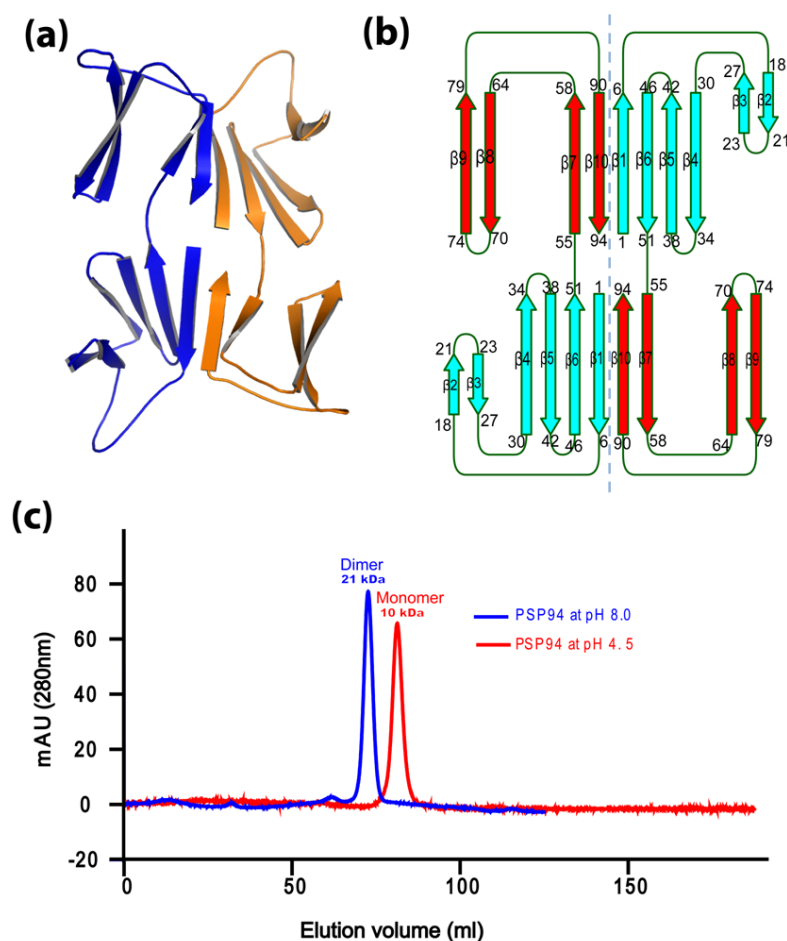


Fig. 2: PSP94 dimer (a) Cartoon representation showing the edge-to-edge interaction of two PSP94 monomers with their polypeptide chains in blue and orange colors. (b) Topology diagram of dimeric interaction showing extension of β -sheet across the dimer interface (broken vertical line). The β -strands in the N-terminal domain are shown in cyan color and those in the C-terminal domain are shown in red color. (c) Elution profile of monomeric and dimeric PSP94. Purified PSP94 (400-500 μg) was subjected to gel filtration chromatography using a Superdex G-75 column (Hi-Load 16/60, Amersham) at a flow rate of 0.5ml/min. The elution buffers used were: 50 mM Tris, pH 8.0 (in blue) and 50 mM acetate, pH 4.5 (in red).

To test whether PSP94 dimer is a manifestation of crystal packing or whether it exists even in solution, gel filtration chromatography was carried out. PSP94 eluted as a single peak corresponding to a molecular weight of $\sim 21\text{kDa}$ (dimer) when eluted with 50mM Tris at pH 8.0. However, when elution was carried out with 50mM Sodium acetate, pH 4.5, PSP94 eluted as a single peak corresponding to a molecular weight of $\sim 10\text{kDa}$ (monomer) (Fig. 2c), suggesting that the acidic pH dissociates PSP94 dimers (21kDa) into monomers (10kDa).

Mechanism of monomer/dimer transition

The dimeric association, which leads to extension of beta sheet across the dimer interface, is stabilized by nine inter-chain backbone hydrogen bonds. The question that initially puzzled us was how by reducing the pH, all these hydrogen bonds are broken. The closer examination revealed that the clue is at the centre of these interactions where a pair of amino and carboxyl ends of the polypeptide chain is held in close proximity (Fig. 3a). At the acidic pH, close to the pKa (~ 4.0) of free carboxyl group, one of the oxygen atoms (O2) of the terminal carboxyl group (of ^{94}Ile) can get protonated and as the protonated hydroxyl (-OH) oxygen of the carboxyl

BARC NEWSLETTER

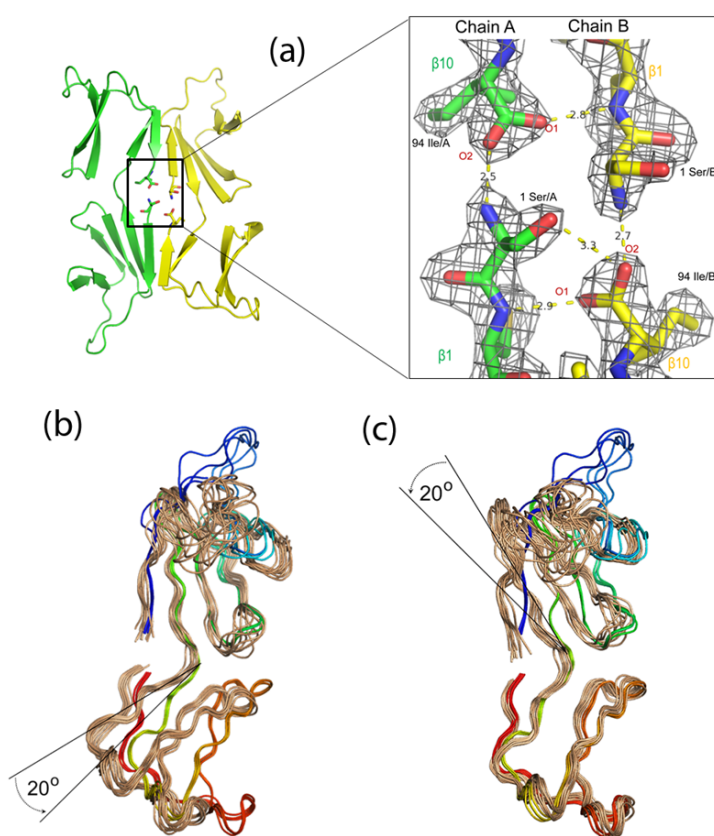


Fig. 3: PSP94 - dimer to monomer. (a) Amino and the carboxyl ends of the two polypeptide chains (green and yellow carbon) at the centre of the dimer interface along with their electron density maps ($2F_o-F_c$) contoured at 1.5σ . Oxygen and nitrogen atoms are colored red and blue respectively. The hydrogen-bond distances are marked in Å unit. Superposition of either (b) the C-terminal domain or (c) the N-terminal domain of the NMR models (from pdb file 2iz3 and shown in brown color) onto the corresponding domain of the crystal structure (four polypeptide chains in rainbow color) showing a shift of $\sim 20^\circ$ in the relative orientation of two domains.

group cannot accept a hydrogen bond³³ from a potential donor group (NH_3^+ of ^1Ser) nearby, the hydrogen bonding interaction holding the amino and the carboxyl ends of the polypeptide chain will be broken. The terminal residues (^1Ser and ^{94}Ile) would then move away from each other to avoid close contacts resulting in disruption the β -sheet interactions at the dimer interface and subsequent dissociation of the dimer. Interestingly, in solution structure of PSP94 by NMR²²⁶, a similar movement of the terminal residues is seen facilitated by twisting of two domains (Fig. 3b, c), where the main chain nitrogen atom of ^1Ser and

carboxyl oxygen atom of ^{94}Ile in different models are far apart (6.0-8.9 Å). Thus the NMR structure, wherein the samples were prepared in water at pH 6.0 without any buffer, would represent the monomeric form of PSP94.

Thus the crystal structure of PSP94 shows how the edges from two PSP94 monomers associate to form a dimer and how by reducing the pH, the dimers dissociate into monomers. This assumes biological significance as PSP94 would function as a dimer in the human semen (pH 7.5-8.0), whereas the dimers may dissociate into 'active' monomers when it comes to vagina (pH 3.8-5.0). The concept of inactive dimers and the active monomers, in the context of PSP94 binding to IgG, was proposed earlier⁴ but the role of vaginal pH in 'activating' PSP94 had not been investigated there. The present work, therefore, provides useful clues to the biological functions of this important family of proteins.

Acknowledgements

We gratefully acknowledge the contribution of our collaborators Dr. Dhanashree Jagtap and Dr. Smita Mahale from NIIRH, Parel, Mumbai, for providing PSP94 for our crystallographic work.

References

1. Laurence M, *PSP94, what is it good for?* (2013), <http://books.google.com/>
2. Ghasriani H, et al. "Solution structures of human and porcine beta-microseminoprotein". *J Mol Biol.* 362 (2006): 502-15.
3. Wang I, et al. "Novel solution structure of porcine beta-microseminoprotein". *J Mol Biol.* 346 (2005): 1071-82.
4. Mori, H, et al. Enzymatic activation of immunoglobulin binding factor in female reproductive tract. *Biochem Biophys Res Commun*, 246, (1998): 409-413.

BARC NEWSLETTER

A NOVEL METHOD USING PULSED EDDY CURRENT FOR DETECTION OF SPACERS IN COOLANT CHANNEL OF PRESSURISED HEAVY WATER REACTOR.

T.V. Shyam
Reactor Engineering Division

Shri T.V. Shyam is the recipient of the DAE Scientific & Technical Excellence Award for the year 2011

Abstract

Conventional Eddy current techniques (ECT) are used for inspection of some of the components like coolant channels of 220 MWe Pressurised Heavy Water Reactor (PHWR). These methods are sensitive to various test object parameters like electrical conductivity, distance between probe and the test object and magnetic permeability leading to ambiguity in measurement of parameter of interest. During en-masse coolant channel replacement operation in one of the PHWR, eddy current signals similar to that of Garter springs were observed which were attributed to localized zones of oxygen rich α -grain phase. With conventional eddy current technique it is quite formidable to distinguish such features. Pulsed Eddy Current (PEC) Technique is broad band in nature and has the capability to probe the test object with broad band of frequencies. The PEC pickup signals carry rich information coded in broad band signals. The signal analysis is carried out by time frequency analysis using wigner ville distribution to extract the information of the parameter of concern.

Keywords. pulsed eddy current, wigner ville distribution, PHWR, ECT, PEC

Introduction

In Pressurized Heavy Water Reactor (PHWR) horizontal coolant channel assemblies submerged under heavy water moderator. The coolant channel assembly consists of horizontal pressure tube (PT) or coolant tube enclosed by calandria tube (CT). Both CT and PT are made of zirconium alloys and are kept separated by annular spacers called garter springs (GS) placed like bangles around PT at pre-determined axial locations. The schematic of coolant channel assembly is shown in Fig. 1.

During garter spring detection scans in fresh pressure tubes (meant for one of the PHWR reactor where en-masse replacement of coolant channels were being carried out), signals similar to that of garter springs

were observed at locations where no garter springs were present. These synonymous signals observed in Eddy Current Technique (ECT) were inverted in phase to garter spring signals and were attributed to localized zones of oxygen rich α -grain phase which exhibited high electrical resistivity (similar instances was reported elsewhere[3]).

The eddy current technique being a multi-parameter sensitive technique, it is usually difficult to separate eddy current sensitive parameters as they influence the output in similar fashion. Conventional mono frequency eddy current technique have limitation to differentiate only maximum two parameters out of many parameters which are subject to variation to various metallurgical transformation due to hostile and radioactive environments existing in operating PHWRs.

BARC NEWSLETTER

To give a wider view to the inspect-ability, pulsed eddy current technique employing broad band of frequencies was used for the inspection for one of the subject fresh pressure tube at Reactor Engineering Division, BARC. The various frequencies in the broad band spectrum of the electromagnetic pulse penetrate the test object and subside as per the skin effect phenomena, wherein higher frequencies subside at lower depths from the surface, where as lower frequencies penetrate and subside at larger depths. The resultant electromagnetic field which induces a pickup voltage signal in receiver coil has initial transient part sensitive to the near surface features and later part of the signal sensitive to the features deeper inside the test object.

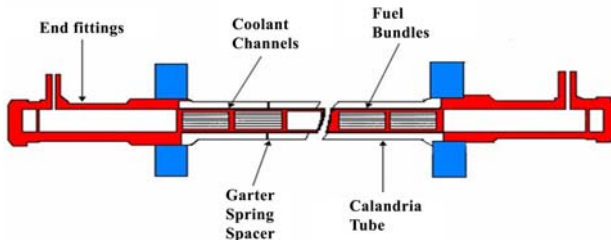


Fig. 1: Schematic of Coolant Channel assembly

The pulsed eddy current signals are encoded with rich information about test object and by application of suitable signal processing technique it would be possible to extract and disseminate the information. Signal processing techniques having both temporal as well as spectral analysis give more perception to separate the parameters from a cluster of unknown parameters. The time frequency analysis using wigner ville distribution has been employed for the analysis of the PEC signals. The output which can mapped into

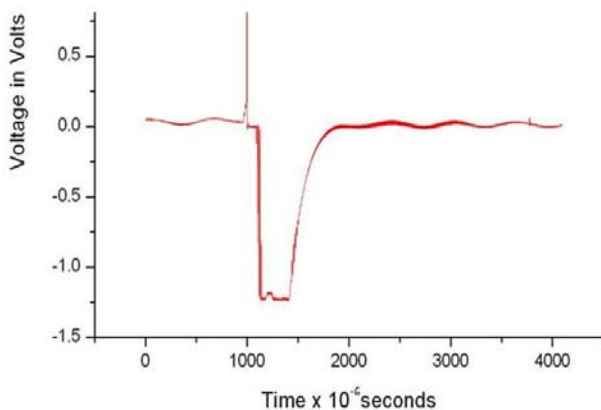


Fig. 2: Typical Response signal of PEC probe

time frequency plane give wider possibility to separate and analyse the effects of the multi -parameters sensitive to eddy current technique. The typical excitation and output waveform of pulsed eddy current system is shown Fig. 2.

The simplified expression for wigner ville distribution [1] of a continuous complex signal $x(t)$ is defined as

$$W_x(t, \omega) = \frac{1}{2\pi} \int x\left(t + \frac{\tau}{2}\right) \cdot x^*\left(t - \frac{\tau}{2}\right) \cdot e^{-j\omega\tau} d\tau$$

where

$$x\left(t + \frac{\tau}{2}\right) \cdot x^*\left(t - \frac{\tau}{2}\right)$$

is the expression for the auto correlation of the signal $x(t)$, τ is a time shift variable, ω is frequency variable and * denotes the complex conjugate. From the above expression, wigner ville distribution can be visualized as the fourier transform of the auto correlation of the signal $x(t)$. The wigner ville time frequency distribution was realized by use of software coded module for wigner ville distribution.

Experimental Setup

Pulsed eddy current garter spring detection probe with bobbin type coils having two sets of primary and secondary coils was fabricated. The secondary coils were configured in differential mode taking into account compatibility to the existing in-service-garter spring detection method. The block diagram of the system setup is shown in Fig. 4.

The garter spring detection probe was excited with pulser module and the secondary coil outputs were fed to signal conditioning unit. The pulser module was designed and developed using 8751H microcontroller for generating pulse which was used to drive a MOSFET driven with the help of associated MOSFET driver. The signal conditioning module was based on instrumentation amplifier. The Pulsed Eddy Current system for Garter Spring Detection is shown in Fig. 3.

BARC NEWSLETTER



Fig. 3: Pulsed Eddy Current System for Garter Spring Detection.

The block diagram of the system setup is shown in Fig. 4.

The signals were acquired using a cPCI based high speed data acquisition system and processed using a software coded wigner ville subroutines for getting time frequency analysis.

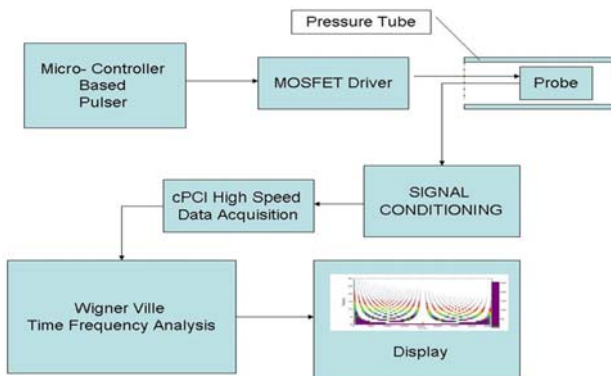


Fig. 4: Schematic of Experimental Setup

Discussion of Results

The pressure tube was scanned initially with garter spring detection probe in conventional technique and locations where conspicuous indications were observed. The pulsed eddy current analysis was carried out at a zone (reference zone) where abnormalities of any nature were not observed. The time frequency analysis of the PEC signal is shown in Fig. 5. The garter spring was placed at another zone where abnormalities of any nature were not observed and pulsed eddy current signals were acquired. The time frequency analysis of PEC signal is shown in Fig. 6.

This time frequency analysis distribution was compared with that obtained at normal or reference zone and it was observed that time frequency representation shows reduction in amplitude in the zone mapped at 1230×10^{-6} s to 1300×10^{-6} s in time axis and frequency at around (8×244) 1952 Hz.

The pulsed eddy current analysis was carried out at location where the in-homogeneity was observed in conventional Garter spring detection technique. The time frequency representation is shown in Fig. 7. The time frequency analysis display was compared with that of template signal observed at reference location. The time frequency representation shows reduction in amplitude in the zone mapped at 1280×10^{-6} s to 1300×10^{-6} s in time axis and frequency at around (15×244) 3660 Hz.

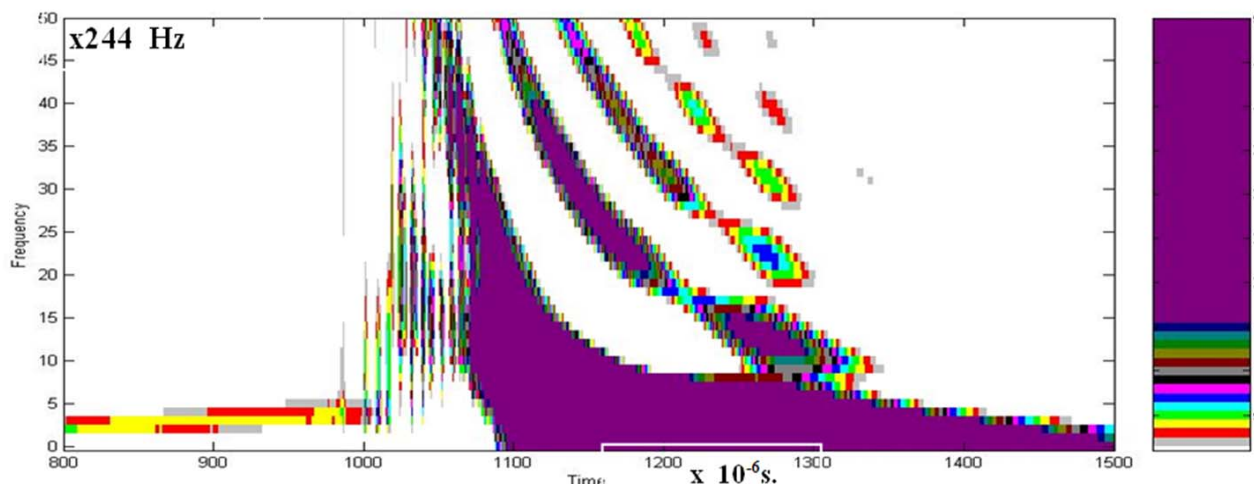


Fig. 5: Typical time frequency analysis of normal zone of pressure tube location

BARC NEWSLETTER

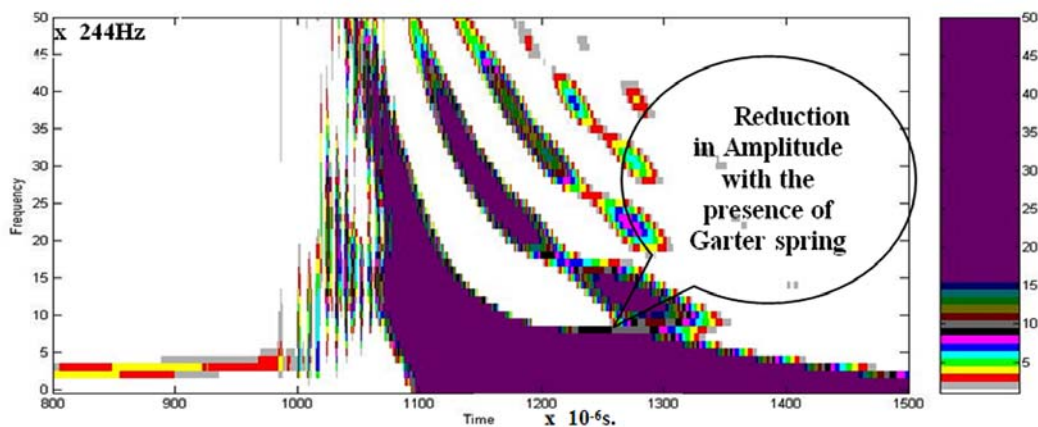


Fig. 6: Time frequency analysis output of location with Garter spring placed over the pressure tube

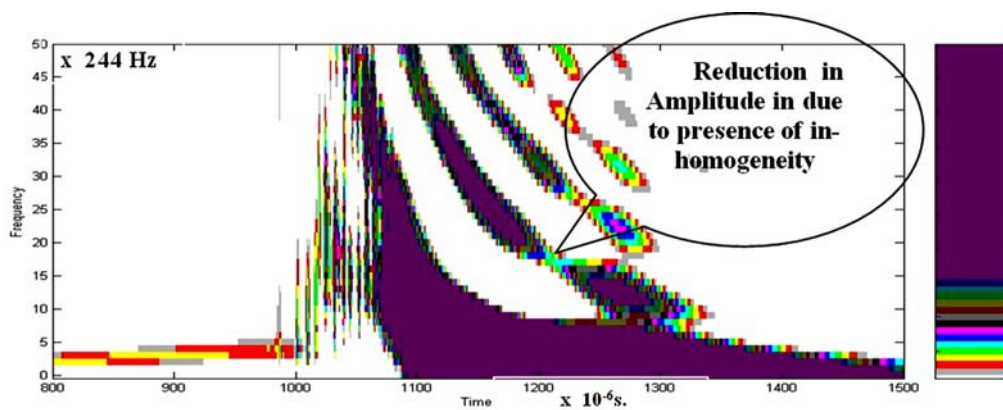


Fig. 7: Time Frequency analysis of location where in-homogeneity was observed

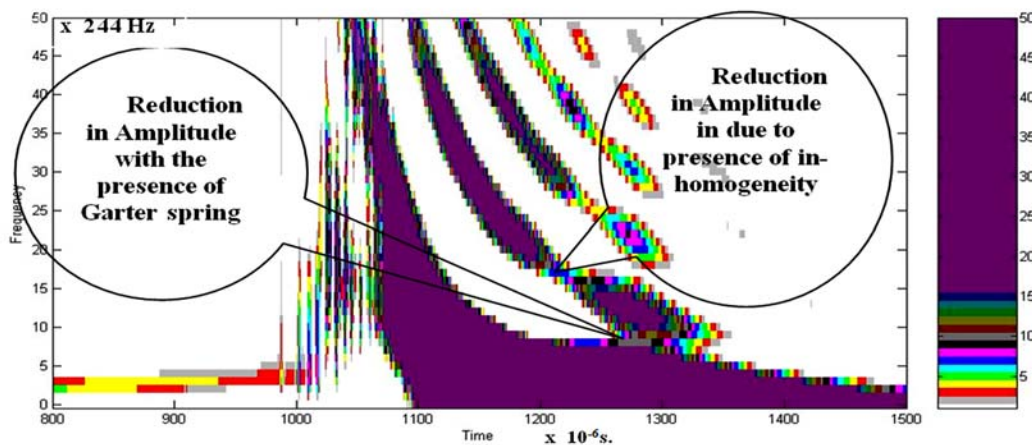


Fig. 8: Time Frequency analysis of location with in-homogeneous zone along with Garter spring

To demonstrate parameter separation capability of garter spring in presence of in-homogeneous localized zone was carried out by placing garter spring at location where in-homogeneity is found. The time frequency analysis shows both the characteristic of garter spring as well as the in-homogeneous zone were distinctly identified at their respective zones at 1230×10^{-6} s to 1300×10^{-6} s in time axis and frequency at around

1952 Hz and at 1280×10^{-6} s to 1300×10^{-6} s in time axis and frequency at around 3660 Hz. The time frequency representation is shown in Figure 8.

Conclusions

The Pulsed Eddy Current (PEC) technique is an emerging field having immense potential especially

BARC NEWSLETTER

in non-destructive testing of critical components related to nuclear reactors. The application of PEC technique gives wide scope for inspect-ability of components of PHWR. By employing suitable signal processing techniques like time frequency analysis, it is shown that the eddy current sensitive parameters can be mapped to specific time frequency zones of the time frequency representation of the PEC signals. With such methodology it will be easier to differentiate the garter spring signals from the in-homogeneity signals in pressure tubes. The broad band nature of the technique gives more dimensions to view the parameters of our interest. The PEC technique can be used as supplement to the existing In-Service Inspection (ISI) whenever ambiguity arises in detection of garter spring using conventional eddy current technique.

Acknowledgement

The author is thankful to Shri K. K. Vaze, Director, Reactor Design and Development Group and Dr. P. K.

Vijayan, Head, Reactor Engineering Division for providing encouragement to carry out such developmental activities.

References

1. M. S. Safizadeh, "Time-Frequency Analysis of Pulsed Eddy Current Signals" in J. Non Destructive Evaluation, vol. 20, No:2, June 2001. pp77-84.
2. P. Brunet, "Evaluation of Time-Frequency Analysis Methods and their Practical Applications" presented in 123rd Convention of Audio Engineering Society, New York, USA, 2007 October 5 -8.
3. R. Choubey et al. "Micro segregation of Oxygen in Zr-2.5 Nb Alloy Materials" Metallurgical and Materials Transactions A Volume 27A, Feb. 1996.

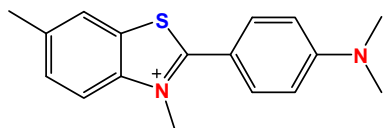
PHOTOPHYSICAL STUDIES OF AMYLOID FIBRIL SENSOR

Sukhendu Nath

Radiation & Photochemistry Division

Dr. Sukhendu Nath is the recipient of the DAE Scientific & Technical Excellence Award for the year 2011

Thioflavin-T (ThT), a benzothiazole based cationic molecule, has been extensively used to detect and monitor the formation of amyloid fibril, a filamentous form of proteins that are responsible for several neurodegenerative disorders, such as Alzheimer's and Parkinson's diseases.^{1,2} ThT is specifically bind to amyloid fibril and do not show any affinity to native protein molecules. Binding with amyloid fibril leads to an increase in its emission yield by several orders of magnitude. Despite of such immense importance of ThT, the basic mechanism that is responsible for its fluorescence sensing activity in amyloid fibril was not known. We have studied the photophysical properties of ThT in detail to understand the basic molecular processes that are responsible for its fluorescence sensing activity.



Scheme-1: Chemical structure of Thioflavin-T

Emission yield of ThT in water is extremely low ($\sim 10^{-4}$). The excited state of ThT in water shows multi-exponential decay kinetics at all emission wavelengths. The average excited state lifetime of ThT in water is estimated to be ~ 1 ps. Detailed analysis of emission transient decays shows that following photoexcitation, ThT undergoes an efficient non-radiative process with time constant of ~ 0.57 ps ($1\text{ps}=10^{-12}$ sec).³ Because of such ultrafast decay process in its excited state, the emission quantum yield of ThT in water is extremely low.

To understand the origin of such ultrafast non-radiative process, excited state properties of ThT have been studied in different homogeneous and heterogeneous

media.³⁻⁸ Such studies show that the emission yield and the excited state lifetime of ThT increases with the increase in the solvent viscosity (*cf.* Fig. 1). Further, detailed time-resolved studies show that the rate of ultrafast non-radiative decay process decreases with increase in the solvent viscosity.⁵ Thus, the time constant for the nonradiative decay in ethylene glycol, a relatively viscous solvent, is found to be 1.8 ps, which is considerably higher than that in water (0.57ps). Increase in the non-radiative time constant with increasing solvent viscosity suggests the presence of a large amplitude torsional motion in its excited state.

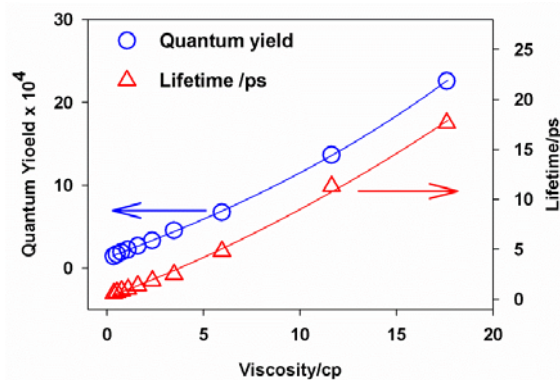
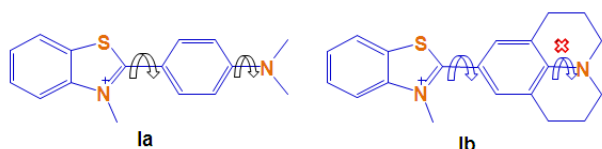


Fig. 1: Variation in the emission quantum yield and excited state lifetime of ThT with solvent viscosity.

From the chemical structure of ThT it is evident that there are two possible torsional motion, one is around central C-C bond, and other is around C-N single bond in the dimethylanilino moiety. Rotation around any one of such bonds can lead to non-radiative decay of the excited ThT molecules. To identify the bond that is mainly responsible for the excited state torsional motion, two derivatives of ThT (*cf.* Scheme 2) have been synthesized.⁶ In derivative 1a torsional motion around both the bonds are possible while the torsion around the C-N bond is prohibited in 1b due to the presence of

BARC NEWSLETTER

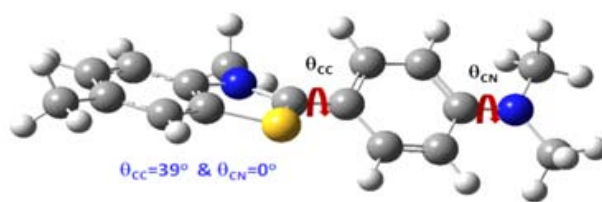
julolidine group. Detail photophysical studies of these two derivatives shows that all photophysical parameters, like quantum yield, lifetime, etc are quite similar for ThT, Ia, and Ib. If the torsional motion around C-N bond were responsible for the observed ultrafast decay, one would expect a large increase in the lifetime and emission yield for Ib in comparison to ThT and Ia. Thus, torsion around the C-N single bond is not responsible for the observed ultrafast non-radiative decay of the excited ThT molecules. This in turn, revealed that the twisting around the central C-C bond is mainly responsible for the observed ultrafast decay and low emission yield of ThT in low viscous solvents.



Scheme 2: Chemical structure of Thioflavin T derivatives.

The torsional motion around the central C-C bond is further confirmed by quantum chemical calculations.³ The optimized geometry of ThT (*cf.* scheme 3) indicates that the molecules in the ground state is non-planer and the benzothiazole moiety makes an angle of $\sim 39^\circ$ with respect to the dimethyl anilino moiety. Further, the dihedral angle between the dimethylamino group and benzene ring is $\sim 0^\circ$.

The potential energy surfaces as function of the torsional angle (θ_{CN}) around the C-N single bond for both ground and first excited singlet state are shown in Fig. 2A. It is evident from the Fig. 2A that configurations with $\theta_{CN} = 0^\circ$ and 90° are separated by a high energy barrier and thus torsion around the C-N bond is not feasible. The potential energy surfaces as a function of the torsional angle (θ_{CC}) around the central C-C bond (*cf.* Fig. 2B) indicate that the local excited state ($\theta_{CC} = 39^\circ$, in S_1 state) has a quasiminimum energy and the twisted state ($\theta_{CC} = 90^\circ$) is the most stable configuration. Thus, the present result indicates that the ThT in its photoexcited state can undergo barrierless torsional motion around the central C-C single bond to form twisted state. Such barrierless torsional motion is mainly responsible for the low emission yield of ThT in less viscous solvents.



Scheme 3: Optimized geometry of ThT in water. The curved arrows show the possible rotations around single bonds.

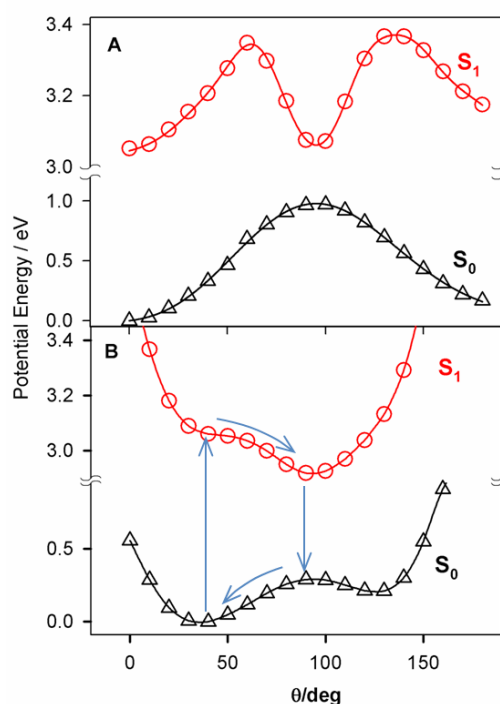


Fig. 2: Variation in the potential energy in the ground (Δ) and excited state (O) as a function of dihedral angles: (A) θ_{CN} and (B) θ_{CC} .

Thus, experimental and quantum chemical calculations indicate that the torsional motion around the central C-C single bond in the excited state of ThT is mainly responsible for its observed ultrafast decay and consequently its extremely low emission yield in water. However, in viscous solvent, such torsional motion is restricted in the excited state and leads to an increase in its emission yield.

Photophysical properties of ThT has been investigated in Insulin fibrillar media.³ The emission quantum yield of ThT is increases by ~ 160 times due to its association with the amyloid fibril. Its excited state lifetime is also increases from ~ 1 ps in water to 1.3 ns in fibrillar media (*cf.* Fig. 3). Absence of any ultrafast non-radiative decay in amyloid fibril indicates that the torsional motion in

the excited state of ThT is completely prevented in the fibrillar solution and leads to large increase in its emission yield.

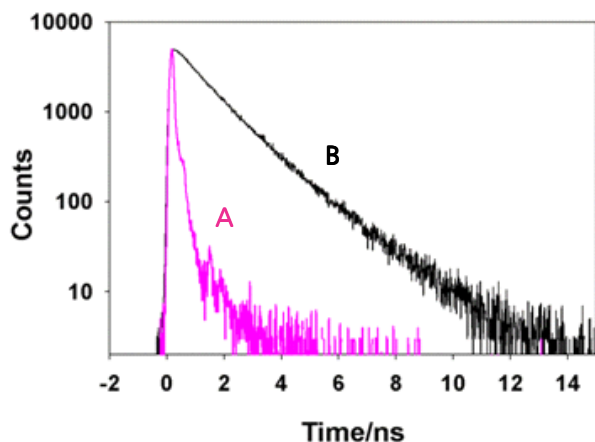


Fig. 3: Emission transient decays for ThT in (A) water and (B) insulin fibrillar solution.

Thus, our studies established for the first time that the ultrafast torsional motion is mainly responsible for the low emission yield of ThT in water. Further, such torsional motion is prevented in amyloid fibril due to the entrapment of ThT in its three dimensional structure and causes large increase in its emission yield.

Acknowledgement

I am thankful to all my coauthors for their significant contribution in the present research work. Sincere and valuable guidance from Dr. T. Mukherjee, Dr. S. K. Sarkar, and Dr. D. K. Palit is acknowledged.

Reference

1. Gilead, S.; Gazit, E. *Angew. Chem. Int. Ed.* **2004**, *43*, 4041.
2. Mishra, R.; Winter, R. *Angew. Chem. Int. Ed.* **2008**, *47*, 6518.
3. Singh, P. K.; Kumbhakar, M.; Pal, H.; Nath, S. *J. Phys. Chem. B* **2010**, *114*, 2541.
4. Singh, P. K.; Kumbhakar, M.; Pal, H.; Nath, S. *J. Phys. Chem. B* **2009**, *113*, 8532.
5. Singh, P. K.; Kumbhakar, M.; Pal, H.; Nath, S. *J. Phys. Chem. B* **2010**, *114*, 5920.
6. Srivastava, A.; Singh, P. K.; Kumbhakar, M.; Mukherjee, T.; Chattopadhyay, S.; Pal, H.; Nath, S. *Chem. Eu. J.* **2010**, *16*, 9257.
7. Singh, P. K.; Kumbhakar, M.; Pal, H.; Nath, S. *Phys. Chem. Chem. Phys.* **2011**, *13*, 8008.
8. Singh, P. K.; Kumbhakar, M.; Pal, H.; Nath, S. *Chem. Commun.* **2011**, *47*, 6912.

INDIGENOUS DEVELOPMENT OF A SPOT PICKER ROBOT FOR PROTEOMICS APPLICATIONS

Ratnesh Singh Sengar, A.K. Upadhyay, D.N. Badodkar, R.K. Puri, Manjit Singh

Division of Remote Handling & Robotics

and

M.G.R. Rajan

Radiation Medicine Centre

and

V.M. Gadre

Department of Electrical Engineering, Indian Institute of Technology Bombay, Mumbai

Shri Ratnesh Singh Sengar is the recipient of the DAE Scientific & Technical Excellence Award for the year 2011

Abstract

Proteomics is a well established subject in medical science, which focuses on the library of proteins specific to a given bio-system, the proteome, and understanding of relationships therein. It is a very challenging task to find out the correct position coordinates of all the proteins in the 2D gel, because proteins change their position in each experiment according to their mass and charge with a lot of noise and non-linear background. The precise excision of the correct protein spots is also important for further analysis. The Spot Picker Robot can be seen as an essential tool in proteomics. It accurately locates and identifies the protein spots from 2D gels and picks and transfers the proteins for further analysis, thus enhancing data quality and reliability in the field of proteomics. The application of this robot has helped in discovering new proteins to develop biomarkers for new diagnostic tests. It provides the necessary automation for high throughput analysis. Our spot picker robot features the non-separable wavelet based novel imaging algorithms, better design of light illumination for detection of faint, irregular & overexposed protein spots in a nonlinear background and generates more accurate reference position coordinates of a dynamic protein object. The system includes a high performance solenoid controlled surgical grade protein spot excision tool and a novel wavelet based accurate positioning algorithm to reduce the effect of jerks on the system. Even with all these features, the cost of the system is very reasonable.

Introduction

The Spot Picker is a 3-axis robotic system (Fig. 1) designed for precise protein spot excision and to accurately pick spots from 2D gel electrophoresis (2DGE). It transfers the picked protein into micro plates for analyzing protein expression. This is important for understanding protein function for the development of new and more effective drugs. The protein separation from the human cells or plant tissue is done by a 2D gel electrophoresis process, which is very non-linear. It introduces a lot of noise and uneven background in the gel. So, a very important task in a 2D gel proteomic

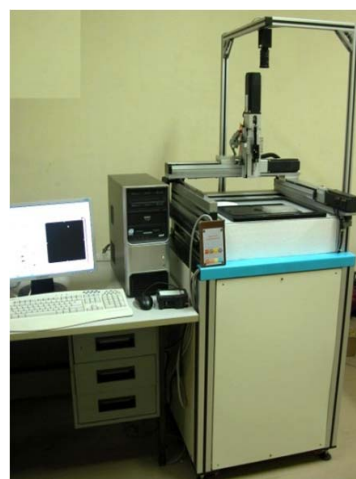


Fig.1: Spot Picker Robot

BARC NEWSLETTER

study is to find out the correct position coordinate of each protein spot. It is a very challenging task to correctly analyze and interpret 2D gel images through image analysis to identify the position of all protein spots. After processing, it generates the spot position co-ordinates and spot picking list, which is the reference coordinates of each dynamic protein spot, which is be directly interfaced with the robotic system for automated protein spot excision.

A typical flow of gel based proteomics is depicted in Fig. 2. In this paper, we explore the steps 4 to 7 in the workflow of a proteomics application, which are related to development of our Spot Picker Robot. The important considerations while designing this precise 3-axes robotic system are high speed, micron level accuracy and minimum vibration. The system should also have uniform illumination for gel images, a high resolution imaging device, precise excision of protein spots without distortion and contamination of the gel and robust imaging algorithms. Rinsing of the probe is required to avoid crossover contamination.

Analysis and interpretation of 2D gel images (as shown in Fig. 3) is the key task in proteomics study. The

commercially available image analysis software packages have limitations for the detection of complex and faint protein spots in a nonlinear background. The faint and complex protein spots also play an important role in the study of proteomics. The non-separable wavelet based processing methods have been developed, due to their inherent ability to better represent directional information. These seem to be promising for the processing of protein spots with low abundance. Our system features new algorithms for noise filtering [1] and image segmentation [2]. Using its powerful spot detection algorithm, it instantly locates and analyses protein spots. We have introduced a novel hardware feature for setting up a very uniform light source in our system to provide better illumination of protein spots in 2D gel for imaging. Excision of individual protein spots from a 2DGE without deformation is another important task. It is designed to minimize damage to the gel or protein carryover from one spot to another. The robot is a critical part for precise picking of the protein spots from 2D gels. The system hardware consists of a 3-axes robotic motion which is highly precise and has a positioning accuracy of ± 10 microns.

1. Sample preparation from cell/tissue
2. Separation of protein in sample by Electrophoresis
3. Image Acquisition: High resolution color CCD camera
4. 2D Gel Image Analysis :
 - a. Image Preprocessing (De-noising)
 - b. Segmentation (Spot detection)
 - c. Image Registration
 - d. Protein Quantification in spot (shape, size, intensity, contrast)
5. Spot Picking Robot for Automation: A 3-axes robot for picking the protein spots from 2D gel surface
6. Protein spot cutting tool
7. Data Analysis and Integration
8. The excised protein is identified by Mass Spectroscopy

Fig.2: Typical flow of gel-based proteomics (2DGE & MS)



Fig.3: Different types of spots

BARC NEWSLETTER

Non Separable Wavelet based 2D Gel Image Analysis

The objective is to locate and identify the protein spots in gel images from the uneven background which has sharp edges, e.g. lines, artifacts and streaks in some areas. Due to the system nonlinearities in gel formation and image acquisition, there will inevitably be overlapped protein spots, saturated spots and faint spots. The nonlinear intensity and narrow lines on the gels make the task more difficult (see Fig. 3). Although our method of de-noising and segmentation has been reported earlier [1] [2], to have a complete view of our system, a brief has been presented here as a review of our earlier work.

The classical methods of filtering, which are fast and efficient for stationary signals, fail for the non-stationary ones with high frequency features. We have also found that the spatial filters destroy the borders of the spots, which create problems for proper detection of spots. The areas and the intensities of spots are also affected. Images obtained from 2DGE contain spots (peaks) of very different sizes and intensities. The Wavelet Transform outperforms spatial filtering, both in terms of Peak Signal to Noise Ratio (PSNR) and in terms of minimizing spot edge distortions [1]. Separable 2-D wavelet transforms extensively focus on the three directions (vertical, horizontal and diagonal) an enormous amount of singular information in other directions cannot be revealed explicitly in the high frequency component. Hence quincunx non-separable wavelets and filter banks have good potential when applied to gel images.

Non-Separable Wavelet Quincunx

We employ a non separable quincunx wavelet transform that outperforms the available methods of de-noising and segmentation. Even though this is a non-separable transform, the computational complexity is not significantly greater. At the same time, it maintains the general form of multi resolution character. Our investigation demonstrates that the high frequency components from this non-separable WT can capture more singular information than traditional wavelets. Therefore, it motivates us to apply an approach based

on the non-separable wavelet to extract the features of 2D Gel electrophoresis images. A quincunx filter bank has the canonical form shown in Fig.4.

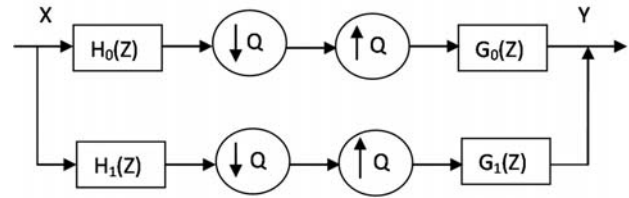


Fig. 4: Quincunx filter-bank

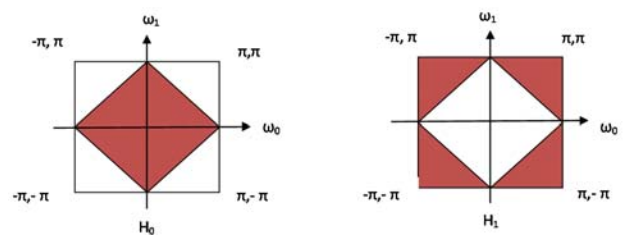


Fig. 5: Frequency supports of filters in Quincunx filter-bank

Non-separable systems have non-rectangular frequency supports for the sub-bands, thus resulting in better frequency selectivity. The simplest decomposition of that type, known as the Quincunx transform (QT), uses non-separable and non-oriented filters, followed by the non-separable sampling represented by the matrix Dq in (1) below. The Quincunx low-pass and high-pass filters are often chosen to have diamond shaped frequency supports, as shown in Fig.5. Since $\det(Dq) = 2$, this transform is performed with a two-channel filter bank. At each level, the input image is decomposed with the multi-resolution scale factor 2, resulting in one low-resolution sub-image and one non-oriented wavelet sub-image.

$$Dq = \begin{bmatrix} 1 & 1 \\ -1 & 1 \end{bmatrix} \quad (1)$$

We have employed the quincunx filter bank in polyphase form, with the analysis and synthesis polyphase filtering each being performed by a ladder network consisting of a number of *lifting* filters P and U as shown in Fig.6. In this manner, quincunx filters of higher order have been constructed with perfect reconstruction property. During our experiments it has been found that the un-decimated version of the quincunx transform performs better than previous

BARC NEWSLETTER

versions, so the decimation operator has been removed from the quincunx lifting scheme and the N-times quincunx up sampled versions of filters are used, where N represents decomposition level.

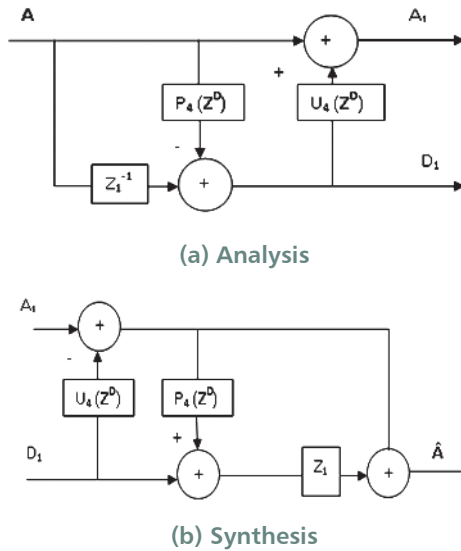


Fig. 6: Lifting Scheme of Quincunx filter bank

We have reported our results of de-noising of gel images [2]. After de-noising, segmentation is another important step in processing the gel image, which extracts individual spots. Although, de-noising in non-separable domain gives the best result, a large of nonlinear variations still pose problems for segmentation. The watershed is a popular medical image segmentation method. The available segmentation methods, including watershed use various global thresholds for obtaining the final results. A lower value of threshold lead to detection of several artifacts as spots and a higher threshold value miss many spots. It is next to impossible to find an optimal threshold value. Depending upon the nature of gel images, global thresholds cannot work and local thresholds are hard to find.

Singularity in 2D gel images across scales is studied in the non-separable domain and it is found that it can provide valuable hints for image segmentation [2]. A gel image is first decomposed using un-decimated quincunx wavelet transform to maintain the shift invariant nature of the transformed image and then a watershed transform enables us to study singularities within a local area (or partition) in the wavelet domain.

The watershed transform on the low resolution image is obtained and each partition (catchment basin) is denoted by $CB(m_k)$, where m_k is the k th minima in the corresponding image. We define the scale product and connected maxima set as follows:

Definition: The scale product $P_{j,j+1}$ shows the correlation between wavelet coefficients of adjacent scales j and $j+1$ and defined as

$$P_{j,j+1}(x,y) = W_j(x,y) \cdot W_{j+1}(x,y)$$

Watershed catchment basins are mapped onto $P_{j,j+1}$ and corresponding to each $CB(m_k)$, coefficients of $P_{j,j+1}$ are found and denoted as $S_{j,j+1}(m_k)$. Now a connected maxima set for $S_{j,j+1}(m_k)$ is defined as follows:

Definition: A connected maxima set $CM_i(m_k)$ is a collection of those coefficient $\{c_q\}$'s of $S_{j,j+1}(m_k)$ which satisfies any of the following criteria:

$$(1) c_q = \{\max_j (c_j) | c_j \in (S_{j,j+1}(m_k) - U_{i \neq i} CM_i(m_k))\}$$

or

(2) c_q is in neighborhood of $CM_i(m_k)$ and it is largest of its neighbors. Also c_q has at least $(k-2)$ neighbors having value less than it (assuming k -neighborhood operation). In a $S_{j,j+1}(m_k)$, there may be more than one connected maxima set. Horizontal and vertical connected maxima sets are identified and neglected in further processing. The remaining connected maxima set is used to calculate the local threshold for each watershed partition [2]. Further, post-processing is also required to remove the artifacts and remaining streaks. Moments, relative pixel intensity and minimum size of spots act together as the constraints to give the final results. Fig. 7 shows the part of original segmented image.



Fig. 7: Segmented Protein Spot

BARC NEWSLETTER

Spot Cutting Tool

Excision of individual protein spots from a 2D electrophoresis gel without deformation is another important task. We have developed a cutting tool made of surgical grade stainless steel with a diamond coated surface. It is depicted in Fig. 8. It is designed to minimize carry over or damage to the gel or membrane when properly handled. The cutting tips of 1.0mm, 1.5mm, 2.0mm, 2.5mm and 3.0mm diameter can be easily attached or detached with the rest of this tool. After cutting, the part of the gel should remain inside the cutter and should expel into the well-plate. A solenoid based pneumatic actuated placement system with silicon diaphragm is used to create pressure inside the cutting tool.



Fig. 8: Spot Cutting Tool

After cutting, the part of the gel should remain inside the cutter and should expel into the well-plate. A solenoid based pneumatic actuated placement system with silicon diaphragm is used to create pressure inside the cutting tool.

introduced a novel hardware feature for illumination in our system. A light source (see Fig. 9) has been designed and developed, which consists of a matrix of 15 x 18 white light LEDs. This LED matrix is encapsulated by a thin plate made of a special type of polymer (PMMA) on the upper side and provides 90% color index rendering, 100% diffused pure white light with low power consumption.



Fig. 9: Light Source

Illumination System

Uniform non-heating illumination is an important requirement for imaging the protein spots without any distortion of the gel or denaturing of protein. We have

Robotic System

The robot is a critical part for precise picking of the protein spots from 2D gels and the transfer of that protein into the right place for further analysis. Hence the system hardware consisting of a 3-axes robotic motion has been designed to be highly precise with a

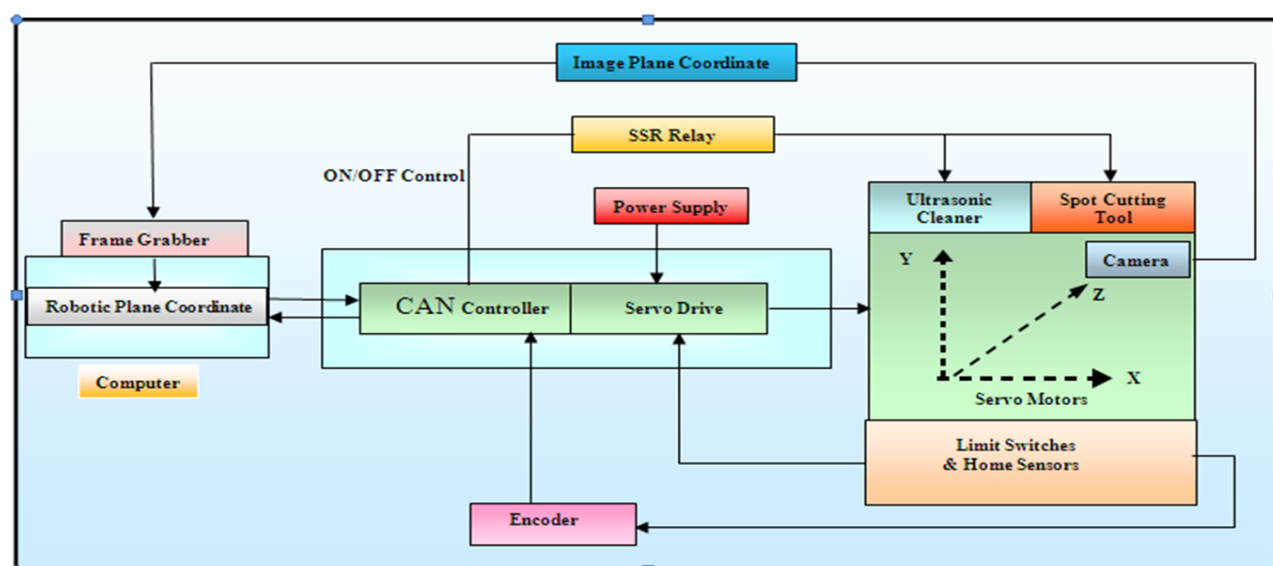


Fig. 10: Computer based control system for Spot Picker Robot

BARC NEWSLETTER

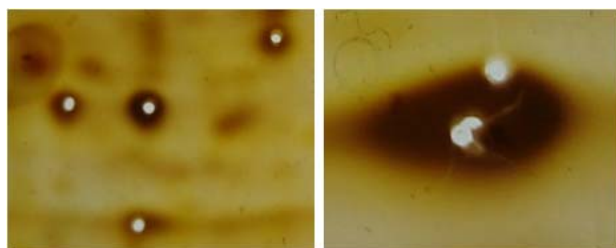
positioning accuracy of ± 10 microns. This can be achieved with the help of servomotors, high resolution encoders, precision ground ball-screw based linear actuator, an advanced control system scheme and a well damped table. A jerk rejection method based upon Haar wavelet has been implemented to generate the motion profiles [3]. A block diagram of the whole system is represented in Fig. 10.

Software

Object oriented multithreading software has been developed to provide real time and user friendly control for each resource of the system. It grabs the image, analyzes it and presents the segmented result of protein spots to the user for automated or manual picking of the spots. The centroid coordinates of the spots in the image plane are converted into the robotic plane and the robot cuts, picks and delivers the spots. After cleaning the cutting tip, the robot picks the next spot and the cycle continues to reach the final spot.

Sample outputs from our system

Sample outputs coming from our system are shown in Fig. 11. One can clearly see the superior quality of the output of the spot picker robot.



(a) by Spot Picker Robot (b) by manual operation

Fig. 11: Spot cut from the gel

Conclusion

We have developed a high quality Spot Picker Robot for the successful application of automation in high quality laboratory equipment and as a life science product for proteomics applications. Novel image processing algorithms have been developed for precise protein spot identification. A spot cutting tool has been designed for uniform and accurate spot excision without distorting the gel. A uniform non-heating

illumination source has been designed which provides fully diffused pure white light and avoids denaturing of proteins.

The hardware and software are both designed to provide high performance automation together with the flexibility required for individual sample handling and custom design. Experimental results indicate that our advanced technology used for this control and automation scheme exhibits superior performance compared to other less sophisticated methods. The developed spot picker robot with its imaging algorithms is a state of the art technology for low cost biomedical systems. This system has been delivered to RMC, Parel.

Acknowledgment

The authors are grateful for the helpful suggestions of Dr. HS Mishra, MBD, BARC and Dr. Savita Kulkarni, RMC.

References

1. Ratnesh Singh Sengar, AK Upadhyay, Pushkar G Patwardhan, Manjit Singh, Vikram M Gadre, "Approaches based on non-separable filter banks in 2D Gel electrophoresis image analysis," *Proceedings of Asia Pacific Signal and Information Processing Association (APSIPA) International Conference, Biopolis, Singapore*, p.p. no. 387-392, December 2010.
2. Ratnesh Singh Sengar, AK Upadhyay, Manjit Singh, Vikram M. Gadre, "Segmentation of Two Dimensional Electrophoresis Gel Image Using the Wavelet Transform and the Watershed Transform," *The eighteenth annual National Conference on Communications (NCC-2012), IIT-Kharagpur, IEEE Xplore DOI: 10.1109/NCC.2012.6176861*, February 3-5, 2012.
3. Ratnesh S Sengar, AK Upadhyay, DN Badodkar, RK Puri, Manjit Singh, MGR Rajan and VM Gadre "Development of Spot Picker Robot for Proteomics Applications", *IEEE International Conference on Robotics & Automation*, May 06-10, Karlsruhe, Germany, IEEE Xplorer DOI-IAN: 978-1-4673-5642, pp 1704-1709.

BARC NEWSLETTER

THE CHILD-LANGMUIR LAW – FROM QUANTUM TO CLASSICAL PHYSICS

Debabrata Biswas

Theoretical Physics Division

Dr. Debabrata Biswas is the recipient of the DAE Scientific & Technical Excellence Award for the year 2011

Abstract

A hundred years after the Child-Langmuir law, its relevance in devices ranging from the nano to the macro remains undiminished. We first show that a more general law can be derived from simple dimensional analysis involving the Schrodinger and Poisson equations. The classical law then follows as a limit on demanding that it should be independent of Plank's constant (\hbar). We also point out a simple modification of the Child-Langmuir law for electromagnetically open systems where radiation may carry away energy out of the device. Finally, we briefly mention results on enhancing efficiency of microwave generation in the Virtual Cathode Oscillator (vircator) via improved beam-wave interaction using Particle-In-Cell codes where a limiting current is implicitly assumed.

The Child-Langmuir law, also known as the 3-halves law, dates back a century now. It was first published by Child [1] in 1911 and was followed up independently by Langmuir [2] in 1913 while investigating the limiting current in thermionic emission. It relates the maximum current density, J , that can be transported across a gap on application of a voltage (V) across two parallel plates separated by a distance (D):

$$J = \frac{4}{9} \epsilon_0 \sqrt{\frac{2e}{m}} \frac{V^{3/2}}{D^2}$$

The law does not concern itself with the emission mechanism. It simply assumes the existence of a sea of electrons at the cathode plate, whether due to thermionic, field or photo-emission. On application of a voltage, electrons start flowing through the diode, their number depending on the net electric field at the cathode. At the maximum transported current, the net electric field at the cathode becomes zero and further electrons cannot be transported even if they are made available at the cathode, for instance by increasing the temperature in case of thermionic emission or light intensity in case of photoemission.

The Child-Langmuir law can be easily derived from Gauss's law of electrostatics and holds for infinite planar electrodes. A similar law for co-axial diodes goes under the name of Langmuir-Blodgett law [3]. It can also be generalized for non-zero injection energy [4] and for finite emission areas [5] without requiring substantially new physics, so long as the devices involved follow "classical" laws. At the nano-scale however, considerations other than electrostatics dictate the maximum current that can be transported under identical assumptions. Here the dual nature of electrons comes into play and they can no longer be treated as point particles whose position and momentum are both known precisely by solving the equations of motion. Instead, their wave nature assumes importance due to the low applied voltages and (small) dimensions of a nano-diode, inside which other electrons reside. There is thus an additional interaction between electrons apart from the electrostatic - a quantum-mechanical interaction dictated by the well known Pauli Exclusion Principle, and, an additional phenomenon that has no parallel in classical physics – that of quantum mechanical tunneling.

BARC NEWSLETTER

Interestingly, quantum mechanics also holds in macro-devices. However, till recently [6], the Child-Langmuir law had never been arrived at from quantum-mechanical considerations. We shall first show how a more general scaling relationship can be derived from simple dimensional analysis, one that holds in nano as well as macro devices.

The starting point of the quantum-mechanical treatment is the Schrodinger equation

$$-\frac{\hbar^2}{2m} \frac{d^2\psi}{dx^2} + V(x)\psi = E\psi$$

where the wavefunction $\psi(x)$ determines the probability density $|\psi(x)|^2$ of finding electrons in any region. The potential $V(x)$ is an effective 1-particle potential that comprises of the electrostatic potential determined by the Poisson equation

$$\frac{d^2V}{dx^2} = -\frac{\rho(x)}{\epsilon_0} = -\frac{e|\psi(x)|^2}{\epsilon_0}$$

and the quantum exchange-correlation potential, arising out of the quantum many-body effects which depends on the electron number density $|\psi(x)|^2$. The two equations must therefore be solved self-consistently using appropriate boundary conditions [6-8].

We are interested here merely in the scaling properties of the maximum transported current J , on application of a voltage V . In quantum-mechanical terms, the current density

$$J = \frac{e\hbar}{2im} \left(\psi^* \frac{d\psi}{dx} - \psi \frac{d\psi^*}{dx} \right),$$

so that a scaling relationship for J if it exists, must depend on various powers of e, \hbar, m, ϵ_0 , the voltage V and the gap D since ψ itself may depend on all of these through the Schrodinger and Poisson equations. A simple transformation $\tilde{\psi} = \psi/\sqrt{\epsilon_0}$ can be used to make the Poisson and Schrodinger equations free of ϵ_0 . The current density can now be expressed as

$$J = \epsilon_0 \frac{e\hbar}{2im} \left(\tilde{\psi}^* \frac{d\tilde{\psi}}{dx} - \tilde{\psi} \frac{d\tilde{\psi}^*}{dx} \right).$$

Since $\tilde{\psi}$ no longer depends on ϵ_0 , $J \sim \epsilon_0 V^\alpha D^{\delta_1} \hbar^{\delta_2} m^{\delta_3} e^{\delta_4}$. We are now in a position to implement standard dimensional analysis to determine the scaling law by expressing each of the quantities in terms of mass, length, time and current (M, L, T, A) and equating their coefficients. We thus obtain a set of four equations:

$$\begin{aligned} \delta_4 - \alpha &= -1 \\ 2\delta_2 + 2\alpha + \delta_1 &= 1 \\ \delta_4 - \delta_2 - 3\alpha &= -4 \\ \delta_2 + \delta_3 + \alpha &= 1 \end{aligned}$$

in terms of five unknown quantities. Four of these can be eliminated to express the scaling as

$$J \sim \epsilon_0 V^\alpha D^{2\alpha-5} \hbar^{3-2\alpha} m^{\alpha-2} e^{\alpha-1},$$

This is the generalized quantum Child-Langmuir law, applicable across all domains. The classical law can be recovered by demanding that it should be independent of \hbar i.e. by equating the exponent of \hbar to zero. Thus $\alpha = 3/2$ and $J \sim \epsilon_0 \sqrt{\frac{e}{m}} V^{3/2}/D^2$ which, barring the dimensionless constants, is the classical Child-Langmuir law. The determination of α in the deep quantum regime is beyond the scope of the article but can be found analytically under certain assumptions for the exchange-correlation potential (see Fig. 1).

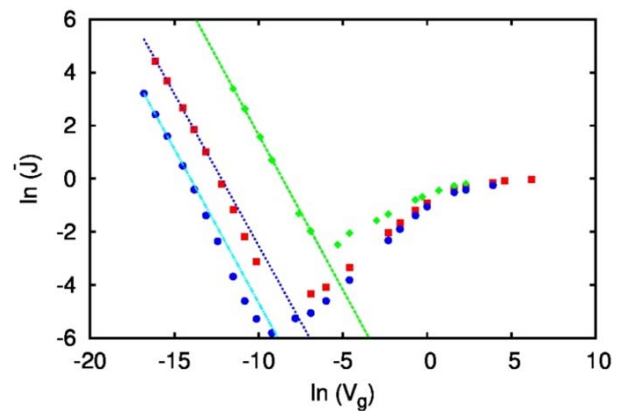


Fig. 1: The limiting current in the quantum case in units of the Child-Langmuir current for three different nanogaps. Here V is the applied voltage. The power law behavior and the exponent α at small voltages is predicted accurately. The classical limit is obtained at large applied voltages [6].

BARC NEWSLETTER

We shall now focus on an important aspect of the Child-Langmuir law – the case where the power radiated by the accelerating electrons leaks out through an opening in the device such as a dielectric window [9-11], as in case of a photodiode. If there are sufficient electrons at the cathode, the current through the diode will be space charge limited and dictated by the voltage drop across the diode. Assuming a uniform electromagnetic power loss through the dielectric window, the applied voltage must account for the energy gained by the electrons in traversing the length of the diode as well as the electromagnetic power loss. For a correct estimate of the Child-Langmuir current, the effective voltage drop across the dielectric window (i.e. P/I) must be subtracted from the measured voltage in an equivalent circuit theory. In the above, P is the electromagnetic power exiting the output port and I is taken to be the diode current. The Child-Langmuir current must therefore be evaluated self-consistently from the equation:

$$\frac{I}{A} = \frac{4}{9} \epsilon_0 \sqrt{\frac{2e}{m}} \frac{(V - P/I)^{3/2}}{D^2}$$

where A is the area of the emitter. Fully electromagnetic Particle-in-Cell simulations for various diode geometries have been used to verify the above equation (see Fig. 2).

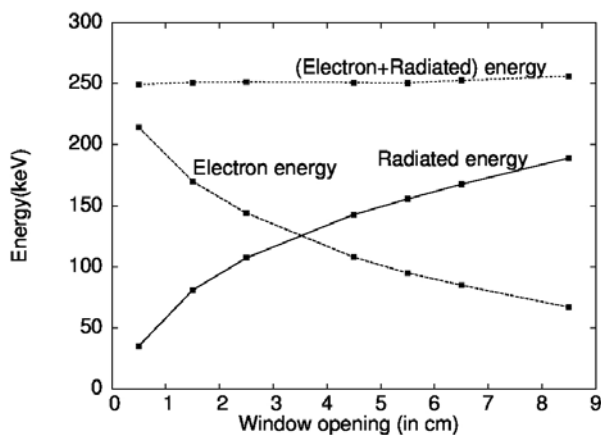


Fig. 2: The radiated energy and the electron energy are plotted separately for several window openings (and hence distinct values of the output impedance). In all cases, they add up to the applied voltage [9].

Finally, we shall touch upon an application of the Child-Langmuir law in a high power microwave (HPM) device - the Vircator or the Virtual Cathode Oscillator. The device primarily consists of a diode and a drift space in addition to a wave-guide and an antenna. It is powered by Marx generator or a flux-compression generator to produce a high voltage power supply. The current through the diode depends on the material-dependent emission mechanisms, but is high enough to be space-charge limited. The Child-Langmuir law thus comes into play in the design of the Vircator. When such a high current density beam enters the drift region, only a fraction of the current passes through. The rest of the electrons form a locally oscillating blob known as the virtual cathode which in turn leads to an oscillation of other electrons between the cathode and virtual-cathode [12]. There are thus two mechanisms that produce narrow-band microwaves – the oscillation of the blob and electrons reflecting between the cathode and virtual cathode.

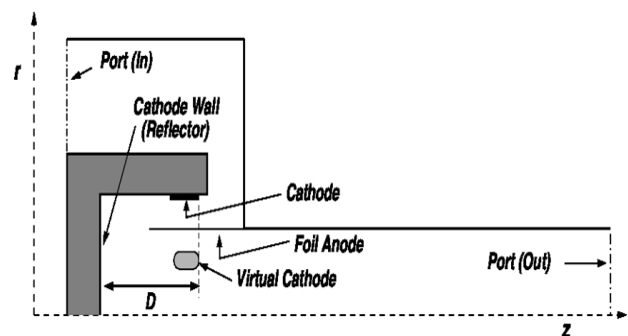


Fig. 3: Schematic of a typical co-axial vircator. Power is injected through the window marked Port(In) and electromagnetic power extracted through the window marked Port(Out) [13].

A requirement for a sustained microwave production is a constructive beam-wave interaction i.e. a mode supported by the drift tube must be in resonance with the natural oscillation of the vircator and should also have an anti-node at the location of the virtual cathode. For the vircator shown in Fig. 3, a means of achieving this is by varying the distance D , provided other parameters are optimum for the formation of an anti-node at the virtual cathode location [13]. The electromagnetic power extracted by varying D is shown in Fig. 4. An optimum distance can thus be chosen to maximize the efficiency.

BARC NEWSLETTER

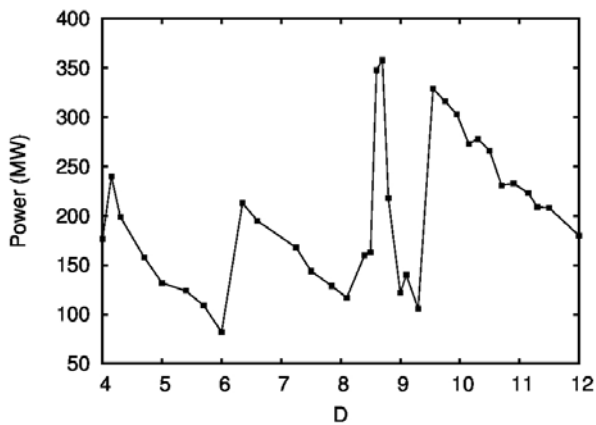


Fig. 4: The power depends sensitively on the distance between the cathode-wall and the virtual cathode. The optimum value may thus be chosen for maximum efficiency [13].

References

1. C.D.Child, Phys. Rev. Ser 1, 32,492(2011)
2. I.V.Langmuir, Phys. Rev. 2, 450 (1913).
3. I.V.Langmuir and K.Blodgett, Phys. Rev. 22,347 (1923); 24, 49 (1924).
4. R.R.Puri, D.Biswas and R.Kumar, Phys. Plasmas, 11, 1178 (2004).
5. Y.Y.Lau, Phys. Rev. Lett. 87, 278301 (2001).
6. D. Biswas and R.Kumar, Europhys. Lett. 102, 58002 (2013).
7. D. Biswas and R.Kumar, Euro. J. Phys. B, 85, 189 (2012).
8. D. Biswas, Phys. Rev. Lett. 109, 219801 (2012).
9. D. Biswas, R. Kumar and R.R.Puri, Phys. Plasmas 12, 093102 (2005).
10. D. Biswas and R.Kumar, Phys. Plasmas, 13, 073101 (2006).
11. D. Biswas, Phys. Plasmas, 15,013103 (2008)
12. D. Biswas, Phys. Plasmas, 16,063104 (2009).
13. D. Biswas and R.Kumar, IEEE Tans. Plasma. Sci. 39, 1573 (2011).

BARC NEWSLETTER

FIRST PRINCIPLES STUDIES ON HIGH PRESSURE EQUATION OF STATE AND PHASE STABILITY OF SOLIDS

P. Modak and Ashok K. Verma

High Pressure and Synchrotron Radiation Physics Division

Dr. P. Modak is the recipient of the DAE Scientific & Technical Excellence Award for the year 2011

Introduction

The equation of state of a material represents a definite relationship between three thermodynamic variables volume (V), temperature (T) and pressure (P). Perhaps pressure possesses the greatest range of all the physical variables — at one end, the pressure in the remotest vacuum of space (10^{-17} atmospheres) and at the other end that found at the center of a neutron star (10^{29} atmospheres). The center of the Earth is at a pressure of 350 GPa (3.5 million atmospheres) and more than 90% of the matter in the solar system exists at pressures above 100 GPa. The optical, electrical, magnetic and chemical properties of a solid depend on the interactions of the outer electrons of its constituent atoms or molecules. In particular, these properties are determined by the arrangements of the electrons in the ground state, and on the energy and electronic characteristics of various excited states. The effect of pressure is to decrease the volume and increase overlap among the electronic orbitals. Since these orbitals differ in their spatial properties (radial extent and shape) they are perturbed to different degrees by compressions which may change the electronic, magnetic and structural properties of solids.

One of the most studied phenomena that may occur under applied pressure is a change in the arrangement of the atoms, i.e., a structural phase transition. The Gibbs free energies of the different possible arrangements of atoms vary under compression, and at some stage it becomes favorable for the material to change the type of atomic arrangement.

The study on equation of state (EOS) and phase stability of solids, denoting which phase is thermodynamically stable at given set of pressure and temperature conditions have enormous importance in many branches of physics and material science. The EOS of solids provides the vital inputs for large-scale complex hydrodynamics simulations to predict performance of nuclear weapon, its safety under various conditions and to predict capsule materials for inertial confinement fusion etc. For all the studies mentioned above a very accurate equation of state data is required which may be obtained from experiment but in most of these cases it is difficult to do experiments or the pressure-temperature conditions are out of reach of experiments. Therefore the first principles calculations are playing an important role in the field of EOS and phase stability because of its predictive power and reliability. Over the past few decades Density Functional Theory (DFT) [1,2] emerged as a leading tool for calculation of the ground state properties of complex systems and has made it possible to obtain quantitative results for geometries and binding energies of systems with large number of atoms and low symmetries. The accuracy of the existing approximations within DFT is often remarkably good and sometimes good enough for a successful prediction of experimental phenomena.

We have studied many elemental solids and compounds having different types of electrons (sp , d and f) in their valence configurations using first principles methods under pressure [3-10]. However, in this paper we are presenting some of the important results on iron (Fe, d -electron system) and uranium mono-nitrides (f -electron system) [3-6].

BARC NEWSLETTER

Method of Calculation

To study the phase stability at a given pressure and temperature, we have calculated Helmholtz free energy for different possible structures. The free energy of the system for a given volume can be written as,

$$F(T) = E_0 + F_H(T) + F_{AE}(T) \quad (1)$$

Where E_0 is the energy of the static lattice, $F_H(T)$ is the contribution to the free energy from harmonic lattice vibrations of the ions, and $F_{AE}(T)$ is the free energy due to electronic excitations and anharmonic phonons. The thermal contribution to the free energy can be obtained using the phonon density of states (DOS) $g(\omega)$ which may be determined from ab initio phonon calculations within quasi-harmonic approximations. Accordingly the phonon contribution to the free energy can be written as,

$$F_H(T) = \int_0^{\omega_{\max}} \left\{ \frac{\hbar\omega}{2} + k_B T \ln \left[1 - \exp\left(-\frac{\hbar\omega}{k_B T}\right) \right] \right\} g(\omega) d\omega \quad (2)$$

Here the phonon DOS is calculated at 0K and hence if the considered structure is not stable at 0K then it is not possible to calculate the phonon DOS. However one can use Wallace's prescription [11], which is based on Debye model and needs sound velocity to calculate the phonon contribution to the free energy. The sound velocity can be obtained from the calculated bulk modulus and the density of the solid. The electronic excitation energy can be calculated following Mermin's [12] extension of DFT to finite temperatures. According to Wallace's prescription the phonon contribution and the contributions from electronic excitation and anharmonic phonons to the free energy can be written as,

$$F_H(T) = -3k_B T \left[\ln(T/\theta_0) - (1/40)(\theta_2/T)^2 + \dots \right] \quad (3)$$

where

$$k_B \theta_0 = \langle \ln(\hbar\omega) \rangle_{BZ} \quad (4)$$

$$k_B \theta_2 = \left[\frac{5}{3} \langle (\hbar\omega)^2 \rangle_{BZ} \right]^{1/2} \quad (5)$$

and

$$F_{AE}(T) = -\Gamma T^2 \quad (6)$$

Here $\langle \dots \rangle_{BZ}$ indicates a Brillouin zone average of a function of the phonon frequencies ω . Γ is a phenomenological parameter determined from available specific heat data of the solid at high temperatures and high pressures.

To calculate static lattice energy we have used different implementations of density functional theory like full potential linear augmented plane wave (FPLAPW) method, pseudopotential method and projector augmented wave (PAW) method etc. The phonon calculations are carried out using both density functional perturbation theory (DFPT) [13] and the small displacement force method where the force constant matrix (given as the second derivative of energy with respect to displacements of atoms from their equilibrium positions) was constructed by calculating the forces on atoms of a periodically repeated supercell arise due to the displacement of few selected atoms from their equilibrium positions. The dynamical matrix can be easily constructed from the force constant matrix which can be diagonalized to get the phonon frequencies. Here, we have taken a $3 \times 3 \times 3$ supercell and two atoms, one from each species are displaced separately by an amount of 0.04 Å and then the self consistent forces on the atoms were determined [6].

Results and Discussions:

Iron

The phase diagram of Fe has been studied extensively because of its geophysical importance. Iron crystallizes in body centered cubic (bcc) structure at ambient conditions, and transforms to hcp structure above 15 GPa at low temperatures, and a face centered cubic (fcc) structure above 1,300 K at low pressures. However, the structure of Fe at moderate pressure-temperature conditions (40-100 GPa and 1,000-2,000 K) is controversial as different sets of experimental data suggest different structures [3]. Also at earth's core conditions (~ 350 GPa and $\sim 6,000$ K) there is a controversy about its structure [4].

BARC NEWSLETTER

Our calculated equilibrium volume (V_0), bulk modulus (B_0), and its pressure derivative (B'_0) both for bcc and hcp phases of iron (see Table I), which we obtained by fitting our calculated total energies to the Birch-Murnaghan equation of state. These are in good agreement with available experimental and theoretical results [4]. At ambient pressure the calculated phonon frequencies also match well with that of inelastic neutron scattering measurements.

Table 1: Equilibrium properties of Fe.

Properties	Present calculations	Expt. [14]
bcc		
V_0 (\AA^3)	11.667	11.732
B_0 (GPa)	179.6	173
B'_0	3.66	5.0
hcp		Others [15]
V_0 (\AA^3)	10.219	10.204
B_0 (GPa)	298.7	291
B'_0	3.55	4.4

The calculated EOS at 0K correctly reproduced the bcc and hcp stability region (see Fig. 1). We have also studied fcc, dhcp and orthorhombic structures as the possible candidates at high pressure and high temperature conditions ($P > 60$ GPa and $T > 1500$ K). At 0K and 100 GPa, we have found that dhcp and fcc structures are very close in energy to that of the hcp structure (~ 3 -4 mRy), and the orthorhombic structure is about 10 mRy higher than the hcp energy. The high

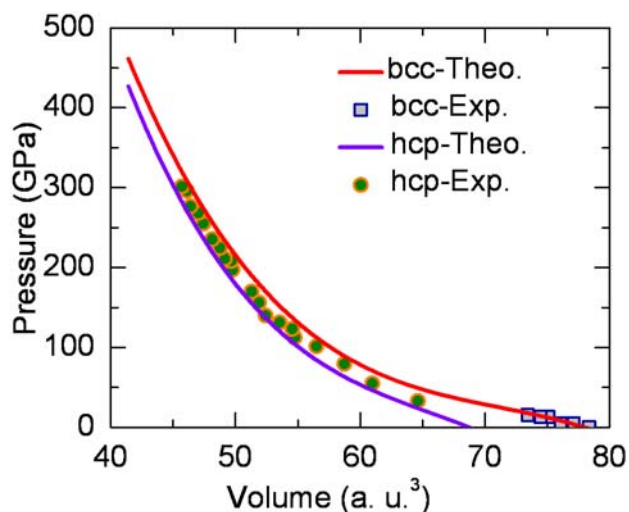


Fig. 1: PV EOS of iron at 0 K (1 a.u. = 0.529177 \AA).

pressure phonon frequency calculations showed that the bcc and orthorhombic structures are vibrationally unstable as some modes give negative frequencies. We have calculated phonon DOS for fcc and hcp iron at 100 and 400 GPa, and then calculated free energy as a function of temperature for these two structures. We have found that the hcp phase is more stable compared to the fcc phase at 100 GPa pressure at least up to 2,500 K (see Fig. 2).

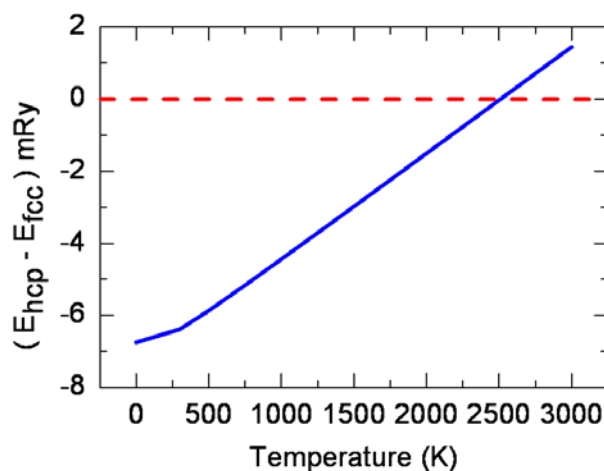


Fig. 2: Comparison of free energy between hcp- and fcc-Fe at 100 GPa.

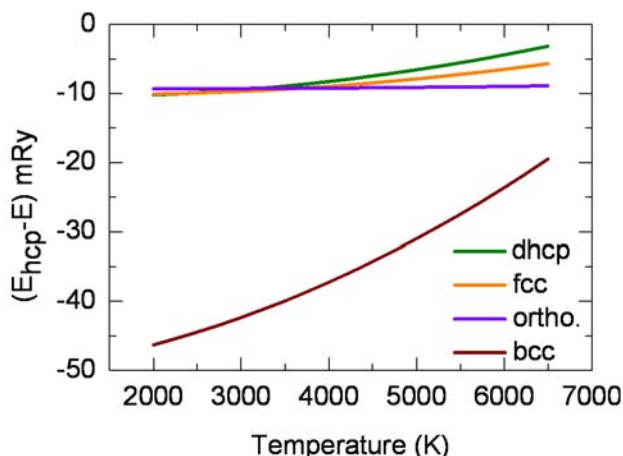


Fig. 3: Free energy of different structures with respect to hcp structure at 400 GPa.

Using Debye temperature (θ_D) for the value of θ_2 in Wallace's prescription, as discussed earlier, we have calculated the phonon contribution to the free energy for other structures. From these calculations we showed that the hcp phase of iron is more stable compared to bcc, fcc, dhcp and orthorhombic phases both at moderate pressure-temperature and earth's core conditions [5]. Though the energy difference between

BARC NEWSLETTER

hcp and bcc reduces at earth's pressure with temperature, at 6,000 K it is still of the order of 15 mRy (see, Fig.3), which is quite large and hence ruled out the possibility of bcc iron at earth's core conditions.

Uranium mono-nitride (UN)

In recent years, actinide mono-nitrides (AcN) have been studied extensively because of their possible use as advanced fuels in the fourth generation nuclear reactors. In comparison to present oxide fuels, the nitride fuels have superior thermo-physical properties (i.e., high thermal conductivity and high melting temperature), higher burn-up, easy re-processing, and higher metal (actinides) density.

At ambient pressure UN crystallizes in NaCl structure (*B1*). The lattice constants (*a*), bulk modulus (B_0) and its pressure derivative calculated at ambient pressure are compared in the Table II with the available data [16, 17]. The LDA/GGA underestimates the lattice constants by 2.21/0.63 %, and overestimates the bulk modulus by 31/11 % compared to that of experimental data. The GGA + *U* calculations improves slightly the ambient pressure lattice constant but fails to improve the bulk modulus, consistent with the earlier self-interaction corrected local spin-density calculations.

We have carried out enthalpy calculations as a function of *c/a* ratios for R-3m structure at few pressures to study the structural stability among *B1*, *B2* and R-3m structures (see, Fig.4). We have found that the R-3m structure relaxes to NaCl structure at zero pressure. However, the R-3m structure becomes stable under pressure and near 18 GPa it becomes both energetically and mechanically stable (see Fig. 4). But the CsCl (*B2*)

Table 2: Equilibrium properties of UN

	<i>a</i> (Å)	B_0 (GPa)	B_0'
LDA	4.781	266.3	3.63
GGA	4.858	225.0	4.00
GGA + <i>U</i>	4.899	233.2	6.28
Expt. [16]	4.889	203.0	6.30
Others [17]	4.858	227.0	

structure remains energetically unstable at least up to 100 GPa [6].

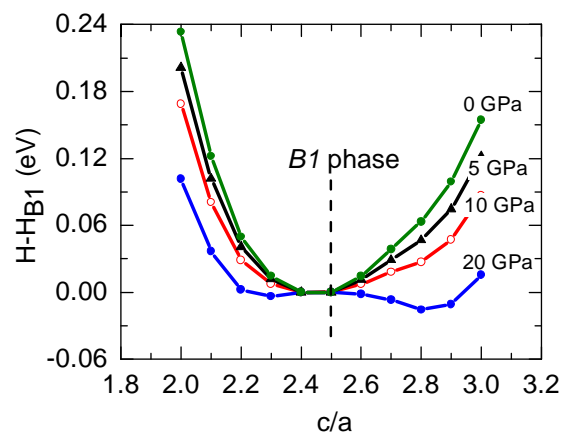


Fig. 4: The GGA enthalpy barriers (eV / f.u.) at different pressures.

These results are in good agreement with the earlier high pressure X-ray diffraction measurements [16] where *B1* to R-3m transition was observed near 29 GPa. The transition pressure mismatch in UN is probably due to the inability of density functional theory to treat narrow *f* bands properly. In fact, the GGA + *U* calculations predict better agreement in transition pressure (26 GPa). It is worth to mention that the LDA transition pressure is 4.7 GPa. Therefore, the LDA underestimation of transition pressure for UN is very large (84 %). The calculated *PV* equation-of states relations together with experimental results are shown in Fig. 5. A small volume change (2.5 %) is found during NaCl to R-3m phase transition which is consistent with experimentally observed value of 3.2 %.

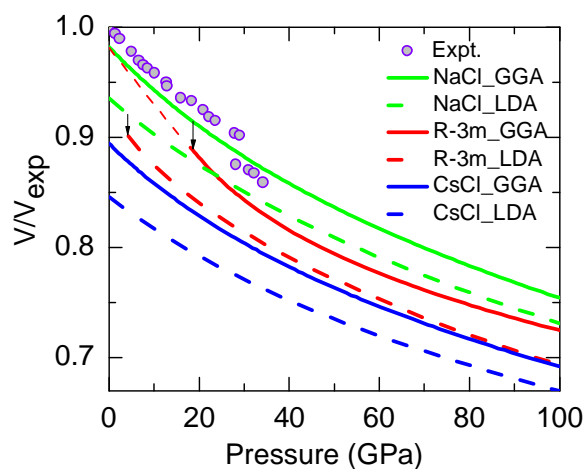


Fig. 5: The GGA and LDA *PV* EOS for different structures. Initial dashed portion of the R-3m phase shows the extrapolated data, as this phase is mechanically unstable in this region.

BARC NEWSLETTER

References

1. P. Hohenberg and W. Kohn, *Phys. Rev.* **136**, B864 (1964)
2. W. Kohn and L.J. Sham, *Phys. Rev.* **140**, A864 (1965)
3. R.S. Rao, P. Modak, B.K. Godwal and S.K. Sikka, *Phys. Rev. B* **59**, 13498 (1999)
4. P. Modak, A.K. Verma, R. S. Rao, B. K. Godwal and R. Jeanloz, *J. Materials Science*, **41**, 1523 (2006)
5. P. Modak, A. K. Verma, R. S. Rao, B. K. Godwal, L. Stixrude and R. Jeanloz, *J. Phys.: Condens. Matter* **19**, 016208 (2007)
6. P. Modak and A. K. Verma, *Phys. Rev. B* **84**, 024108 (2011)
7. A.K. Verma, and P. Modak, *Europhys. Lett.* **81**, 37003 (2008)
8. A.K. Verma, P. Modak, R. S. Rao, B. K. Godwal, and R. Jeanloz, *Phys. Rev. B*, **75**, 014109 (2007)
9. A. K. Verma, P. Modak and Surinder M. Sharma, J. *Phys: Condens. Matter* **20**, 325215 (2008)
10. P. Modak, A. K. Verma, R. S. Rao, B. K. Godwal and R. Jeanloz, *Phys. Rev. B*, **74**, 012103 (2006)
11. D. C. Wallace, *Phys. Rev. B* **58**, 15433 (1998)
12. N. D. Mermin, *Phys. Rev. A* **137**, 1441 (1965)
13. S. Baroni, S. de Gironcoli, A. D. Corso, and P. Giannozzi, *Rev. Mod. Phys.* **73**, 515 (2001)
14. A. P. Jephcoat, H. K. Mao and P. M. Bell, *J. Geophys. Res.*, **91**, 4677 (1986)
15. L. Vocadlo, J. Brodholt, D. Alfe, M. J. Gillan, and G. D. Price, *Phys. Earth Planet. Inter.* **117**, 123 (2000)
16. J. Staun Olsen, L. Gerward and U. Benedict, *J. Appl. Cryst.* **18**, 37 (1985)
17. Raymond Atta-Fynn and Asok K. Ray, *Phys. Rev. B* **76**, 115101 (2007)

BARC NEWSLETTER

RESISTIVE PLATE CHAMBERS FOR THE RE4 UPGRADE OF THE CMS EXPERIMENT AT THE LARGE HADRON COLLIDER FACILITY AT CERN

L.M. Pant
Nuclear Physics Division

Dr. L.M. Pant is the recipient of the DAE Scientific & Technical Excellence Award for the year 2011

Abstract

The Compact Muon Solenoid (CMS) detector operates at the Large Hadron Collider (LHC) at CERN. It was proposed to install the fourth endcap (\pm RE4) consisting of Resistive Plate Chambers (RPCs) for the CMS muon Endcap system, in order to improve its Level-1 trigger efficiency and thereby completing the full implementation of the TDR, after which LHC will run with its full designed luminosity. This station is being installed in the first Long Shutdown (LS1) of LHC during 2013-2014. In this presentation, we will discuss about the entire procedure of fabrication of bakelite gas gaps, standardisation of leak and spacer tests for the gas-gaps, the new design for the Cu cooling system, assembly, testing and characterization of RPCs which would be executed in a synchronised way at the three assembly sites at CERN, BARC-Mumbai and University of Ghent, Belgium. These detectors also have an immense outreach in medical imaging, homeland security and tomography.

The CMS experiment at CERN

The Compact Muon Solenoid (CMS) detector operates at the Large Hadron Collider (LHC) at CERN. It was conceived to study proton-proton (and lead lead) collisions at a centre-of-mass energy of 14 TeV (5.5 TeV nucleon-nucleon) and at luminosities up to 10^{34} $\text{cm}^{-2}\text{s}^{-1}$ (10^{27} $\text{cm}^{-2}\text{s}^{-1}$). At the core of the CMS detector sits a high-magnetic field and large-bore superconducting solenoid surrounding an all-silicon pixel and strip tracker, a lead-tungstate scintillating-crystals electromagnetic calorimeter, and a brass-scintillator sampling hadron calorimeter. The iron yoke of the flux-return is instrumented with four stations of muon detectors covering most of the 4π solid angle. Forward sampling calorimeters extend the pseudorapidity coverage to high values ($\eta \approx 5$) assuring very good hermeticity. The pseudorapidity, $\eta = -\ln[\tan(\theta/2)]$, where θ is the polar angle wrt the beam axis. The overall dimensions of the CMS detector are a length of 21.6 m, a diameter of 14.6 m and a total weight of 12500 t [1], Fig.1.

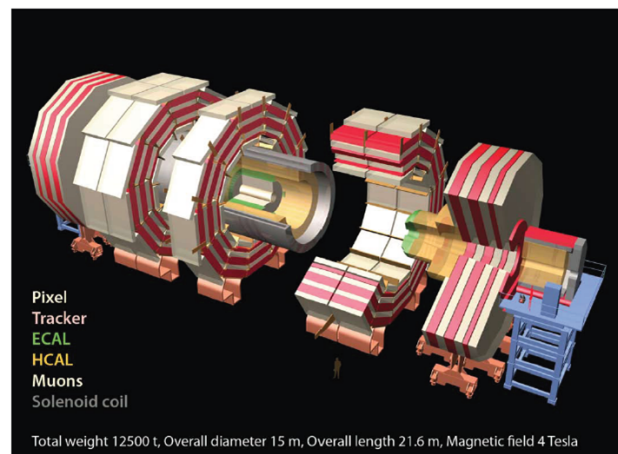


Fig.1: The CMS calorimeter with its sub detector systems. The muon stations are in the periphery in grey colour

The prime motivation of the LHC is to elucidate the nature of electroweak symmetry breaking for which the Higgs mechanism is presumed to be responsible. The experimental study of the Higgs mechanism can also shed light on the mathematical consistency of the Standard Model at energy scales above about 1 TeV. Various alternatives to the Standard Model invoke new symmetries, new forces or constituents. Furthermore,

BARC NEWSLETTER

there are high hopes for discoveries that could pave the way toward a unified theory. These discoveries could take the form of supersymmetry or extra dimensions, the latter often requiring modification of gravity at the TeV scale. Hence there are many compelling reasons to investigate the TeV energy scale.

Muon detection is a powerful tool for recognizing signatures of interesting processes over the very high background rate expected at the LHC with full luminosity. For example, the predicted decay of the Standard Model Higgs boson into ZZ or ZZ^* , which in turn decay into 4 leptons, has been called "gold plated" for the case in which all the leptons are muons (Fig.2). Besides the relative ease in detecting muons, the best 4-particle mass resolution can be achieved if all the leptons are muons because they are less affected than electrons by radiative losses in the tracker material. This example, and others from SUSY models, emphasize the discovery potential of muon final states and the necessity for wide angular coverage for muon detection. Therefore, as is implied by the experiment's middle name, the detection of muons is of central importance to CMS: precise and robust muon measurement was a central theme from its earliest design stages. The muon system has 3 functions: muon identification, momentum measurement, and triggering.

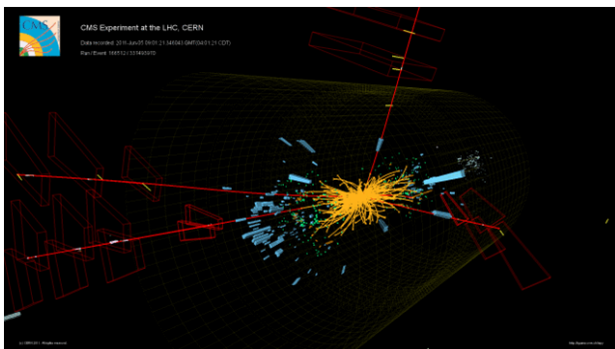


Fig.2: A typical event of $H \rightarrow ZZ \rightarrow \mu^+ \mu^- \mu^+ \mu^-$, for the 8 (4+4) TeV data in CMS

Resistive Plate Chambers for CMS

Resistive Plate Chambers (RPCs), developed by R. Santonico [2] in the early 80's, are parallel plate gas detectors, made of highly resistive plates such as glass or bakelite ($\rho_{\text{bulk}} \sim 10^{10}$ to $10^{12} \Omega\text{cm}$), coated with graphite ($\rho_{\text{surface}} \sim 1 \text{ M}\Omega/\square$, thickness $\sim 100 \mu\text{m}$) to

provide the anode and cathode and are operated either in avalanche or streamer mode with a typical combination of gas mixture consisting of R134a ($\text{C}_2\text{H}_2\text{F}_4$) as the main component ($\sim 95\%$), alongwith other gases such as Iso-butane and SF_6 . RPCs are not a proportional counter. They are designed to create an avalanche and then also configured to arrest the avalanche from spreading out. They have found wide applications in collider and neutrino based experiments [3,4], as trigger and/or tracking detectors, because of following features :

- low cost in fabricating large surface areas units (1 m^2 to 4 m^2), wireless detectors, instead use strips
- excellent count rate capabilities ($\sim 10\text{s kHz/cm}^2$),
- timing resolution ($s \sim 2 - 3 \text{ ns}$)
- efficiency $> 95\%$
- no degradation in performance parameters in hostile radiation environment and
- stable performance over extended period

Fig.3 shows a schematic of an RPC. The resistive plates determine the count rate capability whereas the gap between the plates determines the timing characteristics. Time resolutions of the order of picoseconds have been achieved with multigap timing RPCs (mRPCs) having gas-gaps of the order of 100s of microns, used basically for particle identification via time of flight method.

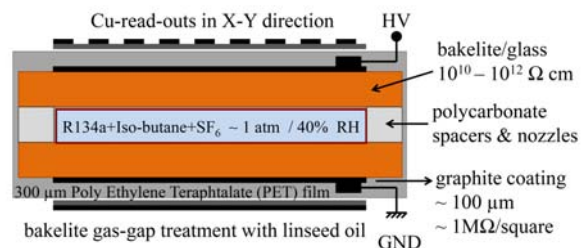


Fig.3: Schematic of an RPC with anode, cathode and read out planes in X and Y

The CMS muon system

The CMS detector consists of Drift Tubes (DTs) in barrel region, Cathode Strip Chambers (CSCs) in the end-cap (forward) region and Resistive Plate Chambers (RPCs) in both the regions. RPCs have very good timing but not a good position resolution, DTs which are slower,

BARC NEWSLETTER

have a good position resolution and not a good timing, whereas CSCs have a good position resolution and acceptable timing [5]. As such, the CMS has two independent muon triggering systems, complementary to each other, thereby providing :

- trigger at high luminosity
- good muon ID over wide range of momenta and angles
- improved tracking momentum resolution above 200 GeV/c

The TDR for the muon trigger for the CMS experiment at the LHC facility, envisages to have four layers of Resistive Plate Chambers (RPCs) in the forward region ($1.2 < \eta < 1.6$). The present CMS experiment has three layers of RPCs in the end-caps and the RPC trigger logic requires hits in at least three layers, which causes the observed drop in efficiency for the endcaps with only three stations. Adding the 4th layer in the endcaps, enabling a 3-out-of-4 trigger logic in those regions, will bring the RPC endcap performance to a similar level as in the barrel region, Fig.4, [6].

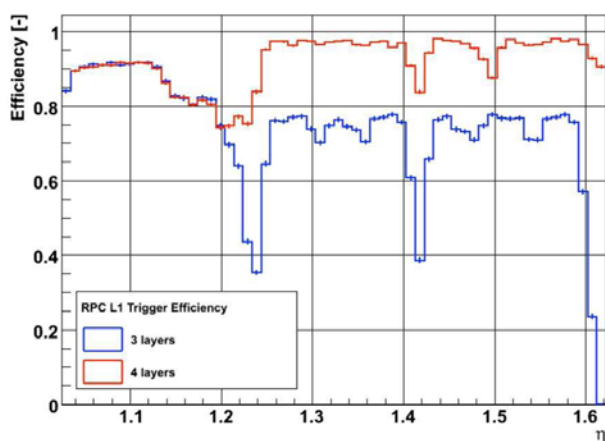


Fig. 4: Comparison of simulated RPC Level-1 trigger efficiency for the upgraded version with the present system with three end caps

The end-caps consist of three trapezoidal bakelite gas-gaps configured as a double gap RPC (Fig.5), [7]. The present forward region (end caps) consists of 432 chambers mounted in a staggered way in two concentric rings on the end cap disks to cover its surface (~ 150 m² per disk). The double gap geometry, improves the efficiency, allows safer operation at higher threshold and also improves the time resolution. In

order to increase the L1 trigger efficiency, it is proposed to install the fourth end-cap layer during the long shutdown (2013-2014), after which LHC will run with its full designed luminosity (more than $10^{34} \text{ cm}^{-2}\text{s}^{-1}$ at 14 TeV). The CMS-RPCs work in the avalanche mode satisfying the following criteria :

- efficiency, $e > 95\%$
- streamer fraction, $f < 10\%$ &
- cluster size, $N_s < 2$

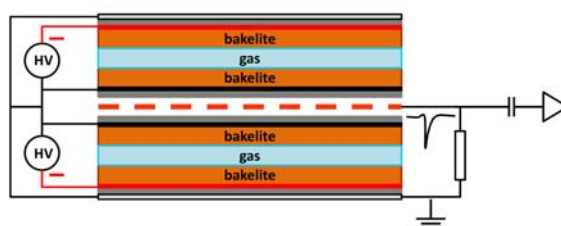


Fig.5: Schematic of a double gap RPC

The construction procedures of RPCs, with the experience gained during the operation of RPCs in the present set-up, has been improved, keeping backward compatibility with the presently installed RPCs. As in the past, the fourth layer will consist of 2 rings denominated as RE4/2 and RE4/3, each having 36 chambers. Both end-caps will be instrumented for a total of 144 chambers with another 56 chambers as spares, adding to 200 chambers for the RPC upgrade project, which then fully restores the TDR version of CMS with RE4 RPCs.

RPC Lab at NPD-BARC

The idea of building an RPC Lab., at NPD-BARC was conceived about six years back, as sufficient infrastructure was required to handle the large area gaseous detectors such as RPCs and characterize them with cosmic muons. Accordingly step by step, gas mixing systems, gas flow dividers, gas recirculation system were developed, installed and commissioned in the lab. Subsequently for characterizing the RPCs, a cosmic hodoscope was built which would provide the muon trigger by scintillators placed on top and bottom of the hodoscope, separated by 2.1m. The RPCs are then inserted in between for characterizing them in terms of their efficiency, cluster size, noise rate and

BARC NEWSLETTER

strip profiles. The hodoscope is shown in Fig.6, which is 3m in height and can handle 6 RPCs simultaneously with a foot print size of each platform being 2m x 1.8m. The hodoscope is instrumented with gas flow lines, HV cables both for the RPCs and the PMTs for the scintillators (Fig.7). The bottom section of the hodoscope houses the VME based DAQ catering to 600 channels of electronic signals to be processed, via the multi hit TDCs for the 6 RPCs each having 100 channel of read outs.



Fig.6: The cosmic hodoscope at NPD-BARC



Fig.7: The top layer of scintillators (each 2m long) on the hodoscope for providing the muon trigger

Mechanical tests for the gas-gaps

Since the gas-gaps are transported through a large distance via air freight and then handled at airports before delivery to the respective assembly sites, their mechanical properties are evaluated through leak and spacer tests before they are assembled. Five tests are being performed for gaps - Visual Test, Leak Test, Resistivity Test and Dark Current Test (I) and Dark Current Test (II). The Dark Current Test I is the HV scan of gaps between 100 Volts and 10,000 Volts while the Dark Current Test II is the Long Term Stability test which aims to monitor the stability of the current in time at a fixed voltage for about 72 hours.

The trapezoidal gas-gaps have nozzles in the four corners for gas flow. The 2 mm gap uniformity is maintained through a grid (10 cm x 10 cm) of button spacers (of height uniformity within 20 μm) between the bakelite sheets. The 20 μm precision ensure that the gap remains uniform over the entire area of the gas-gap providing a uniform electric field. These spacers could also get popped up because of insufficient bonding of the glue at the fabrication site, though sufficient care is taken to keep the spacers pressed, guaranteed by water column, for 14 hours during curing. The spacers can also get popped up because of mishandling of the gas-gap crates at the time of delivery. A gas-gap, even with a single popped spacer cannot be used and is to be rejected. In order to certify these gas-gaps, a new system has been designed where the gas-gaps on arrival from KODEL, undergo a leak



Fig.8, Facility for leak and spacer test of the bakelite gas-gaps at NPD-BARC

BARC NEWSLETTER

and spacer test (Fig.8). The gas-gaps are pressurised at 20 mbar above atmospheric pressure with Argon gas and the pressure is recorded digitally through a transducer (Sensor Technics - CTE7000) with a 20 bit ADC.

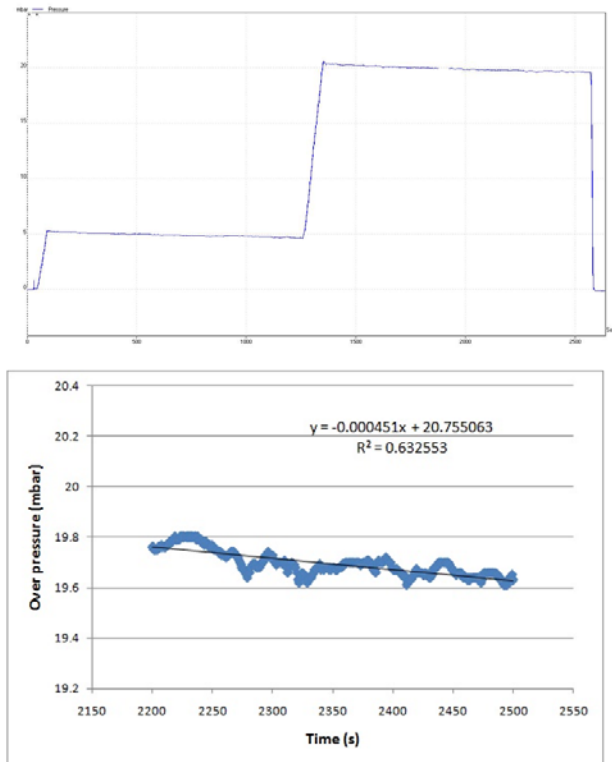


Fig.9: A typical dp/dt plot at 5 mbar and 20 mbar of overpressure (top) and fitted value for leak test measurements at 20 mbar for an RE4/2 Bottom gap (bottom)

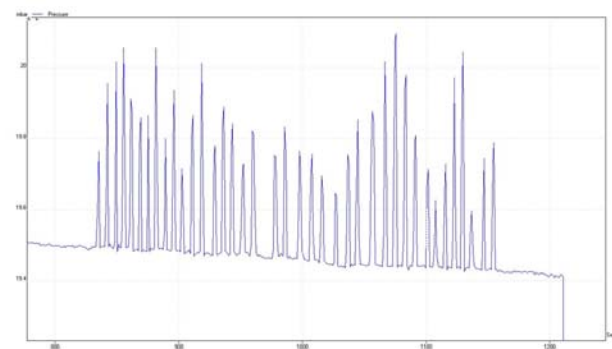


Fig.10: Gas-gaps overpressurised to 20 mbar for spacer test showing acceptable pressure fluctuations (± 0.5 mbar) for all the 39 intact spacers for a Top Wide gap

The QA/QC “as prescribed by the CMS experiment for the leak test” needs the gap to remain overpressurised at 5 mbar, for five minutes, which emulates the situation in the CMS cavern, measure the dp/dt and then overpressurize the gaps to 20 mbar for another five minutes and re-measure the dp/dt and finally release the overpressure to zero. A plot of the fall in pressure with time is shown in the top panel of Fig.9 for the RE4/2-bottom gas-gap with 102 spacers. The bottom panel of Fig.9, shows the fitted value of dp/dt (4.51×10^{-4} mbar/sec). Table 2 shows the maximum allowed pressure drop for different gas-gaps, normalized to 2 litres of gas volume.

Table 2 : dp/dt limits for the gaps

gas-gap	RE	RE	RE	RE	RE	RE
type	4/3	4/3	4/3	4/2	4/2	4/2
→	Top	Top		Top	Top	
→	N	W	B	N	W	B
$[dp/dt]_{max}$ (mbar/300s)						
→	0.3	0.1	0.4	0.1	0.1	0.2

For spacer test, while at an overpressure of 20 mbar, a template with known spacer position is placed over the gap and each spacer position is pressed to record the fluctuations in the pressure. For intact spacers, the fluctuations in the pressure are in the range of ± 0.5 mbar, whereas for the same pressure applied in the non-spacer region, resembling a popped up spacer, corresponds to large fluctuations (± 1 mbar and beyond), as shown in Fig.10, for a Top Wide gap consisting of 39 intact spacers. The gas gap is qualified when no spacer causes an overpressure peak larger than ± 0.5 mbar.

Electrical tests for the gas-gaps :

QA/QCs for electrical tests of the gas-gaps have been formulated to be uploaded on the data base, prior to assembly and dispatch to CERN. Each gas-gaps will be purged with RPC gas mixture (R134a : Iso-butane : SF₆ :: 95.2 : 4.5 : 0.3) with 40 % RH in the gas mixture at a flow rate of 5 litres per hour for 48 hours, with $P_0 = 1010$ mbar and $T_0 = 293^\circ\text{K}$, before undergoing the dark current tests. The gas-gaps will be ramped upto

BARC NEWSLETTER

10 kV of applied HV ($E \approx 50$ kV/cm) and the maximum acceptable dark currents are shown in Table 3.

Table 3 : Dark current limits for the gaps

gas-gap type	RE 4/3	RE 4/3	RE 4/3	RE 4/2	RE 4/2	RE 4/2
→	Top N	Top W	B	Top N	Top W	B
I_{max} (μA)						
→	3.5	2.0	5.1	2.0	2.0	3.5

The gas-gaps are then subjected to stability test for three days at the sites with HV at 9.7 kV. The acceptance criteria for the gas-gaps is that during the stability tests the increase in dark current should be less than 50% and $I < I_{max}$ as mentioned in Table 3. The HV working point depends on temperature and pressure of the environment, where the measurement is being done. Therefore, together with atmospheric pressure [mbar], the values for environmental temperature [$^{\circ}C$], environmental relative humidity [%], gas temperature [$^{\circ}C$] and gas relative humidity [%] are also to be stored in the data base. The HV values should be in volts while

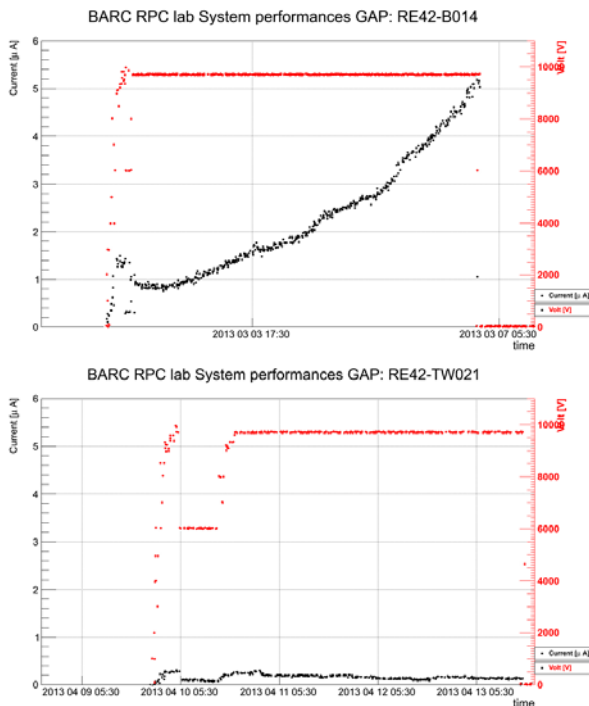


Fig.11: Long term monitoring (> 72 hrs) of gas gaps for leakage currents at 9700 V. The top panel shows a rejected gap and the bottom panel shows an acceptable gap after the HV scan

the I_{mon} values should be in microamperes. The formula used for the effective high voltage value is the following :

$$HV_{effective} = HV_{applied} [(P_o / P) \times (T / T_o)]$$

where $P_o = 1010$ mbar, is the reference atmospheric pressure and $T_o = 293$ K, is the reference ambient temperature. Once, the gas-gaps pass the acceptable criteria of mechanical and electrical tests, they are ready for assembly into an RPC.

Read out strips and electronics

Each RPC in the end-cap has a trapezoidal segmented readout strip divided in 3 η partitions, with 32 strips each, yielding a total of 96 strips per chamber (Fig.12). Each strip is soldered with coaxial cables (50Ω) to a 16 channel adaptor board which get linked to three Front End Boards (FEBs) for each chamber, which are electronically controlled through a Distribution Board (DB). The FEBs generate an LVDS (Low Voltage Differential Signal) which are transmitted to the off-detector electronics consisting of Link Boards (LBs), which perform the synchronization with the LHC clock and the transmission to the Trigger Electronics in the control room. The RPCs provide a fast and highly segmented trigger with a sharp transverse momentum threshold over a large portion of rapidity range $|\eta| < 1.6$. Muon detection is quite central to the CMS detector and the solenoidal field bends muon in the ϕ direction. The bending power of CMS magnet is uniform in the



Fig.12: A trapezoidal read out plane for RE4/2 RPC segmented into three eta sections namely $\eta = A, B$ & C , each consisting of 32 strips

BARC NEWSLETTER

barrel region and is equal to 17 Tm. In the end cap it reduces to 8 Tm at $|\eta| = 2.0$ and to 6 Tm at $|\eta| = 2.4$. Therefore particles of a given p_t bend differently at different $|\eta|$. One has thus to know $|\eta|$ in order to determine p_t from $\Delta\phi$ measurements. The ten degrees RPCs in the end-cap region provide a granularity of $\Delta\eta \times \Delta\phi : 0.1 \times 0.3^\circ$. The precision of 0.1 in η , therefore determines the maximal length of the strips. The high field of the solenoid is the key to excellent momentum resolution of the detector. Drift Tubes (DTs) in the barrel and Cathode Strip Chambers (CSCs) in the end caps provide track segments in each muon station with a spacial and angular precision of 1-2 mm and 10-60 mrad respectively. Muons are reconstructed as objects that have track in the muon spectrometer and a corresponding matched track in the inner tracker. The muon system stand alone resolution, $\Delta(p_T)/p_T$ (%) is about 20 – 40 % at 1 TeV, which when matched with the central tracker, improves to 6 – 17 % at 1 TeV. The CMS detector has been optimized in such a way so as to provide an excellent muon signature for several interesting/exciting events such as :

- a. $H \rightarrow ZZ \rightarrow \mu\mu\mu\mu$,
- b. $H \rightarrow \mu\mu\mu\mu$,
- c. $Z \rightarrow \mu\mu$,
- d. $W \rightarrow \mu\nu$

RPC : assembly and characterization

After the mechanical and electrical tests of the gas gaps, each RPC is configured with the three gaps (Bottom, Top Narrow and Top Wide), enclosed within the Cu mylar Faraday cage and soldered with 96 coaxial cables to the η -segmented read out plane.

An RPC when fully integrated, externally, with the Cu cooling system and the FEBs mounted on it (Fig.13), is tested for its strip connectivity, LV, noise and threshold settings on the FEBs, before being inserted in the hodoscope for evaluation of its performance parameters in terms of efficiency, strip profile, cluster size and noise rate which are shown respectively in Fig.14a,b,c,d for a typical RPC. Fig.14a, shows the efficiencies of the top layer (red), the bottom layer (black) and also a combination of the double layers

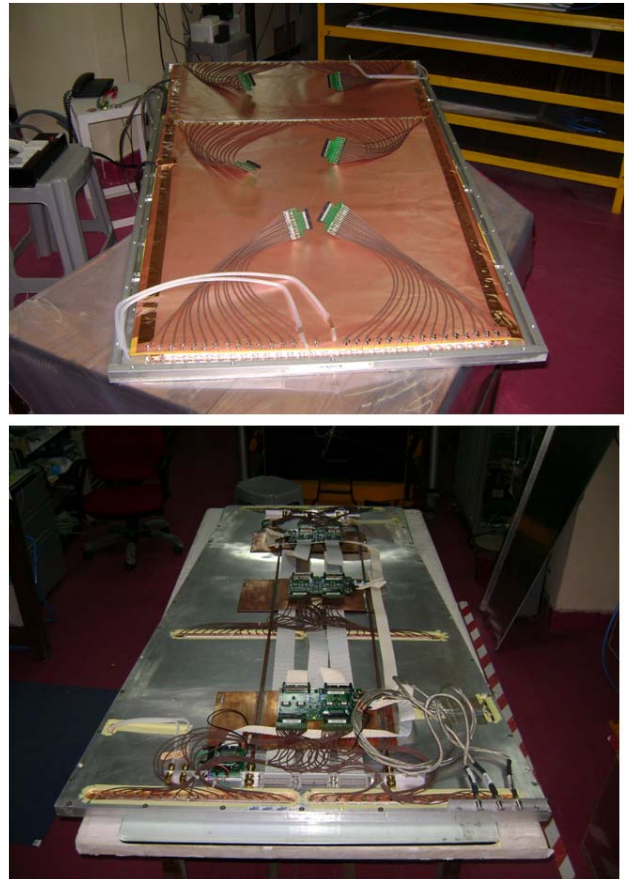


Fig.13: RPC with coaxial cables (top) and fully integrated with Cu cooling & FEBs (bottom)

(brown) alongwith the dark currents for the three types of gaps. The efficiencies, as expected, are better than 95% at the operating voltage (9400 V) and provide a plateau of about 300 V. The strip profiles from all the 96 read outs ensure that there are no dead channels and validates the entire connectivity chain. The cluster sizes and the noise rates are as expected. The software which controls the DAQ, HV power supplies and records the environmental parameters such as room pressure, RH and temperature alongwith evaluating the performance parameters is fully operational in the lab.

Instrumentation for monitoring of the environmental pressure, temperature, and relative humidity to run the HV scripts and for ramping of gas-gaps for dark current measurements have been implemented in all the three sites. The development of software tools for offline analysis and characterization of RPCs is being fine tuned at the moment. All operations are performed via webpages click-by-click and all the actions are logged in the e-log system to easily/simply manage the sites.

BARC NEWSLETTER

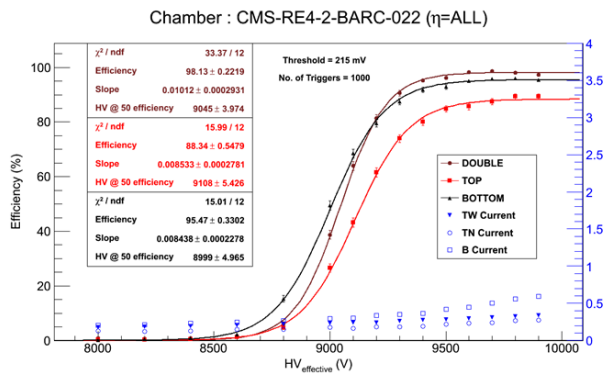


Fig. 14a: Efficiency for the three gaps configured inside an RPC (CMS-RE4-2-BARC-022) along with their dark currents

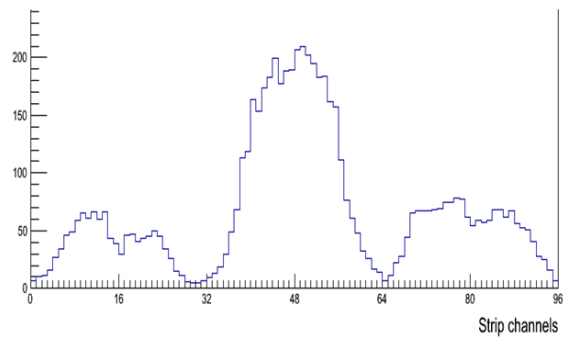


Fig. 14b: Strip profile from the 96 read outs from an RPC at 9900 V for 1000 cosmic triggers

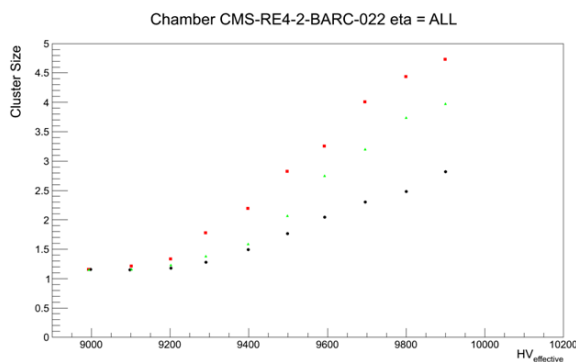


Fig. 14c: Cluster size from the three gaps of an RPC as a function of HV

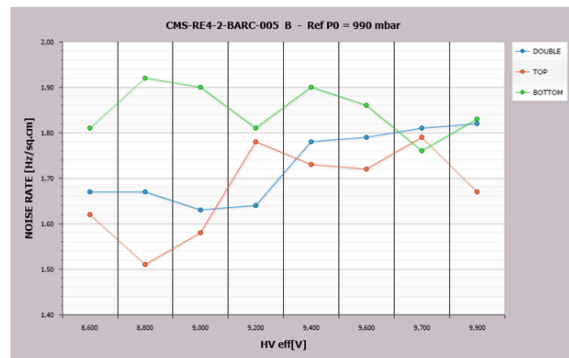


Fig. 14d: Noise rates (Hz/cm²) for the three gaps configured inside an RPC as a function of HV

Redesigned Cu cooling system :

With the experience gained with the installed RPCs in the existing end-caps, the Cu cooling system for the RPCs was redesigned. In the new design, the area of Cu plates has been increased optimally with water flowing through Cu pipes, in a closed circuit. The earlier installed, 8 mm ϕ brass unions with a single ferrule, have been replaced with SS double ferrules to ensure that there is no water leakage at the coupling junctions. Improvement in the cooling system had to be introduced for RE4, due to its particular position facing the electronics of the other muon system based on Cathode Strip Chambers. The new cooling system is envisaged also for RPC that will replace malfunctioning chambers in the other layers, so the design includes backward compatibility.

A prototype of the Cu cooling system was fabricated in BARC, Mumbai, meeting the required specifications and was dispatched to CERN during the pre-production run. The Cu cooling system was fabricated with

Deoxidized High Residual Phosphorus (DHP) semi hard Cu pipes (8 mm OD and 6 mm ID) and Cu sheets with 1 mm thickness. The DHP Copper is a commercially available material of pure copper, which has been deoxidized with phosphorus, leaving relatively high residual phosphorus content. This copper has a lower electrical conductivity and is used where there is need for heat transfer and electrical properties are not important. The Cu cooling system will have chilled water at 19°C running at a pressure of 2 bar, in order to cool the electronics and the body of RPCs through the aluminum honey comb panels on to which it is mounted. A typical Cu cooling system for RE4/3 type RPC is shown in Fig. 15. The Cu pipes were soldered (~200°C) to the Cu plates with soldering material having a composition of Sn : Ag : Pb :: 62 : 2 : 36. After complete assembly, the Cu cooling systems are tested for any possible leakage with Argon gas at 20 bar of pressure. Special jigs were made to ensure that the Cu pipes do not bend and maintain their straightness, while soldering them to the Cu plates. The fabricated Cu assembly was further subjected to leak tests with 20

BARC NEWSLETTER

bar of Argon gas for 30 minutes. Each Cu cooling set is subjected to leak test, three times to ensure that it qualifies the leak standard as set up by CERN ($< 5 \times 10^{-4}$ mbar.litre.sec⁻¹).



Fig.15: Mass production of Cu cooling assemblies (top) and a typical RE4/3 cooling set under leak test at NPD-BARC (bottom)

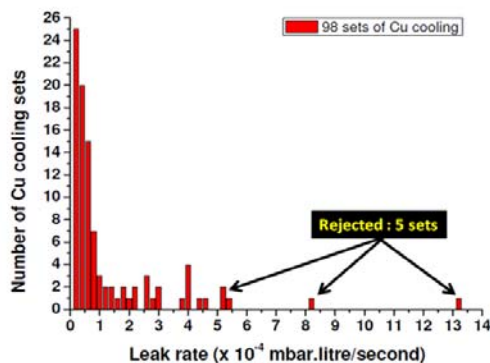


Fig.16: Distribution of the leak rates of 98/200 of the Cu cooling sets (top) and their dispatch in batches of 20 each to CERN and Ghent (bottom)

So far 98 out of 200 of the Cu cooling sets have been fabricated, leak tested and dispatched to CERN. A distribution of the leak rates ($\times 10^{-4}$ mbar.litre.s⁻¹) is shown in the top panel of Fig.16. The five rejected systems having leak rates larger than the prescribed limit were those from the initial pilot production run, where the procedures were being laid out for deciding the acceptable leak rates. A couple of sets were rejected because of improper crimping of ferrules.

The Cu cooling systems for all the chambers are being fabricated and tested at BARC, Mumbai and being dispatched to the other assembly sites at CERN and Ghent, in a phased manner synchronising with the delivery of gas gaps from KODEL (Fig.16, bottom panel). MD&PDD-BARC has the responsibility of the fabrication of entire 200 Cu cooling sets for the RE4 production along with providing engineering support to the RE4 upgrade project at BARC.

Supper Module assembly at CERN :

All the assembled and characterized (QC1, QC2 and QC3) from the three assembly sites arrive at CERN. The first set of ten RPCs from NPD-BARC arrived at CERN in May 2013. They were subjected to visual inspection and after mounting the HV Tripolar connectors were sent to QC4 level, where they are monitored again for 1 week to evaluate the stability in their dark currents. After the Tripolars are mounted the three gaps merge into top and bottom layers and the access to two different gaps (Top Narrow and Top Wide) in the top layer cease to exist (Fig.17). At the time of writing this article, two of the RPCs have qualified the QC4 level and others are in the queue at QC4. Once the chambers have qualified the QC4, they are immediately sent to be configured into a Super Module assembly, where an RE4/2 chamber mates with the RE4/3 chamber and all the interconnections for gas flow, Cu cooling, HV, LV and signal cables are secured. A typical Super Module assembled is shown in Fig.18. A typical existing end-cap in the CMS, when configured at the CMS surface hall is shown in Fig.19 (left). Its overall diameter is 15 metres. At that time the entire end-cap after having been mounted on the iron yoke at the surface hall was later lowered into the cavern, 100 metres below the surface.

BARC NEWSLETTER

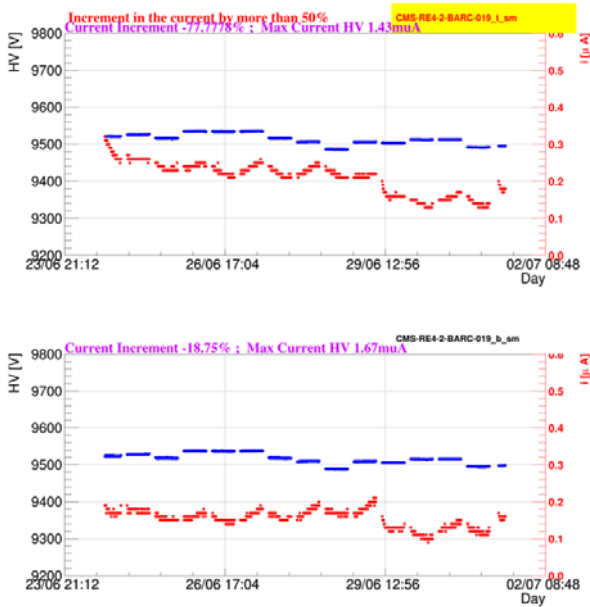


Fig.17: A typical chamber assembled at BARC (CMS-RE4-2-BARC-019) after having qualified the QC4 level for integration into a Super Module



Fig.18: An assembled Super Module under test

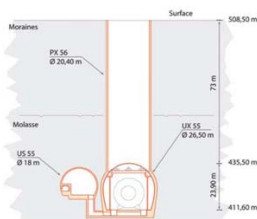
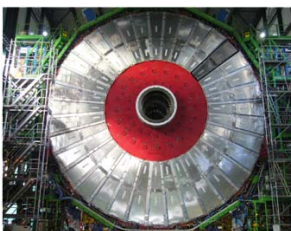


Fig.19: One of the existing end cap, when assembled on the surface hall of the CMS (left). The Super Module is outlined in dark. The schematic of the CMS cavern (right)

During the installation of RE4, however, the procedures would be very different. During the installation of RE4, it will be the Super Modules, which will be lowered down into the cavern and installed on the reverse side of the existing iron yoke in the cavern. All the Super Modules will then be transported from CERN to the

CMS cavern at Point 5 in Cessy in France for installation and commissioning.

The Construction Database

Each of the QA/QCs procedures mentioned above, for each chamber, shall be stored in an Oracle based Construction Database. The database will include all measurements at the gas-gap level, HV scans, characterization of RPCs in terms of efficiency, cluster size and strip profile, performed during the detector assembly and the Super Module assembly. This will enable CMS to follow the evolution of each chamber in time, in case problems related to chamber performance should appear during operation later on [8].

Delivery schedules of RPCs from the assembly sites :

Table 4, below summarizes the RPCs to be built at different assembly sites for the RE4 upgrade. In India, two institutes are collaborating jointly for the project, namely – Nuclear Physics Division-BARC, Mumbai and Panjab University, Chandigarh. CERN site will coordinate the logistics & setting up protocols for QA/QC.

Table 4 : RPCs to be built at the sites

Sr No	RPCs to be built for the RE4 upgrade	# of RPCs
1	BARC (RE4/2)	50
2	Ghent (RE4/3)	50
3	CERN (RE4/2)	50
4	CERN (RE4/3)	50

Construction data base has been implemented for QC from chamber components (bakelite, gaps, electronic etc.) to final chamber Super Module assembly. All the relevant components of the chamber mechanics have been delivered at the respective assembly sites for all the 200 chambers and the RPC assembly work is expected to begin soon after the arrival of first batch of gas-gaps at the assembly sites. Gas-gaps will be produced at a rate of approximately 60 gaps per month at KODEL, and will then be dispatched to the three sites. The chamber production rate is foreseen as five RPCs per month in Mumbai, five RPCs per month at

BARC NEWSLETTER

Ghent and ten RPCs per month at CERN, given the available logistics and infrastructure in these sites. At the time of writing this article, ten RPCs from BARC, ten from Ghent and thirty RPCs from CERN have been built and delivered at CERN, keeping in line with the time schedules. Seventy two chambers are required for configuring 36 Super Modules for the installation of the first end-cap (+). So far ten Super Modules have been built and qualified for installation at Point 5.

Table 5 : Schedule for installation

Sr No.	Installation & Commissioning	Proposed schedule
1	36 SM for Endcap 1 ready for P5	Aug 2013
2	First endcap (+ Z side)	Oct. 2013
3	36 SM for Endcap 2 ready for P5	Jan. 2014
4	Second endcap (- Z side)	Feb. 2014

The entire schedule of installation and commissioning of both the end-caps is shown in Table 5. The procedures for building the remaining 40 RE4/2 RPC at NPD-BARC is in full swing wherein these chambers are to be delivered to CERN by Jan 2014.

Acknowledgements

We are thankful to the Indian agencies, Department of Atomic Energy and Department of Science and Technology for funding the upgrade project, various divisions in BARC such as CDM and MDPDD for providing the engineering support, the CMS-RPC end-cap group at CERN for providing the logistical support and staff and students from Panjab University,

Chandigarh for the help during the execution of the project. I would also like to thank Dr(s). S. Kailas, R. K. Choudhury, A. K. Mohanty and Archana Sharma for their continuous guidance and support for this project. I also express my gratitude to my NPD colleagues R. G. Thomas, Mrs. S. T. Sehgal, R. Sehgal, Ph.D. students V. K. S. Kashyap and C. Yadav and Manish Kumar and his team from MD&PDD, for their vital contributions in this project.

References

1. The CMS experiment at the CERN LHC, 2008 JINST 3 S08004, (<http://iopscience.iop.org/17480221/3/08/S08004>)
2. Development of Resistive Plate Counters, R. Santonico and R. Cardarelli, *Nuclear Instr. & Methods in Physics Research*, 187 (1981) 377
3. Resistive Plate Chambers in running and future experiments, G. Bruno, CMS CR 2004/001, International Europhysics Conference on High Energy Physics, Aachen (Germany), July 17-23, 2003
4. INO/2006/01 Project Report Volume I <http://www.imsc.res.in/~ino/OpenReports/INOReport.pdf>
5. Performance of a large forward resistive plate chamber for the CMS/LHC under high radiation environment, S.H. Ahn et al., *Nuclear Instr. & Methods in Physics Research*, vol. A 469 (2001) 323
6. CMS Collaboration, *The Muon Project*, CMS Technical Design Report, CERN/LHCC 97-32
7. Characterization of CMS end-cap RPCs assembled in India, L. M. Pant, *Nuclear Instr. & Methods in Physics Research A* 661 (2012) S34
8. https://apex.cern.ch/pls/htmldb_cmsr/f?p=106:1

ENHANCEMENT OF CHARGE CARRIER MOBILITY OF ORGANIC SEMICONDUCTOR THIN FILMS

A.K. Debnath, Soumen Samanta, Ajay Singh, D.K. Aswal and S.K. Gupta
Technical Physics Division

Dr. A.K. Debnath is the recipient of the DAE Scientific & Technical Excellence Award for the year 2011

Abstract

Cobalt phthalocyanine (CoPc) films of nominal thickness of 20 nm have been grown on LaAlO₃ (001) and SrTiO₃ bi-crystal substrates using molecular beam epitaxy (MBE) technique. Temperature dependent charge transport was studied in the temperature range 300-20K. Mobility (μ) at 300K was observed 7 and 148 cm²V⁻¹Sec⁻¹ for the films grown on (001) LaAlO₃ and SrTiO₃ bi-crystal respectively. The large increase in μ value is attributed to better ordering of the organic molecules.

Introduction

Most of the work on organic semiconductor films to date has concentrated only on the growth and optoelectronic characteristics of planar stacking molecules viz. metal phthalocyanines (MPcs), and polycyclic aromatic compounds based on naphthalene and perylene as compared to their charge transport properties. Charge carrier mobility (μ) is a very important parameter for device applications. μ of organic semiconductors films is very low (< 0.1 cm²V⁻¹s⁻¹) as compared to inorganic semiconductors [1]. This is because of the large size of molecules i.e large lattice mismatch between organic molecule and inorganic substrate which results in large disorder in films and inherent weak intermolecular forces (van der Waals). Further, low molecular symmetry leads to highly anisotropic conduction. The effective path for charge transport is perpendicular to the molecular plane i.e. direction of maximum π -orbitals overlap [2]. Therefore a close packing of the molecules and ordered crystalline structure are essential to maximize the π -orbitals overlap. Osso et. al. used stepped sapphire as a template to grow ordered F₁₆CuPc films but they did not study μ of the films [3]. We have studied μ of the cobalt phthalocyanine (CoPc) films grown on (001) LaAlO₃ and SrTiO₃ bi-crystal. LaAlO₃ has natural twin boundaries

and SrTiO₃ bi-crystal has single boundary which act as template to grow ordered films.

Film Growth and Measurements

CoPc films were deposited at 200°C using MBE (RIBER system, model EVA 32) with a base vacuum $> 10^{-8}$ Torr. For transport measurements two planar gold electrodes (size: 3 mm x 2 mm) separated by 7 μ m were thermally deposited onto films using a metal mask and silver wires were attached to the gold electrodes using silver paint. The current-voltage (*J-V*) measurements were carried out using Keithley 6487 voltage source/picoammeter and computer based data acquisition system in the temperature (T) range 300–24 K using a closed cycle cryostat.

Structure and electrical transport properties

(i) CoPc films LaAlO₃ substrate

Figure. 1a shows XRD spectrum for the 20 nm CoPc films. Presence of a highly intense (200) Bragg peak at 6.7° corresponding α -CoPc phase, indicates that the film is highly crystalline with *a*-axis normal to the substrate. This is further confirmed by rocking curve of (200) Bragg peak (inset of Fig. 1a), which has an intense

peak at 3.35° with a full-width-half-maximum value of only 0.11° .

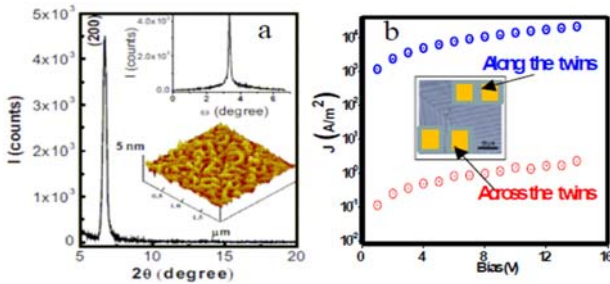


Fig.1: (a) XRD pattern for 20 nm CoPc film. Insets (upper) rocking curve of (200) Bragg peak (lower) AFM image of the film (b) J - V characteristics of the films across (red) and along (blue) the twins. Inset shows the twin boundaries of the bare substrate with gold pads for the electrical measurements

AFM image of the CoPc film (inset of Fig. 1a), reveals that film consists of highly dense CoPc grains. Presence of natural twins (inset Fig. 1b) in LaAlO_3 substrate that might act as a template for the growth of ordered CoPc films. Figure 1b shows J - V characteristics for 20 nm CoPc films along and across the twins which show a vast difference (10^4 order) in J value. J - V characteristics for 20 nm CoPc films at different temperatures as shown in Figure 2a, indicates that variation of current depends on both V and T . Unlike disordered films no hysteresis is observed in the present case. Based on the nature of J dependence on V and T , four distinct regions (marked as I–IV) have been identified. Broadly, regions I and II belong to the temperature region of 300–100 K, whereas regions III and IV lie in the temperature zone below 100 K.

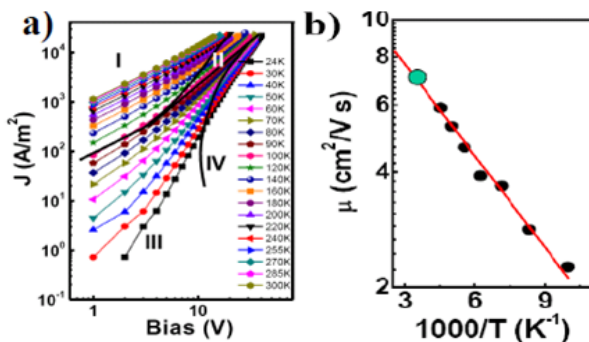


Fig.2: (a) Log-log plots of (J - V) characteristics for 20 nm CoPc films in the temperature range 300–24 K (b) Arrhenius plot of mobility determined from the slope of J - V^2 data in region II.

The slope value in region II is ~ 2 , indicating that the charge transport is via trap-free space charge limited conduction (SCLC) which occurs if the injected carrier concentration exceeds that of thermally generated carriers. For SCLC the J - V characteristics is given by: $J = (9/8)\epsilon\theta\mu(V^2/d^3)$, where ϵ is permittivity of the film, V is the applied bias, d is the electrode separation and θ is a ratio of free to total (trapped and free) charge carrier density. The μ values at different T were calculated from the slopes of J - V^2 plots and shown in Fig. 2(b), which is found to obey the Arrhenius behavior, i.e., $\ln \mu \sim 1/T$. Since in the temperature range 300–220 K, we have only Ohmic region in the entire bias, the value of μ at 300 K was obtained by the extrapolation of data, which is found to be $\sim 7 \text{ cm}^2 \text{ V}^{-1} \text{ s}^{-1}$ [4]. It is two orders in magnitude higher as compared to disordered films [5]. In order to re-confirm the role of twin boundaries for the enhancement of μ we had grown CoPc films (100 μm wide and 20 nm thick) “along the boundary (ATB)” and “in the single crystal region” (SCR) of 36.8° boundary SrTiO_3 bicrystal substrates, as shown in next section.

(ii) CoPc films SrTiO_3 bi-crystal substrate

As schematically shown in Fig. 3, in a bicrystal SrTiO_3 substrate, two single crystals, i.e., A and B share a common (001) surface and at the boundary their (010) are tilted by an angle ϕ (e.g., 36.8°). Bicrystal boundary (BB) is zigzagged along (100) and (010) axes of SrTiO_3 with facets on both A and B sides of the boundary with triangularly shaped grooves.[6]

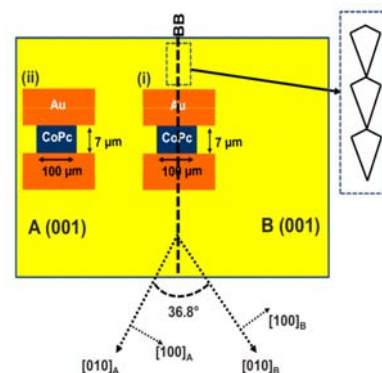


Fig.3: Schematic of Au/CoPc structure deposited (i) along ATB and (ii) in the SCR of SrTiO_3 bicrystal substrates. Both part A and part B of the bicrystal share a common (001) surface. The structure of BB consists of triangularly shaped grooves.

BARC NEWSLETTER

Resistivity (ρ) was measured for films grown on ATB and SCR regions and results are shown in Figure 4a. It is seen that the value of ρ (300K) for ATB films is ($52 \Omega \text{ cm}$) lower by three orders in magnitude as compared to SCR films ($1.08 \times 10^4 \text{ cm}$). In general, ρ (300K) increases as the disorder in the film increases. Temperature dependence of the reduced activation energy [$W = d \ln[\rho(T)/d \ln T]$] [6] for both ATB and SCR films is plotted in Fig. 4b.

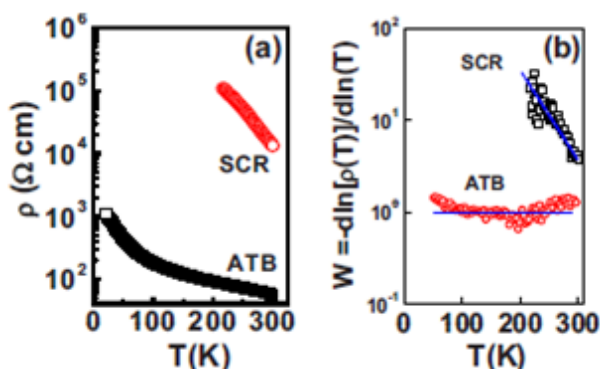


Fig.4: (a) $\rho(T)$ and (b) $W(T)$ plots of ATB and SCR films.

It is seen that for ATB films the value of W is ~ 1 , which is nearly independent of the temperature, i.e., slope is zero. This indicates that ATB films are in the critical regime. On the other hand, a negative slope of $W(T)$ for SCR films reveals their insulating behavior. Figure 5a shows linear room temperature J - V characteristics for ATB films i.e. an Ohmic conduction in the entire bias range, while SCR films exhibit nonlinear behavior. Ohmic conduction ($J = n_0 e \mu V/d$) in molecular semiconductors occurs if the thermally generated carriers exceed that of the injected carriers from the electrode where n_0 is the thermally generated hole concentration, e is electronic charge. In the case of SCR films, three different power law behavior ($J \sim V^\alpha$) is observed. For bias $< 5 \text{ V}$, $\alpha \sim 1$ indicates Ohmic conduction. For the bias range 5 – 15 V , $\alpha \sim 2$ indicates SCLC. Taking literature value of ϵ as $2.43 \times 10^{-11} \text{ F/m}$, the estimated μ was found $4.1 \times 10^{-4} \text{ cm}^2 \text{ V}^{-1} \text{ s}^{-1}$ for SCR films. The value of μ calculated following the approach of Wu *et al.* [6] The obtained value of μ was $3.8 \times 10^{-3} \text{ cm}^2 \text{ V}^{-1} \text{ s}^{-1}$, which was also field-independent.

For bias voltage $> 15 \text{ V}$, $\alpha = 3$ suggests SCLC mechanism in the presence of deep traps i.e, films have a very large structural disorder.

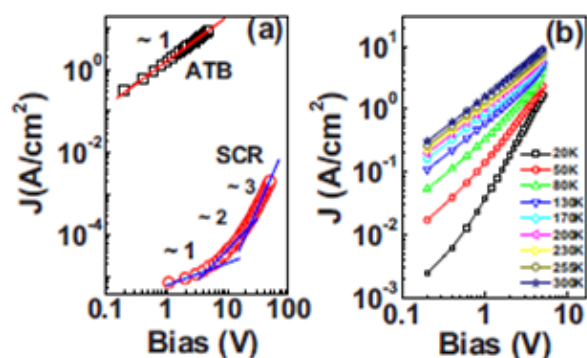


Fig.5: (a) Log-log plots showing the room temperature J - V characteristics of ATB and SCR films. (b) Temperature dependent J - V characteristics of ATB films.

J - V characteristics for ATB films (Fig.5b) shows Ohmic behaviour in the entire bias for temperature region of 300 – 170 K . For $T < 170 \text{ K}$, at low bias the conduction is Ohmic, while for high bias the slope changes to ~ 2 , indicating that charge transport is via trap-free SCLC, that is $\theta = 1$. The μ values, therefore, were directly calculated from the slopes of J - V^2 plots and T vs μ is plotted in Fig. 6.

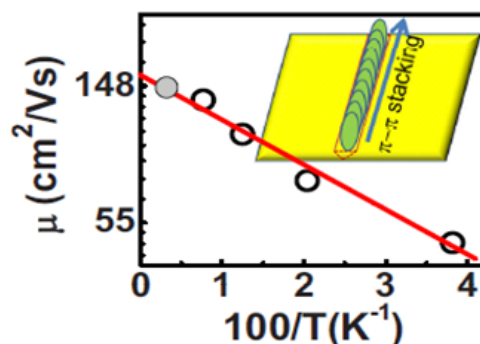


Fig.6: Arrhenius plot of mobility determined from the slope of J - V^2 data in the temperature range of 170 – 200 K for ATB films. Inset shows schematic of the ordering of CoPc molecules in "standing-up" configuration along the BB due to π - π interactions.

The value of μ at 300 K obtained by the extrapolation of data is found $\sim 148 \text{ cm}^2 \text{ V}^{-1} \text{ s}^{-1}$. A straight line fit of $\ln \mu$ versus $1/T$ data indicates that the temperature dependence of μ obeys Arrhenius behavior, i.e., $\mu(T) = \mu_0 \exp(E_{\text{pol}}/2kT)$, where E_{pol} is the polaron binding energy.

From the slope of $\ln(\mu)$ versus $1/T$, the value of E_{pol} comes out to be 0.014 eV . A very low value of E_{pol} in the case of ATB films shows that they are well ordered.

BARC NEWSLETTER

Conclusion

Ordering of the molecules is essential for the enhancement of μ for organic semiconductor films. Highest μ ($148 \text{ cm}^2 \text{ V}^{-1} \text{ s}^{-1}$) achieved in CoPc films grown on SrTiO_3 bi-crystal boundary.

References

1. R. D. Gould, Coordination Chem. Rev. 156, (1996) 237.
2. Jean-Pierre Farges :Organic conductors: Fundamentals and applications Applied physics, Marcel Dekker 1994.
3. J. O. Oss'ó, F. Schreiber, V. Kruppa, H. Dosch, M. Garriga, M. I. Alonso, and F. Cerdeira., Adv. Funct. Mater., 12 (2002) 455–460.
4. S. Samanta, D.K. Aswal, A. Singh, A.K. Debnath, M. Senthil Kumar, Y. Hayakawa, S.K. Gupta and J.V. Yakhmi, Appl. Phys. Lett. 96 (2010) 013305
5. S. Samanta, A. Singh, A. K. Debnath, D. K. Aswal, S. K. Gupta, J. V. Yakhmi, and S. K. Deshpande, J. Appl. Phys. 104, (2008) 073717.
6. S. Samanta, A. Singh, Arvind Kumar, A. K. Debnath, D. K. Aswal, S. K. Gupta, and J. V. Yakhmi, Appl. Phys. Lett. 98 (2011) 143301.

BARC NEWSLETTER

PHOTODISSOCIATION DYNAMICS STUDIES USING LASER INDUCED FLUORESCENCE (LIF) AND RESONANCE ENHANCED MULTIPHOTON IONIZATION – TIME OF FLIGHT (REMPI-TOF) TECHNIQUE

Hari P. Upadhyaya

Radiation & Photochemistry Division

Dr. Hari P. Upadhyaya is the recipient of the DAE Scientific & Technical Excellence Award for the year 2011

Abstract

A brief description of Laser Induced Fluorescence (LIF) and Resonance Enhanced MultiPhoton Ionization - Time of Flight (REMPI-TOF) technique developed in our laboratory is presented in this article. These techniques are used to obtain various dynamics information, such as, distribution of the available energy into the product states. Finally, these dynamics information are correlated to the features of dissociative potential energy of the molecular system.

Introduction

A photodissociation reaction is a unimolecular reaction, where the energy requirement for the reaction (fragmentation/isomerization) is obtained from the absorbed photon by the molecule. To explain its dynamics, it is better to explain the molecules in terms of various potential energy surface (PES), which is a plot of potential energy as a function of various molecular coordinates. Molecules have a ground electronic state, and a large number of excited electronic states. The nature of PES prepared by an absorbed photon, determines the fate of the prepared excited state, such as whether it will fluoresce or dissociates. To obtain the dynamic information, which can be utilized to understand the mechanism of a photodissociation process, state-resolved measurements are employed, where the population of individual states are probed to obtain the microscopic details about the dissociation process. The kind of distribution of the available energy into the product states indicates the nature of the dissociation process. A non-statistical distribution suggest a direct dissociation, where dissociation occurs on a time scale shorter than the rotational period of the molecule.

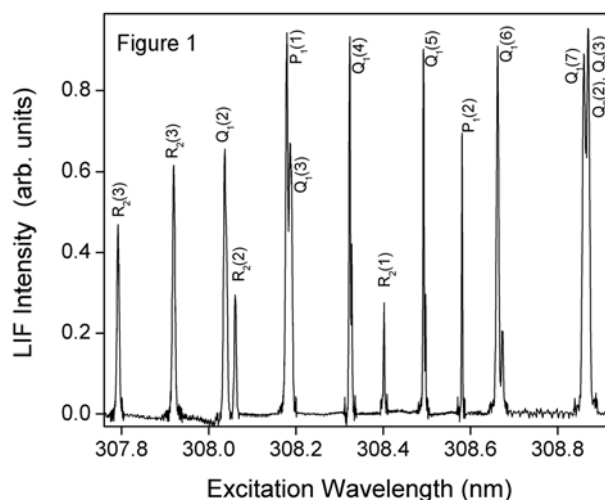
On the other hand, a statistical distribution points out the complex nature of a dissociation mechanism, with a dissociation lifetime longer than the rotational period of the molecule. We have developed and employed two versatile techniques, laser induced fluorescence and resonance enhanced multiphoton ionization- time of flight mass spectrometer, to probe the partitioning of the available energy among different states of a photofragment and deduced the photodissociation dynamics of some atmospherically important molecules.

The available energy in the photodissociation process is related to the photolysis photon wavelength by the relation, $E_{avl} = E_{int}(\text{reactant}) + hv - D_0$, where $E_{int}(\text{reactant})$ is the initial internal energy of the reactant molecule, hv is the photolysis photon energy, and D_0 is the dissociation energy of the molecule for forming the fragments. The available energy is partitioned into the fragments internal energy, electronic (E_e), vibrational (E_v) and rotational (E_r), and relative translational energy (E_t). We have used these two techniques, LIF and REMPI-TOF, to estimate these quantities in the photodissociation process of various molecules to understand their dynamics and mechanism of dissociation.

LIF Spectroscopy for photodissociation dynamics investigation

LIF technique involves the absorption of a monochromatic photon by atomic/molecular species, and monitoring of subsequent emission from the excited species. In LIF technique, the population of molecules from rovibrational state in the ground state is transferred to a rovibrational state in the excited electronic state, using a laser tuned to the requisite wavelength. However, the spectral bandwidth of the laser employed should be less than the rotational-state spacing of the species to be monitored. For this purpose, a tunable dye laser, or an optical parametric oscillator, which has an advantage over the conventional light source in terms of spectral brightness and width is used. In this technique, the intensity of the fluorescence signal, I_{LIF} , is proportional to the population of the species in the excited state, which is related to the initial ground state population before laser excitation. Although, in principle, it can be used for detecting single molecular species, in practice, for most of the systems one might obtain sensitivity of 10^6 particles per cubic centimeter.

The LIF setup was developed at Radiation & Photochemistry Division, B.A.R.C. for investigating photodissociation dynamics of atmospherically important molecules, producing OH radical on photoexcitation. The photolysis laser employed is an excimer laser. The probe beam is the second harmonic output of a dye laser pumped by the second harmonic of a seeded Nd:YAG laser. The photolysis and the probe laser beams traverse orthogonally through two pairs of windows to intersect at the center of the reaction chamber. The fluorescence is collected by a photomultiplier tube. A PC is used to control the scan of the dye laser and to collect data. The spectral resolution of the probe laser is 0.06 cm^{-1} . The OH fragment was probed state-selectively by exciting the $A^2\Sigma \leftarrow X^2\Pi$ (0,0) transition of OH (306–309 nm) and monitoring the subsequent fluorescence. The typical LIF spectra, with appropriate assignments are shown in Fig. 1 for the (0,0) band of the A-X system of OH, produced from acetic acid on photodissociation at 193 nm.^{1,2}



Rotational State Distribution:

The nascent rotational state populations of OH radicals generated on photodissociation were used to construct a Boltzmann plot, for obtaining the rotational temperature of nascent OH fragments.

Estimation of Vibrational State Distribution:

Assuming a Boltzmann distribution, a vibrational temperature can be obtained from the ratio of the normalized LIF intensities of the same rotational excitation line of the various vibrational level.

Average translational energy of OH

After correcting the Doppler profile of the rotational lines for the probe laser linewidth, the linear Doppler width $\Delta\nu_D$ is related to the translational temperature (T_T) by the equation $\Delta\nu_D = 7.16 \times 10^{-7} \nu_0 \sqrt{T_T(OH)/m_{OH}}$, which can be used to determine the average translational energy.

Apart from above mentioned quantities, other parameters such as Spin-Orbit State Distribution and population of the Λ -doublets can also be determined to further understand the dynamics of the dissociation process.

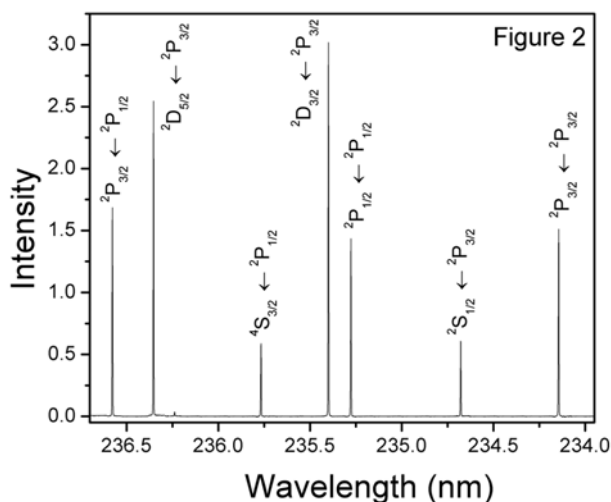
REMPI-TOF mass spectrometer

We have developed TOF-MS for investigating the photodissociation dynamics of reactions channel

BARC NEWSLETTER

forming atomic species, such as Cl and Br.³ A detailed description of the experimental setup is given in our previous paper.⁴ A TOF-MS (two-stage Wiley–McLaren type) was mounted vertically, perpendicular to the horizontal MB, with microchannel plates as detector. The vapours of reactant, seeded in helium, was obtained by bubbling helium through a sample maintained at room temperature. We have employed a single laser for both photodissociation of the parent molecule and ionization of the atomic photoproducts. A Nd:YAG laser pumped dye laser using rhodamine 101 dye, was employed for generating the requisite laser beam in the range 230–236 nm.

For measuring TOF spectra, the MCP signal was fed to an oscilloscope, which was interfaced to a Pentium PC. The laser power was typically 50–100 $\mu\text{J}/\text{pulse}$. The power dependence measurements were also performed. A typical REMPI spectra of Cl atom in the photodissociation of PCl_3 is shown in Fig. 2. A double Fresnel rhomb was used for rotation of the laser beam polarization entering the chamber. TOF profiles were taken for three different experimental configurations, *vertical, horizontal and magic angle*.



Analysis of TOF profile

The measured TOF profile corresponds to the component of the photofragment that speeds along the TOF-MS axis, which defines the lab frame Z axis

and is given as, $f(v_z, \chi) = \int_{1/v_z}^{\infty} \frac{g(v)}{2v} \left[1 + \beta P_2(\cos \chi) P_2\left(\frac{v_z}{v}\right) \right] dv$, where v_z is the velocity component along the Z axis, v is the recoil speed of the fragments, β is the anisotropy parameter, $P_2(\cos \chi)$ is the second Legendre polynomial, and the $\cos(\chi) = \hat{\epsilon} \cdot \hat{z}$, is the projection of the pump laser electric field, $\hat{\epsilon}$, on the detector axis, \hat{z} , which is also defined as the angle between the dissociation laser polarization and the Z axis. The major task of the analysis procedure is to extract the photofragment speed distribution, $g(v)$, and anisotropy, β of each decay channel i active in the photodissociation. The detail of the adopted procedure has been described elsewhere.⁴ The photofragment speed distribution, $g(v)$, thus obtained was converted into the center-of-mass translational energy distribution, $P(E_T)$ and the average translational energy was calculated. Also, the spin-orbit ratio of the halogen atom formed is evaluated, which eventually gives information about the dynamics occurring in the exit channel of the photodissociation process.

References

1. Naik, P.D., Kumar, A., Upadhyaya, H. P., Bajaj, P.N. and Sarkar; S.K. *Laser Induced Fluorescence Spectroscopy, Lasers in Chemistry*, Vol. 1, Ed. M. Lackner, Wiley-VCH Verlag GmbH (2008), p 463
2. Naik, P.D., Upadhyaya, H. P., Kumar, A., Sapre, A. V. and Mittal, J. P. *Dynamics of Acetic Acid Dissociation at 193.3 nm : Selectivity in OH Reaction Channel*, *Chem. Phys. Letters*, **340** (2001) 116-122
3. Naik, P.D., Upadhyaya, H. P., Kumar, A., Bajaj, P.N., Sinha, A.K., Bhatt, S. and Gupta, M.D.P., Development of resonance-enhanced multiphoton ionization system, BARC Report No.: BARC/2009/E/011.
4. Upadhyaya, H. P., Saha, A., Kumar, A., Bandyopadhyay, T., Naik, P.D. and Bajaj, P.N. Photodissociation Dynamics of Phosphorus Trichloride (PCl_3) at 235 nm Using Resonance Enhanced Multiphoton Ionization (REMPI) with Time-of-Flight (TOF) Mass Spectrometry *J. Phys. Chem. A*, **114** (2010) 5271-5278

BARC NEWSLETTER

DESIGN, DEVELOPMENT AND DEPLOYMENT OF INSIDE DIAMETER MEASUREMENT TOOL FOR 220 MWE PHWRs

G. Sharma, S. Bhattacharyya, V.P. Bodile and R.J. Patel
Refuelling Technology Division

Shri G. Sharma is the recipient of the DAE Young Applied Scientist / Technologist Award for the year 2011

Abstract

Inside Diameter (ID) measurement of PHWR coolant channels is required to be carried out for diametral creep assessment. Inside Diameter Measurement Tool (IDMT) has been developed for mass scale ID measurement in water flooded condition using Fuelling Machines. IDMT is having a conical ball actuator which actuates three balls axially outward. The ball actuator is moved by the Ram-C of Fuelling Machine and travel of ball actuator is reflected on potentiometer of the Ram-C. The IDMT is quickly deployable and does not require hose / cable connection to operate. IDMT was first time deployed in KAPS-2 for carrying out measurement in 26 numbers of channels. This experience enabled refinement in the technique before deploying again in KAPS-2 for measurement in 16 channels. Implementation of IDMT has given leverage to reactor operation in terms of significantly reduced man-rem consumption. IDMT is useful for faster scanning of large number of channels to identify bigger diameter channels for further scanning due to its quick deployment capability.

Introduction

Expansion of coolant channels due to creep and growth is one of the major life limiting parameters of coolant channels in Pressurized Heavy Water Reactors (PHWRs). Heavy water at high pressure and temperature flows inside the coolant channels. The radioactive environment causes axial and radial creep in pressure tubes. Expansion due to radial creep increases pressure

tube diameter which may lead to coolant bypass resulting in insufficient cooling to the fuel bundles and is a safety concern. It also results in reduction in gap between pressure tube and calandria tube. Hence periodic radial creep monitoring of pressure tubes of PHWRs under life management program is necessary.

BARC has developed few tools for measuring ID of coolant channels in past viz. 3-point micrometer,

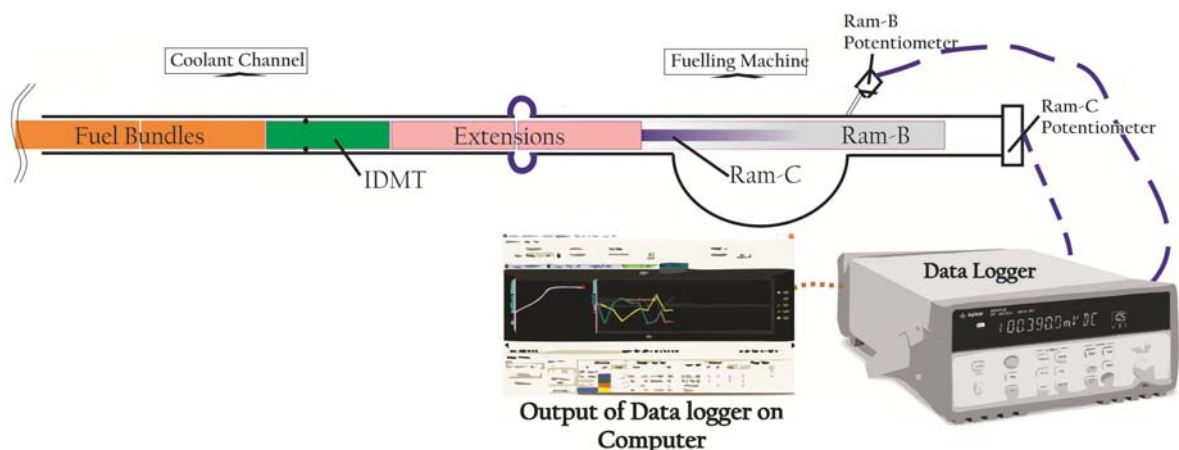


Fig. 1: IDMT schematic

BARC NEWSLETTER

HYdraulic Remote Inside diameter Measurement system (HYRIM) and recently UT based measurement technique incorporated in the BARCIS. Elaborate preparation, more reactor shut-down time and human presence in the vault make these tools less attractive in terms of man-rem consumption and ease of operation.

An innovative IDMT has been evolved for mass scale wet-condition measurements of coolant channel ID remotely using Fuelling Machines (FMs). The tool is having three numbers of balls located equispaced and can be moved radially outward by axial movement of ball actuator. The tool can reach up to centre of channel using extensions. The tool remain sandwiched between fuel column and Ram-B of FM. IDMT is positioned at desired location by moving fuel column and Ram-B. Fig. 1, shows the scheme.

Working Principle

IDMT is assembled with three balls supported on a ball actuator and retained in the radial holes in the body. The balls move radially outward due to axial motion of a taper ball actuator. Fig. 2 depicts cross section of the tool. In normal condition, ball actuator is held backwards by spring force and balls remain in collapsed condition. In this condition, tool is positioned at desired

location using fuelling machine. For measurement of ID, Ball actuator is pushed by Ram-C of FM causing balls to move radially outward to touch ID of Pressure Tube. The radial movement of balls is a linear function of ball actuator travel. Ram-C travel is calibrated in terms of inside diameter.

Major Dimensions of IDMT	
Length	750 mm
Diameter	80.5 mm
Stroke	170 mm
Cone Angle	2°
Measurement range	82-87 mm

Overall Scheme

IDMT is positioned by Ram-B at desired location. During measurement tool front face gets supported against the fuel column. Fuel column at other end is supported by Ram-C of other FM. Extensions are used to position tool inside the channel since reach of Ram-B is limited. Space available in the FM magazine allows maximum four number of extensions to be stored, which can facilitate measurement up to middle of the channel. Other half of channel can be measured by deploying IDMT from other side (refer fig. 3).

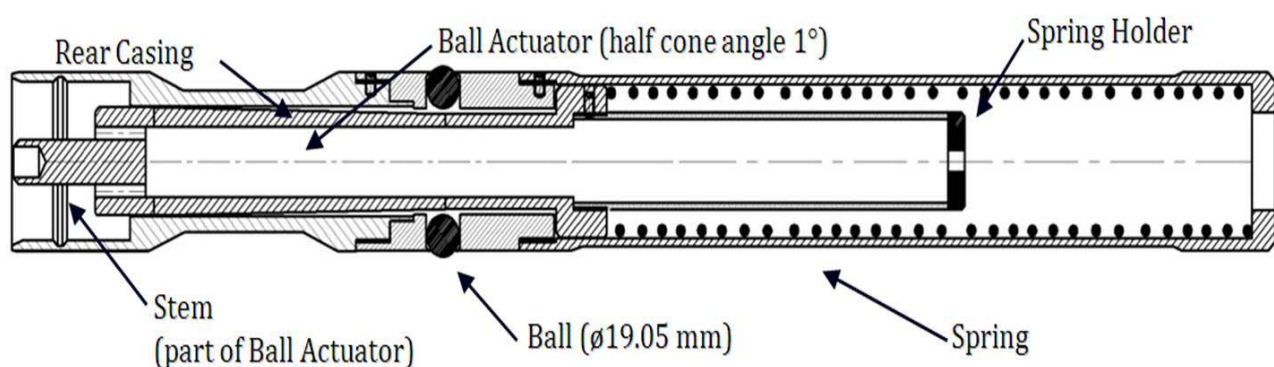


Fig. 2: ID Measurement tool –sectional view and photograph of IDMT

BARC NEWSLETTER

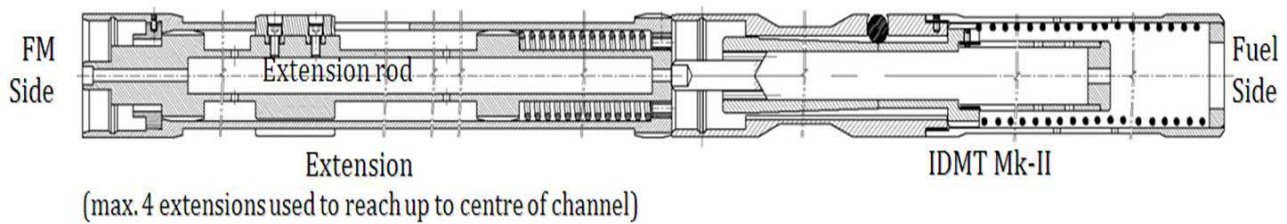


Fig. 3: IDMT with one extension

FM Ram-C (measurement side FM) is advanced to move balls radially outward. As soon as the balls come in contact with Pressure Tube, ball actuator stalls causing Ram-C to stop. The travel of Ram-C is recorded to calculate inside diameter of Pressure Tube.

Design Calculations and Qualification

IDMT has challenges for design and deployment in terms of ensuring safety of Pressure Tube and getting satisfactory accuracy. These concerns were addressed by analysis, calculations and performing elaborate experiments.

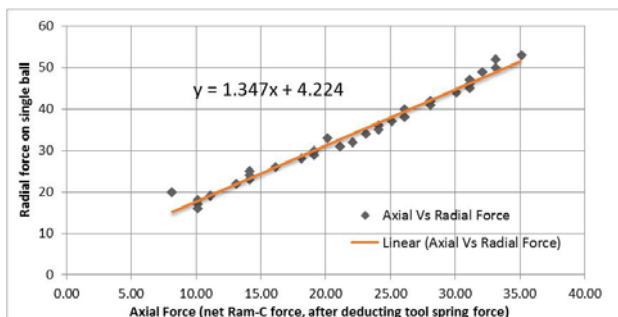


Fig. 4: Relation between axial vs radial force from experimental data

FM Ram-C force get applied on the PT walls through balls. A relation between the FM forces to ball-PT contact is established by analytic calculations. The relation was validated by experimentation and were found to be in good agreement, as shown in Fig. 4. When ball makes contact with Pressure Tube, some area of the Pressure Tube undergo plastic deformation resulting in residual stresses, which can causing Delayed Hydride Cracking (DHC). From DHC point of view allowable force is 250 kgf. From structural integrity point of view, allowable force comes out to be 200 kgf. Fig. 5 shows typical stress intensity plot.

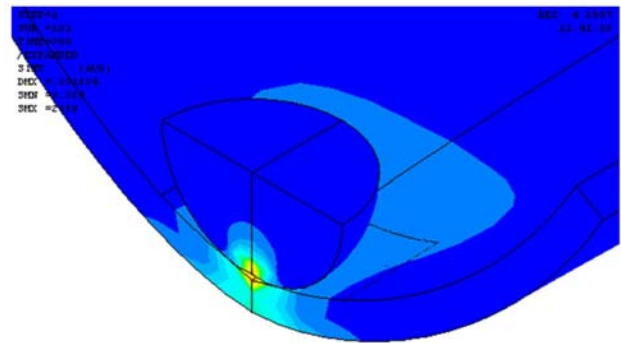


Fig. 5: Stress Intensity Pattern, at PT-ball interface

Insertion of tool and extension in channel restricts the flow through channel and bundle cooling may be affected. A flow analysis was performed to ascertain bundle safety. Current geometry of the tool and extensions allows sufficient flow for bundle cooling after 3 days of shutdown

Full-fledged mock-up trials were conducted at Rehearsal Facility Tube using FM to validate the operating procedure. Theoretical uncertainty in the measurements was estimated using NIST guidelines. IDMT measurement accuracy is within 0.2 mm.

Deployment in the reactor

IDMT was first time deployed in KAPS-2 for carrying out ID Measurement of 26 numbers of channels. Based on this campaign, procedures were further improved to get enhanced accuracy.

IDMT was again deployed in August 2012 for ID measurement in 16 channels. The IDMT measurements were compared with BARCIS. The agreement between both techniques was within 0.24 mm and this variation is within uncertainty margin. The IDMT took about 2 hours to complete half channel scanning.

BARC NEWSLETTER

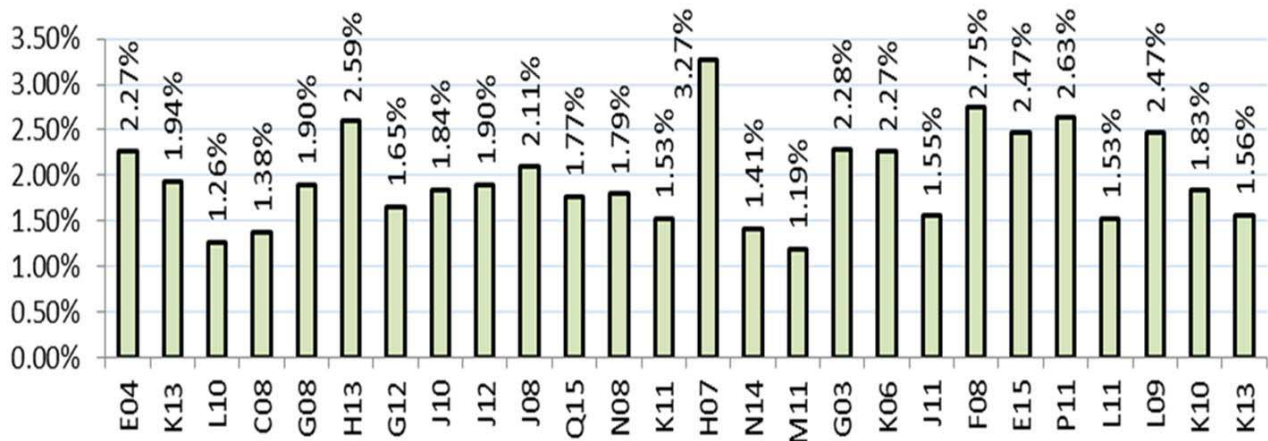


Fig. 6: Bar plot representing radial creep in KAPS-2 as on September 2010

Conclusions

Inside Diameter Measurement Tool (IDMT) has been developed for measurements of coolant channel ID in water flooded condition using Fuelling Machines. The IDMT is a remotely operable tool which can be quickly deployable and do not requires hose / cable connection to operate. The IDMT was used for ID measurement in half the channel from hot end side. The performance

of the IDMT is found to be satisfactory and measurement of a channel can be completed in 2 hours. The IDMT is found to be convenient to use and due to remote operation the consumption of man-rem was negligible. IDMT performed as intended and the ID data generated found useful for safety assessment. IDMT is useful for faster scanning of large number of channels to identify bigger diameter channels for further scanning due to its quick deployment capability.

BARC NEWSLETTER

ANUVI - DEVELOPMENT OF IN-HOUSE SCIENTIFIC VISUALIZATION FRAMEWORK

Venkata P.P.K., S.K. Bose, Dinesh M. Sarode, Pritam P. Shete,
Mohini M. Laghate and R.S. Mundada
Computer Division

Shri P.P.K. Venkata is the recipient of the DAE Young Applied Scientist /
Technologist Award for the year 2011

Abstract

Rapid improvements in the hardware and supercomputing technologies are enabling users to generate Gigabytes of data over millions of grid points through simulations. Fields like Fluid dynamics, medical imaging, monte-carlo simulations require high end visualization systems to understand and the simulated processes. Though graphics hardware is growing rapidly, the software required for scientific visualization is still lagging in terms of usability, customization and compatibility. In this article we describe about the development and customization of *AnuVi* an in-house scientific visualization framework, which is used by large section of the scientific community to support their diverse visualization needs.

Introduction

Though the performance of graphics hardware is growing at astronomical speed, most of the efforts are aimed at the gaming community. The scientific community is lagging behind in terms of graphics usage due to its diverse needs, which include but are not limited to customized GUI, light weight visualizer, advanced visualization system, high resolution display system, scripting interfaces to augment the available algorithms, data conversion, automated data extraction etc. It is very difficult to have a common framework catering to all the diverse requirements of the scientific community.

To cater to maximum of the scientific community requirements, we developed *AnuVi* as a scientific visualization framework with most of the desired features along with possibility for easier customization and made sure that it is portable on most of the environments available ranging from Windows, Linux as well as on the high resolution tiled-display system¹. Various aspects about *AnuVi* development are described in the following sub sections.

Design & Implementation

To facilitate the ease of development, maintenance etc. we have adopted Object Oriented approach for the development of *AnuVi*. To reduce the common errors in the design, we extensively used the Design Patterns. The usage of design patterns in the design of *AnuVi* is detailed by Venkata et. al².

AnuVi is developed in C++/Python hybrid language environment. All the computational and input-output intensive modules are developed in C++ for the sake of high performance where as all the extended features like interface development, scripting facility etc. are implemented in Python with help of its rapid application development features. Instead of using the low level OpenGL library for rendering the graphics primitives, high level VTK³ library is used for supporting both structured and unstructured grids. GUI is developed using the cross-platform WxWidgets library using its python port WxPython. CGNS⁴ is used extensively as a standard file format for data exchange.

BARC NEWSLETTER

Portability

Both for C++ and Python languages, only the standard features available across all platforms were used to reduce the portability problems. To create the compilation scripts we used cross-platform compilation assistance tool CMake to ease the development. To support the multi user development model, source code repository is maintained using the CVS. The recent methodologies like instant integration, document generation through parsing etc. are put to use. The documentation is embedded inside the source code and is generated using the Doxygen automated document generation tool.

To support the high resolution and large visual area required to render the huge datasets generated through the modern simulation software, a parallel graphics cluster with 47 million pixel resolution involving 36 LCD panels arranged in a 6x6 grid is developed and deployed in SCF building. The entire system runs on open source Scientific Linux environment. To mitigate the seams of the LCD panels which are obscuring some of the pixels, new projector based seam-less high resolution display system with 9 projectors and 7 million pixel resolution is developed and is deployed in the SCF building.

We ported *AnuVi* on both of the high resolution tiled-display systems using the Chromium middleware and by customizing the SPU chains required for rendering the visualization on both the tile as well as in the local node. Fig. 1 shows a snapshot of the high resolution Tsunami visualization movie generated using *AnuVi* over LCD tiled display. Fig. 2 shows a snapshot of the *AnuVi*

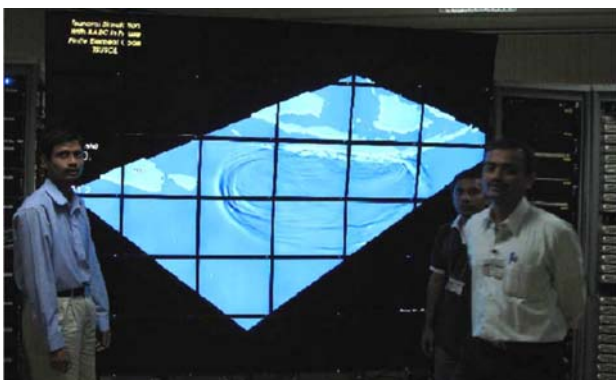


Fig. 1: Tsunami simulation using the LCD based 6x6 tiled display system.

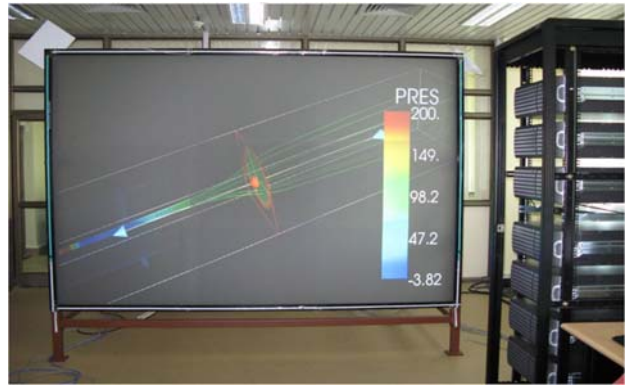


Fig. 2: Simulation result of a chemical reactor shown using the projector based 3x3 seam-less tiled display system

over projector tiled display, the application being stream lines generated over a chemical reactor simulation data.

Customization & Scripting

To customize *AnuVi* for various applications, customization of GUI with modified properties and parameters is essential. To ease the customization, base GUI classes are developed in Python and following the Open-Close philosophy of Object Oriented methodology using the inheritance, sub-classes will be derived and the required content will be over-ridden. A sample property sheet for creating a customized GUI page with a checkbox and two textboxes is displayed below.

```
page = [{"ObjectName": "StaticText", self.name),
        ("ShowAxis:", "CheckBox", 1),
        ("NumberOfLabels:", "TextCtrl", "3"),
        ("LabelFormat:", "StringCtrl", "%-#6.3g") ]
```

Providing all functionality as buttons and clickable objects is impossible. further the diverse nature of the scientific applications always need advanced facilities, so a python shell is integrated with bindings to WxPython GUI module, VTK visualization module as well as with the *AnuVi* high level classes to enable user to develop short scripts for enhancing the functionality of the *AnuVi*. Sample code for changing the visualization to wireframe model is shown below.

```
p = AnuviViewer.GetActor('cgns1').GetProperty()
p.SetRepresentationToWireframe()
AnuviViewer.GetRenderWindow().Render()
```

BARC NEWSLETTER

Usage & Features

Many users from the scientific community within and outside BARC used *AnuVi* to generate visualization as well as to publish their work. Fig. 3 shows an advanced visualization done using the scripting interface of *AnuVi* to extract multiple cut-planes each 15 degree apart from a helical heat exchanger coil spanning a total of 360° and displaying velocity contours on each of these cut-planes⁵.

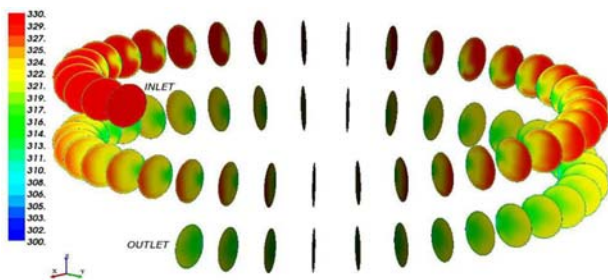


Fig. 3: Contours drawn at various planes over a helical coil.

Some of the standard features of *AnuVi* are listed below.
Plotting: scalar, vector, tensor, contour, stream line, particle trace, ray casting, iso-surface etc.

Manipulation: cut plane, clipping the dataset, extrusion, reflection, triangulation etc.

Export: Images, movies, sessions, scripts, Print etc.

Availability: Windows, Linux, Tiled-display environment etc.

Conclusion

AnuVi is tested by a large section of scientific community for their diverse scientific visualization requirements. It catered positively to many users in customizing applications, visualizing data, automating

data extraction etc. By using *AnuVi* under the high resolution tiled-display environment, simulations can be done in large visual area with very high resolution.

Acknowledgements

We sincerely thank Mr. P.S. Dhekne, former associate director E&I group, BARC and Mr. A.G. Apte, former head, Computer Division, BARC for their valuable suggestions and encouragement. We also thank all the members of computer division as well as the users for their cooperation.

References

1. Bose S K, Sarode D M, Venkata P P K, Shete P P, & Apte A G. "High end scientific visualization with scalable display system". Proceedings of International Conference on Advances in Computer Engineering – ACE (IEEE), (2010): 316-318.
2. Venkata P P K, Bose S K, Dinesh M Sarode, P P Shete, Apte A G. "Design Patterns in development of AnuVi". Proceedings of National conference on ICT: Theory, Applications and Practices organized by SPSU, Udaipur sponsored by CSIR, (2010).
3. Schroeder W J, Avila L S, & Hoffman W. "Visualizing with VTK: a tutorial". IEEE Computer Graphics and Applications, 20(5), (2000): 20-27.
4. Poirier D, Allmaras S R, McCarthy D R, Smith M F, & Enomoto F Y. "The CGNS system". AIAA Paper, (1998): 98-3007.
5. Jayakumar J S, Mahajani S M, Mandal J C, Iyer K N, & Vijayan P K. "CFD analysis of single-phase flows inside helically coiled tubes". Computers & chemical engineering, 34(4), (2010): 430-446.

DEVELOPMENT OF A NOVEL VARIABLE DISPERSION ZOOM OPTICS FOR MAGNETIC SECTOR MASS SPECTROMETER

Rajender K. Bhatia, Varun K. Yadav, Vilas M. Mahadeshwar, Milind M. Gulhane,
E. Ravisankar, T.K. Saha, V. Nataraju and S.K. Gupta
Technical Physics Division

Shri Rajender K. Bhatia is the recipient of the DAE Young Applied Scientist /
Technologist Award for the year 2011

Introduction

Magnetic Sector mass spectrometers are used in the precise isotopic ratio measurement of the inorganic samples in gaseous or solid form. TPD, BARC has been developing these instruments [1] for various applications in DAE. The instruments developed so far are based on conventional design of collector system whereby each collector is mounted on a mechanical motion feed-through [2]. This set-up suffers from the following limitations: a) In case of higher number of faraday cups (5 or more) mechanical assembly is very bulky and unwieldy, b) limited peak flatness (500 – 600 ppm) due to limited aperture size (~ 1 mm), c) difficulty in angular adjustment of the collector cups affecting the peak shape, d) the physical dimensions of the collector viz., 2.5 mm, restricting the placement of collectors at desired locations which limits the mass range for multi-collection ratio measurement to around 250 amu, e) prominent surface bulging effects during the fabrication of collector f) microphonic pick-ups in the collector mounting mechanism leading to higher noise in the amplifier and thus the internal precision.

To circumvent these problems, a new collector set up with variable dispersion zoom optics is developed. The main advantages of this set-up are elimination

of mechanical motion feed-throughs and improved peak flatness leading to better precision and accuracy. This paper discusses the design aspects, experimental study and evaluation using Strontium standard for isotopic ratio measurement.

Design Details

The setup consists of DC quadrupole [3], deflection optics and five fixed collectors with wider input apertures. DC quadrupole adjusts the dispersion of ion beams by suitably varying the potentials such that these are well aligned with the respective apertures on the

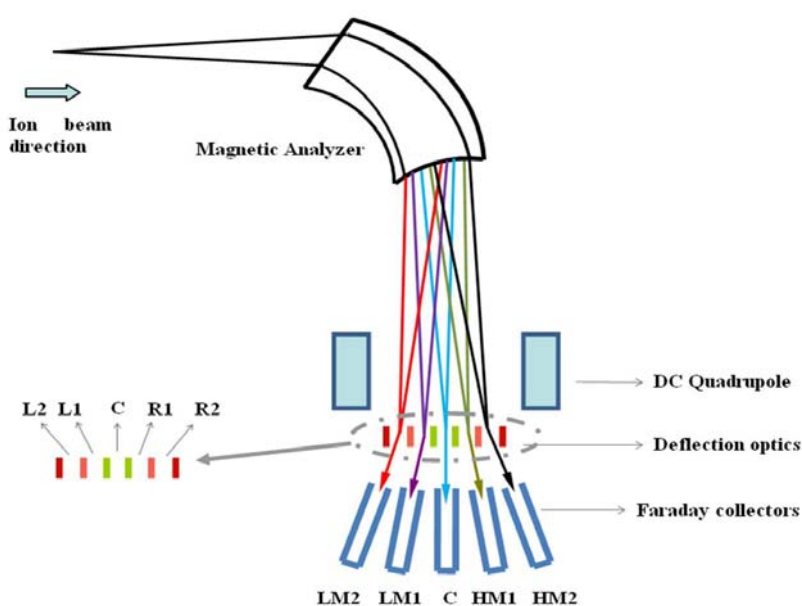


Fig. 1: Schematic of Variable dispersion zoom optics; five masses dispersed by magnetic analyzer adjusted for optimized dispersion by VDZO and collected by respective faraday collectors.

BARC NEWSLETTER

deflection optics. The deflection optics consists of thin metallic plates stacked together but electrically insulated from each other and hence forming different apertures for the passage of ion beams. It deflects the ion beam passing through respective apertures in such a way that the distance between the beams increases when they reach the respective collectors as shown in Fig. 1. The increased distance allows using collectors with wider apertures which leads to more peak flatness. For the collection of ion beam, five faraday collectors with 3 mm aperture are used. These are mounted on a single stainless steel plate enabling simpler and sturdier mechanical assembly.

Computer Simulation

The entire geometry was simulated using SIMION 7.0 software [4] and a study was carried out for the optimum set of potentials for all the ion optical elements that will give the maximum transmission for the isotopes of a given element. Two different potential arrays—one with geometry of DCQ, deflection optics and faraday cups and the other consisting of the 30 cm, 90° deflection stigmatic magnet geometry, were coupled together in the work bench. The ion flight paths through above optics were generated using ion groups having an energy of 7 keV, originating from a source slit of 0.3 mm (placed at 600 mm from the magnet boundary) with a divergence of $\pm 0.5^\circ$. The masses of interest for these simulations correspond to the isotopes of Sr, Nd and U. The ions were allowed to pass through the given geometry of VDZO to be collected on the faraday cups after the dispersion by the magnet. A comparison study was conducted for a variety of design features of each component and the final design was worked out for maximum transmission of the ion beam for all required elements. Simulated

optimum potentials for different elements are summarized in Table 1. The effect of DCQ potentials on the beam width as well beam height was also studied and the dimensions of the Faraday cup were accordingly fixed.

Experimental

A working model based on the outcome of the simulation studies was fabricated for experimentation. The experiments were carried out in three different parts. In the first part a micro-channel plate phosphor screen (MCP-SP) imaging device was used to capture the images of the ion beams to study the effect of variation in voltages on DCQs and deflection optics on dispersion of ion beams. The second part involves placement of final collectors and obtaining flat top peaks by optimizing deflection optics potentials. Third part consists of carrying out isotopic ratio measurements on these collectors for desired elements by optimizing DCQ potentials and small adjustment of deflection optics potentials.

To check the effect of VDZO on performance of the instrument, DCQ potentials were optimized and isotopic ratio measurement for strontium was carried out. The Strontium standard sample (SRM 0978) was used for the measurement of isotopic ratio $^{87}\text{Sr}/^{86}\text{Sr}$ using multi-dynamic mode. The sample was deposited on the rhenium side filaments of triple filament assembly. The data was collected in 10 blocks of 10 ratios each, for the same assembly to estimate the internal precision (calculated as the relative standard error over all 100 ratios). The same sample was analyzed on ten separate filament assemblies on a turret/sample magazine for external precision measurement (relative standard deviation).

Table 1: Optimized values of potentials on VDZO for collecting various ion beams on faraday cups

Element	Potentials on Deflection optics and DCQ in volts L2 / L1 / C / R1 / R2 (-ve in volts) ; DCQ(+/- in volts)	
	Simulations	Experimental
Sr	1000 / 0 / 0 / 0 / 1000 ; 140	1030 / 0 / 0 / 0 / 1100; 120
Nd	1100 / 100 / 0 / 100 / 1100 ; 30	1200 / 150 / 0 / 70 / 1150; 20
U	1000 / 0 / 0 / 0 / 1000 ; 40	1030 / 0 / 0 / 0 / 0 / 1100; 20

BARC NEWSLETTER

Results and Discussion

From the imaging studies involving MCP-PS, it was observed that the dispersions for all the elements were closely matching with the simulated values. For example the dispersions obtained for Sr isotopes before and after the application of DCQ potentials of ± 120 volts (Fig. 2) are almost same as the simulated values of 6.9 mm and 8 mm respectively. Similarly the VDZO parameters were verified for Nd taking their images on MCP-PS.

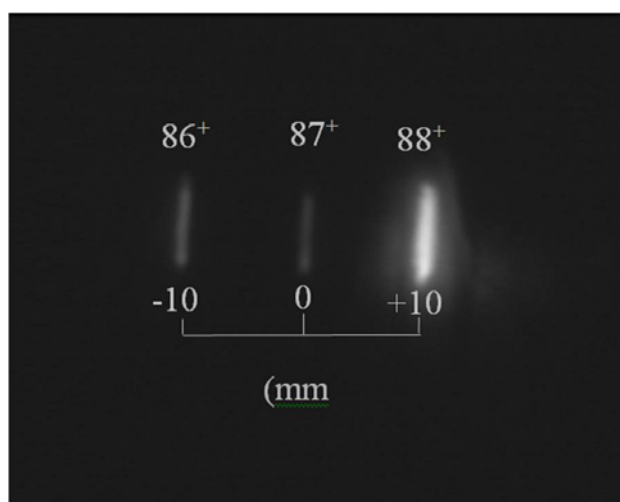


Fig. 2: Images of Sr isotopes on MCP

The peak shapes (for ^{88}Sr isotope) without DCQ potentials (but using deflection optics) were sequentially studied on all the collectors by suitably varying magnetic field. A peak flatness of ~ 3000 ppm of mass and a beam width of 0.8 mm was observed on each of the collectors. The isotopic ratio measurement of Sr, corresponding to masses 86, 87 and 88, on collectors LM2, C and HM2, were carried out at a DCQ potential of ± 120 V. This resulted in an increase in beam width to 1 mm and a decrease in peak flatness to 2500 ppm which is in full agreement with computer simulations. Fig. 3 shows the simultaneous peaks of strontium isotopes on LM2, C and HM2 collectors indicating ability of VDZO in matching the peaks. Similarly, the peak matching for Nd and U isotopes was also carried out.

The results for isotopic ratio measurement of Sr on conventional and the VDZO setup are

tabulated in Table 2. It is seen that internal precision is nearly same in both the systems (conventional and VDZO) but the external precision (8 ppm) is much better with VDZO as compared to that obtained with conventional setup (22 ppm). The accuracies in case of conventional and VDZO systems were found to be 50 ppm and 10 ppm respectively for a true value of 0.710244.

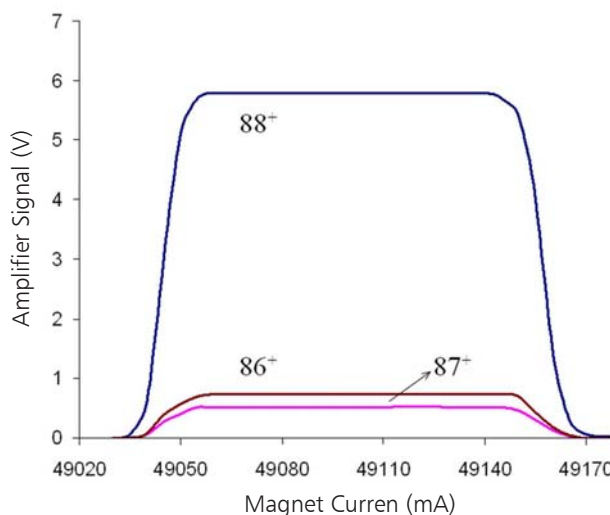


Fig. 3: Peak shape for Sr isotopes (86, 87, 88)

Table 2: Comparison of zoom optics with conventional collector setup for isotopic ratio measurement of standard Sr sample (SRM 987). Average $^{87}\text{Sr}/^{86}\text{Sr}$ ratio with relative standard error (internal precision; in parentheses)[#] has been given for each sample.

Sample Number	Ratio ($^{87}\text{Sr}/^{86}\text{Sr}$)	
	On conventional setup (without zoom optics)	On setup with zoom optics
1.	0.710194 (6)	0.710246 (4)
2.	0.710210 (4)	0.710241 (8)
3.	0.710219 (4)	0.710239 (6)
4.	0.710199 (4)	0.710230 (7)
5.	0.710198 (4)	0.710242 (7)
6.	0.710239 (4)	0.710231 (8)
7.	0.710190 (5)	0.710234 (5)
8.	0.710222 (4)	0.710241 (8)
9.	0.710190 (4)	0.710230 (6)
10.	0.710220 (5)	0.710233 (5)
Average Ratio	0.710208	0.710237
RSD (external precision)	23 ppm	8 ppm

([#] the value in parenthesis is the variation in last significant digit of the ratio value)

BARC NEWSLETTER

Conclusions

A new Faraday collector system (with five cups) for thermal ionization mass spectrometer has been developed based on variable dispersion zoom optics. The system enables fixed collector cups with wider apertures that facilitate analysis of different elements with a simple adjustment of suitable potentials to deflection optics rather than the mechanical movement of collectors. Further, wider collectors help in improvement of peak flatness from 500 ppm to 3000 ppm for Sr⁸⁸. The system design was optimized for analysis of U, Sr and Nd isotopic ratio analysis by simulation. The system enables improvement in both precision and accuracy of analysis. This has been demonstrated by analysis of ⁸⁷Sr/⁸⁶Sr ratio where precision and accuracy have been improved from 22 ppm to 8 ppm and 25 ppm to 10 ppm respectively.

Acknowledgements

Authors wish to thank Dr. S. Kailas Director, Physics Group, BARC for his constant support throughout the

execution of this work. The contributions from all the team members from mechanical and electronics group of Technical Physics Division are highly appreciated.

References

1. Rajender K. Bhatia, Yogesh Kumar, K. Prathap Reddy, V.K. Yadav, E. Ravisankar, T.K. Saha, V.Nataraju, V.K. Handu, International Journal of Mass Spectrometry **313** (2012) 36
2. Rajender K. Bhatia*, R. Datta, Rekhu Chandak, M. M. Gulhane, Pratap R. Kasina, A. M. Kasbekar, N. Ved, M. Gopalakrishna, E. Ravisankar, T. K. Saha, V. Nataraju, and V. K. Handu Proceedings of 11th ISMAS symposium 'TRICON' 2009, Hyderabad, India
3. Peter H. Dawson, Elsevier Scientific Publishing Company, Amsterdam (Netherland)
4. D.A.Dahl, "SIMION version 7.0", Idaho National Engineering Laboratory, 2000

DEVELOPMENT & APPLICATION OF AN EULERIAN RADIATION MAGNETO-HYDRODYNAMICS (RMHD) CODE

C.D. Sijoy and S. Chaturvedi

Computational Analysis Division, BARC, Visakhapatnam

Shri C.D. Sijoy is the recipient of the DAE Young Applied Scientist / Technologist Award for the year 2011

Abstract

A two dimensional (2D) Eulerian multi-material radiation magneto-hydrodynamics (RMHD) code has been developed for the analysis of large deformation hydrodynamics in the presence of self-consistent magnetic fields. The code features a new Volume-Of-Fluid (VOF) based material interface tracking scheme, multi-material MHD scheme, thermal radiation transport and variety of non-linear Equation Of State (EOS) modules (both analytical and tabulated). The MHD scheme is formulated using magnetic vector potential with an implicit magnetic field diffusion calculation. The thermal radiation transport scheme used is capable of handling intense thermal radiation through both optically thin (transport limit) and thick media (diffusion limit). In this paper, we report the details of the algorithm and its application to a sample problem.

Introduction

Numerical simulation of hydrodynamics phenomena involving large material deformation, intense thermal radiation and magnetic fields is a challenging topic. A few examples are 1) laser- or thermal-radiation driven ablative acceleration, including instability growth; 2) the dynamics of Magnetic Rayleigh-Taylor (MRT) instabilities in flux compression systems driven by fusion plasma armatures¹⁻³ 3) plasma formation between the solid surfaces in electromagnetic welding systems, etc. Pure Lagrangian simulation fails when large material deformation occurs. Therefore, an Eulerian or Arbitrary Lagrangian Eulerian (ALE) scheme is necessary. The code described here is based on an ALE scheme with a remapping stage back to the initial grid at each time-step—essentially making it an Eulerian code.

RMHD model and numerical scheme

The governing hydrodynamic equations can be seen in Refs.¹⁻³. A thermodynamically consistent multi-material hydrodynamics formulation⁴ along with our new volume-of-fluid (VOF) interface tracking algorithm⁵ is used to handle multiple materials in a mixed

computational cell (a cell containing more than one material). This formulation avoids commonly used pressure relaxation methods and corresponding iterations in each mixed cell⁶. However, this formulation requires the evaluation of 'M' different energy equations in each mixed cell, where 'M' is the total number of materials^{2,4}.

The VOF based material interface tracking algorithm⁵ consists of three different phases: Interface reconstruction, Lagrangian deformation of material interfaces and finally the Eulerian advection. A Piecewise Linear Interface Construction (PLIC) scheme is used in the first phase of VOF algorithm where the interface is represented by a straight line in a cell. The slope of this interface is obtained from the gradients of volume fraction of each material. Different materials contained in a mixed cell are ordered using a dynamic layered material ordering scheme⁵. The third stage of VOF scheme is material advection. This is done using a second order accurate Monotonic Upwind Scheme (MUSCL)². The mass advected in the Eulerian advection step is calculated using a characteristic trace back scheme⁵ based on the area of intersection between the old and new meshes.

BARC NEWSLETTER

For the simulation of MHD flows, the electromagnetic field components are required to be updated self consistently with the fluid flow and external electric circuit equations¹. This has been achieved using our new MHD algorithms described in Refs^{1,2}. Magnetic diffusion into electrical conductors is solved implicitly using the magnetic vector potential². During the advection/remap step, the magnetic field components are advected using a 2nd order MUSCL scheme.

For practical cases, the material velocity is typically smaller than the speed of light. Therefore, at any instant of time, the radiation field can be regarded as quasi-static. Furthermore, we have used the frequency averaged scheme, i.e., "grey" approximation. The radiation transport equation⁷ is solved in 2D by using a numerical scheme described by Ramis et al⁷. The radiation energy is coupled to material through a Symmetric Semi-Implicit (SSI) scheme⁷.

Application to a sample problem

The algorithm developed has been validated against known analytical solutions of several benchmark problems^{2,5}. Here, we present the results of Magnetic Rayleigh-Taylor (MRT) instability analysis in a direct energy conversion system which converts Inertial Fusion Energy (IFE) plasma kinetic energy into pulsed electrical energy¹⁻³. A schematic of the proposed Magnetic Flux Compression (MFC) system driven by fusion plasma sphere is given in Fig. 1. Preliminary studies¹ show that the proposed MFC system is promising in terms of overall conversion efficiency. However, the plasma expanding across the magnetic field is subject to MRT instabilities.

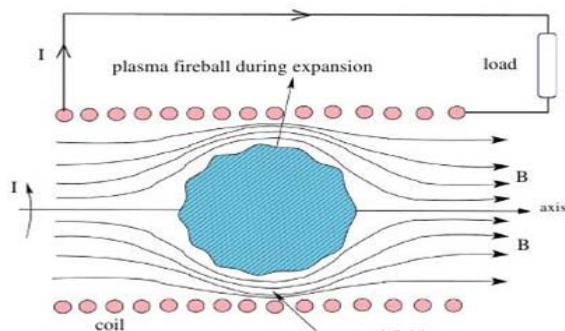


Fig. 1: Schematic showing MFC by expanding plasma sphere (not to scale).

In the sample problem, the initial plasma kinetic energy and mass were taken as 280 MJ and ~ 4.4 mg, respectively, with temperature of 100 keV (fusion-driven) and density of $\sim 10^{-6}$ kg/m³. The initial magnetic field was ~ 5 Tesla. The coil radius and length were 1.5 m and 4.5 m, respectively.

Fig. 2 shows the spatial variation of plasma density. Starting with a uniform density plasma sphere, the plasma evolves into a shell-like geometry near the stagnation time, where the outer surface slows down due to magnetic pressure and the inner region catches up with the outer surface. The thickness of this region is ~ 0.05 - 0.1 m with an average temperature of ~ 30 keV. The electrical conductivity of the plasma near the surface is sufficiently high $\sim 10^9$ S/m to prevent magnetic field diffusion. That is, even at larger expansions, the diffusion of magnetic field into the plasma is found to be negligible.

Towards the stagnation time, we have observed the evolution of MRT instabilities on the surface of the plasma even with an unperturbed initial plasma state, as shown in Fig. 3. Therefore, the analysis is repeated

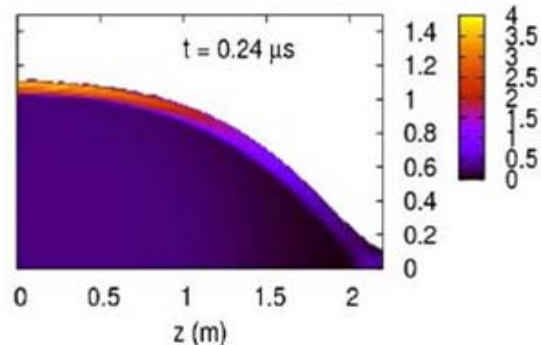


Fig. 2: Spatial variation of plasma density (scaled by 10^6 kg/m³) at stagnation time

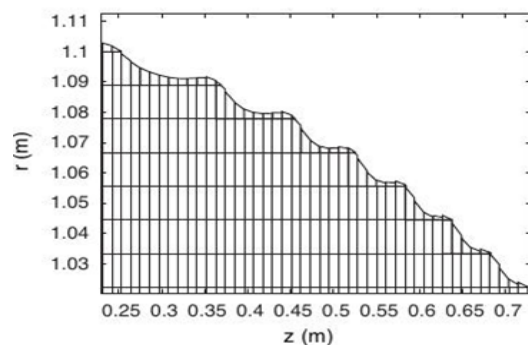


Fig. 3 : Zoomed in plot of plasma vacuum interface near the stagnation time indicate the development of MRT instability.

BARC NEWSLETTER

for plasmas with an initial sinusoidal perturbation of different wavelengths λ and amplitudes α . This helps us identify the critical α and λ which produce significant degradation in system performance.

The instability amplitude growth obtained for different cases of initial perturbation α and λ are summarized in Fig. 4. The perturbation amplitude continues to grow exponentially with nearly constant growth rate (γ) and makes a transition into a nonlinear phase towards the stagnation time. Hence the amplitude growth of modes towards stagnation time, although exponential in nature, is lower than the growth predicted by linear theory. We also note that extremely large flute structures and plasma jetting, which could damage the coil/cavity

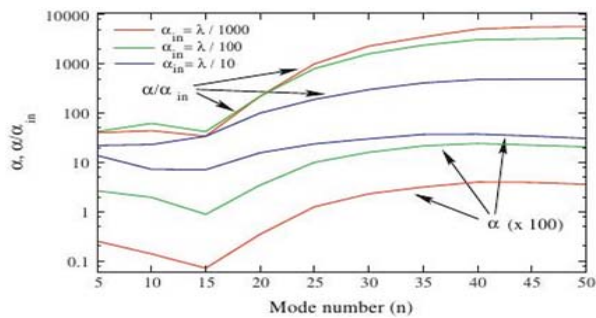


Fig. 4: The variation of maximum α/α_{in} and α ($\times 10^2$ m) for different values of initial mode number (n) and perturbation α_{in} .

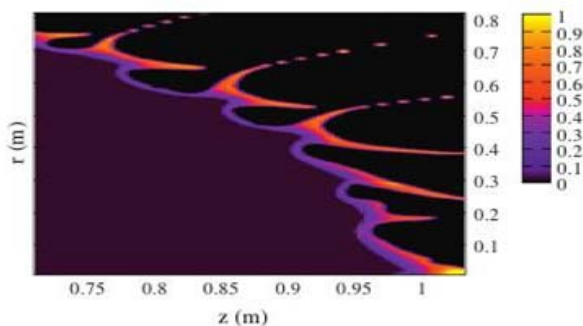


Fig. 5: The evolution of MRT instability for $n=10$ and $\alpha_{in} = \lambda_{in}$. The figure shows the normalized density (normalized to 10^{-5} kg/m³).

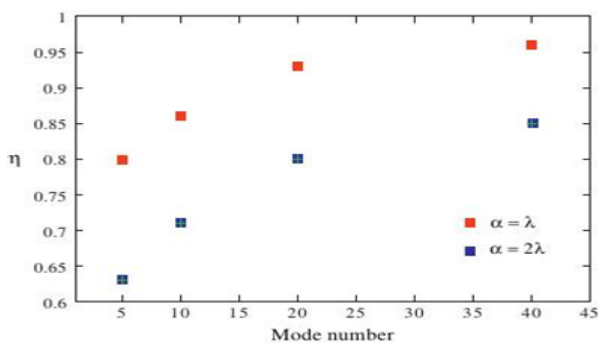


Fig. 6: Flux compression efficiency vs. mode number

wall, is not observed for $\alpha_{in} < \lambda_{in}/10$. However, for $\alpha_{in} > \lambda_{in}$, the instability amplitudes are large enough, especially for longer λ modes, to cause plasma jetting leading to significant reduction in flux compression efficiency, see Fig. 5. In order to quantify the decrease in efficiency (ϵ), we have shown the variation of ϵ for different values of mode number and α_{in} in Fig. 6. In general, a loss of efficiency $\sim 20\%$ is expected for longer λ modes ($n < 20$) and short λ modes ($n > 20$) when $\alpha_{in} \sim \lambda_{in}$ and $\alpha_{in} \sim 2\lambda_{in}$ respectively.

Conclusions

A two-dimensional (2D) RMHD code has been developed and validated. The validated algorithm has been applied to study MRT instabilities in a MFC system driven by expanding high-pressure IFE plasma.

References

1. Sijoy C. D. and S. Chaturvedi, "Conversion of plasma energy into electrical pulse by magnetic flux compression", *Fusion Engineering and Design*, 86, (2011): 174-182
2. Sijoy C. D. and S. Chaturvedi, "An Eulerian MHD model for the analysis of magnetic flux compression by expanding diamagnetic fusion plasma sphere", *Fusion Engineering and Design*, 87, (2012): 104-117
3. Sijoy C. D. and S. Chaturvedi, "Analysis of Magnetic Rayleigh-Taylor instability in a direct energy conversion system which converts inertial fusion plasma kinetic energy into pulsed electrical energy", *Annals of nuclear energy*, 62, (2013): 81-85
4. G. H. Miller and E. G. Puckett, "High-order Godunov method for multiple condensed phases", *Journal of Computational Physics*, 128, (1996): 134-164
5. Sijoy C. D. and S. Chaturvedi, "Volume of fluid algorithm with different modified dynamic material ordering methods and their comparisons", *Journal of Computational Physics*, 229, (2010): 3848-3863
6. Sijoy C. D., V. Mehra, V. Mishra and S. Chaturvedi, "A VOF based multi material method to study impact and penetration problems", *Journal of Physics Conference Series*, 377, (2012): 012106
7. R. Ramis et al, "MULTI2D – A computer code for two dimensional radiation hydrodynamics", *Comp. Phys. Commu.*, 180, (2009):977-994.

BARC NEWSLETTER

DEVELOPMENT OF PHASE CONTRAST IMAGING TECHNIQUES

Yogesh S. Kashyap and Amar Sinha
Neutron and X-ray Physics Division

Shri Yogesh S. Kashyap is the recipient of the DAE Young Applied Scientist / Technologist Award for the year 2011

Abstract

Since the discovery of X-rays in 1895, vast majority of radiographs have been collected and interpreted on the basis of inhomogeneous attenuation of the samples in both basic and applied research. Recently, a new technique, X-ray phase-contrast imaging has emerged. This new technique is capable of providing improved information from weakly absorbing samples, together with improved edge enhancement. The method requires use of coherent X-rays to allow wave interferences to occur and manifest itself as contrast formation in the intensity distribution recorded at the detector plane. This paper presents study of phase contrast imaging technique using X-rays & neutron sources.

Introduction

The basic principles of X-ray image formation and interpretation in radiography have remained essentially unchanged since Röntgen first discovered X-rays over a hundred years ago. The conventional approach relies on X-ray absorption as the sole source of contrast and draws exclusively on ray or geometrical optics to describe and interpret image formation. The conventional absorption X-ray imaging is able to distinguish between hard (high Z) and soft (low Z) materials but it fails to image soft materials like polymers, carbon- composites and soft tissues as the absorption is very less for such materials. This approach ignores another, potentially more useful source of contrast-phase information. Phase-sensitive techniques, which can be understood using wave optics rather than ray optics, offer ways to augment or complement standard absorption contrast by incorporating phase information. In the last few years, this new imaging technique named *Phase Contrast Imaging* is being developed to remove the limitations of conventional X-ray imaging and it promises to revolutionize the way soft material imaging has been conducted till now. In this article we have focused our attention on In-line

phase Imaging techniques. This technique can be implemented in the laboratory using partially coherent source without any need of elaborate instrumentations. A brief discussion on implementation of neutron based phase imaging is also presented.

Free-space propagation based Phase contrast imaging

When a coherent wavefield propagates through an object, phase differences arise between different parts of the wavefront. These are due to spatial variations in the refractive index of the object, which for x-ray wavelengths is given by

$$n = 1 - \delta + i\beta \quad (1)$$

Here, $\beta = \mu\lambda/4\pi$ incorporates the absorption of the x-rays, with μ the absorption coefficient. This term affects the amplitude of the waves. The term

$$\delta = \lambda^2 r_e n_e / 2\pi, \quad (2)$$

with $r_e = 2.818 \times 10^{-15}$ m the classical radius of the electron and n_e the electron density of the material, determines the phase of the waves and causes their

BARC NEWSLETTER

refraction. For sufficiently small wavelengths ($\lambda < 0.1$ nm), β may be as small as 10^{-9} , whereas δ is of the order of 10^{-6} . Phase contrast therefore dominates absorption contrast in the x-ray regime. Phase contrast X-ray imaging therefore has great potential for application in medicine and in biology, enabling one to differentiate between different kinds of soft tissue. The structural detail in a phase contrast image depends on the distance R between the object and the detector. Three regimes for imaging can be distinguished. In the *contact* or near-contact regime, the detector is placed directly behind the object. In this case the observed contrast in the image can only be due to absorption. As one moves further away from the object, interferences build up, and one enters first the *Fresnel* diffraction regime, then the *Fraunhofer* regime. In the Fresnel diffraction regime, phase contrast can be exploited to greatest advantage as the detector records laplacian of the phase which can be directly related to the object features. In-line contrast imposes only modest requirements on the source coherence. Longitudinal coherence is not an issue, because the scattering is nearly in the forward direction. The transverse coherence length only has to exceed the distance over which the density of the object changes appreciably. The interferences in the *Fraunhofer* regime provide us with information on its shape and internal structure on a length scale much shorter than is accessible with visible light. The retrieval of the object's real-space structure from the observed interference pattern is known as coherent diffractive imaging or lensless imaging, which can be regarded as holography without a reference beam.

Experiments in In-Line Phase contrast Imaging using X-rays

We have set-up an experimental facility at our laboratory using a combination of X-ray microfocus source and high resolution CCD camera for carrying out phase-contrast [1,2] x-ray imaging experiments (Fig. 1). We have carried out set of experiments on carbon coated zirconia microspheres to study the feasibility of this imaging system for phase imaging of coated particles. These kind of coated materials are potential candidates for future generation of high temperature nuclear

reactor. Zirconia microspheres of approximately $500\mu\text{m}$ diameter were deposited with different materials in an electrically heated graphite vessel under different conditions so as to make an equivalent fuel particle. This technique provides the unmatched imaging quality for the study of such materials (Fig. 2).

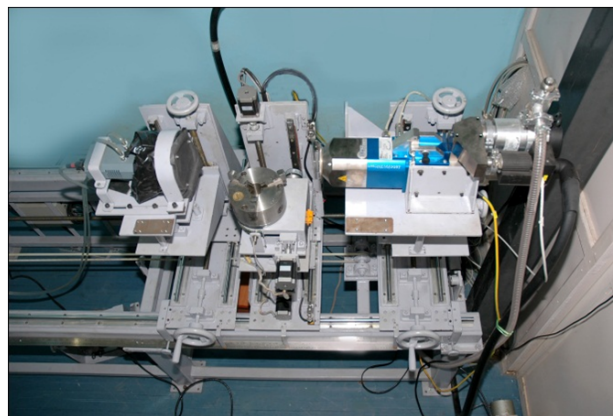


Fig. 1: In-line phase imaging using micro-focus based X-ray source

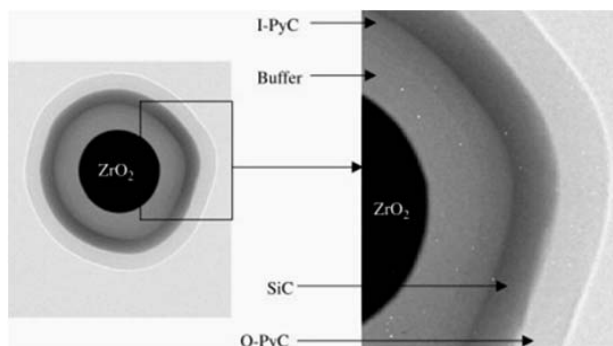


Fig. 2: In-line phase imaging of simulated TRISO particle

An experimental facility using Indus-2 synchrotron source has been set-up at RRCAT, Indore for carrying out experiments in both absorption and phase imaging modes. As synchrotron source provides X-rays with high degree of temporal and spatial coherence various phase contrast imaging techniques such as grating interferometry, diffraction enhanced imaging etc can also be carried out at this experimental facility.

Experiments in In-Line Phase contrast Imaging using neutron

As neutrons provide complementary information about the object to that of X-rays, there is great potential to phase based imaging techniques, if these can be implemented using neutrons. The relative transparency of many high Z elements to the neutrons essentially

allow us to obtain an inside look into objects and to make 3D reconstructions of their internal structure. Similarly materials like Pb, Be, C, Al, Si are more easily probed using neutrons than X-rays. Moreover, the phase sensitive measurements in combination with neutron imaging can also provide 3D spatially resolved information on the scattering length density distribution. A dual collimator assembly based experimental facility at CIRUS reactor was set-up to carry out both the conventional and phase contrast imaging experiments[3]. Figs. 3 and 4 show comparison of absorption and phase contrast images of lead and syringe samples and enhancement at the edges of these samples due to phase effects can be clearly seen.

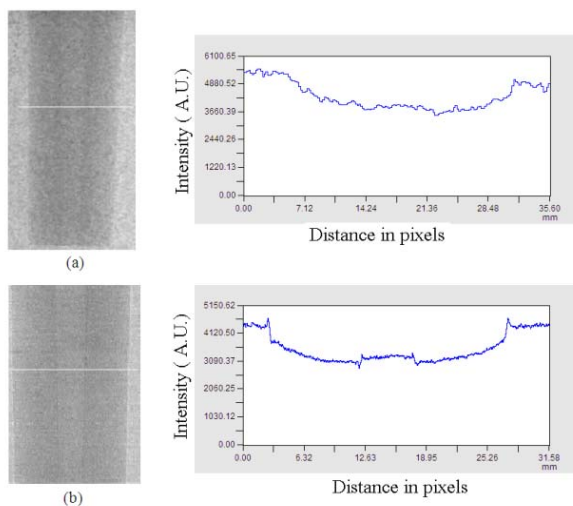


Fig. 3: Neutron radiograph of lead (35mm diameter) containing conical hole and edge profile across the marked line for (a) absorption and (b) phase contrast mode

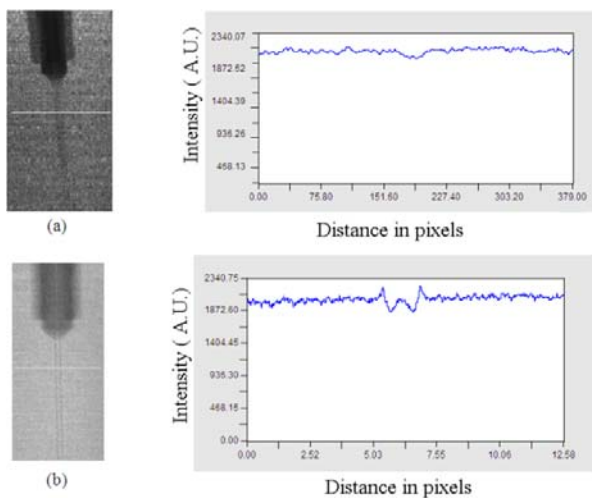


Fig. 4: Neutron radiograph of 1mm iron syringe (a) absorption mode (b) phase contrast mode along with the profile across the marked line

Phase retrieval techniques and their applications

The notion of 'phase retrieval' goes a step beyond phase contrast, in the sense that one now wants to measure, or 'retrieve', a given phase distribution from one or more phase contrast images of that distribution, which are obtained as output from a given phase-contrast imaging system. Adopting this viewpoint, such phase-contrast images are viewed as encrypted or coded images of the desired phase distribution $\phi(x, y)$. The problem of phase retrieval, often termed the 'phase problem', arises on account of the extremely rapid nature of wave-field oscillations at X-ray frequencies.

The existing state of the art, in X-ray detector technology, is still many orders of magnitudes too slow to directly detect the position-dependent phase of a coherent X-ray wave-field, or the position-and-time-

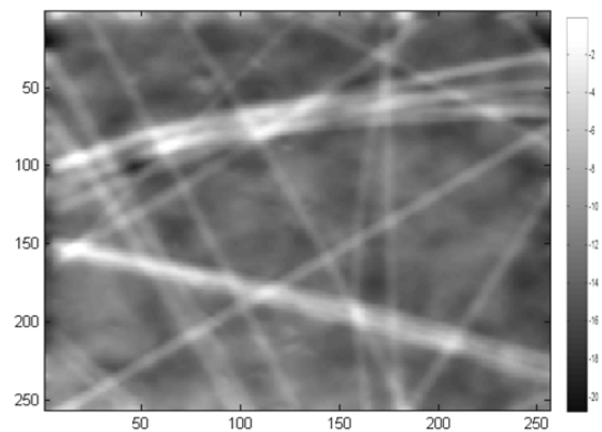


Fig. 5: Phase retrieval (integrated) of silicon-aerogel fibers showing the distribution of fiber networks

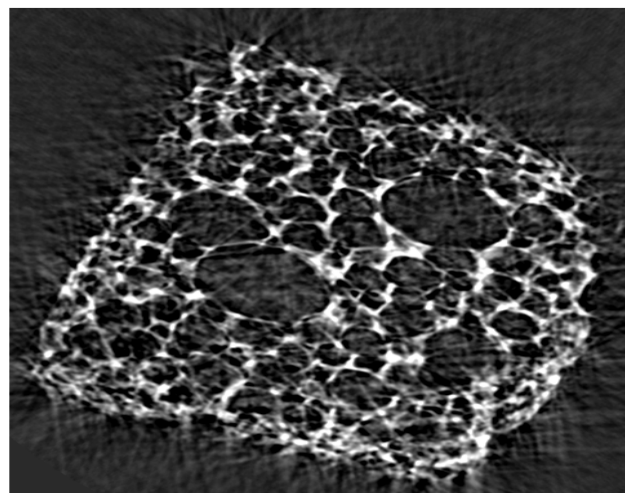


Fig. 6: Reconstructed slice of polyurethane foam using phase retrieval and tomography



Fig. 7 (a) Simulated exit wavefield of cell containing lipid membrane and protein (b) its far-field diffraction pattern (c) Reconstructed object from the diffraction pattern

dependent phase of a partially coherent X-ray wavefield. A large number of algorithms have been developed to retrieve the phase information from recorded intensity in both near as well as far-field regime. The basic idea behind these techniques is to record multiple images through the phenomenon of oversampling the data and then retrieve the phase map by suitable boundary conditions. Moreover one can also combine the phase retrieval step with tomography reconstruction technique to get complete three dimensional distribution of the complex refractive index of the samples. Fig. 5 shows the phase retrieved image of silicon aerogel sample with multi-wavelength approximation technique [4] of phase retrieval in the near field regime. The phase retrieval step was coupled with the x-ray tomography scheme to obtain full three-dimension distribution of refractive index of polyurethane foam (Fig. 6).

Fig. 7(a) shows the exit wavefield of a cell phantom as an illustration of potential of coherent X-ray diffraction microscopy. The membrane of the cell is made by lipid. The cell is filled with soluble protein and has one ellipsoid protein bulk and two protein cylinders inside. The far field diffraction of the cell is shown in Fig. 7 (b) and the reconstructed object is shown in Fig. 7(c). The faithful reconstructions of the object from its diffraction pattern in these simulated phantoms show the remarkable sensitivity of this form of X-ray microscopy for achieving nano-resolution without any aid of focusing optics.

Summary

Phase contrast imaging technique promises to revolutionize the way X-ray imaging has been done till now. It has been particularly useful for advanced materials such as composites which are being used for many industrial applications and for which conventional X-ray imaging was almost impossible. It is also expected to find applications in material science, biological research, medical imaging of soft tissue.

References

1. Laboratory based X-ray phase-contrast imaging technique for material and medical science applications; Y. S. Kashyap, P. S. Yadav, T. Roy, P.S.Sarkar, M. Shukla and A. Sinha, *Applied Radiation and Isotopes*, **66**, 1083 (2008).
2. Phase Contrast Imaging and its applications in materials science; Amar Sinha, Y. Kashyap, Tushar Roy and P.S. Sarkar, *Journal of Non-destructive Testing & Evaluation*, **7**, 1 (2009)
3. Neutron phase contrast imaging beamline at CIRUS, reactor India; Yogesh S. kashyap, Ashish Agrawal, P.S.Sarkar, Mayankshukla, Tushar Roy and Amar Sinha, *Applied Radiation and Isotopes*, **70**, 625 (2012).
4. A variable wavelength based approach of phase retrieval for contrast transfer function based methods; Yogesh Kashyap, Ashish Agrawal, P.S. Sarkar, Mayank Shukla, Tushar Roy and Amar Sinha, *J. Synchrotron Rad.*, **17**, 799 (2010).

BARC NEWSLETTER

DESIGN AND MANUFACTURE OF PROTOTYPE 400 KEV RFQ ACCELERATOR

Abhay Kumar, S. Guha, R.S. Vohra, S.B. Jawale and R.L. Suthar
Centre for Design and Manufacture

and

Rajesh Kumar, Dr. Pitambar Singh and Dr. R.K. Choudhury
Nuclear Physics Division

Shri Abhay Kumar is the joint recipient of the DAE Young Applied Scientist /
Technologist Award for the year 2011

Abstract

400 keV, 350MHz radiofrequency accelerator is a deuteron beam accelerator which will be used in place of dc accelerator of PURNIMA facility at BARC. It is an octagonal shaped complex structure having two pairs of modulated tip vanes with eight rectangular vacuum ports, four RF feed port and sixteen tuner ports. It has 24 cooling holes with NPT threaded connections to carry away heat. High surface profile accuracy of vanes and modulated gap among vanes are essential design requirement. 1.028 metre long RFQ structure involves two stages of brazing at high temperature in vacuum furnace to ensure He leak tight joints and design of suitable brazing fixture. This paper describes mechanical design, analysis and manufacturing aspects of the product.

Design Features of 400 KeV RFQ Accelerator Sub-assembly

400 KeV RFQ (Radio Frequency Quadrupole) Accelerator Sub-assembly is an octagonal shaped (Ref. Fig.1) Proton accelerator. It consists of one pair each of Major and Minor vanes having modulations at tips in longitudinal direction. There are two conflat flanges made up of SS 304L at both ends of the Assembly. A total of 28 nos. ports are present, 8 nos. of which are rectangular vacuum ports, to maintain a vacuum of the order of 10^{-6} torr, 4 nos. are R.F. Power feed ports, to feed RF power at middle of its length, and remaining 16 nos. ports are tuner ports which are meant for frequency tuning of RFQ accelerator. Vane tip of the prototype RFQ are made up of OFHC copper and bolted to the main body which is made of ETP Copper, with SS 304L end flanges. Fig.2 shows the drawing of the Major Vane of the RFQ Sub-assembly.

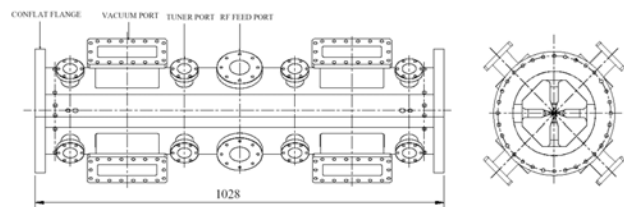


Fig.1: Single segment of RFQ assy

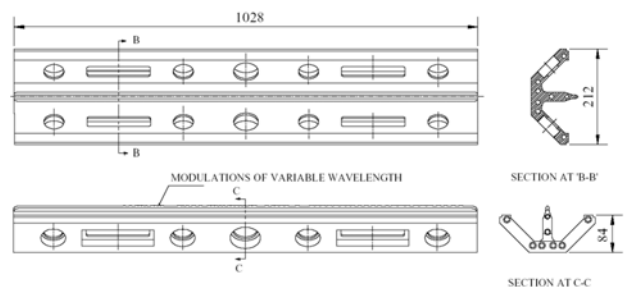


Fig.2: Major Vane of RFQ

Two pairs of Major and Minor vanes have modulations of varying wavelengths at their tips, with tip radius of 1.873 mm. Each RFQ vane has coolant holes, with NPT threaded hydraulic connectors on its surface. Modulations of adjacent vanes are at phase difference

BARC NEWSLETTER

of 90°. Machining of modulated vane, with 0.8 microns (R_a) surface finish; checking of machined profile with theoretical one; different stages of machining and brazing make the entire job challenging.

All ports are vacuum brazed at 830° - 840°C for SS 304L Flange and ETP Copper Nozzle bi-metallic joint. Ends of the RFQ Sub-assembly are machined to circular shape from octagonal shape to permit brazing of SS end flanges. High vacuum application, 1028 mm long ETP Copper material, 162 kg weight of the sub-assembly and Helium leak tightness joints of RFQ Sub-assembly require brazing to be done in a vacuum furnace.

Two stage brazing is required to be done at two different temperatures. For this, a horizontal First stage brazing fixture has been designed and used in brazing. All four Major and Minor vanes are positioned with dowel pins and all geometric features as well as vane tip gaps are checked before brazing operation.

In second stage of vacuum furnace brazing, pre-brazed RFQ Sub-assembly is assembled with 28 nos. ports and additional 2 nos. SS end flanges, with brazing alloy filler material. For this, second and final stage brazing fixture (Ref. Fig. 3) has been designed. Inconel helical springs as well as Nimonic-50 Belleville springs having adequate strength at high temperature are used to keep all ports and flanges in position and to take care of thermal expansion of components in the Vacuum furnace.

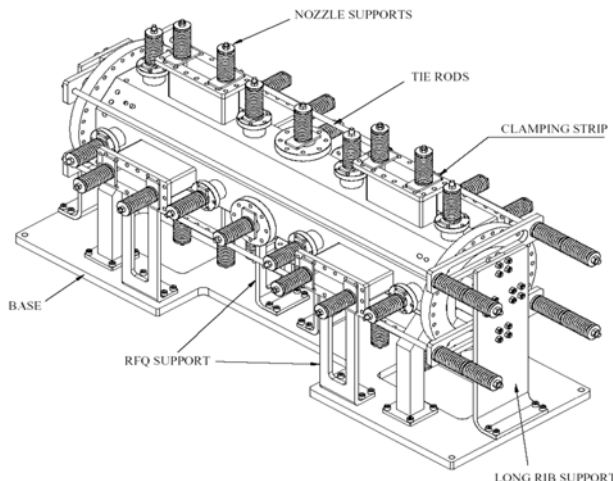


Fig 3: Design of brazing fixture

Manufacturing Features

Raw material

The raw material for Minor and Major Vanes as well as for the Cylindrical and Rectangular nozzles should be Oxygen Free High Conductivity (OFHC) Copper, having Oxygen content less than 10 PPM. It is preferable to have these vanes made from forged raw materials (with forging process followed by stress relieving). The raw materials also need to be tested by Ultrasonic Testing (UT) methods to detect any flaws, as per the ASTM standards, after proof machining of the forged pieces. However the raw material available for the Prototype RFQ sub-assembly at CDM is ETP Copper, wherein porosity defects were observed and water cooling arrangement for the Vanes could not be implemented, even though water cooling holes have been made in all the vanes. To avoid porosity defect in the tip of vanes where modulations are machined were made of OFHC copper. The material of the flanges for the nozzles is of SS 304L - UT tested quality.

Trial machining to assess the capability of the machining processes / facilities:

The profile contour, on the Major and Minor vanes, is of critical nature for achieving the dimensional and geometrical accuracy as well as surface finish. To ascertain this, CDM has first carried out one trial machining of a Major Vane, on (Column and moving Ram type) Horizontal CNC Boring Machine, on a full size Aluminium block. The machining parameters were selected out of the available best tool materials and machining was carried out continuously (round the clock) during the finishing cut. It is a must that finishing cut should continue till the completion of the entire cycle time to avoid the inaccuracies due to unforeseen changes of machine reference points, which would have taken place because of switching on and off the machine. The trial piece was inspected and the dimensional accuracy was observed within 25 microns and with surface roughness of 0.4 micron CLA. Thus the machining parameters and the CNC program which was generated through CAD/CAM were qualified.

BARC NEWSLETTER

Layout of machining process

a) Rough machining to the near final shape of the product, keeping 2 mm machining allowances on the critical portion and an extra portion (on the sides to be used for clamping of the job on table and to be subsequently cut off during finish machining stage) was carried out. Fig 4 shows shape of Major Vane of the RFQ Sub-assembly.



Fig.4: Machined Major Vane

Deep hole drilling of various holes, which provide the water cooling paths. This is to be done with the use of fixtures, while drilling holes from both sides to minimize the inherent drift of the long drill, during deep hole boring (Gun drilling) operation. Fig 5 shows Deep hole drilling of major Vane of the RFQ Sub-assembly.



Fig.5: Deep hole drilling of coolant channel

Plug welding of the deep holes using GTAW processes with pure Copper as a filler rod.

Stress relieving of the rough machined Vanes, at a temperature of 625°C for half an hour, to ensure that the components are free from distortion during finish machining operation. Stress relieving is required as a large amount of material is been removed from the original raw material.

Finish machining of the Vanes: Major and Minor vanes were finish machined, using special grade carbide tool, on the Horizontal CNC Boring Machine, using the machining process which was qualified earlier. The profile details and other features were inspected on the CNC CMM (Co-ordinate Measuring Machine) and the dimensional accuracy of 25 microns was achieved. Fig.6 shows the finish machining of a Vane of RFQ Sub-assembly.



Fig.6: CNC machining of Vane Modulation

To ascertain the alignment of the four Vanes at their assembly (during brazing) matching dowel holes (dowels were made out of Copper material) were also machined on all the Vanes. The Cylindrical Flanges and Rectangular nozzles were finish machined on CNC Lathes and Milling machines respectively and were brazed at a temperature corresponding to the first stage of brazing sequence.

Joining processes

The RFQ Sub-assembly requires three stages of joining processes. Obviously, each subsequent stage of the

BARC NEWSLETTER

joining (welding/brazing) process has to be done at a temperature which is less than the temperature of the previous stage. The following different joining (Welding/ Brazing) processes were adopted:

a) Welding of the plugs for plugging the coolant holes is done by GTAW process at a localized temperature of around 1050°C.

b) Vacuum (1st stage) Brazing of the Vanes to each other, with Palladium Cu-Si 5 Brazing foil. The melting temperature of this alloy is 815°C for which the vacuum brazing cycle operates at 830°C - 840°C and vacuum level maintained at 10^{-5} Torr in the Vacuum furnace. Vacuum brazing of the flanges to the nozzles (28 Nos.) were similarly carried out, as a separate batch, at this temperature.

In the first brazing cycle, RFQ sub-assembly was assembled & made ready for 1st stage of brazing. Fig.7 shows RFQ sub-assembly after completion of the 1st stage of brazing.



Fig. 7: RFQ assembly after 1st stage brazing

c) Vacuum Brazing of all the Nozzles (Large size 2 nos. of End Flanges of the RFQ Sub-assembly and the 28 nos. smaller nozzle / flange sets, with BvAg8 brazing foil. The melting temperature of this alloy is 780°C and brazing is carried out at 810°C to ensure melting of the foil and thus the leak tightness of the joint. The brazing alloy chosen is in foil form of 50 and 100 micron thickness to cover the complete width of the joint, as per drawing, for all the above mentioned brazing filler materials.

Vacuum Furnace

As the Vacuum furnace of requisite capacity is not available in CDM, this job was sub-contracted to M/s. Golden Engineers, Navi Mumbai. In all four brazing loading cycles were envisaged to be carried out at the sub-contracted Vacuum brazing facility. Fig 8 shows the RFQ assembly with mountings inside the furnace. Several thermo-couples were connected to achieve a controlled temperature during brazing.



Fig. 8: RFQ assembly with brazing fixture mounted inside the vacuum Furnace

Vacuum Brazing Cycles

The two different brazing cycles were designed by CDM for the two different temperatures. These involved Ramped up (Controlled rate) Heating, Soaking (at the desired temperature, for the desired time period) and Ramped down (Controlled rate) Cooling. CDM engineers witnessed and supervised the temperature cycle at the vendor's works.

Final brazing which includes 28 sets of Nozzles / Flange and 2 nos. of Large End Flanges, has been successfully completed now.

Vacuum Brazing Fixtures: For carrying out brazing, CDM has designed and manufactured holding fixtures (Ref. Figs. 3 & 9) for use in the corresponding brazing stages. In these fixtures the Orientation and Position of the components during the brazing process is ensured as per the assembly requirement.

BARC NEWSLETTER



Fig. 9: Assembly of 2nd stage brazing fixture

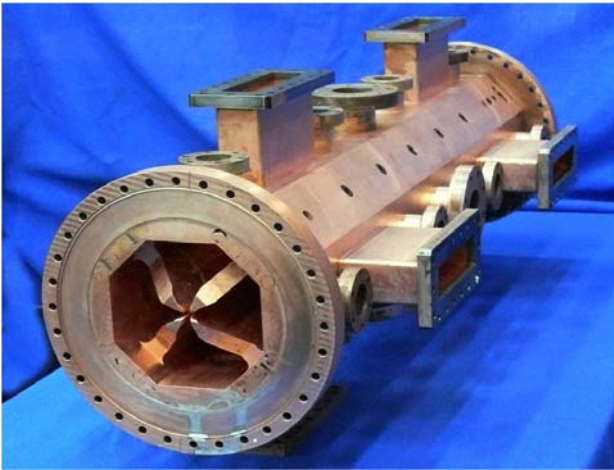


Fig. 10: The Final Product

RF Testing of RFQ prototype assembly

Resonance frequency of the prototype assembly described above was subjected to RF test (Fig. 11) without vacuum conditions and without cooling of vanes. RF test was carried out after first stage brazing and it was meeting RF requirement and resonant frequency was measured as 353 MHz. After second stage brazing RF test was again carried out and was found to be 346 MHz. Tuners are to be added to the



Fig. 11: RF Test Setup

assembly to tune it to a resonant frequency of 350 MHz which is the design requirement.

Conclusion

The design and manufacturing of this 1.028 metre RFQ vane assembly was a prototype system which was aimed at attaining precision manufacturing experience, understanding brazing criticality, complexity of modulation geometry machining and maneuvering of cooling system for the assembly. The trial piece was made of ETP copper and we have experienced problems due to material defects. Machining and brazing were very successful for this prototype. Experience was gained in the design of brazing fixture where we used special spring material which retains stiffness at high temperature. Final product improvements is planned to be done using OFHC copper material for the RFQ vane.

MICROWAVE POWER SOURCES FOR S-BAND ELECTRON LINACS

Shiv Chandan, A.R. Tillu, V.Yadav, R.B. Chavan, D. Bhattacharjee,
K.P. Dixit, K.C. Mittal and L.M. Gantayet
Electron Beam Centre, Accelerator & Pulse Power Division

Shri Shiv Chandan is the recipient of the DAE Young Applied Scientist /
Technologist Award for the year 2011

Abstract

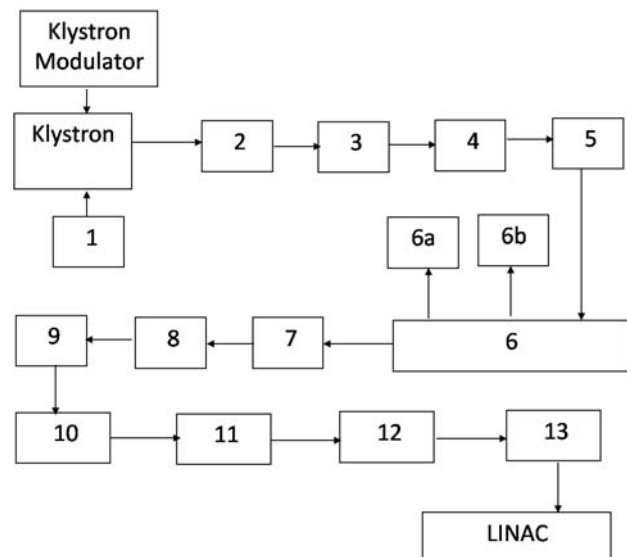
Microwave power sources based on Klystron & Magnetron are used for Industrial & Cargo scanning applications. These sources were tested on matched water load for their rated parameters and then integrated with Linac system. RF conditioning of Linac was first done up to 2.0MW without beam and then with beam loading above 2.0MW. This paper describes the RF source testing details for 10MeV Industrial Linac, 9MeV Linac for test facility at ECIL, Hyderabad and 6MeV linac for cargo application. Design & development of passive RF components is also described.

10MeV Linac for Industrial Application

A 10MeV RF Industrial Electron LINAC [1] has been indigenously designed, developed, commissioned and is being operated regularly at beam power of 3kW for industrial & research applications at EBC, Kharghar. The pulsed S-band bi-periodic standing-wave structure Linac is driven by a Toriy (KIU-147A) make Multi-beam Klystron with peak power of 6MW and average power of 25kW (pulse width 10 μ sec and PRF 415Hz) operating at 2856 \pm 5MHz [2]. The RF source consists of a line type pulse modulator powering the klystron. Microwave components like directional couplers, circulator with matched load, bends with arc detectors and RF window are used for transmission of microwave power from Klystron to LINAC. Pulsed driver amplifier of 110W was used to give low RF power to Klystron input cavity.

Klystron was first tested on water load. For power measurement, a loop type directional coupler with forward & reverse coupling of 55 dB and directivity of 25dB was used. Klystron modulator was tuned to impedance of 16 Ω . Klystron was first operated in the diode mode and its VI characteristics were measured. Beam perveance of 21 μ Perveance was measured.

Klystron was tested up to peak forward power of 5.5MW at 50kV, 235A. Reflected power was less than 1%. All these tests were done at PRF of 50Hz.



- (1) Driver Amplifier
- (2) Flexible waveguide-1
- (3) DDC-1
- (4) E bend-1 with arc detector
- (5) H bend-1
- (6) 4-port Circulator with (6a & 6b) water loads
- (7) H bend-2
- (8) E bend-2 with arc detector
- (9) Flexible waveguide-2
- (10) DDC-2
- (11) Straight waveguide section
- (12) Flexible waveguide-3
- (13) RF Window.

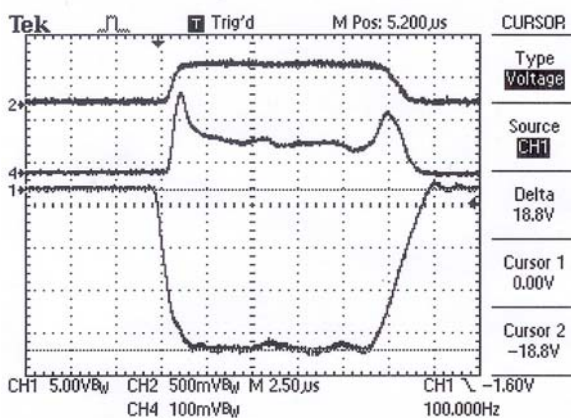
Fig. 1: Schematic of RF source

BARC NEWSLETTER

The schematic for testing the Klystron on LINAC is shown in Fig1. For testing the Klystron on LINAC load, water load at circulator port 2 was disconnected and a second directional coupler (DDC-2) with forward coupling of 66.1dB, reverse coupling of 70.9dB and directivity of 30dB was used & a flexible waveguide were connected in the waveguide line. To isolate the vacuum in the LINAC & pressure in the waveguide line, RF window was connected between DDC-2 & LINAC. Waveguide line was pressurized with 28 psi SF6.

RF Conditioning of LINAC Cavity

Initially frequent arcing was observed at RF peak powers as low as 0.5MW. The arcing was accompanied with heavy out-gassing in the linac region, and total power reflection. On sustained arcing, the ARC detector (at linac side) would trip the modulator at such low



Ch1: Klystron current $I_{kly} = V_{ch1} * 10 = 188A$.
 Ch2: Forward power envelope corresponding to 3.5MW.
 Ch4: Reflected power envelope corresponding to ~200kW.

Fig2: 3.5MW peak, 3.5kW avg. power testing of klystron on LINAC

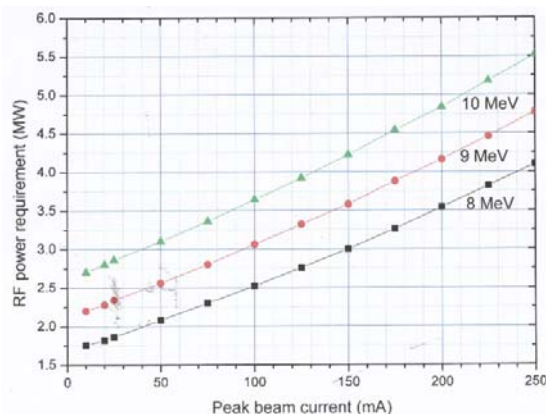


Fig. 3: Beam Energy Relation with Beam Current & RF Power

peak powers. The vacuum level in the linac would deteriorate to 10^{-05} mbar range. Subsequently frequent arcing reduced after the RF conditioning of cavity. RF conditioning of cavity was done at variable PRF (minimum 10 Hz to a maximum of 400 Hz) at each peak power level of 500kW to 4MW in steps of 100kW. This took ~250 hours. During the RF conditioning of the linac cavity, a vacuum of 3.0×10^{-7} mbar was maintained throughout the complete linac system. Vacuum in the cavity & Reflected power signals were monitored to do the RF conditioning of linac Cavity. The value of reflected power was minimized by tuning the frequency at the driver amplifier input within the range of $2856MHz \pm 500kHz$. The reflected power was <10% of the forward power for all the forward power levels. The klystron current pulse and envelope of forward and reflected powers is as shown in Fig. 2.

Dependence of Beam energy on beam current & RF power (Theoretical analysis) is shown in Fig. 3.

9MeV Linac for Linac Test facility (LTF)

Development of a 9 MeV LINAC based X-ray scanning system [3] has been taken up jointly by BARC-ECIL as a Linac test facility for Cargo scanning.

A Klystron (THALES, TH2163) based Microwave power source of 5.5MW peak, 10kW avg., at 2.856GHz frequency has been developed. The Klystron requires RF drive power of 70W, given from a 150W driver amplifier. The pulse cathode voltage of 150kV & current of 110A is given from a Klystron Modulator. For microwave power transmission, components like circulator, directional coupler, water load and RF window are used, rated for 8MW, 15kW power. All components were tested on VNA with VSWR<1.1 and insertion loss<0.05dB. Total insertion loss for the full waveguide line is 0.25dB (i.e. 5.5% power loss). These components were assembled and installed with the Klystron system. Microwave plumb line is pressurized with 28 psi SF6 gas for handling high microwave power. For this, a SF6 filling waveguide is connected in waveguide line and a SF6 gas handling unit has been installed. A gas inlet valves opens if the pressure falls below 21psi and closes when the pressure increases up to 28psi.

BARC NEWSLETTER

A LCW plant is installed for cooling Klystron, Klystron modulator, Electromagnet, Circulator, water-load, RF-window and other LINAC components.

Testing on Water Load

The Klystron was tested on water load at 5.5MW peak, 10kW average power. Its VI characteristics are shown in Fig.4. Beam perveance of $1.9 \mu\text{Perveance}$ was measured. Variation of forward Klystron power with input RF drive power at Modulator voltage of 132kV & current of 92A is given in Fig. 5.

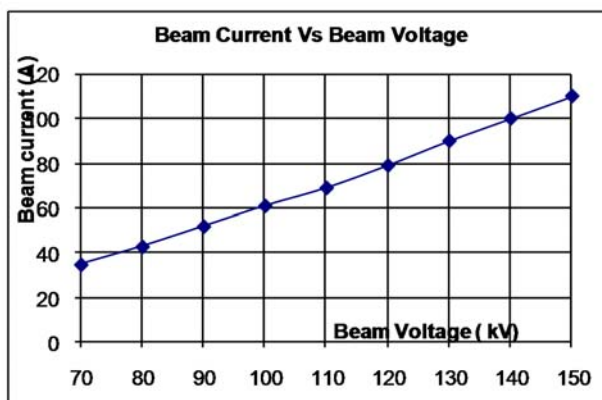


Fig. 4: V-I Characteristics of Klystron

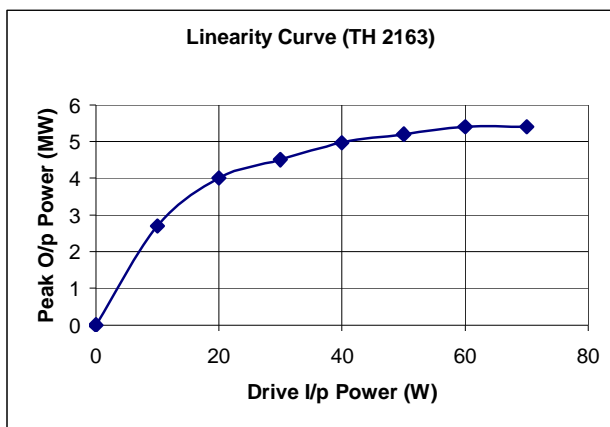


Fig. 5: Klystron Output power variation with input drive power

RF Conditioning of LINAC Cavity

RF conditioning of cavity was done in steps of 100kW. While RF conditioning, both Vacuum and ARC fault are monitored. Pfeiffer make controller has been used to monitor Vacuum in LINAC. The controller has relay contact which has been programmed for fault generation if the vacuum pressure falls below 5×10^{-6}

mbar. For the required operation, the RF conditioning has been done up to 2.8MW, 200Hz. For 9MeV energy at beam current of 75mA, RF power of 2.75MW is required.

6MeV Compact Cargo Linac

Based on the demonstration of 9MeV ECIL LINAC, in order to make the Cargo scanning system more compact, a 6MeV, 700W compact LINAC based on Magnetron as Microwave generator, was developed by APPD, BARC.

The specifications of the linac are given in Table 1 below:

Table 1: Specifications of 6/3 MeV Compact Linac

Beam Energy	: 6 MeV
Peak beam current	: 160 mA
Avg beam power	: 700 W (max)
X-ray beam focal size	: 1-2 mm
X-ray dose	: 8-10 Gy/min/m
X-ray field size	: Std 30° cone
Pulse width	: 3.4 μs
Pulse rep. rate	: 250 Hz (max)
Length of linac	: 0.6 m
RF Frequency	: 2856 ± 2 MHz
Injection voltage	: 85 kV (max)

After the Magnetron RF output, WR 284 rectangular waveguide components were connected, which comprises of flexible waveguide, H-Bend, 90 degree twist, circulator with medium power load and a water load with forward & reverse coupling port of 60dB. Diode detector was calibrated from 0 to 13dBm on signal generator and connected with a 30dB attenuator at water load coupling port. All the interconnecting cables between Magnetron, Modulator, HVPSU and control unit were connected. DM water given to all the components from 5TR chiller system with required flow rates.

Magnetron Filament heating was done at 10V, 6A for 6 minutes. Trigger signal was given to control unit. HV was applied. Magnetron peak power was measured in the range to 1.0MW to 5.0MW by changing the modulator voltage from 25kV to 50kV. Pulse width was 4 μsec and PRF was varied from 10Hz to 250Hz. Magnetron average power was 3kW. Magnetron output power was measured using peak power meter and diode detector.

BARC NEWSLETTER

Magnetron frequency was measured using spectrum analyzer in the frequency band of $2856\text{MHz} \pm 5\text{MHz}$. System was tested at various duty cycles. It was tested for reliable operation at 3MW peak, 3.0kW average ratings for 4 hours continuously.

Baking of Linac beam line

Electron Gun, Linac, beam tube, target and RF window of compact linac were assembled with vacuum sealing gaskets. Vacuum of 6×10^{-7} mbar was achieved with TMP pumping. IR heaters were placed for baking the Linac beam line at uniform temperature of 100°C . Total 120 hours of continuous baking was done. After isolating the TMP, time to reach from vacuum of 1×10^{-5} mbar to 1×10^{-4} mbar was 4 minutes at 100°C . At room temperature, vacuum of 3.4×10^{-4} mbar was measured without any TMP pumping for 20 hours, suggesting the system leak rate of 3×10^{-8} mbarLit/sec.

Magnetron testing on Linac Load

First, Cavity was tested using VNA. Resonant cavity was 2858.150MHz and Beta was 5.0 (45% reflected power). After magnetron testing on water load, load was disconnected from circulator port-2 and connected at circulator port-3. Waveguide components like E-Bend with arc detector, directional coupler (Coupling 60dB), flexible waveguide and RF window were connected at circulator port-2 and integrated with Linac power feed cavity. SF6 was filled in full waveguide line from Magnetron to RF window at 15psi. No leak was detected. Vacuum of 4×10^{-7} mbar was maintained in Linac beam line.

RF conditioning of Linac

Linac under RF conditioning is shown in Fig 6. RF Conditioning was done up to 1.50MW, $4\mu\text{sec}$, 100Hz PRF. Reflected power was 700kW (i.e. 45% of forward power and Beta value of 5.0). Resonant frequency was matched to 2858.150MHz for minimum reflected power. Reflected power was increasing at other frequencies. Vacuum in the cavity was in the range of 3.0×10^{-6} mbar. Cumulative conditioning time was 4.5 hours. Radiation level in operating area was $< 0.3\mu\text{SV/hr}$. No arc fault was observed during conditioning.

collimator focussing coil linac cavity E-gun RF Window



Fig.6: Photograph of 6 MeV linac system

Design & Development of RF components

Passive microwave components like directional coupler, E & H bends and high power RF window were designed and developed for Linacs. Directional coupler measures the forward and reflected power, E & H-bends changes the orientation of waveguide line in the desired direction and RF window passes the microwave power from klystron and also acts as a barrier between vacuum in the Linac & SF6 in the waveguide line. Directional coupler was designed for $\text{VSWR} < 1.1$, Insertion loss $< 0.05\text{dB}$, Coupling of 60dB & Directivity $> 20\text{dB}$. E & H bends are designed for $\text{VSWR} < 1.1$ and Insertion loss $< 0.05\text{dB}$.

RF window was fabricated at $2856 \pm 5\text{MHz}$ with DN100 Flange at Vacuum side and rectangular WR284F flange at pressure side. It was tested for $\text{VSWR} < 1.10$ and insertion loss of 0.05dB (1.1% loss). Vacuum leak rate of 10^{-10} mbar/lit/sec was measured. All the components were pressure tested at 45psi SF6. No leak in 4 hours test was observed.

References

1. K.C. Mittal, Shiv Chandan, et al, "Operating experience of 10MeV Industrial Linac" Proc. InPAC 2011, IUAC, New Delhi.
2. Shiv Chandan, A.R. Tillu, et al, "Development of S bad RF power source for 10MeV Industrial Linac" Proc. InPAC 2011, IUAC, New Delhi.
3. Vivek Yadav, Shiv Chandan, et al, "Microwave source development for 9MeV Rf Electron Linac for Cargo Scanning" Proc. InPAC 2011, IUAC, New Delhi.
4. Shiv Chandan, SR Ghodke, et al, "First beam trials of 6MeV RF Electron Linac for mobile Cargo Scanning applications" Proc. VEDA 2012, CEERI, Pilani.

BARC NEWSLETTER

DESIGN, UPGRADE, INSTALLATION, COMMISSIONING & MAINTENANCE OF PROCESS INSTRUMENTATION FOR RESEARCH REACTORS

Kaustubh Gadgil, Prashant Awale, C. Sengupta, R. Bharathan, G. Bharadhwai
Research Reactor Maintenance Division

Shri Kaustubh Gadgil is the recipient of the DAE Young Engineer Award
for the year 2011

Abstract

Control & Instrumentation of Trombay Research Reactors is maintained by Instrumentation Section of Research Reactor Maintenance Division. Design & up gradation aspects of new reactors as well as existing reactors is also executed by this section. Apart from maintenance of conventional process instrumentation, maintenance & overhauling of hydraulic systems is also handled by instrument maintenance section. Complete project cycle for implementing process instrumentation of Critical Facility for AHWR from conceptualization & design to installation & commissioning was also successfully executed. Up gradation of instrumentation for various reactor systems for research reactor Dhruva was completed which involved Up gradation of Emergency Core Cooling System, Main Control Room, Channel Flow Monitoring System & Fuelling Machine. This also involved development of indigenous solutions for overcoming obsolescence & embargo problems associated with critical equipment which were replaced as a part of upgrade. This paper describes the design, installation & commissioning of process instrumentation for Critical Facility and C&I up gradation for Dhruva reactor along with maintenance aspects.

Keywords: Research Reactors, Process Instrumentation, Critical Facility, Dhruva

Introduction

Process Instrumentation Systems are critical for safe & smooth operation of nuclear reactors. Sound design, maintenance & timely upgrade of these systems are essential for achieving desired performance of these systems. Instrumentation Maintenance Section of Research Reactor Maintenance is responsible for Design, Upgrade, Installation, Commissioning & Maintenance of Process Instrumentation for Research Reactors located in Trombay. Critical facility is a low power research reactor with built in design features that allow arrangement of fuel rods, safety rods and experimental assemblies in variable lattice spacing to simulate different core configurations as per the requirements of various reactor physics experiments for AHWR and

500 MW PHWR. Process instrumentation provided for the reactor is predominantly electronic with a back up of conventional passive instruments for critical parameters.

Research reactor Dhruva is a 100 MWth, heavy water moderated, heavy water cooled metallic uranium fuelled reactor. For handling active heavy water and metallic uranium fuel stringent process instrumentation is designed for monitoring of pressure, flow, level & temperature. The instrumentation has been designed in the late seventies and it was predominantly pneumatic. Upkeep of these systems after more than 25 years of operation with limited spares inventory, is becoming increasingly difficult due to obsolescence & embargo problems. Since the expected life of C&I

BARC NEWSLETTER

systems is typically twenty years, it is considered appropriate to upgrade the important C&I systems in Dhruva. The upgradation was carried out in phased manner ensuring minimum down time of the reactor.

Process Instrumentation for Critical Facility

Instrumentation is provided for monitoring important process parameters such as Level, Flow, Pressure & Temperature. It also generates trips, alarms & interlocks necessary for smooth operation of the process systems and safety of reactor, personnel as well as equipment. Electronic instrumentation has been selected wherever remote transmission of process data is required which also offers advantages such as better accuracy, stability and lesser maintenance frequency. All the important parameters are provided with SMART transmitters and the data from these transmitters is made available in local panel as well as control room for indication/recording.

Direct acting passive instruments such as manometers, pressure gauges & flow glasses are used as backup to electronic instruments and for providing local indication for less important parameters.

Contacts required for generating trips, alarms and interlocks are derived from Indicating Alarm Meters, Contact type pressure gauges and limit switches. Redundant contacts have been provided for generating reactor or equipment trip to improve the reliability.

Indicating instruments have been provided on local panel, control room panels and control console. Indication of the parameter is provided on any of these or all the locations depending on the operating requirements. All the indicating instruments in control room are electronic.

For temperature measurement Resistance Temperature Detectors (RTD-PT-100) have been selected as the primary element due to its high sensitivity, accuracy, reliability and relatively small time dependant drift. For flow measurements venturi elements have been selected because of their highly reproducible output

signals, low-pressure loss and lesser straight length requirements on the upstream & downstream side of the element. For measurement of pressure in field and local panels, bourdon tube type pressure gauges have been chosen as primary element due to their ruggedness and proven design.

Important parameters of the various systems such as Nuclear channels, Reactor Regulating System, Reactor protection system, Start-up logic and other Process parameters have to be monitored & recorded on a continuous basis. For recording this data, digital paperless recorders are used. These have freely configurable input channels to suit signal types & levels. Recorders are having intuitive, touch screen display to enable operators to clearly view data in varying formats including trend of a parameter. For storage of data internal flash memory is used. Data stored on flash memory can be archived on a floppy disc or on a computer magnetic disc through Ethernet. Stringent specifications and rigorous inspection & testing prior to procurement ensured very reliable instruments for important systems for Critical Facility.

Apart from installation of the instrumentation various pre-commissioning tests were carried out which involved volumetric calibration of the tanks, moderator dump test, process interlock checking and light water commissioning of the system.

Upgrade of Process Instrumentation for Dhruva

To overcome embargo & obsolescence problems, instrumentation for following important systems has been upgraded in a phased manner over a period of last ten years.

Fuelling Machine 'A'

Fuelling machine of Dhruva is designed for handling of the heavy water (D₂O) cooled 10 m long, irradiated & fresh fuel assemblies. The machine is having necessary shielding arrangements for safety of plant personnel & adequate cooling provision for hot fuel removed from reactor core.

BARC NEWSLETTER

The machine uses servo hydraulic drives for positioning of this 300 Te machine with an accuracy of ± 0.25 mm in X-Y plane. Hydraulic servo valves for this system were developed indigenously as replacement for obsolete valves. Flow, pressure & dynamic characteristics of the servo valves were tested at manufacturer's lab and the valves were accepted only after satisfactory test results. The valves were installed and hydraulic system was tuned to provide desired positioning accuracy. The servo amplifier control circuit was also replaced with indigenously manufactured modular circuit boards. The performance of the position servo system is satisfactory after this upgrade.

Hydraulic drives are used for handling the fuel rod and tray rod assemblies. These drives were dismantled, serviced and installed back after replacing obsolete components. The commissioning of the hydraulic system involved fine tuning & setting adjustments of various system components in order to get desired performance.

Apart from the hydraulic drives, up gradation of all the C&I systems of the Fuelling Machine was also carried out. Machine positioning system and fuel assembly position indication system were replaced with new systems. Relay logic for Process interlocks was revamped and additional safety interlocks were incorporated. The alarm annunciation & beetle monitoring system were replaced along with control console which houses these systems. Recording of important parameters & contacts was implemented as a part of upgrade along with provision for jumpering of specific interlocks by authorised personnel. Before implementation of the upgrade, the design was thoroughly reviewed by an independent peer review committee.

Important aspect in execution of these jobs was to carry out the jobs to limit the down time of machine as its availability is very critical for operation of reactor. The large wiring density & number of safety interlocks also posed challenge in site execution. Functional checking of large number of safety interlocks after commissioning was critical aspect of the installation & commissioning procedure as the machine handles highly radioactive

irradiated fuel. The upgrade of the C&I has resulted in smoother operation, reduced faults and improved facilities for operators.

Coolant Channel Flow Monitoring System

The Differential Pressure gauges used for coolant channel flow monitoring system at Dhruva, were facing frequent failures over the years & difficulties were experienced in procuring the spares due to embargo & high cost. Considering the same, it was decided to develop a customized Electronic DP Indicating Switch, which could be retrofitted without modifying the existing mounting arrangement or tubing & cabling. As these instruments were for Reactor Protection & classified as safety class 1E instruments, all necessary QA procedures & type tests were carried out as per the requirements of IEEE 323 standard. Further, necessary Failure Mode & Effect Analysis of the hardware along with exhaustive V&V of the micro-controller software, were also carried out.

A total of 387 gauges were replaced in a phased manner during scheduled monthly shutdowns and thereby not affecting reactor availability. The total replacement of all the gauges was completed in four such campaigns, through meticulous planning & man-rem budgeting and the functioning and performance of the instruments till date has been found to be satisfactory.

Upgrade of Main Control Room of Dhruva

The Main Control Room of Dhruva, was having predominantly pneumatic instruments which were facing frequent failures & difficulties were experienced in procuring the spares due to obsolescence. Considering the same, it was decided to replace the control room instruments on six out of nine panels with electronic video graphic recorders & LCD screens. While designing new panels, requirements of Functionality, Ergonomics, Aesthetics and redundancy were taken into account along with provision for future requirements. The design was reviewed by an independent Peer Review Committee.

BARC NEWSLETTER

A total of 6 panels each comprising of around 100 instruments, 1500 terminations catering to 50 parameters were replaced in a phased manner during scheduled monthly shutdowns and thereby not affecting reactor availability. Provision of Temporary Instrumentation was made for monitoring important parameters and keeping the safety interlocks & critical alarms effective during each panel replacement. The replacement of all the six panels was completed in six such campaigns, through meticulous planning and the functioning and performance of the instruments till date has been found to be satisfactory. The feedback from staff manning the control room has been excellent.

Upgrade of Instrumentation for ECCS System of Dhruva

ECCS system of Dhruva was modified in order to improve the reliability of the system. As a part of these modifications, instrumentation associated with ECCS was upgraded from pneumatic to electronic. Also provision was made for additional instrumentation in view of the equipments added to the ECCS system. Total 35 transmitters were installed for monitoring various parameters associated with ECCS. As per original design certain parameters associated with ECCS were provided with indication on the local panel in the reactor hall. After converting instrumentation of these parameters to electronic, there was a need for a new panel for accommodating these parameters along with

additional parameters associated with new equipments. For this purpose, a section of the control room panels (viz. Panel H) was replaced with a new section with cut outs suitable for new set of instruments. The site installation, commissioning & testing of instrumentation & associated interlocks was completed in-house within a span of two weeks.

Conclusion

Upgrading process instrumentation is a continuous process that is essential to meet the performance requirements and ensure maintainability and availability. Field and control room instrumentation for Dhruva is being progressively upgraded in phased manner. Upgrading instrumentation in an operating reactor poses challenges such as limited down time, ensuring continuous monitoring & availability of critical parameters and important safety interlocks during execution. Retrofitting of the new instrumentation poses difficulties such as fitment, compatibility with existing systems & familiarity of operating and maintenance personnel.

Selection of instruments also plays vital role in design of the process instrumentation as it has bearing on performance & maintainability in long term. In view of this due importance is given while selection and designing instrumentation system for research reactors to achieve desired accuracy, stability & reliability.

BARC NEWSLETTER

DESIGN AND DEVELOPMENT OF DOUBLE ACTUATOR CONTROLLER WITH DUAL CAN BUS INTERFACE FOR 6 DOF SHAKE TABLE

Shiju Varghese, Jay Shah, P. Ramakrishna, N.L. Soni, and R.J. Patel

Fluid Power and Tribology Section

Refuelling Technology Division

Shri Shiju Varghese is the recipient of the DAE Young Engineer Award for the year 2011

Abstract

A 5 Ton 6 DOF shake table is being indigenously developed at Refuelling Technology Division, BARC for the seismic qualification of different equipment and structures to be used in nuclear reactors.

This 6DOF shake table is having eight numbers of servo-hydraulic linear actuators connected to the table. To meet the demanding requirements of the control system of the shake table, a particular architecture of the control system has been formulated. In this architecture two actuators are being controlled by a double actuator controller and networked with other three double actuator controllers through a dedicated CAN bus. A double Actuator Controller with dual CAN bus Interface has been designed and validated to control two servo-hydraulic linear actuators with feedbacks from different sensors of actuators. 5 different parameters are sensed for each actuator. Facility for implementation of advanced control algorithms is also available in this system.

This paper describes Digital Signal Controller based hardware design, different sensor interfaces, software and testing of the Dual Actuator Controller with dual CAN bus Interface on simultaneous control of two single DOF shake tables.

Introduction

Seismic shake tables are used to simulate the exact effects of earth quake loading on a specimen and conduct experimental research in the areas of vibration, structural identification, assessment and control. It is one of most effective methods to identify the reliability of a product in real life situation .Refuelling

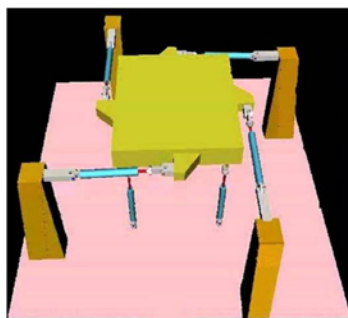


Fig. 1: 5 Ton Six Degrees of Freedom Shake Table being developed by BARC.

Technology Division; BARC is developing a 5 Ton 6 Degrees of Freedom (6DOF) shake table as shown in Fig. 1.

This topology of shake table is widely used in earthquake simulation experimental facilities.

Eight Linear servo-hydraulic actuators having fast response with precise motion control are used in this application. The control performance of shaking tables is greatly affected by the interaction between the table and the test specimen mounted on the table. This is because the dynamic characteristics of large specimens give significant force disturbances to the table . For this reason it is not appropriate to run the table with

BARC NEWSLETTER

conventional PID controllers. A state feedback control strategy is more appropriate and it can give wide bandwidth required for this application. This requires measurement of different state feedbacks of actuators and use of these in the control algorithm. Control system for shake table should implement features like overturning moment compensation, force balance control, offset moment compensation, and three variable controls. This controller uses modern control algorithms that require high order floating point matrix multiplications. The control loop update rate is 1 kHz. Hence, high computational power is required from the processor for actuator control. Modern digital sensor interfaces such as CAN bus and SPI are selected to minimize noise related problems.

Fast and real time communication interface is required for synchronizing the movement of all the actuators. Sufficient memory for storing the position history and control parameters of the actuators is also required. A design for achieving the control and performance requirements of the 6DOF shake table has been planned and concept verification experiments were carried out. This design consists of four numbers of Dual Actuator Controllers with dual CAN bus Interface (DACCI) interconnected via a CAN network. This paper describes a Digital Signal Controller (DSC) based hardware design, different sensor interfaces, software and testing of a DACCI.

Design of the DACCI

Each actuator of the shake table is provided with a magneto-strictive position and velocity sensor with a CAN bus interface, a MEMS accelerometer with SPI interface, a load cell and two pressure transmitters as shown in Fig. 2. Two such actuators are controlled by a single DACCI which has been designed around a DSC.

Digital Signal Controller(DSC)

We have selected a 150 MIPS dual core floating point DSC with a rich built-in peripheral set. This processor has a control law accelerator (CLA) which can be dedicatedly used for executing the control algorithm.

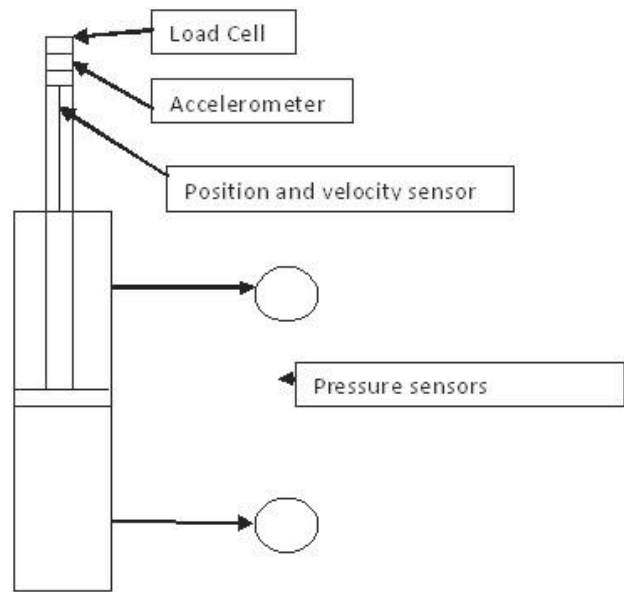


Fig. 2: Instruments connected to an actuator

It has dual CAN controllers (CAN A & CAN B) configurable at 1Mbps and two multi channel buffered serial ports (MCBSp) that can be configured as SPI ports. Six Channel DMA controllers provide very useful data transfer methods without sacrificing the processing power of the DSC core. This processor also has 16 channel 12 bit 12.5 MSPS ADCs and PWM controllers. It has 128K x 16bits Flash and 8K x16 bits RAM. It is possible to control the two servo hydraulic actuators required for this application using a single DSC because of its high processing capabilities and rich peripheral control units inside.

DACCI Architecture

The architecture of a DACCI is shown in Fig. 3. Here, a DSC is connected to two CAN networks, CAN A and CAN B through separate internal CAN controllers. ISO1050 is a galvanically isolated CAN transceiver that meets or exceeds the specifications of the ISO 11898 standard and is used to connect DSC to the CAN networks. ISO1050 can provide isolation up to 5000Vrms. CAN A is the network for inter-controller communication. Four such controllers are connected in the CAN A network. Two numbers of magneto-strictive sensors that can give position and velocity information in a single CAN message are in CAN B network.

BARC NEWSLETTER

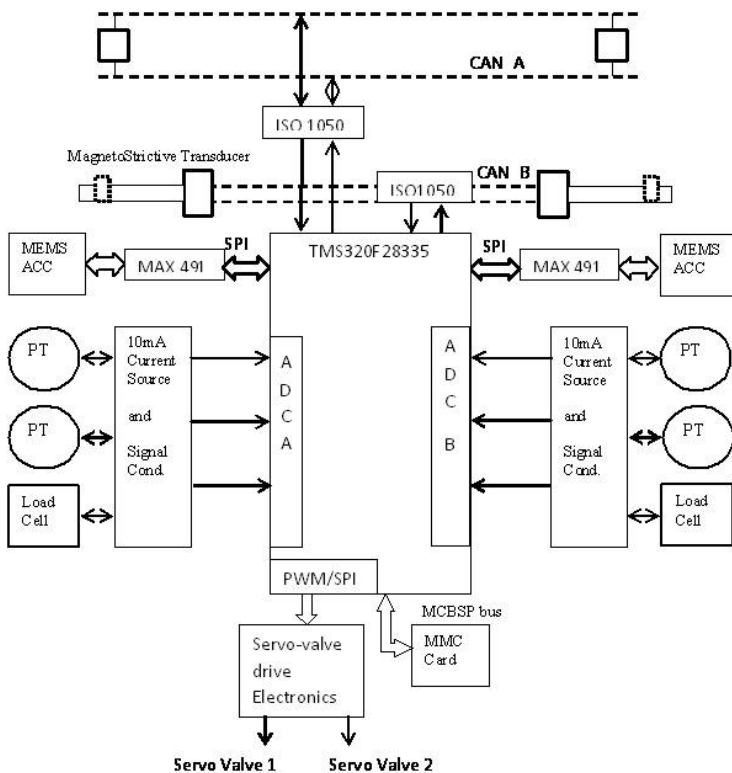


Fig.: 3 Architecture of DACCI

Both these sensors are configured for broadcasting the sensed values every 1 millisecond. By providing an independent CAN network for these sensors, reduced bus traffic and improved deterministic availability of the feedback parameters are achieved. MEMS accelerometer is connected via SPI to the DSC. The load cell and the pressure transmitters are connected to ADCs of the DSC after many stages of signal conditioning such as amplification, level shifting, filtering and isolation.

Sensor Interfaces

Position and velocity sensor interface

This 6 DOF shake table is an over-constrained system. The accuracy requirements of the position sensors are in the order of 5 microns. The stroke lengths of the actuators are 300mm for vertical and 200mm for horizontal actuators. Long range LVDTs are found to have high non-linearity errors. Also, signal conditioning circuits required in LVDTs are analog circuits and noise elimination is difficult especially in an operating

environment which includes noise sources such as hydraulic power packs and solenoids. A comparative study has been carried out to compare a magneto-strictive sensor with an LVDT. It was observed that the LVDT signal conditioner output was highly noisy as compared to the magneto-strictive sensor which has CAN bus digital interface. The position measurements made by both these are shown in Fig. 4. In addition, magneto-strictive sensor has velocity output also. Differentiating LVDT output to get the velocity worsens the noise problem.

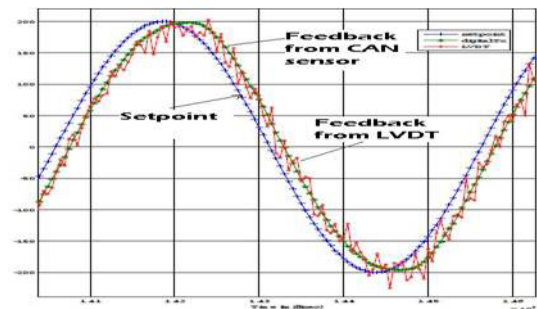


Fig. 4: LVDT vs Magneto-strictive CAN interface sensor

MEMS accelerometer Interface

A dual axis MEMS accelerometer with 1.9 mg ((19mm/s²) resolution at 60Hz of excitation has been chosen for this application. This accelerometer is having SPI (Serial Peripheral Interface) output. SPI controller of the DACCI was configured to update the acceleration data from the sensor at 1Mbps. Since the accelerometer is required to communicate at this rate from a distance of at least 6 meters away from the DACCI, a high slew rate differential transceiver circuit based on MAX 491 was developed, successfully tested and used in the controller. This communication scheme is shown in Fig. 5.

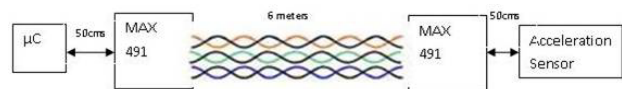


Fig. 5: SPI with MAX 491 interface for accelerometer

BARC NEWSLETTER

Load Cell and pressure transmitter interfaces

The load cell and the pressure transmitters are having Wheatstone bridge type output. An all element variable bridge is internally present in these sensors. The signal conditioning circuit for these has been developed in-house to achieve remote sensing and sufficient bandwidth. This circuit includes a 10mA precision current source for bridge excitation and an AD620 based instrumentation amplifier which amplifies and scales the differential signal output from the sensor bridge to ADC range of 0-3V followed by an anti-aliasing filter with 2 kHz cut-off. The output of the filter is connected to the ADCs of the DSC.

Software Development

Software for execution of the control algorithm and generation of outputs to servo-valve is included in the interrupt routine of the DSC corresponding to the CAN message from the two magneto-strictive sensors plugged into the CAN B network. These sensors are configured to broadcast position and velocity information in a single CAN message every 1 millisecond. One of these CAN sensors has been given a head start of 500 microseconds. This makes a phase difference of 500 microseconds between any two consecutive CAN messages in CAN B network thus avoiding any arbitration requirements for both the

sensors to access the network by both sensors. The SPI controller and the ADCs are configured earlier and triggered with a timer interrupt such that the latest outputs from accelerometers, pressure transmitters and load cell have been sensed at the same sampling time and are available before the execution of the control algorithm. The timing diagram is shown in Fig. 6.

Position history of the actuators consisting of set-points with respect to time is generated using kinematic software in a PC and downloaded to the DSC via RS-232 port. This set-point table is saved in an MMC card via the MCBSp of the DSC configured as SPI. During execution, the set-points are transferred from the MMC card into the DSC RAM in blocks of 512 bytes by a DMA controller. A scheduler program schedules the use of these set-points. The CAN A network is used to synchronize the scheduler program with that of other DACCI's via interrupts. MMC card is also used to save the acquired data during experiments. The RS-232 port is used to transfer the acquired data to the PC from DSC.

Testing

A fifth order linear ordinary differential equation model of the electro hydraulic servo linear actuator mathematically derived from first principles was experimentally validated using this DACCI. This experiment was conducted on a frictionless hydraulic linear actuator on a test bench.

Test bunch is a single DOF shake table. First, the DACCI was used to acquire all the states of electro hydraulic servo linear actuator and control the actuator. Then, this validated fifth order mathematical model of electro hydraulic servo linear actuator was used to develop a high order pole placement controller. Later, this high order pole placement controller was implemented in the DACCI which improved the performance of electro hydraulic

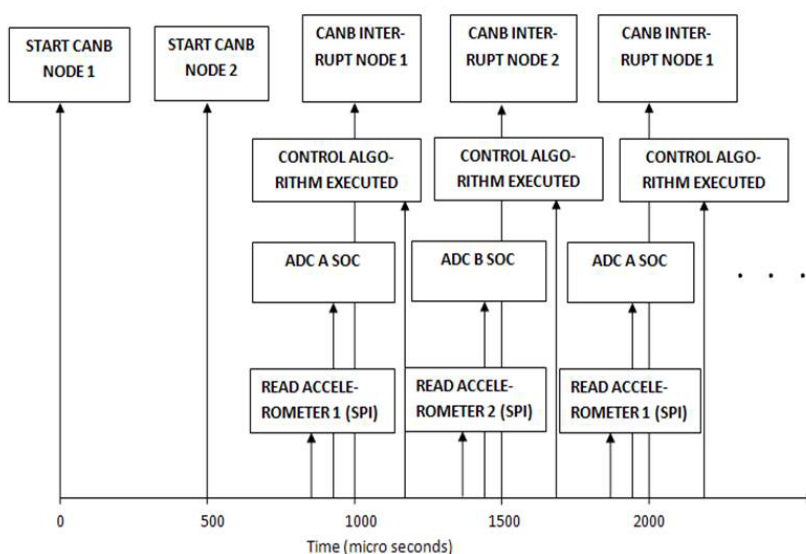


Fig. 6: Software Timing diagram

BARC NEWSLETTER

servo linear actuator greatly. A good match was obtained between the experimental results of all the states and simulated predictions .

Simultaneous control of two such single degree of freedom (SDOF) shake tables were carried out by subjecting both tables to design response spectra compatible time history is shown in Fig. 7. The

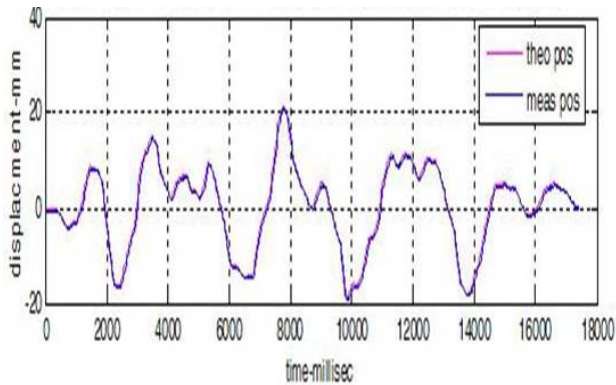


Fig. 7: Faithful reproduction of design response spectra compatible time history on SDOF shake table.

overlapping of the feedback readings and set-points with respect to time in the graph shows faithful reproduction of design response spectra compatible time history.

Conclusion

6 DOF shake table is an application which requires coordinated multi-axis control. A dedicated CAN network (CAN A) is utilized in this design to co-ordinate all actuators and avoid jamming. Simultaneous control of two single degree of freedom (SDOF) shake tables were carried out by subjecting both tables to design response spectra compatible time history. This will be further extended to control the 6DOF shake table. Dedicated CAN A network of this system facilitates this expansion. Double Actuator Controller with Dual CAN Bus Interface is a suitable platform for the development and research in control of multi-axis systems like 6DOF shake table.

BARC NEWSLETTER

RISK MONITOR –A PSA BASED OPERATOR SUPPORT SYSTEM FOR IPHWR

M. Hari Prasad, Gopika Vinod, V.V.S. Sanyasi Rao and R.K. Singh
Reactor Safety Division

Shri M. Hari Prasad is the recipient of the DAE Young Engineer Award for the year 2011

Abstract

For Nuclear Power Plants (NPPs), the major concerns of safety needs to be addressed for the future growth of nuclear power that is essential for reaching at a reasonable index of prosperity level as compared to the international standard. Probabilistic Safety Assessment (PSA) has become a key tool as on today to identify and analyze the NPP systems to address these safety concerns. PSA models have been successfully employed during design evaluation to assess weak links and carry out design modifications to improve system reliability and safety. As a result of the availability of these PSA studies, one can make its use to enhance plant safety and to operate the plants in the most efficient manner. This necessitates development of software tools like Living PSA, Risk Monitor etc. Risk Monitor is a PC based tool, which computes the real time safety level based on the actual status of systems and components and in addition assists plant personnel and regulatory authorities to manage day-to-day activities and can provide solutions to various regulatory decision making issues. This paper discusses various modules and data flow diagrams of Risk monitor being developed for Indian Pressurised Heavy Water Reactors (IPHWR). In Risk Monitor, risk is subjected to the change in the state of the system, which in turn depends on the state of the components and these are explained with a case study.

Introduction

Risk Monitoring can be defined as being the process whereby a complex technical facility is continuously monitored as regards the functioning or non-functioning of its different subsystems and the risk emanating from the facility is evaluated on the basis of this information. In the widest sense it can be regarded as being part of the risk management of a plant. Operation of Risk Monitor is based on PSA methods for assisting in day to day applications. Risk Monitoring programs can assess the risk profile and are used to optimize the operation in NPPs with respect to a minimum risk level over the operating time. Risk Monitoring provides safety status information for a plant and thus aids decision making about whether continued plant operation is tolerable under certain

system function outages. It may also support operations and be of help in deciding on maintenance strategies allowing immediate assessment of different plant configurations.

Reactor Safety Division of Bhabha Atomic Research Centre (India) has developed a PC based tool (Risk Monitor), which can assess the online risk profile. Risk Monitor is user friendly and can re-evaluate Core Damage Frequency (CDF) for changes in component status, test interval, initiating event frequency etc. Plant restoration advice, when the plant is in high risk configuration, is provided in the package. Current status of all plant equipments and equipment prioritisation is also provided in the package. What-If analysis can be done by using this package, which provides guidance to plant operators to choose among various options.

BARC NEWSLETTER

PSA Methodology

Probabilistic Safety Assessment (PSA) is an analytical technique for assessing the risk by integrating diverse aspects of design and operation of NPP. Risk can be defined as the product of the probability of an accident and the consequences from that accident. In the context of a NPP, core damage of the reactor represents an accident and release of radioactivity in the public domain and its effects on them will be the consequence. In order to prevent the occurrence of an accident, various engineered safety features are designed. An accident situation occurs when an initiating event is coupled with the unavailability of one or more Engineered Safety Features. The accident frequency can be minimised by reducing the frequency of initiating event and improving the availability of safety systems. This can be achieved by incorporating robust design, operating practises and selection of reliable components. The consequence of an accident that may occur can be minimised by providing barriers (e.g. reactor containment and exclusion zone) for arresting the release of radioactivity and reaching the public. In general PSA model of a plant has to be updated frequently as and when there is a permanent change in the design and operational procedures in the plan (Living PSA) [1] [2].

Necessity of Risk Monitor

PSA models can be used to quantify risk due to changes in components status, system design and operations consequent to changes in plant configuration. Plant configuration undergoes changes due to changes in component status and/or operating / maintenance procedures. Some components are randomly down and/or others can be planned for test, maintenance and repair. This results in a variation of the risk level over operating time, which is termed as risk profile, and indicates the trends which could lead to deviation from desired CDF. Thus, Risk Monitor helps in computing the risk based on the actual status of systems and components and assists plant personnel and regulatory authorities to manage day-to-day activities and can provide solutions to various regulatory decision making issues [3].

Different Modules of Risk Monitor

The Risk Monitor Software has been developed in Visual Basic. The Data Flow Diagram of Risk Monitor is shown in the Fig. 1. The various modules developed in the package are given as [4] System Modelling Options, Main Summary & On-Line Risk, Component data base, Component Out-of-Service & Restore, What-If Analysis and Probabilistic Precursor module.

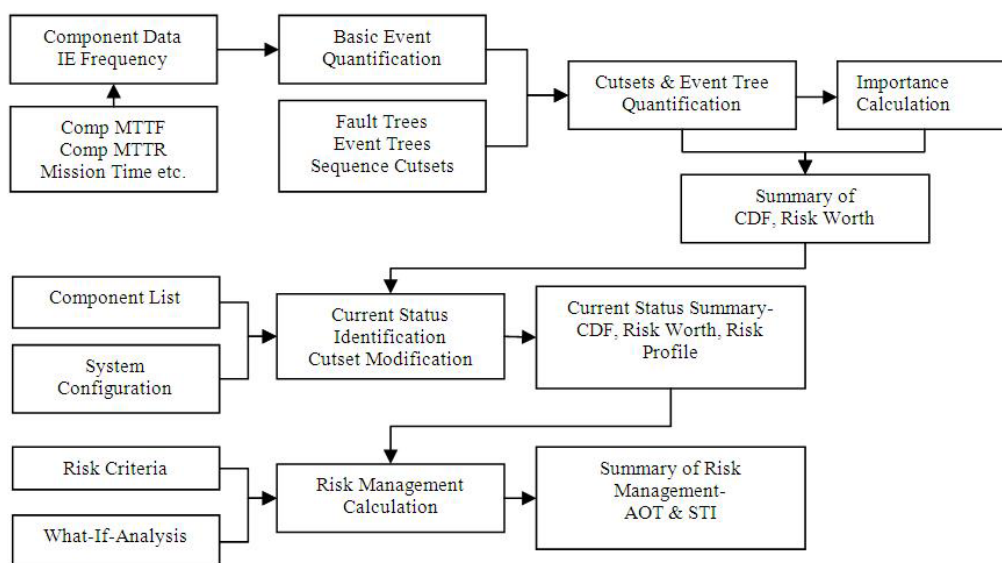


Fig. 1: Data Flow Diagram of Risk Monitor

BARC NEWSLETTER

In *System Modelling Options* user can provide the information on initiating events, safety systems, minimal cut sets of safety systems and core damage frequency, CCFs (this is explained in the following section) or can even import the data from the available PSA results. The *Main Summary & On-Line Risk*, module summarises status of the safety systems based on the status of the components, list of components which have been taken out from the service and risk profile (CDF vs Time). The *Component Database* is a reliability data base used for the management of data which is designed using MS ACCESS which also stores the PSA models and analysis results. The *Component Out-of-Service & Restore* module shows all the components which are in service and out of service as of today on system wise. The user can take any component from out of service (for maintenance, testing or inspection) or can restore by checking the relevant components in the in-service list or out of service list respectively. This changes the configuration of the systems and in turn affects the CDF. *What-If Analysis* is the unique feature of the risk monitor. With this analysis user can analyse different combinations of component states and based on the change in the CDF value decision can be made on which combination of components can be taken for maintenance or can be restored. In *Probabilistic Precursor* module significant events can be analysed to assess their potential to develop into catastrophic accident like core damage situation. In this analysis conditional core damage probability (CCDP) is the parameter with which significance of an event can be estimated. The CCDP value is calculated as:

$$CCDP = T_{\text{event}} \times (CDF_{\text{event}} - CDF_{\text{base}}) / A \quad (1)$$

with A the duration of power operation per year, T_{event} the duration of the operational event (h), CDF_{event} the core damage frequency during the event (1/yr), and CDF_{base} the base value of core frequency during power operation (1/yr).

Presentation of Main Results

The main results in Risk Monitor include risk plot, status of different safety systems, unavailability of different safety systems, list of components taken out of service, components which are due for restoration, Inspection intervals of different components, different Initiating Event (IE) frequencies, percentage contribution of IE to risk, conditional core damage probabilities and What-If Analysis. These results are presented for a typical Indian NPP. The variation of risk (in terms of CDF) along with time is shown in the Fig. 2. Table 1 shows the details of the component which the user wants to take it for inspection or maintenance. Risk Monitor helps the user whether one can perform this action based on the risk with the help of What-If analysis. The risk comparison is also shown in the table. The change in risk when this component taken out from the service is $3.078\text{e-}5/\text{yr}$ and the original risk is $4.487\text{e-}6/\text{yr}$. Since the modified risk is well below the unacceptable risk user can take this component for inspection or maintenance. The output of probabilistic precursor module is shown in Fig. 3 which shows the graph between CCDP vs the operational events occurred in a plant.

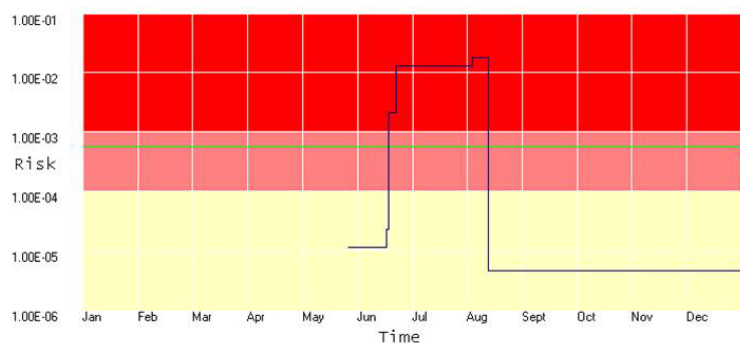


Fig. 2: Graphical representation of Risk varying with time

Table 1: Details of the component which has been taken out from service

General		Parameter	Value
ID	FFW-MV1	Failure Rate	4.75e-6
Description	Motor Operated Valve	Test Interval	720 hr
System	Fire Fighting Water System	Unavailability	1.708e-3
Model Type	Tested		
Existing CDF value			4.217e-6/yr
Change in CDF value when this component is fully unavailable			3.028e-5/yr
Unacceptable Risk Level			> 1.0e-4/yr

BARC NEWSLETTER

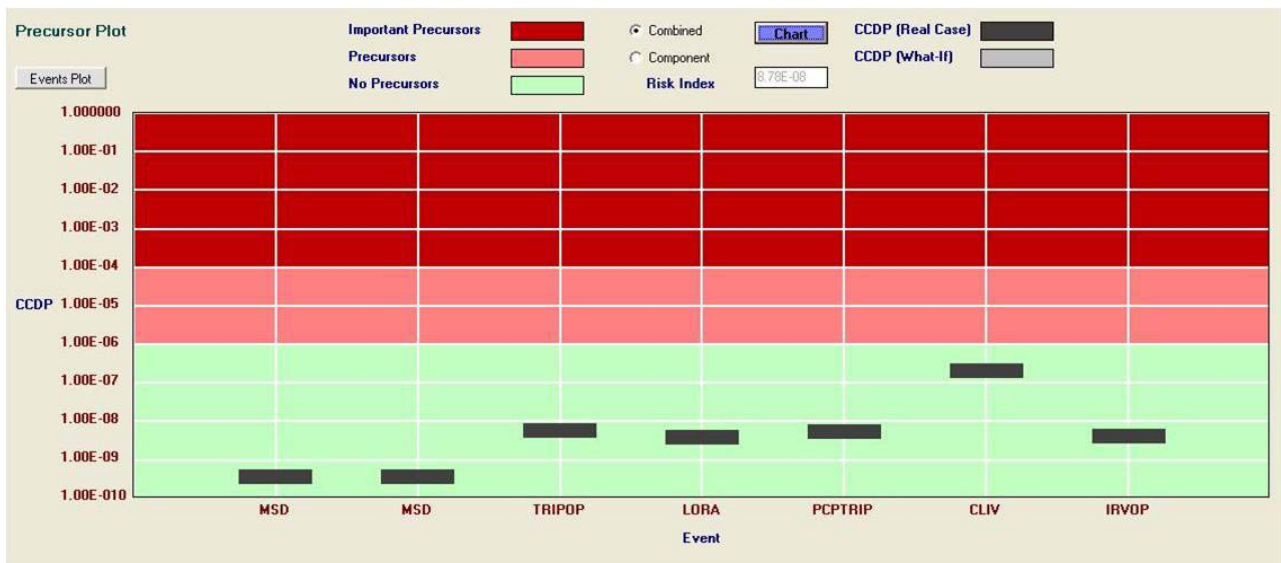


Fig. 3: Graph between CCDP Vs Events for a typical NPP

Conclusions

Risk Monitors are gaining wider acceptance world over. Risk Monitors are being used in various areas related to nuclear power plant operations. Risk monitor can be used as an efficient tool by plant personnel to analyse the change in risk whenever there is a change in component parameters or system configuration. Also it can be considered as an efficient system to track plant history. Risk Monitor can assist plant operators as well as regulators to assess the risk and ensure that plant is in the prescribed safe domain. Various such applications are optimization of technical specifications, operational decision making, risk based and risk informed decision making etc. Risk Monitor developed has been put under pilot study at various NPP sites in India. Depending on operator feedback, modifications were carried out to improve user friendliness of the software.

References

1. R. Nakai and Y. Kani, "A Living PSA system LIPSAS for an LMFBR", International symposium on the use of PSA for operational Safety, PSA '91, Vienna, Austria, 3-7 June 1991.
2. IAEA-TECDOC-1106 (1999), Living probabilistic safety assessment (LPSA), IAEA, Vienna.
3. M. Hari Prasad, Gopika Vinod, R.K.Saraf and A.K. Ghosh, "Application of PSA in Risk Informed Decision Making", International Conference on Reliability, Safety and Hazards, Mumbai, Dec 1-3, 2005.
4. Hari Prasad, Gopika Vinod, R.K.Saraf and A.K. Ghosh, "Risk Monitor a tool for operational safety Assessment", report BARC/2006/E/016, July, 2006.

BARC NEWSLETTER

DEVELOPMENT OF LOW ENERGY DEUTERON ACCELERATOR BASED DC AND PULSED NEUTRON GENERATORS

Tarun Patel and Dr. Amar Sinha
Neutron & X-ray Physics Division

Shri Tarun Patel is the recipient of the DAE Young Engineer Award for the year 2011

Abstract

Neutron sources are in a great demand in many area like research, nuclear waste management, industrial process control, medical and also security. Major sources of neutrons are nuclear reactors, radioisotopes and accelerator based neutron generators. For many field applications, reactors cannot be used due to its large size, complicated system, high cost and also safety issues. Radioisotopes like Pu-Be, Am-Be, Cf, are extensively used for many industrial applications. But they are limited in their use due to their low source strength and also handling difficulties due to radioactivity. They are also not suitable for pulsed neutron applications. In contrast, compact size, pulsed operation, on/off operation etc. of accelerator based neutron generators make them very popular for many applications. Particle accelerators based on different types of neutron generators have been developed around the world. Among these deuteron accelerator based D-D & D-T neutron generators are widely used as they produce mono-energetic fast neutrons and in particular high yield of D-T neutron can be obtained with less than 300KV of accelerating voltage.

Introduction

As a part of departmental programs, various types and size of deuteron accelerator based neutron generators are developed in NXPD at Purnima, BARC. These can produce neutron source strength of $10^5 - 10^{10}$ n/s. Neutrons are produced using following two reactions:
 $D + T \rightarrow {}^4\text{He} + n + 17.6 \text{ MeV}, E_n = 14.1 \text{ MeV}$ (1)
 $D + D \rightarrow {}^3\text{He} + n + 3.3 \text{ MeV}, E_n = 2.45 \text{ MeV}$ (2)
D-T reaction has a large cross-section even at low energy from 50- 300 keV and it is almost 100 times higher

than D-D reaction at this energy. Hence 300 kV accelerator based D-T neutron source is widely used to obtain higher neutron yield.

300 kV deuteron accelerator based neutron generator

This neutron generator (PNGF) has been designed for 300 kV accelerating voltage and 1 mA deuterium beam current installed in Purnima hall [1]. This can produce neutrons strength upto 5×10^{10} n/s neutron yield. It is an Electrostatic DC accelerator. The Schematic layout

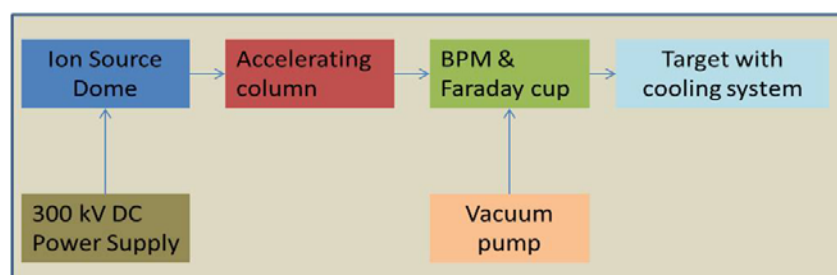


Fig. 1: Schematic layout of 300 kV deuteron accelerator

BARC NEWSLETTER



Fig. 2: Purnima neutron generator facility (PNGF)

and photograph of neutron generator is shown in Fig. 1 and 2 respectively.

System description

Neutron generator consists a Radiofrequency (RF) ion source shown in Fig 3. The deuterium gas is supplied to ion source through a gas inlet and its flow is controlled by a motorised needle valve which is connected with deuterium gas cylinder. The plasma is produced using capacitor coupled 100 MHz, 200W RF power.

D⁺ ion beam is extracted from ion source by applying extraction voltage which is focused by 30 kV DC electrostatic Einzel lens. The ion source, beam chopper and focusing lens with their all power supplies are kept in 300 kV electrically isolated dome. The electrical power of 230 VAC, 50 Hz for ion source power supplies inside the ion source dome is supplied by 300 kVDC isolation transformer.

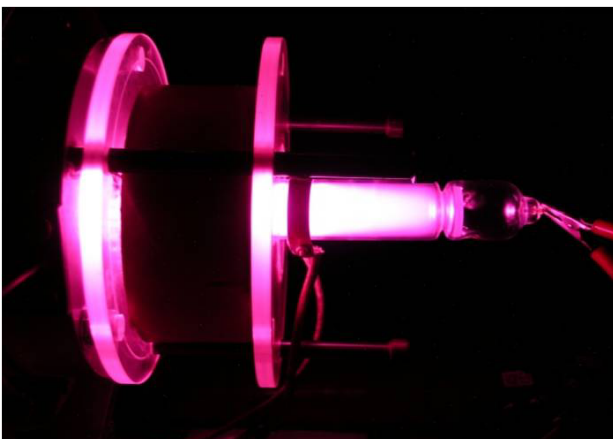


Fig. 3: RF ion source with deuterium gas plasma

The dome is connected with 300 kV power supply for acceleration. It is an 8 stage crocroft-Walton type 300 kV, 10 mA power supply designed by RRCAT, Indore. Accelerating column provides uniform acceleration of ion beam upto 300 kV. To align the beam in X-Y plane on the target, an electrostatic beam steerer is provided. It has two horizontal and two vertical plates connected with regulated 10 kV DC power supply. Beam diagnostic components like beam profile monitor and Faraday cup are incorporated to get the information of beam profile and current of accelerated beam.

At end of accelerator, target holder assembly is installed which can accommodate Tritium or Deuterium target as shown in Fig. 4. Tritium or Deuterium gas adsorption in titanium layer deposited on a copper backing plate of 0.5-1 mm thick is used as a target. Target holder is designed to accommodate 25 to 45 mm diameter target with a cooling system to dissipate beam heat. Target is continuously cooled by closed loop chilled water system.

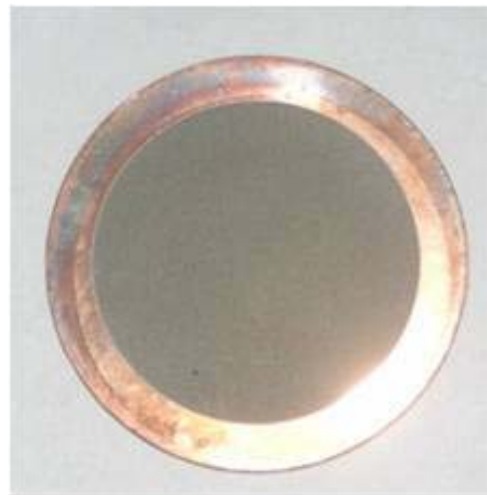


Fig. 4: Tritium or Deuterium Target

High vacuum Turbomolecular pump with rotary pump is used to obtain vacuum in the order of 10⁻⁶ mbar inside neutron generator for its proper operation. Two He-3 detectors and a SSB based neutron monitoring system has been installed for online measurements of neutron yield during operation. These neutron monitors are also used for neutron interlock for safe operation of NG. All important parameters of the neutron generator are controlled and monitored through a computer based centralized system from the control

BARC NEWSLETTER

room. For the safe and reliable operation of the neutron generator, a PLC based interlock system has been incorporated in the facility.

Pulsing of neutron generator

Many applications like fissile material detections, explosive material detection, Keff measurement and dynamic behavior studies of sub-critical system, time of flight measurement require pulse neutron source. For such applications, three different techniques have been developed and installed in the neutron generator to produce pulsed ion beam for pulsed neutron source.

1. Extraction voltage pulsing
2. Beam chopping
3. RF power pulsing

Extraction voltage pulsing

A variable 6 kV extraction power supply has been designed and developed which can be operated in DC as well as pulsed mode. Positive pulse voltage upto 6 kV is applied to probe of RF ion source for extraction of pulsed beam. The power supply can be operated from 1 Hz to 2 kHz repetition rate and 1-100% duty cycle with rise and fall time less than 1 μ S.

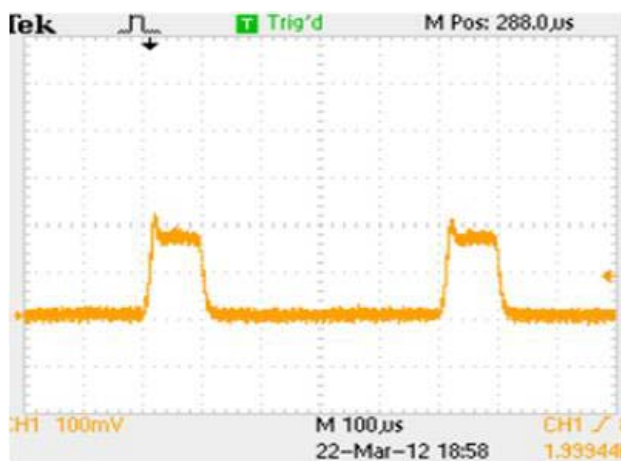


Fig. 5: 100 μ S pulse of deuteron beam by extraction pulsing

Beam Chopping

A specially designed beam chopper has been developed to provide vary accurate beam pulse having rise and fall time in order of 100- 200 nS. It is electrostatic beam

deflector with beam dumper. The beam chopper can be operated at 1kV with 1 Hz to 10 kHz repetition rate and 1-100% duty cycle.

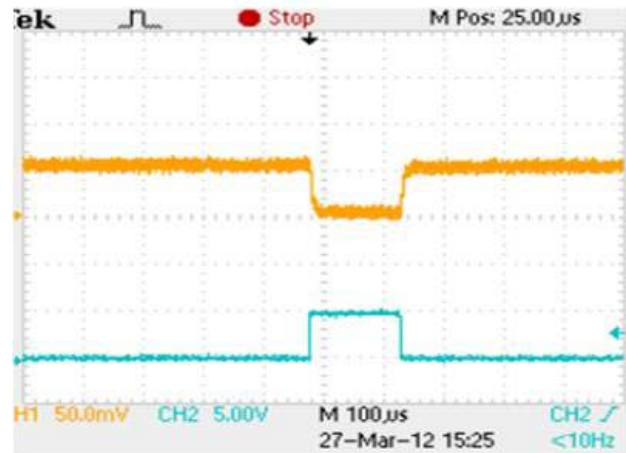


Fig 6: 150 μ S pulse of deuteron beam by beam chopper

RF power pulsing

The easiest way to obtain pulsed beam is to simply pulse the plasma. This can be achieved by modulating the input RF power. Pulsed RF power supply of 13.56 MHz frequency is used to generate the pulsed plasma. Due the limitation of power supply, it can be operated upto 4 Hz with 50% duty cycle.

Transportable neutron generator

Transportable neutron generator is designed and developed for field applications like explosive detection, fissile material detection and waste management applications where neutron yield is required of the order of 10^{8-9} n/s [3]. This deuteron accelerator is similar to

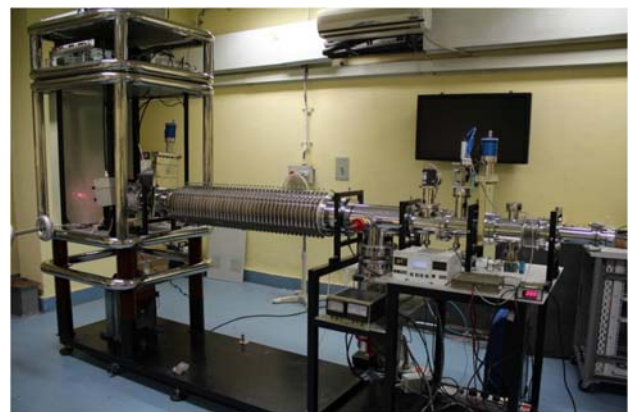


Fig 7: Transportable neutron generator

BARC NEWSLETTER

Purnima neutron generator but designed for 150 kV accelerating voltage. The photograph of the neutron generator is shown in Fig.7. The neutron generator is mounted on a movable trolley to ease maintenance where area is restricted for the occupation.

Compact single gap neutron generator

Accelerator based compact neutron generators are being developed which are capable of producing 10^5 – 10^8 n/s neutrons. The advantage of a compact neutron source Fig. 8 is its small size that makes it suitable for many field experiments and also for various other applications like fissile material detection, baggage inspection for explosive detection, Oil well logging, routine activation analysis etc [4]. Its single gap accelerator which consists an ion source, single and target assembly. The turbo molecular pump constantly evacuates the accelerator. In conventional deuteron accelerator ion source is kept positive floating on accelerating voltage and target at ground potential whereas in this compact neutron generator target is kept at negative 100-125 kV voltage and ion source is kept at ground potential.

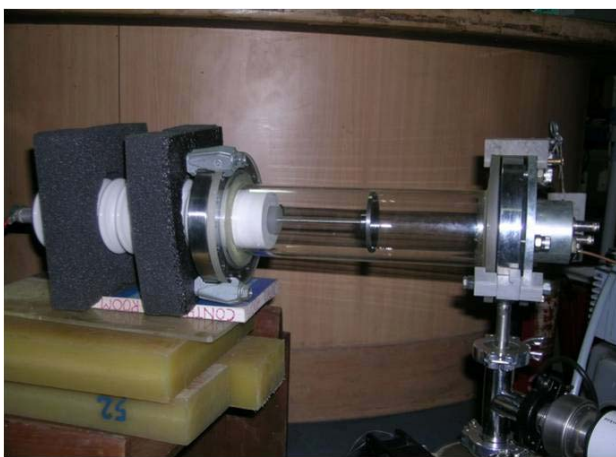


Fig. 8: Compact single gap neutron generator

Conclusion

Purnima neutron generator has been designed and upgraded for safe and reliable operation upto 10^{10} n/s and it is the strongest indigenously developed D-T

neutron source in India. Many experiments have been conducted with this neutron generator by various divisions in BARC. The facility has also been used for experiments of Coincidence and Time of Flight (TOF) measurements using APT technique in collaboration with Padova University, [2] Italy and neutron radiography for VSSC, *Thiruvananthapuram*. At present, PNGF is coupled with India's first sub-critical system. Transportable & a series of compact neutron generators have been designed, fabricated and installed. These generators are under testing for neutron production.

Acknowledgement

The authors would like to thank Dr. Mayank Shukla, Smt. Saroj Bisnoi, and Shri P. S. Adhikari of NXPD for their technical support for development of neutron generators and also conducting the experiments.

References

1. Tarun Patel, Saroj Bishnoi and Amar Sinha "2.45MeV/14 MeV Neutron Generator Facility", , National Symposium on Radiation Physics, November-2009 at MSU, Udaipur, India.
2. Saroj Bishnoi, S.Pesente, D.Fabris, Tushar Roy, P.S.Sarkar, T.Patel, Amar Sinha, G.Viesti, G.Nebbia and S.Kailas "Tagging of D-D and D-T neutrons using Associated Particle Technique at Purnima Neutron Generator facility, India", DAE Symposium on Nuclear Physics, December-2010 at Birla Institute of Technology & Science, Pilani.
3. V. Skorkin, S. Akulinichev, A. Andreev, "The high current deuteron accelerator for the neutron therapy" Proceedings of RuPAC-2010, Protvino.
4. K. N. Leung, "A High Intensity Multi-Purpose D-D Neutron Generator for Nuclear Engineering Laboratories", Report, University of California at Berkeley (2004).

BARC NEWSLETTER

DESIGN, DEVELOPMENT, MAINTENANCE, REFURBISHING, INSTALLATION & COMMISSIONING OF CONTROL & INSTRUMENTATION FOR RESEARCH REACTORS

Parag Punekar, N. Ramkumar, Kallol Roy, M.D. Darbhe and G. Bharadhwaj
Research Reactor Maintenance Division

Shri Parag Punekar is the recipient of the DAE Young Engineer Award for the year 2011

Abstract

The Control & Instrumentation (C&I) Systems in Research Reactors have to be designed, developed maintained & upgraded in a systematic, reliable & effective manner. The entire cycle involves conceptualization of various Control & Instrumentation systems, making system requirement specifications, detailing the concept, design, fabrication, creation of test facilities, testing, validation of system performance, preparation of various documents for the regulatory safety clearances, installation & commissioning of the systems after fine tuning the design for performance. Various C&I upgrades are required for enhancing safety, to mitigate obsolesces, simplification, improved O&M features & import substitute. Executing C&I upgrade projects in operating research reactor pose constraints of high safety requirements & limited time, that necessitates long term planning & implementation strategies based on innovative ideas & careful use of the best available technology. This paper provides technical information on development & implementation of C&I systems for the research reactors with improved diagnostics, operator interface & O&M features and the commissioning experience.

Keywords: Research Reactors, C&I Systems, Dhruva, Critical Facility

Introduction

A Research Reactor is regarded as a fundamental prototype for functional evaluation of all aspects of nuclear science and technology. From validating a code design, evaluating nuclear performance of fuels, studying the thermal hydraulic aspects of energy removal, validating estimated flux profiles, etc. In addition there are various engineering & technology issues, pertaining to metallurgical study of in-core components, flow induced vibrations, performance evaluation of heat exchangers, instrumentation, control techniques, detector development, etc. Effectively all major branches of engineering and applied aspects of physical sciences are encompassed under one single unit — a research reactor.

Control & Instrumentation of Research Reactor consist of different systems, instruments and equipments required for monitoring different parameters, controlling of various processes and provide protection for the reactor. C&I facilitate the normal operation of the plant & provide the operator all the information required to take necessary action for an optimal, reliable & safe performance.

The C&I requirements of Research Reactors are far more complex and diverse in nature than those of a conventional plant. There are several reasons viz. higher safety, availability, non-accessibility of reactor areas during operation of the reactor, challenges arising due to technological advances & obsolesces etc. Considering all these, the design & deployment of C&I systems of

BARC NEWSLETTER

research reactors are based on the design philosophy of simplicity, redundancy, adherence to single failure criteria, fail safe philosophy, common mode failure criteria, facilities for in situ testing, use of proven systems, use of qualified systems (environmental, seismic and LOCA qualification for appropriate systems) and ease of operation and maintenance.

This paper provides comprehensive technical information on recent development & implementation of C&I systems for the research reactors located at BARC, Mumbai.

Control & Instrumentation Systems for Critical Facility

The Critical Facility is a low power research reactor with built in design features which allow arrangements of fuel rods, SORs and experimental assemblies in the variable lattice spacing to simulate different core configuration as per the requirements of various reactor physics experiments for AHWR and 500 MW PHWRs. Maximum power can be achieved is 500W and the core neutron flux is 10^{19} nv. This is a manually controlled reactor where in reactor power is varied by varying the inventory of heavy water used as moderator in reactor vessel. Nitrogen is used as a cover gas for heavy water system.

The neutronic channels for monitoring nine decades of neutron flux from 10^0 nv (fresh core) to 10^9 nv (100% Full Power) independent source, intermediate and power range instrumentation with required overlaps have been developed. The important aspects, like safety, reliability, convenience of operation, ease of maintenance etc. are specifically taken care of in the design. A new type of nuclear channel Log-Linear channel with all the in-situ test facilities was designed for the use in regulation and protection system. An extensive testing of nuclear detectors and channels has been carried out. The details of the nuclear channels & detectors are as follows:

The Start Up Logic System (SULS) is provided for startup permissive for the reactor. The transition from the 'reactor tripped' state to desired power level is accomplished through a set of operation which is to be performed from the control console in a certain

sequence. These operations will not be effective unless certain conditions which are validated by SULS. SULS permits the raising/lowering of SORs in a predetermined sequence & generates an 'SOR out of sequence' alarm whenever operations of raise/lower are done in out of sequence. SULS also generates few time-related trips and alarms, when demanded for, to indicate the performance of shut down devices. SOR Motor Drive Interlock & Phase Sequence Detection and SOR Out of Sequence Raise Facility (OOS) for in-pile testing of a selected SOR is also engineered & deployed.

The primary shutdown system consists of six shut-off-rods with cadmium absorber. During reactor operation they are parked out of core at a fixed elevation and held there by electromagnetic clutch in the shut-off-rod headgears. The protection action is through relay logic, wired in two independent groups for the trip parameters (Group-1 & Group -2) in order to provide two diverse chains of protection action. Each group is capable of independently tripping the reactor. The design also ensures reactor trip, due to one or more parameters in one group resulting in de-energisation of trip relays on the other group. The system is given 48 Volts class-I DC supply and the relays are kept energized during normal conditions. Moderator dumping is also incorporated in the protection system, as a backup protection action, whenever any one of the main group trip relays is in de-energized state. Based on earlier experience with plastic encapsulated relays where the contact resistance degrades due to dust entry, epoxy sealed relays have been used. Check Scram Facility for functional validation of all reactor trips through a test push button on control console which actuates respective relays in protection system is deployed.

Functional tests were carried out for all fabricated Nuclear Channels, Start Up Logic, Alarm Annunciation System, Digital Recording System etc. Climatic tests consisting of dry heat, dry cold and two cycles of damp heat tests are done for PCBs, control cables, electromagnetic relays. Endurance tests like drop, bump and vibration are done on relays to be used in protection system, as per relevant JEE standards. The control room panels and local panels are designed to meet applicable seismic requirements.

BARC NEWSLETTER

Functional tests were carried out on all the nuclear channels. These channels were subsequently kept ON for a continuous operation (burn-in test) to observe their performance. As for the DC channels, measurement accuracy at very low current signal is very important. It was confirmed that the developed DC channels can measure upto 2pA. Further the DC channels were tested at the maintenance laboratory at TAPS-3&4. Subsequently the channels along with the detectors were tested at a calibration facility at RSSD, BARC. Due consideration was given for integrated testing these channels considering gamma field that was estimated at detector location. To evaluate the sensitivities of the detectors and response of the nuclear channels, integrated testing at Apsara reactor was carried out. As the detectors used for the start up range are B-10 lined counters, to observe the effect of gamma field on its performance, the testing was carried out at RSSD. It was verified that there are no changes in the operating characteristics up to 100R/hr.

Finite Impulse Testing (FIT) System for Emergency Cooling System (ECS) in Dhruva

Finite Impulse Testing (FIT) system for Emergency Cooling System (ECS) is used to check healthiness of ECS logic circuits in an online mode. The ECS is an important safety system that ensures the cooling of reactor core during shutdown state of Main Coolant Pumps (MCPs), and hence FIT-ECS that monitors the health of ECS logic circuits in an online (real time) mode is an important part of it. Based on a Safety Related Unusual Occurrence in ECS system due to the malfunction of its earlier single channel FIT system, the new FIT-ECS system has been designed with new features and is commissioned.

The FIT-ECS system feeds the simulated input signals (fine impulses of nominal width 575 μ S) to the ECS logic circuits and read the outputs. These output (predicted) signals from ECS logic circuit are processed in the FIT-ECS system and in event of any discrepancy, the FIT-ECS system displays fault signature on local panel, detailed information of the fault on a PC based Operator Console (OC), and generates an alarm "ECS Logic Fail" in the control room. FIT-ECS also monitors the inputs

and outputs of ECS logic circuit. All the information required is stored as a database that can be subsequently displayed in various formats.

ECS system is designated as Category I-A system and is a hardwired system & FIT-ECS monitors the healthiness of the logics of the ECS System is a computerized system. As per IEC 61226, FIT-ECS is categorized as Category I-B system.

The FIT-ECS system uses standard microcomputer board family designed by RCnD and manufactured by ECIL. Design philosophy was adapted for easy maintainability reduction in PCB cost and component availability. The FIT-ECS hardware was manufactured at ECIL. Climatic testing on the representative board of FIT-ECS system was carried out successfully at ECIL as per CSG: STD: 203 which is based on IS9000. Subsequent to the module testing and individual channel testing, three channels of FIT-ECS system were interconnected and integrated testing was carried out as per approved test plan with the help of ECS simulator. The three channels of FIT-ECS were integrated and tested along with the ECS simulator for more than 5000 hours, partly at RCnD and at RRMD after shifted to the site (Dhruva).

The final integrated test of all the three channels as per approved test plan was completed and detailed test report was submitted to safety committees. Subsequently after the review of FIT-ECS design, documents and test results safety committee recommended Commissioning of FIT-ECS channel-A as per procedure submitted. Based on the satisfactory performance of the channel-A for the period of two months Channel-B & Channel- were commissioned during monthly schedule shutdowns.

Up-gradation of Dhruva Main Control Room (MCR)

The MCR of Dhruva had been designed in the late seventies, where a predominance of pneumatic instrumentation in the field necessitated the usage of a large number of pneumatic recorders & indicators. The Main Control Room of Dhruva has a total of nine panels, A, B, C, D, E, F, G, H & I, of which the central three panels, D, E, F house the plant mimic. While, the

BARC NEWSLETTER

indicators & recorders of most of the process parameters are positioned on the first three panels, the indicators & recorders for channel temperature & other nuclear parameters are positioned in G,H,&I panels. Since there is a plan to progressively replace many of the pneumatic transmitters (pertaining to various process system instrumentation), to electronics, there would be need to replace many of the pneumatic indicators & strip-chart recorders, mounted on the panel fascia and replace the same with multi-input chartless recorders. In addition, as a consequence of the C&I upgrades, whereby the Operator Consoles (OCs) of the entire proposed computer based systems, need to be mounted on the MCR panels, some of the control room panels required changes.

For the upgrade of the Dhruva MCR panels, the preliminary design requirements for a control room, viz. functionality, ergonomics & aesthetics, had to be weighed against the constraints of a retrofit job along with the need to maintain operator familiarity. Considering this, the aim was to replace the panels A, B, C, G, H&I, housing the indicators & recorders, and retain the three mimic panels, D, E, & F. The upgrade design considered complete replacement of the A,B,C and G,H, I panels with chartless recorders & Operator Consoles (for the embedded systems) in panels A,B,H & I (for display & recording of the existing parameters) and large-size screens in panels C (for CC-TV) &G (for display of fuel channel matrix).

The replacement of all the six panels was completed in six campaigns (during monthly shutdowns) as per approved commissioning procedures. Provision of temporary instrumentation was made for monitoring important parameters and keeping the safety interlocks & critical alarms effective during each panel replacement.

Up-gradation of Control & Instrumentation of Fuelling Machine-A of Dhruva:

Fuelling machine-A (FM-A), is used to handle heavy water cooled assemblies of Dhruva Reactor. Owing to

obsolescence of various C&I components, increasing O&M and other related problems, for better operator interface, upgrade of the C&I of the FM-A was initiated & completed. Considering the functional requirements and human machine interface requirements, the control console has been upgraded / modified. The mimic panel, all the switches and push buttons, relays and timers are replaced. DC power supplies are replaced with dual redundant supply. A new microcontroller based Beetle Monitoring Unit, Alarm Annunciation System & Fire detectors are provided. A microcontroller based Extractor position indication system (ELIS) that senses extractor position using multi turn absolute encoder is developed along with CnID, & is commissioned.

Up-gradation of Dhruva Control & Instrumentation:

The existing C&I systems of Dhruva have been designed in the late seventies and are facing not only obsolescence but have limited diagnostic features. As upkeep of these systems with limited spares inventory, is becoming increasingly difficult and the expected life of C&I systems is typically twenty years, it has been considered to upgrade some of the important C&I systems in Dhruva, viz. Coolant Channel Flow Monitoring System & Trip Logic System (termed as the Reactor Trip Logic System (RTL), Start-up Logic System (SULS), Alarm Annunciation System (AAS) & ECCS Instrumentation Logic (ECCS-IL) using newly developed VME bus-based family of microcomputer boards by RCnD . The full scale systems for RTL, SULS, AAS & ECCS-IL were setup at RCnD and exhaustive testing was carried out at RCnD as per the System Validation Procedure. After successful testing and validation of the system at RCnD, RTL & AAS have been shifted to Dhruva & one of the Channels of RTL is commissioned for the performance feedback.

Upgradation of Dhruva Radiation Monitors:

Up-gradation in the instrumentation of Failed Fuel Detection System by enhancement of signal level from the detector by using a detector with higher sensitivity, changing the range of FFD-instrumentation from six

BARC NEWSLETTER

decades to three decades for better resolution were completed. This is of paramount importance considering release of a very low order of fission products activity for detection in case of fuel failure. The development of a microcontroller based Neutron REM Monitor with diagnostic & customized features were initiated along with Electronics Division. The environmental, Seismic, EMI and source calibration test for these units have been carried out following which the units have been installed in research reactors.

Conclusion

The original reactor C&I system of Dhruva reactor was developed in the late seventies. Even if the original C&I system completely met the demands that were put on it, its technical design is becoming fast obsolete. There older technology presents difficulties with maintenance due to a lack of spare parts. Furthermore, to adhere to some new demands on quality and qualification it was

decided to upgrade the existing C&I systems. Compared to the old system, the new C&I system provides better testability and maintainability and uses up-to-date technology in both the hardware and the software. The most important experience during the C&I upgrade & its implementation has been the significance of the complete, correct and unambiguous requirements and the thorough testing of safety and operational features of the upgraded safety system within real reactor conditions. Our experience & collective wisdom has shown that C&I modernization and refurbishment programmes for research reactors must be a continuous activity where small steps must be taken to improve the performance of the reactor with moderate budgets and shorter shutdown periods rather than very extensive refurbishment programmes that require large sums and long shutdown times. However, very well-planning and skilful management of the activities are the essential ingredients for successful implementation methodology.

BARC NEWSLETTER

RARE EARTH BORIDES SYNTHESIS BY REDUCTION DISTILLATION

Abhishek Mukherjee, Uttam Jain, Sanjay Kumar and Nagaiyar Krishnamurthy
Fusion Reactor Materials Section, Materials Group

Dr. Abhishek Mukherjee is the recipient of the DAE Young Engineer
Award for the year 2011

Abstract

A reduction-distillation process was used in the synthesis of borides of lanthanum, neodymium and yttrium. The process involves heating rare earth halides (chlorides or fluorides) with boron and/or aluminium in the range of 1000-1200°C under dynamic argon flow. Borides are formed on reduction of halides and the reduction products are separated *in-situ* by distillation. The thermodynamic basis of the process and experimental results on practical application to the synthesis of borides of selected rare earths are presented in this paper.

Keywords

Borides, oxychlorides, reduction-distillation, borates

Introduction

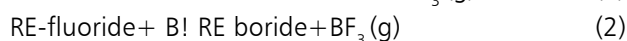
Borides of rare earth metals have attracted attention due to their unique combination of physiochemical properties especially at elevated temperatures¹⁻². Presently, the industrial production of the rare earth borides is limited by the difficulty in preparing a product of satisfactory purity by a process that may be extended to an industrial scale. A common method of synthesis of these borides is by reaction of elemental metal and boron³. It is also well known to prepare boride by reducing oxide by means of boron carbide or elemental boron, under reduced pressure⁴⁻⁷. However, the reaction is carried out at elevated temperatures (1600-1800°C); this not only mandates use of a graphite crucible, but also a high temperature furnace. Many rare earth borides have also been prepared by fused salt electrolysis techniques⁸. However fused salt electrolysis presents the usual problem of recovering the rare earth boride at the cathode, which entails a problem of contamination.

Use of pure metals is expensive and may not always be essential. Use of boron carbide and carbon as reducing

agents may lead to carbon contamination in final boride and fused salt electrolysis involves handling corrosive salts at high temperatures. Techniques which involve leaching operations after reduction can contaminate the final boride product if the byproduct of reaction is not properly removed. It is however quite attractive to have some products of reactions in vapour form so that they can be removed by distillation as in Pidgeon process or in lanthanothermic reduction. An innovative process was reported for the preparation of rare earth borides where the other product of reaction is a gas⁹⁻¹⁰.

In the present paper, synthesis of rare earth borides (namely lanthanum, yttrium, neodymium) by such a reduction-distillation technique is discussed.

Reaction processes (1) and (2) shown below were used to prepare the borides:



(RE: rare earth). Mixtures of rare earth chloride or fluorides with boron and/or aluminium were prepared

and heated at temperature ranges of 1100-1200°C in a flow of pure argon. AlCl_3 and BF_3 are gases at these temperatures. It is carried away by the gas sweep, leaving behind pure rare earth boride product. The choice to use chloride or fluoride as starting materials for the reduction-distillation reaction depends on the respective vapor pressure of the rare earth halide.

Thermodynamics of the reduction distillation process

Fig. 1 shows the variation of free energy changes for all possible reactions (for chlorides) drawn using Factsage 6.1 module using its FACT 53 databases; wherein the data for LaB_6 ¹¹ was entered separately in the FACTSAGE. The free energy data for other borides in this study are not reported in open literature. In this situation, we have assumed the free energy of YB_6 , NdB_6 to be similar to LaB_6 .

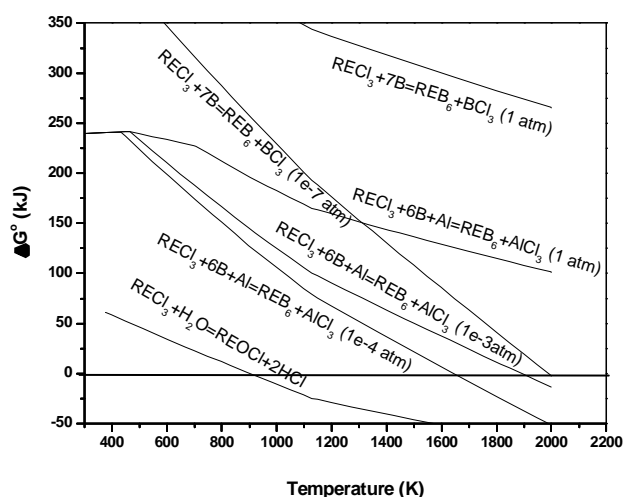
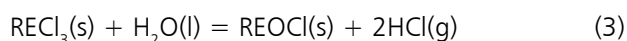


Fig. 1: Free energy of formation of different reactions used in this paper at various pressure

Fig. 1 indicates that the presence of water in the reactants favors the formation of rare earth oxychloride by reaction (3).



Rare earth oxychlorides are very stable compounds and they tend to form more for lighter rare earths. Thus it is important that the starting chloride should either be completely anhydrous and that dehydration of the chloride is completed at lower temperatures. From

Fig. 1, it is evident that addition of Al to chlorides lowers the free energy of reaction, and that the reactions would only occur under reduced pressures.

For YB_6 preparation, it was seen that the vapor pressure of yttrium chloride, is nearly two order of magnitude compared to neodymium chloride and lanthanum chloride in the operating temperature of 1300-1500K (1000-1200°C). Hence, for the preparation of yttrium borides, yttrium fluoride was used as a starting material and reaction (2) was used to prepare the boride. Yttrium fluoride is quite stable and has low vapor pressure. Boron fluoride being a gas at all temperatures was swept away to form the borides. Aluminium for fluoride reaction lowers the free energy of reaction (2), however it requires a temperature beyond 1300°C to distill off AlF_3 , hence only boron was used as reducing agent for fluoride reduction.

Experimental

The starting powders used were as prepared hydrated LaCl_3 , NdCl_3 and YF_3 (Indian Rare Earths make). All the chlorides are hexahydrates, hence before use, these were vacuum dehydrated. The anhydrous chlorides were mixed with 99.99% pure aluminum powders (average particle size 28.64 μm) and technical grade amorphous boron powder (average particle size 10 μm of 95-97% purity) in stoichiometric amount as per reaction (1) and placed in molybdenum boats. For YB_6 preparation, YF_3 was mixed with boron as per reaction (2). These mixtures were then heated at 1200°C in a superkanthal furnace under high pure argon flow of 100ml/min.

Results and Discussions

Experiments for LaB_6 preparation using reaction (1) as reported by us previously⁹, showed that the boride formation only occurred after 1000°C. Similar phenomenon was observed for NdB_6 preparation. The XRD of the as prepared LaB_6 (PCPDF: 340427) and NdB_6 (PCPDF: 110087) are shown in Fig. 2. It can be seen that all the peaks correspond to the borides with no presence of impurity peaks.

BARC NEWSLETTER

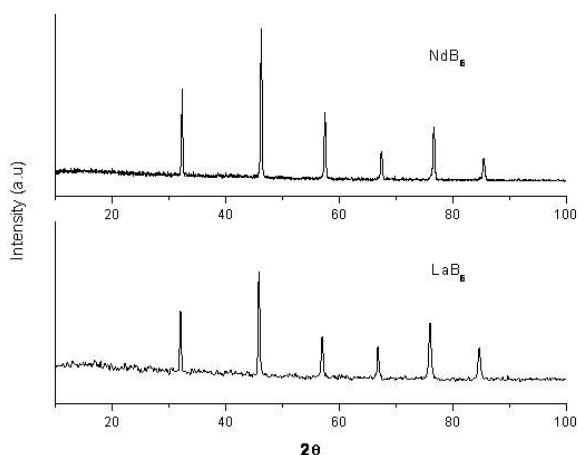


Fig. 2: XRD of as synthesized NdB_6 and LaB_6

As the starting materials of these borides were hydrated chlorides, it was ensured that the starting chlorides were water-free, as the presence of water initiated the formation of LaOCl and NdOCl , which further did not react with Al and B to yield borides. For successful runs, the dehydration schedule (as described in experimental) was done *in situ* followed by the reduction. Synthesis of single phase YB_6 using reaction (2) was not possible. A slight presence of oxygen in system (residual oxygen in pure argon) was sufficient to oxidise the yttrium boride and instead some borates were also formed. The product obtained on boride reduction of yttrium fluoride is shown in Fig. 3. It could be seen that apart from the presence of YB_6 (160732) presence of YOF (060347) and YBO_3 (741929) was also seen. The oxyfluoride was initially present in yttrium fluoride, and as unreacting was expected to be present in the final

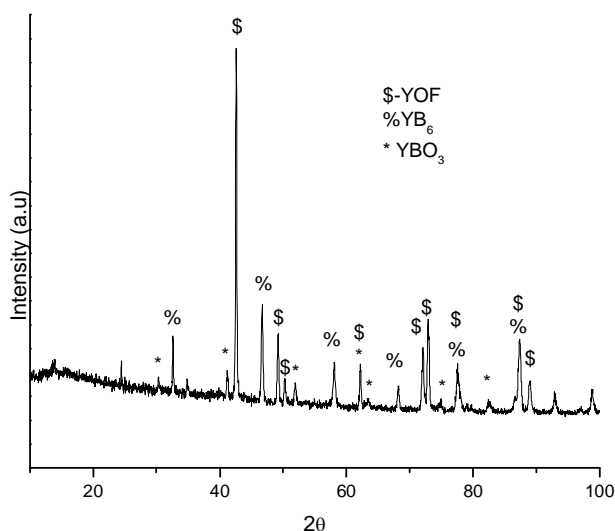


Fig 3: XRD of as synthesized YB_6

product. The borates had formed from oxidation of YB_6 by reaction (4)



B_2O_3 being a glassy phase could not be detected in XRD (Fig. 3).

Conclusions

A novel reduction-distillation technique was used to prepare borides of rare earths lanthanum, neodymium, and yttrium. Lanthanum and neodymium borides could be successfully prepared without any presence of impurity phases. Yttrium hexaboride was seen to be highly oxidation-prone. The reaction yielded borates along with borides. The starting chlorides and fluorides must be free of oxyhalides, as these do not participate in the process and remain as impurities in final borides.

The above work was presented by the authors at the 18th Plansee Seminar held at Reutte, Austria from June 3-7, 2013.

References

1. Brewer, L.; Sawyer, D. L.; Templeton, D. H.; Dauben, C. H., A Study of the Refractory Borides. *Journal of the American Ceramic Society* **1951**, 34, 173-179.
2. Mori, T., Novel physical properties of rare earth higher borides *J. Phys.: Conf. Ser.* **2009**, 176, (01), 2036.
3. Paderno, Y. B.; Ivanchenko, L. A.; Bessaraba, V. I.; Vereshchak, V. M., Preparation of lanthanum hexaboride films by synthesis from the elements. *Powder Metall. Met. Ceram.* **1975**, 14, (6), 515-516.
4. Zheng, S.; Min, G.; Zou, Z.; Wang, X.; Han, J., Synthesis of LaB_6 powder by reaction in La_2O_3 - B_4C system. *Acta Metallurgica Sinica* **2001**, 37, (4), 419-422.
5. Zhang, M.; Yuan, L.; Wang, X.; Fana, H.; Wang, X.; Wu, X.; Wang, H.; Qian, Y., A low-temperature route for the synthesis of nanocrystalline LaB_6 . *J. Solid State Chem.* **2008**, 181, (2), 294-297.

BARC NEWSLETTER

6. Kuzenkova, M. A.; Kislyi, P. S., Preparation of zirconium diboride. *Soviet Powder Metallurgy and Metal Ceramics* **1965**, 4, (12), 966-969.
7. Sonber, J. K.; Murthy, T. S. R. C.; Subramanian, C.; Kumar, S.; Fotedar, R. K.; Suri, A. K., Investigation on synthesis, pressureless sintering and hot pressing of chromium diboride. *International Journal of Refractory Metals and Hard Materials* **2009**, 27, (5), 912-918.
8. Zubeck, I. V.; Feigelson, R. S.; Huggins, R. A.; Pettit, P. A., The growth of lanthanum hexaboride single crystals by molten salt electrolysis *J. Cryst. Growth* **1976**, 34, (1), 85-91.
9. Mukherjee, A.; Gulnar, A. K.; Sahoo, D. K.; Krishnamurthy, N., Gas solid techniques for preparation of pure lanthanum hexaboride. *Rare Metals* **2012**, 31, (3), 285-289.
10. Alain, I.; Patrick, M., Preparation of rare earth borides patent no 07/341809. In USA, 1991.
11. Peshev, P., A Thermodynamic Analysis of Lanthanum Hexaboride Crystal Preparation from Aluminum Flux with the Use of Compound Precursors. *J. Solid State Chem.* **1997**, 133, (1), 237-242.

BARC NEWSLETTER

MATHEMATICAL MODELING OF NUCLEAR SYSTEMS

Raj Kumar Singh, A. Rama Rao
Reactor Engineering Division

Shri Raj Kumar Singh is the recipient of the DAE Young Engineer Award for the year 2011

Introduction

One of the most important advantages of having a mathematical model of a process is that one can experiment with the model rather than the process. Invariably the experiments with the model are best done on a computer. The power of modern computers allows extensive simulations with even very complex models to be done quickly once the model has been programmed. Computer models can often be used to indicate what additional data would be beneficial for refining an existing model to make it more realistic and more useful.

We see the dark clouds, which we equate with imminent rain; we calculate that we can cross the road before the oncoming car reaches us; we choose the fastest moving queue in the supermarket. We don't normally formulate equations for these models and often it wouldn't be useful to anyway. However, there are many processes for which it is very worthwhile to develop explicit mathematical models. Such models are most often used in scientific research to understand how processes work. If there is a process involved, then it can be modeled; if there are significant benefits associated with the process then a key question for the process is how can the process be made more efficient. It may be that the best way to answer that question is to model the process and experiment with the model.

An attempt was made to arrive at mathematical solution to some of the complicated processes and phenomenon that were not fully comprehended. The paper gives highlights of the findings and how mathematical modeling helped in understanding the process more clearly.

Theory of flow pattern prediction in perforated tubes

Perforated tubes are widely used in nuclear industries for many critical process and regulatory purpose. In pressurized heavy water reactors (PHWRs), perforated tubes are used in moderator system, in shutdown system for poison injection and in reactivity mechanism for housing the safety bank inside the core. In the moderator system and in poison injection loop the flow of fluid through perforated tubes match the requirement of the system. The design of perforated tube involves arriving at the size of the holes, its spacing along the length and in the circumference. For PHWRs, the design was achieved by rigorous experimentation.

Through computational methods by solving 3-D Navier Stokes equations, outflow pattern can be predicted for given perforated tube. But, if some flow pattern is needed and perforated tube is to be designed to meet the requirement, CFD method cannot be directly used. CFD methods can predict flow when geometry is known, but cannot easily configure the geometry for a given flow.

So it becomes important to develop theories to study outflow pattern and predict perforations (hole size and pitch variations with length) needed for the desired flow pattern. The model offers an analytical method

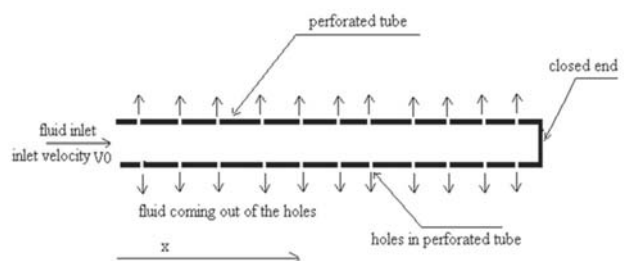


Fig. 1: Simplified illustration of a perforated tube.

BARC NEWSLETTER

required in arriving at the design of perforated tubes that can meet the end objective.

Flow pattern in perforated tubes is modeled by mass and momentum balance. It leads to a nonlinear differential equation whose general solution is obtained. Flow pattern is predicted by this solution. Variation of discharge velocity with length, for tube with uniform hole with equal pitch is shown in Fig. 2. It shows that more water flows out from the holes at the closed end and less flows out from holes at the entry of the tube.

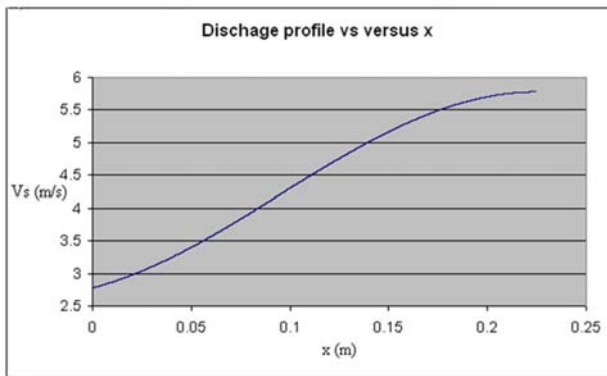


Fig. 2: Profile of discharge (V_s) along the pipe.

These results were compared with simulated experiments and a close match was observed. Furthermore, hole size distribution along the length for desired flow profile was also estimated by proposed theory.

The Study of water ingress phenomena in melt pool cool ability

During a postulated severe accident, the nuclear reactor core can melt and the melt can lead to failure of the reactor vessel. Subsequently, the molten corium can be relocated in the containment cavity, forming a melt pool. The melt pool can be flooded with water at the top for quenching it. However, the question arises in mitigating severe accident is to what extent water can ingress to quench the melt pool. To reveal that, a model was proposed based on the physics of the process. This work is seen as first attempt to model this phenomenon from basic principles, previous modeling were mostly relying on correlations.

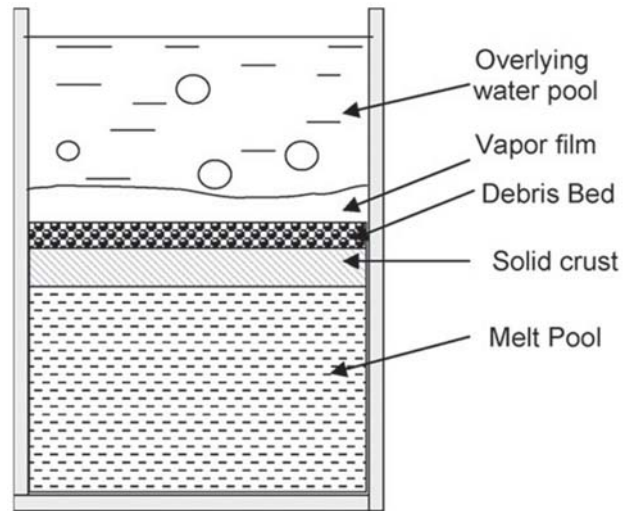


Fig. 3: Schematic of the melt pool with water overlayer considered in the analysis

A computer code MELCOOL was developed based on proposed model. The code considers the heat transfer behavior in axial and radial directions from the molten pool to the overlying water, crust generation, its growth; thermal stresses built-in the crust, disintegration of crust into debris, natural convection heat transfer in debris, molten pool and water ingress into the debris bed.

Phenomena of reverse momentum pulse and fluid leak after poison injection in the shutdown system of PHWR

The secondary shut down system (SDS-2) of 540 MWe PHWR, Tarapur consists of poison tanks connected to perforated injection line in the Calandria. A high-pressure helium circuit connected to the top of the poison tanks provides the required energy for instant injection of poison into the moderator. A polyethylene ball floats on the poison in the tank. When SDS-2 is activated, the high-pressure helium gas pushes the ball and the poison gets injected in Calandria via connected pipes. The ball remains seated at the bottom of the tank after pushing the poison to prevent helium entry into the Calandria.

During the commissioning of secondary shut down system of 540 MWe PHWR in Tarapur, multiple pressure pulse were observed at the inlet pipes, after the poison was injected into the Calandria. On a closer analysis of the data captured during injection, it was observed that

BARC NEWSLETTER

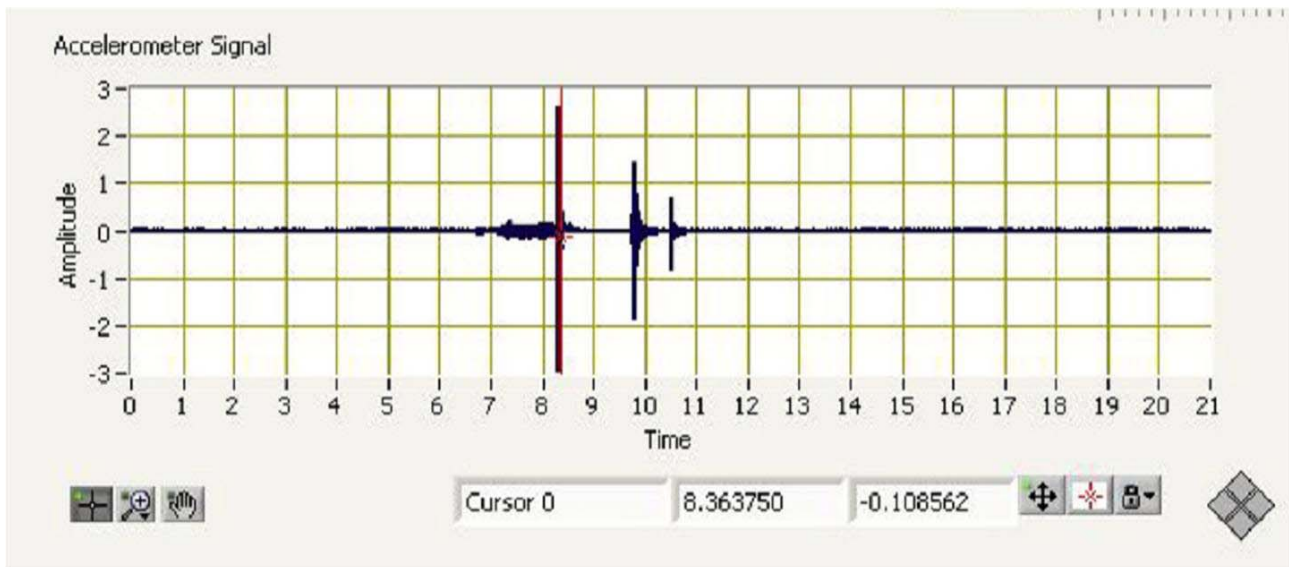


Fig. 4: Vibration signal showing multiple impacts after the injection

after the injection of poison into the Calandria, a strong pressure wave manifests in the loop in the reverse direction moving from Calandria to poison tank. The confirmation of the reverse pulse was seen in the vibration signals from the tank as shown in Fig. 4.

Effort has been made to explain the phenomena by solving the governing equation for fluid flow in piping. The arrival time of the reverse pressure pulse and its intensity has been analytically estimated and compared with measured experimental data.

The possible interaction between the pressure pulse and the ball in the tank has been explained based on experimental data. The concept of minimum residual

poison to be maintained in the tank after the injection in order to avoid leakage of gas into the Calandria, due to the action of reverse pulse on the ball, has been explained.

5.0 Conclusion

Mathematical models are not reality. The real world is often far more complex than a mathematical model used to simulate it, and so that is a limitation. However, often a mathematical model (if correct) can reasonably predict behavior for a system and can help to validate mechanisms in physical processes. Through the above examples, an attempt has been made to show how mathematical modeling helped in understanding the physics behind the complicated processes.

BARC NEWSLETTER

CRYSTAL GROWTH AND MORPHOLOGICAL STUDY OF ADU AND ITS CALCINED PRODUCT

Subhankar Manna and Saswati B. Roy

Uranium Extraction Division

and

Jyeshtharaj B. Joshi

Homi Bhabha National Institute

Shri Subhankar Manna is the recipient of the DAE Young Engineer Award for the year 2011

Abstract

Ammonium diuranate (ADU) and its calcined product uranium oxides (UO_3) are important intermediates for nuclear fuel production. The morphology and Particle Size Distribution (PSD) of ADU powder produced at various stages of precipitation have been observed to study the particle growth of ADU. It has been observed that the ADU particles are basically agglomerates of submicron platelets. The microstructure of ADU is retained in UO_3 even after calcination. Effect of calcination temperature has been studied on tap density, surface area, porosity, O/U ratio and morphology of uranium oxides. It has been observed that O/U ratio, bulk density and tap density of the uranium oxide are reduced with an increase in temperature. Surface area and porosity increase with temperature, pass through maxima and then reduce. These observations have been explained using high resolution SEM.

Introduction

Ammonium diuranate (ADU) and UO_3 are important intermediate compounds in nuclear fuel industries. The production process and properties of UO_2 (power reactor fuel) and uranium metal (research reactor fuel) largely depend upon the characteristics of ADU and UO_3 . The name ammonium diuranate (ADU) has been given to the insoluble product of reaction between gaseous or aqueous ammonia and solution containing uranyl (UO_2^{2+}) ions. However, according to investigations [1-6], the compound precipitated from aqueous solutions does not have the exact composition $(\text{NH}_4)_2\text{U}_2\text{O}_7$, even in the presence of a large excess of ammonia. Several workers [7-11] have reported how the properties of ADU affect the properties of uranium oxide fuel as well as uranium metal fuel. Doi and Ito [7] presented that the ADU precipitate usually consists of elementary particles, primary and secondary agglomerates. However, practically no information is

available in the published literature regarding the morphology and particle growth of ammonium diuranates at different stages of precipitation. Woolfrey [12] reported that the thermal decomposition during calcination occurs in several stages: initially water and ammonia are released and then at higher temperature U_3O_8 is produced by self reduction by ammonia retained within the solid. Das [13] reported reduction of surface area at 650°C onwards due to sintering.

Experimental

Ammonium diuranate (ADU) was produced by the reaction of uranyl nitrate and ammonia mixed with air at the ratio of 1:10. To study crystal growth of ADU powder, samples (aliquot) were withdrawn after regular intervals [14]. Ammonia was fed through sparger until pH of the solution reached to 7. The slurry was then filtered under vacuum using the Büchner funnel and 542 grade Whatman filter paper. The cake obtained

BARC NEWSLETTER

was then washed and dried in an oven at 100 °C for 4 h. The dried cake was calcined in a muffle furnace at the temperatures of 450 °C, 550 °C, 650 °C and 750 °C for a period of 2.5 h [15].

Results and discussion

Variation of pH of the solution and uranium concentration in the filtrate with time is shown in Fig. 1. It shows that there is a flat zone in the pH curve

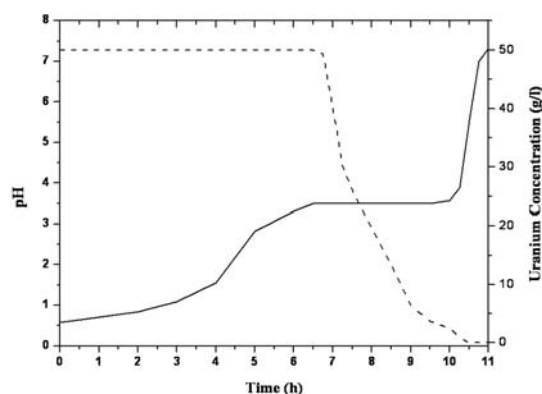


Fig. 1: Change of pH and uranium concentration in filtrate with time.

and most of the precipitation reaction occurs during the period which is indicated by substantial decrease in uranium concentration. The same conclusion was drawn from the study of change in optical density of the samples collected after regular interval during precipitation [14].

Morphology of ADU has been observed using high resolution 'Scanning Electron Microscope' (SEM) and 'Transmission Electron Microscope' (TEM). Fig. 2 shows that morphology of ADU (obtained at pH 7). It basically consists of primary platelets of 250-500 nm width and of 500-1000 nm length. These primary platelets form primary agglomerates. These agglomerates look like woolen balls or cauliflower and primary agglomerates are also connected with each other to form secondary agglomerates. The TEM picture (Fig. 3a) for ADU also confirmed the plate like structure of the final ADU produced in gaseous route. The selected area diffraction (SAD) pattern of ADU (Fig. 3b) indicates that the ADU particle is made of agglomerates of both nano-crystals and larger crystals. The nanocrystals produce ring pattern whereas larger crystals give bright spots.

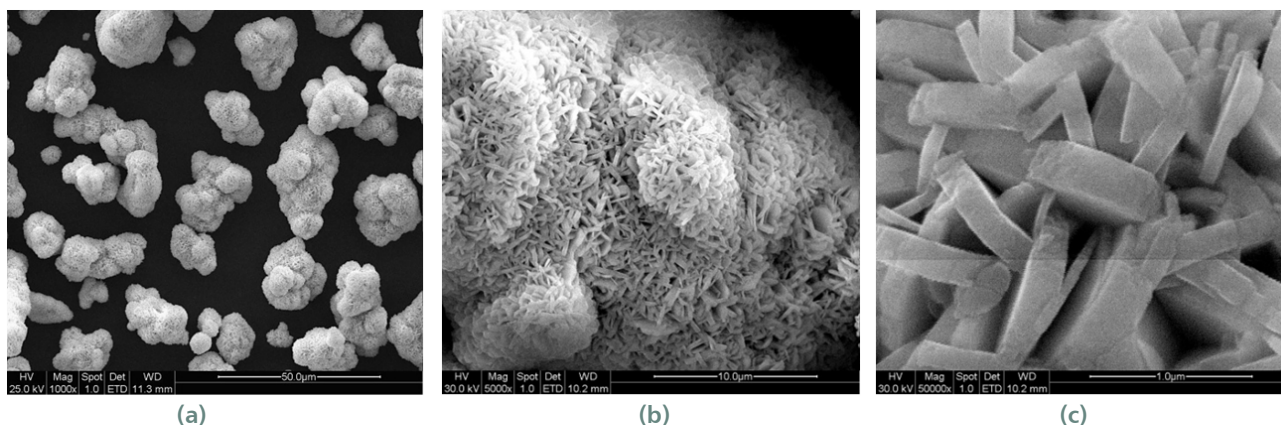


Fig. 2: SEM images of final ADU at different magnifications a)500X, b) 5000X c)50000X



Fig. 3: TEM images of final ADU a) microstructure, b) selected area diffraction pattern

BARC NEWSLETTER

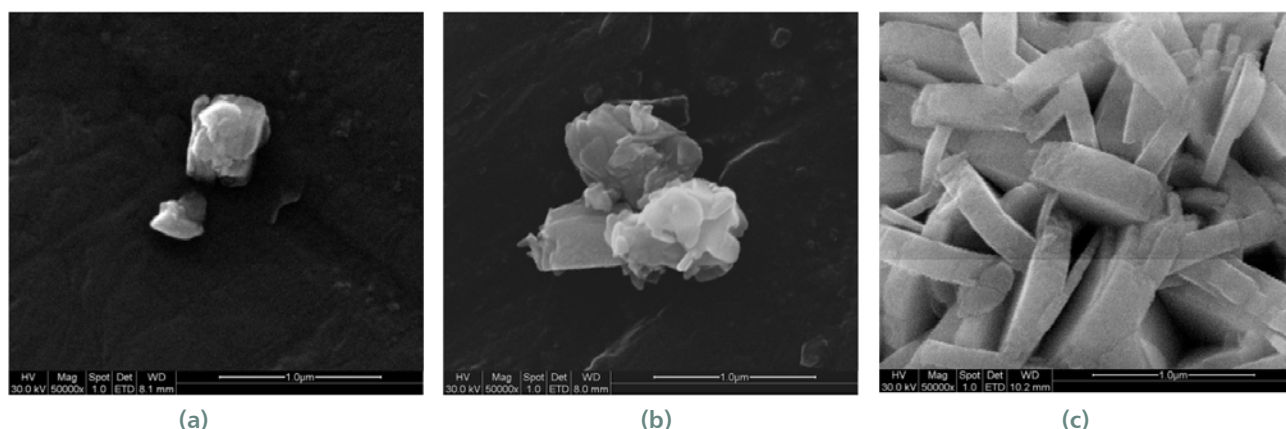


Fig. 4: TEM images of final ADU a) microstructure, b) selected area diffraction pattern

Fig. 4a to Fig. 4c exhibits the SEM images of ADU at different stages of precipitation. Fig. 4a shows platelet like structure of ADU at inception. In the course of reaction platelets connect each other forming agglomerates. As reaction proceeds, the size of both platelets and agglomerates increased. The change of mean particle size of ADU powder with time has been plotted in Fig. 5a. It clearly indicates the growth of particle with time. The particle size distribution (PSD) of ADU at the inception and pH 7 is shown in Fig. 5b. Wide PSD has been observed at the inception but PSD becomes narrower at the final stage of precipitation. ADU powder was then calcined to UO_3 at different temperatures starting from $450^\circ C$ to $750^\circ C$. Effect of calcination temperature on O/U, bulk density, tap density, mean particle size, surface area, porosity & colour has been shown in Table 1. It has been observed that O/U ratio, bulk density and tap density of the

of ADU at the inception and pH 7 is shown in Fig. 5b. Wide PSD has been observed at the inception but PSD becomes narrower at the final stage of precipitation. ADU powder was then calcined to UO_3 at different temperatures starting from $450^\circ C$ to $750^\circ C$. Effect of calcination temperature on O/U, bulk density, tap density, mean particle size, surface area, porosity & colour has been shown in Table 1. It has been observed that O/U ratio, bulk density and tap density of the

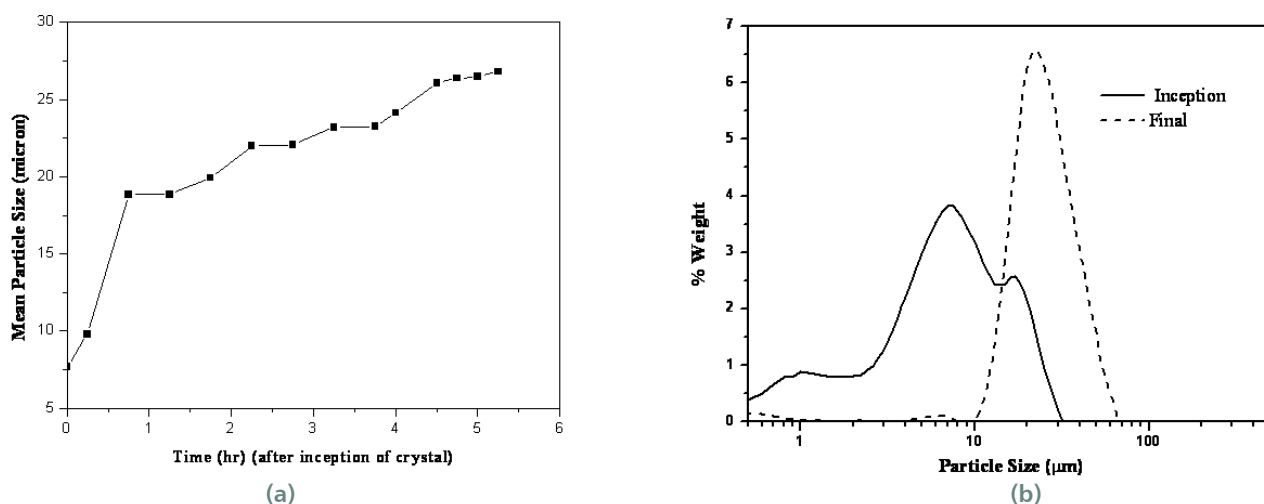


Fig. 5: a) Variation of mean particle size of ADU produced at different stage of precipitation and b) PSD of ADU produced at the inception and at pH 7

Table 1: Effect of calcination temperature on properties of uranium oxide

Sr. No.	Temp. ($^\circ C$)	O/U Ratio	Bulk Density (g/cm^3)	Tap Density (g/cm^3)	Mean Particle Diameter (μ)	Surface Area (m^2/g)	Porosity (cm^3/g)	Colour
1	450	2.82	1.92	2.26	24.68	22.5	0.07	Reddish Black
2	550	2.77	1.89	2.24	25.09	35.39	0.17	Black
3	650	2.71	1.88	2.22	22.83	12.15	0.04	Black
4	750	2.67	1.77	1.90	24.27	7.24	0.03	Black

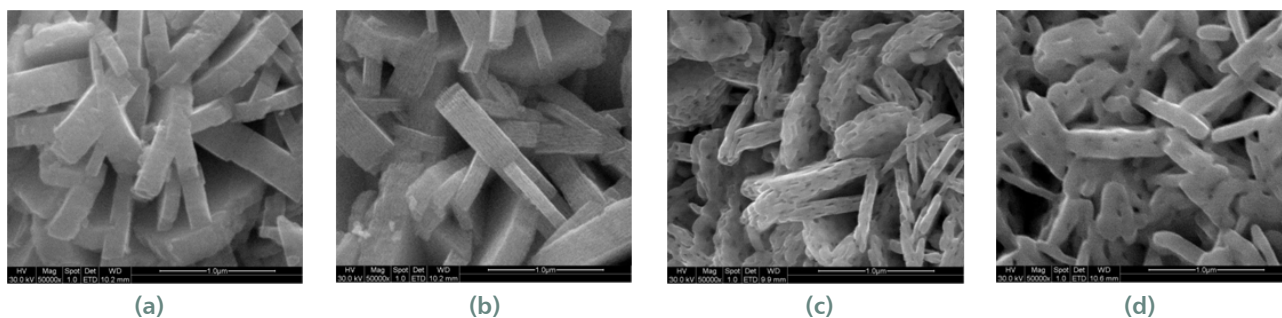


Fig. 5: SEM image of uranium oxide produced by calcination of ADU at different temperatures. a) 450°C, b) 550°C, c) 650°C and d) 750°C

uranium oxide are reduced with an increase of calcination temperature. Colour of the uranium oxide produced at 450 °C is reddish black whereas it was found to be black when produced at temperatures, higher than 450 °C. It is also studied that surface area and porosity pass through a maximum value at 550°C and then reduces.

Fig. 6a to 6d shows the morphology of UO_3 produced by calcination of ADU at different temperatures. It is clear from Fig. 2 and Fig. 6 that the microstructure of ADU and uranium oxide is similar. The uranium oxide particles also consisted of primary platelets and these platelets are connected to form agglomerates. This granular agglomerate structure of uranium oxide improves flowability of the powder significantly. This is much important physical property required for further processing of uranium oxide. The SEM micrograph at 50000X, shows pores on the primary platelet of uranium oxide calcined at 550 °C and at higher temperatures, but no pores were observed in uranium oxide produced at 450°C. These pores are generated due to release of gaseous NH_3 and water vapour during calcination. The micrographs clearly indicate that sintering of UO_3 powder takes place at 650°C onwards. It clarifies that initial increase of surface area occurs due to generation of pores whereas a reduction of surface area occurs because of sintering.

Conclusion

ADU particle basically consists of primary platelets, and these primary platelets form primary agglomerates. Sometimes a number of primary agglomerates are connected with each other to form secondary

agglomerates. In the course of reaction both the size of primary platelets and the agglomerations get increased. It has also been concluded that microstructure of ADU is retained even after its calcination to uranium oxides. It has been observed that O/U ratio, bulk density and tap density of the uranium oxide is reduced with an increase in the calcination temperature. However, the temperature was not found to have significant effect on tap density, bulk density and mean particle size. High resolution SEM has revealed that pores are generated during calcination and at higher temperature sintering of powder takes place. As a result surface area increases with temperature and then reduces after passing through a maxima.

Acknowledgements

The authors acknowledge Prof. G.K. Dey, Dr. A. Awasthi, Shri J. Banerjee, Shri S. Neogy, Dr. C.B. Basak, Dr. A. Mukherjee, and Shri Hareendran of B.A.R.C and Shri P Karthik and Shri R. Bhattacharya of AERB. Shri S. Manna is thankful to Shri S.K Satpati for his kind support and Shri U.R. Thakkar for his help to carry out experiments.

References

1. E. H. P. Cordfunke, "On the Uranates of Ammonium-I: The ternary system $NH_3-UO_3-H_2O$ ", *J. Inorg. Nucl. Chem.* 24 (1962) 303-307.
2. M. Deane, "The infra-red spectra and structures of some hydrated uranium trioxides and ammonium diuranate, *J. Inorg. Nucl. Chem.* 21 (1961) 238-252.

BARC NEWSLETTER

3. P. C. Debets, B.O. Loopstra, "On the Uranates of Ammonium-II x-ray investigation of the compounds in the system $\text{NH}_3\text{-UO}_2\text{-H}_2\text{O}$ ", *J. Inorg. Nucl. Chem.* 25 (1963) 945-953.
4. E. V. Garner, "X-ray diffraction studies on compounds related to uranium trioxide dehydrate", *J. Inorg. Nucl. Chem.* 21 (1961) 380-381.
5. M. E. A. Hermans, T. Markesteyn, "Ammonium urinates and UO_3 -hydrates ammoniates", *J. Inorg. Nucl. Chem.* 25 (1963) 461-462.
6. W. I. Stuart, T.I. Whateley, "Composition and structure of ammonium uranates", *J. Inorg. Nucl. Chem.* 31 (1969) 1639 - 1647.
7. H. Doi, T. Ito, "Significance of physical state of starting precipitate in growth of uranium dioxide particle", *J. Nucl. Mater.* 11 (1964) 94-106.
8. J. Janov, P.G. Alfredson, V.K. Vilkaitis, "The influence of precipitation conditions on the properties of ammonium diuranate and uranium dioxide powders", *J. Nucl. Mater.* 44 (1972) 161-174.
9. N. B. Murthy, P. Balakrishna, R.B. Yadav C. Ganguly, "Influence of temperature of precipitation on agglomeration and other powder characteristics of ammonium di-uranate", *Powder Technol.* 115 (2001) 167-183.
10. S. Rajgopal, T.P.S. Asari, C.S.P. Iyer, "Particle size analysis of ammonium urinate prepared by conventional and homogeneous methods of precipitation and their corresponding oxides", *J. Nucl. Mater.* 227 (1996) 300-303.
11. S. B. Roy, S. K. Satpati, A. M. Meghal, T. K. Mukherjee, . "A gas liquid ADU reaction in stirred tank and the effect of the presence of immiscible inert gas on the product solid". HMT Conference Suratkal (1995) 609 – 613.
12. J.L. Woolfrey, "The preparation of UO_2 powder: effect of ammonium urinate properties", *J. Nucl. Mater.* 74 (1978) 123-131.
13. M. S. Das, T.S. Krishnamoorthy P.V. Ravindran and N. Mahadevan, unpublished internal report of BARC, DAE, India.
14. S. Manna, S. B. Roy, and J. B. Joshi, "Study of crystallization and morphology of ammonium diuranate and uranium oxide", *J. Nucl. Mater.* 424, 94-100, 2012.
15. S. Manna, P. Karthik, A. Mukherjee, J. Banerjee, S. B. Roy, and J. B. Joshi, "Study of calcinations of ammonium diuranate at different temperatures", *J. Nucl. Mater.* 426, 229-232, 2012.

BARC NEWSLETTER

COMPACT INDUCTIVE ENERGY STORAGE PULSE POWER SYSTEM

Senthil K.

Accelerator and Pulse Power Division, Beam Technology Development Group

Shri K. Senthil is the recipient of the DAE Young Engineer Award for the year 2011

Abstract

An inductive energy storage pulse power system is being developed in BARC, India. Simple, compact, and robust opening switches, capable of generating hundreds of kV, are key elements in the development of inductive energy storage pulsed power sources. It employs an inductive energy storage and opening switch power conditioning techniques with high energy density capacitors as the primary energy store. By optimizing the exploding wire parameters, a compact, robust, high voltage pulse power system, capable of generating reproducibly 240 kV, 6 kA, and 200ns pulses has been developed.

Introduction

Inductive energy storage, in combination with opening switch power conditioning switch, offers several attractive features for pulsed power applications when compared with conventional, capacitive technology. The advantages are compactness and low cost of the primary energy store. As only the last stage of pulse conditioner generates high voltage, the complications of oil filled Marx generators, pulse forming lines, and power limiting interfaces can be eliminated. When a wire is heated, considerable energy is required during the metal-to-liquid and (particularly) the liquid to vapour phase transitions, and these must both be produced very rapidly to ensure the best explosive performance. Any capacitor storing sufficient energy to heat an exploding wire (EW) to burst condition can, in principle, cause it to explode. It is necessary therefore for the energy to first be transformed into magnetic energy in an inductor to increase its resistance between 100 and 300 times its initial values during the explosion. There will clearly be an inductance that stores sufficient magnetic energy to explode the EW and provide the optimum performance¹.

Basics of Exploding Wire Switch

The basic circuit diagram of inductive energy storage system² (IESS) is shown in Fig. 1. When the spark gap breaks down, the initially charged capacitor C_s discharges through the inductor L_s and EWA resulting in an under damped RLC series circuit. As the current starts increasing, the resistance of the EWA rises due to Joule heating. Due to high rate of energy deposited in the EWA, it changes from solid state to liquid state and finally vaporizes. This rate of rise of resistance of EWA is linear as it is heated up to melting point. From melting point to the point of vaporization, it increases rapidly (with different slopes). The highest rate of rise of resistance is from liquid to vapour state.

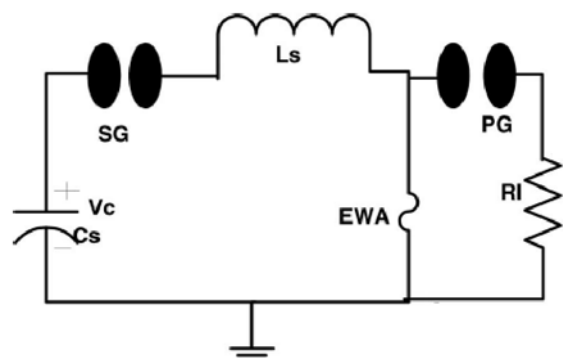


Fig. 1: Schematic of IESS

The current $i_s(t)$ in the circuit is given by

The current $i_s(t)$ in the circuit is given by

$$i_s(t) = \frac{V_c}{\sqrt{\frac{L_s}{C_s}}} e^{-\alpha t} \sin(\omega t) \quad (1)$$

$$\text{where } \alpha = \frac{r_{\text{ewa}}}{2L_s}, \quad \omega_d \sim \omega_n = \frac{1}{\sqrt{L_s C_s}}$$

V_c is voltage on capacitor, r_{ewa} is the cold resistance of EWA

The current $i_s(t)$ will reach maximum peak when time $t_p = T/4$ where T is period of ringing frequency of the circuit. Say, at time $t=t_{\text{exp}}$, the EWA explodes with the current in the inductor L_s , the current is chopped and high voltage i_s generated which is given by

$$V_o = L_s \frac{di_s(t_{\text{exp}})}{dt} \quad (2)$$

From eqn (2), the high voltage generated V_o is proportional to the current $i_s(t_{\text{exp}})$ and inversely proportional to the transition time (time taken to go from ON state to OFF state).

System Description

The capacitor bank has four 2.8 μF , 50 kV, 14kJ capacitors, connected to storage inductor pressurized spark gap. The storage inductor of 4 μH is made of 15 turns copper tube of diameter 8mm wound over Delrin former (EWA housing) of 70 mm diameter of



Fig. 2: Photograph of IESS

length 500 mm. The peaking spark gap is of pressurized rod plane type with a gap of 25 mm. The EWA holder is made of 30 mm \times 700 mm fiber-reinforced plastic (FRP) sheet of 3 mm thickness with end connection with a push fit arrangement. The CuSO_4 load is made of Perspex tube of diameter 50 mm and length 250 mm. The load chamber and inductor chamber are separated by corrugated 100 mm thick Perspex sheet. The Photograph of the system is shown in Fig. 2.

Optimisation of Exploding Wire Array

Experiments were carried out with copper wires of different wire diameter, length and gaseous environment at different pressures for optimising exploding wire array. Initially, the capacitors were charged to 12kV

Number of wires

Table 1 shows the experimental data for capacitor charged to 15kV with different number of wires, it is observed that the input current and conduction time of EWA increases with number of wires.

Table 1

Number of wires	Inductor Current in A	Load voltage in kV	Conduction time in μs
1	5836	45	1.6
2	9728	70	3.52
3	12185	63	4.6
4	14233	52	5.46
5	15667	29	7

The input current increases sinusoidal with the conduction time till the instant EWA starts changing its phase from solid to liquid. It is observed that the input current increases due to reduction in cold resistance of EWA, its increased mass require more energy for vaporization making it to conduct for longer time before vaporization. Due to increased input current, more energy is stored in inductor i.e., more energy is transferred from capacitor, hence maximize the output voltage. The plot of output voltage V_o Vs number of wires is given in Fig. 3.

BARC NEWSLETTER

Length of Wires and Quenching medium

From the equation for length of a fuse was determined, this was used as a base length upon which to do experimental testing on the effect of fuse length on the voltage multiplication ability of the electro-explosive fuse. From the base length, two other lengths up to two times the base length were tested to see the results of voltage multiplication and more clearly define the effects of fuse length on the operation of an EWA.

The twice length factor is primarily due to the experimental setup arrangement in which the storage inductors are continually driven through the entire vaporization process. As discussed previously, initial design considerations for the experimental setup did not account for energy left in the capacitors after fuse opening.

As the capacitor voltage is increased, restrike mechanism³ develops, thereby obstructing the exploding phenomenon. To avoid this, length as well as surrounding medium of EWA is pressurised with gases namely nitrogen and floron. Due to electronegativity nature floron at 3kg/cm², EWA gives similar performance with nitrogen at 5kg/cm². With the optimised EWA of 9 numbers of SWG 40 copper wire, length of 42cm at 3kg/cm² floron yields an output voltage of 240kV, 6kA, 250ns FWHM on reflex triode with rise time of 50ns.

When operated with reflex triode for HPM generation, output pulse 150ns is recorded, due to electron beam get short circuited is shown in Fig. 4. An magnetic field



Fig. 4: Waveform with reflex triode

of 21A/m is measured at distance of 3m with dominant frequency of 0.9GHz and 2.6GHz is shown in Fig. 5.



Fig. 5: HPM signal

Conclusion

Exploding wire array to be used as opening switch with inductive energy storage has been designed and optimised for its physical parameters, quenching medium for chopping a current of 27kA with a rise time of 5 μ s to generate 240kV, 6kA, 200ns on load of 40 Ω with a opening time of approximately 400ns without restrike mechanism.

Acknowledgements

I would like acknowledge all my seniors/ mentors and colleagues of APPD,BTDG and BARC for their constant encourageent and support throughtout carry out the studies on exploding wire array as an opening switch.

References

1. Chace W.G., *Exploding Wires*, vol. 1, New York: Plenum Press, New York 1959, pp.7-16.
2. Naoyuki Shimomura, Hidenori Akiyama, " Compact Pulsed Power Generator by an Inductive Energy Storage System With Two-Stage Opening Switches" *IEEE Transactions of Plasma Science*, Vol. no. 19, pp: 1220-1227.
3. Senthil K.; Mitra S.; Sharma, A.; Nagesh, K.V.; Chakravarthy, D.P." Experimental results of inductive energy storage pulsed power system using exploding wire as an opening switch" *IEEE International Vacuum Electronics Conference (IVEC)*, 2011, Page(s): 479 – 480.

BARC NEWSLETTER

FLUIDIZED BED SYNTHESIS OF CARBON NANOTUBES

Kinshuk Dasgupta

Rare Earths Development Section, Materials Group

Shri Kinshuk Dasgupta is the recipient of the DAE Young Engineer Award
for the year 2011

Abstract

Carbon nanotubes have been prepared in large quantity in a fluidized bed reactor by catalytic cracking of acetylene and methane over carbon black. The reaction mechanism involving various mass transfer and chemical reaction steps has been proposed. The rate controlling step(s) and the activation energy have been found out. The present process can produce carbon nanotubes of good quality with a yield of 95% and has potential for commercialization.

In recent years carbon nanotube (CNT) has drawn attention of the researchers, due to its unique properties and potential applications in the electronic industries, in power generation and storage, in biomedical application, in structural and functional composites, etc. [1-6]. The bulk production of CNTs in an economic way is the route to feasibility of these applications. Out of different techniques, catalytic chemical vapour deposition (CCVD) in a fluidized bed is the most promising technique for bulk production of this exotic material [7-8]. In this method, one needs to fluidize nano-agglomerate particles containing catalysts (generally transition metals or their compounds), using a carrier gas like nitrogen or argon along with a hydrocarbon gas like acetylene. The CNTs grow on the catalyst containing nano-agglomerate particles by the decomposition of the hydrocarbon. The use of cheap precursors and the reduction in processing steps are the key factors in producing CNTs economically. In order to meet these requirements, we have chosen carbon black (N 330 grade, furnace black) as the nano-agglomerate particle, ferrocene as the catalyst and acetylene and methane as the precursor hydrocarbons. The beauty of carbon black is that it has primary particles of size ~ 35 nm, which form agglomerate in the size range of $80 \mu\text{m}$ to $120 \mu\text{m}$ and can be easily fluidized. It does not require any processing prior to fluidization. On the contrary, mesoporous alumina, magnesia and silica that have been reported in the published literature [8] as catalyst-support materials for

CNT growth, require several steps of processing prior to fluidization. Similarly, ferrocene on cracking in inert atmosphere, deposits nascent iron (Fe) nanoparticle on the carbon black surface and it acts as the catalyst for CNT growth. In this article, the growth mechanism of CNTs in a fluidized bed has been discussed.

The schematic of the fluidized bed set up used for the CNT synthesis is shown in Fig. 1. Carbon black is charged inside the furnace at room temperature and is initially fluidized by nitrogen till the temperature of synthesis is reached. At the temperature of synthesis, acetylene/methane flow is added to the nitrogen (1:1). The

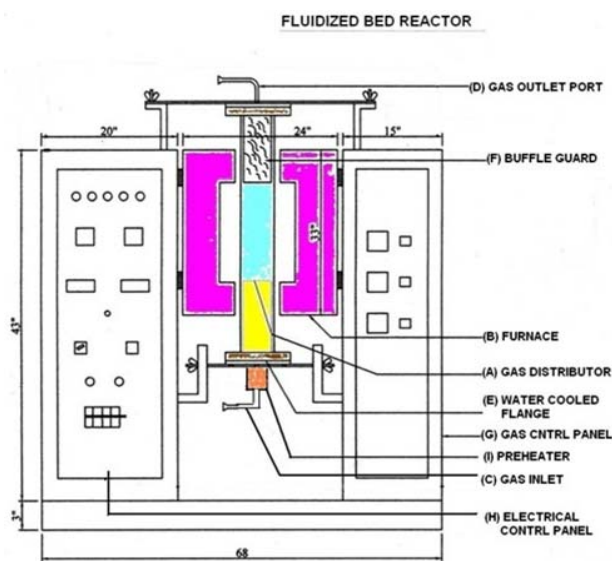


Fig. 1: Schematic of the fluidized bed set up for production of carbon nanotubes

BARC NEWSLETTER

ferrocene is charged inside the pre-heater, which is heated up to 250°C. At this temperature ferrocene is vapourized and is carried inside the furnace by the gas mixture (nitrogen and acetylene/methane). Inside the furnace ferrocene gets cracked into Fe nanoparticles and acetylene/methane gets cracked into C and H₂.

We propose that the fluidized bed process consists of eleven steps related to various mass transfer and chemical reaction steps. These are:

1. The hydrocarbon transfers from the bubble phase to the emulsion phase
2. Mass transfer of hydrocarbon from emulsion to the external surface of the support (carbon black)
3. Diffusion of hydrocarbon from the pore mouth on the surface to the surface of the catalyst
4. Adsorption of the hydrocarbon onto the catalyst surface (active site)
5. Reaction on the catalyst surface to produce carbon molecules
6. Solubilization of carbon molecules in the catalyst
7. Supersaturation of the catalyst with carbon
8. Nucleation and Growth of CNT
9. Desorption of hydrogen and other gaseous products
10. Diffusion of the gaseous products from the catalyst surface to the external surface of support (carbon black)
11. Mass transfer of gaseous products from support (carbon black) to the emulsion phase

In order to investigate the rate controlling step(s), experiments have been performed in a systematic sequence over a wide range of gas superficial velocities, carbon black agglomerate sizes, partial pressures of acetylene and methane, catalyst loadings, temperatures and time of synthesis. Formation of carbon molecules on the surface of the catalyst has been found to be the rate controlling in the temperature range of 700-807°C for acetylene as feed gas, where activation energy is 47 kJmol⁻¹. At higher temperature range (807-1000°C), rate controlling mechanism shifts to diffusion through pores of carbon black, with activation energy 7.6 kJmol⁻¹. However, for methane the former one has been found to be the rate controlling throughout the entire temperature range. There is a continuous deactivation

of catalyst which we have represented with an exponential decay model. During the entire process proper fluidization of the bed must be ensured. In order to get some idea about the quality of fluidization, the pressure drop across the bed (ΔP) has been measured as a function of superficial gas velocity (V_G). Fig. 2 shows such a plot at 30°C and 700°C. The values of minimum fluidization velocities have been found to be 2.95 and 2.75 mm/s, respectively. During the CNT formation experiments, the value of V_G is kept in the range of 5-10 times that of the minimum fluidization velocity.

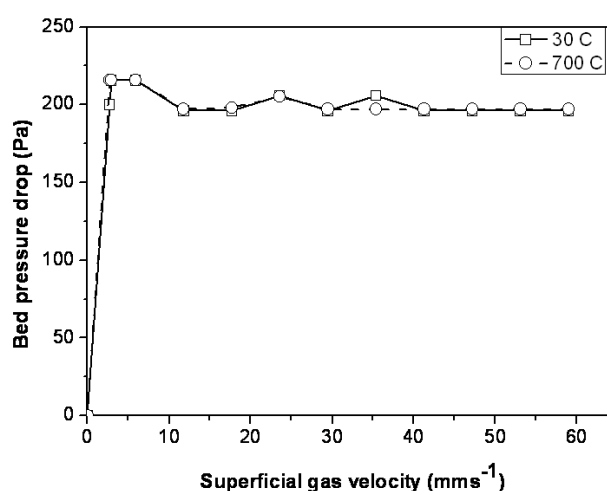


Fig. 2: Bed pressure drop as a function of superficial gas velocity at 30 and 700°C

It is worth mentioning here that the structure of the original carbon black gets modified during processing. The product contains CNT along with modified carbon black and catalyst particles. The product after each experiment is purified by treatment with dilute hydrochloric acid for 2 hours, which removes most of the catalyst particles. Then it is heated in air at 650°C for 1 hour to remove the other forms of carbon except CNT. The temperature has decided based on thermogravimetric (TG) studies [9]. The purified CNTs have been characterized. Fig 3 shows a typical SEM image of the CNT products at 800°C after purification as described above. Fig. 4 shows the TEM image of the CNTs synthesized at 800°C. It is multiwalled in nature with outer diameter 30-50 nm and the hollow core of CNT is visible. High resolution TEM (HRTEM) image in Fig. 5 reveals that the walls are well aligned. The distance between the walls is about 3.4 Å. The Raman spectrum of the purified CNTs is shown in Fig. 6, which give characteristic 'G' and 'D' bands. The above results show that the CNTs are of very good quality.

BARC NEWSLETTER

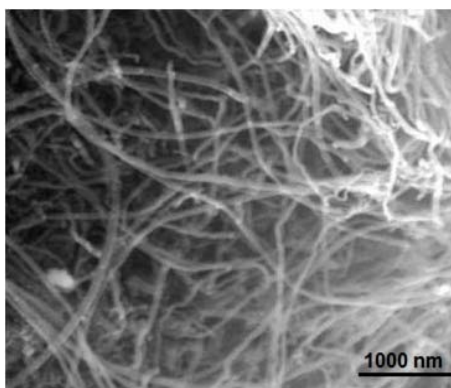


Fig. 3: SEM of CNTs

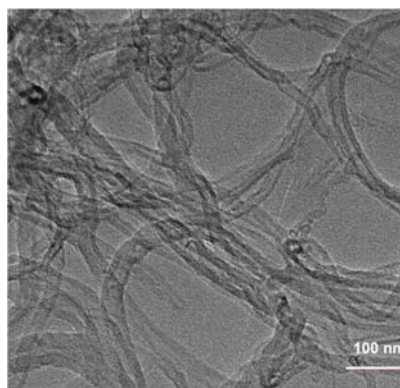


Fig. 4: TEM of CNTs

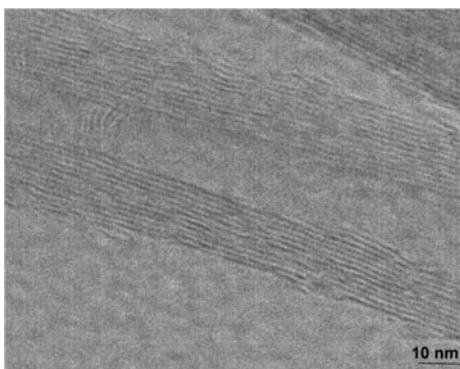


Fig. 5: HREM of CNTs

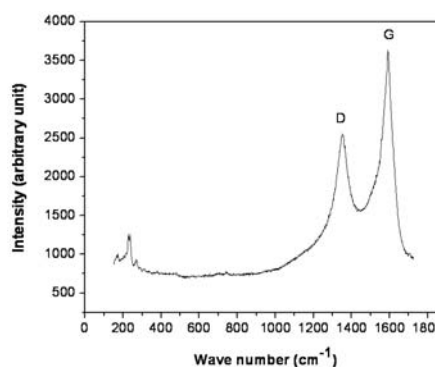


Fig. 6: Raman Spectrum of CNTs

The fluidized bed process can produce CNT at the rate of 650 kg/m³/s with a yield of 95%. The proposed process is economic and can be scaled up for the bulk production.

Acknowledgement

The work has been carried out under the guidance of Prof. J. B. Joshi, DAE-Homi Bhabha Chair, HBNI and Dr. S. Banerjee, DAE-Homi Bhabha Chair, BARC. The author is grateful to Shri H. Singh, Head, REDS for his constant support.

References

1. Baughman RH, Zakhidov AA, de Heer WA. Carbon nanotubes — the route toward applications. *Science* 297 (2002): 781–787.
2. Bonard JM, Kind H, Stockli T, Nilsson LO. Field emission from carbon nanotubes: the first five years. *Solid State Electron.* 45 (2001): 893-914.
3. Dillon AC, Jones KM, Bekkedahl TA, Kiang CH, Bethune DS, Heben MJ. Storage of hydrogen in single-walled carbon nanotubes. *Nature* 386 (1997): 377-9.
4. Fan JP, Zhang DM, Zhao DQ, Zhang G, Wu MS, Wei F, et al. Toughening and reinforcing alumina matrix composite with single-wall carbon nanotubes. *Appl Phys Lett.* 89 (2006): 121910.
5. Tans SJ, Devoret MH, Dai H, Thess A, Smalley RE, Geerligs LJ, et al. Individual single-wall carbon nanotubes as quantum wires. *Nature* 386 (1997): 474-7.
6. Tsukagoshi K, Yoneya N, Uryu S. Carbon nanotube devices for nanoelectronics. *Physica B* 323 (2002): 107-114.
7. Wang Y, Wei F, Luo GH, Yu H, Gu GS. The large-scale production of carbon nanotubes in a nano-agglomerate fluidized-bed reactor. *Chem. Phys. Lett.* 364 (2002): 568–572.
8. Philippe R., Morançais A., Corrias M, Causat B, Kihn Y, Kalck P, et al. Catalytic production of carbon nanotubes by fluidized-bed CVD. *Chemical Vapor Depos.* 13 (2007): 447-457.
9. Dasgupta K, Sen D, Mazumdar T, Lenka RK, Tewari R, Mazumder S, Joshi JB, Banerjee S. Formation of bamboo-shaped carbon nanotubes on carbon black in a fluidized bed. *J. Nanopart. Res.* 14 (2012): 728-736.

BARC NEWSLETTER

INDIGENIZATION IN DESIGN AND DEVELOPMENT OF HIGH PRECISION INSTRUMENTS FOR SYNCHROTRON BEAM-LINES AT INDUS-II, RRCAT, INDORE.”

A.D. Patil

Centre for Design & Manufacturing

Shri A.D. Patil is the recipient of the DAE Young Engineer Award for the year 2011

Ultra high vacuum compatible water cooled Precision slits:

This is an import substitution item and has been developed indigenously for ARPES/PEEM synchrotron beam-lines and Protein Crystallography synchrotron beam-line at INDUS-II, Indore. ARPES/PEEM beam-line is being installed to carry out photo electron spectroscopy for studying the electronic structure of the surface of solids and Protein Crystallography beam-line is being installed to study the protein structures. Function of Precision slit is to control the aperture of synchrotron beam-line to suit the acceptance of successive instruments like D.C.M., P.G.M., and Mirror Mounts etc. Indigenous development of the fully automated primary slits proved to be more compact and user friendly. The remotely operated precision slit is designed to align and move two nos. of slits in a planar spatial space and is attained by two D.O.F. slider mechanisms with a high flexural rigidity link mechanism designed for positional accuracy of 2 microns. For detailed analysis of flexural rigidity of the mechanism ANSYS-11 software was used. The criticality of the instrument lies in positional accuracy, provision of heat sink, remote operation, U.H.V. compatibility, compactness of the instrument & positional stages. The uses of primary slits are not limited to these beam-lines but also required for all the beam-lines to be installed at INDUS-2.

The complete system was first assembled and tested at CDM and then the same has been dispatched and now installed at INDUS –II, RRCAT, Indore.

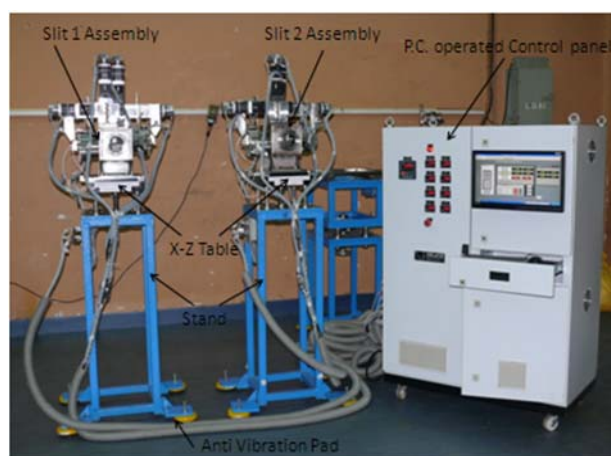


Fig.1: Ultra high vacuum compatible water cooled Precision slits with control panel

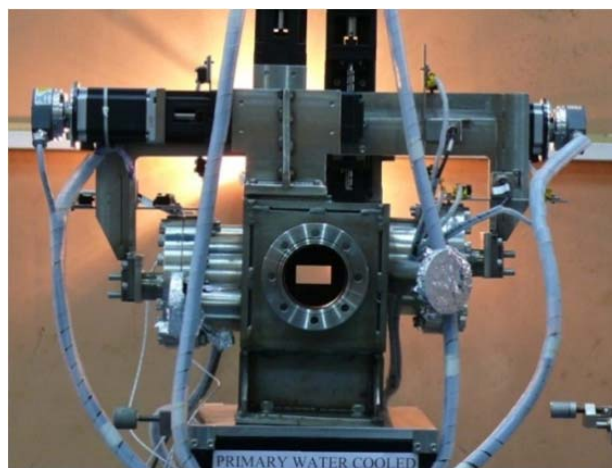


Fig. 2: Slit Aperture with maximum opening size

High Temperature Cell for EXAFS studies of Uranium and Plutonium bearing samples:

This is an import substitution item and has been developed indigenously first time in India. High temperature cell is designed for recording high

BARC NEWSLETTER

temperature EXAFS patterns for uranium and plutonium bearing samples at Synchrotron light source beam line, BL-8 at RRCAT, Indore. This Cell facilitates to heat the sample to 1273 K for recording EXAFS spectrum at various temperatures in different gaseous atmospheres. The high temperature EXAFs helps in the study of the compounds undergoing phase changes with temperature. It shall be useful for characterizing the products formed due to Fuel, Fission product and cladding interactions during reactor operating and transient conditions. Also it is useful to study the change in valency of the compounds specially uranium oxide with temperature. It can give information about amorphous materials also.

Detailed steady state thermal analysis was carried out for positive clamping of samples at high temperature and to take away the heat from the containment and the feed-through. Detailed analysis also calls for

selection of electrical insulation for 100 A current at 8 V supply and thermal insulation.

High temperature cell was successfully tested at CDM and Chemistry Division Lab to achieve temperature upto 800 K and job was handed over to Fuel Chemistry Division, BARC for further experiments for EXAFS studies.

Cylindrical Bendable Mirror:

This is an import substitution item and has been developed indigenously. Function of this Cylindrical Bendable Mirror is to generate different cylindrically shaped surfaces by bending a flat substrate of OFHC copper or Single Crystal Silica flat for micro-focusing the X-Ray beam on to the material to be studied under high pressure using EXAFS beam-line at INDUS-II Synchrotron source. This developmental work is of great

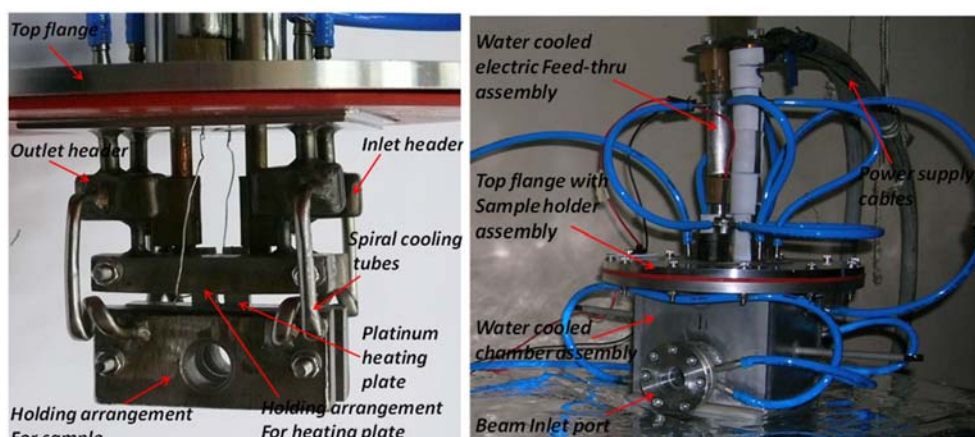


Fig.3: High temperature cell

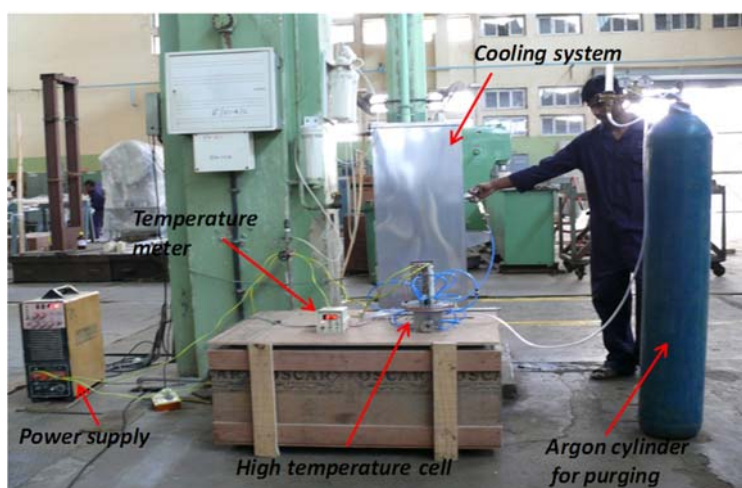


Fig. 4: Experimental Set-up for testing High Temperature Cell

BARC NEWSLETTER

important because, generating highly accurate cylindrical surfaces by conventional grinding and polishing methods or by any other method with the desired optical accuracy is very difficult, whereas flat surfaces of the required accuracy are comparatively easy to produce.

This is one of the critical instruments of the beam-line, where 200 mm long OFHC Cu or Silica crystal flat plate/laminated (having mirror finished reflective surfaces) is bent into cylindrical shape. Euler's theory was effectively used to design the kinematic linkage mechanism to generate pure bending moment on the mirror substrate to achieve constant radius of curvature along the length of the substrate. The most challenging part in the design was to generate different cylindrical surfaces on the same crystal laminate, for doing the experiments with different photon energies (energy level varying from 5 Kev to 20 Kev) and it was done successfully. To achieve the objective a detailed solid modeling and analysis work was carried out to finalize the bending mechanism.

Bendable mirror has been tested optically by HPPD, BARC at CDM, minimum focal spot size, which was obtained by this bendable mirror was

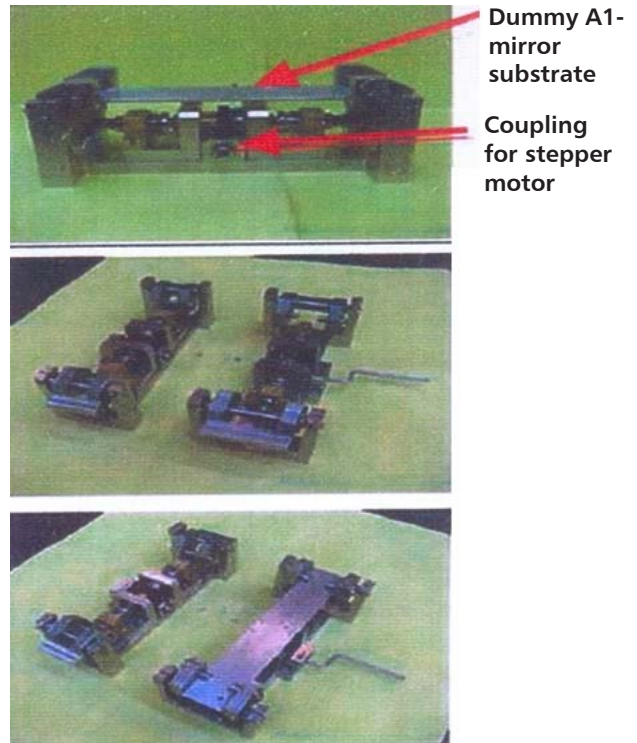


Fig. 6: Cylindrical Bendable Mirrors

$16\ \mu\text{m(H)} \times 20\ \mu\text{m(V)}$ and $37\ \mu\text{m(H)} \times 27\ \mu\text{m(V)}$ for photon energy range of 5 Kev to 20 Kev, and was the achievement for user. The bender can also be used to generate elliptical profile by providing the variable width of the substrate along the length.

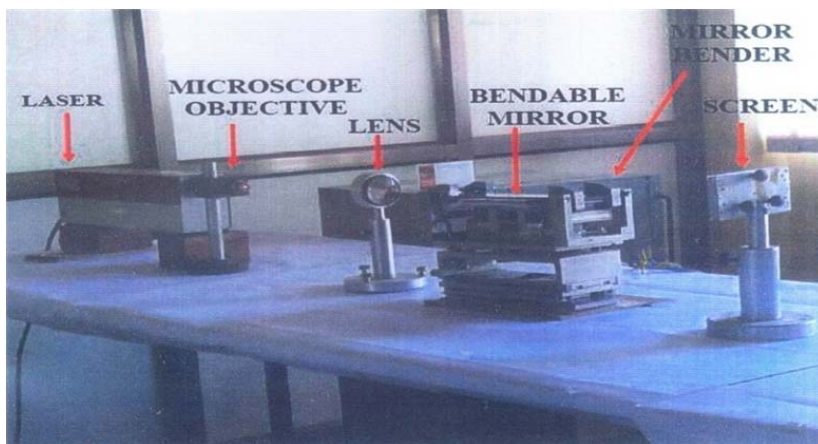


Fig.5: Experimental Setup for recording the focus spot using Laser light

PHOTOPHYSICAL STUDIES IN SUPRAMOLECULAR SYSTEMS

Sharmistha Dutta Choudhury
Radiation & Photochemistry Division

Dr. Kum. Sharmistha Dutta Choudhury is the recipient of the DAE Young Scientist Award for the year 2010

Abstract

Supramolecular interactions have enormous potential for controlling and modulating molecular properties for numerous applications. Our studies have helped in understanding the photophysical properties of guest molecules encapsulated in supramolecular systems and to use these systems as soft templates for creating different kinds of molecular architectures or aggregation patterns. Apart from modulating photophysical properties, the supramolecular systems have also been found to be responsive toward external stimuli, leading to controlled release/exchange processes for prospective use in drug delivery or therapeutic applications.

Keywords: Organized assembly, macrocyclic host, H-aggregate, fluorescence enhancement, stimulus response

Introduction

Supramolecular systems are formed from molecular building blocks held together by 'weak' noncovalent intermolecular forces such as electrostatic interactions, hydrogen bonds, π -stacking or the hydrophobic effect. Although individual noncovalent interactions are weak, the summation of a large number of weak bonds in a 'supramolecule' can lead to strong overall bonding and stability. Supramolecules, however, are quite flexible due to the continuous making and breaking of the weak bonds and it is this process that leads to the rich diversity and complexity of supramolecular systems. The flexibility and selectivity of supramolecular complexes is what has made the "chemistry beyond the molecule" a very versatile and much investigated research area with wide ranging applications. For the past couple of years we have been interested in different kinds of supramolecular systems, such as organized assemblies of surfactants or lipids and also rigid cage like molecules, like cyclodextrins and cucurbiturils that are capable of trapping suitable guest species. Our research focuses on two complementary aspects: the use of photophysics to characterize supramolecular systems and the use

of supramolecular systems to alter the photophysical properties of molecules. We are also interested in the biological aspects of supramolecular systems and their applications for fluorescence on/off sensing or drug release and uptake. This article describes the interesting changes in the photophysical behavior and aggregation patterns of one such biologically important molecule, thiazole orange (TO), in the presence of surfactants, such as sodium dodecyl sulfate (SDS) and sodium bis(2-ethylhexyl) sulfosuccinate (AOT) and macrocyclic hosts, such as cucurbit[8]uril (CB8).

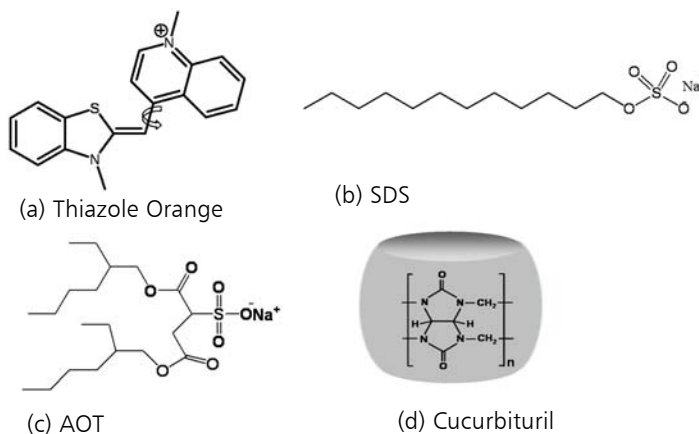


Fig. 1: Chemical structures of the dye, Thiazole Orange (a), Surfactants, SDS (b) and AOT (c) and the macrocyclic host, Cucurbituril (d).

Surfactant Induced Aggregation Patterns of Thiazole Orange

Thiazole Orange (TO) is a cationic cyanine dye (Fig. 1a) that can exist in the monomeric, dimeric or higher aggregated forms in aqueous solutions, depending on its concentration.¹ It is widely used as a fluorogenic probe for the detection of DNA since its fluorescence is enhanced upon binding to nucleic acids.² The TO-DNA binding is very much dependent on the aggregation state of the dye as well as on the dye/nucleic acid ratio. So it is important to have a clear idea about the photophysical characteristics and aggregation behavior of TO in order to understand the DNA binding interactions of this dye. On the other hand, the self-association of organic dyes is in itself a very interesting phenomenon due to its applications in many areas like photography, photodynamic therapy, non-linear optics and photoelectric devices.³ Two types of ordered aggregates are typically observed, J-aggregates, formed by the alignment of molecules in an edge to edge configuration and H-aggregates, composed of dye molecules stacked face to face in a sandwich-like configuration.³ The tendency and type of aggregation depends on a number of factors like the structure of the dye, temperature and the kind of environment. Researchers have studied the role of different additives in controlling and designing the aggregation patterns of dyes. Considering the inherent property of surfactants to form supramolecular assemblies of different morphologies, we expected a pronounced effect on the aggregation behavior of TO in the presence of surfactants, depending on the dye-detergent interactions.⁴ We investigated the aggregation behavior of TO in two different, well-characterized anionic surfactant systems, namely pre micelles/micelles of SDS (sodium dodecyl sulfate) and pre reverse micelles/reverse micelles of AOT (sodium bis(2-ethylhexyl) sulfosuccinate). In the case of SDS/water system, we observed that TO initially exists in the monomer form in aqueous solution. At low

concentrations of SDS, the surfactant induces the formation of H-aggregate/dimer forms of TO. Beyond the critical micelle concentration (CMC), de-aggregation of the dyes occurs due to their incorporation within the SDS micelles.⁵ Interestingly, the observed changes in the absorption and emission characteristics of TO due to the surfactant induced formation of H-aggregates/dimers, is found to be useful for estimating the surfactant concentration parameters for pre-micellar aggregation of SDS.⁵ In the AOT/heptane system, the TO dyes are initially present as H-aggregates due to the clustering of the cationic dyes in the nonpolar solvent.⁴ With increasing AOT concentration, the H-aggregates of TO are disrupted and gradually converted to H-dimers due to the electrostatic interactions between the dye and the AOT head groups, and the association of AOT into pre-reverse micellar aggregates. However, in contradiction to the Poisson distribution statistics, the H-dimer form of TO persists even for AOT concentration much higher than the CMC for reverse micelle formation. The H-dimers are proposed to be facilitated by the combined effect of the strong tendency for self-aggregation of the TO dyes and the favorable electrostatic interactions between TO and the AOT head groups. With increasing water content, the hydration of the dyes favors the disintegration of the H-dimers to the monomer form. Aggregation patterns of TO in SDS/water and AOT/heptane systems gives us information regarding the existence of pre-micellar and pre-reverse micellar aggregates in these surfactants. Interestingly, these initial aggregates serve as templates for bringing two or more TO dyes in close proximity, thus promoting the dye aggregation.⁵ These studies are therefore relevant for the design of molecular

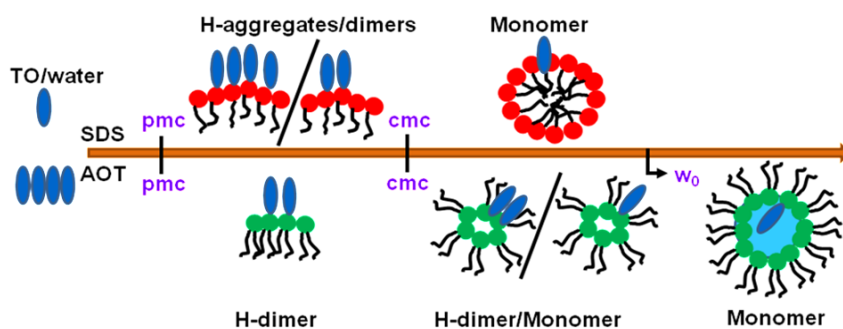


Fig. 2: Schematic of the surfactant induced H-dimer and H-aggregate formation of Thiazole Orange.

assemblies and ordered molecular structures with desired aggregation patterns, for various applications.

Spectacular Fluorescence Enhancement of Thiazole Orange within Macrocyclic Host, Selective Exchange and Release

Studies on recognition-mediated supramolecular assemblies have captured much attention in recent years because of their direct application in fluorescence sensing, on/off switches, controlled drug uptake/release, enzymatic assays, stimulus-responsive functional devices and so on. Cucurbit[n]urils are a class of fascinating host molecules with excellent binding affinities for cationic guests.⁶ Cucurbit[8]uril (CB8) has the special ability to hold two suitably sized guest molecules within its hydrophobic cavity. We observed that CB8 has a strong interaction with TO and forms two types of supramolecular complexes with the dye; a 1:2 complex composed of two TO molecules inside one CB8 moiety (CB8-2TO) and a 2:2 complex composed of two TO molecules capped by two CB8 moieties from either end (CB8-2TO-CB8).⁷ The 2:2 complexation lends immense structural rigidity to the TO molecules and prevents their intramolecular twisting. This leads to a spectacular, 1700 fold enhancement in the fluorescence intensity of TO. Excited by this host induced 'light-up' of TO, we attempted a stimulus responsive stoichiometric control over the host-guest supramolecular assembly. We selected different chemical additives like metal ions (NaCl), tryptophan (Trp), or adamantylamine (AD) as external stimuli, based on their biological importance and varying binding affinity toward CB8. Interestingly,

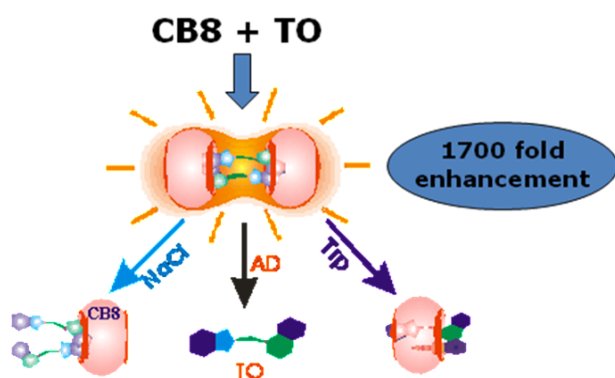


Fig. 3: Schematic of the supramolecular 'light-up' of TO and controlled stimulus responsive exchange/release of guests within CB8.

each of these additives produced a distinct supramolecular response with corresponding photophysical changes. In the presence of NaCl, the CB8-2TO-CB8 complex broke down into the CB8-TO complex, while in the presence of AD, the CB8-2TO-CB8 complex was totally disrupted leading to the release of free TO. With Trp, the CB8-2TO-CB8 complex was converted to CB8-TO-Trp, i.e. one of the TO molecules was replaced by a Trp molecule within the supramolecular complex.⁷ We feel that this controlled exchange and release strategy can be evolved into general protocols for designing functional supramolecular systems for targeted applications.

Acknowledgements

I would like to thank my mentors and co-authors of our published papers. I also thank all colleagues of RPCD and CG for their encouragement and support.

References

1. (a) Nygren, J., Andrade, J. M., Kubista, M. *Anal. Chem.* 68 (1996) 1706. (b) Silva, G. L., Ediz, V., Yaron, D., Armitage, B. A. *J. Am. Chem. Soc.* 129 (2007) 5710.
2. Lubitz, I., Zikich, D., Kotlyar, A. *Biochemistry* 49 (2010) 3567.
3. Mishra, A., Behera, R. K., Behera, P. K., Mishra, B. K., Behera, G. B. *Chem. Rev.* 100 (2000) 1973.
4. Kalyanasundaram, K. *Photochemistry in Microheterogeneous Systems* (Academic Press, London, 1987).
5. Dutta Choudhury, S., Bhasikuttan, A. C., Pal, H., Mohanty, J. *Langmuir* 109 (2005) 8113.
6. (a) Bhasikuttan, A. C.; Dutta Choudhury, S.; Pal, H.; Mohanty, J. *Isr. J. Chem.* 51 (2011) 51, 634. (b) Dsouza, R. N., Pischel, U., Nau, W. M. *Chem. Rev.* 111 (2011) 7941. (c) Dutta Choudhury, S.; Mohanty, J.; Pal, H.; Bhasikuttan, A. C. *J. Am. Chem. Soc.* 2010, 132, 1395–1401.
7. Mohanty, J., Thakur, N., Dutta Choudhury, S., Barooah, N., Pal, H., Bhasikuttan, A. C. *J. Phys. Chem. B* 116 (2012) 130.

BARC NEWSLETTER

CHARACTERIZATION OF DNA PROCESSING MULTIPROTEIN COMPLEX REVEALS THE ROLE OF ITS COMPONENTS IN RADIORESISTANCE OF *DEINOCOCCUS RADIODURANS*.

Swathi Kota and H.S. Misra
Molecular Biology Division

Dr. Smt. Swathi Kota is the recipient of the DAE Young Scientist Award for the year 2011

Abstract

Deinococcus radiodurans is characterized by its extraordinary resistance to various DNA damaging agents including gamma radiation and desiccation. An efficient DNA strand breaks repair and a strong oxidative stress tolerance are amongst the mechanisms attributed to its extraordinary radioresistance. Genome sequence comparison of this bacterium with *E. coli* a radiation sensitive bacterium shows nearly similar sets of DNA repair proteins as that of *E. coli*. Therefore, the possibility of the microenvironment in which these proteins are functioning could be different in radioresistant versus radiosensitive bacteria, was hypothesized. With this hypothesis, a multiprotein complex was isolated, characterized for DNA metabolic functions and components were identified using mass spectrometry. Interestingly, several of the activities of this complex found to be associated with the proteins actually detected in the complex. Complex also contains a large number of hypothetical proteins with unknown functions and these were further characterized for their roles in radioresistance and DNA repair in *D. radiodurans*. Our findings all together suggested the importance of protein-protein and protein DNA interactions in the efficient execution of different cellular functions including gamma radiation resistance in *Deinococcus radiodurans*.

Introduction

Deinococcus radiodurans a member of *Deinococcaceae* family is extremely tolerant to many abiotic stresses including ionizing radiation, UV and water loss (Battista, 1997). Complete genome sequence of this bacterium is available and its analysis shows the presence of nearly similar DNA repair and homologous recombination machinery except RecBC, as known in other radiation sensitive bacteria including *Escherichia coli* (White et al., 1999). Over the years research has revealed that an efficient DNA double strand break (DSB) repair (Zahradka et al., 2006, Slade et al., 2009) and strong antioxidant mechanisms are amongst the processes implicated to its extraordinary tolerance to the deleterious effects of DNA damaging agent. A unique DSB repair mechanism called Extended Synthesis Dependant Strand Annealing (ESDSA), which helps to

mend hundreds of DSBs efficiently, has been demonstrated in this bacterium (Zahradka et al., 2006). Further, the antioxidants such as carotenoids (Tian and Hua, 2010), PQQ (Khairnar et al., 2003, Rajpurohit et al., 2008) and the intracellular ratio of Mn/Fe (Daly et al., 2004) contribution to radioresistance and oxidative stress tolerance by either directly or indirectly protecting the biomolecules from oxidative damage has been documented. Another unique feature of this bacterium is that its genome (the blue print of life) exists in form of a highly condensed and compact toroidal structure. Although the role of toroidal nature of genome contributing to DSB repair is debated, its significance in extraordinary radiation resistance (Levin-Zaidman et al., 2003, Zimmerman and Battista, 2005) of this bacterium has not be ruled out. Since, the compactness of its genome does not alter upon irradiation, and the possibility of some unique mechanisms maintaining the

BARC NEWSLETTER

structural integrity of chromosomes during normal growth and post irradiation recovery could be suggested. Whether it is the efficient DSB repair by ESDSA or packaging of its genome in toroidal form, require several proteins to be together in close proximity for efficient processing and repair of radiation induced DNA breaks. The multiprotein assemblies help in enhancing the speed and specificity of biochemical reactions. Proteins present in multiprotein complexes at times acquire new functions upon interaction with other proteins in vicinity. Also even unknown proteins have been characterized based on the functions of their interacting partners (Takashi et al., 2010). Multiprotein complexes may also act as depots to release protein components depending upon the requirement of the cells (Mazumder et al., 2003). Therefore the idea of characterization of such types of complexes from this bacterium has been a novel thought and that has been realized under this study.

A multiprotein complex having 24 different proteins present together in form of a functional module was

Table 1: Mass spectrometric analysis of protein complex components.

Annotated ORFs in the host genome	Protein size (~kDa)	Deinococcal protein identity
DR0116	13.7	Hypothetical protein
DR0129	67.9	DnaK protein
DR0505	59.3	5' - Nucleotidase family protein
DR0644	20.7	Hypothetical protein
DR0672	17.1	Hypothetical protein
DR0673	19.9	Hypothetical protein
DR0690	38.9	Hypothetical topoisomerase
DR0691	27.0	Hypothetical protein
DR0969	46.1	Hypothetical protein
DR0972	23.4	Conserved hypothetical protein
DR1124	42.6	SLH family protein
DR1483	32.2	Hypothetical protein
DR1706	12.7	Hypothetical protein
DR1707	102.6	DNA - dependent DNA polymerase
DR1736	73.1	Cyclic nucleotide 2' - phosphodiesterase
DR1768	15.0	Hypothetical protein
DR2069	75.4	DNA ligase
DR2310	84.2	Hypothetical protein
DR2417m	63.5	Conserved hypothetical protein
DR2527	20.2	Hypothetical protein
DR2563	7.8	Hypothetical protein
DR A0346	32.0	PprA
DRB0067	109.7	Putative extracellular nuclease
DRB0100	24.3	Putative DNA ligase

isolated and identified from *D. radiodurans*. Biochemical characterization of this complex indicated that it has various DNA metabolic activities closely associated with DSB repair, a process associated with gamma radiation resistance. Mass spectrometric analysis shows that there are 24 different proteins of *Deinococcus radiodurans* are present in this complex as a functional module (Table 1). Different biochemical activities that were associated with this complex are, metal ion and ATP independent super coiled DNA relaxation activity i.e. topoisomerase IB activity, divalent metal ions dependent 5'→3' exonuclease activity, ATP stimulated DNA end joining activity, DNA dependent DNA polymerase activity and protein kinase activity (Kota and Misra, 2008). Majority of these functions are found to be associated with the proteins actually detected in the complex. An intriguing feature of this DNA processing complex is that it harbors two important but mutually incompatible DNA metabolic functions i.e. nuclease (a degradation) and DNA ends joining (a synthetic) activities. Our results revealed that ATP a high-energy biomolecule is the key regulator of the differential regulation of its nuclease and ends joining activities in the complex. Since, the levels of ATP showed a kinetic change during post irradiation recovery of *D. radiodurans* (Kamble et al. 2010), the possibility of ATP regulating both these incompatible functions of such a complex under in vivo conditions could be suggested. Subsequently, we characterized ATP sensitive nuclease activity in two of the deinococcal hypothetical proteins (DR0505 and DR2417) and ATP requirement for the DNA ends joining activity by ATP type DNA ligase (DRB0100) of the complex. This complex also contains another notable DNA repair protein PprA that is present only in member of Deinococcaceae family. Recently we have demonstrated novel function of this protein in genome maintenance of this bacterium.

Functional characterization of DR_0505 as ATP sensitive nuclease

DR0505, a protein component of the multiprotein complex was previously annotated as a 5' nucleotidase. Bioinformatic analysis showed that DR_0505 ORF is having 5' nucleotidase domain both at C terminal of total protein and in the C-terminal region of a

BARC NEWSLETTER

calcinuerin like esterase domain located at N terminal of protein. The possibility of DR0505 protein contributing to nuclease function in the complex was hypothesized and subsequently studied at both molecular and genetics levels. Recombinant DR0505 is characterized as a thermotolerant esterase, which could detoxify both natural, as well as damaged mononucleotides like 8-oxo-GMP. It may be noted that 8-oxo-GMP is product of oxidative damage of DNA and if not detoxify could become harmful to the fidelity and integrity of the genome in the cells. Thus an enzyme like DR_0505 might be assisting this organism in the catabolism and replenishment of nucleotide pools by recycling both normal and damaged bases and thereby helping in the maintenance of genome integrity could be suggested. Esterase function of this protein was also tested on artificially synthesized DNA substrate. The purified DR_0505 enzyme also showed ATP insensitive endonuclease activity with the propensity to ss/ds junction and ATP sensitive 3'→5' exonuclease activities

on both single-stranded and double-stranded DNA substrates (Fig 1). Thus DR0505 a hypothetical protein in complex is characterized as an ATP regulated DNA-processing enzyme and a thermotolerant esterase *in vitro* (Kota et al., 2010a).

DRB0100 is characterized as ATP type DNA ligase

DRB0100 was identified as an uncharacterized polypeptide in complex. Homology search shows that this protein is closer to an ATP type DNA repair ligase of higher organisms including human being. Shortly thereafter, the recombinant protein was made and demonstrated by an independently group, that this protein is inactive *in vitro* (Blasius et al 2006). Since, I had detected this protein in multiprotein complex showing ATP stimulated DNA ligase activity along with other proteins, we hypothesized that DRB0100 seems require other partners for its activity. Previously, Narumi and colleagues have also shown that PprA could

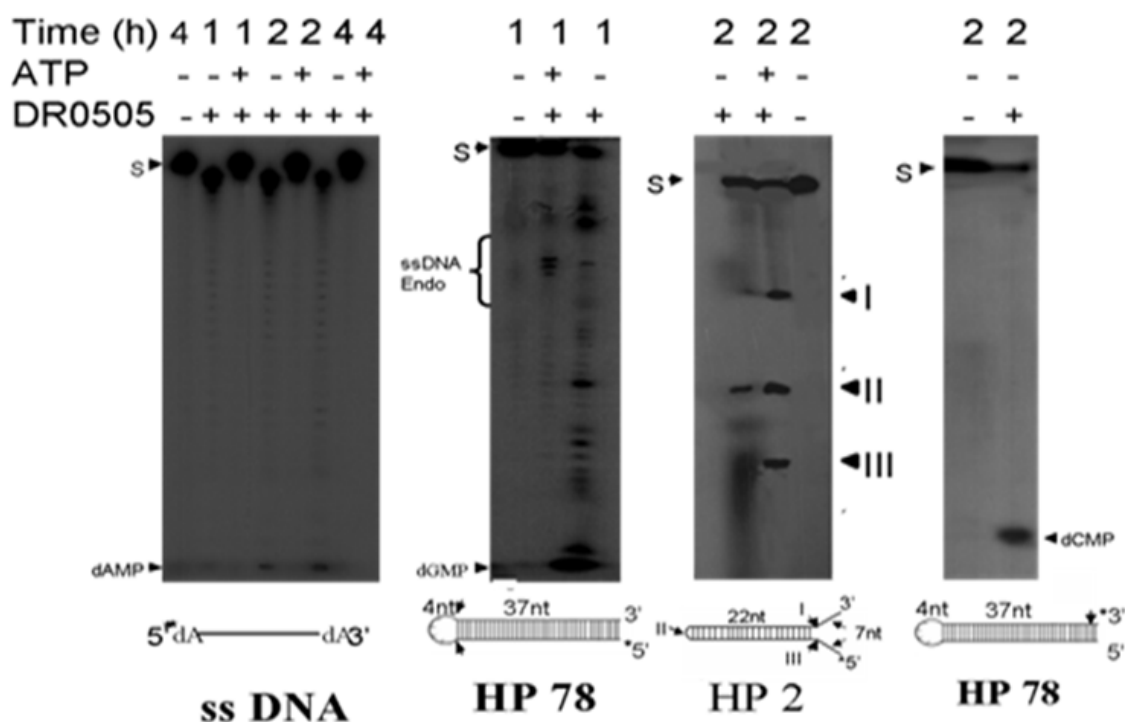


Fig 1: DNA-processing activity assay of DR0505 on DNA substrates with different structures in solution. (A) The single-stranded 40-mer poly dA (dA40), (B) stem-loop 78-mer (HP78) and (C) hairpin-forked 56-mer (HP2) were labelled at the 5' end (D) HP78 also labelled at the 3' end. Purified substrates (S) were incubated with purified protein for the indicated times with dA40, 1 h with HP78 labelled at the 5'end, 2 h with HP2 and 2 h with HP78 labelled at the 3' end both in presence and absence of ATP. Products were analysed by urea/PAGE and radiolabelled DNA bands were visualized by autoradiography. Arrows indicate the position of different substrates and the corresponding products generated from both endonucleolytic and exonucleolytic cleavage of respective substrate as shown in autoradiogram. Labeled deoxy mono nucleotides are released by either the terminal cleavage of the (D) 3'-labelled base (dCMP) or 3'→5' processive degradation of 5'-labelled (A) ssDNA and (B and C) dsDNA substrates.

BARC NEWSLETTER

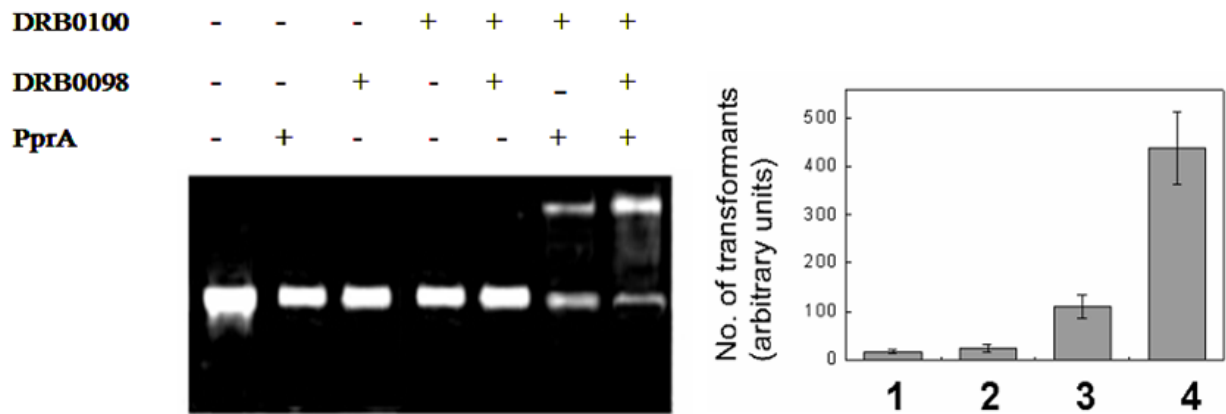


Fig 2: DNA end-joining activity assay of recombinant DRB0100 (LigB) in presence of PprA and DRB0098 proteins. The effect of PprA on DRB0098- supported ligation efficiency of LigB was assayed on agarose gel taking linear plasmid as substrate (A) and (B) Bio assay for DNA end joining activity of DRB0100 protein. The ligation mixtures obtained from incubation of DNA substrate with LigB alone (1) and LigB with DRB0098 (2), PprA (3), and PprA with DRB0098 (4), respectively, were transformed into *E. coli* and number of transformants obtained were plotted.

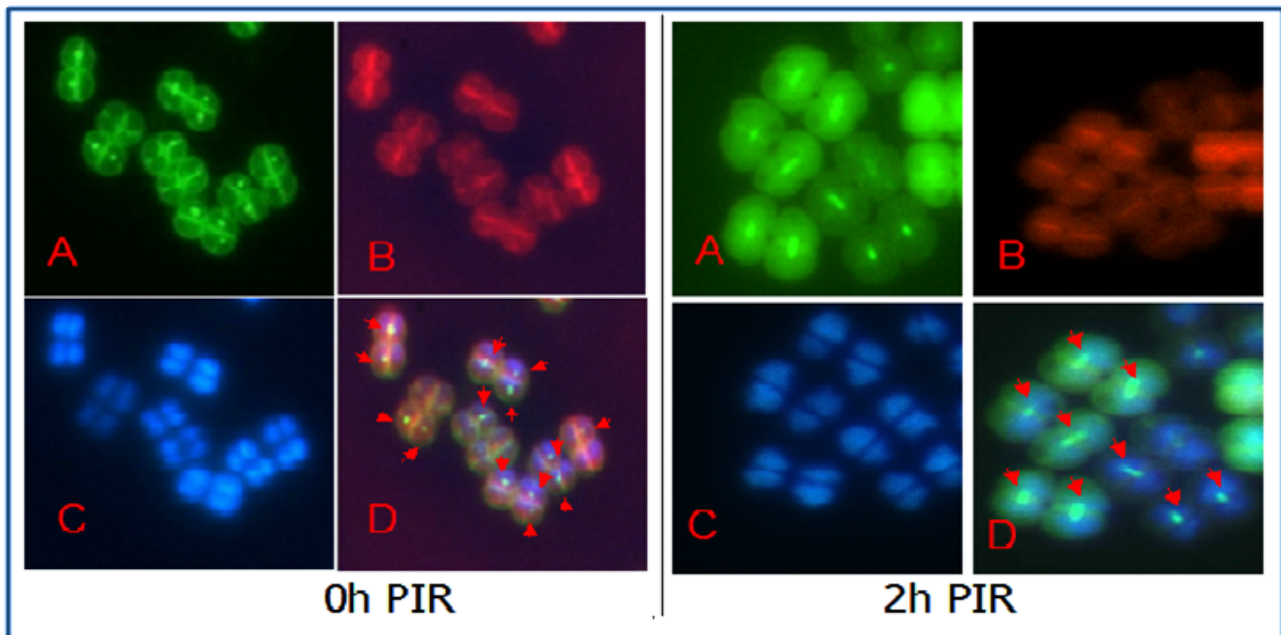


Fig 3: Cellular localization of PprA in *Deinococcus radiodurans*. The *pprA* mutant of *D. radiodurans* (DR), expressing GFP-PprA was irradiated with 4kGy gamma radiation and cells were collected at 0h post irradiation recovery period (0hPIR) and 2h PIR (2hPIR). These were imaged for GFP (A), membrane stained with Nile red (B) and nucleoid stained with DAPI (C). These images were merged (D) to check PprA localization in cells. All these cells were imaged for GFP expression and for DAPI stained nucleoid. Arrow indicated the position of GFP- PprA foci across the field.

stimulate DNA end joining activity of a commercially procured DNA ligase *in vitro* (Narumi et al 2004). We therefore, made recombinant PprA as well as DRB0100 in our laboratory and reconstituted together, checked for DNA ends joining activity. Pleasantly, we could detect DNA ends joining activity in DRB0100 in presence of PprA (Fig 2.). This indicated that DRB0100 a component of multiprotein complex requires interacting partners for its function. This has been the most remarkable

and novel findings demonstrating directly the significance of protein-protein interaction in expression of function in a protein, which alone does not express its activity. The possibility of various other proteins of the complex acting more efficiently when present in complex form cannot be ruled out but could provide a most plausible basis of this bacterium having higher tolerance to DNA damage as compared to other bacteria.

BARC NEWSLETTER

PprA involvement in genome segregation is a novel function of this protein

PprA is a novel radiation-inducible protein found exclusively in member of *Deinococci* family that plays a critical role in the radiation resistance of *Deinococcus radiodurans* (Narumi et al., 2004). It was found to be associated with the DNA processing multiprotein complex we identified from this bacterium. Earlier it was shown that PprA binds to linear double stranded DNA and also stimulates DNA ligase activity (both NAD and ATP dependent). In addition to the role of PprA in the stimulation of ATP dependent DNA ligase activity of DR_B0100 (Kota et al., 2010b), we recently observed that GFP-PprA fusion protein expressing in *D. radiodurans* produced a signature (sitting between growing septum) (Fig 3) that is similar to the proteins involved in the resolution of duplicated intertwined bacterial chromosome and thus genome segregation. We observed that the frequency of anucleate cells in wild type and cells lacking PprA was nearly similar under normal growth conditions. However, upon DNA damage by gamma radiation, the PprA lacking cells showed several fold higher frequency of anucleate cells (Fig 5). These results suggest that PprA has a novel function in the genome segregation and maintenance of radiation damaged genome in *D. radiodurans*.

Conclusions

We have demonstrated the existence of several DNA repair proteins in form of multiprotein complex in the extremophile *Deinococcus radiodurans*. The DNA processing complex showed nuclease activity inhibited by ATP and DNA ligase activity is dependent on ATP. Earlier findings from our laboratory had shown that the levels of different nucleotides change during post irradiation recovery period (Kamble et al., 2010) and during early hours ATP levels are more. Thus the two mutual incompatible processes i.e. DNA degradation and DNA synthesis functions which are very much essential in DNA damage repair are regulated differently in different organisms and the outcome of this process might decide the survival of an organism to the DNA damaging agents. Presence of novel proteins like PprA

which protects the DNA ends and has role in genome segregation besides its stimulatory effects on enzymatic activities like catalase and DNA ligases, and proteins like DR-0505 which functions even at higher temperatures may assist the organism's survival at extreme conditions. Thus the findings from my studies signify the importance of macromolecular interaction in facilitating cellular and molecular processes integral to gamma radiation induced DNA strand break repair and eventually gamma radiation resistance in *D. radiodurans*.

Acknowledgments

I am grateful to Dr. H. S. Misra, Head, Molecular Genetics Section, Molecular Biology Division for being associated with this project as a mentor and his constant encouragement and criticisms. We thank Professor S.K. Apte, AD (B) BMG & Head-MBD for his suggestions and constant supports during the course of this study. I express my sincere gratitude to Dr (Mrs) Vidya A. Kamble, Dr. Y. S. Rajpurohit, Shri Vijaya Kumar Charaka for their support in this work and other lab colleagues for their valuable suggestions and upfront criticisms.

References

1. Battista, J.R. Against all odds: the survival strategies of *Deinococcus radiodurans*. *Annu. Rev. Microbiol* 1997; 51: 203-224.
2. Blasius, M., Buob, R., Shevelev, I.V., and Hubscher, U. 2007. Enzymes involved in DNA ligation and end-healing in the radioresistant bacterium *Deinococcus radiodurans*. *BMC Mol. Biol.* **8**(1): 69.
3. Daly, M.J., Gaidamakova, E.K., Matrosova, V.Y., Vasilenko, A., Zhai, M., Venkateswaran, A., Hess, M., Omelchenko, M.V., Kostandarithes, H.M., Makarova, K.S., Wackett, L.P., Fredrickson, J.K., Ghosal, D. (2004). Accumulation of Mn(II) in *Deinococcus radiodurans* facilitates gamma-radiation resistance. *Science* 306, 1025–1028.
4. Kamble, V. A., Rajpurohit, Y. S., Srivastava, A. K. and Misra, H. S. (2010). Increased synthesis of signaling molecules coincides with reversible

BARC NEWSLETTER

inhibition of nucleolytic activity during postirradiation recovery of *Deinococcus radiodurans*. *FEMS Microbiol. Lett.* **303**, 18–25.

5. Khairnar, N. P., Misra, H. S., and Apte, S. K. (2003). Pyrroloquinoline-quinone synthesized in *Escherichia coli* by pyrroloquinoline-quinone synthase of *Deinococcus radiodurans* plays a role beyond mineral phosphate solubilization. *Biochem Biophys Res Commun* 312:303-308.
6. Kota, S., and Misra, H.S. (2008). Identification of a DNA processing complex from *Deinococcus radiodurans*. *Biochem Cell Biol* 86: 448–458.
7. Kota, S., Kumar, C.V., Misra, H.S. (2010a). Characterization of an ATP-regulated DNA-processing enzyme and thermotolerant phosphoesterase in the radioresistant bacterium *Deinococcus radiodurans*. *Biochem. J.* 431, 149-157.
8. Kota, S., Kamble, V.A., Rajpurohit, Y.S., and Misra, H.S. (2010b) ATP-type DNA ligase requires other proteins for its activity in vitro and its operon components for radiation resistance in *Deinococcus radiodurans* in vivo. *Biochem Cell Biol* 88: 783-790.
9. Kota, S., and Misra, H.S. (2006) PprA: A protein implicated in radioresistance of *Deinococcus radiodurans* stimulates catalase activity in *Escherichia coli*. *Appl Microbiol Biotechnol* 72: 790-796.
10. Levin-Zaidman S., Englander, J., Shimon, E., Sharm, A.K., Minton, K.W., Minsky, A. (2003) Ringlike structure of the *Deinococcus radiodurans* genome: a key to radioresistance? *Science*. 299:254-6.
11. Mazumder, B., Sampath, P., Seshadri, V., Moitra, R.K., DiCoreto, P.E., and Fox, P.L. (2003). Regulated release of L13a from the 60S ribosomal subunit as a mechanism of transcript-specific translational control. *Cell* 115: 187-198.
12. Narumi, I., Satoh, K., Cui, S., Funayama, T., Kitayama, S., and Watanabe, H. (2004) PprA: a novel protein from *Deinococcus radiodurans* that stimulates DNA ligation. *Mol Microbiol* 54: 278-285.
13. Rajpurohit, Y.S., Gopalakrishnan, R., and Misra, H.S. (2008) Involvement of a protein kinase activity inducer in DNA double strand break repair and radioresistance of *Deinococcus radiodurans*. *J Bacteriol* 190: 3948-3954.
14. Slade, D., Lindner, A.B., Paul, G., and Radman, M. (2009). Recombination and replication in DNA repair of heavily irradiated *Deinococcus radiodurans*. *Cell* 136, 1044-55.
15. Takashi, O., Bancinyane, L. S., Qian, W., Dimitri, Y., Victor, M., Bolanos, G., and Blundell, T.L. (2010). Structural biology of DNA repair: Spatial organization of the multiprotein complexes of nonhomologous end joining. *Nucleic Acids*. Vol 2010:19 pages doi:10.4061/2010/621695.
16. Tian, B., and Hua, Y. (2010) Carotenoid biosynthesis in extremophilic *Deinococcus-Thermus* bacteria. *Trends Microbiol* 18:512-20.
17. White O, Eisen JA, Heidelberg JF, Hickey EK, Peterson JD, Dodson RJ, et al. (1999). Genome sequence of the radioresistant bacterium *Deinococcus radiodurans* R1. *Science* 286: 1571-7.
18. Zahradka, K., Slade, D., Bailone, A., Sommer, S., Averbeck, D., Petranovic, M. et al., (2006) Reassembly of shattered chromosomes in *Deinococcus radiodurans*. *Nature* 443: 569-573.
19. Zimmerman, J.M., and Battista, J.R. (2005). A ring-like nucleoid is not necessary for radioresistance in the *Deinococcaceae*. *BMC Microbiol.* 31:15:17.

BARC NEWSLETTER

APPLICATION OF IMMOBILIZED ENZYME AND CELLS IN BIOSENSORS FOR THE DETECTION OF GLUCOSE AND METHYL PARATHION

Jitendra Kumar

Nuclear Agriculture and Biotechnology Division

Dr. Jitendra Kumar is the recipient of the DAE Young Scientist Award for the year 2011

Abstract

Biosensors are analytical devices composed of a recognition element of biological origin and a physico-chemical transducer. Immobilization plays a key role in developing stable biocomponent for integration with transducers, which lead to the development of biosensor. This article describes the study carried out on immobilization of glucose oxidase (GOD) enzyme and microbial cells on suitable matrices for the development of stable biocomponent and its integration with the transducer for the detection of glucose and methyl parathion.

Introduction

A biosensor is a compact analytical device, incorporating a biological or biologically derived sensing element, either closely connected to, or integrated within a transducer system. The principle of detection is the specific binding of the analyte of interest to the complementary biorecognition element immobilized on a suitable support matrix. The specific interaction results in a change in one or more physico-chemical properties (viz. pH change, electron transfer, mass changes, heat transfer, uptake or release of gases or specific ions) which can be detected and measured by the transducer. The aim is to produce an electronic signal, which is proportional to the concentration of a specific analyte or group of analytes, to which the biosensing element binds. Biosensors can be classified according to biorecognition system. The biological elements used in biosensor technology are enzymes, antibody/antigens and nucleic acids/complementary sequences. In addition, microorganisms, animal or plant whole cells and tissue slices, can also be incorporated in the biosensing system. Depending on the method of signal transduction, biosensors can also be divided into different groups: electrochemical (amperometric, potentiometric or conductometric), optical,

thermometric and piezoelectric. Biosensors offer many advantages over conventional analytical techniques. The selectivity of the biological sensing element offers an opportunity for the development of highly specific devices for real-time analysis in complex mixtures, without the need for extensive sample pre-treatment or large sample volumes. The function of a biosensor will depend on the biochemical specificity of the biologically active material. Biosensors also promise highly sensitive, rapid, reproducible and simple-to-operate analytical tools.

The basic requirement of a biosensor is that the biological material should bring the physico-chemical changes in close proximity of a transducer. In this direction, immobilization technology has played a major role. Immobilization not only helps in forming the required close proximity between the biomaterial and the transducer, but also helps in stabilizing it for reuse. The biological material has been immobilized directly on the transducer or in most cases, in membranes, which can subsequently be mounted on the transducer. Biomaterials can be immobilized either through adsorption, entrapment, covalent binding, cross-linking or a combination of all these techniques. The choice of technique and support should be such that, it should retain the enzyme activity and have reusability as well

BARC NEWSLETTER

as storage stability. A variety of synthetic as well as natural materials have been exploited in our laboratory, for immobilization of biocatalysts and their use in biosensor development.

This article summarizes all our studies related to immobilization of glucose oxidase (GOD) and microbial cells having OPH enzyme on different supports using suitable techniques for the development of biosensors for methyl parathion and glucose monitoring.

Immobilization of GOD enzyme for glucose biosensors

Enzymes are well-known as biological sensing materials in the development of biosensors due to their specificity and play a key role in clinical diagnosis. Detection of glucose has been the most studied analyte in clinical diagnosis for diabetic patients. Most of the glucose biosensors are based on glucose oxidation, catalyzed by GOD enzyme. In our study GOD enzyme was immobilized on suitable support for better stability and reusability and associated with suitable transducers for biosensor monitoring of glucose. Immobilized GOD converts glucose into gluconolactone with the consumption of oxygen. Amperometric response was monitored, by measuring the depletion of oxygen from sample using oxygen-sensitive dissolved oxygen (DO) electrode.

In one of our study a method was optimized to prepare a synthetic polyvinyl alcohol (PVA) membrane from a homogenous mixture of 12% low DOP PVA, 8% high DOP PVA and 2% benzoic acid in 50 mM sodium phosphate buffer containing 20% acetone. 2 mL GOD (2000 units/mL) was added to the mixture and mixed homogeneously. The mixture was overlaid as a thin membranous layer, air-dried, peeled off carefully and placed under UV light for cross-linking and integrated with the DO probe for biosensor application (Fig. 1). Detection range of this biosensor was estimated to be between 0.9 and 225 mg/dL glucose. GOD-PVA membrane was reused for 32 reactions and was stable for 30 days without significant loss of activity¹.

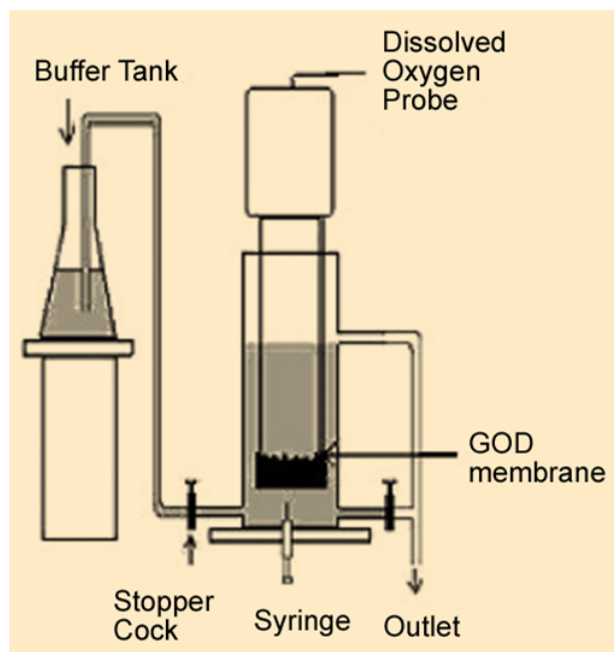


Fig.1: Schematic diagram of association of GOD immobilized membrane with the DO probe biosensor

In another study GOD was immobilized on inner epidermal membrane of the onion bulb scales as a natural support and applied for biosensor application for detection of glucose in association with DO probe². Natural polymers in living organisms are composed of biomolecules like carbohydrates, lipids and proteins and therefore they can provide a biocompatible microenvironment for enzyme immobilization. This natural membrane is also mechanically stronger because it consists of microfibrillar cellulosic biological components and served as a biocompatible immobilizing support, for optimum enzyme activity. Onions (*Allium cepa* L.) were cut into half, bulb scales were separated and inner epidermis from outer fleshy scale was stripped. Circular pieces of 1.5 cm diameter were cut and stored at 4°C in the refrigerator. An aliquot of 100 µL GOD (250 units/ml prepared in 50mM sodium phosphate buffer) was added on each membrane. After 30 min, 10 µL of 2% glutaraldehyde solution was added to the surface of the membrane and spread uniformly. After GOD immobilization on surface of onion membrane, many changes like depressions and uneven distribution of microfibrillar structure were observed on the surface morphology (Fig. 2). GOD immobilized onion membrane has shown a high reusability (127

BARC NEWSLETTER

reactions) and stability (45 days) but low sensitivity (detection range 22.5 - 450mg/dL) for glucose detection, for the development of the biosensor.

analyte. As the OPH is a periplasmic enzyme, whole cells can be immobilized directly on the matrix and integrated with transducers for biosensor development.

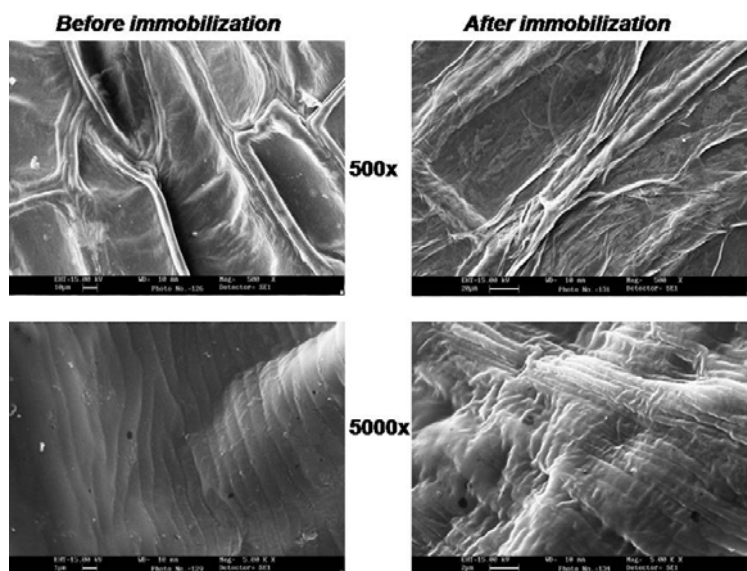


Fig. 2: SEM micrograph of onion membrane after immobilization of glucose oxidase

Immobilization of microbial cells for methyl parathion biosensors

Methyl parathion pesticide is extensively used in the field of agriculture despite its high toxicity and contributes major share in terms of restricted uses in India. Among the various biosensors for methyl parathion determination, systems based on acetylcholinesterase (AChE) and organophosphorus hydrolase (OPH) enzymes contribute major share. AChE biosensor is based on enzyme inhibition mechanism; hence it requires longer incubation time and also has poor specificity because of interference from carbamate pesticide and metals. OPH catalyzes hydrolysis of methyl parathion pesticide into detectable product *p*-nitrophenol (PNP) and generates two protons as a result of the cleavage of the P-O bond. Products that are chromophoric and/or electroactive can be detected by colorimetric and electrochemical methods, and were exploited to develop biosensors for detection of methyl parathion pesticide. The analyte can be determined as the rate of product formation is directly proportional to the concentration of the

In our laboratory different types of microbial biocomponents (from disposable to reusable) were developed by immobilizing microbial cells on different supports and associated with different transducers (optical and electrochemical) for analysis of single to multiple samples at a time.

In our first study for detection of methyl parathion, an optical microbial biosensor was developed in which disposable biocomponent was prepared by immobilizing whole cells of *Flavobacterium sp.* on glass fibre filter paper disc and associated with an optical fibre transducer. Detection range of the biosensor was 4 – 80 μ M methyl parathion which required only 75 μ L of sample and its biocomponent was disposable in nature and can be used for field sample analysis³.

In the second study, *opd* gene, which codes for OPH enzyme, was cloned to make recombinant *E.coli* with high periplasmic expression of enzyme. Recombinant *E.coli* cells were immobilized on screen-printed carbon electrode (SPCE) for preparing the biocomponent. Surface morphologies of the working area of both blank and whole cells immobilized SPCE were studied by SEM. As observed in SEM micrograph (Fig. 3), bacterial cells (size 0.5–2 μ m) were present in immobilized SPCE and were absent in the micrograph of blank SPCE. An

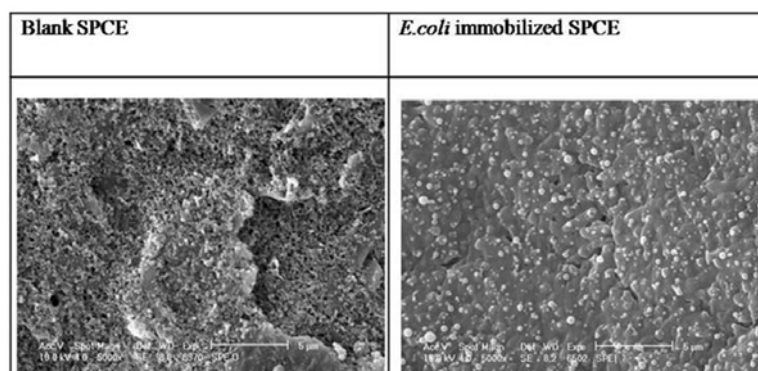


Fig. 3: SEM micrograph of *E.coli* immobilized SPCE

BARC NEWSLETTER

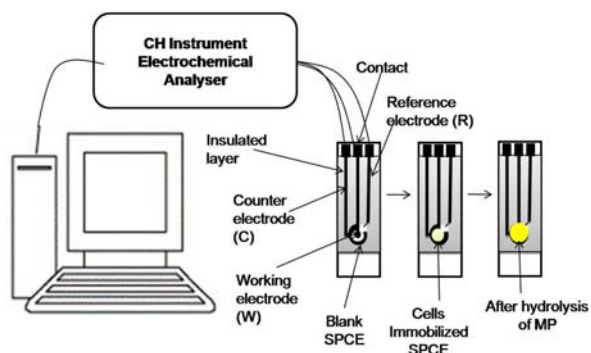


Fig. 4: Schematic diagram of experimental set up of electrochemical biosensor

electrochemical microbial biosensor was developed based on cyclic voltammetry for the detection of methyl parathion using cells immobilized SPCE (Fig. 4). In this study, detection range of the biosensor was 2 - 80 μM methyl parathion but the biocomponent was reusable upto 32 reactions and biosensor requires low volume (20 μL) of sample hence it can be used when very low sample amount is available⁴.

In our third study, an optical biosensor was developed for detecting large number of samples in a single platform in a short period of time (5 min). For this, a bacterium was isolated from soil and identified as *Shingomonas sp. JK1* which hydrolyzes methyl parathion. Microbial cells were then immobilized onto the surface of the wells of microplate (96 wells) and used as a reusable (upto 75 reactions) biocomponent. Surface morphologies of the immobilized area of both blank and whole cells-immobilized microplate were imaged by SEM (Fig. 5). SEM micrographs were acquired on interior surface of the wells of microplates. A bunch of bacterial cells (sizes 0.4 - 0.8 μm) were observed in the micrograph of cells-immobilized surface of well and were absent in the micrograph of unimmobilized surface of well. Microplate based technology was utilized to develop an effective biosensor

tool for detection of multiple numbers of samples because of the time independent measurement of the whole microplate plate irrespective of the number of samples present on the plate (96 wells) that enable to handle multiple number of samples simultaneously on a single platform (Fig. 6). In another experiment, *Shingomonas sp. JK1* was also immobilized on natural support, inner epidermis of onion bulb scale and a bunch of bacterial cells (sizes 0.4–0.8 μm) were observed in the micrograph of cells immobilized inner

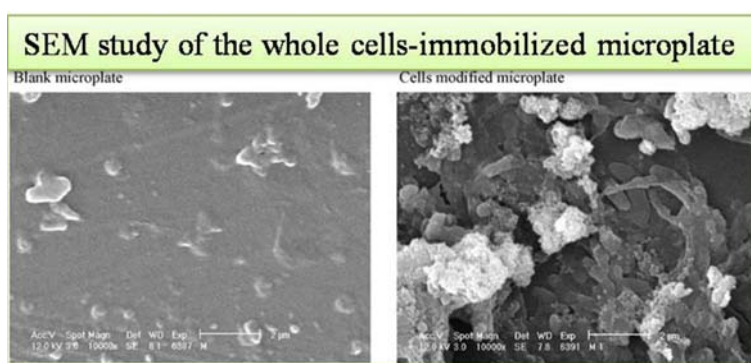


Fig. 5: SEM micrograph of microbial cells (*Shingomonas sp.*) immobilized microplate

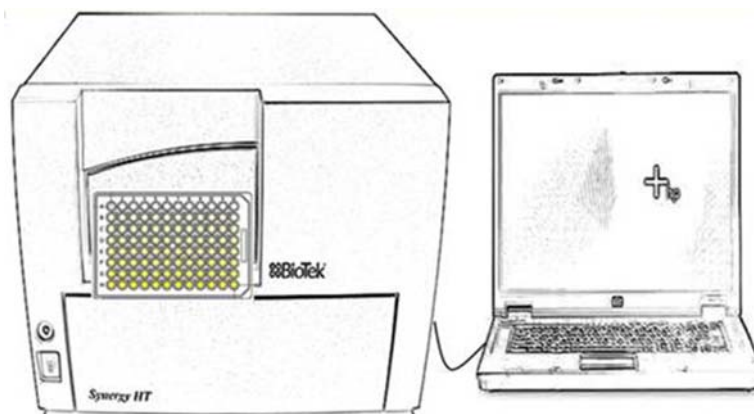
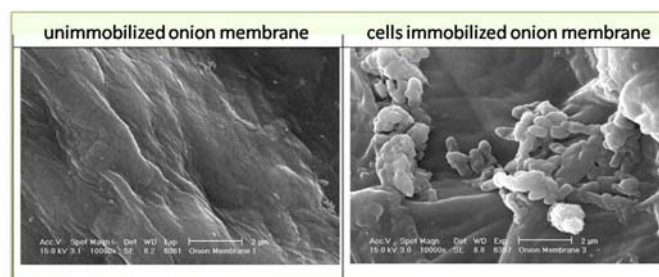


Fig. 6: Schematic diagram of experimental set up of microplate based biosensor



SEM study of the cells (*Shingomonas sp. JK1*) immobilized onion membrane at 10,000x.

Fig. 7: SEM micrograph of microbial cells (*Shingomonas sp.*) immobilized on onion membrane

BARC NEWSLETTER

epidermis of onion bulb scale and was absent in the micrograph of unimmobilized surface (Fig. 7). Cells immobilized biocomponent was directly placed in the wells of microplate and associated with the optical transducer for monitoring of methyl parathion pesticide⁶.

Conclusion

GOD was successfully immobilized on PVA membrane as a synthetic support and inner epidermal membrane of the onion bulb scales as a natural support for application in DO based glucose biosensors. Microbial cells having OPH was immobilized on different types of supports for developing biocomponents (from disposable to reusable) and associated with different transducers for biosensor detection of methyl parathion pesticide.

References

1. Kumar, J., and D'Souza, S. F. Preparation of PVA Membrane for Immobilization of GOD for Glucose Biosensor. *Talanta* 75 (1), (2008): 183-8.
2. Kumar, J., and D'Souza, S. F. Inner Epidermis of Onion Bulb Scale: As Natural Support for Immobilization of Glucose Oxidase and its Application in Dissolved Oxygen Based Biosensor. *Biosensors and Bioelectronics* 24 (6), (2009): 1792-5.
3. Kumar, J., Jha, S. K., and D'Souza, S. F. Optical Microbial Biosensor for Detection of Methyl Parathion Pesticide using *Flavobacterium Sp.* Whole Cells Adsorbed on Glass Fiber Filters as Disposable Biocomponent. *Biosensors and Bioelectronics* 21 (12), (2006): 2100-5.
4. Kumar, J., and D'Souza, S. F. "Microbial Biosensor for Detection of Methyl Parathion using Screen Printed Carbon Electrode and Cyclic Voltammetry." *Biosensors and Bioelectronics* 26 (11), (2011): 4289-93.
5. Kumar, J., and D'Souza, S. F. An Optical Microbial Biosensor for Detection of Methyl Parathion using *Sphingomonas Sp.* Immobilized on Microplate as a Reusable Biocomponent. *Biosensors and Bioelectronics* 26 (4), (2010): 1292-6.
6. Kumar, J., and D'Souza, S. F. Immobilization of Microbial Cells on Inner Epidermis of Onion Bulb Scale for Biosensor Application. *Biosensors and Bioelectronics* 26 (11), (2011): 4399-404.

TUNABLE STRUCTURAL AND MAGNETIC CORRELATIONS IN MULTIFUNCTIONAL HEXACYANOMETALLATE $A_N[B(CN)_6]_M \cdot zH_2O$ COMPOUNDS WITH POSSIBLE TECHNOLOGICAL APPLICATIONS

Amit Kumar

Solid State Physics Division

Dr. Amit Kumar is the recipient of the DAE Young Scientist Award for the year 2011

Abstract

Bulk polycrystalline and nanocrystalline samples of hexacyanometallate, $A_n[B(CN)_6]_m \cdot zH_2O$ (A and B being magnetic ions) based molecular magnetic compounds have been studied in order to investigate the role of crystal structure, structural defects, and type of magnetic ion in determining various magnetic properties of these materials. Our study emphasizes the importance of these structural aspects in the rational design of magnetic properties of these multifunctional magnetic compounds. Possible applications of the studied hexacyanometallate compounds in magnetoelectronic and magnetocaloric devices, such as magnetic memory and magnetic cooling/heating based constant temperature bath have been revealed.

Molecular magnets are new class of magnetic materials that show the possibility of incorporating various molecular functionalities along with their interesting magnetic properties. Unlike traditional atom (mainly 3d/4f metals) based magnets, molecular magnets can be synthesized/ manipulated at ambient conditions using synthetic chemistry methods. These low density (~ 1 gm/cc) magnetic materials have the potential to replace/improve the currently used magnetic materials in our daily life as well as in industry. The hexacyanometallate, $A_n[B(CN)_6]_m \cdot zH_2O$ (A and B being magnetic ions) or Prussian blue based molecular magnets show various novel functionalities, e.g., photo-induced magnetization, electrical conductivity switching, and pressure sensitivity that are suitable for practical applications [1]. However, it is very much essential to understand the factors that can fine tune their structural and magnetic properties for optimal functionality. We have studied the hexacyanometallate compounds (where $A = Mn, Fe, Ni, Co,$ and Cu and $B = Fe$ or Cr) [2-11] with an aim to tune and tailor their magnetic properties by varying chemical composition and/or structural defects. We have also demonstrated

the physics principles of the utilization of these magnetic materials in magnetic memory and magnetic cooling/heating based constant temperature bath applications. This article gives an overview of our investigations on the above magnetic materials.

The bulk polycrystalline samples [3-7, 9-11] of the hexacyanometallates were prepared by simple precipitation method whereas the nanocrystalline samples [2,8] were prepared by carrying out the precipitation reaction in a controlled environment using microemulsions. We employed neutron and X-ray diffraction, infrared and Mössbauer spectroscopy, dc magnetization, ac susceptibility, and transmission electron microscopy experimental techniques as well as Rietveld refinement and reverse Monte Carlo (RMC) computational techniques.

Fig. 1(a) shows the room temperature neutron diffraction pattern for $Fe[Fe(CN)_6] \cdot 4H_2O$ compound. Our structural investigations employing Rietveld refinement technique reveal that this compound crystallizes in the face centred cubic (*fcc*) space group *Fm3m* with lattice

BARC NEWSLETTER

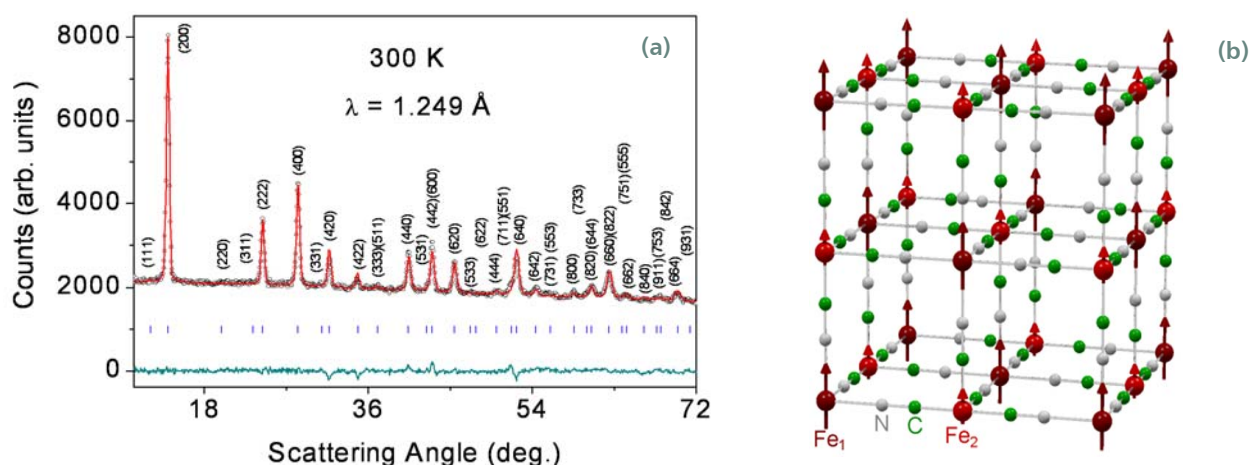


Fig. 1: (a) Rietveld refined neutron diffraction pattern of $\text{Fe}[\text{Fe}(\text{CN})_6]\cdot 4\text{H}_2\text{O}$ compound, depicting a *fcc* structure (b) chemical and magnetic unit cell. For clarity, water molecules are not shown.

constant $a \sim 10.2 \text{ \AA}$. The other hexacyanometallate compounds studied by us also possess the same *fcc* structure. The structure of the studied $A_n[\text{B}(\text{CN})_6]_m \cdot z\text{H}_2\text{O}$ compounds consists of *A*-NC-*B*-CN-*A* type linear chains along the unit cell cube edges [Fig. 1(b)]. In this structure, *A* (*B*) type cations are octahedrally coordinated to N (C) atoms and usually possess high (low) spin owing to a strong (weak) crystalline field at this site. We have succeeded in increasing magnetic ordering temperature (T_c) to 17.4 K in $\text{Fe}[\text{Fe}(\text{CN})_6]\cdot 4\text{H}_2\text{O}$ compound by substituting a paramagnetic Fe^{3+} ion in place of the diamagnetic Fe^{2+} ion in the parent Prussian

blue ($\text{Fe}^{3+})_4[\text{Fe}^{2+}(\text{CN})_6]_3 \cdot 14\text{H}_2\text{O}$ compound ($T_c = 5.6 \text{ K}$). Our low temperature neutron diffraction study infers a collinear ferromagnetic ordering of the high-spin Fe^{3+} (Fe_1 , $5 \mu_B$) and low-spin Fe^{3+} (Fe_2 , $0.8 \mu_B$) ion moments in this compound [5,11]. The chemical and magnetic unit cell of the $\text{Fe}[\text{Fe}(\text{CN})_6]\cdot 4\text{H}_2\text{O}$ compound is shown in Fig. 1(b).

Our study has revealed that the water molecules in the studied hexacyanometallate compounds exist as coordinated water at the empty $[\text{B}(\text{CN})_6]$ sites and as non-coordinated water at the interstitial sites. We have

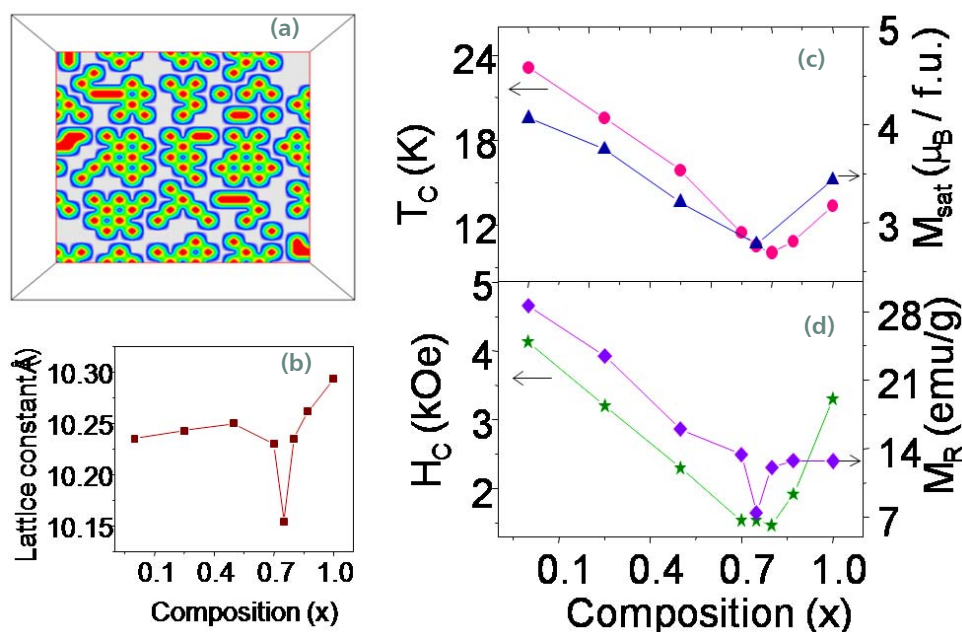


Fig. 2: (a) 2D plot of O atoms in a $4a \times 4a \times 4a$ (a being the lattice constant) cell showing the local ordering of the water molecules in $\text{Co}_{1-125}\text{Ni}_{0.375}[\text{Fe}(\text{CN})_6] \cdot z\text{H}_2\text{O}$ compound. Variation of (b) lattice parameter, (c) T_c , M_{sat} , (d) H_c , and M_R as a function of composition (x) in the $(\text{Co}_x\text{Ni}_{1-x})_{1.5}[\text{Fe}(\text{CN})_6] \cdot z\text{H}_2\text{O}$ hexacyanometallate compounds.

BARC NEWSLETTER

shown that the partial occupancies of the $[B(CN)_6]$ ($B = \text{Fe}$ or Cr) and the non-coordinated water molecular sites and the random substitution of more than one type of magnetic ions at the $4a$ $(0, 0, 0)$ site, are the main structural defects in these compounds. Our neutron diffraction data and RMC analysis establish a local ordering of water molecules at the empty $[B(CN)_6]$ sites in these compounds [Fig. 2(a)]. We have investigated the crucial role of structural defects and quenched disorder in controlling various magnetic properties like T_C , saturation magnetization (M_{sat}), coercive field (H_C), and remanence (M_R) in the $(\text{Co}_x\text{Ni}_{1-x})_{1.5}[\text{Fe}(\text{CN})_6] \cdot z\text{H}_2\text{O}$ compounds by varying Co ion concentration [4,9,10]. A strong correlation between the structural [Fig. 2(b)] and magnetic parameters [Fig. 2(c) & 2(d)] has been found from our dc magnetization study. The various magnetic properties like T_C , M_{sat} , H_C , M_R , etc., show a dip in their values around the $x = 0.75$ where the largest amount of structural disorder is present. The observed structural defects also play an important role in establishing low-spin (LS) and

high-spin (HS) ground states of various magnetic ions by tuning crystalline electric field around them.

By tuning the ferromagnetic (between Cu^{2+} and Fe^{3+} ions) and antiferromagnetic (between Mn^{2+} and Fe^{3+} ions) exchange interactions, we have shown the novel phenomenon of negative magnetization in the $\text{Cu}_{0.73}\text{Mn}_{0.77}[\text{Fe}(\text{CN})_6] \cdot z\text{H}_2\text{O}$ compound [Fig. 3(a)]. The first microscopic experimental understanding [Fig. 3(b)] of this peculiar phenomenon has been obtained by employing RMC and Rietveld refinement techniques on the neutron diffraction data [3]. These two computational techniques help us to derive the ordered magnetic moments and their orientation at the Cu^{2+} / Mn^{2+} and Fe^{3+} sites. Our mean-field theory based calculation also reproduces the observed temperature dependant magnetization reversal very well [Fig. 3(a)]. We have demonstrated a reversible and bipolar switching of magnetization [Fig. 3 (c)] in the $\text{Cu}_{0.73}\text{Mn}_{0.77}[\text{Fe}(\text{CN})_6] \cdot z\text{H}_2\text{O}$ compound when the applied magnetic field is switched between two positive (e.g.,

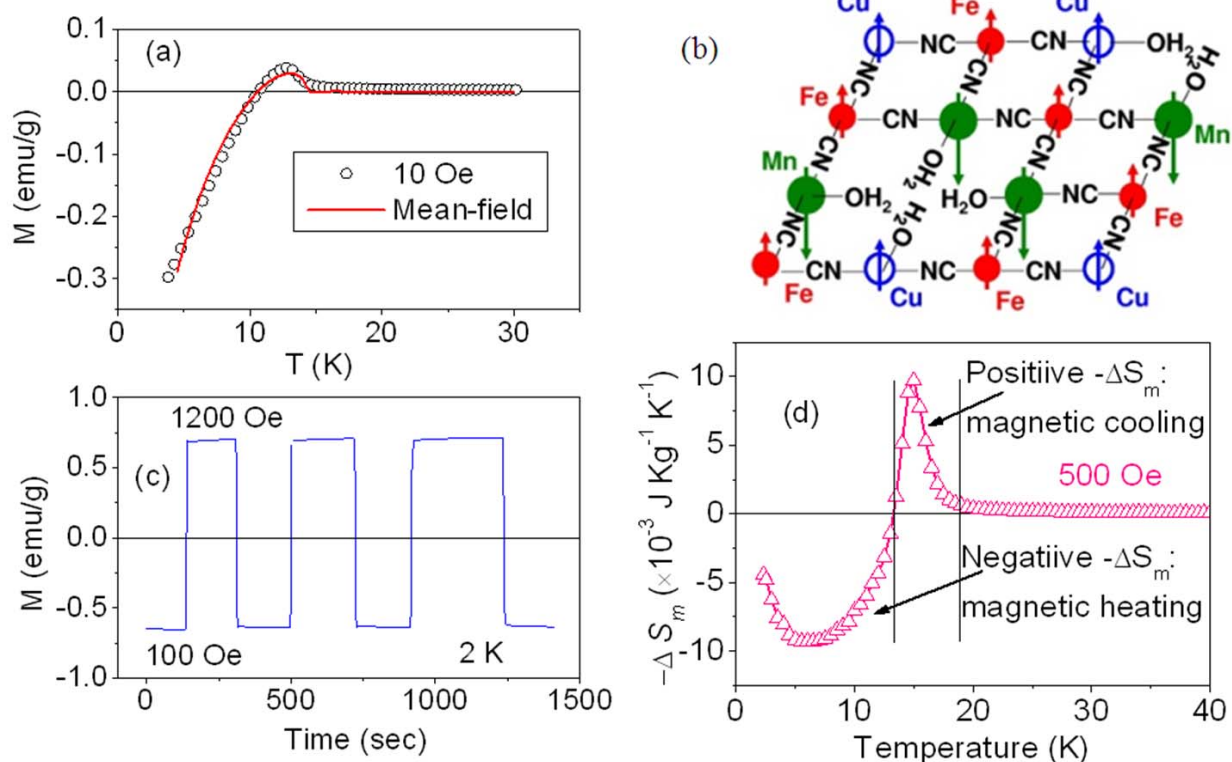


Fig. 3: Multifunctional properties of the $\text{Cu}_{0.73}\text{Mn}_{0.77}[\text{Fe}(\text{CN})_6] \cdot z\text{H}_2\text{O}$ compound. (a) Observed (o), field-cooled at 10 Oe, and calculated (line), using mean-field theory, magnetization (M) vs temperature (T) curves (b) Magnetic structure (planar view) at 1.7 K (c) Switching of magnetization between positive and negative values (memory effect) under the application of low applied fields in a cyclic manner. (d) Positive and negative values of magnetic entropy change ($-\Delta S_m$) at two different temperature ranges.

BARC NEWSLETTER

100 Oe and 1200 Oe) values. This highly reproducible bi-stability in the low-field magnetization data can be utilized for a volatile magnetic memory application [6]. Moreover, this compound shows a pole reversal of magnetic entropy change ($-\Delta S_m$) across the magnetic compensation temperature [Fig. 3(d)]. The existence of both normal (positive ' $-\Delta S_m$ ') as well as inverse (negative ' $-\Delta S_m$ ') magneto-caloric effect in this compound over two temperature ranges can be exploited for a magnetic cooling/heating based constant temperature bath application [6].

We have also investigated the variation of magnetic properties of $\text{Fe}[\text{Fe}(\text{CN})_6]\cdot 4\text{H}_2\text{O}$ [8] and $\text{Cu}_{1.5}[\text{Cr}(\text{CN})_6]\cdot 6.5\text{H}_2\text{O}$ [2] compounds with crystallite sizes, which is an important issue in the design of nanomagnets for practical applications. Magnetic study of the nanoparticles of above compounds has revealed a weaker magnetic properties (e.g., T_c , M_{sat}) with particle size. This behavior may be attributed to an increasing surface spin disorder with decreasing particle size.

Acknowledgment

The author is grateful to Dr. S. M. Yusuf for important suggestions to this article and his guidance during this

entire work. Generous thanks are also due to other co-authors for their contributions.

References

1. H. Tokoro and S. Ohkoshi, *Dalton Trans.* **40**, 6825 (2011).
2. Amit Kumar, S. M. Yusuf, and J. V. Yakhmi, *Appl. Phys. A* **99**, 79 (2010).
3. Amit Kumar, S. M. Yusuf, L. Keller, and J. V. Yakhmi, *Phys. Rev. Lett.* **101**, 207206 (2008).
4. Amit Kumar, S. M. Yusuf, L. Keller, J. V. Yakhmi, J. K. Srivastava and P. L. Paulose, *Phys. Rev. B* **75**, 224419 (2007).
5. Amit Kumar, S. M. Yusuf and L. Keller, *Phys. Rev. B* **71**, 054414 (2005).
6. S. M. Yusuf, Amit Kumar, and J. V. Yakhmi, *Appl. Phys. Lett.* **95**, 182506 (2009).
7. S. M. Yusuf, N. Thakur, Amit Kumar, and J. V. Yakhmi, *J. Appl. Phys.* **107**, 053902 (2010).
8. M. D. Mukadam, Amit Kumar, S. M. Yusuf, J. V. Yakhmi, R. Tewari, and G. K. Dey, *J. Appl. Phys.* **103**, 123902 (2008).
9. Amit Kumar, S.M. Yusuf, L Keller, *Physica B* **385–386**, 444 (2006).
10. Amit Kumar and S. M. Yusuf, *Physica B* **362**, 278 (2005).
11. Amit Kumar and S. M. Yusuf, *Pramana-J. Phys.* **63**, 239 (2004).

BARC NEWSLETTER

ADVANCED LASER SPECTROSCOPY AT BULK AND INTERFACES

Jahur Alam Mondal and Dipak K. Palit
Radiation & Photochemistry Division

Dr. Jahur Alam Mondal is the recipient of the DAE Young Scientist Award for the year 2011

Abstract

Understanding the physicochemical properties and excited-state dynamics of molecules at bulk and interfaces is of essential importance in fundamental sciences and applied fields. Advanced laser spectroscopy techniques such as, heterodyne-detected vibrational sum frequency generation (HD-VSFG) and femtosecond transient absorption spectroscopy revealed important interrelations between the physicochemical properties/excited-state dynamics of molecules and their functional groups and properties of bulk and interfacial media.

Introduction

Photoinduced intra-/intermolecular processes (electron/energy transfer, conformational/configurational changes, etc.) are vital in many natural (e.g. photosynthesis, vision, phototropism) and artificial (photovoltaics, molecule-based electronics, etc.) systems.[1] In general, absorption of UV-Vis. photon lands a molecule on an excited potential energy surface, which while relaxing to the ground-state, undergoes electron/energy transfer or conformational/configurational changes in an extremely fast rate ($\sim 10^{12} \text{ s}^{-1}$). By using femtosecond transient absorption spectroscopy, we directly monitored the excited electronic states of various model molecules and unravel the role of functional groups and the properties of bulk solvent media on various photoinduced processes. Previous studies indicated that interfacial chemistry, which plays important roles in chemistry (solvent extraction, food technology, catalysis), biology (cell membrane interface), and environmental sciences is different from bulk phase chemistry. Nevertheless, because of the technical difficulty of selectively probing of an interface (\sim a few nm thick), the molecular level understanding of interfacial phenomena is limited. Very recently, we applied heterodyne-detected vibrational sum frequency generation, HD-VSFG[2] to selectively

probe the vibrational characteristics of molecules located at a few molecular layer thick interfaces. Our HD-VSFG investigations revealed unique organization of water at cationic, anionic, and zwitterionic lipid containing cell membrane-water interfaces.

Excited-state dynamics of photoinduced processes in bulk liquid phase

Intramolecular electronic energy transfer (EET) in bichromophoric molecule.

In some bichromophoric molecules, the energy levels of the two chromophores, although not perturbed significantly by each other, are coupled enough to participate in rapid non-radiative energy transfer from the excited-state of one chromophore (donor) to the other (acceptor). We investigated the EET dynamics in a special kind of bichromophoric molecule, (2-(9-anthryl)-1H-imidazo [4,5-f] [1,10]-phenanthroline (AIP)) whose donor (anthracene (AN)) and acceptor (1H-imidazo [4,5-f] [1,10]-phenanthroline (IP)) groups are directly linked. Thus, the donor and acceptor groups in AIP are very short distance (one σ bond) apart (Figure 1). Transient absorption studies showed that the rate of energy transfer decreases with increasing viscosity of the medium.[3] This means the energy transfer in

BARC NEWSLETTER

such directly linked bichromophoric molecule is accompanied by conformational change, which is required for the efficient orbital overlap in the EET process.

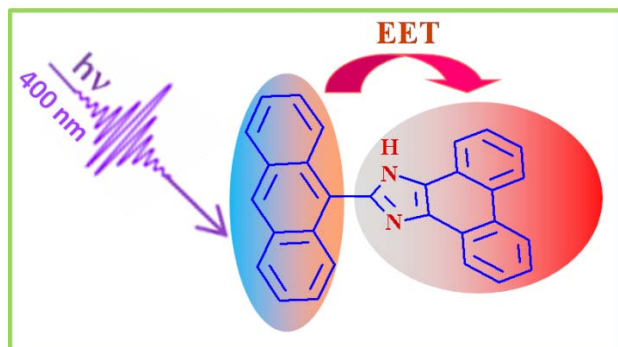


Fig.1: Intramolecular-EET in AIP (from anthracene to imidazophenthroline). Because the donor and acceptor groups are directly linked in AIP, the rate of EET is inherently fast ($1.8 \times 10^{11} \text{ s}^{-1}$ in methanol) and depends upon the relative orientation of anthracene and imidazophenthroline moieties in the photoexcited state.

Intramolecular charge transfer (ICT) in donor-acceptor molecules.

Like the energy transfer in bichromophoric AIP, a molecule with two types of functional groups- one electron rich and the other electron deficient, can undergo ICT on photoexcitation. We investigated the ICT dynamics in several electron donor-acceptor molecules (e.g. Michler's ketone (MK), 2-dimethylamino-7-nitrofluorene (DMANF) and 4-(N,N-dimethylamino)-4'-nitrostilbene (DMANS); Figure 2a) in different bulk liquid phases. In Michler's ketone (MK),

for example, the electron donating N,N-dimethylanilino groups are attached with an electron withdrawing carbonyl group and because of the steric hindrance, the two N,N-dimethylanilino groups are not in the same plane (pre-twisted in ground-state). On 400 nm photoexcitation, the pre-twisted locally excited S_1 state undergoes two consecutive conformational relaxation processes. First, an ultrafast *anti*-twisting motion of the dimethylanilino groups takes the molecule to a near-planar geometry with high mesomeric interaction (ICT-state). Then, in highly polar solvents, the N,N-dimethylamine groups ($-\text{N}(\text{CH}_3)_2$) undergo $\sim 90^\circ$ twisting with respect to their phenyl rings. This leads to the conversion of the intermediate ICT-state to a highly polar twisted intramolecular charge transfer (TICT) state.[4] To look into the intricacies of the excited-state ICT and twisting processes, we investigated 2-dimethylamino-7-nitrofluorene (DMANF) where the 'dimethylanilino-like' electron donor and 'nitrophenyl-like' acceptor groups are rigidly bonded (not free to twist). It is observed that in the case of DMANF, the nitro group is twisted to accommodate the charge in the lowest energy excited-state. Thus, unlike in the well-studied dimethylamine benzonitrile[1] where the electron donating N,N-dimethylamino ($-\text{N}(\text{CH}_3)_2$) is twisted, it is the electron accepting nitro group that is twisted in the excited-state of DMANF.[5] In fact, we found that it is the electron donating and accepting ability of the donor and acceptor groups that determines the site of conformational change in a molecule.

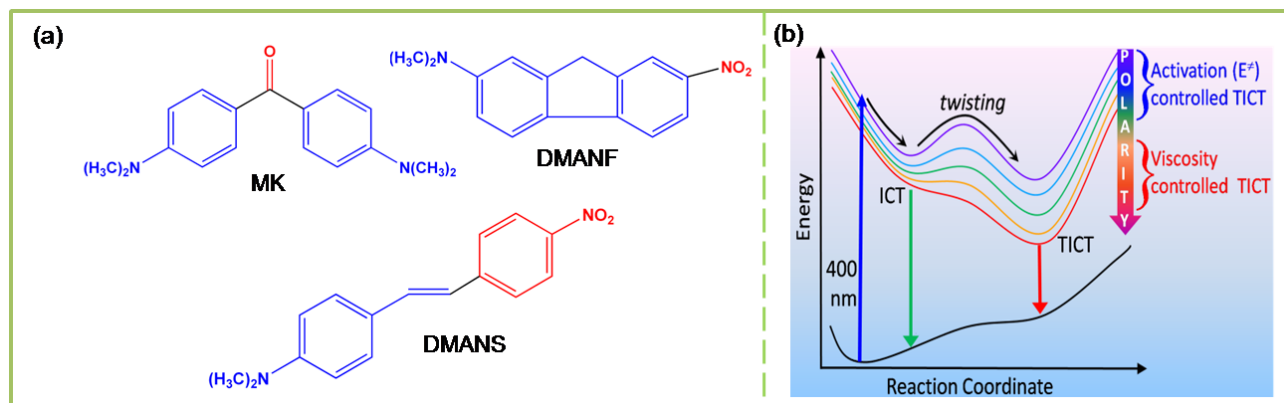


Fig.2: (a) Chemical structures of different molecules used in photoinduced charge transfer and conformational/configurational relaxations studies. MK: Michler's ketone; DMANF: 2-dimethylamino-7-nitrofluorene; DMANS: trans-4-(N,N-dimethylamino)-4'-nitrostilbene. (b) Typical role of solvent properties on the TICT dynamics: in less polar solvent, the TICT is activation barrier controlled and in highly polar solvent it is governed by the viscosity of the medium.

BARC NEWSLETTER

Donor-acceptor molecules in which the electron donor and acceptor groups are separated by long conjugations are active ingredients of optoelectronic and molecule-based devices. However, the additional conjugations (mesomeric bridge between the donor and acceptor) are likely to provide potential deactivation pathways to the excited states that may have adverse effect on the desired photo-processes. Investigations of the dynamics of *trans*-4-(N,N-dimethylamino)-4'-nitrostilbene (DMANS), which has a C=C bond in between the donor (N,N-dimethylanilino) and acceptor (nitrophenyl) groups, showed different behavior in different solvents. For example, in nonpolar cyclohexane, it undergoes photoisomerization whereas, in polar acetonitrile, TICT is the dominant relaxation processes in the excited-state. Moreover, the rate of formation of the TICT state increases exponentially with the polarity of moderately polar solvents ($ET^N < 0.3$), which signifies a solvent (polarity) dependent activation barrier for the TICT process. Nevertheless, in highly polar solvents ($ET^N > 0.4$), the activation barrier is negligible and the rate of TICT depends on frictional interaction (viscosity) with solvents (Figure 2b).[6]

Photoisomerization in azo-compounds:

Photoinduced isomerization is an important elementary process in liquid crystals, optical switching, memory storage, and photoregulation of biofunctions. As a result, extensive researches were carried out to understand the photoisomerization dynamics of azobenzene and related compounds. Using transient absorption spectroscopy, we investigated the photoisomerization dynamics of a different class of azo-compounds (N-1-methyl-2-(tolylazo)imidazole (MTAI)) and its metal complexes (Figure 3). From time evolution of the transient spectra and global analysis of the temporal profiles, it has been observed that isomerization occurs in the S_1 state of MTAI via the inversion at one of the azo-nitrogen atoms.[7] However, on complexation with Cu(II), $[Cu(\textit{trans}\text{-MTAI})_2]Cl_2$, the photoinduced isomerization of the azo-backbone is inhibited.

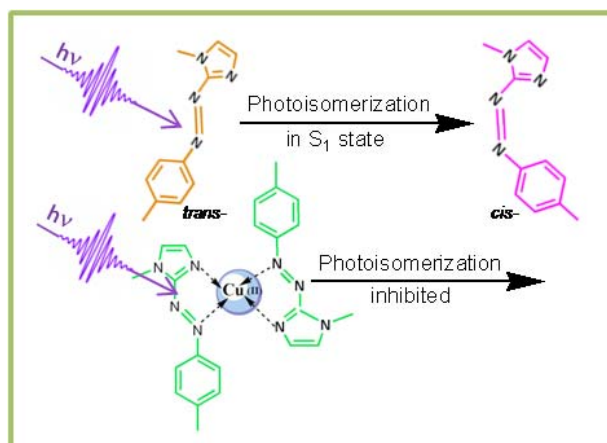


Fig. 3: Photoinduced *trans* → *cis* isomerization in MTAI. Independent upon the state of electronic excitation, the photoisomerization occurs in the S_1 state of *trans*-MTAI by inversion at one of the azo-nitrogen atoms. On complexation with Cu(II), the isomerization is arrested.

Physicochemical properties of water at model membrane/water interfaces

An interface is a common boundary across two immiscible bulk phases and has properties that are different from either of the bulk phases. As a consequence, chemistry at interface is different from that in bulk of a medium. Recently, we have demonstrated distinct properties of water at model membrane/water interfaces by using a novel HD-VSFG technique.[8] Measurement at different charged and zwitterionic lipid monolayer/water interfaces revealed unique organization of water at membrane interfaces (Figure 4). For instance, at charged lipid interfaces, water is preferentially oriented by the interfacial electric field created by the charge on lipid headgroups.[9] Water takes H-up (water dipole is pointed toward the lipid phase) orientation at negatively charged interfaces and H-down (water dipole is pointed toward the aqueous phase) orientation at positively charged lipid interfaces. On the other hand, at the net neutral zwitterionic lipid (phosphatidylcholine) interface, water takes a net H-up orientation. This means that the anionic phosphate has stronger water orienting ability than that of the cationic choline in phosphatidylcholine. In fact, there are distinct water structures around the

BARC NEWSLETTER

phosphate and choline groups.[10] In general, interfacial water is more inhomogeneous than the bulk water and there is very weakly or non H-bonded water species at lipid interfaces.

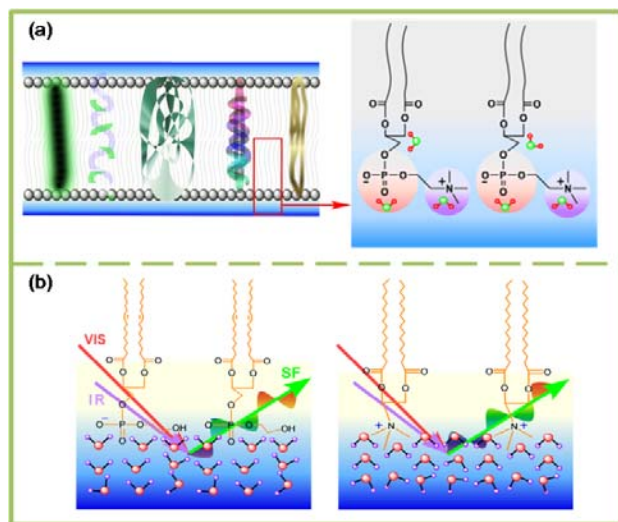


Fig. 4: Schematic representation of (a) Distinct hydration structures around the phosphate and choline groups at phosphatidylcholine lipid interface. The water around the phosphate is strongly H-bonded and H-up oriented whereas, that around the choline is relatively weakly H-bonded and H-down oriented (b) preferential orientation of interfacial water at cationic and anionic lipid interfaces.

Acknowledgements

The authors acknowledge Prof. A. Samanta, Hyderabad Central University for providing the aminonitrofluorene compounds and Prof. C. R. Sinha, Jadavpur University, West Bengal, for providing the arylazoimidazole compounds. Dr. C Singh and Mr. R. Ghosh for their kind help in transient absorption studies. JAM acknowledges Prof. T. Tahara and his team in Molecular spectroscopy laboratory, RIKEN, Japan, for the interfacial studies and Japan society for the promotion of sciences (JSPS) for the financial support during his postdoctoral research in RIKEN.

References

1. Grabowski, Z.R., K. Rotkiewicz, and W. Rettig, Structural Changes Accompanying Intramolecular

Electron Transfer: A Focus on Twisted Intramolecular Charge-Transfer States and Structures. *Chem. Rev.*, 2003. **103**(10): p. 3899-4032.

2. Nihonyanagi, S., et al., Structure and Dynamics of Interfacial Water Studied by Heterodyne-Detected Vibrational Sum-Frequency Generation. *Annu. Rev. Phys. Chem.*, 2013. **64**: p. 579-603.
3. Mondal, J.A., et al., Ultrafast intramolecular electronic energy-transfer dynamics in a bichromophoric molecule. *J. Phys. Chem. A*, 2004. **108**(39): p. 7843-7852.
4. Mondal, J.A., et al., Twisting dynamics in the excited singlet state of Michler's ketone. *J. Phys. Chem. A*, 2006. **110**(10): p. 3432-3446.
5. Mondal, J.A., et al., Charge-transfer-induced twisting of the nitro group. *J. Phys. Chem. A*, 2007. **111**(28): p. 6122-6126.
6. Singh, C., et al., Excited state dynamics of a push-pull stilbene: A femtosecond transient absorption spectroscopic study. *J. Photochem. Photobiol. A: Chem.*, 2013. **263**(0): p. 50-60.
7. Mondal, J.A., et al., Photoisomerization dynamics of N-1-methyl-2-(tolylazo) imidazole and the effect of complexation with Cu(II). *Phys. Chem. Chem. Phys.*, 2012. **14**(37): p. 13027-13034.
8. Nihonyanagi, S., et al., Direct evidence for orientational flip-flop of water molecules at charged interfaces: A heterodyne-detected vibrational sum frequency generation study. *J. Chem. Phys.*, 2009. **130**(20): p. 204704.
9. Mondal, J.A., et al., Structure and Orientation of Water at Charged Lipid Monolayer/Water Interfaces Probed by Heterodyne-Detected Vibrational Sum Frequency Generation Spectroscopy. *J. Am. Chem. Soc.*, 2010. **132**(31): p. 10656-10657.
10. Mondal, J.A., et al., Three Distinct Water Structures at a Zwitterionic Lipid/Water Interface Revealed by Heterodyne-Detected Vibrational Sum Frequency Generation. *J. Am. Chem. Soc.*, 2012. **134**(18): p. 7842-7850.

BARC NEWSLETTER

THERMAL HYDRAULIC DESIGN VALIDATION OF STEAM DRUM INTERNALS, MODERATOR AND LIQUID POISON INJECTION SYSTEMS FOR AHWR

D.S. Pilkhwal, N.K. Maheshwari, R.K. Bagul, A.M. Vaidya, A. Kansal and P.K. Vijayan
Reactor Engineering Division

Shri D.S. Pilkhwal and his team received the DAE Group Achievement Award for the year 2011

Abstract

Two experimental test facilities for thermal-hydraulic studies in steam drum, moderator flow and liquid poison injection system have been designed, fabricated, installed and commissioned in Engineering Hall-7, BARC, which are important for AHWR technology development. Setting up of the test facilities involved design of various components, selection of appropriate materials, elaborate mock up tests, fabrication of components, installation of instruments and their controls. Measures were taken to ensure safety of the experimental set-up and the personnel working on the setups. The task was highly complicated and challenging because of fabrication of large number of components, requirements of flow visualization of single-phase and two-phase flow and hundred percent leak proof joints with various nozzles. The scaling of the facilities has been done by simulating various non-dimensional numbers. The heat generation in the moderator has been simulated by electrically heated calandria tubes. Experiments were performed in these facilities. This paper deals with the work performed and results obtained in brief.

Introduction

The design of Advanced Heavy Water Reactor (AHWR) is in progress in BARC. The steam-water separation is achieved in AHWR steam drum naturally without the use of a mechanical separator. This necessitated the use of gravity separation in the steam drum. Liquid-vapour separation without aid of a mechanical device may not be fully effective and may lead to two undesirable phenomena, namely, carryover and carryunder. The adequacy of the gravity separation phenomenon in the steam drum needs to be ensured. Two in-house developed computer codes, GSEP-CO and GSEP-CU, to predict the carryover and carryunder require experimental data for their validation. A multichannel Air Water Loop (AWL) was designed, fabricated and installed to experimentally investigate the phenomena such as carryover and carryunder relevant to AHWR steam drum.

In AHWR, heavy water moderator is used to thermalize the neutrons inside the calandria. Calandria is a vertical cylindrical vessel containing vertical calandria tubes. A large amount of heat is generated in moderator due to the thermalisation process. Hence, to maintain its temperature, heavy water moderator is circulated through heat exchangers. In the calandria, the flow is mainly affected by momentum of inlet jets and buoyancy due to heat generation. The design and location of the inlet and outlet nozzles should be such that the maximum moderator temperature and impact velocity on the calandria tube bank are within limit.

Shut down system-2 (SDS-2) of AHWR is a fast acting system in which liquid poison is injected in the calandria vessel. This system is designed to shut down the reactor in a very short span. A Moderator and Liquid Poison Injection Test Facility (MLPITF) was designed, fabricated and installed to investigate the duration and get proper

BARC NEWSLETTER

distribution of poison in the moderator. To optimize calandria configuration for moderator flow distribution, experiments are being conducted in a scaled model. Further, experiments are carried out to optimize performance of shut down system -2. For this purpose a Moderator and Liquid Poison Injection Test facility was designed, fabricated and installed to investigate the duration and dispersion of poison in the moderator.

Brief overview of facilities

Two experimental test facilities named, Air Water Loop (AWL) and Moderator and Liquid Poison Injection Test Facility (MLPITF) have been designed, fabricated, installed and commissioned in Engineering Hall-7, BARC. The details of the facilities are described below.

Air Water Loop (AWL)

AWL has been designed and installed to study carry out thermal hydraulics experiments relevant to AHWR steam drum. The major objectives include investigation of the carry-over and carry-under phenomena in steam drum of AHWR, measurement of swell in the steam drum (pool void fraction) and testing performance of steam drum internals. The AWL consists of a semi-circular air-water drum simulating scale down AHWR

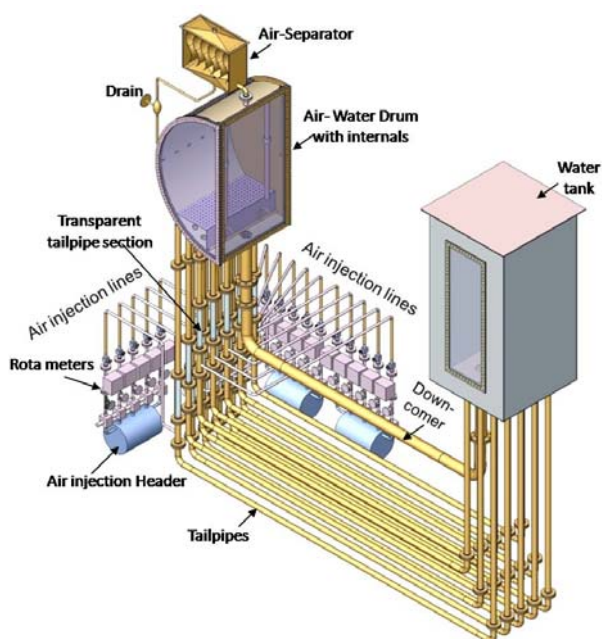


Fig. 1: Isometric View of AWL

steam drum with internals, rectangular water tank, piping simulating the risers and downcomer (Fig. 1). The air injection lines to simulate the two-phase flow at drum inlet, air-separator to separate the air at drum exit were also designed and fabricated.

The steam drum is 1/8th slice of the prototype, with 15 tail pipes (62.7 mm ID) and one downcomer (134.5 mm ID). Superficial velocities of individual phases in the prototype and model are same. One end of these tail pipes and downcomer is connected to the air-water drum as in the prototype while other end is connected



(a) Steam Drum and Water Tank



(b) Air injection system



(c) Tail pipes

Fig. 2: Photograph of AWL components and piping

BARC NEWSLETTER

to a storage tank. Air is injected at the bottom end of the vertical tail pipes. The loop flow is generated due to the density difference between two-phase air-water mixture in the tail pipe and single-phase water coming from water tank via downcomer. The two-phase flow of air-water mixture then enters in the air-water drum and air gets separated by gravity. The separated water flows towards water tank via downcomer. Some of the photographs of the installed facility are shown in Fig. 2.

The different parameters to be measured are swell level, pool void fraction and entrainment in air-water drum, pressure drop in tail pipe and downcomer. The swell in the air-water drum is measured by change in measured levels. Flow measurement in the single-phase horizontal pipe is carried out by calibrated pipe taps (pipe flow meter). Pressure drop and level is measured with differential pressure transducers or transmitters. Bubble and droplet size distributions are measured using high speed photography. Special provisions are built in the facility to measure the entrainment and pool void fraction.

Experimental work in Air Water Loop (AWL)

Steady state experiments on two-phase natural circulation were carried out with different initial water inventory and varying the air injection flow rates simulating the AHWR conditions (Fig. 3). Steady state circulation flow rates, pressure drop in single and two-phase regions of the facility were measured and are

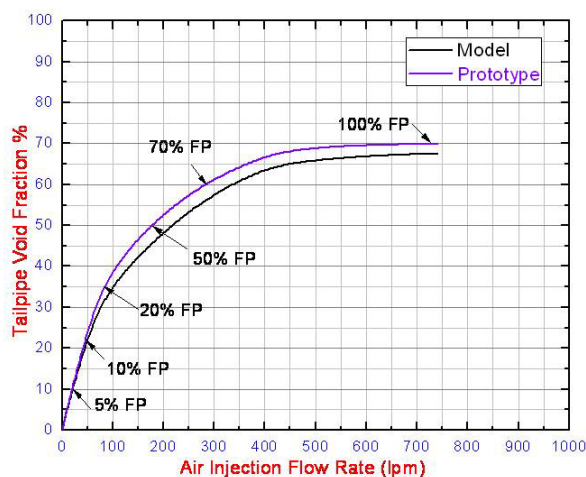


Fig. 3: Simulation of AHWR Void Fraction

validated using in-house developed code. Also a scenario similar to on-load refueling was experimentally simulated in AWL. Initially all the channels are subjected to same air injection flow rate. Air injection flow is reduced to zero in one of the channel. The channel acts as downcomer and reverse flow is observed. With initiation of air injection in that channel flow is still observed to remain in reverse direction. Only upon further increasing the air injection flow rate, flow becomes forward. Such hysteresis effect was found to be dependent on the rate of change of air injection flow rate. Fig. 4 shows the flow reversal phenomenon observed experimentally. Figs. 5a and 5b show some of the photographs taken for flow visualization during experiments.

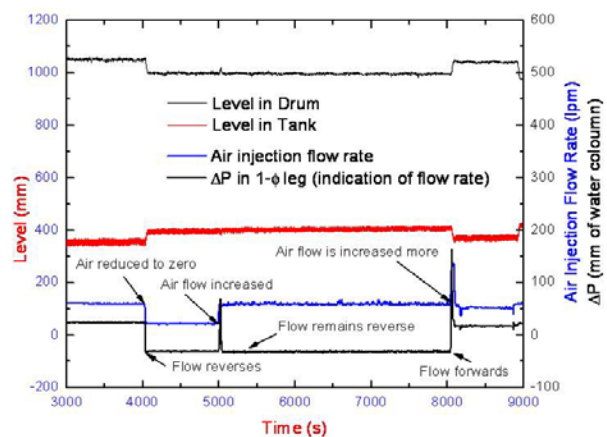


Fig. 4: Simulation of Flow Reversal Phenomenon



Fig. 5a: Flow visualization in the steam drum



Fig. 5b: Flow visualization in the water tank

BARC NEWSLETTER

Moderator and Liquid Poison Injection Test Facility (MLPITF)

A semitransparent scaled experimental setup of AHWR calandria was designed, fabricated and installed for moderator flow distribution studies. The model has been designed in such a way that Archimedes number is same as prototype. The model consists of calandria shell with calandria tubes, inlet-outlet nozzles, etc. The acrylic flanges and acrylic windows in the calandria shell are provided for visualization purpose. In the model, heat generation is simulated by direct electrical heating of calandria tubes. The calandria tubes are connected to the electrical supply through motorized auto transformers. Local electrical control panel is provided to operate the power supply system. The current, voltage and power are measured. Various instruments like magnetic flow meters, thermocouples, rotameters, pressure gauge, level indicator and level transmitter were installed in the test setup for measurement purpose. Spatial temperature distribution was measured using large number of thermocouples. Spatial velocity distribution is measured by using pitot tube. The data obtained are being utilized for computational fluid dynamics code validation. The test facility has been hooked up to a PLC based SCADA System. The instrument signals from field are terminated to PLC remote I/O modules in a local instrumentation control panel. For safety purpose, software and hard wired trips are provided based on high temperature signals. Earthing was provided on calandria shell, transformers and armour of cable for personal safety. Fig. 6 shows the photographs of some of the components of MLPITF. To carry out experiments on liquid poison injection and its distribution inside the calandria, the components of SDS-2 are installed and commissioned. The model consists of a gas tank for pressurization of poison, poison tanks and injection tubes for injecting the poison into the moderator. Liquid Poison is injected in scaled calandria through perforated headers. Eight poison segmental circumferential injection headers are provided at the middle of calandria. Each header has nozzles for injecting poison into the moderator. On the bottom tube sheet, perforated injection headers are also provided. Poison and gas tank are connected with these injection headers. A gas tank for pressurizing

poison tank was connected through a quick opening solenoid valve. Pressure gauge, pressure transmitter, relief valve, nitrogen supply line, level gauge and level transmitter were provided. Facility is hooked up to a PLC based SCADA System. Experiments are conducted at different injection pressures. Some of the photographs of the installed facility are shown in Fig. 6.



(a) Scaled Model of Calandria



(b) Electrical and instrumentation connection at the top the calandria



(c) Poison and gas tanks of liquid poison injection system

Fig. 6: Photographs of the Moderator and Liquid Poison Injection Test Facility (MLPITF)

BARC NEWSLETTER

Experimental work in Moderator and Liquid Poison Injection Test Facility (MLPITF)

The experimental studies on moderator flow distribution have been carried in the test facility. Experiments were also performed on the liquid poison injection system

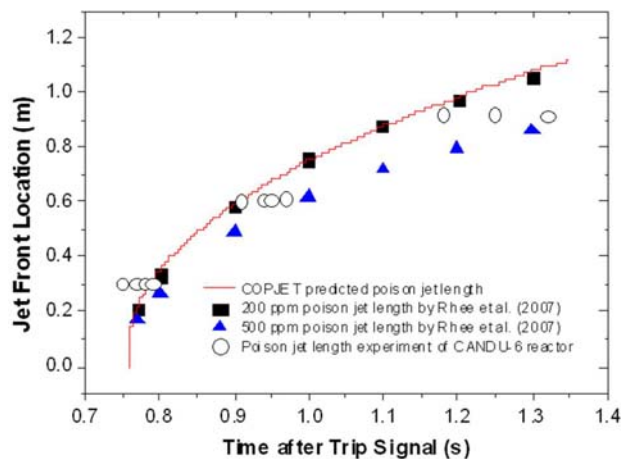


Fig. 7: Comparison of predicted poison jet front progression with experimental data

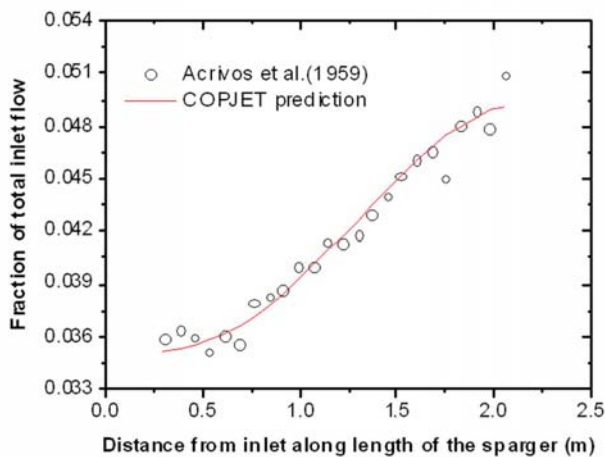


Fig. 8: Validation of COPJET prediction with test data from literature

for different cover gas pressures. Moderator flow and Temperature distribution were complimented by detailed three dimensional CFD simulations. CFD simulations were performed using PHOENICS CFD code. The poison distribution inside calandria was also computed. Further, a computer code, COPJET is developed which simulates gas expansion, system piping, perforated injection headers and poison progression into the calandria. The code results have been compared with the data available in the literature and with the PHWR data (Figs. 7 & 8).

Conclusions

Two experimental test facilities (AWL & MLPITF) for thermal-hydraulic studies in steam drum, moderator flow and liquid poison injection system have been designed, fabricated, installed and commissioned. Steady state experiments on two-phase natural circulation were carried in AWL. Measured steady state circulation flow rates, pressure drop in single and two-phase regions of the facility have been validated using in-house computer code. Flow reversal phenomenon was experimentally studied and hysteresis effect was found to be dependent on the rate of change of air injection flow rate.

The experimental studies on moderator flow and temperature distribution were carried out. The results were simulated using a CFD code. A computer code, COPJET was developed which simulates gas expansion, system piping, perforated injection headers and poison progression into the calandria. The code results have been compared with the experimental data and data available in the literature.

BARC NEWSLETTER

DESIGN, DEVELOPMENT AND COMMISSIONING & CAPACITY DEMONSTRATION OF 6000 A ELECTROLYTIC FLUORINE GENERATION CELL

C.S.R. Prasad, S.Sarkar, T.M. Sudhakar, S.V.G Rao and V.K. Misra
Chemical Technology Group

Shri C.S.R. Prasad and his team received the DAE Group Achievement Award for the year 2011

Abstract

For the past several years, the electrolytic fluorine generation cells of 1500 A capacity are being operated for the production of HEX gas. These Medium Capacity Cells (MCC) were initially deployed to meet the fluorine requirement for producing HEX Gas needed for strategic purposes. Subsequently, it is felt that development of economically viable higher capacity fluorine generation cells are essential for the future expansion programs. With the experience/expertise gained over the period of years of operation of MCC, a 6000A capacity cell was contemplated, designed and developed with improved techno- economic parameters. A test cell of this rated capacity was fabricated and subjected to plant trials to collect vital operational data. Based on the collected information, appropriate design modifications have been incorporated and a 6000 A cell has been commissioned successfully and integrated with fluorination plant. This higher capacity compact cell is not only catering to the increased in-house requirement of fluorine, but also paves way for the indigenous development of other fluorine based compounds such as production of SF₆ & MoF₆.

Introduction

Elemental fluorine is a pale yellow gas which is chemically the most reactive of all the elements. It is capable of reacting with all of the elements, except for the lighter noble gases. Generation of fluorine is possible through a chemical process, but it is not considered to be an efficient or practical method. Electrochemical route is the principal method for the industrial production of elemental fluorine. The electrochemical route of fluorine generation, developed by H. Moissan, originally used anhydrous hydrofluoric acid as the media. The process was not particularly efficient due to the low conductivity of HF. The molten salt method was established later, using molten anhydrous KF·2 H₂O electrolyte with carbon anode and steel cathode. Fluorine has been produced industrially for the past 70 years, a majority of that production going towards the nuclear industry for the manufacture of HEX gas for

the isotopic enrichment of fuel for nuclear reactors. Other applications of fluorine include its use in metallurgy, the preparation of semi-conductors, organic fluorine chemicals, sulphur hexafluoride, and other inorganic fluorides.

For the past several years, the electrolytic fluorine generation cells of 1500 A medium capacity are being operated for the production of HEX gas at Chemical Technology Group. Though these small cells were initially deployed to meet the fluorine requirement, for producing HEX Gas needed for strategic purposes, there was a need for suitable scaling up so as to develop economically viable fluorine generation cells, for the future expansion programs. In this backdrop, the 6000 Amp cell was designed. Novel concepts like usage of cheaper construction materials, high current density and the consequent lower footprint were aimed at, in making fluorine production more economical [2].

BARC NEWSLETTER

Technical challenges were anticipated as regards obtaining sustained high current density at the electrodes, heat removal, avoidance of explosive recombination, corrosion inhibition etc. The cell that was initially designed and fabricated had to undergo changes so as to meet many challenges. The commissioning of the 6000 A cell, in the final configuration, involved extensive trials and modifications, the details of which are discussed in this paper.

Design Consideration

The design involved understanding the hydrodynamics, heat & mass transfer, and kinetics, apart from electrochemical aspects. In contrast to the existing MCC, the following design philosophies were taken into account to make the cell compact and economically cheaper in terms of capital and operational costs. The cardinal approach for making the cell compact is based on adopting an innovative anode activation procedure. It is a prerequisite step that enables the carbon anode to carry about 2 ½ times higher current density compared to that of the existing MCC. By implementing this concept, compactness of the cell size has been accomplished. The higher capacity cell generates about 50 KW of heat. The heat removal is a herculean task due to the reduction in cell volume. This calls for better heat removal arrangement. This has been facilitated by incorporating cooling coils for every single anode assembly apart from jacket cooling of the body. Carbon steel has been used for fabrication of tank and cooling coils, which assumes a cathodic potential, thus getting galvanically protected. During the idling condition, these parts are cathodically protected through an external arrangement. Due to the change of MOC to carbon steel in lieu of Monel, the cost of the equipment has been reduced significantly.

Configuration Of Test Equipment

The cell has eleven anode assemblies with individual cooling arrangements. The cooling coils are wound around the anode assembly in a box like pattern with close pitch. This is meant for effective heat removal and lowering of the current density. In this

arrangement, both the cooling coils and carbon steel sheets act as cathode. The cell is loaded with 30 % additional electrolyte compared to MCC. As the tank has a negative potential, it is insulated from anodes by fastening a PTFE mat at the bottom. In addition, each anode assembly has been provided a PTFE strip at the bottom as a barrier. The skirt & diaphragm of the cell are connected by a flange joint & several small PTFE parts have been used to achieve electrical isolation between them, anticipating enhanced corrosion of the diaphragm. This has also been introduced to circumvent the recombination in the skirt region due to prevalence of bipolar cell at the diaphragm .

Plant Trials & Observations

The test equipment has been evaluated for its performance (Fig .1). During the trial run operations, the following problems were encountered:-

- a. Very high body to cathode voltage due to formation of gas blanket in the coil corrugation and also non-uniform current density which is attributable to the coil contour;
- b. Burning of the PTFE strip at the anode bottom consequent to high amperage operation;
- c. Dislocation of PTFE mat as a result of buoyancy.



Fig. 1: Photograph of 6000 A cell

Post-trial Modifications

Few skirt-diaphragm assemblies were operated without isolator and were found to be satisfactory. Based on this observation, the skirt was welded with the diaphragm, avoiding several small components which are difficult to assemble. Removal of the flange in

BARC NEWSLETTER

between, gave more clearance between anode & cathode, to facilitate easy assembly and more leverage on ensuring verticality of the anode & cathode assemblies to avoid electrical short circuit. The old & new arrangements are depicted in the Fig.2. Similarly, for making it more operator friendly with respect to assembly and maintenance of the cell, many components were also integrated.

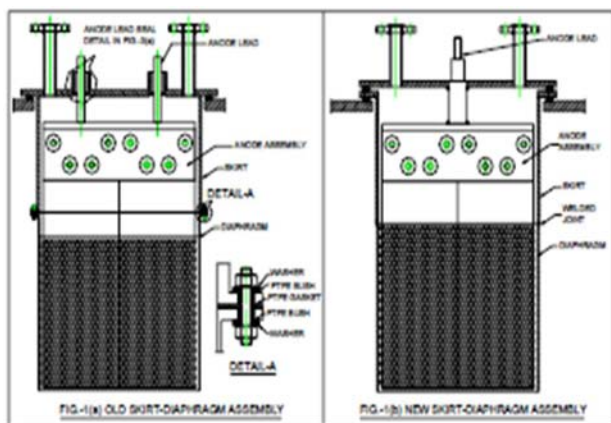


Fig. 2: Showing pre & post Modification of skirt diaphragm assembly

Modifications of the cathode

The rectangular box type cathode used in the test equipment was replaced by a plain cathodic plate with attached cooling coils on the rear side as shown in Fig.3. This facilitated easy detachment of hydrogen bubbles from the surface apart from more cathodic area & uniform inter-electrode gap thus paving the way for reduced cathodic voltage.

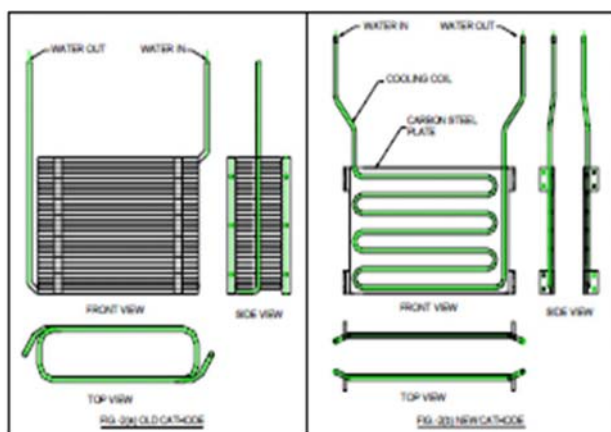


Fig. 3: Showing pre & post Modification of cooling arrangement

Improvements on the anode seal

Failure of seals and insulations, due to concentrated heating resulting from anodic overvoltage, was reduced [5] by the welding of anode lead to a cover plate and shifting the insulation point to the periphery of the cover plate, thus facilitating thermal dissipation (Fig.4).

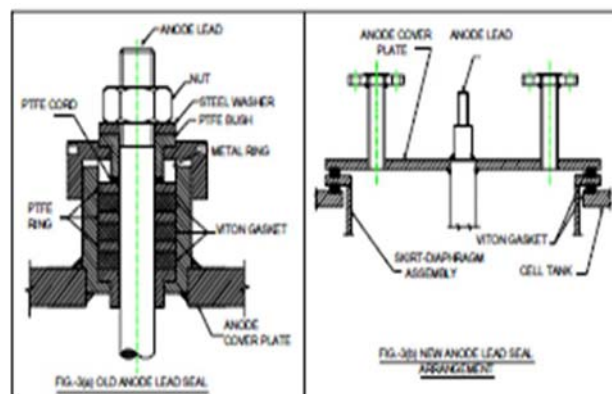


Fig. 4: Showing pre & post Modification in anode seal assembly

Activation of carbon anodes

Technique was developed for in-situ activation of carbon anodes to improve wettability of anode [3]. This resulted in lowering of the working voltage and easy detachment of evolved gaseous bubbles from the anode surface. This could eventually modify the effective surface area manifesting in very high current density. The advantages of activation are elaborated in Table-1.

Table 1: Significant advantages of Activation

Figure of merit	Pre-activation	Post-activation
Current efficiency	90-95%	90-95%
Voltage efficiency	19.8%	22.2%
Energy efficiency	18.3%	20.5%
Anode to body voltage	6.5 V	5.5 V
Cell working voltage	9.6 V	8.6 V
Specific energy consumption (kWhr/kg)	14.6	13
Space time yield (kg/m ³ .hr)	1.9	4.8
Service life (Amp-hrs)	5 X 10 ⁵	More than double

BARC NEWSLETTER

Miscellaneous

Contact resistances at anode clamping areas were reduced by nickel plating [4], thus reducing the working voltage and anode damage due to resistive heating at the contact areas. The steel chamber of the cell has been given suitable cathodic protection to deter galvanic reaction with the electrolyte during idling. PTFE mat is fastened to each cooling coil frame as a barrier/masking.

Conclusions

Designing of a higher capacity electrolytic fluorine generation cell merely based on operational experiences of MCC and first principles and then executing it to the level of continuous industrial operation is true demonstration of technical skills of various disciplines. The 6 kA cell has been successfully designed, tested and operated to its rated capacity continuously, for the production of HEX gas. Based on the availability of fluorine at high production rates, a plant for the production of sulphur hexafluoride gas has also been commissioned, which would be a stride towards indigenization of the SF₆ production technology. It is also envisaged to use this cell for the production of MoF₆ and other allied fluorine compounds.

Acknowledgements

The authors wish to thank Shri T.K. Bera, Project Director for his whole hearted encouragement and support. We

also wish to thank all the staff and members of CF, EISS, EPS, ACL, FMS and USS, who were directly and indirectly associated with the developmental work.

References

1. A.T.Khun, "Industrial Electrochemical Processes".
2. B. Bhattacharjee, in: Proceedings of symposium on advances in chemical engineering-97, BARC, Mumbai, October, 1997, PP. 127-151, "Fluorine technology in India and its emerging applications in industry".
3. C.S.R.Prasad : Proceedings of symposium on New vistas in Electrochemistry, 1995 organised by SAEST & IGCAR, "Carbon anodes – selection, conditioning and electrochemical performance for elemental fluorine generation".
4. S.V.G.Rao : Proceedings of international conference on advances in surface science & engineering (INSURE-2001) at Chennai, organized by ISAS, "Nickel plating on electrical contact area of the carbon anodes for improving the fluorine cell performance".
5. S.V.G. Rao : Proceeding of International Conference on Advances and Recent Trends in Electrochemistry (ELAC-2013) at Hyderabad, organized by Indian Society for Electro Analytical Chemistry, (ISEAC), Mumbai, "Art & Science of Fluorine Generation".

BARC NEWSLETTER

DEVELOPMENT OF A TB-PCR KIT FOR THE DIAGNOSIS OF TUBERCULOSIS

Savita Kulkarni and M.G.R. Rajan

Radiation Medicine Centre, BARC

and

Papia Hazra, A. Islam, R. Seshadri

JONAKI, BRIT, CCMB campus, Hyderabad

Dr. Smt. Savita Kulkarni and her team received the DAE Group Achievement Award for the year 2011

Abstract

Complex chemistry of mono-functional to multi-functional extractants such as: phosphine oxides, sulfoxides, N-oxides, carbamoyl methyl sulfoxide, carbamoyl methyl pyrazole, diglycolamide, thiodiglycolamide and crown ether with uranyl nitrate, uranyl bis (β -diketonate) and lanthanide nitrates was studied by using IR, NMR spectroscopy, elemental analysis and single crystal x-ray diffraction methods. The structures of most of the isolated complexes of uranyl nitrate with the ligands show that the uranyl group is surrounded by two nitrate groups and one or two ligand(s) in a hexagonal bi-pyramidal geometry. The structures of uranyl bis (β -diketonate), mono-functional ligand complexes show that the uranyl group is surrounded by seven oxygen atoms in a pentagonal bi-pyramidal geometry. The structures of lanthanide nitrate complexes show that the metal ion has either a bi-capped square prismatic or tri-capped trigonal prismatic coordination geometry, depending upon the ligands used.

Introduction

Tuberculosis caused by *Mycobacterium tuberculosis* (*MTB*), is a public-health problem of global importance. India carries one-fifth of the global burden of TB with more than 350,000 deaths every year. The emergence of HIV infection and a rising prevalence of multi-drug resistant (MDR) tuberculosis have threatened the effectiveness of standard chemotherapy such as Directly Observed Treatment (DOTS)¹. The rapid diagnosis of pulmonary TB (PTB) is the most important step in TB control as these patients are responsible for the respiratory transmission of tuberculosis. As the conventional techniques like AFB smear microscopy lack sensitivity as well as specificity and 'gold standard' culture technique is labour intensive and takes too long, it is important to develop a test which is rapid, sensitive and specific. A test based on polymerase chain reaction (PCR) fulfills all these criteria and hence such a test was developed at RMC for diagnosis of tuberculosis.

Many of the PCR tests for *MTB* detection, described in the literature, are based on amplification of *IS6110* sequences that is believed to be restricted to members of the *MTB* Complex². The presence of multiple copies of this element in the majority of *MTB* strains undoubtedly enhances the sensitivity of PCR. However, the discovery of occasional *MTB* strains lacking *IS6110* in India³ however implies the possibility of a few false negative results in the test with *IS6110*-based PCR. To overcome these problems, a PCR test was developed in our laboratory targeting a house keeping gene of *M.tuberculosis* coding for a 38 kDa protein, involved in phosphate transport⁴.

Methods

Standardization of PCR test

PCR was standardized using a primer pair KD1 and KD2 targeting 340bp segment of the 38kDa gene of *MTB*.

BARC NEWSLETTER

The analytical sensitivity of the PCR test was found to be 10fg which is equivalent to the DNA for 3 bacilli. The test was shown to be specific only to *M. tuberculosis* complex strains and did not give amplification with various bacterial DNA as well as human DNA.

PCR test validation for pulmonary (PTB) as well as extra-pulmonary tuberculosis (EPTB)

The PCR test was validated for PTB (168 sputum samples from TB patients) as well as extra-pulmonary tuberculosis (EPTB) (50 abdominal biopsies from suspected abdominal TB patients and 60 CSF samples from patients with TB meningitis cases (TBM). The test was always performed in duplicate and one of the test samples was spiked with positive control DNA to look for inhibition of the PCR. Various procedures for extracting DNA from clinical samples were evaluated for their extraction efficiency and ability to remove inhibitors. Silica spin column based extraction method with modifications was found to be the most satisfactory procedure. **An indigenous TB-PCR kit containing silica columns and indigenously produced Taq polymerase was developed by RMC and JONAKI, BRIT.** The prototype kit was again validated using 110 sputum samples from PTB patients and 72 samples from healthy controls.

Results

Initial validation of the standardized PCR test performed with 168 sputum samples exhibited 77% positivity in

AFB positive samples with 10 % of samples showing PCR inhibition. Study with abdominal biopsies showed sensitivity and specificity of 77% and 68% respectively⁵. In the double-masked study of TBM patients, 73.3% sensitivity observed with ethidium bromide staining which increased to 90%⁷ by using Southern hybridization and Enhanced Chemiluminescent (ECL) method with biotinylated internal probe⁶. The prototype kit showed sensitivity of 84% and specificity of 97% respectively. A small batch of kits was then produced and the kits were given to different hospitals for evaluation. After a satisfactory feed-back, a bulk production was carried out and a **totally indigenous kit which contains both column based DNA extraction as well as PCR reagents was launched in the market in Aug 2009 by BRIT and BARC (Fig 1 a & b).**

Discussion

TB-PCR fulfills all the criteria for being an ideal diagnostic test, in comparison to existing tests for early detection of TB and hence justifies being the choice of test. PCR is theoretically capable of amplifying even a single copy of DNA. Further, all types of biological specimens such as sputum, blood, bronchoalveolar lavage, CSF, biopsies, pleural and ascitic fluid are amenable to PCR analysis.

The PCR target used by us showed a very high sensitivity and specificity and can detect cases infected by MTB strains lacking IS6110, proving its usefulness. The elimination of inhibitors is one of the most difficult



DNA extraction kit



PCR reagents kit

Fig 1. Indigenous TB-PCR kit

BARC NEWSLETTER

challenges in the diagnostic PCR test. Use of silica membrane in existing kit was observed to have great efficacy for removing Taq polymerase inhibitors from blood, sputum and other biological material and hence no inhibition of PCR was seen, resulting in no false negativity with our kit.

The diagnostic sensitivity and specificity of our kit is comparable to the one observed by different laboratories. Additionally, our test could also detect 52% of smear negative–culture positive TB cases and 22% of smear and culture negative TB cases which are considered to be a challenge in TB diagnosis. TBM is one of the common EPTB with high mortality where definitive diagnosis is not possible as smear and culture are rarely positive. A PCR test like ours with 90% sensitivity will be very useful in the early diagnosis of TBM. Abdominal tuberculosis is another important EPTB which is difficult to diagnose due to the diagnostic dilemma in histopathology. When AFB and culture are negative, PCR is the only reliable technique that can confirm the presence of *MTB* in the affected site and further help in ruling out malignancy.

Simultaneously, a PCR test targeting *IS6110* was standardized at RMC and was evaluated for the diagnosis of bovine tuberculosis, tuberculous meningitis and TB osteomyelitis (TBOM)⁷. After the success of these studies, a multiplex PCR targeting both 38kDa gene (RV0934) and *IS6110* was developed at RMC to further increase the sensitivity of existing TB-PCR kit especially for the samples with lower bacterial load and having *MTB* without *IS6110*. The test was evaluated using sputum samples from PTB patients and non-TB controls. The multiplex PCR test is now going to be part of modified TB-PCR kit marketed by BRIT.

References

1. WHO Tuberculosis Global Factsheet (2012) World Health Organization. Available: <http://www.who.int/mediacentre/factsheets/fs104/en/>
2. Caws M, Wilson SM, Clough C, Drobniowski F. "Role of IS6110 Targeted PCR, culture biochemical clinical and immunological criteria for diagnosis of tuberculous meningitis". *J. Clin. Microbiol.* 38 (2000) : 3150-3155.
3. Van Soolingen D, DeHaas PEW, Hermans PWM, Groenen PMA, van Embden JDA. "Comparison of various repetitive DNA elements as genetic markers of strain differentiation of epidemiology of Mycobacterium tuberculosis". *J. Clin. Microbiol.* 31 (1993) : 1887-1895.
4. Kadival GV, D'Souza CD, Kolk AHJ, Samuel AM. "Polymerase chain reaction in the diagnosis of tuberculosis comparison of two target sequences for amplification". *Zbl. Bakt.* 282 (1995): 353-361.
5. Kulkarni SP, Jalil MA, Kadival GV. "Evaluation of polymerase chain reaction for the diagnosis of tuberculous meningitis in children". *J Med Microbiol.* 54 (2005):369-373.
6. Kulkarni SP, Vyas SP, Kadival GV. "Use of Polymerase chain reaction in the diagnosis of abdominal tuberculosis". *J Gastroenterol and Hepatol.* 21 (2006) : 819-823
7. Jambhekar N.A., **Kulkarni S.P.**, Madur B. P., Agarwal S. & Rajan M.G.R. (2006), Application of the polymerase chain reaction on formalin–fixed , paraffin–embedded tissue in the recognition of tuberculous osteomyelitis . *J Bone & Joint Sur. (Br.)*, 88-B:1097-1101A.

BARC NEWSLETTER

DEVELOPMENT OF FLUIDIZED BED THERMAL DENITRATION TECHNOLOGY FOR AMMONIUM NITRATE BEARING WASTE STREAMS OF BACK END OF THE NUCLEAR FUEL CYCLE

Hanmanth Rao
Chemical Engineering Division

Shri Hanmanth Rao and his team received the DAE Group Achievement Award for the year 2011

Abstract

Uranium Oxide Facility (UOF) being set up at Kalpakkam shall process Uranyl nitrate pure solution to convert the uranium values into Uranium oxide product. The filtrate after Ammonium Diuranate (ADU) separation is a waste liquid stream from this plant which mainly contains ammonium nitrate (~1M). A Denitration Plant (DNP) is to be set up in the UOF premises, for thermal decomposition of ammonium nitrate into nitrogen/ NO_x and water. The DNP will be based on fluidized bed thermal denitration process technology developed in the bench and pilot plant facilities at Chemical Engineering Division (ChED). The pilot plant has a 300 NB denitration column and a feed capacity of 50 lph. The paper shares the operating experience gained with the nitrate stream in the pilot plant facility.

Introduction

In uranium refining, purification of uranium by TBP in nitrate medium is still the most acceptable technology. Effluents containing nitrate are either sold for their nitrate value after removal of activity or disposed adopting dilution-dispersion methodology. These methods, being site-specific and driven by market forces, have their own limitations. Further, groundwater is widely used as drinking water and nitrate concentration in groundwater sources has been increasing over the years due to extensive use of fertilizers and discharge of industrial effluents. This may bring further constraints on disposal by dilution-dispersion method.

Uranium Oxide facility (UOF) is being set up at Kalpakkam for conversion of uranyl nitrate solution generated at the back end of the nuclear fuel cycle to uranium oxide. The facility shall adopt ADU precipitation route i.e. wet route for this conversion

and thus generate ammonium nitrate at a concentration of ~75 g /lit as liquid waste. Process feasibility has been established for fluidized bed thermal denitration of ammonium nitrate on the bench scale facility starting with synthetic solution. Based on bench scale experimental data, a pilot plant facility has been set up at ChED. Information and design data collected and technology developed on bench and pilot scales is being deployed for treating ADU filtrate generated from UOF plant, Kalpakkam. In case the situation demands, this can be deployed for overcoming the problem of disposal of ADU filtrate stream generated at the front end.

The denitration process utilizes thermal energy to decompose the ammonium nitrate into N_2 , water vapor and some NO_x and is essentially an endothermic process. In a fluidized bed denitrator, a bed of granular solids viz. silica particles is fluidized by forcing air upwards through a distributor plate and through the bed of solids at a rate that suspends and causes rapid

BARC NEWSLETTER

mixing of the solids to make them behave like a fluid. The bed density is decreased roughly by 40% upon fluidization. The rapid mixing that accompanies fluidization results in uniform composition and uniform temperature.

ADU filtrate can be concentrated before feeding to the denitration column to increase efficiency of the process and throughput. The solution is sprayed on the silica particles in the form of droplets, which denitrates very rapidly upon impact on the surface of the hot bed granules. The process heat needed is supplied by induction heater. Off gas generated is passed through off-gas system. Unconverted ammonium nitrate solution can be recycled back to the denitration column after concentration.

Fluidized Bed Thermal Denitration Pilot Plant

The plant has 300 NB denitration column and has been designed for a capacity of 50 lph of feed. The plant uses twin feed nozzle system i.e. two nozzles can be used at a time for feeding. Each nozzle has a stand-by that can be put on line if the active one gets choked. Two induction heaters axially divided over the length of the column have been used. The two heaters are controlled independently using PID controllers. There are 10 nos. K-type thermocouples provided at different radial and axial positions inside the column for monitoring bed temperature and additionally there are 3 thermocouples for measuring surface temperature of the column. Preheated air is supplied to the column for fluidization of the bed material. Bed inventory is measured by using a differential pressure transmitter and is controlled by varying the solid withdrawal rate from the column using a non mechanical valve in the withdrawal line. There is continuous addition of silica particles at controlled rate to maintain particle size distribution inside the bed.

The off-gas system comprises of two cyclone separators and filter housings to remove entrained solid from the off-gas. Unconverted ammonium nitrate is retrieved along with the solution water in a heat exchanger. After retrieval the gas is passed through water scrubber for removal of NO_x , NO , NO_2 and N_2O concentrations are

monitored at various points in plant using on-line gas analyser.

Experimental Work

Parametric studies were carried out in the 300 NB denitration column with synthetic ammonium nitrate solution for optimization of operating conditions. Effects of feed flow rate, temperature, fluidization air flow rate, air to liquid ratio and nozzle orientation on conversion have been studied. Feed concentration was varied between 130 - 180 g/l in all the runs. Feed can be introduced inside the reactor through single or two nozzles at a time. It is observed that splitting of feed through two nozzles gives higher conversion. Also increase in conversion is observed with increase in



Fig. 1: Pilot Scale Denitration Column

BARC NEWSLETTER

Table 1: Conversion as function of various operating parameters

Parameter	Temp.C	No. of Feed Nozzles and orientation	Feed rate LPH	ALR Slpm of air/ lpm of feed	Fluidization Air flow rate slpm	Conversion %
RUN 1	300	1 , 45° upwards	20	830	800	42
RUN 2	300	1 , 45° upwards	15	830	800	54
RUN 3	300	1 , 45° upwards	15	780	800	57
RUN 4	350	1 , 45° upwards	15	830	800	62
RUN 5	350	2 , 45° upwards	20	780	800	61
RUN 6	350	2 , 45° upwards	30	780	800	48
RUN 7	350	2 , 45° upwards	40	780	800	38
RUN 8	350	2 , horizontal	30	780	800	48
RUN 9	350	2 , horizontal	30	780	600	49
RUN 10	370	2 , horizontal	30	780	800	56
RUN 11	370	2 , horizontal	30	580	800	64
RUN 12	380	2 , horizontal	30	520	800	71
RUN 13	380	2 , horizontal	30	520	800	69

temperature from 300°C to 380°C. Nozzle orientation was kept upward initially and later other column was used with feed nozzles placed horizontally. There is not any effect observed on the conversion with the change in orientation of nozzles. Fluidization air flow rate has some effect on wall heat transfer coefficient. However it does not seem to have much effect on nitrate conversion. Operations with feed flow rates 20 lph, 30 lph and 40 lph show that there is decrease in conversion with the increase in feed flow rate. Decrease in ALR (Air to Liquid ratio) also favours higher conversion.

Experimental runs were carried out with two designs of spray nozzles, SN1 and SN2. First set of runs were carried out with SN1 nozzles and feed concentration 130 g/l, while the remaining runs were carried out with higher concentration of 180 g/l and SN2 nozzles

requiring lower ALR for the same sauter mean feed droplet diameter. Increase in bed temperature, feed concentration and decrease in ALR has resulted in high ammonium nitrate conversion in later runs. The analysis of various samples for ammonium nitrate concentration has been carried out by Analytical Chemistry Division, BARC.

Effects of various operating parameters on conversion have been represented in the Table 1.

Conclusion

Thermal denitration of ammonium nitrate at a concentration level of 150 g/l has been demonstrated in the pilot plant. Upto 70 % conversion of ammonium nitrate has been achieved and yield to N₂ obtained is ~90 %.

BARC NEWSLETTER

DEVELOPMENT OF HEAVY LIQUID METAL TECHNOLOGY FOR FUSION REACTOR TECHNOLOGY FOR FUSION REACTOR MATERIAL CHARACTERIZATION

R.K. Fotedar, N. Krishnamurthy, S. Kumar and P. Chakraborty

Fusion Reactor Materials Section

and

P.K. Pradhan and B. Paul

Materials Processing Division

and

S. Malhotra

Control and Instrumentation Division

Shri R.K. Fotedar and his team received the DAE Group Achievement Award for the year 2011

Introduction

One of the challenges in developing suitable structural materials for fusion reactor (ITER and DEMO) is to make sure that they are compatible with the heavy metals and alloys which have been proposed as potential coolants. India has proposed Lead-Lithium eutectic ($Pb_{83}Li_{17}$) cooled Ceramic Breeder (LLCB) as the blanket concept for testing at ITER. The LLCB blanket concept proposes $Pb_{83}Li_{17}$ eutectic as neutron multiplier, secondary tritium breeder, and coolant for the CB zones [1-2]. In the initial stages, a number of structural materials, including various classes of stainless steels, SiC/SiC_f and vanadium based alloy (V-5Cr-5Ti) had been considered for the construction of TBM. The best suited material will be chosen by considering its thermo-mechanical properties, capability to withstand high neutron flux and most importantly compatibility with the coolant. Lead lithium eutectic ($Pb_{83}Li_{17}$), has been found to be highly corrosive to most of the structural materials where the corrosion is mostly due to dissolution of the constituent elements and not due to chemical reaction. [3]. Thus, the extent of dissolution of constituent elements from the proposed containment materials will be the critical factor in choosing the best candidate for fusion reactor structurals. BARC took up this challenge and successfully created and commissioned elaborate experimental

facilities for development of heavy liquid metal technology. Quick and significant progress has been achieved in the materials front in a short time and foremost among these is the development of certain key aspects of liquid metal technology. Liquid metal technology development in the context of Indian TBM for ITER is one of the principal group efforts in the Fusion Reactor Materials Section (FRMS), BARC.

Liquid Metal Test Facilities

Liquid Metal loops

FRMS already had expertise to handle liquid metals like lead-bismuth eutectic for the ADS project and had operated liquid metal buoyancy loops for extended periods of up to 10,000 h. With the ITER project in hand, the above experience was used to develop liquid metal technology related to lead-lithium eutectic. Initially, buoyancy driven lead-lithium loops were designed and fabricated. The hot leg and the cold leg temperatures were maintained at 500°C and 400°C respectively. The loops were operated for 1000 h by keeping samples of 9Cr-1Mo (P91) material inside for corrosion studies. The exposed 9Cr-1Mo samples were characterised fully and the corrosion phenomenon was studied in detail [4].

BARC NEWSLETTER



Fig. 1: The first Buoyancy Loop installed with Pb-17Li

After successful operation of two such loops, a pump driven (forced circulation) lead-lithium loop was designed which demanded indigenous development of liquid metal based components like electromagnetic pumps, heat exchangers and flow meters. The electromagnetic pump comprised of a SS316L channel having a wall thickness of 1 mm and a rectangular cross section. The overall channel diameter was 300 mm and the thickness of liquid metal contained by it was 8 mm. The channel was housed between two rotating discs where Samarium –Cobalt magnets were placed on the discs with pairs facing each other. The electrically conductive fluid ($Pb_{83}Li_{17}$) between these magnetic pairs was moved by a Lorentz force generated by rotating of the magnets. The magnitude of pressure developed is given by equation (i).

$$P_{\max} = 0.5 \times \sigma \times V_B \times B^2 \times S \times L_{ch} \times K \quad (1)$$



Fig 2: Sectional View of the Electromagnetic Pump.

Where B is the magnetic field (T), σ is the electrical conductivity of the liquid ($S.m^{-1}$), V_b is the velocity of the magnetic field (m/s); L_{ch} is the length of the active part of pump channel (m), S is the slip and K is the coefficient accounting for transversal end effects. The average flux between poles of the opposite magnets was 0.42 T and the maximum pressure developed by the pump at a speed of 1400 RPM was 4 bars. The maximum discharge obtained till date has been 60 l/m.

All components were fabricated and a pump driven loop was operated on lead-lithium eutectic for 1000 h continuously keeping P91 samples inside. The temperature of test section was kept at $550^\circ C$ while the temperature of heat exchanger was at $350^\circ C$. At a rotation speed of 650 RPM from the electromagnetic pump a liquid metal flow rate of 30 l/m was obtained.

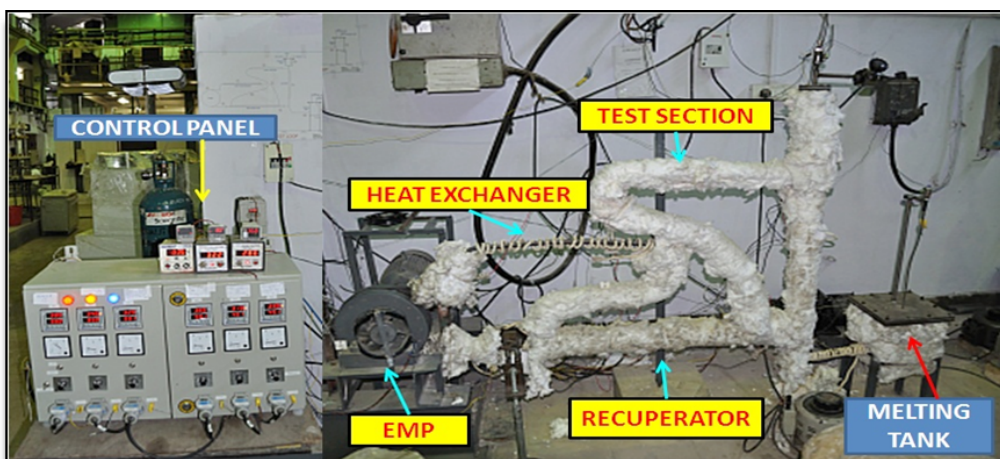


Fig 3: Liquid Metal Forced Circulation Loop showing all components.

BARC NEWSLETTER

Recently, a 1.8T electromagnet has been procured and a pump driven liquid metal loop based on lead-bismuth eutectic was developed with the electromagnet attached over the corrosion test section. After successful operation of this loop for 1000 h, a similar loop with lead-lithium eutectic is being now fabricated for corrosion testing of P91 in the presence of magnetic field.

Rotating Disc Test facility

Velocity of liquid metal flow is an important factor affecting is corrosion behaviour at a particular temperature. To study the effect of different flow velocities on the corrosion behaviour of $Pb_{83}Li_{17}$ on structural materials, rotating disc experiments been planned at FRMS. For This purpose a magnetic coupling based rotating disc reactor has been indigenously designed and fabricated in house and has been successfully commissioned. The initial experiment was carried out to study the compatibility of P91 material at 550°C in $Pb_{83}Li_{17}$ at a rotation speed of 1200 RPM for 2000 hrs. An improvised rotating disc type test facility was designed to study the compatibility of Indian Reduced Activation Ferritic Martensitic Steel (IN-RAFMS) with $Pb_{83}Li_{17}$ eutectic and experiment has been completed by exposing an In RAFMS disc to $Pb_{83}Li_{17}$ at 550°C for 3000 h.

Static test facilities

A number of static test facilities have been designed for studying the compatibility of structural materials with $Pb_{83}Li_{17}$ under various conditions of temperature and material history. The corrosion behavior of Fe9Cr1Mo steel samples in a static $Pb_{83}Li_{17}$ eutectic melt at 823K was analyzed in an especially designed necked quartz capsule [5]. The samples were kept isothermally for 2000 h. The changes in microstructure and depletion of alloying components of the samples were studied using scanning electron microscope (SEM), energy disperses X-Rays (EDS) and electron probe beam microanalysis (EPMA). Weight loss and thinning of the walls were calculated by gravimetric analysis method. Using these data the change in thickness per year was calculated.



Fig 4:- Rotating disc Corrosion test facility

Compatibility of Fusion Reactor Structural Materials

Corrosion of SS316L in $Pb_{83}Li_{17}$

The Corrosion mechanism of SS316L in flowing $Pb_{83}Li_{17}$ has been interpreted in detail based on the data obtained from buoyancy driven loop and static experiments. It has been observed among all the alloying elements, nickel has the highest affinity to dissolve into $Pb_{83}Li_{17}$ and thereby is the main factor responsible for the formation of a porous ferritic layer on the exposed surface of the steel facing $Pb_{83}Li_{17}$ [6]. The effect of oxygen ingress in $Pb_{83}Li_{17}$ loop has also been analyzed thoroughly [7]. Novel techniques to reduce the corrosion rate of SS316L through introduction of nickel and oxygen in $Pb_{83}Li_{17}$ have been investigated upon and satisfactory results have been obtained.



Fig 5: Corroded layer on the surface of SS316L exposed to $Pb_{83}Li_{17}$ at 500°C for 1000 h

BARC NEWSLETTER

Corrosion of 9Cr-1Mo steel (P91) in Pb-17Li

The corrosion mechanism and corrosion rate of P91 at 500°C in flowing $Pb_{83}Li_{17}$ has been established based on the data obtained from buoyancy and pump driven loops [4]. It has been observed that P91 is more resistant to corrosion than SS316L primarily because of the negligible quantity of nickel present in P91. The deposition of corrosion products in the cooler regions of the loops have been analysed and the deposition rate of chromium has been found to be higher than nickel 400°C. The corrosion rate of P91 disc exposed to $Pb_{83}Li_{17}$ at 550C in the rotating disc test facility after 2000 h has been found to be 0.119 mm/yr at a flow velocity of 700 RPM. It has been observed that the presence of magnetic field enhances the corrosion rate by 2-3 times of the initial value and the interaction of this magnetic field with the flowing liquid metal results in results in localized corrosion leading to formation of evenly spaced surface irregularities [8].

Table 1: Corrosion and Deposition rate of P91 samples obtained from buoyancy loop.

Samples	Corrosion rate at 500°C after 1000 h ($\mu\text{g}/\text{cm}^2\cdot\text{h}$)	Deposition rate at 400°C after 1000 h ($\mu\text{g}/\text{cm}^2\cdot\text{h}$)
9Cr-1Mo (10mmx40mmx2mm)	17.4	1.25

Recent Developments

A unique experimental set up has been designed and fabricated to test the creep behavior of structural steels in the presence of $Pb_{83}Li_{17}$ at a high temperature and under a uni-axial tensile load. The stress on the sample is indirectly applied through pressurizing of bellows which are connected to the sample but placed above the level of molten eutectic. The displacement of sample along with time /temperature is measured by an LVDT connected to the sample but isolated from the bellows. The first experiment has been started in this set up with a 170 mm long IN- RAFMS creep sample exposed to $Pb_{83}Li_{17}$ at 823 K and under a uniaxial tensile load of 200 MPa.

The effect of magnetic field of the corrosion behavior of INRAFMS will be studied in a unique set up where the movement of liquid metal would be controlled by a rotating magnetic field. The fabrication of such a set up has been started and the data generated would add to the earlier database and help in understanding the corrosion mechanism of ferritic martensitic steel exposed to $Pb_{83}Li_{17}$ under magnetic field at the operating temperature of ITER.

Acknowledgements

We would like to acknowledge the dedicated effort of all workshop and technical staff of MPD, BARC for fabrication and setting up of all the test facilities.

References

1. Y. Seki, Journal of Nuclear Science and Technology; 26:1 (1989) 189–194.
2. E. Rajendra Kumar et.al. , Fusion Engineering and Design, 83 (2008) 1169–1172
3. O. K. Chopra and D. L. Smith, Journal of Nuclear Materials 155-157 (1988) 715-721
4. P. Chakraborty, P. K. Pradhan, R. K. Fotedar and N. Krishnamurthy, Journal of Materials Research and Technology, doi.org/10.1016/j.jmrt.2013.04.001
5. S. Kumar and N. Krishnamurthy, Fusion Engineering and Design; 2012; doi 10.1016/j.fusengdes.2012.01.014
6. P. Chakraborty, C. Das, S. Kumar and R. K. Fotedar, The Transactions of Indian Institute of Metals, [2012] 65(5):503–506
7. P. Chakraborty, R. K. Fotedar and N. Krishnamurthy, Journal of Nuclear Materials, [2012] Volume 432, Issue 1, p. 239-242
8. E. Platacis, A. Ziks, A. Poznjak, F. Muktepavela, A. Shisko , S. Sarada , P. Chakraborty, K. Sanjay, M. Vrushank, R. Fotedar, E. K. Rajendra, A.K. Suri, Magnetohydrodynamics, (2012), Vol. 48 No. 2, pp. 343–350.
9. P. Chakraborty, S. Kumar, R. K. Fotedar, N. Krishnamurthy, AIP Conference Proceedings, Vol 1538, pp. 34-37; doi:<http://dx.doi.org/10.1063/1.4810028>

BARC NEWSLETTER

O&M OF HEAT TREATMENT VACUUM FURNACES AND THEIR LIFE ENHANCEMENT BY INNOVATIVE MAINTENANCE TECHNIQUES

James Jacob M., Shanmugavelu P., Eswaramoorthy C. and Vaiyapuri K.
Chemical Technology Group

Shri James Jacob M. and his team received the DAE Group Achievement Award for the year 2011

Abstract

Vacuum heat treatment processes such as solution annealing and age hardening are being employed during the manufacture of thin walled Special high strength steel tubes required for "High Speed Machines Program" of the department. Three vacuum furnaces are being used for the past 2 ½ decades for supporting the heat treatment activities. Innovative maintenance techniques were introduced for enhancing its service life beyond the design life by about 2 folds that avoided expenditure of few crores of rupees, apart from providing energy efficient safe operation. The throughputs from the furnaces have been enhanced considerably by the use of suitably designed fixtures to cater to different sizes of our jobs. From the expertise gained over the period of several years of operation of vacuum furnaces, a furnace has been designed, developed and commissioned indigenously by incorporating additional features providing O&M friendly controls along with safe & energy efficient systems.

Introduction

Special High Strength Steels (SHSS) derive their strength not from carbon but from precipitation of intermetallic compounds and martensitic transformation⁽¹⁾. The commonly available SHSS contain Ni, Co, Mo, Ti and Al. These steels develop very high strength by martensitic transformation and subsequent age-hardening. Hardness comes due to formation of intermetallic phases of Ni₃Ti, Ni₃Mo and Fe₂Mo. SHSS have found applications where ultrahigh strength and high toughness are essential. Due to their high strength/density ratio, SHSS have been used for making thin walled cylindrical tubes. The process of making the SHSS tube is a complex one that involves heat treatment processes such as solution annealing and age hardening at different stages. In order to manufacture the cylindrical tube, flow forming technique is employed. SHSS preforms of about few mm thickness are cold formed by multi stage flow forming operations and are brought down to less than 0.5 mm thick thin walled tubes of desired length. Intermediate solution annealing

process is carried out on the pre-forms to make them suitable for further cold working operations. Solution annealing process involves controlled heating of the charge under vacuum to about 900° C and furnace cooling to an intermediate temperature followed by forced cooling using dry nitrogen gas. This process is typically the precursor to an age-hardening operation for precipitation of hardenable alloys. Solution annealing provides complete re-crystallization and ensures the formation of a fully austenitic structure from which martensite can form on cooling. The finished assembly is age hardened that provides the optimum strength and toughness. The nature of the Special high strength hardening mechanism is such that close dimensional control can be maintained in component that are finish machined in the soft, annealed condition and subsequently hardened. The solution annealing and age hardening of the SHSS tubes are carried out in vacuum furnace due to its neutrality of vacuum as a protective atmosphere and the ideal surface quality obtained during the course of heat treatment. In vacuum systems, there is a total separation of the

BARC NEWSLETTER

furnace working area from the environment which permits precise and effective heat treatment processes to be carried out. Additionally, continuous advancement in the area of effective gas quenching makes vacuum furnaces a sophisticated, economical and environmentally friendly alternative to the majority of atmospheric heat-treatment technologies and oil quench.

Three Vacuum Heat Treatment Furnaces (VHTFs) have been installed and operated for the past 2 ½ decades for providing the heat treatment support to our program. Innovative maintenance techniques were introduced to extend its service life beyond the design life, enhance the process throughput and make it energy efficient for safe operation. In this paper, the innovative maintenance techniques followed by us are described.

Use of VHTF for our program

Three vacuum furnaces have been installed and operated for the past 2 ½ decades for providing the following heat treatment support.

- Age Hardening Treatments on finished SHSS rotors.
- Intermediate solution annealing treatment of cold serviced SHSS Preforms.
- Baking of electroless nickel plated components to enhance the adhesion of the coating.
- Heat treatment of Inconel rings.

The vacuum furnaces used for the above applications are made up of double walled stainless steel chamber with all-metallic-hot zone using Molybdenum as heating elements and radiation shields. The hot zones are of modular type having 3 zones of total connected power load of 250 KVA. Effective hot zone size of the furnace is of diameter 700 x 2200 mm height having maximum charge loading capacity of 400 kg at 1000°C. Ultimate vacuum achievable is 1×10^{-6} mbar with vacuum pumping system consisting of diffusion pump, roots pump and rotary vane pumps. It has inbuilt inert gas recirculating fast cooling system.

Innovative Maintenance Techniques Followed

The vacuum furnaces are being operated and maintained in good working condition for more than

25 years till date by adopting innovative techniques for its operation and maintenance. We have successfully carried out few thousands of heat treatment process cycles in each furnace. From the beginning, we have implemented Total Productive Maintenance concepts to make effective use of the equipment and maintain good production conditions. Few of the noteworthy maintenance techniques adopted are mentioned here.

Reconditioning of heat shields for Life enhancement

All metallic hot zone of the vacuum furnaces consists of heating elements, charge carriers and inner two radiation shields made of molybdenum and the outer three radiations shields made of stainless steel (Fig.1). The design life of the molybdenum radiation shields are limited to about 10 years. Replacement of heating shields after its designed service life is essential that incurs a large expenditure in foreign exchange. But we have adopted an innovative technique of overhauling the hot zone that involved multistage buffing followed by ultrasonic cleaning using suitable



Fig. 1: Top-Overall view of hot zones of Vertical furnace; Bottom- Dismantled view of single hot zone

BARC NEWSLETTER

solvents. This process had brought back the original emissivity to the radiation shields enhancing the life of the hot zones apart from providing improved surface quality of the heat treated parts. This maintenance process is a herculean task that involved handling of molybdenum radiation shields which are highly brittle in nature. Implementation of this innovative maintenance concept not only avoided a large expenditure in foreign exchange, but also enhanced the service life beyond 25 years.

Hot zone cleaning cycle

The heat treatment process temperature is limited to 900° C for our routine production activities. During this process, there is a possibility of deposition of volatile materials originating from the charges. This may reduce the efficiency of the heat shields. In order to overcome this problem, a hot zone cleaning cycle is implemented for every 25 batch of process. In this cleaning process, the furnace is heated to 10000° C for an hour by which the efficiency of the heat shields is increased as a result of burning out the deposited volatile materials.

Upgrade of furnace control system enhancing the availability factor

The originally supplied furnace had relay logic based hard wired control system, making it impossible to maintain the equipment in good working condition. Furnace has been upgraded to PLC & HMI based control system that provides flexibility to alter program logic sequences, apart from providing supervisory control and data acquisition. Subsequent to the implementation of the PLC based Control System, a number of modifications in the process interlocks and their sequence were introduced. The additional logic introduced in the sequence of operation for the pumping system has resulted in energy saving of the order of 100 KWH per process cycle amounting to 40% reduction approximately.

Introduction of Safety interlocks

The overall safety features of the High Temperature High Vacuum Furnaces have been enhanced considerably

by adding a number of safety interlocks as detailed below.

- Introduced a pre-condition to initiate fast cooling cycle, ensuring elimination of accidental admission of dry nitrogen gas at elevated temperature.
- To avoid accidental incident of switching on the pumping system when furnace lid is in open condition, proximity sensor was mounted which acted as fail safe precondition to initiate the process cycle.
- Position sensors were also incorporated in the fore-vacuum rough-vacuum and holding line valves ensuring fail safe operation.

Reconditioning of ceramic insulators

The furnace has three heating zones each of which is equipped with cylindrical Mo sheet as heat reflector and Mo heating wire. All-Metallic- Hot zones of these furnaces are separated from the furnace body with the aid of high purity alumina based ceramic electrical insulators. Each furnace has around 200 such ceramic insulators in the shape of bobbins and sleeves. After few years of operation, we have observed frequent blowing of fuses in the thyristor based heater control systems. This was finally attributed to electrical short circuiting in the heater assemblies. Upon investigation, the ceramic insulators were found to be coated with Mo to few microns thickness as confirmed by EDXRF spectrometer. Deposition of Mo over the ceramic insulators has taken place due to the use of Mo radiation shields/heating elements in vacuum condition during the operation of furnace over a period of several years. This resulted in deterioration in the insulating property of the ceramic insulators. As spare ceramic insulators of special dimensions are not readily available, a special reconditioning procedure was developed. All the insulators were removed from the furnace and subjected to suitable chemical treatment process for the selective removal of Mo deposits from the ceramic insulators. All the insulators are salvaged by adopting this innovative chemical treatment process and reassembled successfully for the safe operation. Based on this experience, this *reconditioning procedure has been included in the Total Preventive Maintenance protocol.*

BARC NEWSLETTER

Design and fabrication of fixtures

We had designed and fabricated different fixtures for loading tubes as well as the finished products for annealing/age hardening respectively in the vacuum furnaces. The requisite design & material selection for the fixtures were based on the properties at elevated temperature of the order of 1000° C.

Fixtures for age hardening and annealing

In our earlier design of the fixture used for age hardening, the rotors are directly resting on the fixture's bottom plate, which in turn are placed on the hearth of the furnace. This fixture cannot be used for our newer designs of the work, having flexible elements, due to the possible distortion on the thin sections. So, we had developed a different design of fixture as shown in Fig 2. In this design, the long 'Tube-Assemblies' are loaded in the suspended conditions from the top plate. An intermediate plate takes care of guiding at the bottom. This design eliminates the possible distortion of the Tube-Assemblies'.

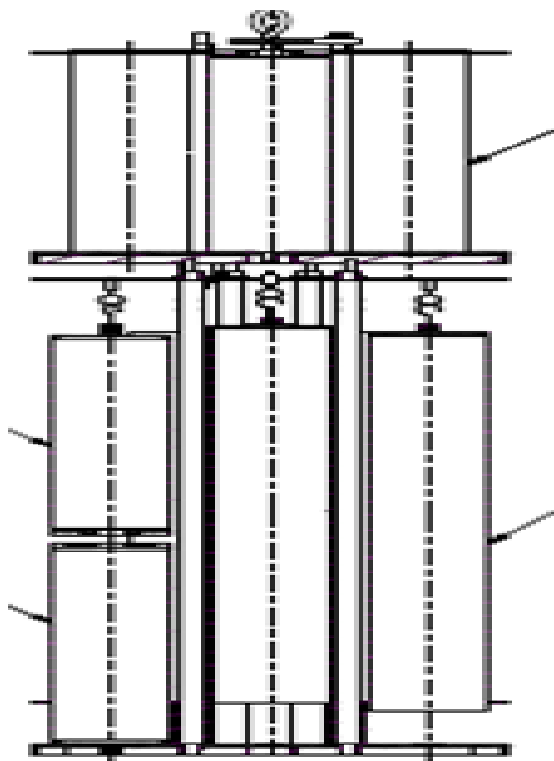


Fig. 2: Universal type age hardening fixture accommodating different designs of rotors in multi tired orientation

In order to reduce the inventory of fixtures for different sizes/designs of the finished products, we had also developed fixtures that can be universally used for accommodating different sizes/designs of the finished products/tubes in multi tire orientation. This resulted in enhanced throughput apart from considerable cost saving in manufacturing of multiple fixtures. Similarly universal fixture as shown in Fig.3 is fabricated for annealing treatment of SHSS preform tubes for increasing the process throughput. In this design, regular diameter pre-form tubes are placed inside the higher diameter pre-form tubes.

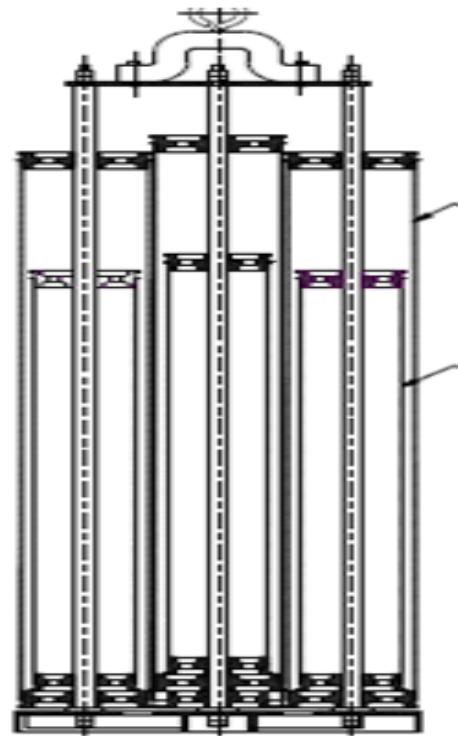


Fig. 3: Annealing fixture for accommodating regular dia preform tubes inside the higher dia tubes

Fixture for vacuum baking of Nickel plated components

Few of the carbon steel components of the HSR machines are coated with nickel to few micron thickness by the process of electro less nickel plating. During the process of nickel plating, hydrogen gas is likely to be trapped in the coating, which needs to be removed. Vacuum baking at about 200°C for few hours often relieves the hydrogen and also enhances the adhesion of the deposit ⁽²⁾. Furnace used for baking operation imposed a limitation on the length of plated components such as housing whose length is about 2

BARC NEWSLETTER

meters. In order to accommodate such lengthy components for baking, special fixtures had been designed & fabricated to load the job in an inclined manner as shown in Fig. 4 taking the advantage of increased space diagonal of the effective hot zones.

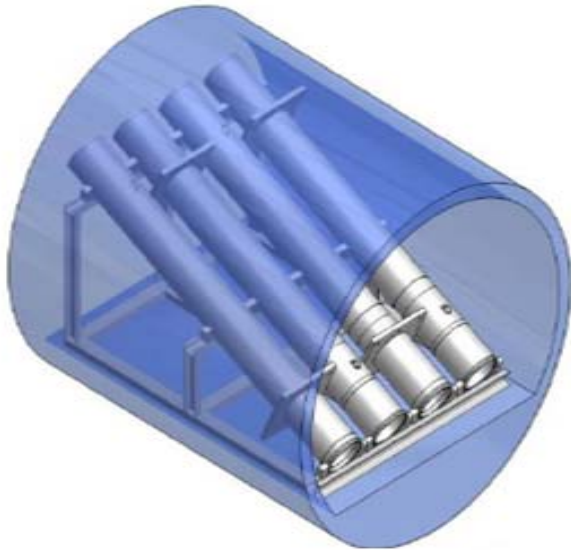


Fig. 4: Fixture used for baking of long housing in inclined orientation

Indigenous development of Vacuum Furnace

Based on the expertise gained over the decades of operation and maintenance of the furnaces, work was undertaken to design and develop Vertical Vacuum Furnace Indigenously in association with NFC, Hyderabad. The following additional features were also incorporated in the indigenously developed vertical vacuum furnace (Figs.5-6).

- Wide Band Heating Elements for uniform heat distribution.
- Fully Automatic operation through PC mode and also manual mode through Control Desk mode.
- Doped Molybdenum based Hot Zone for life enhancement.
- Low Voltage across Heating Elements
- Health monitoring gauges for individual pumps for easy maintenance.
- Incorporation of quadruple mass spectrometer gas analyzer.
- Gas Plenum for effective fast cooling.

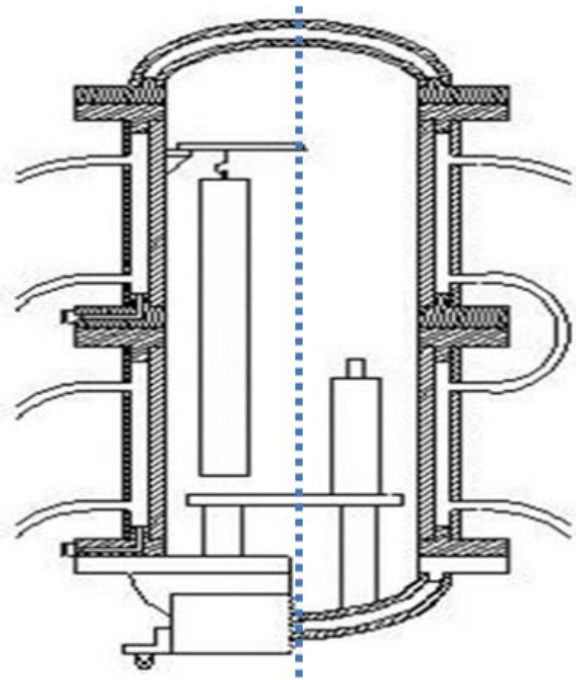


Fig. 5: Comparison of additional features incorporated in the indigenously developed furnace (Left half) with one (Right half)



Fig. 6: Overall view of vertical vacuum furnace

- Avoided looping of cooling water circuits by providing individual cooling water line to the chambers.
- Load hanging fixtures for flexible membered tubes.
- Drain ports for complete removal of water from the jackets to avoid corrosion.

BARC NEWSLETTER

- Wheels on the bottom lid frame for easy maintenance.

Conclusions

From the past experience gained during the operation and maintenance of industrial vacuum furnaces for heat treatment applications, a number of design features have been incorporated for the indigenously developed vacuum furnace, which results in safer and energy efficient operation.

Acknowledgement

We wish to express our gratitude to Shri. T.K. Bera (Project Director), Shri. M. R. Srikanthan (Project

Manager, Mechanical), Shri S. Sarkar (Project Manager, Process) and Shri A. Nandakumar (Head MQF) for their whole hearted support and encouragement. We would also express our sincere thanks to all officers and staff members of RMP especially those from AF-II, EPSS, EIS, USF, FMS, MQF and ACS, who are directly or indirectly associated with this job.

References

1. Physical Metallurgy and Advanced Materials, edited by R. E. Smallman and A. H.W. Ngan. Seventh edition (2007) Published by Elsevier Ltd.
2. G.O.Mallory, *Plat. And Surf. Fin.*, 63(6), 34(1976).

BARC NEWSLETTER

SYNTHESIS OF DICYCLOHEXANO 18 CROWN 6 LIGAND ON BENCH SCALE & DEVELOPMENT AND DEMONSTRATION OF SELECTIVE RECOVERY OF STRONTIUM FROM THORIUM LEAN RAFFINATE (TLR) WASTE IN THE BACK END OF NUCLEAR FUEL CYCLE USING THE LIGAND

K.T. Shenoy

Chemical Engineering Division

and

C.P. Kaushik

Waste Management Division

Dr. K.T. Shenoy and his team received the DAE Group Achievement Award for the year 2011

Abstract

Chemical Engineering Division (ChED) has successfully developed the process for synthesis of Di-Cyclo Hexano 18 Crown 6 ether (DCH18C6) ligand, which is selective for strontium, on bench scale. Initial extraction experiments were carried out in ChED with simulated waste solution and later by radiometric analysis in FRD and WIP laboratories. Finally, quantitative recovery of strontium was successfully demonstrated from the actual Thorium Lean Raffinate (TLR) using the in-house synthesized solvent in five stage mixer – settler experimental facility set up in a fume hood of WIP laboratory. The details of these developmental studies are described in this paper.

Introduction

The crown ether, DCH18C6, has a very important application in back end of the fuel cycle for recovery of strontium from the actinide-free waste streams. TLR stream is generated at FRD during the processing of J-rods of CIRUS reactor. The composition of the raffinate stream after recovery of uranium and thorium are given in Table – 1. Major radioactive elements are Cs and Sr in acidic medium. There is a good demand for Sr⁹⁰ which is required for generation of Y⁹⁰ which is an important radionuclide for therapy in nuclear medicine. Sr⁹⁰ finds use as heat source in radio isotope thermoelectric generators and as radioactive tracer in medicine & agriculture. It is proposed to recover Sr from the active waste stream first by solvent extraction with DCH18C6 followed by recovery of Cs with Resorcinol Formaldehyde resin.

Synthesis of DCH18C6 on bench scale

The bench scale synthesis set up has a batch size of 1 kg of the crown ether DCH18C6 and its precursor DB18C6. The set up consists of 85 liter hastelloy reactor, 25 and 10 liter glass reactors for solvent recovery, 25 liter SS autoclave for hydrogenation, electrode boiler, 5 TR chiller unit etc. The bench scale synthesis runs were conducted through round the clock shift operations. The DB18C6 was synthesised in a ventilated enclosure with about 35% yield and more than 98% purity. Bio Organic Division, BARC has assisted in improving the yield of product. DCH18C6 was synthesized through high pressure catalytic hydrogenation in 25 liter SS autoclave in a semi open area, custom made for this purpose from safety point of view. DCH18C6 was synthesized with more than 90% yield and more than 98% purity.

BARC NEWSLETTER

Table 1: The composition of TLR used for mixer settler experiments

Properties	TLR waste	Adjusted TLR Feed to MS
Molarity (M, H ⁺)	2.0	3.7
Specific Activity, mCi/l		
Gross Beta	16.64	15.07
Gross Alpha (Th)	1.56×10^2	1.3×10^2
Isotopic Constituents, mCi/l		
Cs-137	7.00	6.0 (0.0697 ppm)
Sr-90	4.60	3.92 (0.0284 ppm)
Sb-125	1.37×10^2	1.22×10^2
Tc-99	5.0×10^3	4.44×10^3
Ru-106	3.2×10^3	2.84×10^3
Al (g/l)	2	1.77
F (ppm)	300	267

Strontium extraction – Batch experiments

A set of experiments involved batch contacts of aqueous and organic samples intimately contacted at least for 10 min for attaining the equilibrium condition before separation for analysis. All the strontium analyses were carried out by doping with necessary amounts of active Sr⁸⁵⁺⁸⁹. Pure component data for distribution coefficient of strontium and various impurities likely to be encountered in waste streams, effect of nitric acid concentration, etc. were studied.

Effect of molarity of nitric acid in the feed solution:

Experiments were conducted to optimize the concentration of nitric acid in the feed to achieve maximum uptake of Sr using 0.1M DCH18C6 in the mixture of 20% Octanol + 80% Toluene. It was found that Sr extraction increases with increase in conc. of nitric acid upto 4 M, thereafter, it remains more or less constant. Hence, optimized concentration of 4 M is used for further studies.

Studies on pure components:

The major elements present in the HLW matrix were studied for their extraction by the DCH18C6 and the distribution coefficients were evaluated. It was noted

that most of the constituents of the HLW like Cs, Ru, Ce, Eu, Am, U, etc are not extracted to any significant level. It was also noticed that Pu is significantly extracted especially at higher acidities ($K_d=25$ at 3N and 26.5 at 4N).

Studies on selectivity of DCH18C6 in octanol diluent for Sr in presence of competing actinide elements:

The effect of major elements which are likely to be present in HLW or TLR like Pu, U, Th and Na were studied for their effect on Sr extraction and to find any limiting concentration for better selectivity. It was noticed that thorium is extracted to a small extent at 4.0M acidity in feed. But upto a concentration of 2000 ppm, no significant effect is seen on D_{Sr} (2.8 to 3.2 at 4M). Less than 3 mg/l Pu content in HLW does not affect Sr extraction.

Strontium extraction – Continuous contact experiments

Continuous counter current studies were carried out using 5 stage mixer settler, each stage having 125 ml mixer and 375 ml settler (Fig. 2). All the experiments were carried out in one of the fume hoods having adequate shielding at Process Control Laboratories of WIP with the DCH18C6 synthesised in ChED.

BARC NEWSLETTER

Since the TLR waste had free acidity of about 2M, the same was adjusted to about 3.7M by the addition of conc. nitric acid to exploit the higher distribution coefficient. The details of extraction and stripping parameters are given below:

Feed activity of Sr: 3.92 mCi/l
Concentration of Sr = 0.0284 ppm (based on specific activity of Sr⁹⁰ as 138Ci/g)
Flow rate of Aqueous: 25 ml/min; Flow rate of Organic: 25 ml/min
Volume of organic: 7l (0.1M DCH18C6)
Activity of loaded Organic (based on activity balance during extraction): 3.86 mCi/l

Only aqueous streams could be analysed for Strontium. Strontium in organic was estimated based on average D value of 3.2. Cumulative raffinate was found to

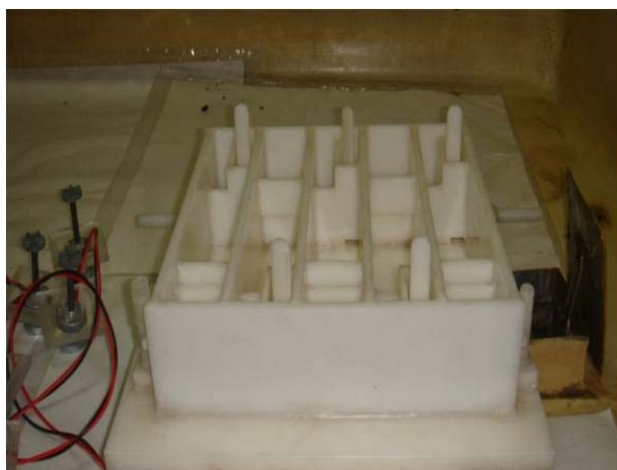


Fig. 2: 5 stage mixer settler unit

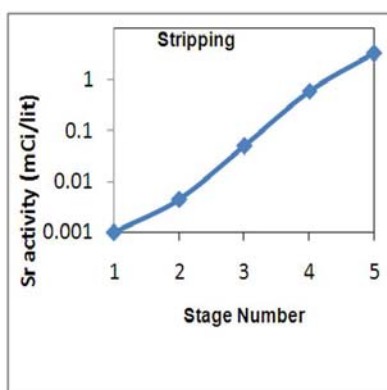
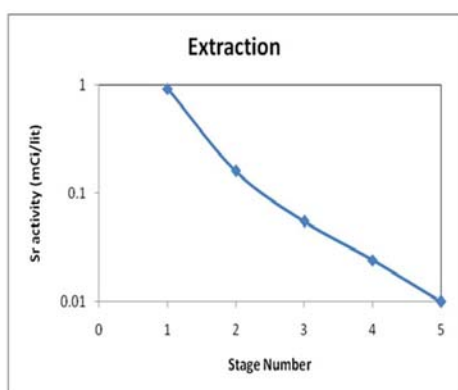


Fig. 3: Steady state stage wise concentration profiles of Sr in the mixer settler

contain 6×10^{-2} mCi/l of Sr and 5.8 mCi/l of Cs. Based on Sr and Cs activity in the feed and raffinate, the Decontamination Factor (DF) with respect to Sr works out to be 65.

More than 99% strontium was stripped in 3 stages. Activity balance shows complete stripping of the loaded organic. Concentration profiles of strontium in various stages of mixer settler for extraction and stripping are given in Fig. 3. Product solution showed 3.86 mCi/l of ⁹⁰Sr and 0.12 mCi/l of ¹³⁷Cs indicating negligible crosstalk of Cs during extraction and stripping cycle.

Conclusion

The demonstration of the extraction experiment has shown overall recovery of strontium from TLR is more than 98.5% based on the feed activity and cumulative raffinate activity. Three diluent combinations were tested namely Octanol, Octanol + Toluene and Octanol + Xylene. All were found suitable for strontium recovery. Octanol is better suited for feed streams, which does not have impurities like Ba, K, etc. from the point of view of lower volatility. The vapor pressure and flash point of octanol are close to dodecane. The only impurity identified in the product is Cs which is about 3% of the total product activity. Purity of the product can be improved to the desired extent by incorporating acidic scrubbing step. The Sr⁹⁰ content can be concentrated from the final product strip solution by evaporation followed by carbonate

precipitation. The recovery of Sr⁹⁰ from feed stream to strip is more than 98%. DCH18C6 solvent system is also suitable for strontium recovery from actinide-free HLW. The flowsheet finalization may require some experimental work with HLW.

BARC NEWSLETTER

PROCESS DEVELOPMENT FOR PLASMA SPRAY DEPOSITION OF YTTRIUM OXIDE COATINGS FOR CONTAINMENT OF MOLTEN URANIUM

A.K. Das, P.V.A. Padmanabhan, Jaya Mukherjee, T.K. Thiyagarajan, S. Sethi, Anupama Prabhala, A. Nagaraj, Y. Chakravarthy, RU. Satpute, M.K. Verma, N.V. Patil, S.L. Songire, A.J. Almeida, S.S. Dehade and S.B. Gaikwad
Laser & Plasma Technology Division

A.K. Das and his team received the DAE Group Achievement Award for the year 2011

Abstract

This paper reports indigenous development of a plasma spray coating process as a corrosion barrier for containment of molten uranium. The uniqueness of this work arises from the fact that the entire process was developed in-house starting from raw powder from IREL, the preparation of spray grade feed material, achievement of optimised plasma spray coating of yttrium oxide on graphite and tantalum substrates and finally extensive qualification tests that included development of necessary equipment and procedures. Commercially available yttrium oxide powder (2-5 micron size) from Indian Rare Earth Limited, India is used as the starting material to prepare plasma spray grade yttria powder (30-75 micron). The plasma spray coating was optimised through process modeling, experiments, post processing and coating characterization to evolve the range of operating parameters for best results. Long term corrosion experiments of yttria-coated tantalum coupons immersed in molten uranium at 1573K showed that yttrium oxide-coated tantalum crucible and substrates withstood more than 400 hours of continuous exposure to molten uranium.

Introduction

Plasma sprayed coatings of metals and ceramics are used for protecting materials in many specialized applications involving thermal barrier, corrosion barrier, electrical insulation etc. where basic structural strength of the base material is maintained. In nuclear industry in particular, development of long duration corrosion resistant coatings to handle actinides in high temperature liquid or vapor phase is one of the key applications of plasma spray technology. Though, for a number of years, aluminum oxide coatings are being used for casting uranium metal, it has certain drawbacks due to its poor thermal shock resistance and its instability under reducing conditions. Above 1200°C, alumina is reduced to its gaseous sub-oxides in vacuum or in presence of carbon, hydrogen, and other reducing

gases. Further, aluminum oxide is not suitable for long duration handling of molten uranium and other reactive metals. Therefore, development of alternate ceramic coatings for containment of uranium and its alloys has been a major research issue.

Amongst the alternate materials, Yttrium oxide has excellent thermal stability up to its melting temperature and also possesses superior resistance to aggressive chemical attack by molten metals, salts and slag at high temperatures. Though commercial yttrium oxide powders are available, they are mostly not spray grade and hardly any literature exists on methods of preparation of thermal spray grade Y_2O_3 powder and development of plasma sprayed yttrium oxide coatings. In view of the urgent need of the Department, developmental study on plasma spray deposition

BARC NEWSLETTER

of yttrium oxide was undertaken. Since the precursor powder used for plasma spray deposition is not locally available and is to be imported, a process to make free flowing yttria powder was developed as a part of indigenization of this entire technology.

Synthesis of plasma spray grade yttrium oxide powder

Plasma spray-grade yttrium oxide powder, synthesized in our laboratory, was used as the feedstock material for plasma spray deposition. Commercially available 99.9% chemically pure yttrium oxide powder from IREL, India, was compacted at about 207 MPa and sintered at 1873K for 4 hours. The sintered mass was crushed into smaller chunks, milled and the powder fraction in the size range of 38–75 micron was used for plasma spray deposition studies. This powder was found to have near-spherical morphology and good flow characteristics¹.

Modeling and Simulation of Plasma Spray Process

Computational fluid dynamic and heat transfer simulation was carried out for the powder laden plasma jet to estimate the velocity and thermal history of yttrium oxide particles in the plasma jet. A two-dimensional axisymmetric plasma jet model was developed to simulate the plasma jet velocity and temperature for different gas flow rates and input powers. This was used to obtain heat and momentum transfer from the plasma to the particle. Particle temperature and velocity at various operating parameters obtained from simulation studies provided a window of operating parameters for process optimization. Experimental studies were then limited to the range of parameters within this window to optimize the process. Coating adhesion strength was used as the response parameter for process optimization, which was done by maximizing coating-substrate adhesion. For an average particle size of 60 micron, 24 kW input power is seen to be the optimum to get adherent yttrium oxide coatings with adhesion strength of about 8 MPa.

Plasma spray deposition

Plasma spray deposition was carried out using a 40kW atmospheric plasma spray system developed in our

laboratory at BARC. Deposition was carried out on various substrates including stainless steel, graphite and tantalum coupons. A mixture of argon and nitrogen was used as the plasma gas, which was injected through a side inlet provided in the insulator. Input power to the plasma torch was varied from 16 kW to 30 kW by controlling the gas flow and arc current. Nitrogen was used as the secondary plasma gas. The primary gas flow was varied from 20-30 standard litres/minute (SLPM). Based on data generated on plasma stability and nozzle erosion at various process operating conditions, experiments were carried out only at 25 and 30 SLPM of primary gas (argon) flow rate. Similarly, the carrier gas flow rate was kept constant at 12 SLPM and the torch to substrate standoff distance was kept constant at 100 mm based on a large number of trial experiments and operational experience.

Coating characterization and Evaluation

Coatings deposited on stainless steel substrates were used for characterization studies by x-ray diffraction, Raman spectroscopy, scanning electron microscope (SEM), thermal shock resistance and tensile adhesion tests. Coatings deposited on graphite substrates were used for studying corrosion attack on the substrates by differential thermal analysis and thermo-gravimetric analyses. Long duration corrosion studies with molten uranium were carried out using yttria coated- tantalum coupons at UCUF.

X-ray diffraction pattern and Raman spectra of the coated specimens showed that the phase composition of the coating was identical with that of the starting material consisting of a single homogeneous phase of cubic Y_2O_3 . The SEM photographs of plasma sprayed deposits showed molten/ partially molten lamellae with scattered porosity. The fraction of un-melted particles and porosity were seen to be higher in coatings deposited at 12 kW. As the power is increased to 16 kW and 20 kW, the porosity and fraction of un-melted particles reduced. The SEM photograph, shown in Fig. 1, of plasma deposited yttrium oxide at 24 kW and gas flow rate of 42 SLPM of argon + 3 SLPM nitrogen gas showed a morphology of fully molten and flattened lamellae. The coating-substrate interface

BARC NEWSLETTER

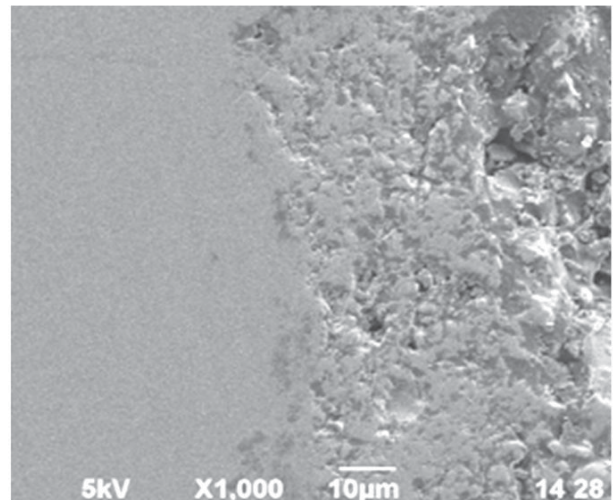
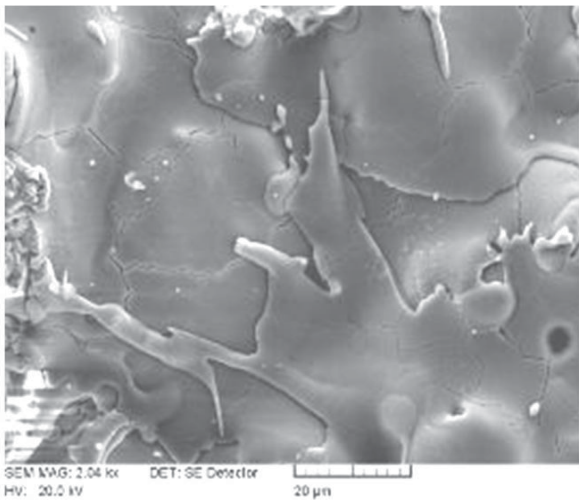


Fig. 1: SEM photograph of surface morphology and cross section of yttrium oxide deposited at 24 kW

showed no de-lamination indicating good adhesion with the substrate surface².

Results of thermal shock resistance of the coatings deposited on stainless steel substrates gave highly encouraging results. The coating-substrate interface was visually examined after each thermal cycling experiment using a magnifying glass of magnification 20. It was observed that the coating-substrate integrity was maintained and that the interface did not develop any visible crack even after 30 thermal cycling experiments.

Corrosion experiment on yttrium oxide coated graphite sample with uranium was carried out by DTA in the temperature range 300 to 1500K. DTA results showed that the coating offered sufficient protection of the graphite substrate against attack by molten uranium. EDX analysis of the coated sample after the DTA/TGA run showed no uranium peak.

Experimental setup for thermal cycling and liquid uranium corrosion studies

Thermal cycling tests were conducted using a 10 KW induction furnace with a graphite susceptor used for heating the coupons held in an alumina tube having dimensions of 80 mm OD and 800 mm long. The coupons were hung using Kanthal wire of 0.5 mm diameter, and were shielded from direct heating from the coil using a grounded graphite cylinder. The heating

and cooling rates used for cycling experiments are as shown in Fig. 2a and the general assembly of the experimental setup is shown in Fig. 2b.

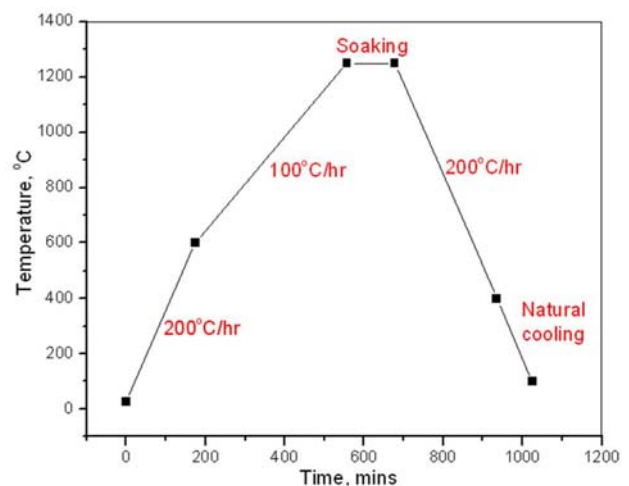


Fig. 2a: Heating and cooling cycle for thermal cycling experiments.

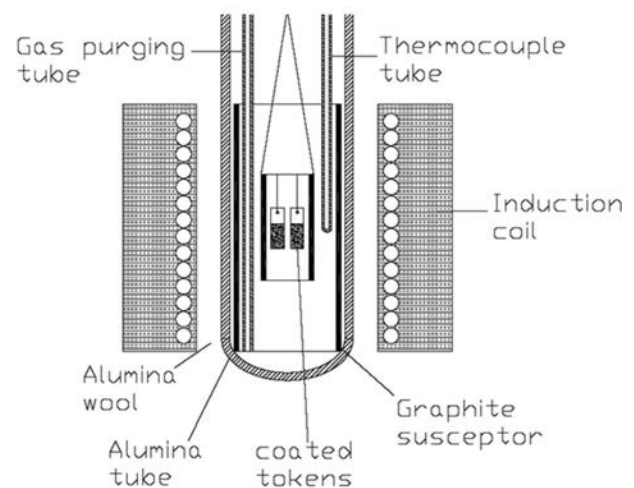


Fig. 2b: General assembly of the thermal cycling setup

BARC NEWSLETTER

The schematic of the corrosion experiment assembly is shown in Fig. 3. The experiments were conducted in a one end closed alumina tube with the open end connected to the vacuum system with the help of a tee. The flange at the other face of the tee had leak tight feed-throughs for coupon holder and thermocouple. The closed end of the tube was placed inside a resistively heated furnace. The length of the alumina tube is suitably chosen so that forced air cooling suffices to keep the temperature of O ring seals below 373K. Vacuum of 1E-6 mbar was maintained by an oil diffusion pump backed by rotary pump. A pack

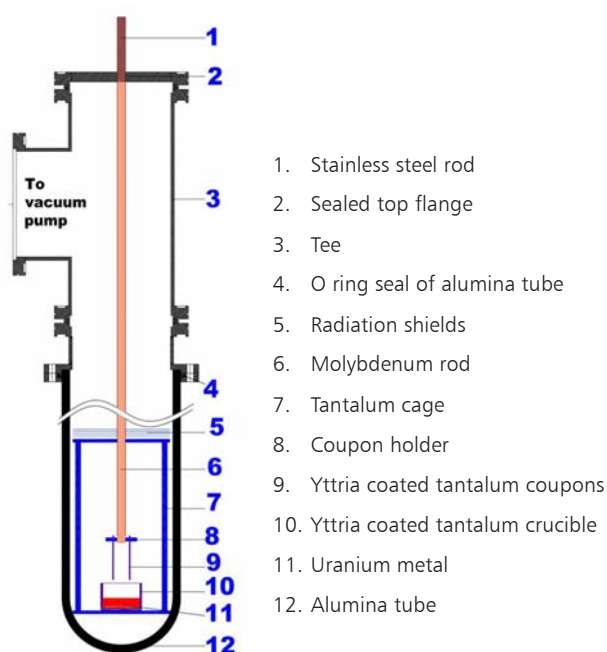
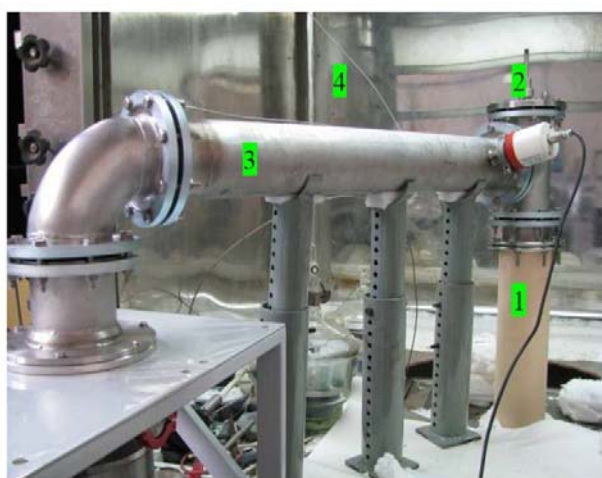


Fig 3a: Schematic of the experimental assembly



1. Alumina tube
2. Sealed top flange with feed through for coupon holder
3. Connection to the vacuum line
4. Complete setup assembled inside a fumehood

Fig. 3b: Photograph of the experimental assembly

of radiation shields ensure a uniform temperature over 150mm length in the hot zone. A tantalum cage was used to support the crucible containing uranium. The crucible was formed from 2mm thick tantalum sheet having dimensions of 50mm outside diameter and 30mm height. This tantalum crucible was coated with 80-110 μm thick yttrium oxide and contained about 230 gm of nuclear grade uranium to provide a molten pool depth of about 8mm. It was planned to change the uranium charge after each experiment if any scum is formed on the surface. However, in the experiments reported, there was no scum observed. Hence, the same melt was used for all the experiments. The experimental setup went through a formal safety audit and approval process. The tantalum coupons used were 40mm x 8mm x 1mm thick with rounded edges and corners to reduce the stresses in the coating. Coating was done up to 15mm from one end of the coupon and the other end had provision to fix in a tantalum coupon holder. Coating thickness varied from 60 μm -110 μm . The coupon holder was a tantalum plate of 30mm x 30mm x 3mm thick with rectangular slots to pin the coupons. The coupon holder was connected to a molybdenum rod, which was in turn connected to a stainless steel rod, projecting through the vacuum feed-through on the top flange. This was used to immerse/remove coupons from the metal pool. Two coupons were used in each experiment. Pre-experimental qualification for defect free coupons was done by optical microscopy at 200X, and thermal cycling tests of a few coupons of the batch.

Thermal cycling and liquid uranium corrosion studies

The thermal cycling tests were performed at 1573K with continuous purging of purified argon containing oxygen below 0.1 ppm and also in vacuum. Each cycle consists of heating the coupons to 1573K in a controlled way, and soaking at that temperature for 2 hours, followed by controlled cooling. The weight changes of the coated samples were measured to a precision of 0.01 mg. At least two samples were tested in identical conditions so that the average weight gain/loss of the samples can be obtained. The samples were considered as failed when cracks were observed at 100X magnification in an optical microscope.

BARC NEWSLETTER

For the corrosion studies, the heating, cooling and holding cycles adopted in the experiments consisted of heating the setup to 823K at 200K/hr and holding it for 2 hours, followed by heating to 873K at 200K/hr and holding for 2 hours for complete out-gassing of the system. Heating was continued at 100K/hr to 1573K to melt uranium, and thermally equilibrate the metal pool and coupons for 2hrs, followed by immersion of coated coupons into metal pool up to 7mm. Separate experiments were conducted by continuous immersion for 10, 20, 40, 80, 120, 200 and 400 hrs durations. Coupons were removed from the metal pool and held above the pool for 1hr for liquid uranium to trickle down. Post experiment analysis included observation of full area under an optical microscope at 200X for any defects. Defect free coupons were cold mounted and cut with a diamond wheel to observe the cross-section. Polishing was intentionally avoided to retain the micro structural features. A Zeiss EVO 40 SEM with Bruker EDX analyzer was used for micro-structural and chemical analysis.

Results and Discussions

Figs. 4 and 5 show the micrographs of the tantalum and of yttria coating interface, and Fig. 6 shows the surface morphology of yttria coating. It can be observed that the coating is uniform, and absence of large open / closed pores show that the coating quality is quite good.



Fig. 4: Optical micrograph of Yttria coating on Ta

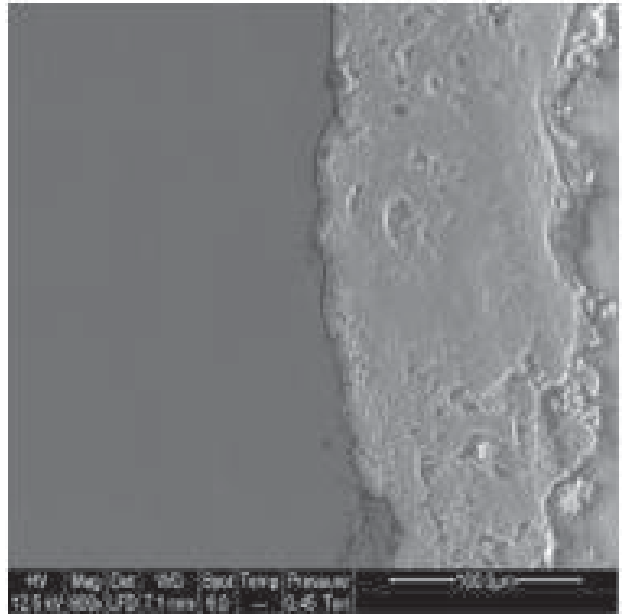


Fig. 5: SEM Picture of interface of coating

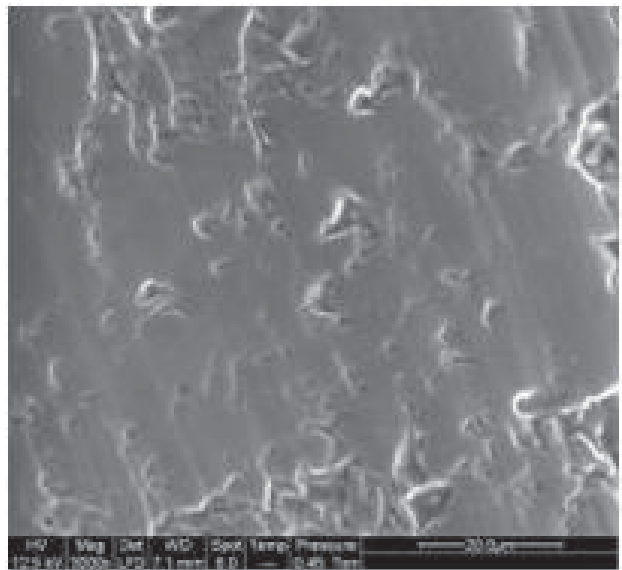


Fig. 6: SEM picture of coating

It was observed that the coatings produced by the in-house sintered and prepared powder did not develop any cracks when viewed at 100X magnification up to 26 cycles. Further testing was not done as the process requirement criterion was satisfied up to 4 times the required number of cycles.

Environmental influence on the performance of the coating was studied by introducing air and moisture leaks into the system. Both oxygen and moisture introduction have resulted in reaction with the substrate and peeling of the coating. In case of moisture entry it was observed that oxide along with TaC formation has

BARC NEWSLETTER

taken place by reaction of hydrocarbon gases / CO produced by reaction of moisture with graphite at high temperature. Oxygen leak into the system resulted in oxidation of tantalum coupons and peeling of the coating.

After the corrosion experiments, the coating was examined for interface integrity. None of the coupons showed de-lamination or interfacial cracks. No significant change was observed in the average thickness of the coating after immersion. The coupons

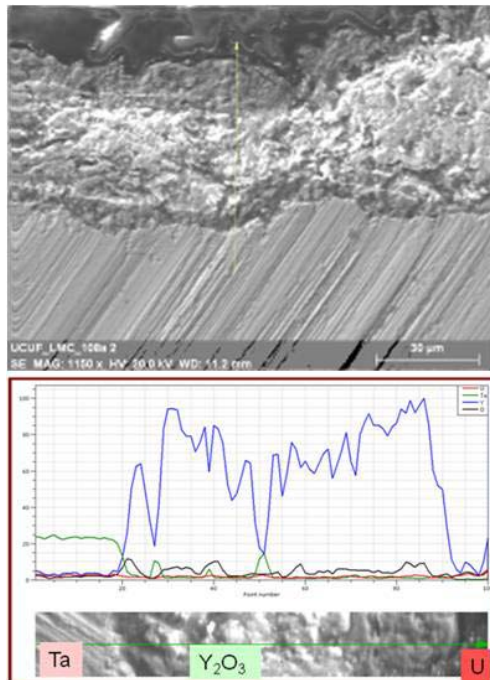


Fig. 7: SEM image and line scan for elements along the cross section of the coating interface-80hrs

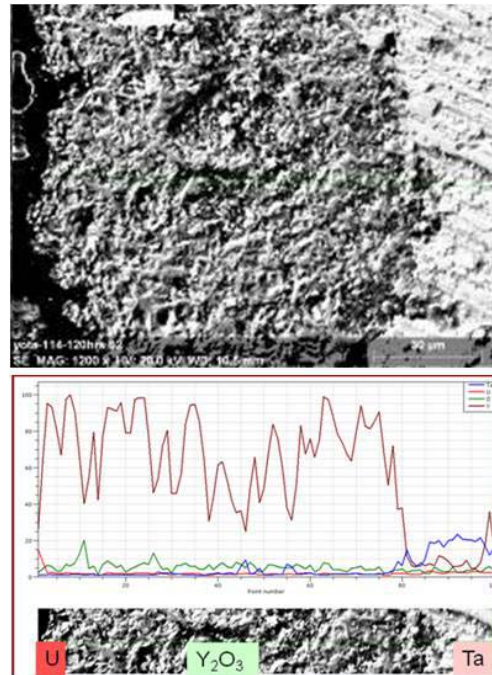


Fig. 8: SEM image and line scan for elements along the cross section of the coating interface-120hrs

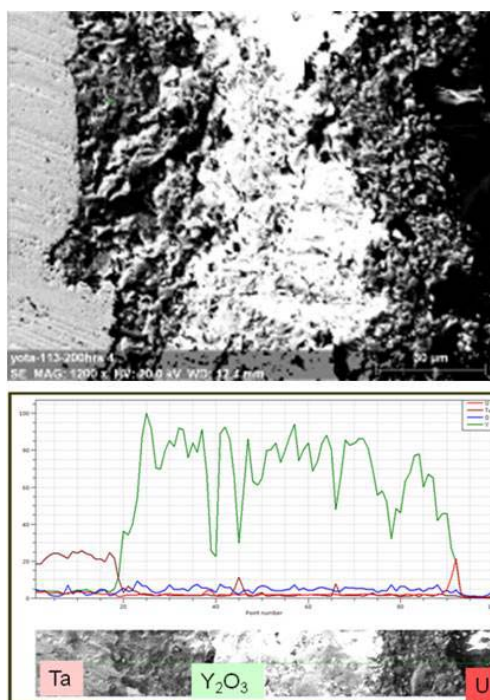


Fig. 9: SEM image and line scan for elements along the cross section of the coating interface-200hrs

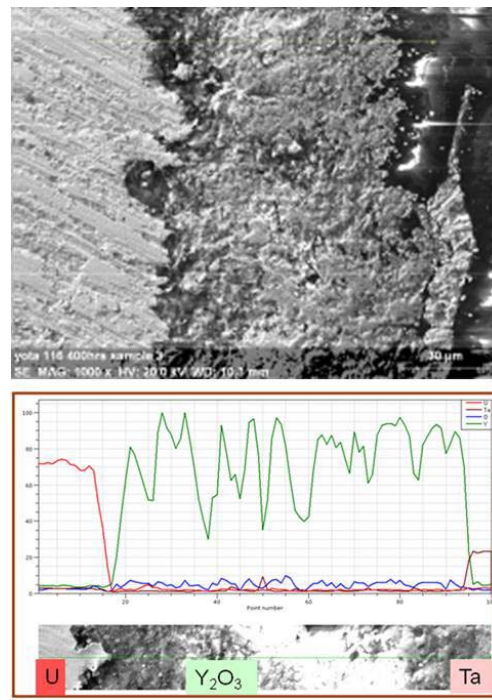


Fig. 10: SEM image and line scan for elements along the cross section of the coating interface-400hrs

BARC NEWSLETTER

always reported a weight gain due to adherence of uranium, and no scum was observed on top of the melt that would have resulted from either reduction of yttrium oxide by uranium metal or due to spalling of the coating³. Figs. 7-11 show the cross-sectional view of the coupons of the four different runs where the coupons were immersed for 80, 120, 200 and 400 hrs respectively in liquid uranium at 1573K. The microstructural features as well as EDX results showed no specific reaction products at the liquid/ Y_2O_3 interface in all the coupons. However, gradual conversion of white stoichiometric Y_2O_3 to black non-stoichiometric Y_2O_3 with increasing contact time with liquid uranium was observed. Tournier et.al⁴ also reported similar observation in his corrosion experiments carried out at 1673K. This kind of non-stoichiometric oxide is not observed across the thickness of coating even after 400 hrs of contact time with liquid uranium. This possibly suggests that kinetics of the formation of non-stoichiometric oxides is very slow as the temperature of our experiment is lower by 100K. However, black/brown color is observed on the surface of the immersed area of the coupon, which may be due to oxidation of uranium that was adhering to the coupon after removal from the metal pool. The coating integrity with the tantalum substrate was found to be intact after 400 hours of corrosion experiments. Subsequent experiments involving longer duration of immersion in molten uranium showed that the coatings were stable even after 1000 hours.

Conclusion

In house development of a complete process for plasma spray deposition of yttrium oxide coatings on graphite and tantalum substrates for protection against long-duration corrosion by molten uranium is reported in this article. The indigenously developed free flowing yttrium oxide powder could be successfully used for plasma spray deposition. Experiments at UCUF

laboratories showed that yttrium oxide-coated tantalum crucible and substrates withstood more than 400 hours of continuous operation exposure to molten uranium, demonstrating the efficacy of yttrium oxide coatings for long duration protection of substrates against corrosion by molten uranium. The total indigenization of the plasma spray technology offers enormous scope of application of this technology to nuclear fuel cycle.

Acknowledgement

The authors thank Dr. L.M. Gantayet, Director, BTDG, BARC for his guidance, continuous support and encouragement.

References

1. P.V.A. Padmanabhan, S. Ramanathan, K.P. Sreekumar, R.U. Satpute, T.R.G. Kutty, M.R. Gonal, L.M. Gantayet, Synthesis of thermal spray grade yttrium oxide powder and its application for plasma spray deposition, *Materials Chemistry and Physics* 106, (2007): 416–421
2. T. K. Thiagarajan, P. V. Ananthapadmanabhan, K. P. Sreekumar, Y. Chakravarthy, A. K. Das, L. M. Gantayet, B. Selvan and K. Ramachandran, Experimental and simulation approach to plasma spray deposition of yttrium oxide, *Surface Engineering*, 28(9), (2012):646-56.
3. Nagaraj Alangi, Jaya Mukherjee, P. Anupama, M.K. Verma, Y. Chakravarthy, P.V.A. Padmanabhan, A.K. Das and L.M. Gantayet, Liquid uranium corrosion studies of protective yttria coatings on tantalum substrate, *J Nucl Mater* 410, (2011): 39–45
4. C. Tournier, B. Lorrain, F. Le Guyadec, L. Coudurier, N. Eustathopoulos, Kinetics of interfacial reactions in molten U/solid Y_2O_3 system, *J Nucl Mater* 254, (1998): 215–220.

BARC NEWSLETTER

DEVELOPMENT OF THREE TANK PLATING CYCLE (TTPC) FOR ELECTROLESS NICKEL PLATING

Ramprasad V. and Dinesh K.P.

Plating Facility, Rare Materials Project, BARC, Mysore

Shri V. Ramprasad and his team received the DAE Group Achievement Award for the year 2011

Abstract

Nickel plating plant at RMP, Mysore, is a special facility to deposit corrosion resistant High Phosphorous Electroless Nickel (HPEN), a highly corrosion resistant coating, on carbon steel and Aluminium components deployed in corrosive fluoride environment. Plating line was designed to plate carbon steel components with the maximum dimension as 1500mm. Necessity arose to plate hollow cylinders of 2000 mm long, which are larger than the designed size of the tanks.

Conventional plating cycle consists of a series of tanks for surface activation and components move from one to another in a sequential manner. Space constraints did not permit to create a separate line for the new requirement. Instead, if chemicals are pumped one after the other into the same tank, number of tanks and footprint will be considerably reduced. This new line of thinking for a compact plating line has been evolved into Three Tank Plating Cycle (TTPC).

This paper presents the conceptualization, technical details, challenges and strategies adopted in developing TTPC to carry out electroless nickel plating on long components successfully.

Introduction

Plating of metals is generally carried out to improve or alter some of the engineering properties of the base material, like hardness, wear resistance, corrosion resistance, conductivity etc. In Electroplating, deposited metal gets reduced from its ionic state to metallic state with the help of electrical energy supplied externally. If the metal is reduced by a chemical reducing agent without using electricity, it is known as Electroless plating. Electroplated Nickel is pure nickel, whereas electroless nickel is a supersaturated alloy of Nickel and Phosphorous or Nickel plus Boron. High Phosphorous Electroless Nickel (HPEN) coating consists of 10-12% Phosphorous and exhibits superior corrosion resistance and higher degree of thickness uniformity than the electroplated nickel. At BARC, Mysore, a special facility to plate carbon steel and Aluminium components of

varying dimensions and geometry, exposed to severe corrosive fluoride environment, are coated with 50 microns of HPEN.

Quality of the surface coating depends on good surface preparation and Electroless Nickel is no exception to it. Proven Pretreatment cycle for Electroless Nickel deposit on Carbon Steel components consists of degreasing, soak cleaning, pickling, anodic activation with intermediate water rinse (single or double) prior to entering the plating bath, making a plating line to consist 12-14 tanks of identical height and width.

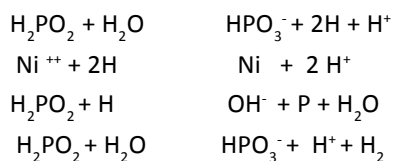
A new requirement has come up, to plate 2000 mm long hollow carbonsteel cylinders, to meet the growing needs of the Project. These components are longer than the existing tank size, and the requirement demands for setting up of a new plating line with larger foot print and

BARC NEWSLETTER

investment. But, limited floor area as well as inadequate head room became constraints to accommodate a new plating line and the new requirement became a challenge. It called for an out of the box thinking to plate these oversized components within the existing facility. This gave birth to a new concept of compact plating line with only 3 tanks instead of 12-14 tanks as in the conventional plating line.

Electroless Nickel

In Electroless plating, nickel gets deposited from an aqueous solution of Nickel salt using a chemical reducing agent without external electrical energy. Electroless Nickel deposit can contain 2-14% of Phosphorous. HPEN contains 10-12% Phosphorous and this gives the deposit metallic glass like structure with unique properties such as higher wear resistance, higher corrosion resistance, non magnetic nature etc. Specific advantage of Electroless Nickel over electroplated nickel is its higher degree of uniformity in thickness distribution. Agitation of plating bath and efficient filtration are to be ensured to achieve quality plating. Reaction mechanism of Ni-P coating on a catalytic surface is as given below:



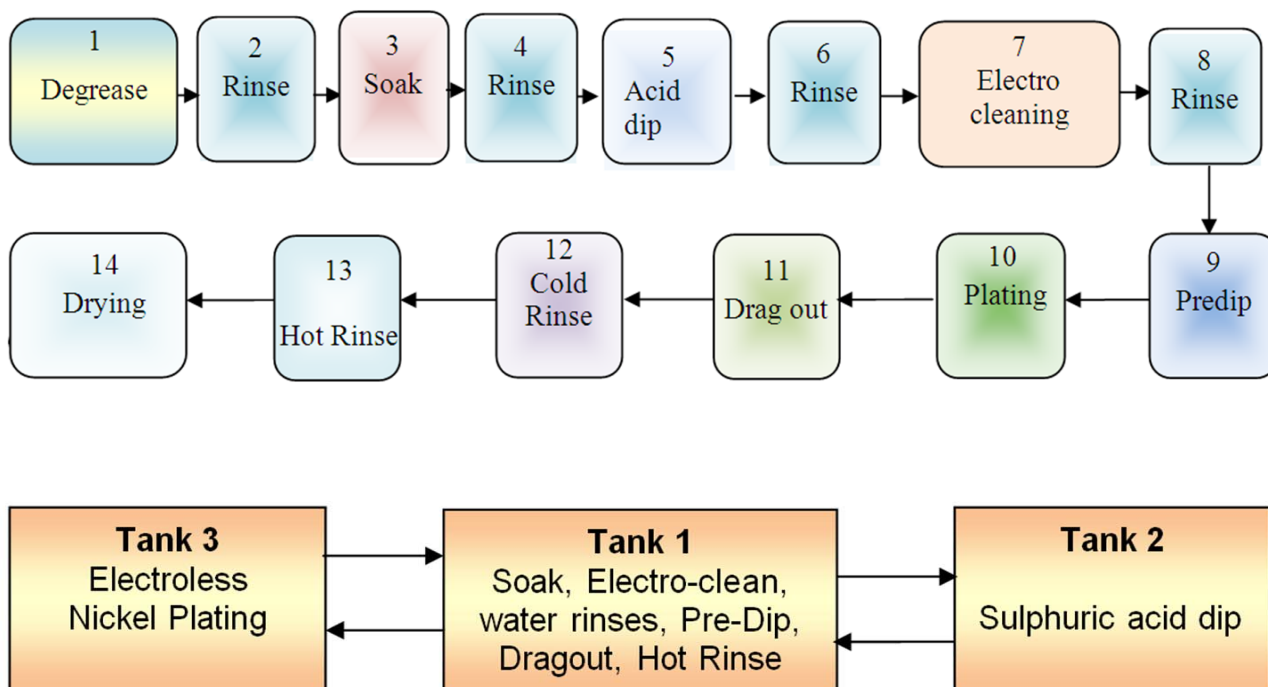
Surface Preparation

Adhesion, porosity, continuity, appearance, finish, coverage and corrosion resistance are the quality parameters for any Nickel coating and pretreatment / surface preparation plays an important role in ensuring the same. Removal of surface contamination to leave a clean, oxide-free surface prior to plating is essential for good quality of the deposit. Following is the generally practiced pretreatment cycle for Ferrous substrates :

Same number of operations are carried out in TTPC in 3 tanks by carrying out multiple operations in a single tank, as shown below.

Design and development of TTPC

In any conventional plating line, components are processed by moving from one tank to another with predecided immersion times. Thorough water rinsing



BARC NEWSLETTER

between any two treatments is essential to avoid cross contamination of chemicals and also to keep the surface free from foreign particles. Naturally it demands as many tanks as the number of steps involved in pretreatment cycle. To plate HPEN on carbon steel it needs 12-14 tanks of identical height and width. Contrary to the conventional practice, if components are made stationary and chemicals are pumped into the same tank, one after the other, then the requirement of number of tanks and their footprint can be considerably minimized.

With this new concept, initial trials were taken in an experimental set up with a single tank for all the operations. Though plating could be accomplished, a few practical problems like intermixing of chemicals, over exposure of active surface to atmosphere, complexity in discharge of chemicals to different destinations, long processing time etc. were experienced. To overcome them, entire operation was divided into three groups namely alkaline cleaning, acidic etching and nickel plating bath, and 3 tanks were installed accordingly.

To make the system efficient and user-friendly, the following engineering works were designed, executed, finetuned and adopted for regular production.

Process Tanks

To minimize the cross contamination of chemicals and total processing time, three tanks i.e. SS316L tank for HPEN plating, Polypropylene tank for activation with sulfuric acid and MS tank for soak, electro cleaning and rinses. Dimensions of these tanks are 2500 X 700 X 1000 mm, facilitating horizontal loading of cylinders. Both MS and SS tanks are fitted with heating/filtration/pumping systems. Vertical tanks were not considered due to limited headroom of the building. There was no space to accommodate 14 tanks of such dimensions in the existing plant, where as, three horizontal tanks could be accommodated with minor adjustments.

Pumping of Chemicals

Filling and draining time of chemicals has to be as minimum as possible to avoid exposure of activated

area to atmospheric oxygen. Accordingly, three high capacity centrifugal pumps along with necessary piping were installed to pump the chemicals from their respective storage tanks to TTPC and back. Sloped bottom, multiple drains and water jetting arrangements were made to flush out the last traces of chemical before the next chemical enters the same tank.

Preheating

Heating time of chemicals is more than their residence time. *In situ* heating of the solutions is a time consuming one and hence, chemicals are preheated in their respective storage tanks and hot solutions (60° - 85° C) are pumped to TTPC to minimize the processing time. Existing vertical tanks of nearby plating line are utilized as storage tanks for all the chemicals.

Loading pattern

Horizontal loading pattern was selected for long components due to space constraint. It has given an additional benefit of avoiding critical sealing area (N_6 face with no tolerance for rough deposit) in horizontal plane, thus ensuring smooth plating on critical surface. A SS304L fixture was designed and fabricated in-house to accommodate two tiers of cylinders with two numbers in each tier. For easy and uniform flow of plating solution filled inside the cylinders, and to ensure easy dislodging of Hydrogen bubbles from the plating surface, 5° inclination was given to all the components.

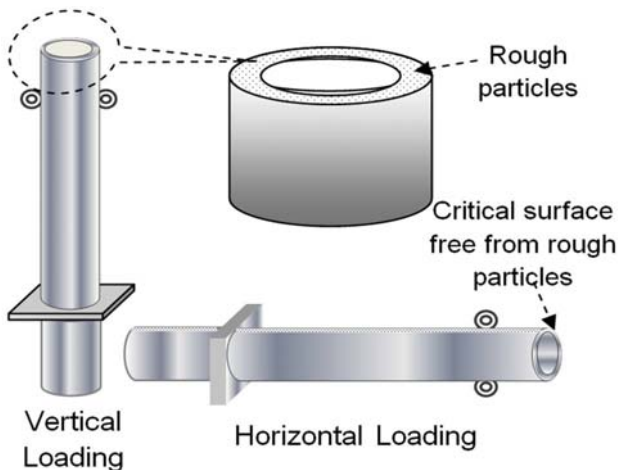
Material handling

Plating operation needs the components to be lifted from the ground level to a height of 3000 mm, longitudinal movement for processing over 3 tanks and again bringing back to zero level after the plating is over. This requirement is also different from conventional plating lines, where in, a loading stand and a Wagon are used in combination for this purpose. Here, both the operations i.e. lifting and longitudinal movements are to be combined in a single material handling Wagon trolley. The conceptual design for such a wagon with telescopic mast was designed totally in-house and executed by a vendor.

BARC NEWSLETTER

Automation

Frequent and precise operation of valves and pumps is important for this process and for this purpose, pneumatically actuated ball valves were installed and all the operations of valves / pumps were planned from a panel to avoid manual intervention and manpower requirement.



Air agitation

There is a likelihood of plating solution filled inside the hollow cylinder experiencing lesser agitation, leading to temperature and concentration gradients. To overcome this problem, an air sparger with apertures on 360° was designed, fabricated and inserted in all the four components to improve internal circulation of plating solution, which has helped a lot in attaining high degree of uniformity in thickness distribution.

Roller Jig

Rotation of components during plating helps in minimizing the un-plated spots at firm contact areas and also gas trapping areas on the internal surface. For this purpose, smooth rollers have been positioned to rotate the heavy components freely during plating thus avoiding jig marks / patch marks.

Operational Sequence:

- i. Make the horizontal jig of degreased components and position it in Tank no.1
- ii. Pump the preheated soak cleaner into Tank no.1
- iii. After 20 minutes, pump back the soak solution to its storage tank.
- iv. Fill the Tank 1 with rinse water.
- v. Transfer the components to Tank 2.
- vi. After 1 minute, transfer the components to Tank 1 for rinsing.
- vii. Drain the water and pump the preheated electro-cleaning solution to Tank 1 from its storage tank.
- viii. Anodic electrocleaning at 60°C for 5 min. with a current density of 1-2 A/dm²
- ix. Pump back electrocleaning solution to its storage tank, and fill Tank 1 with water.
- x. After rinsing, drain the rinse water and pump hot DM Water for Pre-dip.
- xi. Transfer the components to Tank 3, containing plating solution at 88° C.
- xii. Maintain the plating bath at optimum parameters to deposit 50 micron thickness.
- xiii. DM Water in Tank 1 will be heated to use it as dragout tank for postplating cleaning.

Major Benefits

- It has occupied minimum floor space and could be accommodated within the existing plant, thus saving considerable time and investment of creating a new facility.
- Rejection rate of plated components is bare minimum due to horizontal loading.
- Processing of a single jig is enough instead of processing multiple jigs.

BARC NEWSLETTER

- Higher and constant Operating ratio (Area/Volume) can be maintained throughout the plating time.
- For future needs, this concept can be upgraded for still longer components.

Conclusion

This in-house developed set-up has been under continuous usage and till now plating on a few hundreds of long components has been accomplished successfully. This developmental work has immensely helped in plating the 2000 mm long components and

played an important role in achieving the overall targets of the Project.

Acknowledgements

Authors wish to profusely thank Shri T K Bera, Project Director, RMP, Shri M R Srikanthan, Project Manager (Mechanical), Shri F M Patil, Former Head, USF and staff of Electrical, Instrumentation and Workshop for their sincere involvement, guidance and enthusiastic cooperation in transforming a new concept into a successful reality.

1 KILO JOULE COMPACT MARX SOURCE AND REFLEX TRIODE BASED REPETITIVE HIGH POWER MICROWAVE GENERATOR

Archana Sharma, A. Roy, S. Mitra, S.K. Singh, V.K. Sharma, A.S. Patel, Rakhee Menon, K. Senthil, Ritu Agarwal, K.C. Mittal, K.V. Nagesh, D.P. Chakravarthy and A.K. Ray
Accelerator and Pulse Power Division, Beam Technology Development Group

Shri D.P. Chakravarthy and his team received the DAE Group Achievement Award for the year 2011

Abstract

A research effort to develop an efficient and compact High Power Microwave (HPM) source system based on a Marx-generator-driven reflex triode is taken up at BARC. A 1-kJ 300-kV 300-ns FWHM, 10 HZ repetition rate Marx generator and a reflex triode have been developed at the Bhabha Atomic Research Centre (BARC), Mumbai, India, for the generation of high-intensity high-power electron beams and HPMs and their applications.

System description

Bipolar charging of a Marx generator scheme has been adopted to get a faster rise time and relatively low charging voltage. The faster rise time is due to the reduced number of spark gaps down to six for 12 in-series capacitors ($0.15 \mu\text{F}$ and 50 kV) of a six-stage bipolar-charging Marx generator (Fig.1). Interstage inductive charging further enhances the efficiency of the overall system as compared to resistive charging. The complete assembly of the Marx generator is tested first with the resistive load that characterizes the Marx generator operation at the critically matched condition (25Ω matched impedance).

Reflex Triode

A vacuum diode is used to generate Intense Relativistic Electron Beams (IREB) by an explosive electron emission

process in the Reflex Triode (RT) geometry. The RT is basically a space charge device of the vircator category that operates by emitting an electron beam from a cathode and accelerating it through a semitransparent anode. The formation of the space charge and subsequent electron reflexing causes electromagnetic radiation in the HPM regime (few GHz). The RT is housed inside a vacuum chamber having six ports. Fig. 2 shows a front view of the reflex triode assembly with the vacuum pumping system. The Marx generator assembly is fitted to the left-hand-side port of the vacuum diode. The other two ports are used for adjustable cathode holder, voltage, and current diagnostics, and one is for radiating the HPM as an open-ended waveguide. The anode is a 170-mm-diameter SS mesh with 70% transparency connected to the high-voltage terminal.

HPM Generation

In the RT geometry, IREB and HPM were generated for various anode-cathode (AK) gaps. The typical electron-beam parameters were 200 kV, 4 kA, and 300 ns, with a current density of a few hundreds of amperes per square

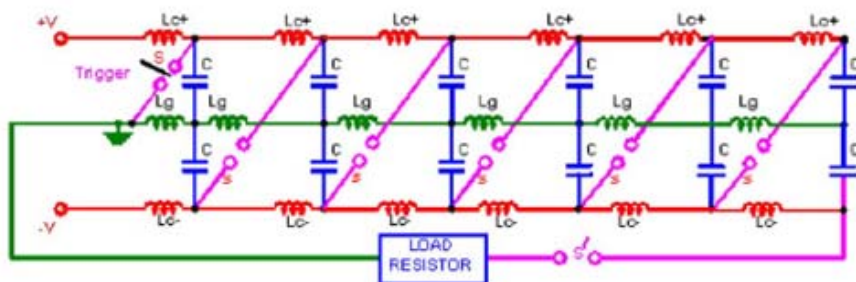


Fig. 1: Circuit diagram of the bipolar- and inductive-charging Marx generator

BARC NEWSLETTER

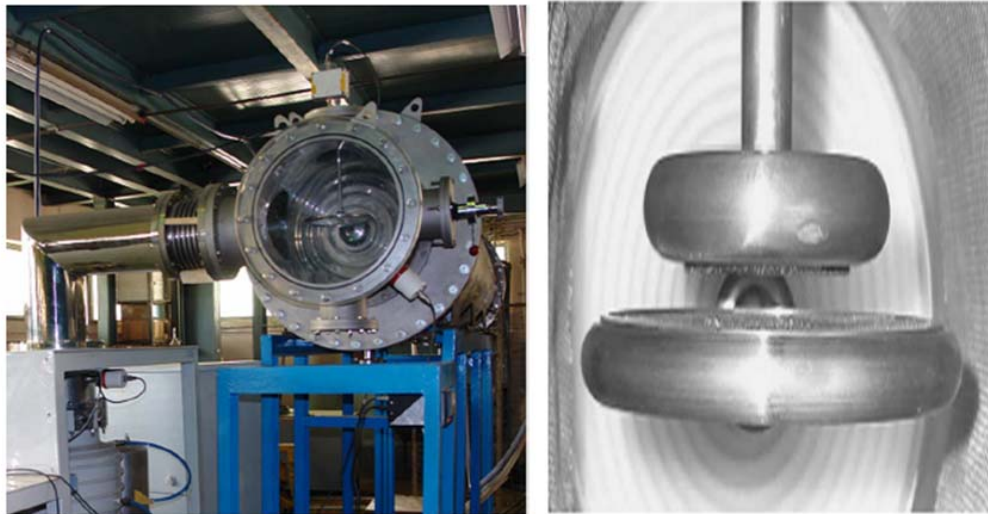


Fig. 2. Front view of the reflex triode assembly with the vacuum pumping system

centimeter. The HPM signal was captured by the double-ridged horn antenna and a B-dot probe placed at far field and sent to a high-speed digital storage oscilloscope (with a sampling rate of 20 GS/s) kept in the shielded room through a coaxial RF cable. Fig.3 shows the beam voltage, current and HPM and its FFT waveforms.

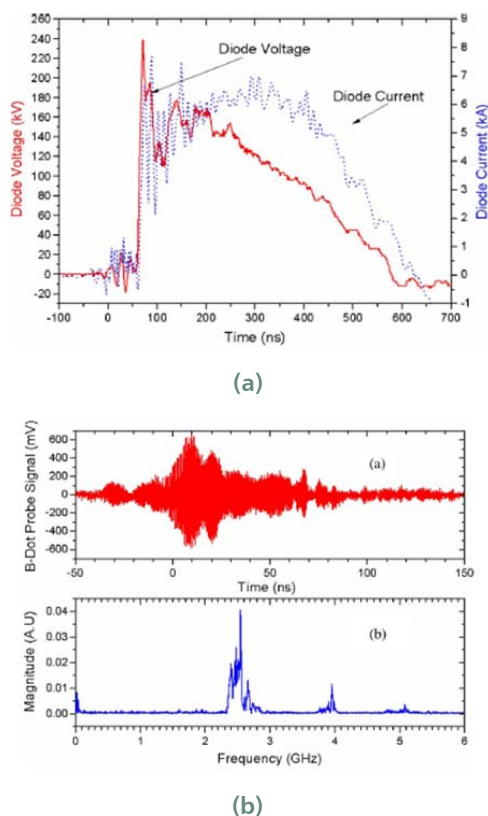


Fig. 3: (a) Electron-beam diode voltage and current waveforms for 15-mm- AK-gap (b) B-dot signal and its FFT

The most fundamental issues in virtual cathode oscillator (vircator)-based high-power microwave devices are efficiency improvement and oscillation frequency control. The time-dependent behavior of the RT vircator oscillation frequency has been studied for various AK-gap distances. It was found that the measured HPM power and the E -field are highest for a 15-mm AK-gap distance (Fig.4). It was found that the oscillation frequency increases with time for all the AK-gap distances studied. The RT vircator emits several frequency components, and maximum power is emitted when all the power goes into a single frequency.

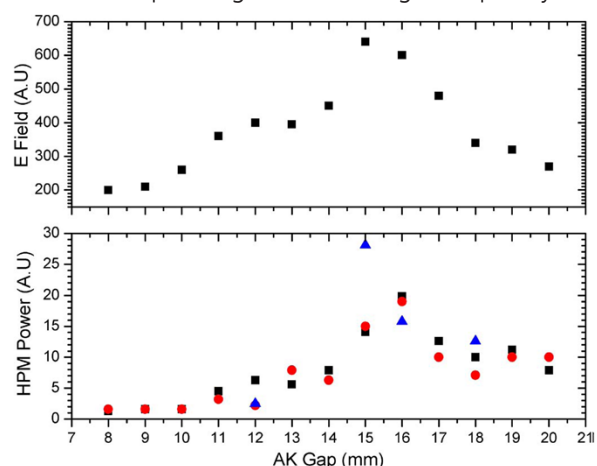


Fig. 4: Variation of the microwave peak power and the E -field with the AK-gap distance

Cathode Materials

The effect of the cathode materials on radiated HPM field and frequency were studied for graphite, stainless

BARC NEWSLETTER

steel nails, and Carbon Fiber (CF) needle type cathodes. The electrode plasma expansion velocity has been estimated from the perveance data and is least for CF cathode. The graphite cathode exhibited maximum radiated HPM field and pulse duration. The RT vircator emits a single frequency for SS nail and CF cathode when subject to a shorter voltage pulse duration.

Maximum E field

The HPM electric fields measured using the B-dot probe at 4.5 m distance from the reflex triode window was maximum for 15mm AK gap and is 14 kV/m at 35 kV charging. The free space radiation pattern was plotted by varying the position of the B-Dot probe radially in the far field region, at a distance of 4.5 m from the reflex triode window. The gain (G_T) of the open ended

wave guide of the reflex triode was estimated from the radiation pattern and is 4.35 dB for 2.4 GHz dominant frequency.

Conclusion

A reflex triode based HPM source with REB diode pulse of 200kV,4kA, 200ns is optimised for its anode cathode gap, cathode material and its dimensions to generate an electric field of 14kV/m at a distance of 4.5m is developed.

Acknowledgement

Authors are grateful to Dr.L.M.Gantayet, Director, BTDG for his continuous support , valuable suggestions and encouragement in development of this technology.

BARC NEWSLETTER

DEVELOPMENT & SUCCESSFUL DEPLOYMENT OF WELD INSPECTION MANIPULATOR (WIM) IN REACTOR PRESSURE VESSEL OF TAPS-1

H. Chatterjee, J.P. Singh, R. Ranjon, M.P. Kulkarni and R.J. Patel
Refuelling Technology Division

Shri R.J. Patel and his team received the DAE Group Achievement Award
for the year 2011

Abstract

The Reactor Pressure Vessel (RPV) of TAPS-1 contains six longitudinal and four circumferential welds. Periodical in-service inspection of these weld joints has been a regulatory issue pending for long. During the 22nd refuelling outage in July 2012 the inspection of L1-1, L1-2 longitudinal welds as well as their junctions with C1 circumferential weld was proposed to be done using ultrasonic technique. Approaching these welds from outer side of the RPV is a difficult and tedious task. Therefore it was decided to examine these welds from inner side of the RPV by filling the cavity with water and approaching the RPV from top. No technology was available to take the probes at a depth of 10-12 m under water. Based on NPCIL requirement, development of weld inspection manipulator was taken up as a challenge. The design was completed in just one month including concept finalization. The manipulator was fabricated on a war footing basis, tested and successfully deployed in the reactor for the first time in TAPS history. The entire activity was completed in three months time. This has helped the department to fulfill its commitment toward health assessment of RPV by direct monitoring of hitherto inaccessible areas and has paved the way for many other similar applications.

Introduction

The Reactor Pressure Vessel (RPV) of TAPS-1 is 3916 mm in outer diameter and 124 mm thick made of SA 302 grade B low alloy steel. It is internally clad with 5.6 mm thick SS 308L austenitic stainless steel weld deposits. There are six longitudinal and four circumferential welds in the RPV as shown in fig. 1. The vessel welds are to be inspected periodically as a part of regulatory requirement. These welds cannot be approached for inspection from outer side of the vessel due to the presence of thermal shield. However during planned shut-down of the reactor L1-1, L1-2 welds and their junctions with C1 weld become accessible for inspection from inner side of the vessel after removal of drier and separator assembly from the RPV top shell.

Weld Inspection Manipulator has been developed to assess the integrity of L1-1 and L1-2 weld joints as well as their junctions with C1. The manipulator clings on to the RPV wall using permanent magnets and can be lowered or raised along the weld on the vessel using refuelling grapple. The motorized weld cleaning brush attached to the manipulator can be traversed laterally using cross travel at any location of the weld to clean the deposited materials on the clad covering the Heat Affected Zone (HAZ). By operating sequentially the grapple for vertical motion and cross travel for transverse motion, the clad covering weld and its HAZ can be cleaned. Subsequently the weld cleaning brush is replaced by a probe holder to scan the entire weld and its HAZ.

BARC NEWSLETTER

Brief Overview of Design

The weld inspection manipulator performs four important functions namely:

- i. Clinging on to RPV wall, while supported on wheels, by magnetic force; attaching to or detaching from RPV wall and moving on the RPV wall along a longitudinal weld

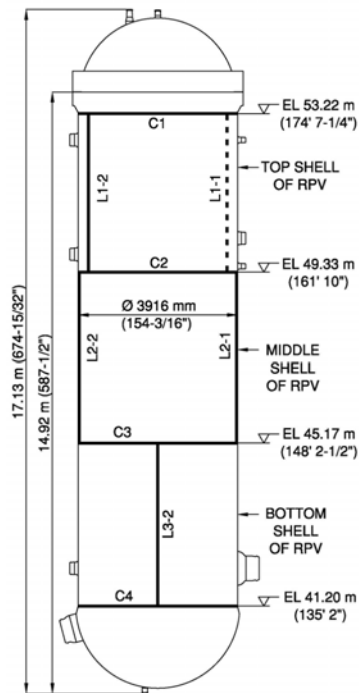


Fig. 1: Schematic of reactor pressure vessel of TAPS 1

- ii. Transverse motion of probe holder or weld cleaning brush across the HAZ
- iii. Weld cleaning
- iv. UT scanning of welds.

To perform these functions WIM has the following major subassemblies:

Main Body

Main Body consists of a triangular platform about which all other components of WIM are configured (fig. 2). The bail is similar to the bail of TAPS fuel assembly to make it compatible with refuelling grappler. WIM is parked on a stand in the fuel storage pool of the reactor building using gantry. From there it is picked up by the grappler and shifted to the RPV. Wheels are mounted on the platform to facilitate longitudinal travel.

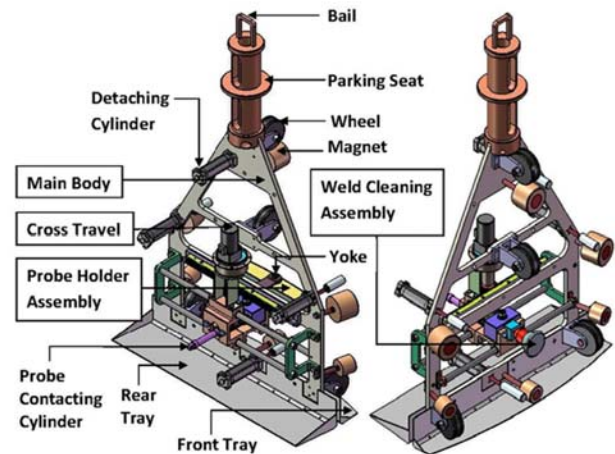


Fig. 2: CAD Model of Weld Inspection Manipulator

Permanent magnets are mounted on the platform for clinging WIM to the RPV wall. Four pneumatic cylinders are used to detach WIM from RPV as and when required.

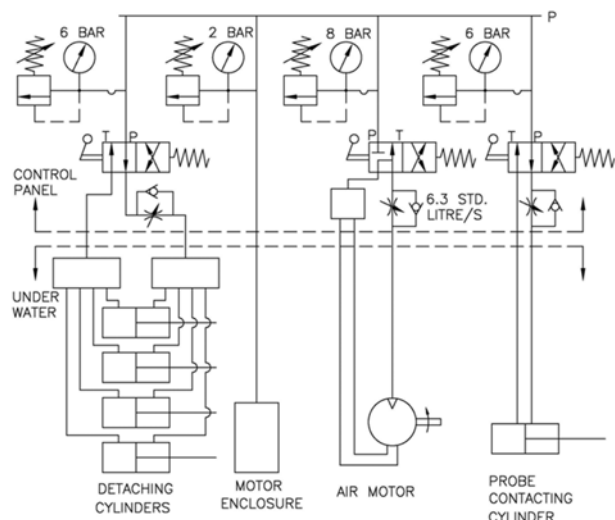


Fig. 3: Pneumatic Scheme for WIM operation

The scheme for operating pneumatic cylinders for WIM operation is shown in fig. 3.

Cross Travel

Cross Travel consists of a cross travel guide block with bush to move horizontally on three guide rods (fig. 4). A rack is attached to the WIM platform. The cross travel guide block carries an enclosure containing a brushless DC motor with gear head and a rotary potentiometer. The enclosure is kept pneumatically pressurized to avoid water-ingress (fig.3). The DC motor drives a pinion

BARC NEWSLETTER

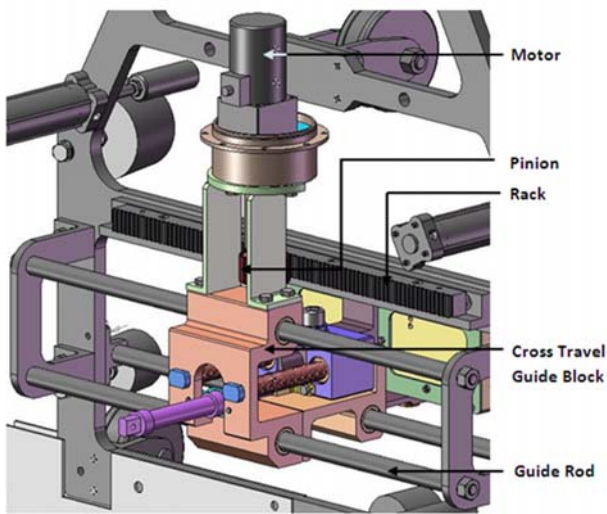


Fig. 4: Cross Travel Assembly

which engages with rack and causes transverse motion of the cross travel guide block. The position of the cross travel is sensed by potentiometer. The velocity of the cross travel is regulated by PC based control scheme (fig. 5).

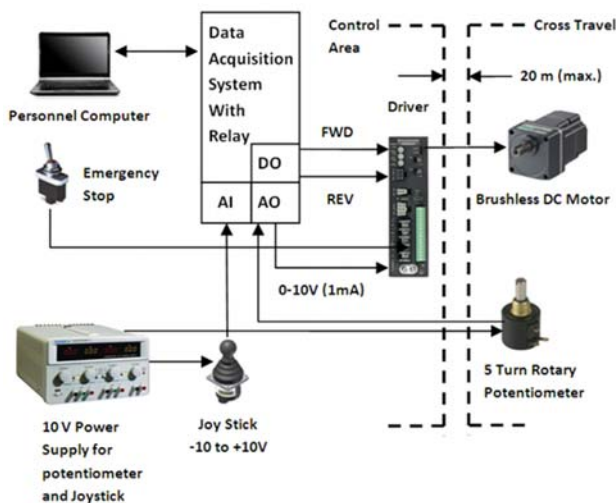


Fig. 5: Schematic of Cross Travel Control Scheme

Operator interface software programme facilitates operation in various modes selectable by operator. A backup hard-wired control scheme is also provided for redundancy.

Weld Cleaning Assembly

Weld Cleaning Assembly consists of an air motor and a cleaning brush with Nylon bristles which are fitted on to the WIM main body (fig. 6). The pneumatic cylinder

presses the brush against the clad above the weld joint area to be cleaned and the air motor rotates the brush for cleaning. In this condition the refuelling grapppler moves up and down sequentially with a cross feed to clean the entire area of clad covering the HAZ. The pneumatic scheme for probe contacting cylinder and air motor is shown in fig. 3.

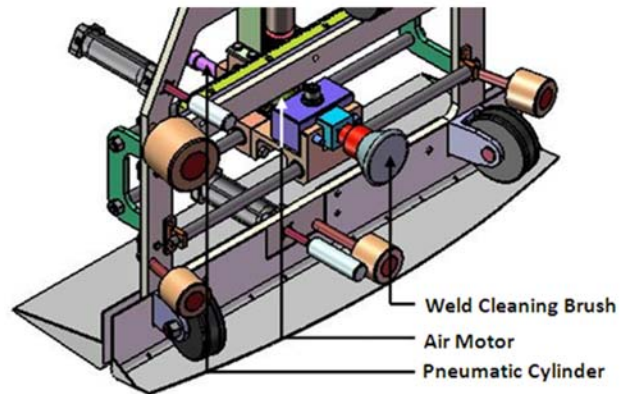


Fig. 6: Weld Cleaning Assembly

Probe Holder Assembly

Probe Holder Assembly consists of eight different types of spring loaded UT probes fitted to a nylon body pivoted centrally about a yoke. A pneumatic cylinder presses the probe holder assembly to create contact of probes with RPV while it is moved up and down sequentially with a cross feed and the UT machine collects weld-scan data. Probe holder assembly is of two types which are identical in shape and used one at a time. Horizontal probe holder is provided for detecting vertical weld defects (fig. 7). Vertical probe holder is provided for detecting horizontal weld defects.

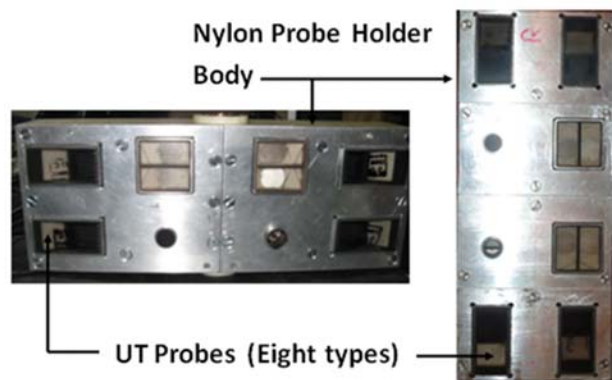


Fig. 7: Horizontal Probe Holder Assembly (left); Vertical Probe Holder Assembly (right)

BARC NEWSLETTER

Manufacturing and Qualification for Reactor Use

A test set-up was fabricated for functional testing of WIM (fig. 8). Standard notches were machined at several locations of the test set-up for demonstrating the notch sensing capability of WIM using UT probes. Performance testing of WIM was carried out at supplier's premises. All functional aspects were successfully demonstrated. WIM was shifted to the Additional Away From Reactor fuel storage pool of TAPS 1&2 for qualification trials. The capability of WIM for weld inspection was demonstrated in the pool by conducting under-water trials (fig. 9). Training was given to the operating personnel.



Fig. 8: WIM with test setup

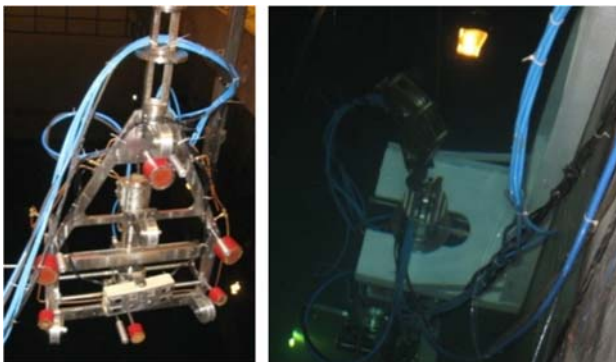


Fig. 9: WIM lowered to AAFR Pool (left), WIM parked on GOM Stand (Right)

Deployment in the Reactor

WIM was successfully deployed in TAPS-1 in August 2012. Welds L1-1, L1-2 and their HAZ were cleaned by weld cleaning brush. Subsequently UT scanning of these welds and their junction with C1 were successfully carried out (fig. 10).



Fig. 10 WIM Performing Weld Inspection

Conclusion

Weld inspection of reactor pressure vessel of TAPS 1&2 was a long pending regulatory requirement. A unique weld inspection manipulator was developed in a short span of three months to enable underwater inspection of longitudinal welds of the upper shell of RPV. The manipulator was successfully deployed for inspection of L1-1, L1-2 welds and their junction with C1 weld in the 22nd refuelling outage of TAPS-1. This development is the first of its kind inspection for BWR. This has helped the department to fulfill its commitment toward health assessment of RPV by direct monitoring of hitherto inaccessible areas and has paved the way for many other similar applications.

PROCESS FOR RETAINING PERICARP COLOR AND EXTENDING SHELF LIFE OF LITCHI

S. Gautam, B.B. Mishra, S.N. Hajare, S. Kumar, S. Saxena, V.S. More,
S. Wadhawan, N. Bandyopadhyay and A. Sharma
Food Technology Division

Dr. S. Gautam and his team received the DAE Group Achievement
Award for the year 2011

Abstract

Litchi is a highly juicy and nutritious fruit. However, it has very short life (2-3 days) at ambient temperature, mainly due to microbial and physiological spoilage. The fruit loses its appeal because of pericarp browning due to anthocyanin degradation and enzymatic oxidation of phenolics. A sequential dip treatment using GRAS (Generally Recognized As Safe) chemicals has been developed which reduced polyphenol oxidase activity by 85%, retained major anthocyanins, cyanidin-3-O-rutinoside and cyanidin-3-O-glucoside by 82 and 97%, respectively, and reduced microbial load to below detectable levels. This resulted in retention of attractive pericarp colour, and shelf-life extension of litchi up to 45-60 days at low temperature storage. To overcome quarantine barrier for export the treated fruits were gamma irradiated at 400 Gy. Processing helped in reducing the spoilage of plucked fruits, maintaining their overall quality attributes, and market access in non-producing regions. The technology has been successfully demonstrated to farmers, transferred to entrepreneurs for its commercialization, and also a patent has been filed (Application No. 2484/MUM/2012 dated 27 August, 2012).

Introduction

Litchi (*Litchi chinensis*, Sapindaceae) is a tropical, non-climacteric, highly juicy and nutritious fruit, which is eaten fresh or used to prepare juice, vinegar, jelly, wine, ice creams and sorbets. The freshly harvested fruit has pinkish-red pericarp, surrounding a white and translucent fleshy aril, having a sweet and unique pleasant flavour. The litchi fruit is highly perishable in nature due to microbial and physiological spoilage, and lasts only for 2–3 days at ambient temperature ($26\pm 2^\circ\text{C}$). Once harvested, the pericarp browning also occurs within 48 h which significantly affects the eye appeal resulting in reduced commercial value of the fruit. Oxidation of pericarp phenolics to quinones and their polymerisation to brown pigments, coupled with accelerated degradation of anthocyanins, have been reported to cause browning of litchi (Jiang et al., 2004). Enzymes such as phenylalanine ammonia lyase (PAL), polyphenol oxidase (PPO), and peroxidase (POD) have been reported to contribute to this browning process,

by regulating the biosynthesis of phenolics and their oxidation (Jiang et al., 2004; Mishra et al., 2011). In the current study, an attempt has been made to explore the possibility of using food grade GRAS chemicals in combination with low temperature storage ($4\pm 2^\circ\text{C}$), to restrict the postharvest pericarp browning and microbial growth in litchi and thus, maintain its eye appeal, and extend shelf life. The quality parameters such as physical, biochemical, microbiological and organoleptic, as well as health protective activities such as antioxidant, and radioprotective capacity were also periodically evaluated during storage.

Materials and methods

Processing of litchi fruit

Fruits of Indian litchi cultivars 'Shahi' and 'China' were procured from a local market within 6–8 h of harvest. Screening was performed to eliminate damaged fruits having any visual blemish. Later, the litchi fruits were

BARC NEWSLETTER

subjected to GRAS chemical dip treatment at various concentrations in different permutations and combinations to select the best treatment conditions, concentration and timing of treatment for significant inhibition of pericarp browning. Furthermore, the fruits were air dried and packed (10 fruits per packet) in low-density polyethylene bags. As a quarantine treatment, packaged samples were irradiated at 400 Gy dose of gamma radiation and stored at $4\pm 2^{\circ}\text{C}$. Controls and treated fruits were analysed for quality parameters during storage.

Preparation of pericarp powder for analysis of browning related parameters

Periodically, pericarp of the fruit was cut into pieces, lyophilized and mechanically ground to fine powder, which was further used for analysing the browning index and related parameters.

Analysis of browning index (BI) and browning parameters

The BI of litchi fruit pericarp was determined by extracting the pigments in ethanol (67%) and measuring the absorbance at 420 nm using a spectrophotometer. Activities of browning associated enzymes, such as polyphenol oxidase (PPO), peroxidase (POD) and phenylalanine ammonia lyase (PAL), as well as, total soluble phenolics from litchi fruit pericarp were determined by methods discussed earlier (Mishra et al., 2011; Sun et al., 2009). Total anthocyanin content was determined and major anthocyanins were characterised. PPO activity measurement was based on oxidation of 4-methyl catechol, whereas, POD activity on oxidation of guaiacol to tetraguaiacol and PAL activity on deamination of L-phenylalanine to trans-cinnamic acid. These activities were measured spectrophotometrically at 410, 470, and 290 nm, respectively. One unit of enzymatic activity was defined as the amount of enzyme which catalysed a change of 0.001 in absorbance per min and expressed as U/g of fresh pericarp weight. The total phenolic content was expressed in mg GAE (gallic acid equivalent)/g of fresh pericarp weight. Anthocyanin content was calculated in terms of cyanidin-3-glucoside (cyn-3-glu) equivalents

and expressed as mg cyn-3-glu/g of fresh pericarp weight.

Physical and biochemical analyses

Pulp were ground in a mixer-grinder and centrifuged (6000 g for 30 min at 4°C). The clear juice was used to determine the quality attributes. Effect of treatment on the physical properties was performed as described earlier (Hajare et al., 2010). In brief, pH of litchi juice was measured using a pH meter. Percentage titratable acidity (TA) was determined by titrating with 0.1 N NaOH and calibrating with citric acid. Moisture was determined by drying the samples at $100 \pm 2^{\circ}\text{C}$ in a hot air oven and quantifying the percentage weight loss. Total soluble solid (TSS) was measured using a hand-held refractometer. Texture was analysed using TA-HD Plus Texture Analyser. Similarly, effect of treatment on biochemical and antioxidant properties of litchi fruit juice was also analysed, as per the method described earlier (Hajare et al., 2010; Saxena et al., 2011). In brief, the reducing sugar was determined using 3,5-dinitrosalicylic acid (DNSA) reagent. The total sugars (mainly consisting of sucrose, fructose, and glucose) were determined after complete inversion of sucrose into reducing sugar by acid treatment. The total phenolic content was determined by the Folin-Ciocalteu method. The total flavonoid content was measured by the aluminium chloride spectrophotometric assay. Total vitamin C content was measured by microfluorometric method. Antioxidant property was analysed by measuring DPPH radical scavenging activity and ferric reducing antioxidant power (FRAP), whereas, radioprotective potential was evaluated based on the protection of plasmid DNA from gamma radiation mediated oxidative damage.

Microbiological analysis

The total bacterial count and yeast and mould count of unpeeled fruit were determined as described earlier (Hajare et al., 2010). To show the efficacy of the treatment for inhibiting microbial growth, fruits were spiked with 10^3 – 10^4 cfu/ml of *Escherichia coli*, *Saccharomyces cerevisiae* and spores of *Aspergillus niger*, separately. Later, the fruits were dried at ambient

BARC NEWSLETTER

temperature, subjected to chemical dip treatment and periodically analysed for residual microbial load in spiked samples during storage.

Sensory analysis

Sensory evaluation of litchi fruits was performed by an expert panel of 15 trained and experienced panelists on a 7-point hedonic scale (7-excellent, 6-very good, 5-good, 4-satisfactory, 3-fair, 2-poor, 1-very poor). Fungal growth on fruits was considered as indicator of spoilage and hence, no further sensory evaluation was carried out with such spoiled samples.

Results and discussion

Pericarp browning

The appeal of litchi fruit is severely affected by pericarp browning, which happens due to phenolic oxidation and concomitant anthocyanin degradation, resulting in brown discolouration of the pericarp (Gautam et al., 2010; Jiang et al., 2004, Kumar et al., 2012). Enzymes like polyphenol oxidase (PPO), peroxidase (POD) and phenylalanine ammonia lyase (PAL) were found to play a role in the browning process of fruits (Mishra et al., 2011; Sun et al., 2009). PPO and POD are involved in oxidation of phenolics to quinones, which polymerise to brown pigments, whereas, PAL is involved in the phenylpropanoid pathway and plays

a key role in the biosynthesis of phenolics (Jiang et al., 2004). Anthocyanins, which are responsible for the attractive red colour of pericarp, undergo accelerated degradation during storage (Jiang et al., 2004). Dip processing was found to be quite effective in controlling these browning related enzyme activities. It inhibited the oxidation of phenolics and maintained the red pigmented anthocyanin, and thus reduced the overall browning (BI) (Table 1, Fig. 1). In processed samples polyphenol oxidase activity was found to be reduced by 85%, whereas, major anthocyanins, cyanidin-3-O-rutinoside and cyanidin-3-O-glucoside were retained upto 82 and 97%, respectively (Fig. 2).

Microbiological analysis

One of the major factors contributing to litchi fruit spoilage is microbial growth (Hajare et al., 2010). Total bacterial count (TBC), yeast and mould count (YMC) were found to be ~4 and ~2.5 log cfu/ml, respectively, in the unpeeled and unprocessed litchi cultivars, whereas, TBC or YMC was found to be nil (below



Fig. 1: Retention of pericarp colour and extension of shelf life of litchi by combination dip treatment: (A) control fruits stored at 4°C for 15 days; (B) dip processed fruits stored at 4 °C for 45 days.

Table 1: Effect of processing on the browning associated parameters of litchi pericarp.

Days of storage	Control		Dip processed			
	0 d	15 d	0 d	15 d	30 d	45 d
BI (A_{420})	0.79±0.05	1.0±0.04	0.79±0.02	0.88±0.04	0.91±0.01	0.94±0.05
PPO (U/g)	832±68	988±67	128±10	118±6	115±10	81±7
POD (U/g)	3899±151	3699±150	3258±235	3033±297	2066±211	1758±180
PAL (U/g)	3455±404	2383±259	3218±215	3111±227	2590±172	2331±176
Total soluble phenolics (mg GAE/g)	4.2±0.2	6.1±0.3	28±1	25±2	27±1	27±2
Total anthocyanins (mg cyn-3-glu/g)	0.21±0.06	0.03±0.01	0.26±0.04	0.31±0.05	0.29±0.05	0.30±0.04

BARC NEWSLETTER

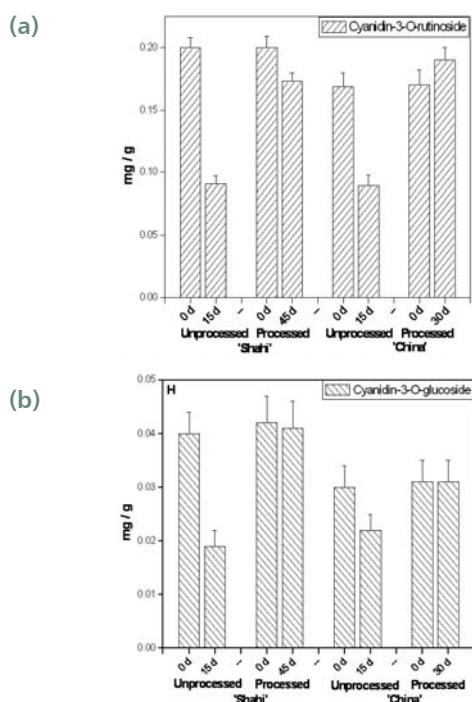


Fig. 2: Retention of major anthocyanins in the pericarp of processed litchi fruits compared to unprocessed control.

detectable level) in the processed samples during storage. Even in artificially spiked litchi fruits with bacteria (*E. coli*), yeast (*S. cerevisiae*) or mould (*A. niger*) in separate set of experiments, treatment lead to complete elimination of these microbes and no microbial load was detected in these samples during storage.

Analysis of physical, biochemical, and sensory properties

Dip processing did not affect the quality parameters of litchi such as moisture content (%), pH, titratable acidity (%), total soluble solid (TSS), sugars, phenolics and flavonoids (Table 2 and 3). Antioxidant and radioprotective properties were also not affected. The observed decrease in texture by dip processing was not reflected during sensory evaluation by taste panelists. A marginal decrease in vitamin C content was noticed during storage, however, processing was not found to have any adverse effect on vitamin C content as earlier reports have also indicated the postharvest decrease in ascorbic acid level in litchi fruits regardless of storage conditions (Holcroft & Mitcham, 1996). The processed litchi samples remained organoleptically acceptable till 45-60 days.

Conclusion

A combination treatment involving dip processing, packaging and low temperature (4°C) storage was found to be effective in almost completely eliminating the microbial load, leading to extension in shelf life of litchi up to 45-60 days, whereas, unprocessed samples

Table 2: Effect of processing on the physical attributes of litchi fruit.

Days of storage	Control		Dip processed			
	0 d	15 d	0 d	15 d	30 d	45 d
Moisture (%)	75±4	72±2	75±2	74±3	72±1	71±3
pH	4.3±0.4	4.3±0.1	4.4±0.2	4.6±0.8	4.5±0.4	4.8±0.1
Titratable acidity (%)	0.31±0.02	0.29±0.03	0.33±0.01	0.35±0.03	0.25±0.01	0.20±0.02
Total soluble solid (° Bx)	15±2	17±3	16±2	18±1	17±1	16±2
Texture (g)	108±16	90±15	73±16	81±15	74±17	65±17

Table 3: Effect of processing on the biochemical and antioxidant properties of litchi fruit.

Days of storage	Control		Dip processed			
	0 d	15 d	0 d	15 d	30 d	45 d
Total sugars (g%)	10±1	11±0.4	10±0.4	10±0.2	10±0.3	10±0.5
Reducing sugars (g%)	9±1	9±1	9±0.4	9±0.2	9.3±0.3	9±0.4
Vitamin C (mg%)	20±1	17±1	21±1	20±1	16±1	14±2
Total soluble phenolics (mg GAE/g)	0.31±0.003	0.32±0.007	0.31±0.009	0.33±0.004	0.33±0.003	0.34±0.005
Flavonoids (mg CE/g)	0.031±0.003	0.032±0.007	0.034±0.004	0.034±0.005	0.028±0.004	0.025±0.006
DPPH scavenging (%)	89±2	93±3	91±2	91±3	90±2	90±3
FRAP (A ₇₀₀)	0.22±0.03	0.26±0.03	0.22±0.04	0.20±0.05	0.26±0.04	0.24±0.04

BARC NEWSLETTER

Table 4. Effect of processing on the sensory attributes of litchi fruit.

Days of storage	Control		Dip processed			
	0 d	15 d	0 d	15 d	30 d	45 d
Appearance	4.7±1.1	4.6±1.2	6.2±1.3	5.8±0.8	6.4±0.9	5.4±1.5
Colour	4.6±1.0	4.3±1.3	5.9±1.2	5.4±1.0	6.4±1.2	5.0±1.5
Odour	4.7±1.4	4.5±1.2	5.1±1.1	5.6±1.2	6.3±0.5	5.0±1.5
Flavour	4.7±1.0	4.6±1.6	5.4±1.3	4.8±1.2	6.0±1.1	5.0±0.8
After taste	5.3±1.0	5.3±0.5	5.2±1.7	4.4±1.7	5.6±1.2	4.8±1.5
Texture	5.4±1.2	5.2±1.3	5.8±0.9	5.7±0.9	6.3±0.7	5.4±0.8
Juiciness	5.5±1.0	5.0±1.3	5.8±0.8	5.9±0.9	6.1±0.6	5.4±0.9
Overall acceptability	5.0±1.0	4.7±1.4	5.7±1.3	5.0±1.4	6.0±1.0	5.2±0.5

spoiled within 15 days of storage at 4°C. The processing drastically reduced the activity of polyphenol oxidase resulting in inhibition of fruit pericarp browning, and allowing significant retention of anthocyanins and hence the attractive reddish colour of the fruit. The processing did not adversely affect any quality attributes of litchi fruits. Thus the current finding can help in expanding the market access for the fruit in non-producing regions. The technology has been well received by the entrepreneurs under DAE-societal initiative including AKRUTI-program.

Acknowledgement

Authors thank Dr. S. P. Kale, Head, TT&CD; and colleagues Shri B. K. Pathak, Smt. S. S. Mule, Dr. Nutan V. Khalap, and Shri G. R. Ursal for their help during transfer and promotion of this technology, as well as technical staffs of Food Science & Safety Section, FTD, Smt. V. Gaonkar, Smt. Nisha Bhadrige, and Shri A. K. Chaubey and also Ex-BARC employee Shri M. N. Parte for their help during course of this study.

References

- Gautam S., Saxena S., Kumar S., Hajare S. N., Wadhawan S., Mishra B. B., More V., & Sharma A. (2010). Shelf life extension of Litchi (*Litchi chinensis*) and overcoming quarantine barriers to international trade using radiation technology. *BARC Newsletter*, 317, 29-34.
- Hajare, S N., Saxena S, Kumar S, Wadhawan S, More V, Mishra B B, Parte M N, Gautam S, & Sharma A. (2010). Quality profile of litchi (*Litchi chinensis*) cultivars from India and effect of radiation processing. *Rad. Phy. & Chem.*, 79, 994–1004.
- Holcroft, D. M., & Mitcham, E. J. (1996). Postharvest physiology and handling of litchi (*Litchi chinensis* Sonn.). *Postharvest Biol. and Tech.*, 9, 265–281.
- Jiang, Y., Duan, X., Joyce, D., Zhang, Z., & Li, J. (2004). Advances in understanding of enzymatic browning in harvested litchi fruit. *Food Chem.*, 88, 443–446.
- Kumar S., Mishra B.B., Saxena S., Bandyopadhyay N., More V., Wadhawan S., Hajare S. N., Gautam S., & Sharma A. (2012). Inhibition of pericarp browning and shelf life extension of litchi by combination dip treatment and radiation processing. *Food Chem.*, 131, 1223-1232.
- Mishra B. B., Kumar S., Wadhawan S., Hajare S. N., Saxena S., More V., Gautam S., & Sharma A. (2011). Browning of litchi fruit pericarp: Role of polyphenol oxidase, peroxidase, phenylalanine ammonia lyase, and effect of gamma radiation. *J. Food Biochem.*, DOI: 10.1111/j.1745-4514.2011.00572.x.
- Saxena S., Hajare S. N., More V., Kumar S., Wadhawan S., Mishra B. B. Parte M.N., Gautam S., & Sharma A. (2011). Antioxidant and radioprotective properties of commercially grown litchi (*Litchi chinensis*) from India. *Food Chem.*, 126, 39–45.
- Sun, J., Xiang, X., Yu, C., Shi, J., Peng, H., Yang, B., et al. (2009). Variations in contents of browning substrates and activities of some related enzymes during litchi fruit development. *Sci. Hortic.*, 120, 555–559.

BARC NEWSLETTER

INDIGENOUS DEVELOPMENT OF A 10 METER OPTICAL PERISCOPE FOR PROTOTYPE FAST BREEDER REACTOR (PFBR)

D.V. Udupa, Sanjiva K. and N.K. Sahoo
Applied Spectroscopy Division

and

R.V. Sakrikar, A. Kadu and M. Singh
Division of Remote Handling & Robotics

and

SS Bhavsar and R.K Garg
Technical Services Division

and

V. Rajan Babu and V. Balasubramanian
Reactor Component Systems Division, IGCAR

and

R.L. Suthar
Ex-Head, Centre for Design & Manufacture

and

G.P. Kothiyal
Ex-Head, Glass & Advanced Ceramic Division

Shri R.L. Suthar and his team received the DAE Group Achievement Award for the year 2011

Introduction

An optical periscope is an instrument which facilitates visual inspection of objects in a remote or out of line of sight location [1, 2]. In a nuclear reactor, the periscope can be a vital in-service inspection tool for regular maintenance and other operations. For the Prototype Fast Breeder Reactor (PFBR) under development at Kalpakkam, pre-commissioning and periodic in-service visual inspection of reactor vessel internals under shut down condition is a mandatory regulatory requirement. In view of this, a 10 meter long optical periscope has been indigenously designed and developed with the collaborative efforts of Applied Spectroscopy Division (ASD), Division of Remote Handling & Robotics (DRHR), Centre for Design & Manufacture (CDM) of BARC and Reactor Component Systems Division (RCSD) of IGCAR [3]. The instrument



Fig. 1: Photograph of the Periscope

BARC NEWSLETTER

has been fabricated by BHAVINI and is ready for use at PFBR, Kalpakkam. During operation, the periscope will be inserted into the PFBR from the top roof slab vertically for inspecting objects present in the space above the liquid sodium level filled with argon cover gas inside the PFBR. The development of this custom designed instrument is presented here (see Fig. 1).

PFBR

The PFBR has a main vessel of 12.9 meters diameter and 13.2 meters height, with a roof slab and Large Rotatable Plug (LRP) at the top (see Fig. 2). The roof slab has six openings, four openings for intermediate heat exchanger and two for primary sodium pumps. The LRP has openings for in-vessel fuel transfer machine and control & safety rod drive mechanisms. The various equipments are installed inside the reactor through their respective openings and are partially submerged in liquid sodium. The gap between the top of the sodium level and bottom of roof slab is filled with argon cover gas. During inspection campaigns, the periscope is introduced in to the reactor from the roof slab through a 600 mm diameter opening on the LRP for inspection of the various assemblies in this space. There are also some components like purified sodium inlet pipe, argon inlet pipe, siphon break pipe that are fixed from the top of roof slab. The periscope will also facilitate visual inspection of these components.

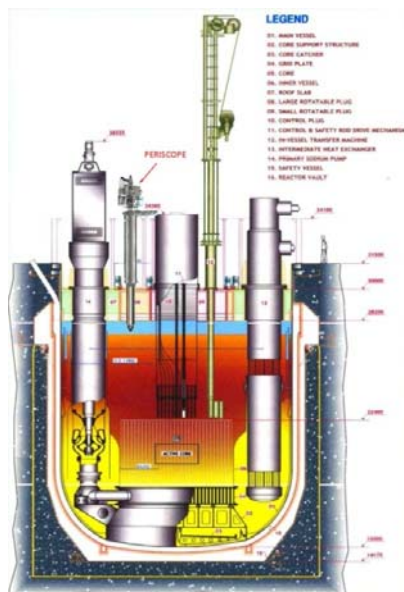


Fig. 2: Schematic of PFBR internals

Periscope Design Features

The periscope will be used for inspection of the main reactor vessel under shutdown condition in presence of the reactor cover gas (argon). The maximum radiation level in the reactor after 10 days of shutdown is 1.3 R/h during which inspection can be carried out. The main design features of the periscope are as follows:

- Length of the periscope: 10 meter
- Object distance from the periscope end: 2 – 4 meter
- Periscope is to be mounted on top of the reactor vessel and inserted vertically through a sealed 600 mm diameter opening on the LRP of the reactor.
- Spatial resolution: 2 mm without zoom and 0.2 mm with zoom
- The maximum field of view: 15 arc degrees
- Operating temperature: 150 °C (cover gas temperature)
- Object space scanning in the vertical plane: from 0° (vertical) to 115° (15° above horizontal)
- Horizontal scanning: 360° by rotating the periscope on vertical axis.
- The periscope provides the facility of video recording in addition to visual inspection.
- The optics of the instrument towards the lower objective end is fabricated with radiation hard glasses for avoiding coloration.
- Final image formed by the periscope is erect with no lateral inversion.

The conceptual design of the instrument was based on fulfilling the above requirements while working with the constraints imposed during handling and operation at site. An elaborate periscope handling and installation procedure has been evolved to carry out the complete inspection campaign in a leak tight manner. This is by using associated accessories such as Leak Tight Chamber, Preheating Chamber and Gate Valves. The periscope is also sealed, purged with argon and maintained at slightly higher pressure compared to the reactor cover gas, so that there is no leakage of reactor argon in case of the failure of the seal.

BARC NEWSLETTER

Optical Design

The basic optical design concept is to image the object field by an objective lens and then to relay this image to the eye-piece at the periscope end by a set of relay lenses. Fig. 3 shows the schematic optical layout in the periscope. The object field is scanned in the vertical direction by using set of prisms while the horizontal field is scanned by rotating the entire periscope about the optical axis. The rotation of the prism during scanning also rotates the image. A compensating additional image rotation is made by rotating a Pechan prism in order to maintain the image orientation. The overall design ensures that the image is finally seen in a proper perspective and no lateral inversion is introduced.

The system is designed with a maximum magnification of 9X for resolving an object of 0.2 mm at 4 meters, considering the angular resolution of the normal human eye [4]. The primary image is formed by a zoom lens objective having zoom ratio of 3 placed behind the scanning prism. An optically compensated [5] three element zoom lens has been designed keeping in mind the simplicity of the mechanical drive needed for linear lens movements in such a system. The focal length of this lens varies continuously in the range 100 - 300 mm. The semi-field covered is 2.5° for 300 mm focal length and 7.5° for 100 mm focal length. The relayed image is focused at the image plane in the eyepiece module. The periscope consists of two arms each for visual inspection and for photography respectively. The optical aberration correction and the design optimizations for best image quality were carried out using optical ray tracing techniques by computer programs developed in-house.

Mechanical Design

The periscope is housed in a single main tube to facilitate ease of handling during deployment and removal of the unit. The main design requirement is the correct alignment of optical elements and the maintenance of optical alignment during movement of optical components for zooming, scanning and

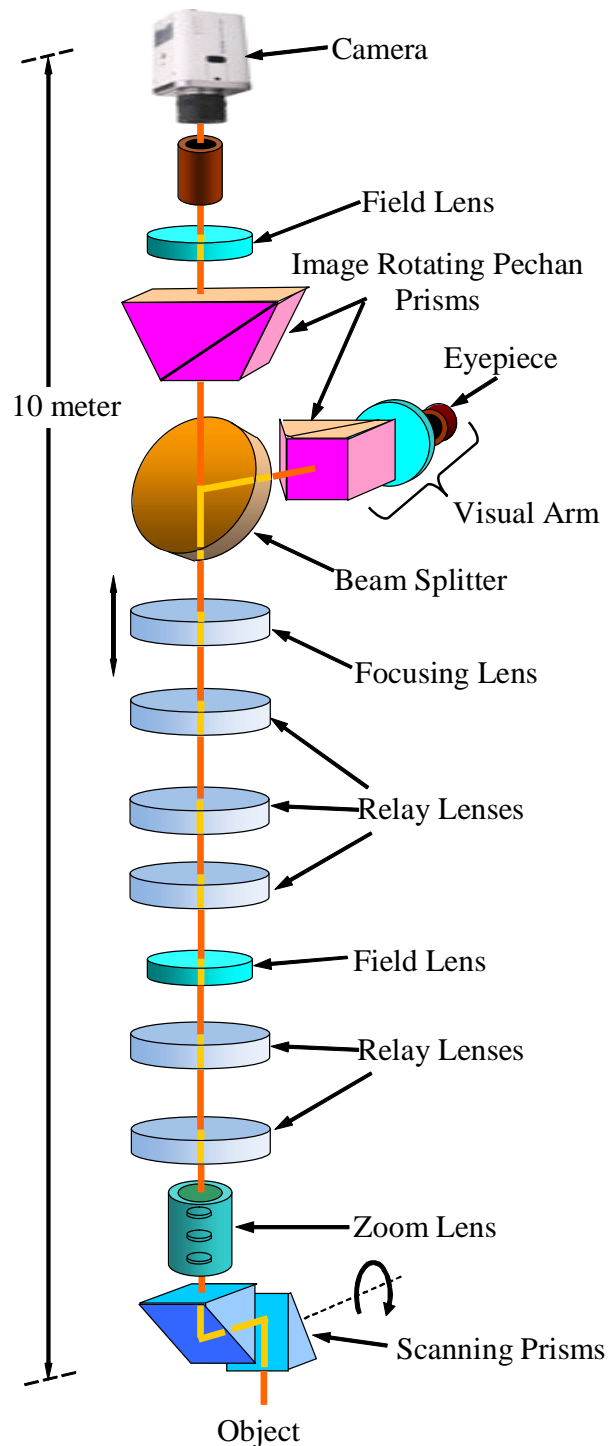


Fig. 3: Schematic optical layout of the periscope

focusing. The design is based on modular construction of optical mounts for ease of assembly, alignment, optical testing and disassembly of optical elements if needed during alignment. The periscope consists two main mechanical sub-systems viz., Main tube assembly and Viewing tube assembly (see Fig. 4).

BARC NEWSLETTER

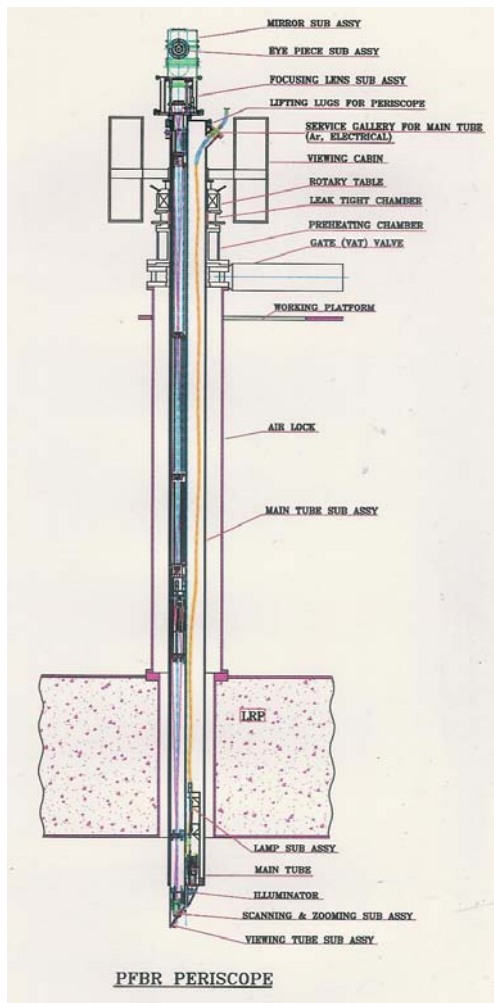


Fig. 4: Mechanical assembly layout of periscope

Main Tube Assembly

Main outer tube is a 400 mm OD and 380 mm ID, SS304 pipe and is hard chrome plated and ground from outside to have scratch proof surface, as per the sealing requirements. The bottom plate fixed to the main tube provides support for lamp modules and associated systems. The main tube assembly provides the required support and rigidity to the Viewing assembly. The top portion of the main tube is provided with lifting lugs and openings for services such as cooling argon, electrical cables, motors and switches etc. The main tube also supports the control panels and the operator cabins mount. The main tube is installed on the rotating table to facilitate axial rotation and the linear axial movement of the periscope.

Viewing tube Assembly

Viewing tube assembly houses all the various optical elements with high mechanical accuracy as per the optical design. This assembly consists of accurately machined lens mounts, connected to each other by tie rods, which are machined precisely and fixed into reamed holes of corresponding lens mounts. The design of the lens mounts is such that the concentricity of 0.05 mm is maintained throughout the relay lens system. The lens mounts have provision of spacers for fine axial distance adjustment and viton 'O' rings for cushioning.

Scanning prism assembly consists of two prisms mounts with a rotation mechanism for the front prism to facilitate scanning by 115 degrees in vertical plane. Zoom lens assembly consists of a set of 3 lens mounts arranged longitudinally with the central lens mount fixed. The two extreme lenses are held at a constant distance and are moved as a unit longitudinally for zooming operation. The eyepiece assembly houses the field lens, Pechan prism and the eyepiece with a high degree of concentricity. This assembly gets located in a ball bearing mechanism and is rotatable for image correction.

Illuminator Design

An illuminating system is housed just beside the viewing canal at the periscope end for illuminating the objects under inspection (see Fig.5). This system has been

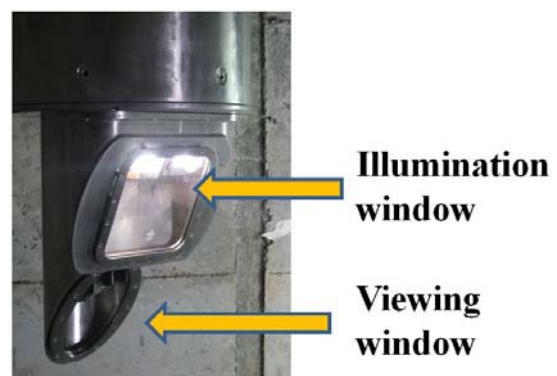


Fig. 5: Periscope end showing illumination and viewing windows

BARC NEWSLETTER

designed to provide light levels of the order of 700 to 1000 lux for comfortable viewing. Considering the light transmission efficiency of the visual canal consisting of multiple elements and surfaces, the light intensity provided on the object is 2500 lux. Two xenon arc lamps of 300 W power consisting of an integral reflector are used for the illumination. One lamp with ellipsoidal reflector and another lamp with parabolic reflector are housed side by side. The lamp with ellipsoidal reflector provides a diverging light which is controlled to 18° by an associated focusing lens system. The lamp with parabolic reflector provides a low divergence light beam of 8° . This arrangement allows for the operator to selectively choose higher illumination in the central field for any inspection with high magnification if required. A system of scanning prisms at the ends for both the lamps allow for directing the illuminating beam in the desired direction for inspection.

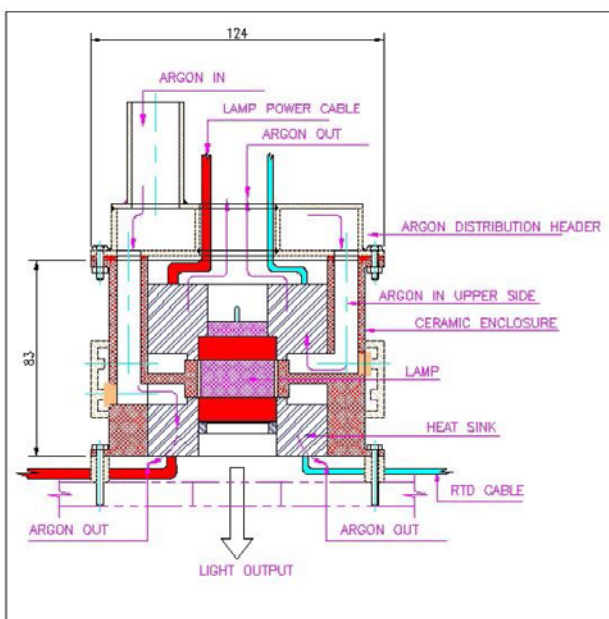


Fig. 6: Diagram showing xenon lamp cooling arrangement

The xenon lamps used in the illuminator has heat-sinks mounted on copper electrodes operating with 25 kV striking pulse. The lamps are originally designed for operation in air with forced cooling. Since the periscope is a sealed device and has argon as operating environment, an additional arrangement with ceramic enclosure on the lamp for electrically isolating the electrodes, while facilitating cooling with argon flow has been designed (see Fig. 6). The heat-sinks on the

lamps are provided with resistance type temperature detection probes. The operation of the lamps is interlocked with temperature to ensure that the lamps are operated within their safe operating zone. The requirements of cooling argon were arrived at on the basis of detailed thermal analysis. The argon supply is taken from the argon header available in the Reactor Containment Building. The supply is routed to the lamp modules through SS flexible hoses having arrangements for quick disconnection from the illuminator modules to facilitate maintenance of lamp modules.

Periscope Controls

The optical component displacements in the periscope for vertical scanning, zooming, focusing, light deflection and the periscope rotation are motorized using stepper motors compatible to argon environment and 130°C temperature. The motors are controlled by individual controllers with adjustable speeds. Non-contact type of magnetic position sensors are used for home position sensing and limiting the movements. The control systems in the periscope is PLC based and has interface for operation, display of status information and monitoring of the operational interlocks. A remote I/O panel situated at 15 to 20 meters away from the periscope houses the main control PLC and its



Fig. 7: Operator control panel

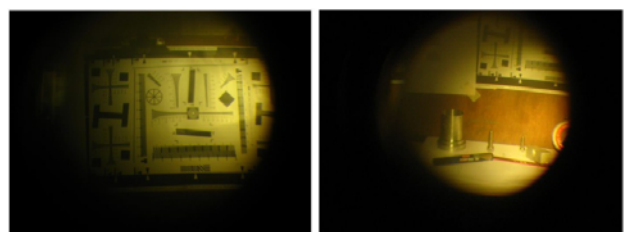


Fig. 8: Test images recorded using the periscope

BARC NEWSLETTER

associated local I/O interfaces and motor controllers. An additional ergonomically designed operator panel is mounted below the eyepiece assembly on the periscope (see Fig.7). Both the panels have joystick interface, for operation of various motions with a touch screen for setting of various parameters and for information display.

References

1. Francis B Patrick, "Military Optical Instruments" in Applied Optics and Optical Engineering, Vol. V Part II, R. Kingslake, Ed. Academic Press, New York, 209-214 pp (1969).
2. M Born and E Wolf, "Principles of Optics", Pergamon Press London, New York, 6th Ed., 243-245 pp (1980)
3. "Development of Periscope for Prototype Fast Breeder Reactor", M. Singh, R. V. Sakrikar, A. M. Kadu, D. V. Udupa and S. Kumar Presented in "Technical Meeting on Fast Reactors In-service Inspection and Repair: Status and Innovative Solutions" at IAEA, Vienna, Austria during 19-20 December 2011, ([http:// www.iaea.org/NuclearPower/ Downloads/ Technology/ meetings/ 2011-12-19-20-TM-FR/ WorkingMaterial.pdf](http://www.iaea.org/NuclearPower/Downloads/Technology/meetings/2011-12-19-20-TM-FR/WorkingMaterial.pdf))
4. W J Smith, "Modern Optical Engineering", MC Graw Hill Book Company, London 214-215 pp (1966)
5. Kingslake R, "Lens Design Fundamentals", Academic Press, London, 63-66 pp (1978).

BARC NEWSLETTER

DESIGN AND DEVELOPMENT OF EXPLOSIVELY DRIVEN HELICAL FLUX COMPRESSION GENERATORS

Anurag Shyam, Partha Banerjee, Rohit Shukla, Rishi Verma
Energetics and Electromagnetics Division, E&I Group

Dr. Anurag Shyam and his team received the DAE Group Achievement Award for the year 2011

Magnetics Flux compression generation or FCG is one of different kinds of explosively driven pulse power source which finds versatile applications. The helical Flux compression generator coils have been indigenously designed and in-house fabricated. Single ended Helical Flux compression generator experiments using 300gm of high explosive were started. All the experiments were conducted with keeping explosive quantity constant. The team efforts in indigenous development of the HFCG resulted in a remarkable achievement in very high magnetic field generation experiments for high power microwave generation and quasi spherical implosion for fission or fusion experiments. A figure of helical flux compression generator is shown in Fig. 1. The salient features of the results are as given under.

Brief write-up on #RI-X.X coil

In the successive dynamic trials with subsequent modifications in coil design, the average overall efficiency has been attained up to the level of ≥ 0.75 . In the dynamic trials, with coil designs briefly designated as #RI-1.X, #RI-2.X and #RI-3.X, maximum current gains of 48x, 61x and 72x have been demonstrated, producing peak currents of 162kA, 225kA and 554kA with seed currents of 3.4kA, 3.7kA and 7.7kA respectively. In terms of energy gain and overall efficiency (α), the initial inductive energies were amplified to $\sim 9.4x$, $\sim 15x$ and $\sim 18x$, where as the maximum overall efficiency (α) were obtained as 0.70, 0.73 and 0.75 respectively. It may be noted that weight of Comp-B explosive used in these experiments was

limited to 0.3kg and all trials have been conducted inside 1.4kg containment chamber.

The brief description regarding performance of compact single-ended flux compression generator designs #RI-1.X, #RI-2.X and #RI-3.X that were dynamically tested in field trials is as followed:

An important aspect of #RI-3.X coil design was that the enhanced utilization of same explosive mass (which was limited to ~ 0.3 kg in all coil designs) has been successfully demonstrated. In comparison to coil designs #RI-

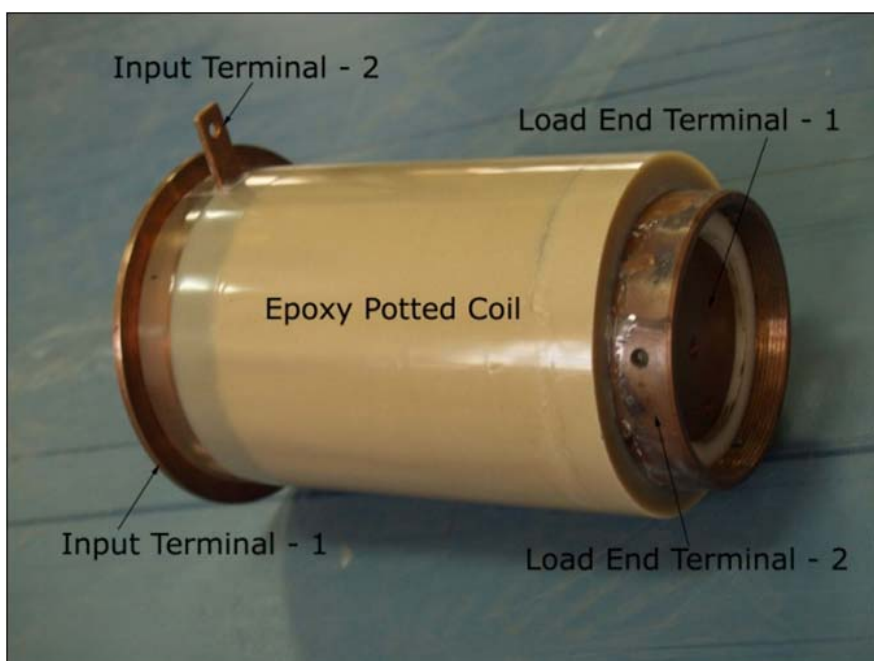


Fig. 1: Helical Flux Compression Generator Coil

BARC NEWSLETTER

1.X & #RI-2.X, #RI-3.X has resulted in much superior performance even at higher seed currents, while the explosive mass remained same. (As mentioned above, its dynamic trial has resulted in most efficient performance yielding highest ever-obtained current gain of 72× (i.e. 554kA of current output) at seed current level of 7.7kA, along with improved overall efficiency i.e. ~0.75).

Brief write-up on #PA-X.X coil

Shri Partha Banerjee is working on Helical Flux Compression Generator (HFCG). He has designed and developed HFCGs for use with ~300 gms of Composition – B high explosive. He modified the design of SIN – 3 – 179 – T28 (I,S) – PA – 7.# series HFCG. The modified version, SIN – 3 – 179 – T28(I,S) – PA – 8.# series was designed to prove that he plasma formation due to adiabatic compression of the medium inside the HFCG volume, can be controlled and the coil turns can be protected from the plasma generated so that the unwanted voltage breakdown between the turns is avoided. The modified version of the HFCG has been tested. The test achieved a current gain of 105 from a seed current of 4.3 kA. The final output current achieved is 450 kA. To note that this is the highest ever achieved current gain from HFCG experiments in India.

Brief write-up on #RO-1.X coil

The helical flux compression generator coils were designed developed and tested with an aim of achieving

more than 300kA currents with seed currents of 20kA in the ongoing series of experiments of flux compression generator current amplifiers. Helical Flux Compression Generators were designed and developed and tested for delivering 400kA & 450kA currents in two successive shots using a seed current of 29kA. Interestingly the load part was in the form of parallel strip type geometry which is expected to offer higher load inductance. They were made using a rectangular strip of copper wire. The crowbar was pin type but tilted at an angle. The end of the coil was extended to receive expansion cone half-angle. The FCG coils and were utilizing 300gm explosive and have delivered maximum peak current with almost perfect repetition seen in the fixed explosive Composition – B with given dimensions. The self-integrated Rogowski coils made employing multilayered winding to enhance the time constant for current measurement were also designed and made for the flux compression generator experiments. Extensive modeling of the Flux compression generator coils were also done to get results in short time in order to analyze and predict the operational parameters of coils.

Acknowledgements

The accomplishment of above mentioned work could have been possible with the efforts of team of Dr. T.C. Kaushik, Shri G. Pandey, P.B. Wagh, S.V. Ingale, Amit Rav, Amit Sur, S. P. Nayak from Applied Physics Division under the esteemed leadership of Dr. Satish C. Gupta.

ROOM TEMPERATURE OPERATED FLEXIBLE AMMONIA SENSOR

Ajay Singh, Soumen Samanta, A.K. Debnath, D.K.Aswal and S.K.Gupta
Technical Physics Division

Shri Ajay Singh received the INSA Medal for Young Scientist for the year 2012

Abstract

The structural, charge transport and chemi-resistive gas sensing characteristics of cobalt phthalocyanine (CoPc) films deposited on flexible bi-axially oriented polyethylene terephthalate (BOPET) substrates were investigated. CoPc films exhibited a preferential (200) orientation with charge carrier mobility of $\sim 118 \text{ cm}^2\text{V}^{-1}\text{s}^{-1}$ (at 300 K). Charge carrier mobility in these films systematically decreases upon bending, which implies that bending reduces π - π interactions among molecules. At room temperature, these films exhibited a reversible change in resistance on exposure to ammonia (5 – 50 ppm) along with high sensitivity and selectivity as well as fast response and recovery. The sensing properties were found to improve significantly under bend conditions owing to creation of more numbers of interaction sites.

Introduction

Development of high mobility flexible organic semiconductor devices is highly desired for the fast and low cost next generation flexible electronic applications.¹ Metal phthalocyanines, which have shown tremendous potential as a key component in organic photovoltaic and gas sensing devices, have never been investigated for flexible devices. In this work, we demonstrate very high charge carrier mobility of $118 \text{ cm}^2\text{V}^{-1}\text{s}^{-1}$ (at 300 K) in cobalt phthalocyanine (CoPc) films grown on transparent flexible bi-axially oriented polyethylene terephthalate (BOPET). These high mobility flexible CoPc films are found to be suitable for detection of ammonia gas in parts per million (ppm) range.

Experimental details

CoPc films (thickness: 20 nm) were deposited on pre-cleaned flexible BOPET substrates by molecular beam epitaxy (vacuum $\sim 2 \times 10^{-8}$ mbar).¹ After film deposition, four pairs of planar gold electrodes (size: 3mm x 2mm) separated by 12 μm were thermally evaporated onto films using a metal mask. Subsequently, silver wires were

attached to the gold electrodes using silver paint. The bending measurements were performed by attaching the flexible samples to curved surfaces of different radius. Current-voltage (*I-V*) measurements were carried out using Keithley 6487 voltage-source/picoammeter and computer based data acquisition system.

Results and discussions:

The atomic force microscope (AFM) image of 20 nm thick CoPc films grown on BOPET substrate, Fig. 1(a), reveals that film consists of elongated grains with rms

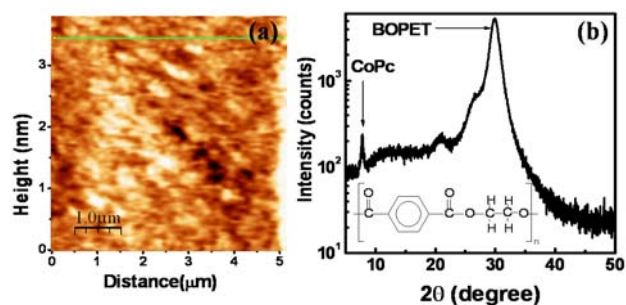


Fig. 1: (a) AFM image of the 20 nm thick CoPc film grown on BOPET substrate and the height profile across the line drawn in the image. (b) XRD pattern reordered for the CoPc films grown over BOPET substrate. Inset shows the molecular structure of PET.

surface roughness of 1.1 nm. Presence of Bragg peak at 7.8° in the XRD pattern shown in Fig 1(b) suggest the (200) orientation of the α -CoPc phase i.e. film is crystalline with a -axis normal to the substrate plane.¹

A typical 2-dimensional pole figure contour recorded for the (200) Bragg peak ($2\theta = 6.9^\circ$) is shown in Fig. 2(a). From pole figure data it can be seen that the intensity is maximum at the center which decreases sharply with increasing azimuthal angle (Ψ) and the contour is highly symmetric with respect to the polar angle (Φ). This suggests that the grown films have reasonably good out-of-plane texturing but there is no preferential texturing in the plane of the films.¹

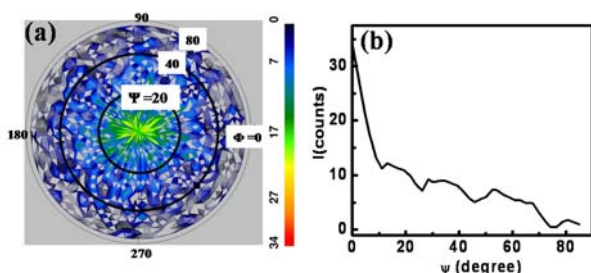


Fig. 2: (a) X-ray pole figure contour recorded for the (200) Bragg peak of 20 nm thick CoPc films grown on BOPET substrate. (b) I - Ψ plot at $\Phi = 171^\circ$ derived from the pole figure data.

A good texturing of CoPc films on BOPET is attributed to the presence of polar groups i.e. C=O and O-C=O in the PET molecular chains, as shown in the inset of Fig. 1(b), that can electrostatically interact with CoPc molecules and a relatively stronger π - π interaction among CoPc molecules.¹

A photograph showing the flexible nature of CoPc films with deposited gold electrodes and schematic of our bending set up along with the charge transport measurement arrangement is shown in Fig. 3(a). Typical room temperature J - V characteristics measured for CoPc films under flat (without bending i.e. bending radius $r \rightarrow \infty$) and for r are shown in Fig. 3(b). It can be seen that with an increase in bending (i.e. a decrease in r) the J decreases. In the inset of Fig. 3(B), the J - V data's are plotted in log-log scale, it is seen that J - V characteristics are non-linear, and exhibits two different power law behavior ($J \sim V^\alpha$) as a function of applied

bias with varying α values. At room temperature, for low bias ($< 15V$) $\alpha \sim 1$ indicates ohmic conduction. For ohmic conduction the J - V characteristics can be described by $J = n_0 e \mu V/d$; where n_0 is the concentration of thermally generated holes, e is the electronic charge, μ is the hole mobility, and d is the electrode separation. For high bias ($> 15V$), $\alpha \sim 2$ indicates the shallow trap mediated space charge limited conduction (SCLC). SCLC occurs if the injected carrier density is higher than n_0 and J depends on applied bias through the relation:

$J = \frac{9}{8} \theta \epsilon \mu \frac{V^2}{d^3}$, where ϵ is permittivity (experimentally determined value of ϵ for our films is $2.45 \times 10^{-11} F/m$) and θ is the ratio of free to total (trapped and free) charge carrier density. The μ values were estimated from the slopes of J - V^2 plots for different r , and the results are plotted in the Fig.1(c). The value of μ in the flat condition of the films was found to be $\sim 118 \text{ cm}^2 V^{-1} s^{-1}$, which systematically decreases on bending.²

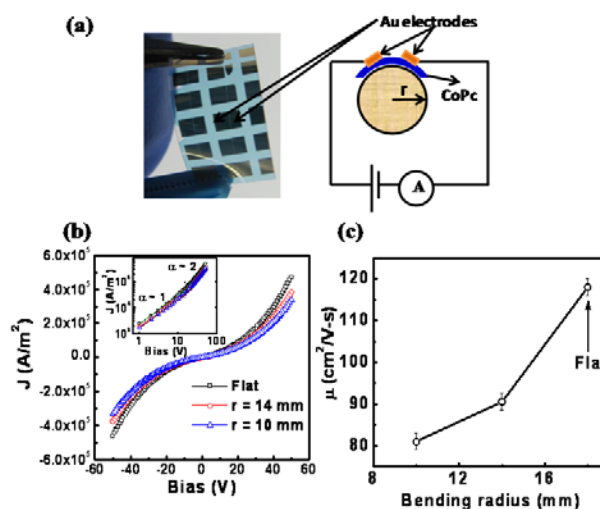
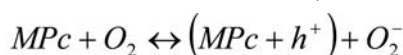


Fig. 3: (a) Temperature dependent J - V characteristics of flexible CoPc films under flat condition. Inset shows the Log-log plots of J - V characteristics. (b) Temperature dependence of the mobility (μ) obtained from the analysis of SCLC characteristics. Inset shows the Log-log plot of J versus d (electrode separation).

Metal phthalocyanines (MPC) are intrinsically insulators under high vacuum environment and turn semiconductors only when exposed to ambient conditions. This is because ambient oxygen gets chemisorbed at the surface, which in turn, induces hole carriers in the films via the process:²



MPC films acts as chemiresistive sensors because the analyte gases (both reducing and oxidizing) can interact with O_2^- as well as metal surface sites, which results in a change of electrical resistivity. The interaction of MPC with the reducing gases (such as NH_3) shows an increase in resistivity, which is attributed to the hole trapping within the films by the electrons donated from reducing gas.

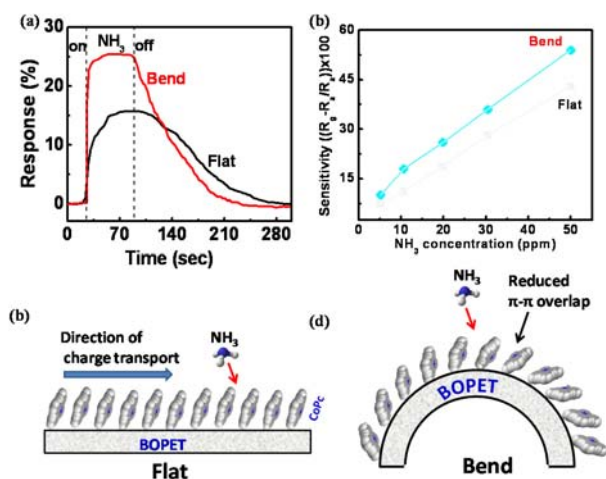


Fig. 4: (a) Comparative response curve of CoPc films under flat condition and under extreme bend condition (bending radius: 10 mm) for 20 ppm of NH_3 . Inset shows the chemical structure of CoPc molecule. (b) Sensitivity versus NH_3 concentration for flat and bend condition Schematic showing the ordering of CoPc molecules on flat BOPET (c) and on bend BOPET substrate (d).

Fig. 4 (a) shows the comparative response/recovery curves i.e. change in film resistance as a function of time on exposure to 20 ppm of NH_3 under flat and bend conditions. It can be seen that under flat condition the response time (i.e. time required to reach 90% of the saturation resistance upon NH_3 exposure) is ~25 s and recovery time is ~156 s, which under bend condition reduces significantly to ~2 s and 100 s, respectively. The sensitivity (defined as: $S(\%) = \left| \frac{R_x - R_a}{R_a} \right| \times 100$,

where R_a and R_x are the resistance values of CoPc films in the air and NH_3 respectively) versus NH_3 concentration curves clearly shows (Fig. 4(b)) that sensitivity is higher under the bend condition

Above results clearly show that under bend conditions high mobility flexible CoPc films exhibit enhanced sensitivity as well as fast response and recovery. In order to explain this behavior in Fig. 4(c, d) we schematically draw the arrangements of CoPc molecules on BOPET substrate under flat and bend conditions. Under flat

condition, CoPc molecules are arranged in edge-on configuration, which results in improved $\pi-\pi$ interaction, and hence high charge carrier mobility is observed. In this case, NH_3 molecules can only interact with surface of the films as Co metal sites are unavailable owing to close packing. Under the bend condition, as shown in Fig. 4(d), the stress enhances the separation among CoPc molecules, which facilitates NH_3 molecules to interact with chemisorbed oxygen present on Co metal sites. An increase in the numbers of interaction sites under bend condition is responsible for high sensitivity as well as fast response/recovery. Due to high toxicity of the gas, any leak in the system can result in a life-threatening situation. Traditional method of detection of presence of ammonia by chemical analysis is a time-consuming and complicated process. However, the sensors based on metal oxides are sensitive to NH_3 but require high temperatures for operation. In this respect, highly flexible CoPc films exhibiting high sensitivity and fast response/recovery under bend condition makes them an attractive candidate for ppm level of NH_3 sensing.

Conclusion

In conclusion, we have demonstrated the growth of highly ordered CoPc films on transparent flexible BOPET substrates with a charge carrier mobility of $\sim 118 \text{ cm}^2 \text{ V}^{-1} \text{ s}^{-1}$ at 300 K. These flexible films show excellent response/recovery for ammonia in the concentration range of 5 to 50 ppm at room temperature. The low cost, room temperature operation, high sensitivity, fast response/recovery of CoPc flexible films makes them attractive candidates for flexi-gas sensor devices.

References

1. A. Singh, A. Kumar, Ashwini Kumar, S. Samanta, A. K. Debnath, P. Jha, R. Prasad, Z. Salmi, S. Nowak, M. M. Chehimi, D. K. Aswal, S.K. Gupta, Appl. Phys. Lett. 101 (2012) 222102
2. A. Singh, Ashwini Kumar, A. Kumar, S. Samanta, N. Joshi, V. Balouria, A. K. Debnath, R. Prasad, Z. Salmi, M. M. Chehimi, D. K. Aswal, S.K. Gupta, Appl. Phys. Lett. 102 (2013) 132107.

BARC NEWSLETTER

INVESTIGATION OF STRUCTURAL AND MAGNETIC PROPERTIES OF SPIN-CHAIN OXIDES

Anil Jain
Solid State Physics Division

This Paper received "IPA's Anil K. and Bharati Bhatnagar Best Ph.D. Thesis Award" at the 57th DAE Solid State Physics Symposium held at IIT Bombay, during December 3–7, 2012

Abstract

The present thesis work on the spin-chain oxides has revealed the role of intrachain and interchain interactions in tuning the magnetic properties. For the compounds $\text{Ca}_3\text{Co}_{2-x}\text{Fe}_x\text{O}_6$ ($x \leq 0.4$), a deviation from "1D character" has been observed with increasing the concentration of Fe. The compounds $\text{Ca}_3\text{Co}_{2-x}\text{Fe}_x\text{O}_6$ ($x \leq 0.4$) and $\text{Ca}_{2.75}R_{0.25}\text{Co}_2\text{O}_6$ ($R = \text{Lu}$ and Dy) order magnetically in an incommensurate spin-density wave structure. Field induced magnetic phase transitions, from the incommensurate-to-commensurate, and then to a ferrimagnetic state (at higher field), are observed. A time dependent magnetic order has been observed in $\text{Ca}_3\text{Co}_2\text{O}_6$.

Keywords: Spin-chain system, geometrical frustration, neutron diffraction, triangular lattice

Introduction

The one-dimensional cobaltate $\text{Ca}_3\text{Co}_2\text{O}_6$ and its derivatives have recently attracted much interest due to their peculiar physical properties [1-6]. The compound $\text{Ca}_3\text{Co}_2\text{O}_6$ crystallizes in a rhombohedral structure (space group $R\bar{3}c$) and its crystal structure contains spin chains, made up of alternating face-sharing CoO_6 octahedra (Co^{3+} , $S = 0$) and CoO_6 trigonal prisms (Co^{3+} , $S = 2$). Besides, the Co^{3+} spins at the trigonal prisms (TP) sites have an Ising-like anisotropy. The ferromagnetic (FM) intrachain and antiferromagnetic (AFM) interchain interactions, combined with a triangular arrangement of spin chains give rise to a geometrical frustration in the compound.

In this thesis, the structural and magnetic properties of the compounds $\text{Ca}_3\text{Co}_{2-x}\text{Fe}_x\text{O}_6$ ($x = 0, 0.1, 0.2, 0.4$, and 1) and $\text{Ca}_{2.75}R_{0.25}\text{Co}_2\text{O}_6$ ($R = \text{Lu}$ and Dy) have been investigated. The choice of the Fe substitution was motivated by the consideration that the Co^{3+} ions, in $\text{Ca}_3\text{Co}_2\text{O}_6$, have large orbital moment, while the Fe^{3+} ions have zero orbital momentum. Moreover, the ionic radii of the Co^{3+} and Fe^{3+} are very close. No strong

lattice effect will, therefore, be introduced, and changes only due to the different magnetic character of the spins of Co^{3+} (Ising) and Fe^{3+} (Heisenberg) are expected. The choice of R^{3+} substitution is motivated by the theoretical prediction that magnetic properties of the compound $\text{Ca}_3\text{Co}_2\text{O}_6$ can be tuned by electron doping.

Experimental

Polycrystalline samples studied in this thesis work were prepared by solid state reaction method. The neutron diffraction (ND) measurements were carried out at Dhruva reactor, Trombay and other neutron scattering facilities, located elsewhere. The dc magnetization measurements were carried out using a commercial vibrating sample magnetometer.

Results and Discussion

Structural Characterization

Rietveld refinement of room-temperature x-ray and ND patterns [Fig. 1(a) for $x = 0.2$ and 0.4] confirmed that all compounds, except $\text{Ca}_3\text{CoFeO}_6$, crystallize in the

space group Rc [1]. For the Fe- substituted compounds ($x \geq 0.4$), the Rietveld refinement of ND patterns and Mössbauer study confirm that the Fe^{3+} ions (with spin $S = 5/2$) are located only at the TP site [1, 2].

Magnetic Properties

A. $Ca_3Co_{2-x}Fe_xO_6$ ($x = 0, 0.1, 0.2, \text{ and } 0.4$)

Dc Magnetization Study: Intrachain and Interchain Exchange Interactions

From the dc-magnetization study, we have derived the values of the intrachain J (positive) and interchain J' (negative) exchange constants. The values of J have been derived by fitting the high temperature χT vs T curves with a theoretical model [Fig. 1(b)]. The values of the J' , have been derived from the ferri-to-ferromagnetic like transition field. A decrease in the intrachain positive exchange constant J and an increase in the interchain negative exchange constant J' have been observed with substitution of iron [Ratio $|J'/J| = 0.025$ and 0.451 for $x = 0$ and 0.4 , respectively], which result in deviation from "1D character" in these spin-chain compounds [1].

Magnetic Ground State: ND Study

In the first approximation, two different commensurate magnetic structures, (i) amplitude-modulated (AM) structure with a propagation vector $\mathbf{k} = \{0, 0, 1\}$ and

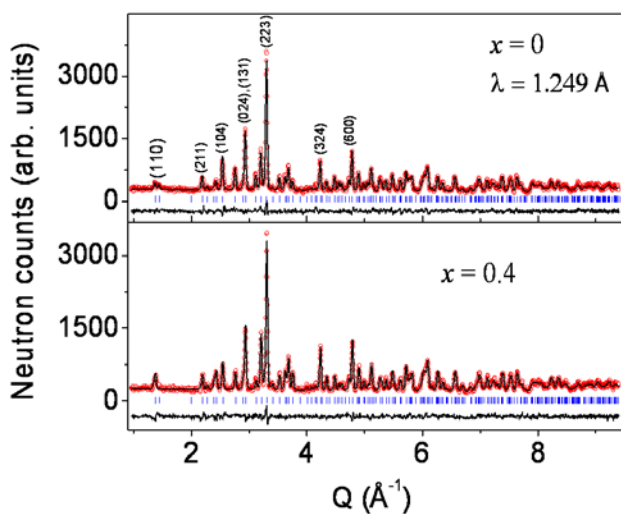


Fig. 1: (a) The Rietveld refined ND patterns (recorded on powder diffractometer II at Dhruva reactor, Trombay) of $Ca_3Co_{2-x}Fe_xO_6$ at 297 K.

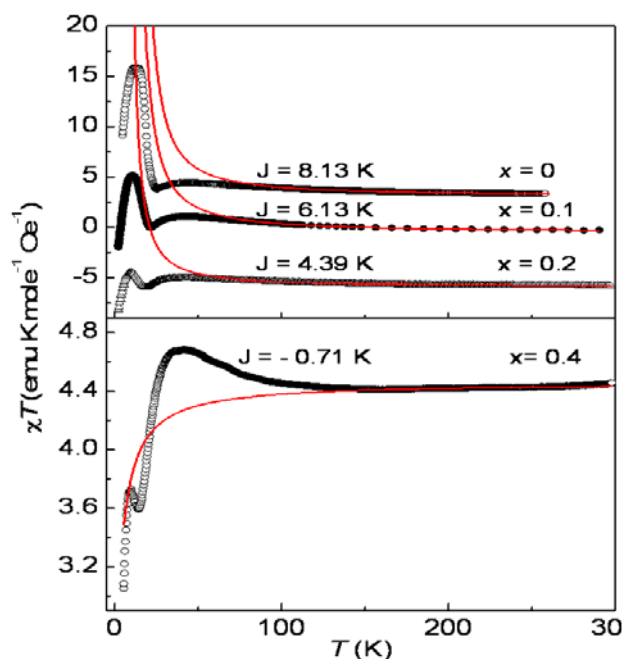


Fig. 1: (b) Plots of χT vs T for $Ca_3Co_{2-x}Fe_xO_6$ derived from FC magnetization curves. Solid lines represent the fitted curve with the expression of χT , for $S = 2$ Ising spin chains as described in Ref. [1].

(ii) partially disordered antiferromagnetic (PDA) structure, are able to fit the neutron diffraction patterns [Fig. 2(a)-(b)] below their respective Néel temperatures ($T_N = 25, 20$ and 17 K, for $x = 0, 0.2$, and 0.4 compounds, respectively) [3, 4]. However, a detailed analysis reveals that these compounds order magnetically in an incommensurate spin density wave (SDW) structure with $\mathbf{k} = \{0, 0, 1.0182(9)\}$ [Fig. 2 (c)-(d)]. Further, a coexistence of the magnetic long-range and short-range ordering has been observed down to 1.5 K (below T_N) [5]. For the parent compound $Ca_3Co_2O_6$, in addition to the magnetic Bragg peaks with SDW order, a second set of magnetic peaks corresponding to the commensurate antiferromagnetic (CAF) structure with a propagation vector $\mathbf{k}_2 = \{0.5, 0.5, 0\}$ appears in the neutron diffraction patterns below ~ 15 K. Moreover, the magnetic Bragg peaks, corresponding to the CAFM and SDW structures, exhibit an unusual time dependence below ~ 12 K.

For the $x = 0.2$ compound, under an applied field of ~ 2 T, a field induced incommensurate-to-commensurate magnetic phase transition has been observed. At higher magnetic field (~ 4 T), the commensurate AM magnetic structure transforms into a ferrimagnetic structure [5].

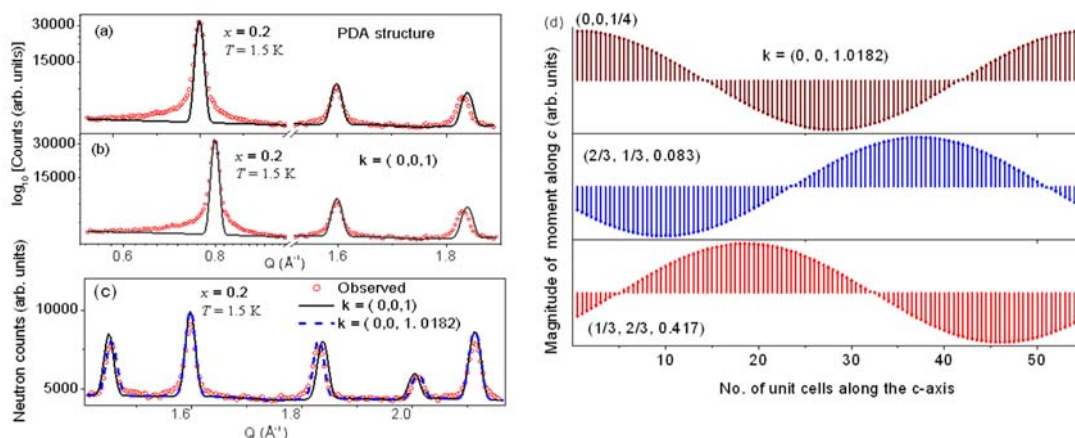


Fig. 2 : The Rietveld refined neutron diffraction patterns for $\text{Ca}_3\text{Co}_{1.8}\text{Fe}_{0.2}\text{O}_6$ at 1.5 K using (a) PDA structure and (b) AM structure with $\mathbf{k} = \{0,0,1\}$. (c) The Rietveld refined patterns shown for $\mathbf{k} = \{0, 0, 1\}$ and $\{0, 0, 1.0182(9)\}$. (d) Schematic of the proposed SDW structure.

B. $\text{Ca}_{2.75}\text{R}_{0.25}\text{Co}_2\text{O}_6$ ($R = \text{Lu}$ and Dy)

For the compounds $\text{Ca}_{2.75}\text{R}_{0.25}\text{Co}_2\text{O}_6$ ($R = \text{Lu}$ and Dy), a detailed analysis of ND patterns reveals that the magnetic structure is an incommensurate SDW structure with $\mathbf{k} = \{0, 0, 1.02\}$, with c axis as direction of both moment and modulation. Neutron diffraction and dc magnetization studies have also confirmed that the oxidation state of a fraction of the cobalt ions at the TP site is reduced from Co^{3+} to Co^{2+} . The observed decrease in the value of T_N with rare-earth substitution ($T_N \sim 25$ K for $\text{Ca}_3\text{Co}_2\text{O}_6$) indicates a reduction in the value of positive FM intrachain exchange interaction J , which is consistent from the crystal structure studies, where an increase in the lattice constants, with the substitution of the R^{3+} ions, has been observed. In the field dependent magnetization study, signatures of the field induced metamagnetic-like phase transitions have been observed [6].

Conclusion

The present thesis work emphasizes the role of intrachain and interchain interactions in tuning the magnetic properties of the quasi-one-dimensional spin-chain oxides. The importance of geometrical frustration and type of spin (Ising or Heisenberg) in the determining the magnetic ordering on the triangular lattice Ising AFMs has been brought out. The role of external magnetic field in tuning the magnetic properties of these spin-chain compounds has been highlighted. The derived results in the present thesis work have given a broader understanding of the physics of the observed

magnetic behavior in these spin-chain oxides and will help in designing the materials with predictable magnetic properties.

Author is grateful to Dr. S. M. Yusuf for his excellent guidance throughout the thesis work.

References

1. A. Jain, S. Singh, and S. M. Yusuf. "Structural and magnetic properties of spin chain compounds $\text{Ca}_3\text{Co}_{2-x}\text{Fe}_x\text{O}_6$ ". *Phys. Rev. B* **74** (2006):174419.
2. I. Nowik, A. Jain, S. M. Yusuf, and J. V. Yakhmi. "Effect of Fe substitution on the magnetic ordering in $\text{Ca}_3(\text{Co}_{1-x}\text{Fe}_x)_2\text{O}_6$ ". *Phys. Rev. B* **77** (2008):054403.
3. A. Jain, S. M. Yusuf, J. Campo, and L. Keller. "Magnetic ordering in the spin-chain compounds $\text{Ca}_3\text{Co}_{2-x}\text{Fe}_x\text{O}_6$ ($x = 0.2$ and 0.4): A neutron diffraction study". *Phys. Rev. B* **79** (2009):184428.
4. A. Jain and S. M. Yusuf. "Short-range and long-range incommensurate magnetic ordering in the frustrated antiferromagnets $\text{Ca}_3\text{Co}_{2-x}\text{Fe}_x\text{O}_6$: A neutron diffraction study". *Phys. Rev. B* **83** (2011):184425.
5. S. M. Yusuf, A. Jain, and L. Keller. "Field induced incommensurate-to-commensurate magnetic phase transition in $\text{Ca}_3\text{Co}_{1.8}\text{Fe}_{0.2}\text{O}_6$: a neutron diffraction study". *J. Phys.: Condens. Matter* **25** (2013): 146001.
6. A. Jain, S. M. Yusuf, S. S. Meena, and C. Ritter. "Stabilization of the spin density wave structure with rare-earth substitution in $\text{Ca}_3\text{Co}_2\text{O}_6$ ". *Phys. Rev. B* **87** (2013): 094411.

BARC NEWSLETTER

¹⁷⁷LU IN TARGETED RADIOTHERAPY: A TRANSITION FROM BENCH TO BED

Sudipta Chakraborty

Isotope Applications & Radiopharmaceuticals Division

This Paper received the IANCAS Dr. Tarun Datta Memorial Award 2012, at the Nuclear & Radiochemistry Symposium 2013 (NUCAR 2013), held at Jabalpur between 18-23rd February, 2013

Introduction

Radionuclide therapy using target specific radiopharmaceuticals is in existence for several decades. Radioiodine (Iodine-131) therapy has been the most successful therapeutic modality for the treatment of thyroid cancer over the last six decades. Better understanding in molecular biology and advances in the field of drug design the last couple of decades have unraveled the possibility of developing new therapeutic radiopharmaceuticals for the treatment of a wide variety of cancers other than thyroid as well as for certain other diseased states, such as rheumatoid arthritis. The availability of radionuclides, having suitable decay properties, in large quantities and with high specific activity for radiolabeling biomolecules targeted to receptors is another important parameter in the success of radionuclide therapy. Towards this direction, the potential of ¹⁷⁷Lu-labeled agents for targeted therapy applications was realized by the researchers of a few institutes across the world in the late 90's and BARC is one of those institutes. ¹⁷⁷Lu is an attractive radionuclide for the development of targeted radiotherapeutic agents owing to its suitable nuclear decay characteristics [$E_{\beta(\max)} = 497$ keV, $E_{\gamma} = 113$ keV (6.4%) and 208 keV (11%)], comparatively longer half-life [$T_{1/2} = 6.65$ d] and ease of production with high specific activity. Indigenous production of the radioisotope in large quantity and with adequate specific activity at an affordable cost was itself a challenge. As a result of extensive research on production of this isotope in varying specific activities, by careful alterations of irradiation parameters (flux, duration, enrichment etc.), ¹⁷⁷Lu is now an indigenously produced therapeutic radioisotope and is being supplied from BARC for use in several nuclear medicine centres in India. Using the

present reactor facilities in our institute, ¹⁷⁷Lu in adequate specific activity and radiochemical purity is being routinely produced and its utilization in developing therapeutic radiopharmaceuticals for the benefit of cancer patients in our country have of a plethora of molecules have been successfully demonstrated.

Production of ¹⁷⁷Lu

¹⁷⁷Lu can be produced by two different routes, namely, by direct neutron activation of natural (¹⁷⁶Lu, 2.6%) or enriched (in ¹⁷⁶Lu) Lu₂O₃ target and also by indirect route involving the irradiation of enriched (in ¹⁷⁶Yb) Yb₂O₃ target followed by radiochemical separation of ¹⁷⁷Lu from Yb isotopes. The above two production routes lead to the product having different specific activities. Although the specific activity obtained in (n,γ) activation is usually low, owing to the high thermal neutron capture cross-section of ¹⁷⁶Lu ($\sigma = 2090$ b) coupled with strong resonance very close to thermal region, direct neutron activation results in reasonably high specific activity of ¹⁷⁷Lu. Therefore it is feasible to produce high specific activity ¹⁷⁷Lu suitable for developing agents for targeted radiotherapy applications by simple (n,γ) reaction using enriched ¹⁷⁶Lu as target in medium flux research reactors. However, a careful optimization of the time of irradiation is required in order to obtain the ¹⁷⁷Lu with maximum specific activity as there will be considerable target burn up owing to the high thermal neutron capture cross-section of ¹⁷⁶Lu. The ¹⁷⁷Lu activity produced at the end-of-bombardment (EOB) as a function of irradiation time at different thermal neutron flux is shown in Fig. 1. It is evident from the figure that depending on neutron flux, the activity of ¹⁷⁷Lu produced will be maximum

after certain duration of irradiation, beyond which the activity will decrease owing to the high target burn up.

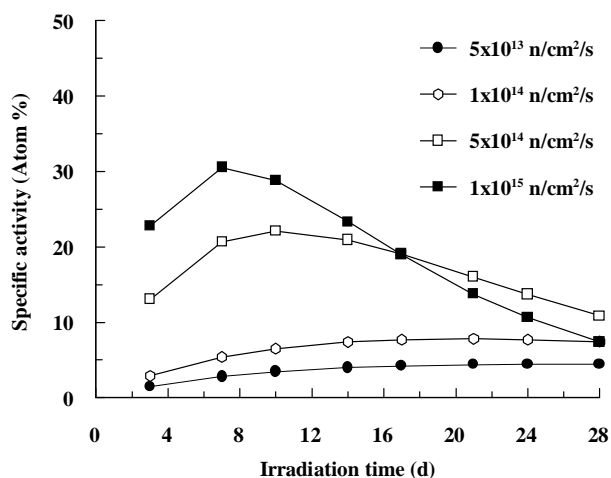


Fig. 1: Variation of ¹⁷⁷Lu specific activity with respect to duration of irradiation at different thermal neutron fluxes

¹⁷⁷Lu is regularly produced by irradiation of enriched (82% in ¹⁷⁶Lu) Lu₂O₃ target at a thermal neutron flux of 1×10¹⁴ n/cm².s for a period of 21 d at the Dhruva reactor. A maximum specific activity of ~925 GBq/mg (25 Ci/mg) was achieved. The radionuclidic purity of ¹⁷⁷Lu is determined by analyzing the gamma ray spectrum of radiochemically processed ¹⁷⁷Lu sample. The average level of radionuclidic impurity burden in ¹⁷⁷Lu due to ^{177m}Lu is found to be ~ 5.5 kBq of ^{177m}Lu / 37 MBq of ¹⁷⁷Lu (~ 150 nCi / 1 mCi) at EOB, which indicates ¹⁷⁷Lu is produced with 99.985% radiochemical purity.

¹⁷⁷Lu-EDTMP in palliation of bone pain due to skeletal metastasis

Skeletal metastases or secondary cancerous lesions in bone are common in patients suffering from breast, lung and prostate cancer in the advanced stage of their diseases. These metastatic lesions in skeleton often lead to excruciating pain and other related symptoms, such as lack of mobility, neurological deficits, depression etc., which adversely affect the quality of life. Radionuclide therapy employing radiopharmaceuticals labeled with β⁻/conversion electron emitting radionuclides is an effective option for bone pain palliation and could

provide significant improvement in quality of life of patients. The major challenge in developing effective agents for palliative treatment of bone pain arising from skeletal metastases is to ensure the delivery of adequate dose of ionizing radiation at the site of skeletal lesions with minimum radiation induced bone marrow suppression. ¹⁷⁷Lu is presently being considered as a potential radionuclide for developing the palliative agents for bone pain arising due to skeletal metastases. The tissue penetration range of the β⁻ particles from ¹⁷⁷Lu are adequately low which ensures minimum bone marrow suppression, a major advantage of this radiotherapeutic application.

Multidentate polyaminopolyphosphonic acid ligands are reported to have high affinity towards skeletal lesions and known form stable chelates with many metals, particularly with lanthanides. Ethylenediaminetetramethylene phosphonic acid (EDTMP) is one of the most widely used polyaminophosphonate ligands for developing radiolabeled agents for bone pain palliation. ¹⁵³Sm-EDTMP (Quadramet[®]) is currently being used extensively for pain palliation due to skeletal metastases. Working in this direction, ¹⁷⁷Lu-EDTMP complex was synthesized and studied with an objective to develop a suitable ¹⁷⁷Lu-based viable alternative of ¹⁵³Sm-EDTMP. ¹⁷⁷Lu-EDTMP complex was prepared in high yield and excellent radiochemical purity (>99%) in our laboratory using EDTMP synthesized in-house. The complex exhibited excellent *in vitro* stability at room temperature. Biodistribution and imaging studies in Wistar rats and imaging studies in New Zealand White rabbits and dogs with spontaneous bone cancer showed selective skeletal uptake with rapid blood clearance and minimum uptake in any of the major organs/tissue. After the successful outcome of studies carried out in animal models, human clinical studies of ¹⁷⁷Lu-EDTMP in cancer patients was initiated. First, pre-clinical evaluation was carried out in patients suffering from bone metastases due to prostate carcinoma to determine the distribution pattern of the agent in human patients. For this, a tracer dose of ¹⁷⁷Lu-EDTMP (111-148 MBq, 3-4 mCi) was injected to the patients. In the next step, Phase I/II clinical trials were initiated in human patients suffering

BARC NEWSLETTER

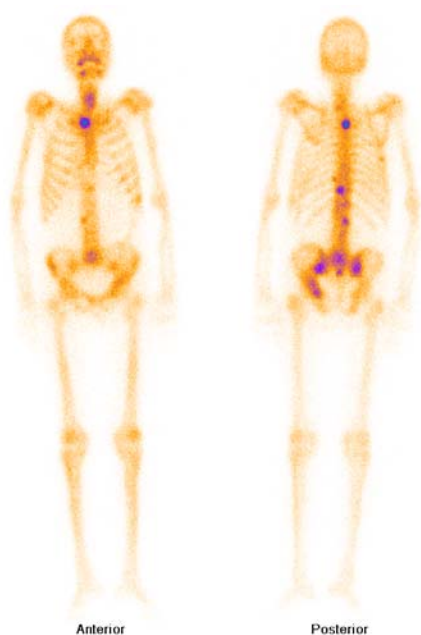


Fig. 2: Whole-body scan of a patient 24 h post-administration of ^{177}Lu -EDTMP showing excellent localization in osteoblastic lesions

from metastatic bone pain due to prostate carcinoma, where 2.59 GBq (70 mCi) dose of ^{177}Lu -EDTMP was administered to each patient. No adverse effect due to the therapy has been detected in any of the patients till date and all of them have experienced excellent pain-relief. The whole body scintigraphic image of a human patient recorded 24 h post-administration of the agent is shown in Fig. 2. Presently, ready-to-use ^{177}Lu -EDTMP is an approved radiopharmaceutical for use in India.

^{177}Lu -DOTA-TATE in peptide receptor radionuclide therapy (PRRT)

Peptide receptor radionuclide therapy (PRRT) using radiolabeled somatostatin analogues is a novel therapeutic modality for patients with somatostatin receptor-positive tumors. ^{177}Lu is being considered as a promising radionuclide to develop new agents for PRRT which will particularly useful for targeted therapy of smaller lesions owing to the small tissue penetration range of β^- particles of ^{177}Lu (maximum range $\sim 2\text{mm}$). ^{177}Lu labeled DOTA-TATE, the ^{177}Lu complex of the somatostatin analog octapeptide, Tyr³-Octreotate conjugated to DOTA, was envisaged as a promising agent for the treatment of patients suffering from inoperable neuro-endocrine originated tumors over-

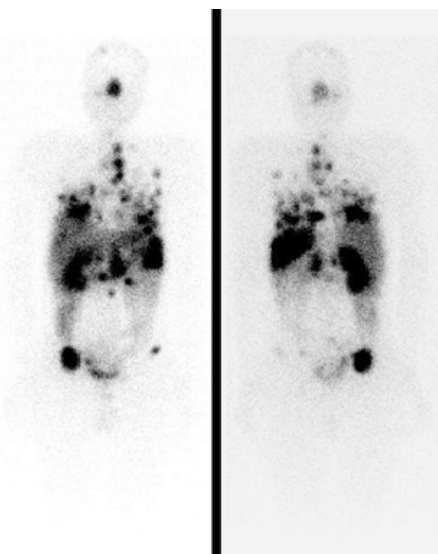


Fig. 3: Post-therapy scintigraphic images of a patient 24 h post-administration of 7.4 GBq of ^{177}Lu -DOTA-TATE

expressing somatostatin receptors. ^{177}Lu labeled DOTA-Tyr³-Octreotate (^{177}Lu -DOTA-TATE) was synthesized in high radiochemical purity and with maximum achievable specific activity by varying various reaction parameters. The preparation demonstrated encouraging results in *in vitro* cell binding studies as well as HT29 tumor bearing nude mice model. Subsequently, human clinical application of ^{177}Lu -DOTA-TATE were initiated in patients suffering from various forms inoperable neuroendocrine originated tumors. An optimized protocol for the preparation of therapeutic dose (5.55-7.4 GBq, 150-200 mCi) with maximum achievable specific activity and stability was developed in our laboratory by extensive variation of several parameters using ^{177}Lu with specific activity varying within a range. More than 1000 patients suffering from various types of neuroendocrine originated tumors have been treated in five major nuclear medicine centers across the country using ^{177}Lu -DOTA-TATE prepared following the developed protocol Fig. 3 shows the scintigraphic images of a patient with neuroendocrine tumor having extensive metastases recorded at 24 h post-administration of 7.4 GBq (200 mCi) of ^{177}Lu -DOTA-TATE.

^{177}Lu -HA for treatment of arthritis: Approximately 1% of the adult population worldwide is affected by rheumatoid arthritis which is manifested in pain, joint immobility and disability. Radiation synovectomy is a

BARC NEWSLETTER

radiotherapeutic modality for the treatment of rheumatoid arthritis wherein a β^- emitting radionuclide is administered locally by intra-articular injection in the form of colloid or radiolabeled particulate. ^{177}Lu could be considered as a promising radionuclide for use in radiation synovectomy owing to its favorable decay characteristics. Hydroxyapatite particles (HA) $[\text{Ca}_{10}(\text{PO}_4)_6(\text{OH})_2]$, regarded as one of the most suitable agents used as the carrier for applications in radiation synovectomy, have been envisaged for labeling with ^{177}Lu to develop a suitable radiopharmaceuticals for radiation synovectomy. Working in this direction, ^{177}Lu labeled HA particles could be prepared in high radiochemical purity ($\sim 99\%$) and excellent in vitro

stability by using ready to use kits of HA particles (particle size 1-10 μm) synthesized in-house. Biological efficacy of the radiolabeled preparation was tested both in normal as well as arthritis-affected knee joints of Wistar rats. The study showed complete retention of activity within the synovial cavity with no measurable activity leaching out from the joint till 168 h post-injection. Based on successful outcome of animal studies, ~ 370 MBq (10 mCi) dose of the agent was injected into the synovial cavity of the knee joints of patients suffering from rheumatoid arthritis after quality control studies. The scintigraphic images of the patients (Fig. 4) showed near-complete retention of the activity in the synovium even after 30 d post-injection. Six patients undergone treatment with ^{177}Lu -HA had reported significant symptomatic relief such as, reduced pain and increased joint mobility.

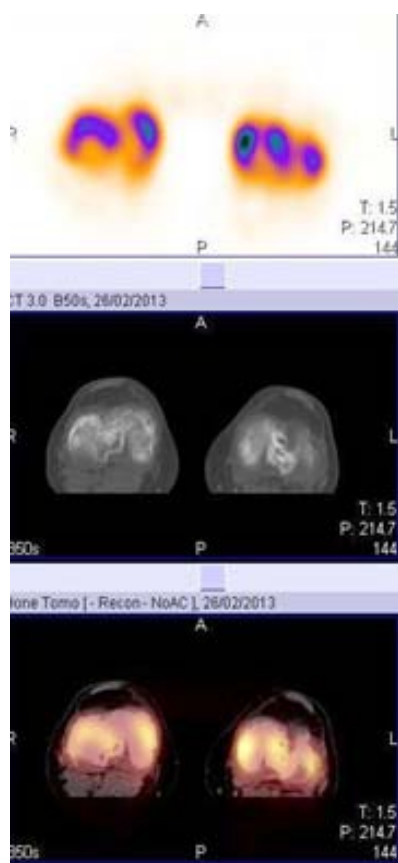


Fig. 4: SPECT, CT and fusion images of knee joint of a patient 1 month post-administration of 370 MBq of ^{177}Lu -HA

Acknowledgements

The author acknowledges IANCAS for bestowing the 'Tarun Dutta Memorial Young Scientist Award'. The encouragement and support of Dr. K.L. Ramakumar, Director, Radiochemistry and Isotope Group; Dr. Gursharan Singh, Associate Director, Radiochemistry and Isotope Group and Head, Isotope Applications Radiopharmaceuticals Division; Dr. A. Dash, Head Radiochemicals and radiation Sources Section and Dr. S. Banerjee, Head Radiopharmaceutical Chemistry Section, Isotope Applications Radiopharmaceuticals Division are gratefully acknowledged. The author is thankful to Dr. H.D. Sarma and staff members of Laboratory Animal House Facility of BARC and all the clinical collaborators. Development of ^{177}Lu radiopharmaceuticals in India is the outcome of a teamwork. The author expresses his sincere gratitude to all his co-workers, especially, Dr. Tapas Das and Shri K.V.V. Nair of Isotope Applications and Radiopharmaceuticals Division.

EFFECT OF SURFACE FINISHING OPERATIONS ON HIGH TEMPERATURE OXIDATION BEHAVIOUR OF ALLOY 800

Geogy J. Abraham, Kushal Singla, B. Sunil Kumar and Vivekanand Kain

Materials Science Division

This Paper received the Best Oral Paper Award at the East Asia Pacific Area Corrosion Conference (CORCON 2012), held at Goa, from 26-29th September, 2012

Abstract

Alloy 800 is being increasingly used as steam-generator tubing material for nuclear power plants. It is used for nuclear application with different surface finishes due to operations such as grinding, machining and buffing on the component. This results in a work hardened layer on the surface that alters the high temperature oxidation behaviour of alloy 800. The studies were aimed at characterizing the work hardened layer of the surface finished alloy 800 using x-ray diffraction (XRD) and electron back scattered diffraction (EBSD) to understand the residual stress and grain boundary character distribution. Also autoclaving of these alloys at 400 °C in steam showed varied oxide morphology which is observed under scanning electron microscopy –field emission gun (SEM-FEG). The variation in the oxide film formation rate due to the surface layer is different for different surface finishing operation. The oxide film morphology and composition plays an important role in localized corrosion resistance of alloy 800. The oxide film instability results in local breakage which acts as a precursor for stress corrosion cracking initiation in alloy 800.

Key words: alloy 800, surface finishing, residual stress, XRD, EBSD, autoclaving

Introduction

Surface finishing is an indispensable stage in the industrial fabrication process. Surface finish of the component is dictated by the last of the fabrication operations practiced like machining, grinding, wire brushing, shot peening etc. of components. The surface states can compromise corrosion resistances (pitting corrosion and SCC) of stainless alloys¹. Corrosion rates depend strongly on the surface condition of the material, and in particular the benefit of electropolishing surfaces has been demonstrated². These processes affect the electrochemical and mechanical stabilities of passive film and that of the near surface layers, by changing the surface reactivity and altering the near-surface residual stress/strain state. Surface preparation operations can alter the susceptibility of stainless alloys to SCC and its resistance to the initiation and propagation of pitting. Surface

finishing operations affect predominantly the surface layers of a component and stress-corrosion cracks initiate from the surfaces³.

The studies were aimed at characterizing the work hardened layer of the surface finished alloy 800 using XRD and EBSD to understand the residual stress and grain boundary character distribution. The surface properties would affect the oxidation rate and oxide morphology. Also autoclaving of these alloys at 400 °C in steam showed varied oxide morphology which is observed under SEM-FEG. The variation in the oxide film formation rate due to varied surface layer is different depending on the surface finishing operation. The oxide film morphology and composition plays an important role in localized corrosion resistance of alloy 800. The oxide film instability results in local breakage which would then act as a precursor for stress corrosion cracking initiation in alloy 800.

BARC NEWSLETTER

Table 1: Chemical Composition of alloy 800 used for study

Element	Ni	Cr	Fe	C	Mn	Si	Ti
(wt %)	27.2	21.6	45.49	0.05	2.31	1.37	0.71

Experimental

The composition of the alloy used for the present study is given in the Table 1:

The surface working operations were carried out on as received alloy 800. The grinding, machining and buffing operations were carried out on the lathe using different attachments. The operations led to the formation of surfaces with different finishes. These samples were then subjected to other characterization analysis to identify the thickness of the work hardened layer using the optical microscopy after electrolytic etching in 10 % oxalic acid solution, microhardness measurements on the surface was carried out, residual stress measurements were done by the XRD analysis using the $\text{Sin}^2\Psi$ method. The work hardened layer was characterized by the electron backscattered diffraction (EBSD) technique. The autoclaving of the samples in steam environment was simulated in the autoclave by using demineralized water at 400 °C for 72 h. The resulting oxide layer was characterized by scanning electron microscopy – field emission gun (SEM-FEG).

Results and Discussion

Microstructural observations

Following are the micrographs obtained for cross-section of grinding, machining and buffing coupons after electrolytic etching in 10% oxalic acid for 45 seconds at 10 V potential after diamond polished to

obtain a 0.5 μm surface finish. The red line drawn over the microstructure shows the work hardened layer on the ground, machined and buffed cross section of alloy 800. The work hardened layer for grinding is thicker than machined and buffed layer for alloy 800.

Electron Back Scatter Diffraction

The EBSD analysis along the cross section of the surface finished as well as on the as received and machined alloy 800 (fig. 3) revealed information regarding the

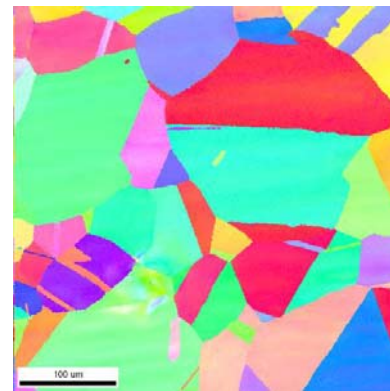


Fig. 3: EBSD mapping of (a) grain orientation in as received alloy (b) grain orientation and nano grain formation in machined alloy 800

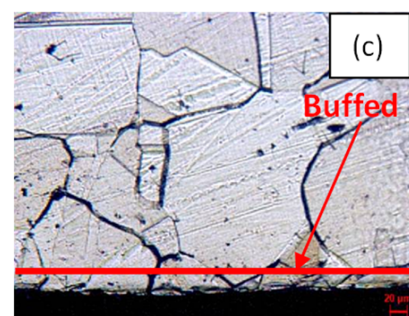
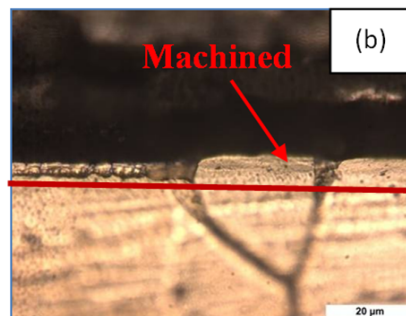
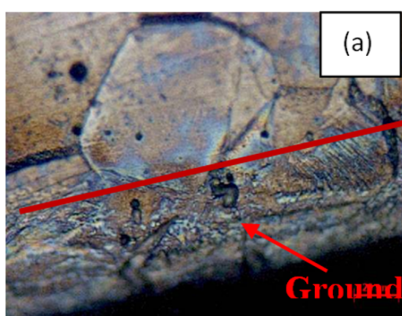


Fig. 2: Optical micrographs of the transverse section of surface worked alloy 800 showing the work hardened layer in (a) grinding (b) machining (c) buffing. The work hardened layer is denoted by the red line in the micrograph

BARC NEWSLETTER

grain boundary characteristics as well as nano grain formation in case of surface finished samples. The nano grain formation was seen in case of machining, grinding and buffing samples since these operations result in surface layer changes taking place and the grain boundaries close to the surface are only affected rest of the bulk material remain unchanged. The layer

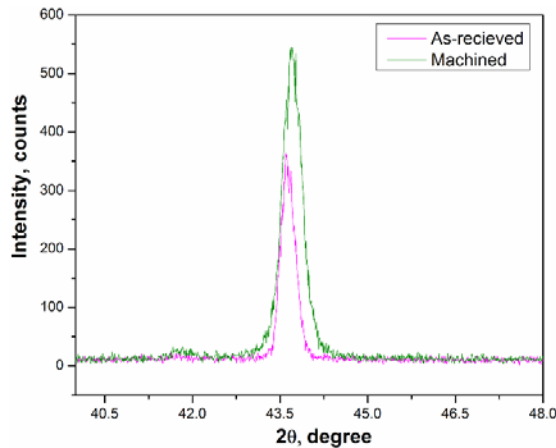


Fig. 5: XRD spectra for alloy 800 in the as received and machined condition showing peak broadening and shifting due to machining operation and nano hardness measurements.

Material condition	Hardness values (HV)
As- received (500 gf)	166
Machining (200 gf)	375
Grinding (200 gf)	325
Buffing (200 gf)	394

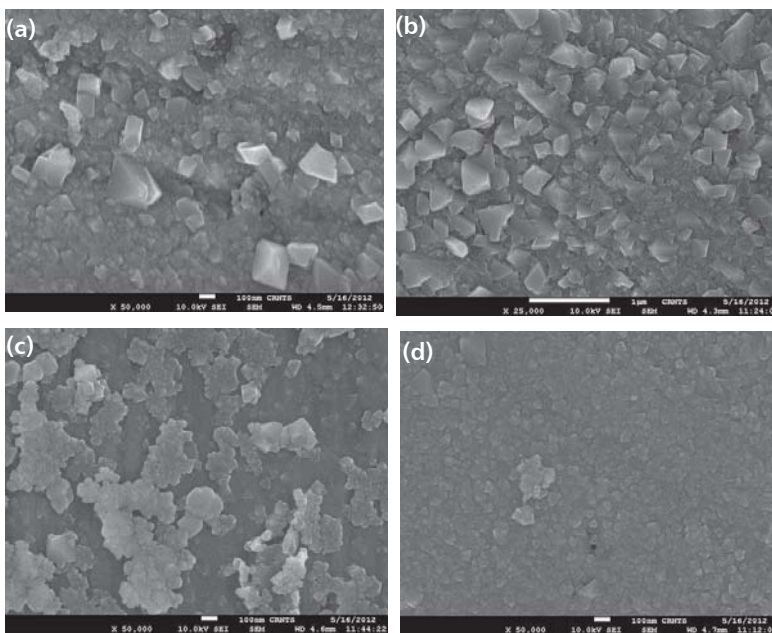


Fig. 7: SEM-FEG images of alloy 800 after autoclaving in (a) as received (b) machining (c) grinding (d) buffing surface operations showing varied oxide morphology

thickness of these nano grain formation was in the range of 40-60 μm .

XRD analysis

The XRD spectra showed in fig.5 (a) gives peaks that correspond to the austenite phase that is present in the alloy. The surface working has resulted in the shifting of the peaks due to the residual stress present in the alloy surface and presence of nano structure on the surface has resulted in the XRD peak broadening.

The normal stress for the as received alloy 800 is negative -97.5 MPa which denotes a compressive stress while in case of machining the values are positive 49.9 MPa indicating a tensile stress presence. The presence of tensile component on the surface results in the oxide film formed being less corrosion resistant since the defect densities within the oxide film increases. The nano hardness measurements were carried out on surface worked layer grinding, buffing and machining since the work hardening is restricted to a few tens of microns on the surface (Table 4).

SEM-FEG analysis

The SEM-FEG analysis on the alloy 800 as received and surface worked samples were done after autoclaving in steam at 400 $^{\circ}\text{C}$ for 72 h. Figure 7 shows SEM micrographs of oxide film formed on the different surface worked condition highlighting the difference in the oxide morphology. The as-received which was given a 600 grit emery polish showed blocky oxide characteristics. The oxide morphology on the surface worked alloy 800 shows similar behavior with flaky type of oxide platelets and they are much denser. The oxidation behavior of surfaces which have been given prior to cold work or subjected to surface finishing operations have been studied on stainless steels and nickel alloys⁵⁻⁷. In machining cubical oxides were observed as compared to the ground and buffed samples.

BARC NEWSLETTER

The conglomeration effect is seen in case of the ground sample which could be a result of the close proximity of the asperity lines thus increased roughness as compared to machined and buffed samples. The composition from EDS analysis confirms that the outer layer of the oxide film which is a spinel oxide of Ni, Fe and Cr as reported in literature.

Conclusions

- Surface working resulted in presence of tensile residual stresses on the surface as shown by XRD measurements.
- The surface roughness and residual stress on the alloy 800 after surface working operation result in change of oxide morphology.
- Grinding operations showed an increased oxidation rate as compared to the other surface working operations as seen by the conglomeration of oxide islands.

References

1. Truman J. E., Perry R., British corrosion journal, 1 (1965) 60-66.
2. Ziemniak, S.E., Hanson, M., Corrosion Science 50 (2008) 2465
3. Wit G., Bogdan K., Adam R., Surface Integrity of Machined Surfaces Chapter in the book 'Surface Integrity in Machining', Ed. J. Paulo Devim, Springer Publishers, (2010) 172-200.
4. Prevey, P.S. "Metals Handbook: Ninth Edition," Vol. 10, ed. K. Mills, pp 380-392, Am. Soc. for Met., Metals Park, Ohio (1986)
5. Higginson R. L., Green G., Corrosion Science, 53 (2011) 1690-1693.
6. Otsuka N., Nishiyama Y. and Kudo T., Oxidation of Metals, 62 (2004) 121-139.
7. Lu Y. H., Peng Q. J., Sato T., Shoji T., Journal of Nuclear Materials, 347 (2005) 52-68.

MARINE CYANOBACTERIA AS SUITABLE CANDIDATES FOR URANIUM RECOVERY FROM AQUATIC ENVIRONMENT

Celin Acharya and Shree Kumar Apte
Molecular Biology Division, Bio-Medical Group

This Paper received the Best Oral Paper Presentation Award at the Indo-US Workshop on Cyanobacteria, held at Lonavala, from Dec. 16-20, 2012

Abstract

Biorecovery/bioremediation of uranium from natural environment and from nuclear wastes is an important program of research in our division. We investigated the interactions of uranium with two marine cyanobacteria- a unicellular cyanobacterium *Synechococcus elongatus* BDU 75042 and a filamentous cyanobacterium *Anabaena torulosa* at a pH of 7.8, where the soluble carbonate complexes of UO_2^{2+} i.e. $[UO_2(CO_3)_2]^{2-}$ or $[UO_2(CO_3)_3]^{4-}$ are the predominant anionic species. The marine, unicellular cyanobacterium, *S. elongatus* was found to remove 72% (53.5 mg U g⁻¹ dry wt) of uranium from test solutions containing 100 μM uranyl carbonate within 1h. Light and scanning electron microscopy coupled with energy dispersive X-ray fluorescence (EDXRF) spectroscopy confirmed the uranyl adsorption by this organism. The filamentous, heterocystous cyanobacterium, *A. torulosa* was also found to bind uranium efficiently from aqueous solutions containing 100 μM uranyl carbonate at pH 7.8. The uranyl sequestration kinetics exhibited (a) an initial rapid phase, binding 48% uranium within 30min resulting in a loading of 56 mg U g⁻¹ of dry wt, followed by (b) a slower phase, binding 65% uranium with resultant loading of 77.35 mg U g⁻¹ in 24h. A detailed study revealed the involvement of acid soluble polyphosphates in uranium accumulation by this brackish water cyanobacterium. Also, long term experiments involving repeated exposure of *Synechococcus* biomass to fresh simulated sea water every third day, showed a loading of 2,960 μg U g⁻¹ in 4 weeks.

Introduction

Increasing contamination of the environment by uranium on account of its mining and disposal of tailings, nuclear power/weapons production, nuclear testing or nuclear accidents, is a worldwide problem. The versatility of microbial systems to remove heavy metals and radionuclides from their immediate environment is well recognized. Microbial interactions with metals form an important part of the natural biogeochemical processes and have important consequences for human society. It, is therefore, vital to advance our understanding of the metal-microbe interactions in order to develop suitable bioremediation strategies for metal contaminated sites.

Cyanobacteria represent a morphologically diverse group of oxygenic, gram-negative photosynthetic prokaryotes, which are widely distributed in freshwater, marine and terrestrial environments¹. They can tolerate, accumulate and detoxify metal contaminants in aquatic environments, thereby affecting the mobility and bioavailability of metals^{2, 3}. Their mass cultivation is economic and feasible which qualifies them as suitable bioremediation agents for the recovery and recycling of target metals⁴. Cyanobacterial cell surface harbours functional groups like carboxyl, phosphoryl, hydroxyl, amine, which bind metal ions to form metal ligand surface complexes. This potential is available even when the cells are dead. Cyanobacterial cells have been shown to concentrate several metals within the cells.

BARC NEWSLETTER

Intracellularly, the metal ion sequestration is facilitated either by polyphosphate bodies or small, cysteine rich proteins, called metallothioneins⁵.

Uranium exists primarily as U (VI) in oxic aqueous systems in the form of free divalent oxocomplex, UO_2^{2+} at $\text{pH} \leq 5$. The aqueous speciation of uranium undergoes major changes within a pH range of 5 to 7 because of complexation with carbonates and hydroxides⁶. Its contamination in surface, ground or natural waters (ponds, lakes, sea water), resulting from activities like mining, storage of radioactive waste, nuclear energy production, is a subject of intense public concern. Uranium is known for its chemical toxicity rather than radiotoxicity and its contamination in surface or ground water poses health hazards. In microbial systems, no specific mechanism has been attributed for uranium toxicity.

We carried out studies on uranium sequestration from micromolar concentrations of uranyl carbonate solutions ($\text{pH} 7.8$) by two marine cyanobacteria, one being unicellular i.e. *Synechococcus elongatus* BDU/75042 and another being a filamentous, heterocystous,

nitrogen fixing brackish water cyanobacterium, *Anabaena torulosa*.

Uranium sequestration by unicellular cyanobacterium, *Synechococcus elongatus* BDU/75042

Synechococcus elongatus cells exposed to $100\mu\text{M}$ or 23.8 mg L^{-1} U at $\text{pH} 7.8$ for 5h, bound 72% U resulting in a loading of 53.5 mg U g^{-1} dry wt⁷. Such U loaded cells exhibited black deposits around the cell margins as compared to control untreated cells (Figs. 1a and b). Treatment of U loaded cells with 0.1N HCl showed loss of black deposits from the cell surface along with $\sim 80\%$ U desorption (Fig. 1c). Energy Dispersive X-ray fluorescence (EDXRF) spectroscopy of uranium loaded biomass revealed all components of UL X-rays (UL_γ , UL_α , $\text{UL}_{\beta 1}$ and $\text{UL}_{\beta 2}$) confirming the association of uranium with the cells (Fig. 1d). Further, studies revealed that the uranium was predominantly associated with the EPS and the FT-IR results confirmed that the carboxyl and amide groups harboured within the EPS, were found to be involved in uranyl binding⁷. The uranyl binding efficiency of the heat killed or the non-viable *Synechococcus* cells was similar

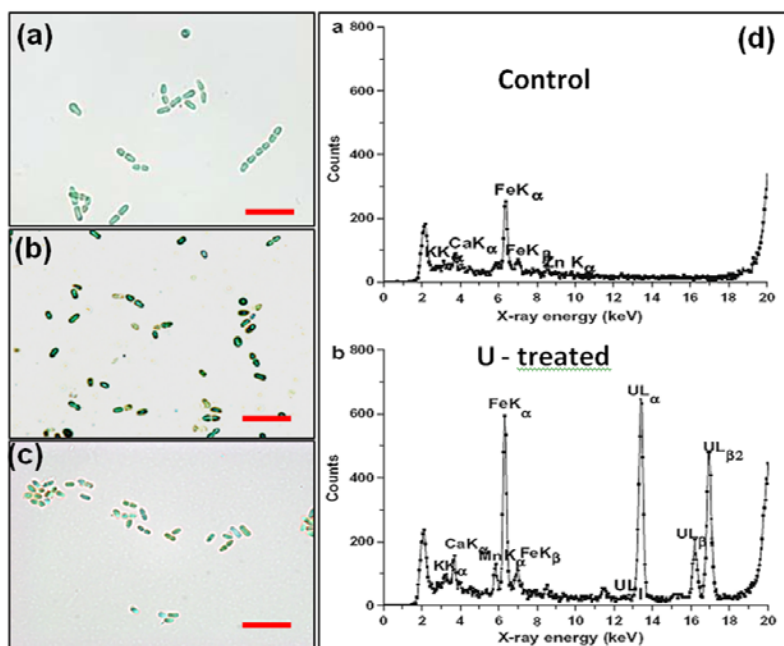


Fig. 1:Uranium exposure to *S. elongatus* cells. The mid-exponential phase cells were incubated (a) under control conditions or (b) were exposed to 23.8 mg L^{-1} uranyl carbonate $[\text{UO}_2(\text{CO}_3)_2]^{2-}$ at $\text{pH} 7.8$ for 5h resulting in loading of 53.5 mg U g^{-1} dry wt and (c) subsequently washed with 0.1N HCl . Cells were observed using bright field microscopy in a Carl Zeiss Axioscop 40 microscope, with oil immersion objectives (magnification 1500X), the bars in figs 1a, b and c represent $5\mu\text{m}$.(d) EDXRF spectra of control (i)and U loaded (ii) (53.5 mg U g^{-1} dry wt) *S. elongatus* biomass.

to that of live cells, corroborating their extracellular localization⁷.

Uranium sequestration by filamentous cyanobacterium, *Anabaena torulosa*

Our recent studies on uranium binding by *A. torulosa* have revealed the involvement of acid soluble polyphosphate bodies in uranium accumulation at pH 7.8⁸. On being challenged with 100 μ M uranyl carbonate for 24h at pH 7.8, under phosphate limited conditions, *A. torulosa* cells bound 65% (15.47 μ g mL⁻¹) of input U (23.8 μ g mL⁻¹) resulting in a loading of 77.35 mg U g⁻¹ dry wt. The kinetics of uranyl binding by live *A. torulosa* cells revealed a rapid phase (lasting for 30 min) resulting in 48% binding or a loading of 56 mg U/g dry wt., followed by a slower phase extending up to 24h and resulting in 65% binding or loading of 77.35 mg U/g dry wt., of the initially added 100 μ M U. Cells challenged with 23.8 mg L⁻¹ U for 24h showed dense dark granular structures resembling polyphosphate bodies as compared to the unchallenged cells (Figs. 2a, b and d). Nearly 80% (12.37 μ g mL⁻¹) of bound uranium (15.47 μ g mL⁻¹) could be released from 24h U challenged cells on desorption with 0.1N HCl. These 24h uranium challenged cells exhibited distinct 'hole' like structures upon acid desorption (Fig. 2c). Treatment of uranium loaded cells with 1N HCl at 100°C for 15 min resulted in complete extraction of total cell bound uranium and inorganic phosphate demonstrating co-localization of uranium with acid soluble polyphosphates⁸.

Uranium concentration from sea water using *Synechococcus elongatus* BDU/75042

Sea water is an inexhaustible and green source of uranium with an estimated uranium content of 4.5 billion tonnes. However, the uranium concentration in sea is very low i.e. 13nM or 3 μ g L⁻¹. Uranium sequestration from simulated sea water containing 3 μ g L⁻¹ U by the marine cyanobacterium, *S. elongatus* was assessed over short (24h-5d) or long (38d) exposure time periods⁹. The organism could remove 90-98% uranium resulting in a loading of 42 μ g U g⁻¹ in 5d (Fig. 3a). When evaluated for its ability to sequester uranium from simulated sea water under continuous replenishment conditions, *Synechococcus* biomass immobilized in dialysis bags, demonstrated superiority over the other tested chemical and biological alternatives in terms of high uranium loading values (2960 μ g g⁻¹) in 4 weeks, and tolerance to the high salinity of sea water (0.5M NaCl) (Fig. 3b). Nearly 85-90% of cell bound uranium could be desorbed using 0.1N HCl. The organism could sequester uranium (13,306 μ g U g⁻¹ in 24h) from aqueous solutions supplemented with 0.6 M NaCl and ~5 mg L⁻¹ [UO₂(CO₃)₂]²⁻ at pH 7.8 (simulated brine reject solutions)⁹.

Conclusions

Cyanobacteria represent an important component of aquatic environments like ponds, sea or oceans which receive direct or indirect metal contamination. Our recent

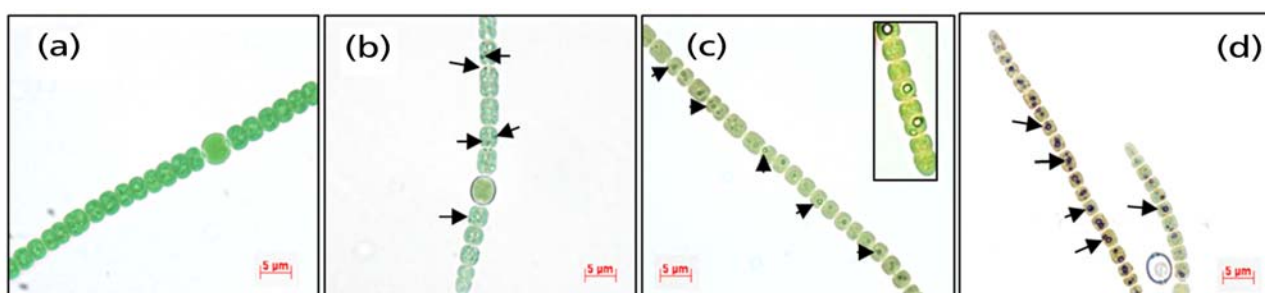


Fig. 2: Light microscopy of uranium exposed *A. torulosa* cells. The mid-exponential phase cells were incubated (a) under control conditions or (b) were exposed to 23.8 mg L⁻¹ uranyl carbonate [UO₂(CO₃)₂]²⁻ at pH 7.8 for 24h resulting in loading of 77.35mg U g⁻¹ dry wt. or (c) subsequently washed with 0.1N HCl and (d) the polyphosphate bodies in U loaded *A. torulosa* were stained using standard staining procedures with 0.05% toluidine blue. The arrows indicate the dense dark granular structures in uranium loaded *A. torulosa* cells (b) or the 'hole' like structures formed after their desorption by HCl (c) or (d) the distinct, dark red spheres, characteristic of polyphosphate bodies in U loaded *A. torulosa* cells after staining with toluidine blue, (magnification 1500X). The inset in (c) shows an enlarged view (magnification: 4000X) of morphological alterations caused by HCl washing of uranium loaded cells.

BARC NEWSLETTER

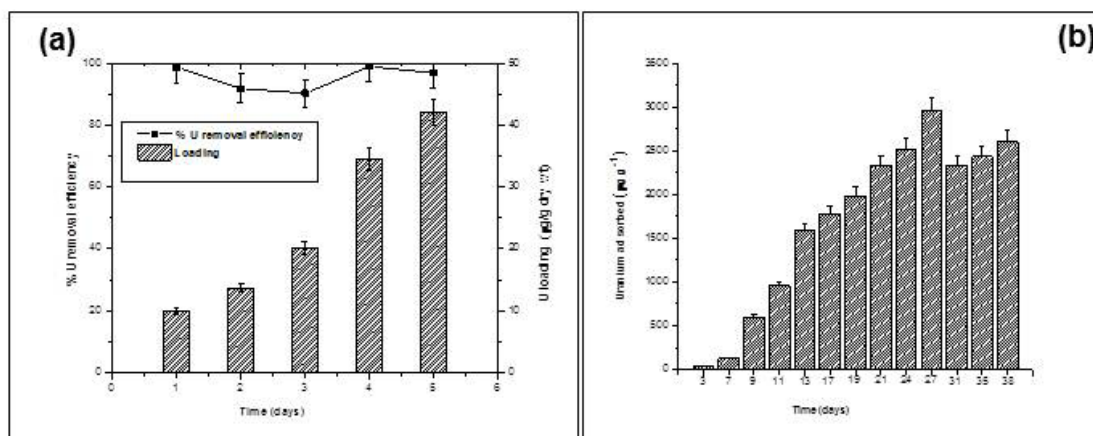


Fig. 3:Uranium sequestration by *S. elongatus* in simulated sea water supplemented with 13 nM of $[\text{UO}_2(\text{CO}_3)_2]^{2-}$. (a) Experiment wherein mid-log phase cells equivalent of $0.363 \text{ mg dry wt mL}^{-1}$ were exposed to fresh experimental solution (1L) everyday for 5 d and analyzed for cell bound uranium at specified intervals by ICP-MS (b) Cells, equivalent of 2.19 g dry wt., were distributed among 12 dialysis bags which were exposed to 3L test solution containing 13 nM uranium at pH 7.8 under continuous stirring and illumination. Test solution (3 L) was changed at 3 days interval. At specified time intervals, biomass was analyzed for cell bound uranium by ICP-MS

studies have identified two marine cyanobacteria with a high potential for uranyl sequestration from aqueous solutions above circumneutral pH. A fundamental understanding of mechanisms employed by cyanobacterial cells to resist/alleviate uranium toxicity will prove useful for development of strategies for either uranium recovery or remediation from aquatic environments.

Acknowledgements

The authors thank Prof. L. Uma and N. Thajuddin, NFMCC, Tiruchirapally, India for providing *Synechococcus elongatus* BDU/75042, Dr. Daisy Joseph, Nuclear Physics Division, BARC, for extending technical help in EDXRF analyses and Dr. S. A. Kumar, Analytical Chemistry Division, BARC, for extending technical help in ICP-MS analyses of uranium in cyanobacterial biomass samples.

References

1. Fogg GE, Stewart WDP, Fay P, Walsby AE. The Blue-green Algae. Academic Press, London (1973).
2. Li PF, Mao ZY, Rao XJ, Wang XM, Min MZ, Qiu LW, Liu ZL. Biosorption of uranium by lake-harvested biomass from a cyanobacterium bloom. *Bioresour Technol* 94, (2004):193-195.
3. Zhou PJ, Lin J, Shen H, Li T, Song LR, Shen YW, Liu YD. Kinetic studies on the combined effects of lanthanum and cerium on the growth of *Microcystis*

aeruginosa and their accumulation by *M. aeruginosa*. *Bull Environ Contam Toxicol* 72, (2004):711-716.

4. Garcia-Meza JV, Barrangue C, Admiraal W. Biofilm formation by algae as a mechanism for surviving on mine tailings. *Environ Toxicol Chem* 24, (2005):573-581.
5. Daniels MJ, Turner-Cavet JS, Selkirk R, Sun H, Parkinson JA, Sadler PJ, Robinson NJ. Coordination of Zn^{2+} and Cd^{2+} by Prokaryotic Metallothionein. *J Biol Chem* 273, (1998):22957-22961.
6. Choppin GR. Actinide speciation in the environment. *J Radioanal Nucl Chem* 273, (2007):695-703.
7. Acharya C, Joseph D, Apte SK. Uranium sequestration by marine cyanobacterium *Synechococcus elongatus* strain BDU/75042. *Bioresour Technol* 100, (2009):2176-2181.
8. Acharya C, Chandwadkar P, Apte SK. Interaction of uranium with a filamentous, heterocystous, nitrogen-fixing cyanobacterium *Anabaena torulosa*. *Bioresour Technol* 116, (2012):290-294.
9. Acharya C, Chandwadkar P, Joseph D, Apte SK. Uranium (VI) recovery from saline environment by a marine unicellular cyanobacterium *Synechococcus elongatus*. *J Radioanal Nucl Chem* 295, (2013):845-850.

BARC NEWSLETTER

DETERMINATION OF VAPOR PRESSURE OF H₂O OVER LaCl₃.7H₂O AND THE INTERMEDIATE COMPOUNDS BY DYNAMIC TRANSPIRATION METHOD

D.K. Sahoo

Rare Earths Development Section, Materials Group

and

R. Mishra and D. Das

Chemistry Division

and

N. Krishnamurthy

Fusion Reactor Materials Section, Materials Group

This Paper received the Best Oral Presentation Award (First Prize) at the 18th DAE-BRNS International Symposium on Thermal Analysis, held at Mumbai from 31st January to 2nd February, 2012

Abstract

The decomposition pattern of LaCl₃.7H₂O(s) was studied by thermogravimetric technique. Thermal decomposition of LaCl₃.7H₂O(s) results in the formation of LaCl₃.6H₂O(s), LaCl₃.3H₂O(s), LaCl₃.H₂O(s) and LaCl₃(s) in the temperature range 320 to 455K. The vapor pressure of over LaCl₃.7H₂O(s) and the intermediate compounds were determined employing dynamic transpiration technique. The vapor pressure of water for the decomposition of LaCl₃.7H₂O(s), LaCl₃.6H₂O(s), LaCl₃.3H₂O(s) and LaCl₃.H₂O(s) are found to be $\ln p_{\text{H}_2\text{O}}/\text{Pa} (\pm 0.01) = -13441.1/T + 48.1$ (328 < T/K < 333), $\ln p_{\text{H}_2\text{O}}/\text{Pa} (\pm 0.02) = -16655.4/T + 52.2$ (359 < T/K < 370), $\ln p_{\text{H}_2\text{O}}/\text{Pa} (\pm 0.004) = -17012.5/T + 52.4$ (380 < T/K < 385), and $\ln p_{\text{H}_2\text{O}}/\text{atm} (\pm 0.05) = -19733.9/T + 56.1$ (399 < T/K < 408), respectively.

Introduction

Lanthanum and its alloys have been extensively their use in varieties of functional materials [1]. The element is also found to be very effective in improving corrosion resistance of the stainless steel. Production of lanthanum metal from molten chloride electrolysis demands the use of anhydrous lanthanum chloride to increase current efficiency. However, this compound is highly hygroscopic and absorbs moisture when exposed to atmosphere. The main difficulty in obtaining lanthanum chloride in pure form is the formation of lanthanum oxychloride during dehydration process. Presence of small quantity of oxychloride inhibits the reduction process. It is necessary to find out an effective way to remove moisture from the raw material. For the production large quantities of anhydrous lanthanum chloride from LaCl₃.7H₂O(s), the knowledge of

thermodynamic stability of LaCl₃.7H₂O and its intermediates and mechanism of the dehydration processes are necessary. The present study was undertaken to determine the partial pressure of water over LaCl₃.7H₂O(s) and its intermediate hydrates.

Experimental

LaCl₃.7H₂O(s) used for the vapor pressure measurement experiments has been prepared from La₂O₃ of 99.99% purity. The sample was characterized by TG-DTA-EGA and XRD techniques..

The thermodynamic stability of the LaCl₃.7H₂O(s) and its decomposition products was determined by measuring vapor pressure of H₂O using a novel dynamic thermogravimetric transpiration instrument described elsewhere [2]. Experimental details involving the

measurement of temperature and flow rate are given in Refs [3,4]. The equilibrium condition for the measurement of vapor pressure was established by monitoring the mass loss of the sample per unit volume of the carrier gas (argon) swept over it as a function of flow rate at the mean temperatures of mass loss corresponding to each vaporization step. The flow rate where the apparent vapor pressure of water is independent of flow rate was used for measurement of vapor pressure.

Results and discussions

XRD plot of $\text{LaCl}_3 \cdot 7\text{H}_2\text{O}(s)$ sample, matches well with the standard pattern of $\text{LaCl}_3 \cdot 7\text{H}_2\text{O}(s)$ (PCPDF No03-0069). The composition of $\text{LaCl}_3 \cdot 7\text{H}_2\text{O}(s)$ was established by recording the thermogram of the sample. Fig.1 gives the TG-DTA plot of $\text{LaCl}_3 \cdot 7\text{H}_2\text{O}(s)$ recorded at the heating rate of 2 K/min under argon flow rate of 1 l/h. The compound under goes mass losses in four successive steps, in the temperature ranges 305-320 K, 328-370K, 370-391 K and 396-422 K, respectively. The second step which is the combination of two water loss steps was further resolved by differentiating the TG curve. The DTG curve indicated a kink at 349 K, which could be attributed to one more step for the water loss. The evolved gas analysis of the sample indicates the loss of only water molecule over the entire range of mass loss steps. No mass peak for the mass numbers 36 and 38 due to HCl molecules produced by the hydrolysis of the $\text{LaCl}_3(s)$ with the evolved water vapor could be observed. From Fig.1 it could be observed that for 219 mg of sample the mass loss obtained in different steps are 4.9 mg, 41.19 mg, 21.12

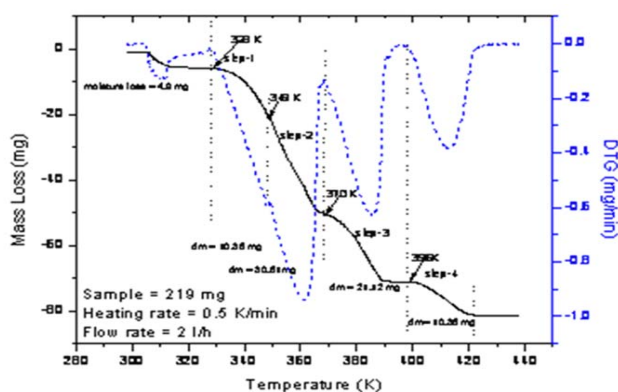
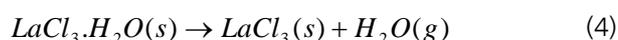
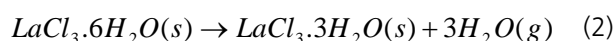
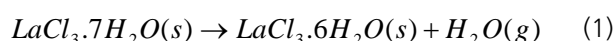


Fig. 1: TG-DTA plot of $\text{LaCl}_3 \cdot 7\text{H}_2\text{O}$ recorded at a rate of 0.5 k/minute under flow of argon atmosphere

mg and 10.38 mg in the temperature ranges 305-320 K, 328-370K, 370-391 K and 396-422 K, respectively. The mass loss 4.9 mg in the first step corresponds to the loss of adsorbed water. The mass loss of 41.19 mg in the second step, which may be further resolved into two steps (10.38 mg + 30.81 mg) is attributed to the combined loss of one and three water molecules. Similarly the third and fourth steps correspond to the loss of two and one water molecules, respectively. This is evident from the ratio of the number of moles of water lost from the sample in the corresponding steps i.e. 0.47: 3.96: 2.03: 1.0. Based on the above observations the decomposition mechanism of the $\text{LaCl}_3 \cdot 7\text{H}_2\text{O}$ can be described as



The above mechanism of decomposition of $\text{LaCl}_3 \cdot 7\text{H}_2\text{O}$ matches well with the recent reported data .

Measurement of vapor pressure

Fig. 2 gives the apparent pressure versus flow rate of the carrier gas for $\text{LaCl}_3 \cdot 6\text{H}_2\text{O}(s) \rightarrow \text{LaCl}_3 \cdot 3\text{H}_2\text{O}(s) + 3\text{H}_2\text{O}(g)$ reaction measured at 363 K for eq. (2). The apparent pressure of water vapor over the sample is independent of flow rate of the carrier gas in the flow rate region 1.90 5 to 2.25 l/h, indicating the establishment of equilibrium condition. Similar experiments were carried for the vaporization reactions eq(1), eq.(3) and eq.(4) under exactly similar conditions. It was observed that in all these steps the flow rate independent region of the apparent pressure (plateau) also falls within 1.5 to 2.5 l/h. Hence a constant flow rate of 2 l/h was chosen for the measurement of temperature coefficient of vapor pressure for each step.

The vapor pressure of water as function of temperature was calculated from the rate of mass loss for given

BARC NEWSLETTER

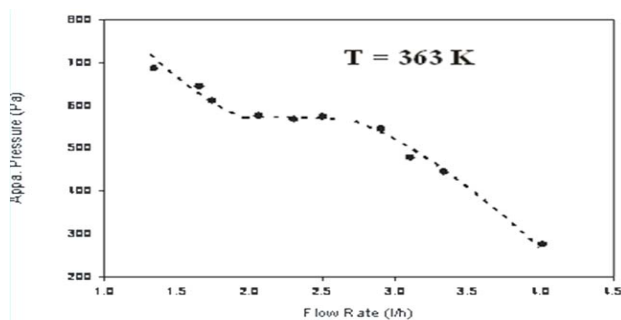


Fig. 2: The apparent pressure vs flow rate of carrier gas for $\text{LaCl}_3 \cdot 6\text{H}_2\text{O}(\text{s})$ $\text{LaCl}_3 \cdot 3\text{H}_2\text{O}(\text{s})$ reaction measured at 363K.

volume of carrier gas passed over the sample. The least square fitted vapor pressure data for the four consecutive steps are given in Fig.3. The corresponding linear equations could be expressed as $\ln p_{\text{H}_2\text{O}}/\text{Pa} (\pm 0.01)$

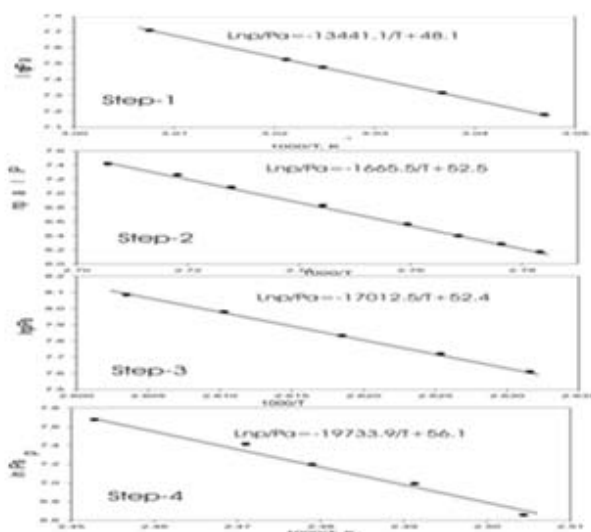


Fig. 3: Plots of $\ln p$ versus $1/T$ for the vaporization reaction $\text{LaCl}_3 \cdot 7\text{H}_2\text{O}(\text{s}) \text{LaCl}_3 \cdot 6\text{H}_2\text{O}(\text{s}) + \text{H}_2\text{O}(\text{g})$, $\text{LaCl}_3 \cdot 6\text{H}_2\text{O}(\text{s}) \text{LaCl}_3 \cdot 3\text{H}_2\text{O}(\text{s}) + 3\text{H}_2\text{O}(\text{g})$, $\text{LaCl}_3 \cdot 3\text{H}_2\text{O}(\text{s}) \text{LaCl}_3 \cdot \text{H}_2\text{O}(\text{s}) + 2\text{H}_2\text{O}(\text{g})$ and $\text{LaCl}_3 \cdot \text{H}_2\text{O}(\text{s}) \text{LaCl}_3(\text{s}) + \text{H}_2\text{O}(\text{g})$

$= -13441.1/T + 48.1$ ($328 < T/\text{K} < 333$), $\ln p_{\text{H}_2\text{O}}/\text{Pa} (\pm 0.01) = -16655.4/T + 52.2$ ($359 < T/\text{K} < 370$), $\ln p_{\text{H}_2\text{O}}/\text{Pa} (\pm 0.05) = -17012.5/T + 52.4$ ($380 < T/\text{K} < 385$) and $\ln p_{\text{H}_2\text{O}}/\text{atm} (\pm 0.05) = -19733.9/T + 56.1$ ($399 < T/\text{K} < 408$), respectively. The standard molar enthalpies of are found to be $111.7.1 \pm 2.8$, 138.5 ± 2.4 , 141.4 ± 1.6 and 164.1 ± 10.8 $\text{kJ} \cdot \text{mol}^{-1}$. Similarly the standard molar entropies of vaporization are found to be 399.9 ± 8.9 , 433.9 ± 6.7 , 435.7 ± 4.3 and 466.5 ± 26.6 $\text{J} \cdot \text{mol}^{-1} \text{K}^{-1}$, respectively.

Conclusions

The decomposition pattern of $\text{LaCl}_3 \cdot 7\text{H}_2\text{O}$ was established by thermogravimetric technique. The equilibrium vapor pressure of $\text{H}_2\text{O}(\text{g})$ over $\text{LaCl}_3 \cdot 7\text{H}_2\text{O}$ and the intermediate compounds were determined.

References

1. "Sophie Legeai, Sebastian Diliberto, Nicolas Stein, Cltilde Boulanger, Julien Estager, Nicolas Papaiconomou, Micheline Draye" *Electrochemistry Communications 10* (2008) 1661-1664.
2. 20. S.R. Dhanvadkar. A.S. Kerkar and M. S. Samant. *Themmchim. Acta.217* (1993) 175.
3. 21. S.R. Dhuvmdkar. M.S. Samant and AS. Kerkar, in PIV Ravindran.M. Sudersanan.S.R. Bharadwaj and S.R. Dhanvadkar (eds.), *From.Ninth National Symp. OnThemudAnalysis. Gw Uniwrsity. Gw.8-10* November 1993. p.590.
4. O.M. Sridharan, S.R. Dharwadkar and M.S. Chattdnsckharaiah. *BARC Int. Rep. No. i-239. 1973.*

MAGNETIC NANOPARTICLES FOR TARGETED-DRUG DELIVERY: A COMBINATORIAL APPROACH OF HYPERTHERMIA AND RADIATION FOR THE IMPROVEMENT OF CANCER THERAPY

Neena V. Jadhav, Amit Kumar and Badri N. Pandey

Radiation Biology and Health Sciences Division

and

R. S. Ningthoujam and R. K. Vatsa

Chemistry Division

This Paper received the 'Best Idea Award' at the International Conference on Radiation Biology (ICRB-2012) and 11th Biennial Meeting of the Indian Society for Radiation Biology, held at Navi Mumbai, from November 22-24, 2012

Abstract

Despite the several technological developments and extensive research in cancer therapy, a high success rate of cancer treatment still needs to be achieved. Limitations posed by conventional therapeutic modalities include side effects associated with damage to normal organs/tissues and resistance exerted by cancer cells. Emerging advantages of magnetic nanoparticles (MNPs) based drug delivery and therapy offers opportunities for targeted delivery of drugs to tumor site as well as to overcome the resistance of cancer cells upto some extent. When MNPs are placed under alternating current magnetic field conditions, they generate heat at the tumor site sufficient enough to kill cancer cells. Such ability of MNPs provides a potential to combine them with another modality of cancer therapy i.e. hyperthermia, in which increased temperature (40-43 °C) at tumor site kills the cancer cells. MNPs overcome the limitations of conventional modalities of hyperthermia application. The ability of MNPs to induce localized heat can be further exploited to release the drug from temperature sensitive liposomes at hyperthermic temperature. The article provides overview of the potential of MNPs for drug delivery and basis of employing them for combinatorial approach to improve the cancer radiotherapy.

Introduction

Cancer remains one of the leading causes of death all over the world. The classical anticancer modalities like chemo- and radiation- therapy present limitations such as non-specific targeting of chemotherapeutic drugs, therapeutic resistance of tumor cells to anticancer agents and radiation, and adverse side effects in normal tissues/organs [1-3]. These limitations necessitate the need for combinatorial approach(s) for cancer therapy. In recent years, super-paramagnetic iron-oxide nanoparticles (SPIONs), due to their unique magnetic properties and biocompatibility, have gathered immense attention in the field of cancer-nanotherapeutics [4]. Moreover, functionalization of

SPIONs with various fluorophores or tumor-specific markers would provide additional advantages of developing newer approaches of imaging and tumor specific-drug delivery. In addition, these functionalized-SPIONs can be co-encapsulated with anti-cancer drugs in temperature-sensitive liposomes (TSLs) for combinatorial cancer hyperthermia and chemotherapy. Hyperthermia not only enhances blood flow (by vasodilation) and oxygen supply in tumor, (which allows an effective drug distribution), but also sensitizes tumor cells to chemo- and radiation- therapy, thus offers a combinatorial modality for cancer therapy.

Combinatorial approaches require the development of magnetic nanocarriers with the following properties:

BARC NEWSLETTER

(i) a uniform size distribution, (ii) good dispersibility under physiological conditions, (iii) chemical stability and biocompatibility, and (iv) amenable to surface functionalization for targeted delivery of both chemotherapeutic drug and magnetic nanoparticles (MNPs) to tumor site. Due to high surface-to-volume ratio, MNPs tend to form aggregates and show undesirable chemical reactions. Therefore, development of effective surface protection strategies is important to improve chemical and physical stability of MNPs for their better biological action at cellular and molecular level. These strategies involve coating of MNPs with small organic molecules or surfactants, polymers (e.g. dextran) or inorganic molecules [2, 5]. These nanocarriers in-turn can be suitably modified and utilized for targeted-drug delivery and hyperthermia applications. One of the strategies to co-deliver MNPs and anti-cancer drugs at tumor site involves their co-encapsulation in TSLs, which in-turn can be made specific-to target a tumor by functionalizing them with a ligand, antibody or a tumor-specific cell surface marker. TSLs composed of a special type of lipid molecules are sensitive to release their contents beyond a specific temperature, such as hyperthermic temperature of $>42^{\circ}\text{C}$. Hence, tumor specific-functionalized-TSLs loaded with MNPs and anti-cancer drugs can be developed and evaluated to release their cargo for enhanced anticancer effect in combination with hyperthermia. Thus, present rationale of combination of MNPs and TSLs in a single chemical

entity termed as 'magneto-liposomes' is expected to overcome limitations of conventional cancer therapy. These 'magneto-liposomes' may offer following potential advantages: (i) suitable for new generation cancer nano-diagnostics; (ii) may improve drug delivery; (iii) may enhance efficacy of hyperthermia in combination with radiation.

In present work, iron-oxide MNPs-coated with oleic acid (MN-OA) were synthesized and characterized by using various physico-chemical techniques. The anticancer efficacy of MN-OA in combination with hyperthermia was evaluated in mouse fibrosarcoma tumor cells, WEHI-164, under culture conditions. Further, therapeutic effect of MN-OA in combination with hyperthermia treatment was validated in fibrosarcoma tumor-bearing animal models. Based on these promising results, further development is in progress to formulate magneto-liposomes for tumor radiosensitization by hyperthermia.

Synthesis and evaluation of anticancer activity of MN-OA in WEHI-164 cells under magnetic hyperthermia conditions

MNPs were synthesized by co-precipitation method using ferrous sulphate and ferric chloride mixed in a molar ratio of 1: 2. The MNPs were functionalized with oleic acid (OA) and further characterized for size, which was found to be ~ 10 nm by transmission electron

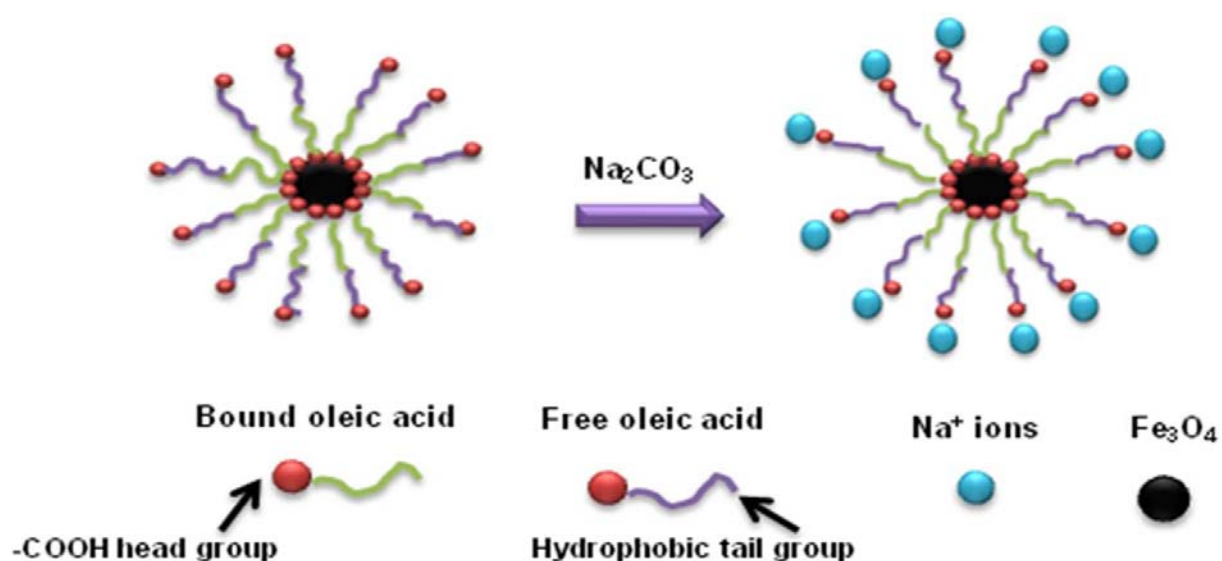


Fig. 1 Scheme for dispersion of MN-OA in aqueous medium using sodium carbonate

microscopy and X-ray diffraction studies. Their superparamagnetic behavior was confirmed by magnetization study using Superconducting Quantum Interference Device. For better biological applicability, it is necessary that the MNPs are dispersible in physiological medium. However, due to hydrophobic nature of OA, MN-OA is not water dispersible. Therefore, based on understanding of chemistry, a condition was optimized using sodium carbonate as a dispersing agent to enable proficient dispersion of MN-OA in physiological medium. The mechanism of dispersion was revealed by FT-IR analysis, which showed that OA is covalently bound to the Fe_3O_4 core via carboxylic group. Sodium ions were found to interact with the carboxylic group of loosely bound OA, whereas its tail interacts with bound-OA by hydrophobic interactions (Fig. 1). The heat generation ability of MN-OA was studied under alternating current magnetic field conditions (AMF, 265 kHz radiofrequency, 335 Oe magnetic field, coil diameter of 6 cm having 4 number of turns). Under AMF conditions, MN-OA induced temperature rise in hyperthermic range even at low concentration (5 mg/ml) [5].

Further, the interaction of MN-OA with mouse fibrosarcoma (WEHI-164) was examined by staining tumor cells with prussian blue for iron localization, and with Nile blue A (a fluorescent probe) for OA distribution using bright field and confocal microscopy. Results

showed that MN-OA interacts prominently with the plasma membrane of tumor cells (Fig. 2) [5]. Further, their hyperthermia efficacy was evaluated in tumor cells by trypan-blue assay. MN-OA treatment in combination with hyperthermia showed a significant reduction (~64%) in viability of tumor cells. The mode of cell death was found to be apoptosis, which was increased from ~ 2.7 folds in cells-treated with MN-OA only -to~ 4.8 folds in cells treated with MN-OA plus hyperthermia [5].

Evaluation of hyperthermia efficacy of MN-OA in fibrosarcoma tumor model in BALB/c mice

To study *in-vivo* hyperthermia efficacy of MN-OA, a fibrosarcoma tumor model was developed by injecting WEHI-164 cancer cells subcutaneously in hind leg of BALB/c mice. Once palpable tumors were visible, they were subjected to treatment with MN-OA and hyperthermia (Fig. 3A). Animals treated with MN-OA in combination with induction heating showed significant tumor regression as compared to control. To further validate these results, *in-vivo* imaging was employed to measure the tumor size more accurately and sensitively. This was accomplished by stably transfecting the WEHI-164 tumor cells with luciferase gene (Fig. 3B). These results indicate the suitability of MN-OA as a potential candidate for the development of magneto-liposomes for combinatorial therapy of cancer, wherein the efficient hyperthermia ability of MN-

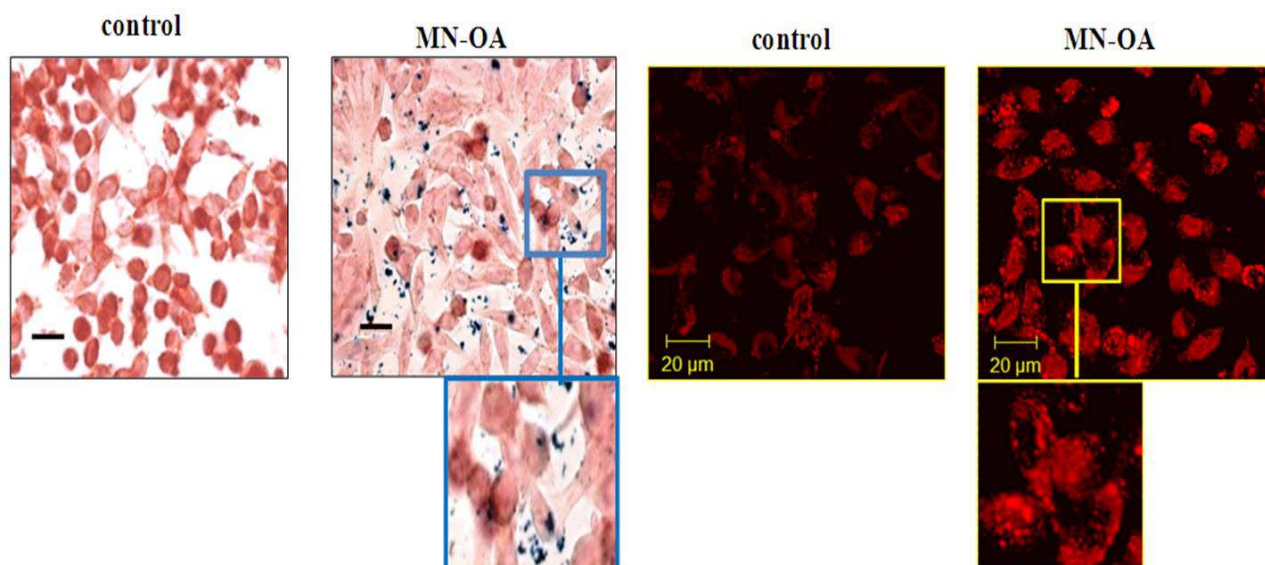


Fig. 2: Cellular localization of MN-OA in WEHI-164 tumor cells studied by (A) Prussian blue staining (B) confocal laser scanning microscopy after Nile blue staining.

BARC NEWSLETTER

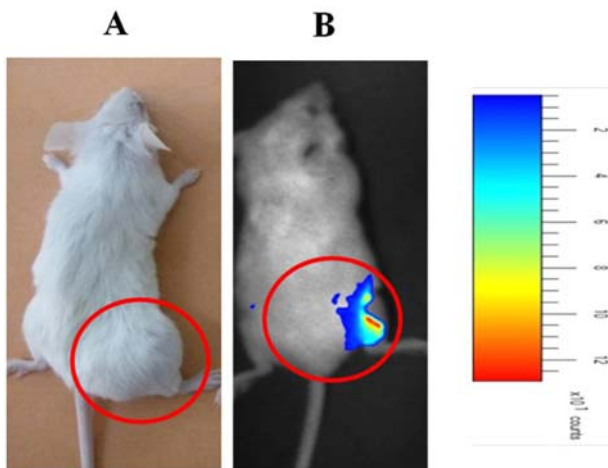


Fig. 3: Image of (A) BALB/c mice bearing fibrosarcoma tumor on hind leg (B) luminescence of WEHI-164 tumor cells (stably transfected with luciferase gene). Tumor was visualized after intraperitoneal injection of D-luciferin (substrate) by Live Animal Imaging System

OA can be combined with temperature-sensitive liposomes (encapsulating anti-cancer drugs) for targeted drug delivery and combined chemo, hyperthermia and radiation therapy of cancer.

Proposed idea for design and development of magneto-liposomes for combinatorial therapy of cancer

Development of magneto-liposomes involves synthesis of TSLs incorporating MN-OA in the membrane and anti-cancer drugs (e.g. doxorubicin) in hydrophilic core. MN-OA would induce magnetic heating of TSLs at the tumor site. When *AMF* is applied, the heat generated by MN-OA in tumor would result in efficient release of anti-cancer agent from TSLs. In addition, the heat dissipation from MN-OA under magnetic induction would lead to the hyperthermic therapy of cancer (Fig. 4). Furthermore, magneto-liposomes, in combination with radiotherapy, would enhance anticancer effect by radio-sensitizing mechanisms. Thus, anticancer magneto-liposomes exhibit an immense potential which however needs to be evaluated for its radiation enhancement effect using suitable tumor models.

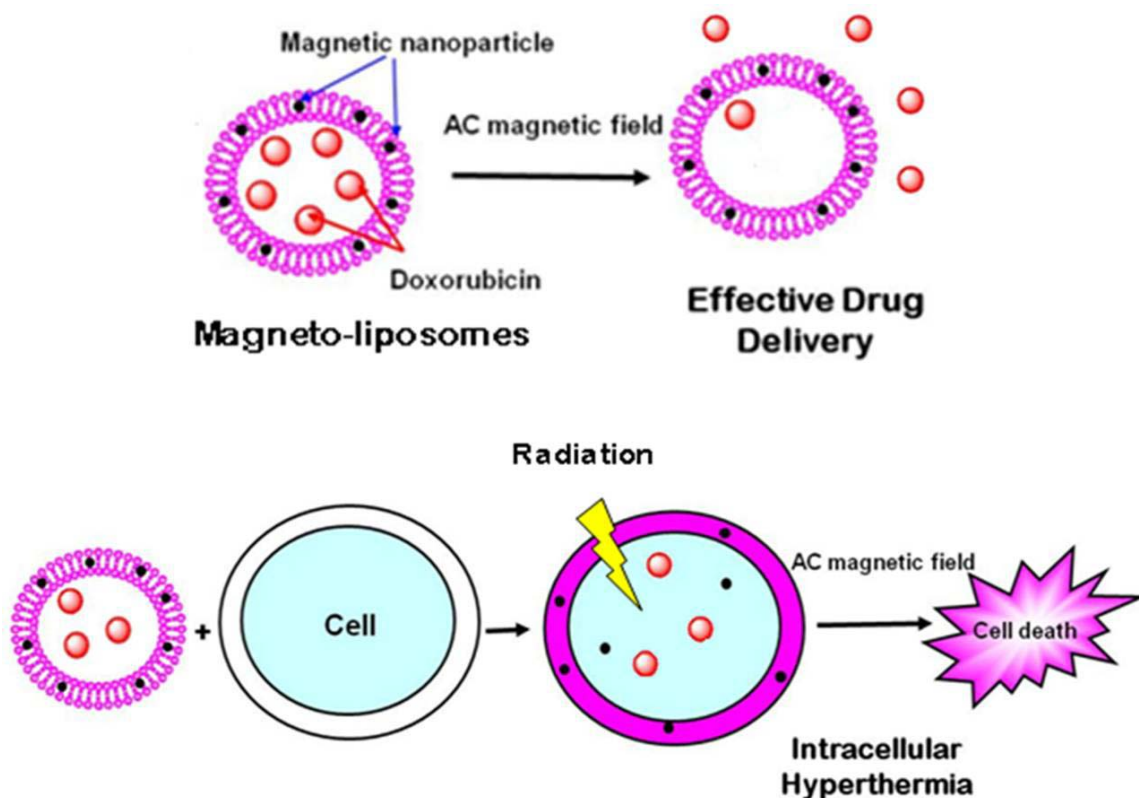


Fig. 4: Scheme for application of magneto-liposomes for combinatorial therapy of cancer

BARC NEWSLETTER

Acknowledgement

WEHI-164 cell line stably transfected with luciferase gene was constructed at ACTREC, Navi Mumbai by obtaining plasmid from Dr Pritha Ray. Authors acknowledge the help of Shri Manjoor Ali and Mrs. R. Vasumathy, Radiation Biology & Health Sciences Division for their technical assistance during confocal microscopy imaging.

References

1. K. Cho, X. Wang, S. Nie, Z. Chen and D. M. Shin, "Therapeutic nanoparticles for Drug Delivery in cancer", *Clin Cancer Res* 14 (2008) 1310.
2. W. Wu, Q. He and C. Jiang, "Magnetic Iron Oxide Nanoparticles: Synthesis and Surface Functionalization Strategies", *Nanoscale Res Lett* 3 (2008) 397.
3. R. S. Ningthoujam, R. K. Vatsa, Amit Kumar, B. N. Pandey, "Functionalized Magnetic Nanoparticles: Concepts, Synthesis and Application in Cancer Hyperthermia", *Functionalized Materials*. 2012, Editors: S. Banerjee and A. K. Tyagi, Elsevier Publications (pages 229-260).
4. K. C. Barick, S. Singh, N. V. Jadhav, D. Bahadur, B. N. Pandey and P. A. Hassan, "pH-Responsive peptide Mimic Shell Cross-Linked Magnetic Nanocarriers for Combination Therapy, *Adv. Funct. Mater.* 22 (2012) 4975.
5. N. V. Jadhav, A. I. Prasad, Amit Kumar, R. Misra, S. Dhara, K. R. Babu, C. L. Prajapat, N. L. Misra, R. S. Ningthoujam, B. N. Pandey and R. K. Vatsa, "Synthesis of oleic acid functionalized Fe₃O₄ magnetic nanoparticles and studying their interaction with tumor cells for potential hyperthermia applications, *Colloids and Surfaces B: Biointerfaces*, 108 (2013) 158.

BARC NEWSLETTER

INTEGRATED APPROACH FOR ENZYME PURIFICATION FROM NON-CLARIFIED CRUDE HOMOGENATE USING MACROPOROUS CRYOGEL MATRIX

Anuj Tripathi

Nuclear Agriculture and Biotechnology Division

and

Ashok Kumar

Department of Biological Sciences and Bioengineering, Indian Institute of Technology Kanpur

This Paper received the Best Paper Award at the DAE-BRNS Biennial Symposium Separation Science & Technology 2012, (SESTEC 2012), held at Mumbai, from February 27 - March 1, 2012

Abstract

This study presents the application of macroporous polymeric cryogel as a continuous chromatographic matrix for the purification of β -glucosidase from non-clarified crude homogenate. The monolithic cryogel showed high flow-rate and could easily transport the macromolecules due to the large pore size in the range of 30-110 μm . Cu^{2+} -iminodiacetic acid modified cryogel was further used for separation of histidine-tagged β -glucosidase directly from the disrupted cell homogenate. Under the three repetitive runs, the average purification factor, percent recovery and yield was approximately 2, 93% and 80%, respectively. These results showed that continuous macroporous cryogels can be potentially utilized for direct capture of labile products from suspensions and cell homogenate.

Introduction

One of the most promising strategies for achieving a better operational economy is the reduction of the number of steps by integrating the primary separation and capture of the product from the cell suspension with the initial purification. Such integrated downstream processing implies the application of the separation technologies capable of processing particle-containing solutions. Recently supermacroporous monolith cryogel matrix with pore size up to 200 μm has emerged as potential stationary phase for chromatographic applications. Cryogel has large pores to accommodate cell debris and even the cells without being blocked. Since one decade we have shown various biomedical and bioengineering applications of cryogel.

In this work we aimed to investigate the monolithic macroporous cryogel column as a robust and integrated

chromatographic technique for the isolation of recombinant protein (thermostable β -glucosidase, $(\text{His})_6$ -TnBglB, MW: 81 kD) from non-clarified crude cell homogenate. The synthesis of macroporous polymeric cryogel and its further modification as immobilized metal affinity chromatographic (IMAC) column was accessed for purification of enzyme.

Methodology

Cultivation and recovery of E. coli containing recombinant β -glucosidase

The recombinant *E. coli* strain Turner (DE3) was grown overnight on LB-agar plate with ampicillin (100 $\mu\text{g}/\text{ml}$) at 37°C. Single colony was used for the mass culturing of cells into LB broth^{+amp} medium by incubating at 37°C on shaker with rotor speed 200 rpm. 1mM IPTG induction was given to the fermentation broth when

BARC NEWSLETTER

O.D.₆₀₀ reached to 0.6 to 0.8 and incubated at same conditions for next 4 to 5 h. The resulting mass culture was centrifuged at 6,500 g for 30 min, and the cell pellet was collected and stored at -20°C.

Synthesis of poly(acrylamide-co-allylglycidyl ether) cryogel

Monomers of acrylamide (AAm) (4%; w/v), Bis-acrylamide (MBAAm) (1%; w/v) and allyl glycidyl ether (AGE) (1%; v/v) were dissolved in deionized water. Then APS (98 mg) and TEMED (115 µl) were mixed in the solution followed by pouring into glass column. This glass column was incubated at -12 °C for 16 h. The obtained gel was thawed in dH₂O and further modified for chromatography application.

Coupling of Cu²⁺-IDA to poly(acrylamide-co-allylglycidyl ether) cryogel column

The poly(AAm-co-AGE) cryogels were activated by 100 ml of 0.5 M Na₂CO₃ solution at a flow rate of 2 ml/min. The IDA solution (0.5 M) was cyclically circulated through the cryogel column at room temperature for overnight followed by washing with dH₂O until the pH reached to neutral. Then CuSO₄ solution (0.5 M) was applied for 4 h. Finally, the column was washed with dH₂O for purification process.

Purification of β-glucosidase using IMAC cryogel column

Microbial cell pellet was disrupted by sonication to release the protein from the cells. This non-clarified

crude was directly loaded (0.5 ml min⁻¹) on to the Cu²⁺-IDA coupled poly(AAm-co-AGE) cryogel with equilibration buffer (20 mM Tris-HCl, 100 mM NaCl, pH 7.5). The column was washed with four column volumes of washing buffer (20 mM Tris-HCl, 100 mM NaCl, 5 mM imidazole, pH 7.5) at 2 ml min⁻¹. Elution was started with elution buffer (20 mM Tris-HCl, 100 mM NaCl, 250 mM imidazole, pH 8.0) at 1 ml min⁻¹. All the chromatographic fractions were collected and analyzed.

Results and Discussions

Properties and modification of poly(acrylamide-co-allylglycidyl ether) cryogel

The poly(AAm-co-AGE) cryogel was synthesized by polymerization of monomers at sub-zero temperature. The water saturated poly(AAm-co-AGE) cryogels were soft, spongy and squeezable in nature. The pore diameter of cryogel was found in the range of 30 - 110 µm and the average pore size was in the range of 65 - 80 µm with 90 % porosity confirmed by SEM (Fig. 1A). The thick pore wall suggested that the cryogels could withstand at high solvent flow and provide strong support for immobilization of ligands and biomolecules. The smooth surface of cryogel suggests protection from non-specific binding. The large interconnected pores in cryogel act as capillaries and can quickly absorb large amount of water with high flow rate. Hydraulic permeability (1 × 10⁻³ m⁴N⁻¹s⁻¹) suggests interconnected porous architecture in the cryogel. The large and interconnected pores of cryogel matrix render the possibility of accommodating molecules and their

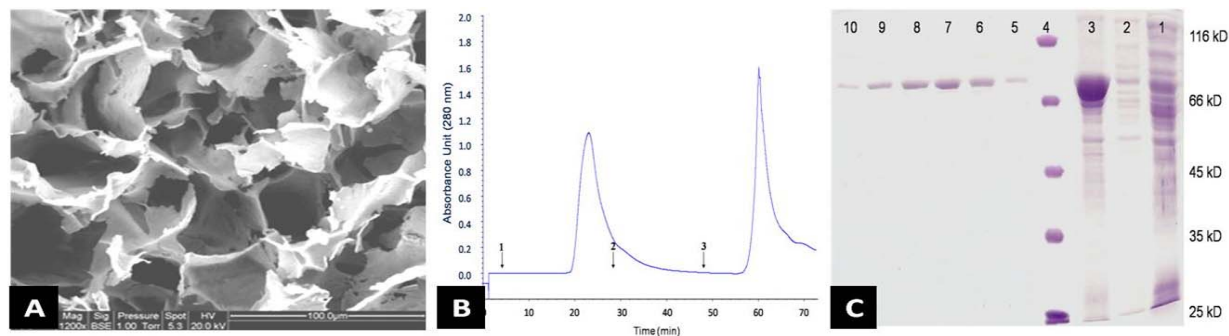


Fig. 1: Scanning electron micrograph of poly(acrylamide-co-allylglycidyl ether) cryogel (A). Chromatography profile of non-clarified β-glucosidase purified using cryogel column (B), where the first peak shows the unbound protein and second peak shows the elution pattern of (His)₆-β-glucosidase bound on the column. The SDS-PAGE electrophoresis of β-glucosidase protein samples at different stages of chromatography (C).

BARC NEWSLETTER

passage. These potential characteristics demonstrate the suitability of prepared cryogel column for affinity chromatography. AGE was chosen to insert the reactive epoxy groups into the cryogel. IDA was later introduced through these epoxy groups. IDA is a tridentate ligand, which binds to metal ions through three co-ordination sites and leaves equal number of sites for proteins to bind. Cu^{2+} shows higher protein retaining capacity compared to others ($\text{Cu}^{2+} > \text{Ni}^{2+} > \text{Zn}^{2+} > \text{Co}^{2+}$). Thus Cu^{2+} -IDA coupled poly(AAm-co-AGE) cryogel was further used as a IMAC column for separation of His₆-tag- β -glucosidase.

Purification and quantification of β -glucosidase enzyme

The sharp elution profile of β -glucosidase protein was obtained during the chromatography process, which suggest good performance of the IMAC cryogel column (Fig. 1B). The slow flow rate (0.5 ml/min) for protein loading was chosen to increase the interaction time with surface ligands of the column (Fig. 1B; arrow 1). Washing was started at 28 min (Fig. 1B; arrow 2). There was no protein peak was observed in the washing step, which suggested strong and selective binding of protein to the Cu^{2+} -IDA cryogel column. Imidazole shows more affinity towards the metal ions (Cu^{2+}) at higher concentration than the histidine. Thus, elution was started at 48 min (Fig. 2A; arrow 3) with imidazole containing buffer, which results in dissociation of His₆-tag-proteins to metal ions and fractions were collected for qualitative and quantitative analysis.

The SDS-PAGE of the purified (His)₆- β -glucosidase showed sharp bands of the purified enzyme (Fig. 1C; fractions 1 to 6 in lane 5 to 10, respectively). The results suggest that large quantity of target protein was bound to the Cu^{2+} -IDA cryogel column. The SDS-PAGE electrophoresis was also performed with the supernatant (lane 1), unbound (lane 2) and pellet (lane 3) of the crude cell-lysate along with the molecular weight standard (lane 4) suggested that the eluted fractions were about the molecular weight of 80 kD, and most of the targeted protein was in aggregated pellet form. Results showed that the pooled unbound protein sample have very less protein of interest but have sufficient amount of other non-specific proteins

compared to eluted fractions as shown in lane 2 of Fig. 1C (unbound), while lane 5 to 10 showed single peak of β -glucosidase (elution fractions). These results support that the Cu^{2+} -IDA- poly(AAm-co-AGE) cryogel column has high affinity for binding a protein from unprocessed crude cell-lysate. The protein concentrations of the different pooled samples were determined by standard BCA assay. The combined concentration of unbound and eluted fraction was found less than the initial total concentration of protein, though the loss of protein during the whole chromatographic process was very less (0.035 mg of total protein loaded i.e. 2 mg). The binding of target protein sample and its purity in eluted fractions was confirmed by calculating the total activity of β -glucosidase present in different pooled sample. The average recovery and the purification factor was 93% and 2, respectively. The low purification factor was mainly because of the production of target enzyme as major protein. During the chromatography, particulate material was not accumulated in the cryogel column. Three repetitive runs of β -glucosidase purification from non-clarified crude homogenate, the cryogel column did not show any pronounced decrease in performance. Importantly, the pore size like in conventional gels (e.g., Sepharose beads) is usually smaller than 0.1 μm , which are about two orders of magnitude less than the cryogel. These advantages of macroporous cryogel suggest its potential use for purification application of micromolecules.

Conclusion

Supermacroporous cryogel was developed and further modified with affinity ligands for protein purification application. Cryogel column is integrating the recovery and purification of protein, which is governed by the presence of large interconnected pores with functionalized specific ligands on surface. Moreover, the used polymer precursors and initiators are common components of routine experiments of electrophoresis, which are easily available and cost effective. These results showed advancement in bio-separation applications using macroporous cryogels for large molecules like plasmid, viruses, cell organelles and even individual cell type.

BARC NEWSLETTER

SIMULTANEOUS OBSERVATION OF LASER-INDUCED PHOTOIONIZATION AND FLUORESCENCE SIGNALS IN ATOMIC URANIUM

M.L. Shah, G.P. Gupta, Vas Dev, B. Dikshit, M.S. Bhatia and B.M. Suri
Laser and Plasma Technology Division

This Paper received the Best Paper Award at the DAE-BRNS National Laser Symposium, (NLS 20), held at Chennai, from 9-12th January 2012

Abstract

Laser-induced photoionization and fluorescence signals were simultaneously recorded in atomic uranium using a single Nd: YAG-pumped dye laser for two specific cases. The uranium atoms in the ground state were ionized by single-color, three-photon photoionization technique resulting in the photoionization signal. The fluorescence signal was simultaneously obtained from the first-excited state involved in the photoionization process. The photoionization and the fluorescence signals were also estimated theoretically for several values of the photoionization cross-section for the transition between the second-excited state and the autoionization state using density matrix formalism. From the comparison of theoretically calculated ratios of fluorescence signals in the two specific cases with the experimentally obtained values, the photoionization cross-section for the 33801.06-50701.59 cm^{-1} transition was obtained.

Introduction

Resonance ionization spectroscopy (RIS), which is based on multi-step resonant photoionization of atoms by laser pulses, is an excellent technique for studying highly excited states of atoms [1]. It has provided very useful information on atomic structures as well as laser-atom interaction dynamics. This technique in conjunction with a mass spectrometer, which is known as resonance ionization mass spectrometry (RIMS), has been extensively used by various groups for studying atomic spectra of uranium and ultra-sensitive detection of trace elements [2-4]. As an alternative to RIS, laser-induced fluorescence (LIF) is another powerful laser spectroscopy technique to study high-lying energy levels of atoms [5-7]. In LIF technique, the resonant absorption of laser photons excites the atoms in the initial state to a final state of higher energy and then the excited state relaxes by spontaneous emission of fluorescence radiation to a lower state which could be the initial state or some

other intermediate state. The LIF signal strength is directly proportional to the atomic population left in the excited state. Thus, the observation of LIF signals along with RIS signals indicates incomplete ionization of atoms present initially before laser irradiation [8]. Using LIF, the photoionization efficiency of every step involved in excitation and ionization process can be monitored. Hence, the simultaneous detection of LIF and RIS signals plays an important role for monitoring the photoionization process. In the present work we have monitored the photoionization dynamics by simultaneous observation of RIS and LIF signals in atomic uranium using a single Nd: YAG-pumped dye laser. We have analyzed these signals using density matrix (DM) formalism. We have compared the theoretical ratios of these signals in the two specific cases with the experimentally measured ratios and obtained the photoionization cross-section for the 33801.06-50701.59 cm^{-1} transition.

BARC NEWSLETTER

Experimental details

The experimental setup for simultaneous detection of RIS and LIF signals is shown in Fig. 1. It consists of a high temperature atomic vapor source in a vacuum chamber, a dye laser (Quantel TDL 90) pumped by a Q-switched Nd:YAG (Quantel YG 980) laser, a U-Ne hollow cathode discharge lamp (HCDL), a photo-multiplier tube (PMT), a 0.5 m monochromator, a 1.5 m high-resolution monochromator, a pyrometer, a high voltage power supply and an oscilloscope. A pencil-type electron gun of 8 kW power (32 kV, 250 mA) is mounted in the vacuum chamber at an angle of 45° relative to the horizontal axis. The electron beam is turned through another 45° by an external magnetic field so as to ensure normal incidence of electron beam on the surface of the material to be evaporated. The pulse duration, repetition rate and line width of the dye laser were 7 ns, 20 Hz and 0.05 cm^{-1} (1.5 GHz), respectively. The laser pulse energy in the interaction zone was 2.5 mJ. The laser beam diameter in the interaction zone was 5 mm. The laser beam passed through the atomic

beam of uranium in cross-configuration. Resonance and near-resonance excitation was ensured with the help of OG signal which was monitored by passing the laser beam through the HCDL during the experiments. The fluorescence light emitted from the first-excited level was collected in a direction perpendicular to both laser and atomic beams and focussed onto the entrance slit of the 0.5 m monochromator by a suitable lens assembly. The photoion signal was detected using a parallel-plate configuration and applying -2 kV to the plates across a load of $5 \text{ k}\Omega$. The monochromator here is used as a filter. The output slit of the monochromator was coupled with a PMT (gain of 10^7).

Results and discussions

The $0-16900.38 \text{ cm}^{-1}$ transition at 591.5 nm in atomic uranium is well studied as it is one of the strongest atomic transitions in uranium in the visible region [9]. This transition also serves as a first-step transition in the RIS of ground-state atoms of uranium using single-color three-photon photoionization pathway to

the autoionization state at 50701.59 cm^{-1} . Considering this transition, we have conducted the experiments for simultaneous observation of LIF and RIS signals in atomic uranium in two specific cases. In the first case, the laser was resonantly tuned to this first-step transition, which excited the uranium atoms in the ground state to the 16900.38 cm^{-1} energy level as shown in Fig. 2A. Two photons of the same laser further photoionized the excited uranium atoms via a near-resonant intermediate state at 33801.06 cm^{-1} . Both the three-photon photoionization signal and the resonant fluorescence signal have been observed using an oscilloscope. Typical RIS and LIF signals were recorded. In the second case,

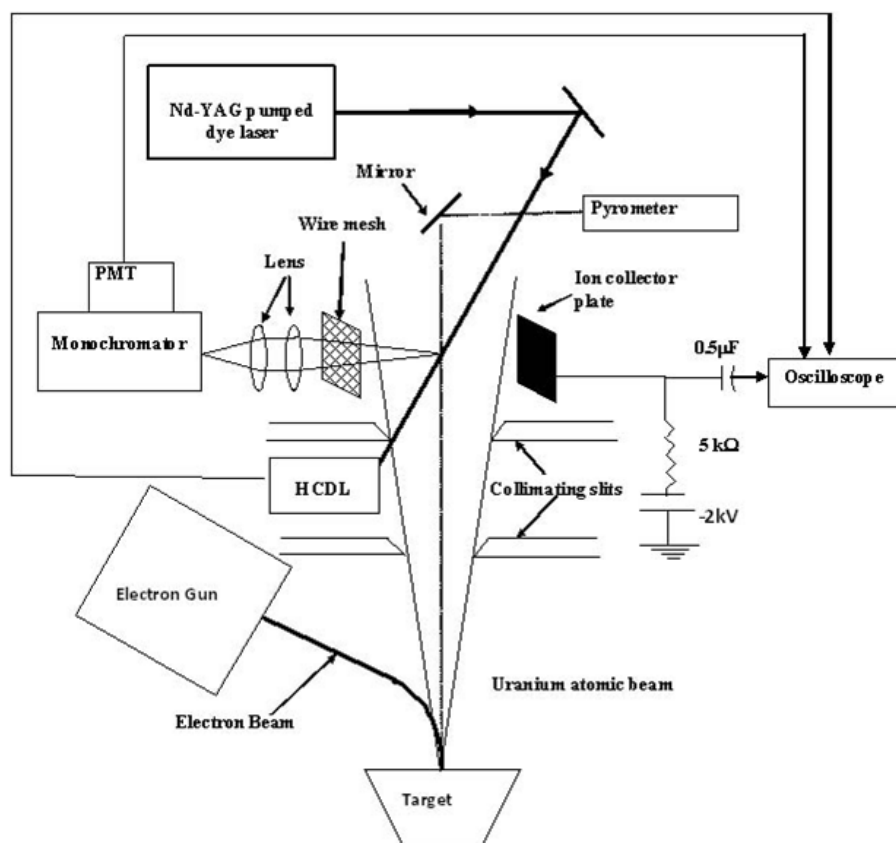


Fig. 1: Experimental setup for simultaneous observation of LIF and RIS signals.

BARC NEWSLETTER

the laser was slightly detuned from the first-step transition by 0.15 cm^{-1} so that it became two-photon resonant at 33801.06 cm^{-1} as shown in Fig. 2B. Typical RIS and LIF signals were also recorded in this case. The RIS signal increased relative to the first case owing to the two-photon resonance transition and its connection to autoionization resonance⁴ at 50701.59 cm^{-1} . However, the LIF signal decreased relative to the first case, owing to detuning of the laser from the first-step resonance. All the experiments were done by taking an average of 64 laser pulses. The experimental ratios of RIS and LIF signals were determined by dividing the signal value measured in the first case to that in the second case. These experimental ratios were obtained by repeating the experiments six times for both the cases. The arithmetic mean of the six values of the ratios is represented as the average value of the ratio. We have taken these average values as the measured ratios. We have found the uncertainty in the signal ratios within $\pm 20\%$ from the spread in the data obtained in the six experiments. This can be attributed to the change

in the experimental conditions such as fluctuations in pulse-to-pulse laser power, atomic number density and the optimization of signals for both cases. The measured ratios of LIF and RIS signals are thus deduced as 3.0 ± 0.6 and 0.5 ± 0.1 , respectively.

We have employed DM formalism to analyze the RIS and LIF signals observed in the two specific experimental cases. The DM formalism for three level open atom interacting with a pulsed narrowband laser relevant to the experiment is discussed in detail in our recent work [10]. From the DM calculations, we have obtained the ratios of photoionization as well as fluorescence signals in the two specific cases, considering several values of the photoionization cross-section as shown in Table 1. By comparing the theoretically calculated LIF and RIS ratios with the experimentally measured values, it is observed that the theoretical LIF ratio (2.9) corresponding to the photoionization cross-section of $5 \times 10^{-16} \text{ cm}^2$ matches well with the measured ratio (3.0) within the experimental error whereas the theoretical

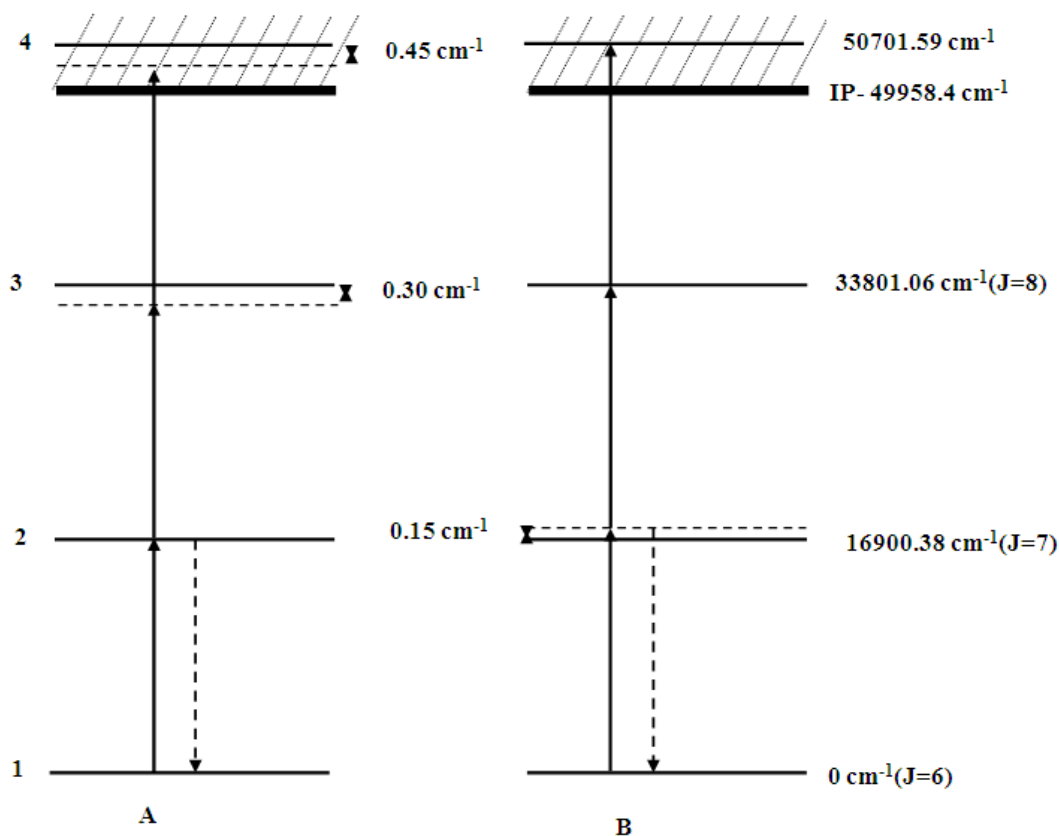


Fig. 2: Energy level diagram for single-color, three-photon photoionization and single-color laser-induced fluorescence when (A) The laser is tuned to resonance in first step transition ($0-16900.38 \text{ cm}^{-1}$), (B) The laser is detuned from resonance in first step transition by 0.15 cm^{-1} , so that it became two-photon resonant at 33801.06 cm^{-1}

BARC NEWSLETTER

Table 1. Theoretical Ratios of LIF and RIS Signals for Several Values of the Photoionization Cross-Section σ_3 .

σ_3 (10^{-16} cm ²)	Theoretical ratio	
	LIF	RIS
1	1.2	0.7
2	1.5	0.6
3	1.9	0.6
4	2.3	0.6
56	2.93.6	0.60.6
8	5.8	0.6
10	9.0	0.6

RIS ratio (0.6) reasonably matches with the measured ratio (0.5) within the experimental error for many values of the photoionization cross-section including 5×10^{-16} cm². The value of the photoionization cross-section for the transition 33801.06-50701.59 cm⁻¹ is thus determined as $(5 \pm 1) \times 10^{-16}$ cm² from the comparison of the theoretical and experimental ratio of LIF signals observed simultaneously along with RIS signals.

Conclusion

We have measured the photoionization cross-section for the 33801.06-50701.59 cm⁻¹ transition in atomic uranium using simultaneous observation of RIS and LIF signals under two specific experimental cases and comparing the experimental results with density matrix calculations.

Acknowledgements

The authors are thankful to Dr. L. M. Gantayet, Director, Beam Technology Development Group and Dr. A. K. Das, Head, Laser and Plasma Technology Division, Bhabha Atomic Research Centre for their encouragement and support.

References

1. V. S. Letokhov, *Laser Photoionization Spectroscopy* (Academic, New York, 1987).
2. L. R. Carlson, J. A. Paisner, E. F. Worden, S. A. Johnson, C. A. May, and R. W. Solarz, *J. Opt. Soc. Am.* **66**, 846 (1976).
3. B. M. Suri, K. Dasgupta, P. N. Bajaj, K. G. Manohar, R. Talukdar, P. K. Chakraborti, and P. R. K. Rao, *J. Opt. Soc. Am B* **4**, 1835 (1987).
4. K.G. Manohar, P.N. Bajaj, B.M. Suri, R. Talukdar, K. Dasgupta, P.K. Charaborti, and P. R. K. Rao, *Appl. Phys. B* **48**, 525 (1989).
5. E. Miron, R. David, G. Erez, S. Lavi, and L. A. Levin, *J. Opt. Soc. Am.* **69**, 256 (1979).
6. A. K. Pulhani, M. L. Shah, V. Dev, and B. M. Suri, *J. Opt. Soc. Am. B* **22**, 1117 (2005).
7. M. L. Shah, A. K. Pulhani, G. P. Gupta, and B. M. Suri, *J. Opt. Soc. Am. B* **27**, 423 (2010).
8. Y. Jonghoon, J. T. Kim, P. Hyuamin, R. Sipyoo, R. Yongjoo, and L. Jongmin, *J Korean Phys. Soc.* **37**, 707 (2000).
9. V. Dev, M. L. Shah, A. K. Pulhani, and B. M. Suri, *Appl. Phys. B* **80**, 587 (2005).
10. M L shah, G P Gupta, Vas Dev, B Dikshit, M S Bhatia and B M Suri, *J. Opt. Soc. Am B* **29** (2012)

BARC NEWSLETTER

STATUS REVIEW ON SPENT DESALINATION MEMBRANE MANAGEMENT

T.L. Prasad D. Goswami and P.K. Tewari
Desalination Division

This Paper received the 2nd Best Technical Paper Award at the National Symposium, WAVE 2012, held at Mumbai on 27th & 28th September, 2012

Abstract

With growing use and market of membrane technologies in desalination and water purification, disposal of used and spent membrane elements is going to be a serious issue for water industry in future. Keeping this in mind, various schemes/protocols can be planned for spent membrane management. Advanced oxidation processes for aqueous organic waste handling are known and are being practiced in industries. Exploratory studies on these lines for handling spent membrane management are planned and primary exploratory experiments based on hydro thermal processes have been initiated. The processes for waste treatment and conditioning practiced in industry need to be revisited in the light of technical developments.

The paper reviews the information available in the open literature concerning these developments and briefly highlights the initiation of the spent membrane management programme.

Keywords: Desalination Membranes; De-polymerisation; Hydro thermal processes; Mineralisation

Introduction

To meet the increasing demand for fresh water under growing environmental awareness and constraints, desalination is being practiced widely. Potable water by desalination can be produced by thermal process or membrane processes. Membrane application has grown in market share, as membrane processes operate at ambient temperature and offer one step separation for dissolved constituents on molecular level. The large desalination plants around the world are running with RO technology. The polymers [1,2] those are used on a commercial basis to prepare membranes for various applications such as ultra-filtration and RO are Cellulose acetate, Poly acrylonitrile, Polyamide and Polysulphones and the elements are mostly in spiral configuration. Depending on process and operating conditions, these modules have design life and needs to be replaced after 3 to 5 years. This generates a lot of spent membrane elements. With growing market of membrane

technologies, disposal of these spent modules is going to be of concern in years to come. Hence, eco-friendly disposal of spent membrane elements is an important issue for desalination industry.

In our initial approach, we initiated carrying out lab scale studies on various hydrothermal process techniques on mineralisation of polyamide as well as polysulphone membranes. These processes otherwise widely practiced in aqueous organic wastes would be adopted for spent membrane management as an exploratory study. The relatively mild reaction conditions help to minimize the plant capital costs and simplify the control logistics.

Status of Processes Technologies for different forms of wastes

This paper reviews the status of technologies currently deployed in the field. Most of these technologies concern aqueous organic wastes generated in the

BARC NEWSLETTER



Fig. 1: Waste treatment status in India

industry and in domestic sectors. Management of solid waste in terms of spent membrane management has attracted BARC's initiative as a spin-off R&D in social sector. The waste treatment status in India is typically as shown in Fig.1. Hydro thermal process techniques provide alternative solution to incineration and land filling technologies.

The salient features of some of the Advanced Oxidation Process techniques being explored by various researchers as well as other industrial practices are presented in Table 1 below.

Table 1: The Salient Features of the AOP techniques and other Industrial Practices

Sl.no	Research / Location	Substrate/ Technique	Technical features	Remarks
1.	Shanghai university China	Nylon-6/ Catalytic hydrothermal depolymerisation	i. Water medium at temperatures of 553 K to 603 K and pressures of 6.4 to 12.8 MPa ii. Reported Reaction Activation Energy is 77.38 KJ/mol	
2.	IBM Almaden Research Center, San Jose, CA, USA	Polyethylene terphthalate/ Catalytic hydrothermal depolymerisation	i. PET organo-catalytic de-polymerisation for chemical recycling. ii. Heating at 190 deg.C with catalyst and ethylene glycol iii. Reactants and catalysts can be recycled many times	Research on Green chemistry of PET bottles with KACST and Stanford university to facilitate recycling
3.	Department of Chemical Technology, Mumbai India	Dye bath waste/ membrane wet oxidation (MEMWO)	i. NF membrane (MPT-30) was used to remove color and 97% COD of dye compound ii. The concentrate treated by wet oxidation at 160-225 deg.C and oxygen partial pressure of 7 to 14 bar using homogeneous CuSO ₄	Hybrid system
4.	Universidad Complutense, Madrid Spain	Phenol / Catalytic wet oxidation	i. Mineralisation at 127 to 180 deg.C at oxygen partial pressure of 3 to 16 bar using Cu-203T catalyst in the range 4 to 1150 g/l ii. Used Stirred tank reactor and Fixed bed reactors	
5.	Shanghai university China	Thermosetting resin/ Catalytic hydrothermal depolymerisation	i. Used heteropolyacid HPW catalyst with water (1:5 in mass) medium at temperature of 275 to 350 deg.C ii. Depolymerised products are phenol and Bispheno-A iii. Activation energy for polymerization is 83.15 kj/mol	DGEBA/EDA thermosetting resin used in composite industry
6.	UAEM-UNAM Mexico	Industrial park waste water/ Electrochemical and Ozonisation	i. aluminium electrodes with current densities of 16-66 mA/sq.cm were used ii. Ozone flow of 60ml/min at pH 9 iii. COD removal reported is 79%	
7.	CNR-Istituto di Metodologie Chimiche, Rome Italy	Land fill leachate / radiolysis and ozonolysis	i. used Cobalt-60 gamma rays from 12 to 400 kGy ii. used 50 mg of ozone of 5% concentration	
8.	University Jinan China	Brilliant red K-2BP / sirling jet-induced cavitation and Fenton process	i. Jet induced cavitation has given improvement of 2-3 orders compare to ultrasonics at 6 bar and 323 K ii. Reported 90% removal of TOC by hybrid process iii. 30% hydrogen peroxide and Ferrous sulphate used with pH adjustment by HCl/NaOH	Textile industry; 25L scale

BARC NEWSLETTER

Sl.no	Research / Location	Substrate/ Technique	Technical features	Remarks
9.	Nicholas Piramal India Ltd, India	p-anisaldehyde & 2-aminothiophenol / UV Fenton	i. hydrogen peroxide (30%) and ferrous sulphate heptahydrate (50 ppm) were used to generate radicals ii. 16W photo reactor was used iii. 80% reduction in COD after 5hr reported	Pharma industry
10.	Washington State Univ, Pullman, Washington	Acrylonitrile industry waste water/ Wet Air Oxidation	i. COD ranges from 30000 to 60000 ppm and cyanide ranges from 500 to 3000 ppm ii. Two step treatment of WAO followed by biological oxidation is proposed iii. WAO reported to remove 99% of cyanide and COD reduction of 97%	Acrylonitrile manufacture industry

Desalination membranes

Cellulose acetate was one of the earlier materials for RO membrane prepared by phase inversion with a solution cast on a non woven and immersed in water. Though this has high chloride tolerance and stability, it is not suitable for feed containing organic solvents, high

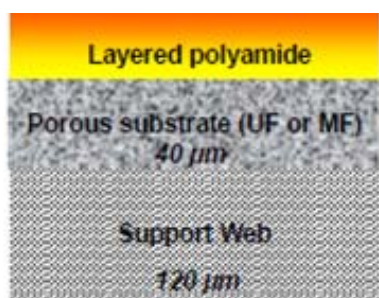


Fig.2: Typical Thin Film Composites used in RO

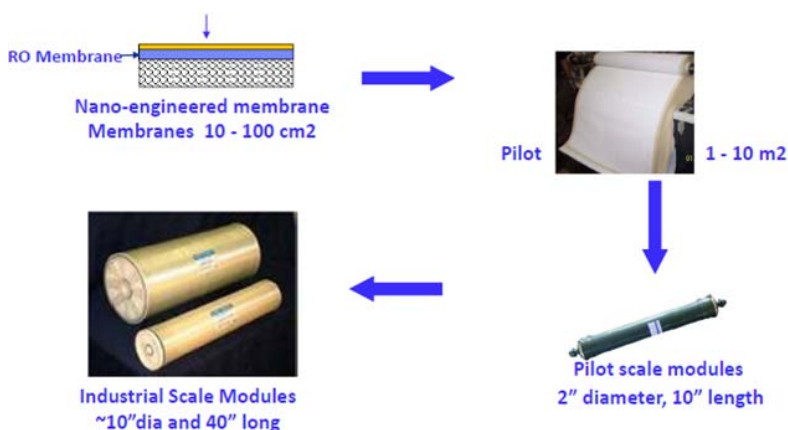


Fig. 3: RO module in spiral configuration



Fig. 4: Typical Spent desalination membranes

temperature and pH. Better membranes for such applications are aromatic polyamides. Also desalination requires large flows to be handled and Thin Film Composites (TFC) are better membranes for this application. TFC's are prepared by interfacial polymerization on surface of porous support and operate in pH range of 2-11. The RO membranes presently used is based on polyamide with thin film composites shown in Fig. 2.

These membranes with optimized coating are configured into spiral modules as shown in Fig. 3 below to provide maximum surface area in minimum volume.

The clean membranes, oil fouled membranes and bio fouled membranes respectively are shown in Fig. 4 below.

Based on Environmental regulations that have to be implemented and keeping in mind the release criteria and BAT (Best Available Technologies), the logic diagram for managing solid form of wastes such as desalination membranes can be represented as shown in Fig. 5 below.

Conclusions

Water industry needs to address the spent membrane management, keeping in mind to provide integrated solution. It is an obvious paradox to desire stability of membranes while in use but instability after the service life of the membranes. AOP's are effective techniques to treat

BARC NEWSLETTER

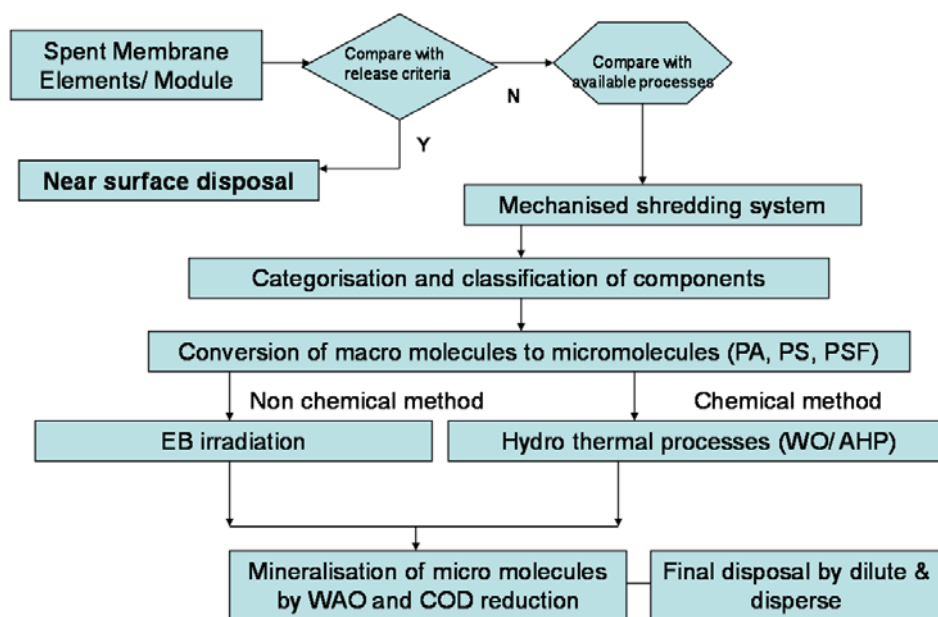


Fig. 5: Logic diagram for spent desalination membrane management

high degree industrial wastes. These techniques have bright prospect in nearby future due to ongoing research initiatives. There are still large many compounds, on which AOP research has not been performed. Best Available Technologies needs to be explored to supplement the conventional biological and chemical methods.

Acknowledgements

The authors wish to thank Director Chemical Engg Group for giving encouragement to the programme.

References

1. Drioli, E., Giorno, L., Comprehensive membrane science and engineering by Elsevier publishers
2. Treatment of spent ion exchange resin for storage and disposal, IAEA-TRS-254
3. Prasad, T.L., Smitha Manohar., Srinivas, C., " Advanced Oxidation Processes for Treatment of Spent Organic Resins in Nuclear Industry " Presented at Indian Chemical Engineering congress, Organised by Indian Institute of Chemical Engineers in collaboration with Central Leather Research Institute, Chennai, December 19-22, 2001
4. Hwubert, D., Simon,C., and et.al., " Wet Air Oxidation for treatment of industrial waste water and domestic sludges, design of bubble column reactors", Chemical Engineering Series 54(1999) 4953-4959
5. Freeman, H.M., Standard Handbook for Hazardous Waste Treatment and Disposal, McGraw-Hill, New York.

HYDROGEN SORPTION-DESORPTION STUDIES ON ZrCo-HYDROGEN SYSTEM

Ram Avtar Jat, S.C. Parida, Renu Agarwal and S.G. Kulkarni
Product Development Division

This Paper received the Mettler Toledo Best Poster Award at the 18th DAE-BRNS International Symposium on Thermal Analysis, held at Mumbai from 31st January to 2nd February, 2012

Abstract

The ZrCo-H₂ system was investigated in this study owing to its importance as a tritium storage material. Hydrogen desorption pressure-composition isotherms were generated in the temperature range of 524-624 K. A van't Hoff plot was constructed using the plateau pressure data of each isotherm and the thermodynamic parameters were calculated for the hydrogen desorption reaction of ZrCo hydride. Hydrogen absorption kinetics of ZrCo-H₂ system was studied at four different temperatures in the range of 544-603 K and the activation energy for the absorption of hydrogen by ZrCo was calculated by fitting kinetic data into suitable kinetic model equation.

Introduction

An intermetallic compound ZrCo seems to be a suitable candidate material for storage, supply and recovery of hydrogen isotopes in ITER [1-4] as it is non-radioactive and non-pyrophoric at room temperature and has similar tritium storage properties as uranium [5, 6]. It is reported [3] that ZrCo can absorb hydrogen at room temperature to form the hydride with a maximum stoichiometry of ZrCoH₃. A comparison of ZrCo and other getter materials for tritium handling and storage is well presented by Penzhron et al. [5] and Shmayda et al. [6]. However, the data reported in the above literatures shows considerable scatter. Therefore, to generate a reliable set of thermodynamic data for ZrCo-H₂ system, an effort is made in this work to reinvestigate desorption pressure-composition isotherms (PCIs) for ZrCo-H₂ system. A van't Hoff plot is constructed using the plateau pressure data of these isotherms. A comparison is made with available experimental data in order to access the reliability of the present investigation. In addition to PCIs, kinetic data also are of prime importance in the design of delivery systems. Hence, kinetics measurement are carried out in this study for hydrogen absorption reaction by ZrCo and the kinetic parameters are evaluated by fitting the

experimental kinetic data to suitable model including the effect of pressure and concentration in the rate equation..

Experimental

Material Preparation and Characterization

ZrCo intermetallic compound was prepared by arc-melting method followed by annealing in an evacuated sealed quartz tube at 973 K for 3 days and water quenching to room temperature. The formation of alloy and its hydride was confirmed by XRD and their surface morphology was investigated by SEM. The homogeneity of the alloy was investigated by compositional analysis at different morphological positions of the alloy by EDS. Lattice parameters of ZrCo and ZrCoH₃ were determined using the XRD data and compared with the reported literature values.

Pressure-Composition-Temperature and Kinetic measurements

Prior to generating the Pressure-Composition Isotherms (PCIs), ZrCo sample was activated by hydriding - dehydriding method. The hydrogen desorption PCIs for

BARC NEWSLETTER

ZrCo-H₂ system were generated at six different temperatures in the range of 524-624 K with step of 20 K, using the Sievert's -type volumetric apparatus. At each experimental temperature desorption equilibrium was established by evacuating a known amount of hydrogen from the reservoir and allowing the system to attain equilibrium and this equilibrium pressure was recorded. This allows to simultaneously calculate the value of x ($= H/M$) and the corresponding equilibrium hydrogen desorption pressure at the experimental temperature. Thereafter, the value of x was altered by aliquoting a known amount of hydrogen from the reservoir and allowing the attainment of a new equilibrium. This process was repeated till the entire isotherm was generated. Following this procedure, six isotherms were generated.

The hydrogen absorption kinetic measurements were carried out in the temperature range of 544-603 K with step of 20 K. High purity hydrogen gas at a known pressure was introduced into the reaction vessel of known volume containing activated sample and pressure change with time was monitored until thermodynamic equilibrium was attained. These data were fitted in to suitable kinetic model and temperature dependent rate constants were calculated from which the activation energy for hydrogen absorption by ZrCo was calculated.

Results and Discussion

Material Characterization

The formation of ZrCo phase and its hydride phase are confirmed by comparing their XRD patterns (Fig. 1) with

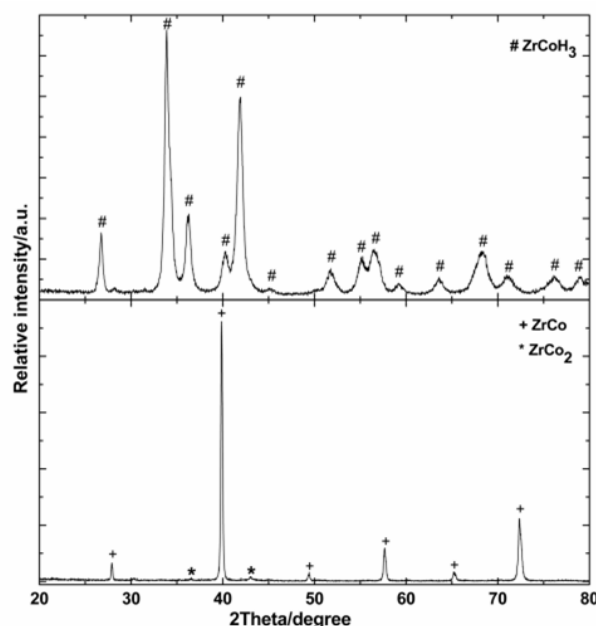


Fig. 1: XRD patterns of ZrCo and its hydride

the JCPDS files [7]. It is observed that trace amount of ZrCo₂ impurity phase is present in the ZrCo phase. The lattice parameters of ZrCo obtained in this study is compared with the literature values in Table 1 and found to be in excellent agreement. The SEM images of ZrCo alloy and its hydride with different magnification are shown in Fig. 2 which reveals that ZrCo alloy exhibits a cleavage type surface whereas its hydride shows a cleavage type fracture surface. The cracks generated in the hydride phase are attributed to the lattice expansion of ZrCo alloy upon hydrogenation. The EDS microanalysis carried out at different morphological positions of the alloy reveals an average composition over the entire sample and in accordance with the nominal composition ZrCo.

Table 1: Comparison of room temperature lattice parameters of ZrCo and ZrCoH₃ obtained from X-ray diffraction data

Compounds, Crystal Structure, Space Group	Lattice parameters/Å		
	This study	Literature	Ref. No.
ZrCo, Cubic, (221)	$a = 3.1957(1)$	$a = 3.196$	[17, File No. 18-0436]
ZrCoH ₃ , Orthorhombic, Cmc ₂ m(63)	$a = 3.5303 (42)$ $b = 10.4820 (118)$ $c = 4.3016 (57)$	$a = 3.53$ $b = 10.48$ $c = 4.3$	[17, File No.33-0416]

BARC NEWSLETTER

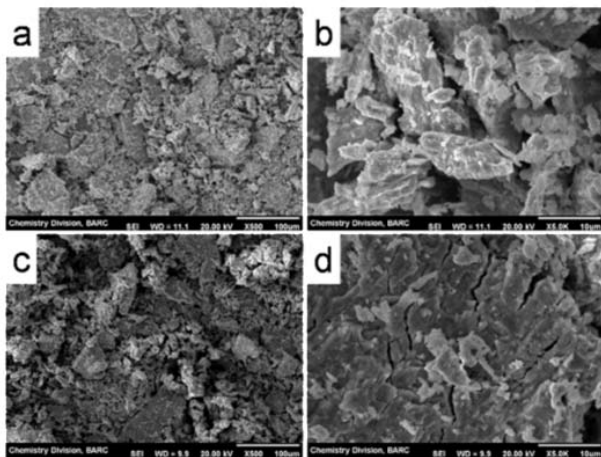


Fig. 2: SEM images of ZrCo and its hydride at magnifications of 500X and 5000X; (a) and (b) ZrCo alloy; (c) and (d) Hydride phase

Pressure-Composition-Temperature measurements

Hydrogen desorption PCIs at different experimental temperatures for ZrCo-H₂ system is shown in Fig. 3. It is evident from Fig. 3 that this system exhibits a single plateau at all experimental temperatures and the plateau width decreases with increasing the temperature. The temperature dependence of the equilibrium plateau pressure for ZrCo-H₂ system is best represented by the van't Hoff plot, shown in Fig. 4. From the van't Hoff plot, temperature dependence of the plateau pressure was found to be expressed by the equation:

$$\log (p_{eq}/\text{Pa}) = -4369.4/T + 11.39 \quad (1)$$

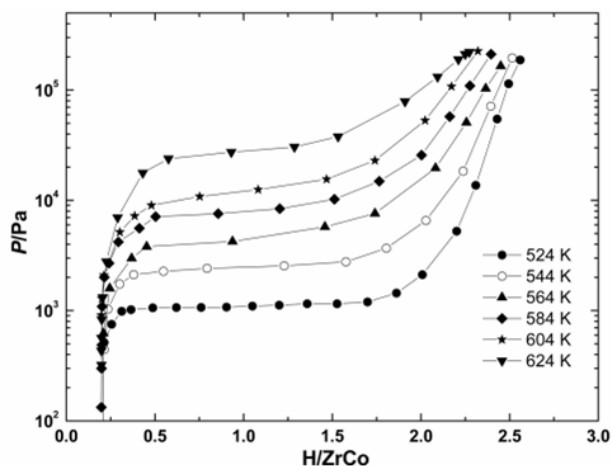


Fig. 3: Desorption pressure-composition isotherms for ZrCo-H₂ system

From this relation, the enthalpy change and the entropy change of the dehydrogenation of ZrCo hydride were deduced to be 83.7 ± 3.9 kJ/mol H₂ and 122 ± 4 J/(mol H₂·K), respectively. The variation of desorption plateau pressure with temperature obtained in this is compared with those reported in the literature [4, 8-11] as shown in Fig. 4. It is evident from this comparison that there is considerable scatter in the data. However, the data obtained in this study are encompassed within the extreme limits of scatter reported in the literature. For a better assessment of PCT data, a direct comparison of the thermodynamic parameters like enthalpy and entropy change of dehydrogenation reactions is made in Table 2. It is evident from this table that the enthalpy and entropy data obtained in this study are very close to the average of all the reported literature data. Moreover, thermodynamic analysis of different metal/alloy-Hydrogen systems by Anderson [12] suggests that the entropy of dehydrogenation reaction should be ~ 130 J/(mol H₂·K) which roughly corresponds to the gain in entropy due to the translational degree of freedom when hydrogen is desorbed from the metal hydride to the gas phase. In the present study the entropy of dehydrogenation reaction was found to be 122 ± 4 J/(mol H₂·K) which is close to the value suggested by Anderson [12]. This suggests that the data obtained in this study are reasonably accurate.

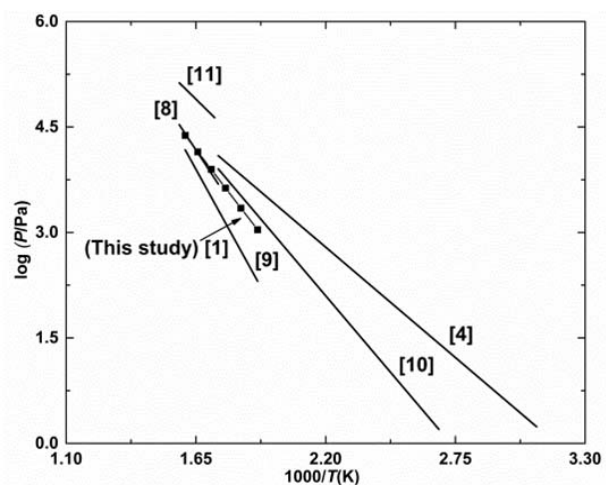


Fig. 4: Comparison of van't Hoff plot obtained in this study with those reported in literature for the desorption isotherms of ZrCo-H₂ system

BARC NEWSLETTER

Table 2: Comparison of thermodynamic parameters of dehydrogenation reaction of ZrCo-H₂ system

Authors/year [Ref.]	$\Delta_r H/\text{kJ mole H}_2$	$\Delta_r S/\text{J/mole H}_2 \cdot \text{K}$	$x = \text{H/ZrCo}$	Temperature Range/K
Jat et al./2012 (this study) [1]	83.7	122.0	1.0	524-624
Bekris et al./2000 [4]	54.7	77.9	1.0	323-573
Gongli et al./2007 [8]	97.8	145.5	—	573-633
Kost et al./1980 [9]	116.5	171.1	0.8	523-623
Heics and Shmayda/1992 [10]	75.8	111.1	0.8	373-623
Zhuo et al./2006 [11]	63.1	101.9	—	578-633

Hydrogen absorption kinetic measurements

Owing to the complexity of gas-solid reaction, many often simple kinetic models fail to fit the experimental kinetic data. It has been observed in many cases that the simple kinetic models lead to negative activation energy which has no physical significance. Hence, in the present study the kinetic data are fitted in the rate equation proposed by Wang and Suda [13] which involves both the hydrogen pressure and concentration in the rate an can be written as;

$$dC/dt = k(T) \cdot f(C,P) \quad (2)$$

$$f(C,P) = (P/P_{\text{eq}})^a \cdot \{1 - (P/P_{\text{f}})^a \cdot (C/C_{\text{f}})^b\} \quad (3)$$

where, $k(T)$ is the absorption rate constant; P and P_{f} are the pressure at time t and final pressure, respectively. C and C_{f} are the concentrations (H/M) at time t and at final pressure P_{f} , respectively. P_{e} is the equilibrium

plateau pressure at experimental temperature obtained from PCT measurements. The constant a and b are the order of the reaction with respect to the hydrogen pressure and concentration (H/M), respectively. The decrease in relative pressure (P/P_{f} , P = pressure at time t , P_{f} = initial pressure) with time is shown in Fig. 5. It is evident from Fig. 5 that at higher temperatures, the final P/P_{f} ratio increases which can be attributed to the increasing extent of desorption reaction at higher temperatures.

The experimental kinetic data obtained in this study are plotted in Fig. 6 as dC/dt vs. $f(C,P)$ at different temperatures. The data were found be best fitted to Eq. (2) at all the experimental temperatures with the adjustable parameters $a = 2$ and $b = 0.1$ which indicates that the hydrogenation reaction is second order with respect to hydrogen pressure ($a = 2.0$) whereas it is almost independent of hydrogen concentration ($b = 0.1$).

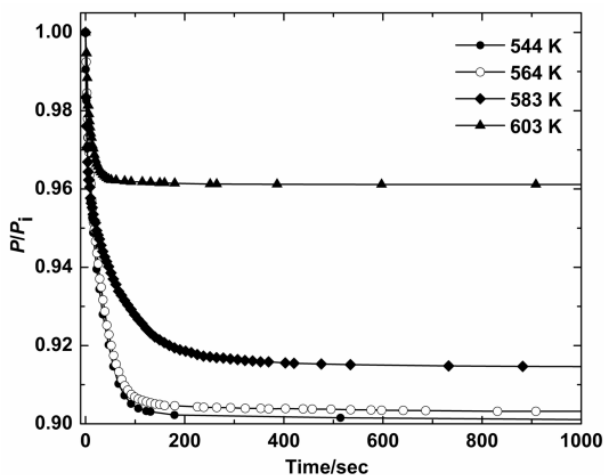


Fig. 5: Variation of relative pressure (P/P_{f}) with time for hydriding kinetics of ZrCo alloy

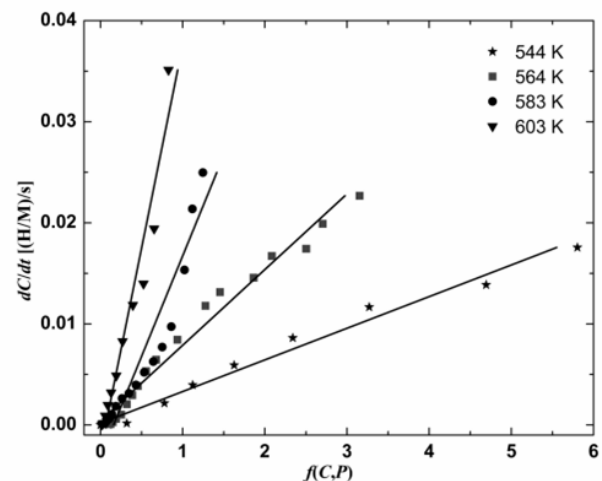


Fig. 6: Hydriding reaction rate vs. $f(C,P)$ at different temperatures

BARC NEWSLETTER

In this study the rate constants at different temperatures were calculated from the slope of the linear fitted lines in Fig. 6 and the corresponding values of rate constants were plotted as $\ln k(T)$ vs. $1/T$ in Fig. 7. From this plot the activation energy of hydrogen absorption reaction was calculated using the Arrhenius equation. The value of E_a was found to be 120 ± 5 kJ/mol H_2 which is comparable to the value 96.6 ± 5.1 kJ/mol H_2 reported by Susic [14] from differential scanning calorimetry (DSC) measurements.

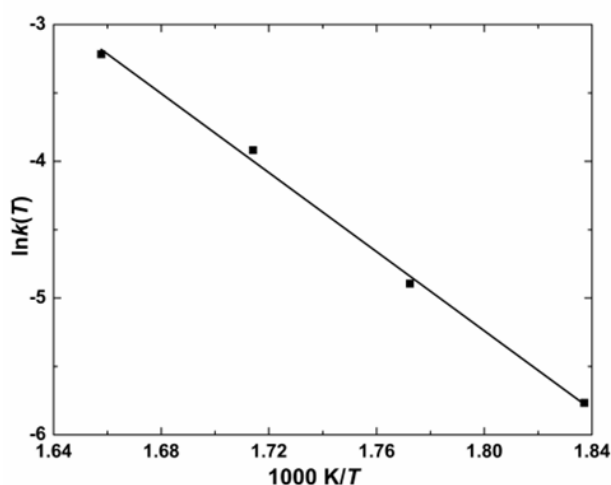


Fig. 7: Arrhenius plot for the hydriding reaction of ZrCo alloy

Conclusion

ZrCo alloy prepared by arc-melting method shows the presence of trace amount of $ZrCo_2$ phase. Microstructure analysis reveals cleavage type surface for ZrCo alloy and cleavage type fracture surface for its hydride. Hydrogen desorption PCT measurements on ZrCo- H_2 system exhibits a single plateau at all experimental temperatures and the plateau width decreases with increase in temperature. The enthalpy and entropy change for the dehydrogenation of ZrCo hydride are 83.7 ± 3.9 kJ/mol H_2 and 122 ± 4 J/(mol

$H_2 \cdot K$), respectively. Constant volume kinetic measurements on hydrogen absorption by ZrCo alloy shows that the hydrogenation reaction is second order with respect to hydrogen pressure ($a = 2.0$) whereas it is almost independent of hydrogen concentration ($b = 0.1$). The activation energy of hydrogenation of ZrCo alloy to form its hydride is 120 ± 5 kJ/mol H_2 .

References

1. Jat RA, Parida SC, Nuwad J, Agarwal R, Kulkarni SG. *J Therm Anal Calorim.* 2013;112:37–43.
2. Jat RA, Parida SC, Agarwal R, Kulkarni SG. *Int J Hydrogen Energy.* 2013;38:1490-1500.
3. Nagasaki T, Konishi S, Katsuta H, Naruse Y. *Fusion Technol.* 1986;9:506-9.
4. Bekris N, Besserer U, Sirch M, Penzhorn RD. *Fusion Eng Des.* 2000;49-50:781-9.
5. Penzhorn RD, Devillers M, Sirch M. *J Nucl Mater.* 1990;170:217-31.
6. Shmayda WT, Heics AG, Kherani NP. *J Less-Common Met.* 1990;162:117-27.
7. PCPDFWIN Version 2.2, 2001, JCPDS-ICDD
8. Gongli T, Xiaopeng L, Lijun J, Shumao W, Zhinian L, Hualing L. *Trans Nonferrous Met Soc China.* 2007;17:s949-53.
9. Kost ME, Padurets LN, Chertkov AA, Mikheeva VI. *Russ J Inorg Chem.* 1980;25:471–3.
10. Heics AG, Shmayda WT. *Fusion Technol.* 1992;21:1030-4.
11. Zhuo H, Xiaopeng L, Lijun J, Shumao W. *Rare Metals.* 2006;25:200-3.
12. Andreasen A. PhD thesis: Hydrogen storage materials with focus on main group I-II elements. Risø National Laboratory, Denmark, 2005
13. Wang XL, Suda S. *Int J Hydrogen Energy.* 1992;17:139-47.
14. Susic MV. *Int J Hydrogen Energy.* 1988;13:173-9.

BARC NEWSLETTER

DETECTION OF ${}^4\text{He}$ GENERATED DURING THE REACTION OF ${}^3\text{He}({}^3\text{He},2\text{p}){}^4\text{He}$ IN A PLASMA FOCUS DEVICE USING LEXAN SOLID STATE NUCLEAR TRACK DETECTOR

Ram Niranjana, R.K. Rout, Rohit Srivastava and Satish C. Gupta

Applied Physics Division

and

R.V. Kolekar

Radiation Safety Systems Division

This Paper received the Z.H. Solapurwala Award for Fusion Research 2012 (Best Poster), at the 27th PSSI National Symposium on Plasma Science & Technology (PLASMA 2012), held at Puducherry, from December 10-13, 2012

Abstract

The plasma focus device is a well known laboratory fusion device. It has been reported to produce neutrons due to D-D or D-T fusion reaction. Fusion of heavier elements is difficult to achieve in laboratory due to high coulomb barrier for reaction. One such type of fusion ${}^3\text{He}({}^3\text{He},2\text{p}){}^4\text{He}$ was attempted here using a compact 11.5 kJ (40 μF , 24 kV) plasma focus device operated with high purity ${}^3\text{He}$ gas at 4mb filling pressure. Detection of ${}^4\text{He}$ along with proton generated during the reaction of ${}^3\text{He}({}^3\text{He},2\text{p}){}^4\text{He}$ was done using Lexan and CR-39 (covered with 24 μm thick aluminium foil) solid state nuclear track detectors respectively. The estimated ratio between the fusion products is close to expected ratio in such reaction. The observation of tracks in Lexan film (for ${}^4\text{He}$) and in CR-39 film (for proton) suggests the occurrence of fusion reaction ${}^3\text{He}+{}^3\text{He}$ in a plasma focus device.

Introduction

The fusion reactor appears to be the promising energy source for the galloping mankind. The fuel (D-D, D-T) for fusion reactions proposed to be used in a fusion reactor for energy generation will produce neutrons of high energies. Such neutrons are likely to cause the components of the reactor vessel radioactive on bombardment. Moreover, indirect ways like thermal process similar to the fission reactor will be required for the power generation. Helium-3 (${}^3\text{He}$) as a fusion fuel is more attractive because of aneutronic nature of its reaction products. The fusion products alpha and proton can be contained using electric and magnetic fields. These particles will not induce any radioactivity in components of the reactor vessel. The fusion products can directly be used for the electricity generation. Thus ${}^3\text{He}$ is conceived as the third generation fusion fuel. Because of the higher coulomb

barrier, the energy required for ${}^3\text{He}_2 + {}^3\text{He}_2$ fusion will be much higher than the conventional ${}^2\text{D}_1 + {}^2\text{D}_1$ or ${}^2\text{D}_1 + {}^3\text{T}_1$ fusion. Display of ${}^3\text{He}$ fusion in a laboratory will have positive impact on the commercial viability. The plasma focus (PF) device [1] is a simple and low cost fusion unit. It produces intense pulsed neutrons on use of deuterium gas with or without tritium gas. The working principle of this unit is based on plasma pinching phenomena. Most of the neutrons produced in this device are due to beam target mechanism. Experiment has been done [2] with deuterium and helium as filling gas in a plasma focus device to measure the energy of the produced protons and to locate the spatial distribution of the fusion regions. But for the ${}^3\text{He}({}^3\text{He},2\text{p}){}^4\text{He}$ reaction for cross section study [3] underground accelerator facility was employed. We have attempted here to fuse ${}^3\text{He}$ with ${}^3\text{He}$ in a compact 11.5 kJ compact plasma focus device. The fusion products ${}^4\text{He}$ (α particle) and proton are measured using

BARC NEWSLETTER

Lexan and CR-39 (covered with 24 μm thick aluminium foil) solid state nuclear track detectors respectively. The experimentally estimated ratio between the fusion products is close to the expected ratio for such reaction products. The detailed of the experiments and the results are reported here.

Experimental Set Up

The schematic of the setup is shown in Fig. 1. The device used for the fusion of ^3He is a compact plasma focus device developed [4] in house. The central electrode (anode) of the unit is of 77 mm effective (exposed) length and 60 mm in diameter. Twelve SS304 rods each of 12 mm in diameter and 122 mm in length arranged in a circle (122 mm PCD) around the anode formed the cathode (squirrel cage geometry). A quartz tube of 50 mm effective (exposed) length, 54 mm outer diameter and 2 mm wall thickness separates the anode

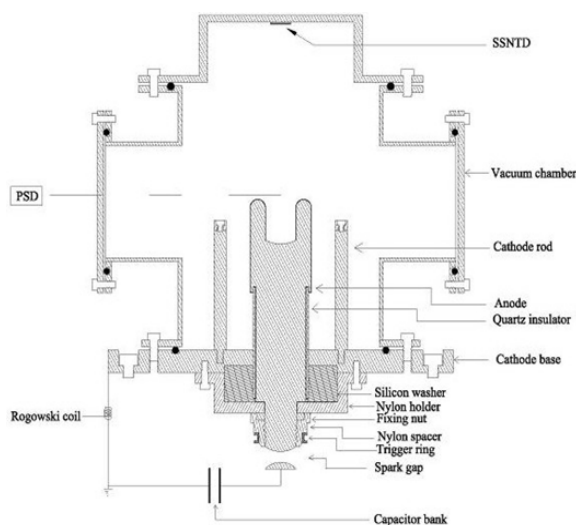


Fig. 1: Schematic of the experimental setup

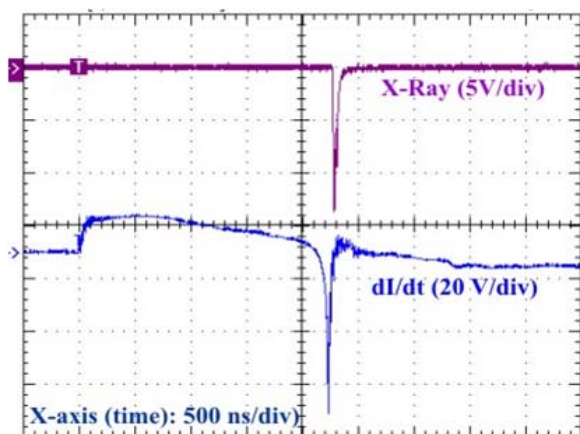


Fig. 2: X-Ray and current derivative signals.

and the cathode at the bottom. The electrode assembly is put inside a high vacuum compatible experimental plasma chamber as shown in Fig. 1. The plasma chamber is fabricated using SS304 material and it has a volume of about 7.5 L. The device is driven by an 11.5 kJ (40 μF , 24 kV) capacitor bank. The PF device is operated with high purity ^3He gas at 4mb filling pressure. The device is evacuated using a diffstac vacuum pump up to 10^{-5} mb of pressure before filling the required gas. The current derivative (dI/dt) of the discharge circuit is monitored by a multi-turn Rogowski coil. The time resolved hard X-ray emission is recorded with a plastic scintillator detector (PSD) positioned at 2 m from the PF device. The PSD consists of a NE102 plastic scintillator and a photomultiplier tube (XP 2012) housed in a cylindrical brass casing covered with lead shields. One of the fusion products, ^4He (α particle, 4.3 MeV) generated during the reaction of $^3\text{He}(^3\text{He},2p)^4\text{He}$ inside the plasma focus device is measured with a Lexan solid state nuclear track detector (SSNTD) film. The other product, the proton is recorded using a CR-39 SSNTD film. The CR-39 film is covered with a 24 μm thick high pure (more than 99%) aluminium foil to stop α particle or any accelerated ^3He particle reaching the film. The SSNTD (Lexan, CR-39) is kept at a distance of 16 cm from the top of the anode in axial direction and is irradiated one at a time. The Lexan film is exposed to 6 PF shots and CR-39 film is exposed to 3 PF shots. After exposing the film to the desired PF shots, it is removed and is etched off line under the standard conditions (6N KOH at 60 $^\circ\text{C}$) for a period of 4-7 hours to develop visible tracks. The tracks are counted using Zeiss axioscope motorised microscope at 100X magnification.

Result & Discussion

The typical current derivative (dI/dt) signal with hard X-ray signal is shown in Fig. 2. The sharp dip in dI/dt signal suggests maximum compression of plasma due to plasma pinching action. The width of hard X-rays is 40 to 50 ns. The production of hard X-ray indicates the generation of high energy electrons due to creation of high electric and magnetic fields. It also envisages the production of high energy ions the necessary condition for fusion reaction. The energy of α particle produced

BARC NEWSLETTER

in fusion reaction of ${}^3\text{He}+{}^3\text{He}$ is around 4.3 MeV. The Lexan film can detect alpha particles when its energy loss rate is nearing Bragg peak (4 MeV/mg/cm²). The alpha tracks recorded in Lexan film are shown in Fig. 3. This is the accumulated tracks in the film exposed to 6 PF discharges. The measured track density is 5.4×10^6 tracks/cm². The energy of the other particle, the proton is also around 4.3 MeV. The accelerated ${}^3\text{He}$ will have energy up to a few hundred keV. The Lexan film is insensitive for ${}^3\text{He}$ and protons [5]. Thus it is evident that the tracks in Lexan film are due to ${}^4\text{He}$ generated in fusion of ${}^3\text{He}$ and ${}^3\text{He}$. The proton tracks appeared in CR-39 film covered with 24 μm aluminium filter are displayed in Fig. 4. The film is exposed to 3 PF discharges. The proton track density is 4.9×10^6 tracks/cm². The range of 4.3 MeV α particles in aluminium is less than 18 μm [6]. The range of accelerated ${}^3\text{He}$ will be much less than 24 μm (used filter). Since ${}^4\text{He}$ and ${}^3\text{He}$ are stopped by the aluminium filter, it is clear that

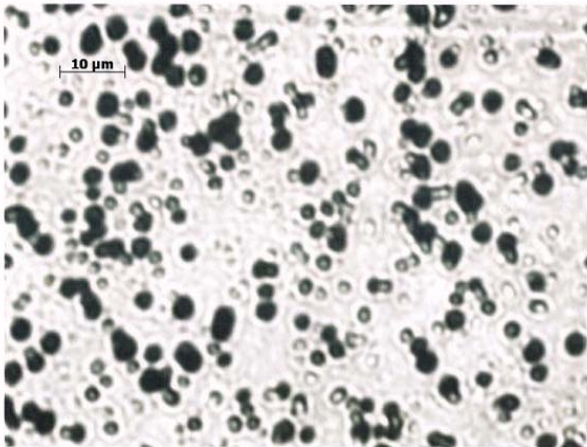


Fig. 3: Tracks of ${}^4\text{He}$ in Lexan film

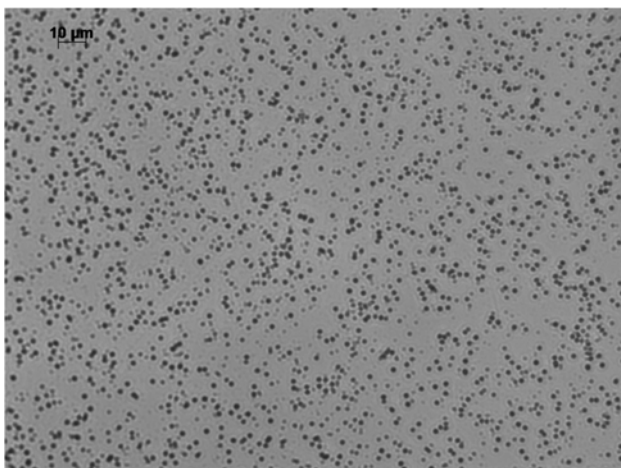


Fig. 4: Tracks of proton in CR-39 film

the tracks in CR-39 film are due to protons produced in the ${}^3\text{He}+{}^3\text{He}$ fusion reaction. Moreover, in a ${}^3\text{He}+{}^3\text{He}$ fusion reaction, two protons and one ${}^4\text{He}$ are produced. The ratio of number of protons to number of α particles is 2.0. The estimated ratio from the recorded track densities (Figures 3 & 4) is 1.8, which is close to 2.0. From the above observations it is quite clear that fusion of ${}^3\text{He}$ with ${}^3\text{He}$ is possible in a compact plasma focus device.

Conclusion

It is shown here for the first time, the possibility of fusion of ${}^3\text{He}$ with ${}^3\text{He}$ in a compact plasma focus device operated at 11.5 kJ of bank energy with pure ${}^3\text{He}$ as filling gas. The fusion products ${}^4\text{He}$ and proton are recorded quite convincingly to establish the claim. Generation of hard X-ray during the fusion process indicates the presence of high energy electrons. This also envisages the presence of high energy ${}^3\text{He}$ ions, which is required for fusion. The estimated ratio of fusion products proton to ${}^4\text{He}$ recorded through SSNTDs is 1.8. It is close to the expected ratio of 2.0.

References

1. Mather J. W., 'Dense plasma focus', Meth. Exp. Phys., 9B, 1971, 187.
2. Springham S. V., Sim T. H., Lee P., et al., ' Fusion reactions in a plasma focus operated with ${}^3\text{He}-\text{D}_2$ and ${}^4\text{He}-\text{D}_2$ gas mixtures', Phys. Scr. T123, 2006, 124.
3. Junker M., Alessandro A. D., Zavatarelli S., et al., 'Cross section of ${}^3\text{He}({}^3\text{He}, 2p){}^4\text{He}$ measured at solar energies', Phys. Rev. C., 57(5), 1998, 2700.
4. Ram Niranjan, Rout R.K., Srivastava Rohit and Gupta Satish C., 'Development and study of 13 kJ capacitor bank and plasma focus device', 25th Nat. Symp. on Plasma Sci. and Technol. (PLASMA -2010), IASST, Guwahati, India. 2012, p.79.
5. Durrani S. A. and Bull R. K., Solid State Nuclear Track Detection (Pergamon Press, Oxford and New York), III, Appendix 1, 1987, 275.
6. Ziegler J. F., Biersack J. P., and Ziegler M. D., SRIM - The Stopping and Range of Ions in Matter. SRIM Co. ISBN 0-9654207-1-X, 2008.

BARC NEWSLETTER

COMBINED RADIATION AND BIOLOGICAL TREATMENT FOR THE DECOLOURATION OF REACTIVE RED-120 DYE

Jhimli Paul and Lalit Varshney

Radiation Technology Development Division

and

A.A. Kadam and S.P. Govindwar

Department of Biochemistry, Shivaji University, Kolhapur

and

Pranaw Kumar

Fuel Chemistry Division

This Paper received the Dr. Hari Mohan Memorial Award for Best Poster at the DAE-BRNS 11th Biennial Trombay Symposium on Radiation & Photochemistry (TSRP 2012), held at Mumbai, from 4th-7th January, 2012

Abstract

The influence of low dose irradiation pretreatment on the microbial decolouration and degradation of Reactive Red-120 (RR-120) dye was investigated in detail by using *Pseudomonas sp.* SUK1. About 27, 56 and 66% decolouration of 150 ppm RR-120 dye solution was observed by applying 0, 0.5 and 1 kGy doses, respectively, in the first step followed by microbial treatment for 24 h under static condition. Similarly, about 70, 88 and 90% TOC removal was observed by applying 0, 0.5 and 1 kGy doses, respectively, in the first step followed by the microbial treatment for 96 h under static condition. The radiation induced fragmented products of RR-120 at doses of 0.5 and 1 kGy were investigated by ESI-MS and FTIR analysis. The induction of the enzymes viz. laccase, tyrosinase and azoreductase was studied in the decolourised solution obtained after irradiating 150 ppm RR-120 dye solution with 0 and 1 kGy doses followed by the microbial treatment for 96 h under static condition. The enzymatic degradation products were studied by FTIR and GC-MS. The toxicity study of the treated dye solution on plants revealed the degradation of RR-120 into non-toxic products by combined radiation-microbial treatment. This study explores a reliable and promising way to use industrially viable dose (≤ 1 kGy) and microbial strain viz. *Pseudomonas sp.* SUK1 for permissible safe disposal of dye solutions from textile industries.

Introduction

Synthetic dyes are extensively used in textile, printing, leather and cosmetic industries. Decolouration and degradation of dyestuffs, before releasing them into the main water stream, are being a major environmental concern of dye effluent treatment plants. Reactive Red-120 (RR-120) is one of the frequently used reactive azo dyes in textile industries and it is a potential threat to the aquatic environment because of its high solubility in water and poor biodegradability. The biological

treatment which is an eco-friendly, cost-competitive alternative, is being used in the conventional dye effluent treatment plants. The bacterium *Pseudomonas sp.* SUK1, (isolated from the waste disposal sites of textile processing and dye manufacturing units in Solapur (India)) showed the capability of decolourising reactive textile dyes [1]. However, it has few limitations owing to the toxicity of the dyestuffs to the microorganism and the time span of the process. The radiation technology is one of the promising advanced oxidation processes, which can effectively degrade a

BARC NEWSLETTER

wide variety of dyes in aqueous solution. Complete decolouration and degradation of any organic pollutant by only radiation treatment requires very high dose, which would not be economical from the industrial point of view. On the other hand, low dose irradiation of the same and subsequent biological treatment can make the process industrially viable.

High energy radiation induced decolouration and mineralization of RR-120 were investigated in our laboratory by employing gamma as well as electron beam, where the authors have found a noticeable increase in the biodegradability (in terms of increase in the BOD/COD ratio) of RR-120 dye solutions after radiation treatment [2, 3]. Therefore, the influence of low dose gamma-irradiation pretreatment on the microbial decolouration and degradation of RR-120 dye by *Pseudomonas sp.* SUK1 under static incubation was investigated in this paper.

Experimental

Steady state radiolysis of 150 ppm (initial dye concentration) aqueous RR-120 dye solution was carried out at pH 6.8 by using ^{60}Co gamma radiation with a dose rate of 2.5 kGy h^{-1} at 0.5 and 1.0 kGy doses. Henceforth, the 150 ppm unirradiated and irradiated RR-120 solutions at doses of 0.5 and 1 kGy will be designated in this paper as RR-120-0, RR-120-0.5 and RR-120-1, respectively. The pure culture of *Pseudomonas sp.* SUK1 was grown for 24 h in a static temperature controlled incubator at $30 \pm 2 \text{ }^\circ\text{C}$. The grown bacterial cells were incubated with RR-120-0, RR-120-0.5 and RR-120-1 along with nutrient broth at $30 \pm 2 \text{ }^\circ\text{C}$ under static condition upto 96 h. Henceforth, 96 h biologically treated RR-120-0, RR-120-0.5 and RR-120-1 will be designated in this paper as RR-120-0-B, RR-120-0.5-B and RR-120-1-B, respectively. Decolouration, TOC, FTIR, GC-MS and ESI-MS of dye solutions were studied by Hitachi U-2800 spectrophotometer, Automated TOC analyzer (Hach, USA), Perkin Elmer 783 Spectrophotometer, Shimadzu 2010 MS Engine and MicrOTOFQ-II (Bruker Daltonics) mass spectrometer, respectively.

Results and discussion

Decolouration and mineralization of RR-120 dye solution

Fig. 1A and Fig. 1B show that about 87, 94 and 97% decolouration and 78, 88 and 90% of TOC removal were observed in RR-120-0-B, RR-120-0.5-B and RR-120-1-B, respectively. At the initial stage of the radiolysis process, the dye molecules break down into smaller fragments. Therefore, the higher decolouration as well as the higher TOC removal in case of combined treatment of RR-120 might be due to the acceleration of the fragmentation of the dye molecules upon irradiating with high energy gamma rays.

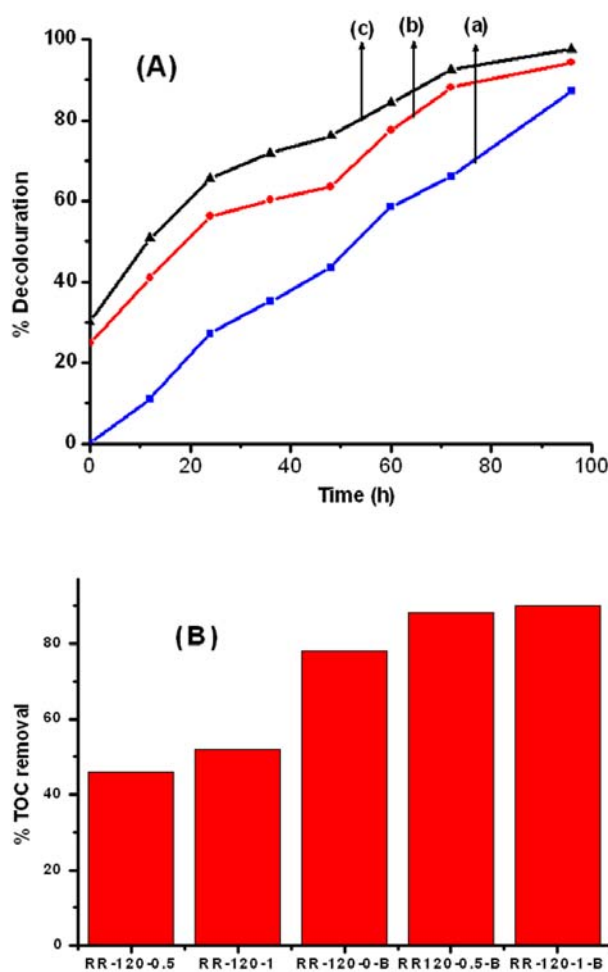


Fig. 1: The extent of (A) % decolouration and (B) % TOC removal of (a) RR-120-0-B, (b) RR-120-0.5-B and (c) RR-120-1-B.

BARC NEWSLETTER

Toxicity test

The assessment of the toxicity level of the treated textile effluent is one of the important factors for the seed germination and plant growth in the irrigation fields. The extent of seed (*Phaseolus mungo*) germination was decreased to 30% in pure dye solution with respect to the distilled water (control) and it was recovered to 90% with respect to control in combined radiation-microbial treated RR-120 solution. The combined radiation-microbial treatment on RR-120 solution showed better reduced toxicity than the unirradiated dye solution.

Investigation on the mechanism of the decolouration and degradation process

ESI-MS analysis was carried out with 25% and 30% decolourised RR-120-0.5 and RR-120-1 solutions, respectively, in order to investigate the probable solution compositions of the irradiated dye solutions used for the biodegradation studies. The spectra of RR-120-0.5 and RR-120-1 revealed the emergence of hydroxybenzosulphonic, aminobenzosulphonic and di-hydroxybenzosulphonic acids, which were formed by the reaction of water radiolysis products (e^-_{aq} and OH) with RR-120-0 during irradiation of aqueous dye solution.

The FTIR spectra of RR-120-0.5 and RR-120-1 compared to RR-120-0 revealed the appearance of primary aromatic amines, cyclohexadiene ring and increase in the population of the phenolic OH groups which supports the inference drawn from ESI-MS spectra. The FTIR spectrum of RR-120-0-B, RR-120-0.5-B, RR-120-1-B showed the disappearance of the azo ($-N=N-$) group and formation of primary aromatic amines.

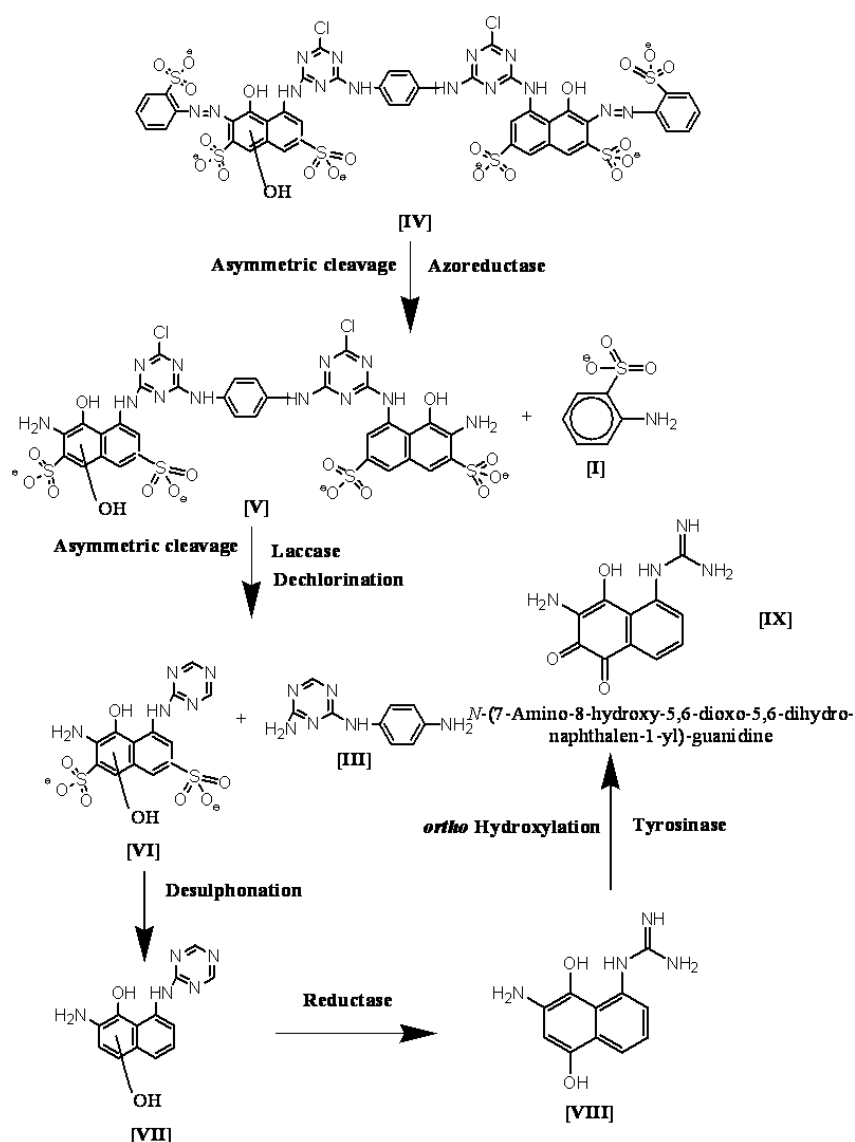
The scheme 1 shows the decolouration of dye solutions in the combined radiation and biological treatment process. The major mechanism behind the biodegradation of azo dyes in static condition is the synchronised action of several oxidative and reductive enzymes, viz. laccase, tyrosinase, azoreductase leading to the degradation of dye molecules and their fragmented products. Radiation induced fragmented products like hydroxybenzosulphonic, di-hydroxybenzosulphonic acid, aminobenzosulphonic acid etc., helped to recover the laccase activity and also helped to increase tyrosinase activity in RR-120-1-B solution as compared to RR-120-0-B. The activity of azoreductase was decreased in RR-120-1-B solution as compared to RR-120-0-B because of the occurrence of lesser number of azo groups in the irradiated dye solution.

On the basis of various enzyme inductions and GC-MS analysis, the possible biodegradation pathways of irradiated RR-120 dye solution adapted by *Pseudomonas* sp. SUK1 are illustrated in Scheme 2. The azo group of the product [IV] formed in the irradiated dye solution might have been reduced by azoreductase to 2-aminobenzenesulfonic acid [I] of m/z 170 and reactive intermediate [V]. Asymmetric cleavage of the reactive intermediate [V] by laccase and subsequent dechlorination formed another reactive intermediate [VI] and one stable product N-(4-aminophenyl)-1,3,5-triazine-2,4-diamine [III] of m/z 154. Subsequent desulphonation of [VI] led to the formation of [VII], which produces N-(7-amino-8-hydroxy-5,6-dioxo-5,6-dihydronaphthalen-1-yl)-guanidine [IX] having m/z at 246 by further attack of reductase and tyrosinase, subsequently.



Scheme 1: The stepwise combined radiation and biological treatment process

BARC NEWSLETTER



Scheme 2: The possible biodegradation pathways of irradiated RR-120 dye.

Conclusion

The detailed mechanistic investigation on the microbial decolouration and degradation of RR-120 showed that the radiation treatment of RR-120 helped to increase the process efficiency in two ways, firstly it decreased the concentration of RR-120 significantly before the commencement of the microbial treatment and secondly the radiation induced fragmented products showed diverse enzymatic activities. However, the above results demonstrate that irradiating the RR-120 solution with a lower dose (≤ 1 kGy) and then microbial treatment of the irradiated solution with *Pseudomonas sp.* SUK1 under static condition increased the performance of the decolouration and degradation of RR-120 dye solution.

References

1. Kalyani, D.C., Patil, P.S., Jadhav, J.P., Govindwar, S.P., 2008. Biodegradation of reactive textile dye Red BLI by an isolated bacterium *Pseudomonas sp.* SUK1. *Bioresour. Technol.* 99, 4635–4841.
2. Paul, J., Naik, D.B., Sabharwal, S., 2010. High energy induced decoloration and mineralization of Reactive Red 120 dye in aqueous solution: a steady state and pulse radiolysis study. *Radiat. Phys. Chem.* 79, 770–776.
3. Paul, J., Rawat, K.P., Sarma, K.S.S., Sabharwal, S., 2011. Decoloration and degradation of Reactive Red-120 dye by electron beam irradiation in aqueous solution. *Appl. Radiat. Isot.* 69, 982–987.

CARBOXYMETHYL CELLULOSE-POLYVINYL ALCOHOL-CLOVE OIL ACTIVE FILMS FOR MEAT PRESERVATION

Shobita Rao Muppalla, Sweetie R. Kanatt, S.P. Chawla, Arun Sharma
Food Technology Division

This Paper received the First Prize for Poster at the Innovations in Food Science and Technology to fuel the growth of the Indian food industry, (XXI ICFOST), held at Pune, on 20th & 21st January, 2012

Abstract

The aim of this study was to develop composite active films from carboxymethyl cellulose (CMC) and polyvinyl alcohol (PVA) containing clove oil, study their properties and application in meat preservation. Films were prepared by the casting method using CMC-PVA and clove oil in different ratios. Mechanical, permeability and antibacterial properties were studied using the standard methods. Addition of PVA led to increase in puncture force, tensile strength of the films. However, the water vapor transmission rate was found to decrease. All the films were impermeable to oxygen. The films containing 3% (v/v) clove oil were found to be effective against *Staphylococcus aureus* and *Bacillus cereus*. These films decreased bacterial counts in minced meat and increased its shelf life by 12 days during chilled storage. The efficacy of these films was further analyzed by packed inoculum studies using *S. aureus* and *B. cereus* in minced meat. These films show promise as active packaging material for meat preservation.

Introduction

Food packaging is important for food processing industry. Bio-based polymeric films for food packaging application have drawn the attention of researchers as an alternative approach to deal with the problem of disposal of plastic packaging materials (1). Active packaging is an emerging food packaging technique. It provides additional functions in comparison to the traditional packaging (2). The main cause for meat spoilage is microbial growth on product surface. Incorporation of antimicrobial agents in packaging material is useful in preventing the growth of microbes and leads to their shelf life extension. Clove oil is a natural preservative and flavoring substance. The aim of this study was to investigate properties of CMC-PVA-clove oil films and evaluate the efficacy of these films in improving shelf life of mince meat model system.

Materials & Methods

Film preparation

The polymer films were prepared by the casting method. CMC solution (1% w/v) and PVA solution (5% w/v) were mixed at various ratios (1:1, 1:2 & 2:1). Clove oil was added to the film forming solution at a concentration of 1, 2, and 3%. The films were prepared by casting and drying at 50°C in a ventilated oven at 50% relative humidity (RH) to obtain films of uniform thickness. Film characteristics were determined after all sample films were preconditioned in a constant temperature humidity chamber set at 23°C with 50% RH for 24 h.

Film properties

Film thickness was measured using a micrometer. Tensile strength (TS) and puncture strength were measured using Texture Analyzer in accordance with ASTM D882-

BARC NEWSLETTER

91 method (3). Water vapor transmission rates and oxygen permeability were analyzed using an automatic water vapor permeability testing machine and automated oxygen permeability testing machine.

Antibacterial activity

Antibacterial activity of all the film samples against *Bacillus cereus* MTCC 470 and *Staphylococcus aureus* ATCC 6538P was determined using tube method. On the basis of its good mechanical and antibacterial activity CMC1PVA2 film containing 3% clove oil was evaluated for its ability to enhance shelf-life of meat samples. Meat packed in LDPE pouches constituted control whereas, other lot consisted of meat packed in the film. All the samples were stored at 4°C for 16 days. At regular intervals the samples were analyzed for their microbial quality. The efficacy of this film in reducing the load of *S. aureus* and *B. cereus* was validated by packed inoculum studies. Samples were irradiated at 10 kGy to eliminate the normal flora. Meat samples were inoculated with cultures individually and packed in film. The samples were stored at chilled temperature and viable counts were analyzed at regular intervals of time.

Results & Discussion

The composite films formed from CMC and PVA were visually homogeneous, had smooth surface and could be easily peeled from the casting plates. The films were free standing and had thickness of 150-200 μm . Ratio of CMC/PVA or addition of clove oil did not change significantly ($p > 0.05$) the average thickness of the films. The films formed of CMC/PVA were transparent and colorless whereas the films containing clove oil had slight yellowish color. Increase in concentration of PVA

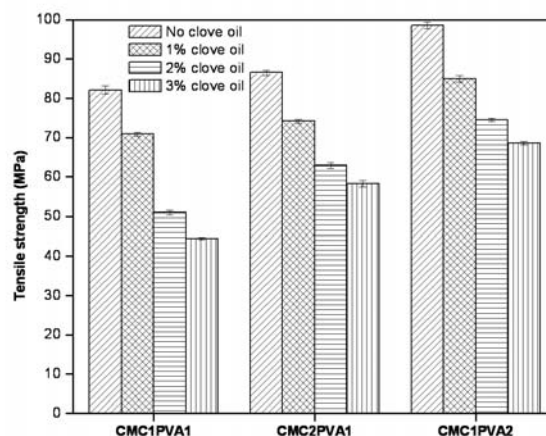


Fig. 1: Tensile strength of CMC-PVA films containing clove oil

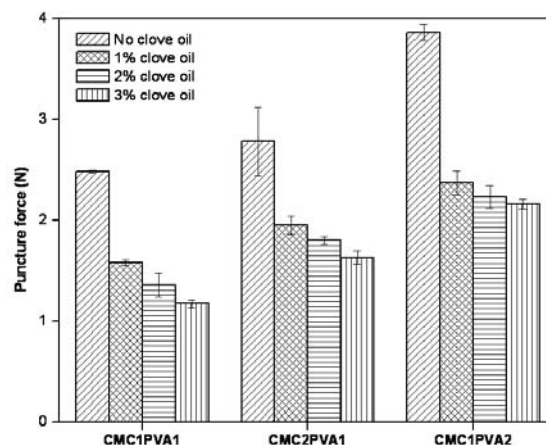


Fig. 2: Puncture force of CMC-PVA films containing clove oil

in film led to increase in tensile strength and puncture force (Fig 1, 2). Addition of PVA has been reported to increase TS of fish myofibrillar protein based film (4). However, incorporation of clove oil in CMC-PVA films led to decrease in both TS and puncture force. The WVTR values of CMC-PVA films are shown in Table 1. Film containing higher percentage of CMC had slightly higher WVTR. The hydrophilic nature of films increases

Table 1 Water vapor permeability of CMC-PVA films

Sample	Water vapor transmission rate (g/m ² /day) ^a			
	0% clove oil	1% clove oil	2% clove oil	3% clove oil
CMC1PVA1	4041 ± 116	4123 ± 106	4202 ± 167	4261 ± 120
CMC1PVA2	3809 ± 174	3764 ± 110	3843 ± 153	3664 ± 158
CMC2PVA1	4261 ± 216	4219 ± 137	4156 ± 172	4080 ± 143

^a the results shown are mean ±SD of three independent experiments.

BARC NEWSLETTER

with increasing carboxymethyl groups therefore resulting in greater WVTR. Addition of clove oil did not result in significant changes in WVTR. All the films had negligible oxygen permeability. PVA is known to have excellent gas barrier property due to its small, dense and closely packed monoclinic crystal structure (5).

The results of antibacterial effects of CMC-PVA films incorporated with different concentration of clove oil against *S. aureus* and *B. cereus* are shown in Fig (3, 4). Films containing higher concentration of PVA showed better antibacterial activity against both the cultures. This can be attributed to hydrophilic nature of PVA which makes release of antibacterial additive easy. The mechanism of antimicrobial activity of essential oils is related with the attack on the phospholipid present in cell membranes, which causes increased permeability and leakage of cytoplasm, or in their interaction with enzymes located on the cell wall (6).

Effect of active film on the natural microflora of minced meat is shown in Fig 5. It can be seen that films containing clove oil reduced the initial load of meat by 2 log cycle. Control samples spoiled within 4 days of

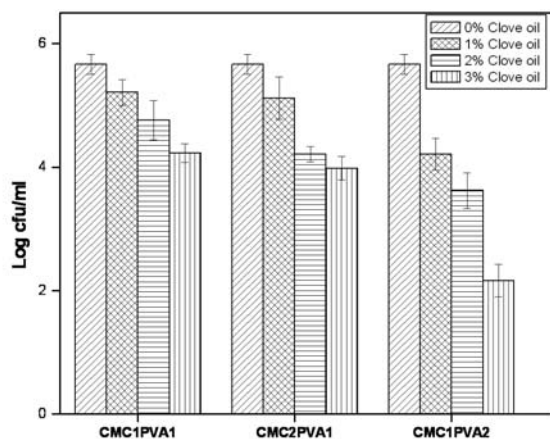


Fig. 3: Antibacterial activity of CMC-PVA-clove oil films against *S. aureus*

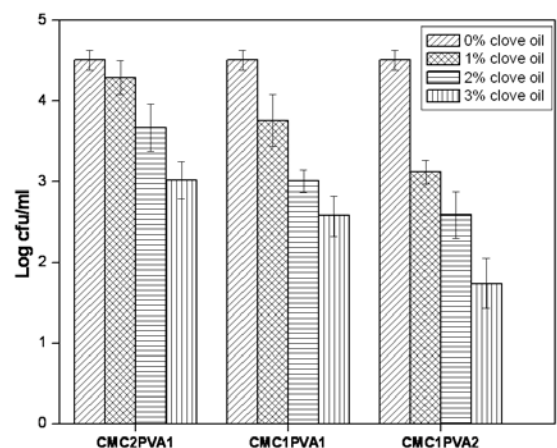


Fig. 4: Antibacterial activity of CMC-PVA-clove oil films against *B. cereus*

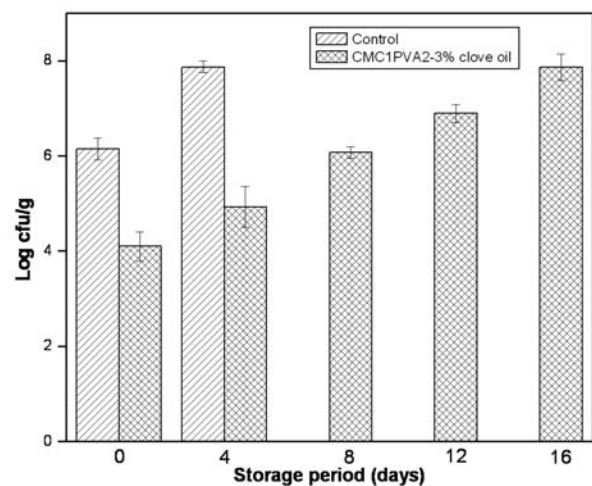


Fig. 5: Antibacterial activity of CMC-PVA-clove oil films against natural flora of minced meat

storage, whereas sample packed in active films had shelf life of 12 days. This inhibition could be attributed to the hydrophobic nature of clove oil to partition in the lipids of the bacterial cell membrane and mitochondria while disturbing the structures and rendering it more permeable (7). The results of packed inoculum studies are shown in Table 2. Initial counts of *S. aureus* in control meat sample were 3.37 log cfu/g which

Organism	Days							
	0		4		7		11	
	Control	Film ^a	Control	Film	Control	Film	Control	Film
<i>S. aureus</i>	3.37±0.23 ^b	2.32±0.11	3.89±0.10	1.30±0.24	5.42±0.21	0	6.07±0.31	0
<i>B. cereus</i>	4.41±0.15	4.09±0.26	4.61±0.13	0	4.82±0.16	0	4.94±0.29	0

^a CMC1PVA2 film with 3% clove oil

^b Counts expressed as log cfu/g

BARC NEWSLETTER

increased up to 6.07 log cfu/g during chilled storage. Packing meat in active film led to initial reduction by 1 log cycle and organism was completely eliminated after 7 days of storage in chilled condition. In case of *B. cereus*, the counts did not increase in control samples during storage but active packaging led to complete elimination of *B. cereus*. These results clearly suggest the potential of CMC-PVA films containing clove oil in ensuring the safety of meat.

Conclusion

This study demonstrated that active CMC-PVA films can be made by incorporation of clove oil. Addition of PVA led to improvement in mechanical and permeability properties of the film. The films improved the shelf life of minced meat during chilled storage. These films were also effective in eliminating inoculated Gram-positive food pathogens in meat thereby enhancing the safety of meat. Thus, this study demonstrated that addition of clove oil to films has the potential for being developed into functional packaging material for food. Further research on feasibility of such films in improving quality and safety of commercial meat products is needed.

Bibliography

1. Farris, S., Schaich, K.M., Liu, L., Piergiovanni, L., Yam, K.L. "Development of polyion-complex hydrogels as an alternative approach for the production of bio-based polymers for food packaging applications: a review". *Trends in Food Science and Technology* 20 (2009):316-332
2. Scannell, A.G.M., Hill, C., Ross, R.P., Marx, S., Hartmeier, W. & Arendt, E.K. "Development of bioactive food packaging materials using immobilised bacteriocins Lacticin 3147 and Nisaplin". *International Journal of Food Microbiology* 60 (2000):241-249.
3. ASTM D 882-91. "Standard Test Methods for Tensile Properties of Thin Plastic Sheeting". In: Annual book of ASTM standards. American Society for Testing & Materials, Philadelphia, PA, 1991.
4. Limpan, N., Prodpran, T., Benjakul, S. & Prasarpran, S. "Influences of degree of hydrolysis and molecular weight of poly(vinyl alcohol)(PVA) on properties of fish myofibrillar protein/PVA blend films". *Food Hydrocolloids* 29 (2012): 226-233.
5. Jang, J., & Lee D.K. "Plasticizer effect on the melting and crystallization behavior of polyvinyl alcohol". *Polymer* 44 (2003): 8139-8146.
6. Emiroglu, Z.K., Yemis, G.P., Coskun, B.K., & Candogan, K. "Antimicrobial activity of soy edible lms incorporated with thyme and oregano essential oils on fresh ground beef patties". *Meat Science* 86 (2010): 283-288.
7. Sikkema, J., de Bont, J.A.M., & Poolman, B. "Interaction of cyclic hydrocarbons with biological membranes". *Journal of Biological Chemistry* 269 (1994): 8022-8028.

BARC NEWSLETTER

γ -TOCOTRIENOL INDUCED APOPTOSIS IN TUMOR CELLS THROUGH ACTIVATION OF INTRINSIC AND EXTRINSIC PATHWAYS

Chandan Wilankar, Nazir M. Khan, Rahul Checker, Deepak Sharma,
R. S. Patwardhan, Santosh. K. Sandur and T.P.A. Devasagayam

Radiation Biology & Health Sciences Division

and

Vikram Gota

Clinical Pharmacology, ACTREC, Tata Memorial Centre

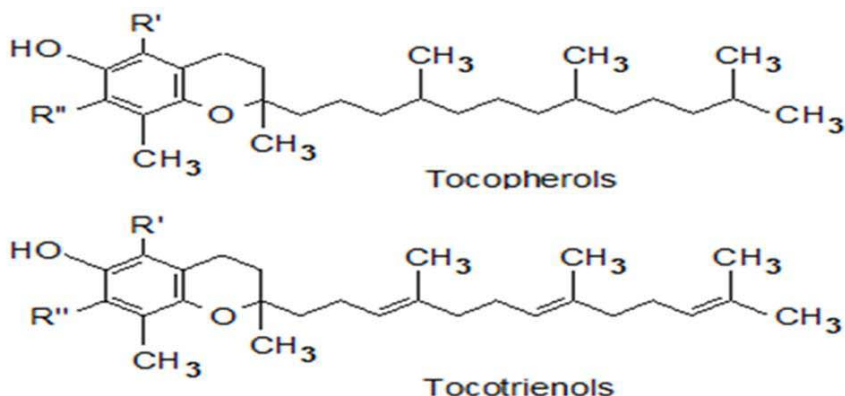
This Paper received the Best Poster Award at the International Conference on Free Radicals, Antioxidants and Nutraceuticals in Health, Disease & Radiation Biology, held at Kolkata, from 12-14 January, 2012

Introduction

Vitamin E is a well known antioxidant and is an important nutrient in the human diet that is readily available in lipid-rich plant products. The vitamin E family consists of eight isomers known as alpha-, beta-, gamma-, and delta-tocopherols and alpha-, beta-, gamma-, and delta-tocotrienols [1]. Tocopherols are predominant in olive, sunflower, corn, soya beans oils, and tocotrienols are the major vitamin E components of palm oil, barley and rice bran [2]. Structurally, tocopherols and tocotrienols are very similar. The main difference is that tocopherols have a long saturated carbon side chain with chiral centers, while tocotrienols have three unsaturated bonds in the carbon side chain with one chiral center. The unsaturated side chain present on tocotrienols facilitates their better cellular uptake than tocopherols. This higher cellular uptake has been attributed to their superior biological activities

as compared to tocopherols. Several studies have reported that tocotrienols may have more potent antioxidant and anticancer effects than tocopherols [3]. Studies have also reported that tocotrienols possess lipid-lowering, anti-atherogenic, blood-pressure lowering, anti-diabetic, neuroprotective and anti-inflammatory effects [4]. The abundance of literature suggests that the use of tocotrienols for therapeutic purposes is very promising.

There are several reports on antitumor activity of γ -tocotrienol (GT) on human mammary tumor cells, hepatocellular carcinoma, colon cancer cells, melanoma cells, gastric adenocarcinoma and prostate cancer cells [5]. Further, GT has been shown to suppress multiple signaling pathways that include suppression of NF- κ B, STAT3 and phosphatidylinositol 3-kinase (PI3K)-AKT signaling. However, there is no consensus on unique identifiable targets of tocotrienols relating to their



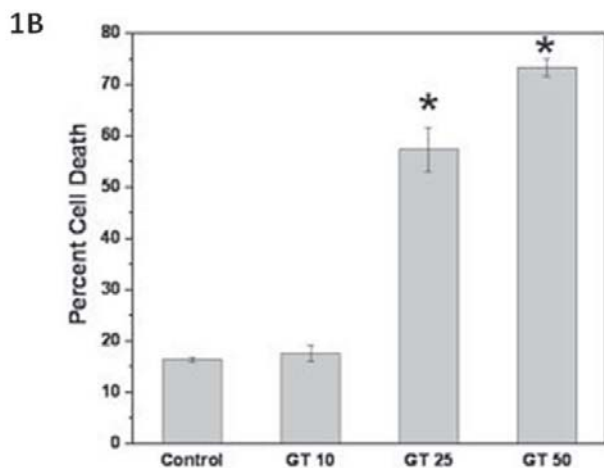
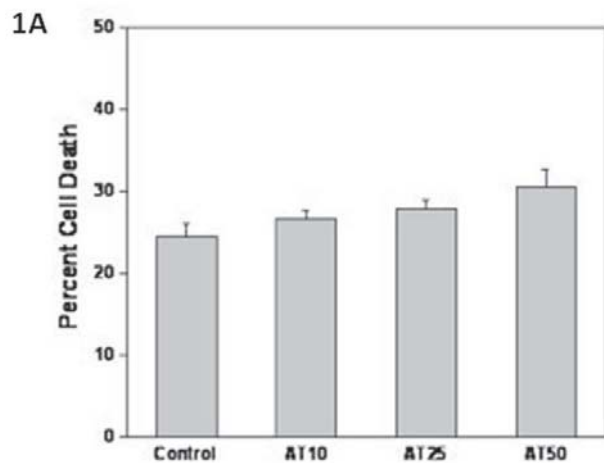
α : R' = CH₃, R'' = CH₃
 β : R' = CH₃, R'' = H
 γ : R' = H, R'' = CH₃
 δ : R' = H, R'' = H

BARC NEWSLETTER

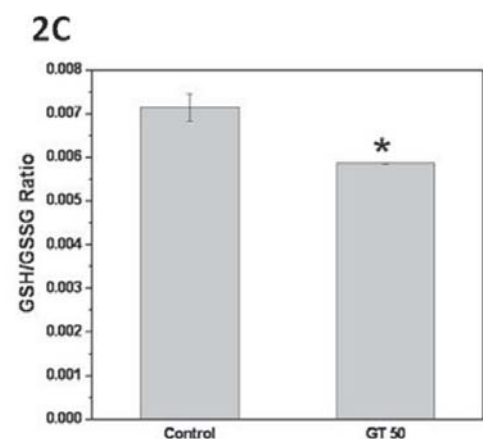
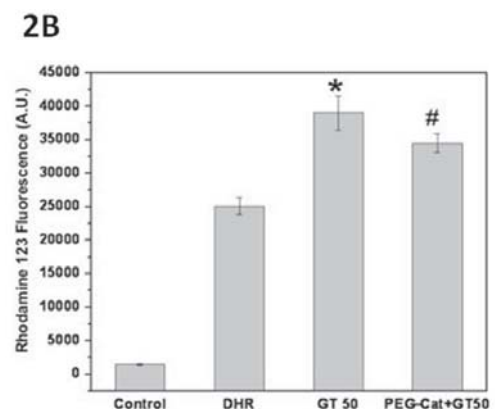
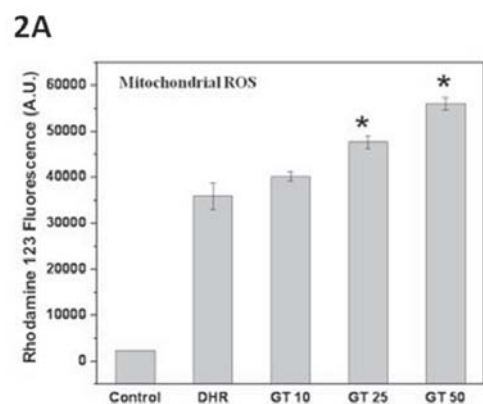
antitumor activity in different tumor cells. The relative antitumor activity of different tocotrienols isoforms is also not clearly established. Further, there is also no evidence for antitumor effect of tocotrienols against human lymphomas. In the present study, we examine the potential of α -tocotrienol and γ -tocotrienol in inhibiting the proliferation of human T cell lymphoma and also elucidate its molecular mechanisms of action using in Jurkat cells.

Results

1. GT was more potent than AT in inhibiting the proliferation of Jurkat cells: To examine the potential anti-tumor properties of γ -tocotrienol (AT) and α -tocotrienol (GT), we investigated the cytotoxic effect of AT or GT in Jurkat cells using propidium iodide staining followed by flowcytometry. We observed that AT did not have any cytotoxic effect in Jurkat cells, whilst GT showed significant cytotoxicity in a concentration dependent manner (Fig. 1A and B).



2. GT induced mitochondrial ROS and decreased GSH/GSSG ratio in Jurkat cells: Treatment of cells with GT led to a dose dependent increased in the mitochondrial reactive oxygen species (ROS) as measured by changes in fluorescence of rhodamine123 which was abrogated by PEG-catalase suggesting an involvement of H_2O_2 (Fig. 2A and B). Further, GT treatment significantly decreased the GSH/GSSG ratio in these cells suggesting that GT induced cell death in Jurkat cells may be mediated by induction of oxidative stress (Fig. 2C).



BARC NEWSLETTER

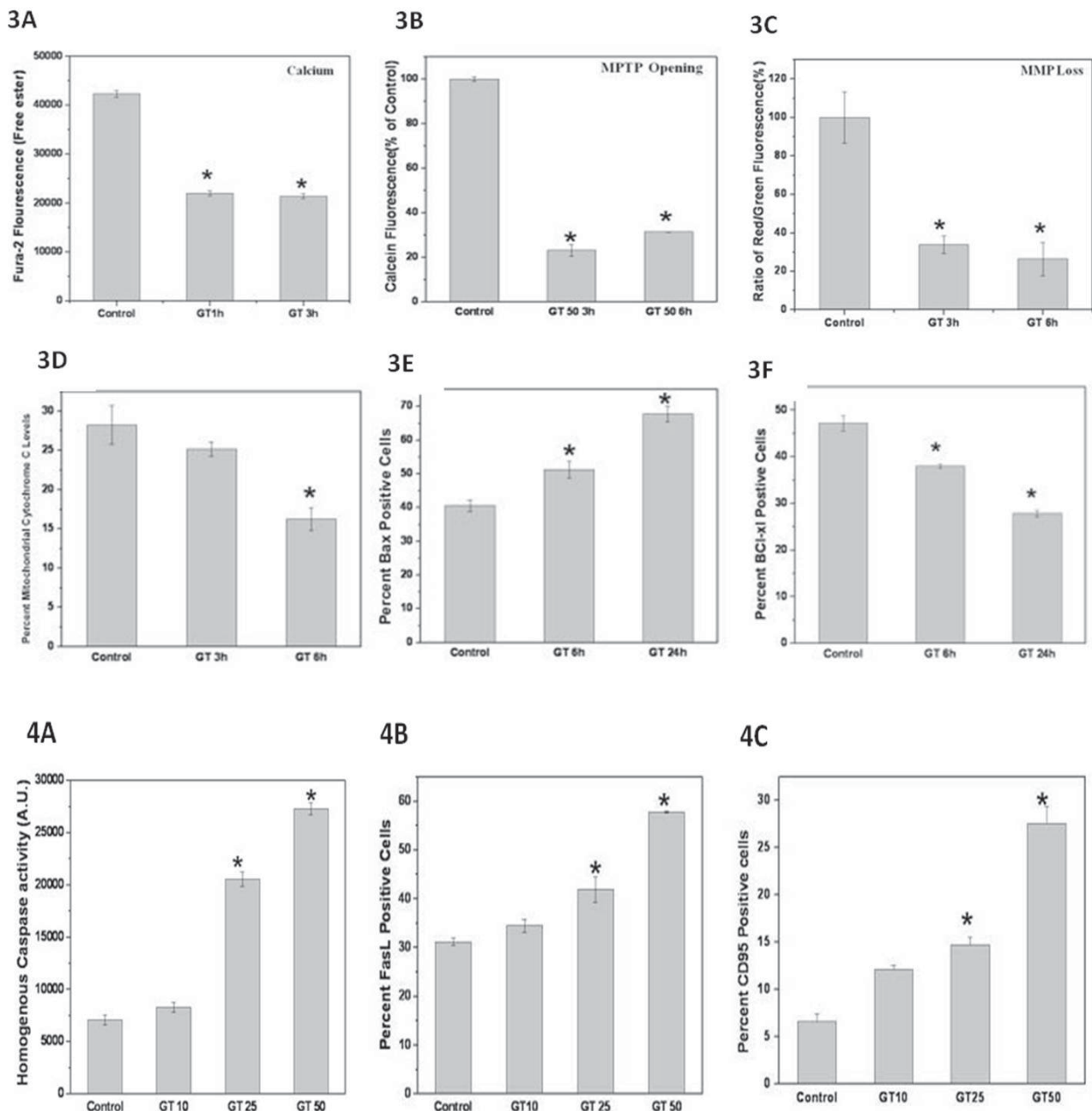
3. GT treatment induced loss of mitochondrial membrane potential induced calcium release and cytochrome c release from the mitochondria:

It was observed that GT treatment led to Ca^{2+} release from intracellular Ca^{2+} stores as measured using fluorescence of free ester of fura-2AM (Fig. 3A). Increased mitochondrial transition pore (MPTP) opening (Fig. 3B), disruption of the mitochondrial membrane potential (Fig. 3C) and decrease in mitochondrial cytochrome c levels were observed in GT treated Jurkat cells (Fig. 3D). Further, a significant increase in Bax levels, a proapoptotic protein (Fig. 3E), and

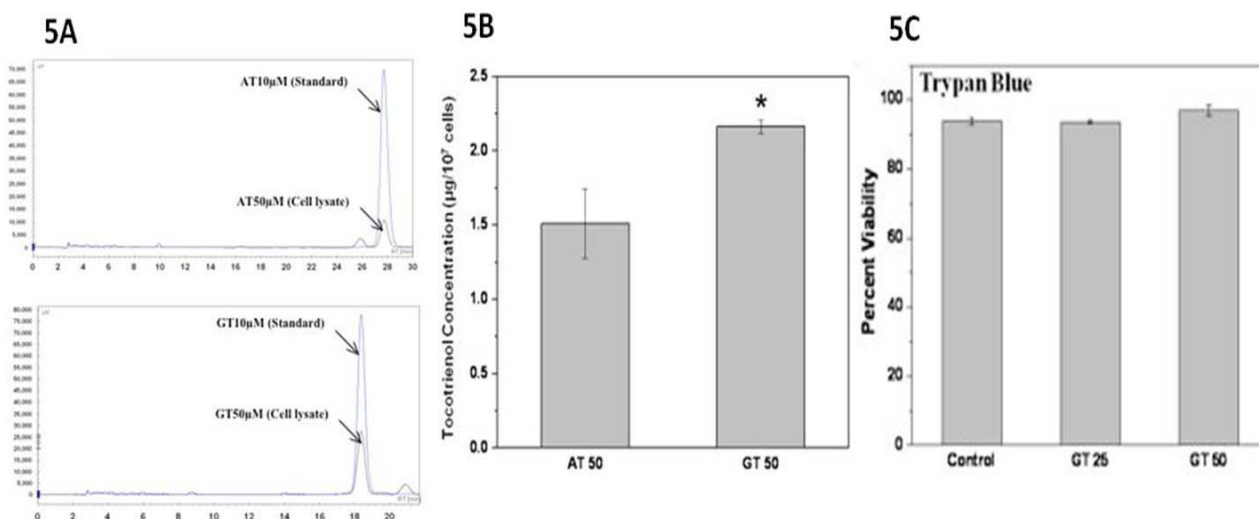
decrease in Bcl-xl levels, an antiapoptotic protein, were observed in Jurkat cells following incubation with GT (Fig. 3F).

4. GT Induced Caspase Activation and Degradation of PARP and Activated Extrinsic Apoptotic Pathway:

It was observed that GT treatment increased homogeneous caspase activity in a concentration dependent manner in Jurkat cells (Fig. 4A). Further, GT (25 μ M) treatment to cells also increased the surface expression of FasL and Fas on Jurkat cells as estimated by flow cytometry (Fig. 4B and C).



BARC NEWSLETTER



5. Cellular Uptake of GT was Higher than AT: To investigate whether the cytotoxic effects exhibited by GT but not by AT are due to their differential cellular uptake, HPLC analysis coupled with UV absorption detection was performed using lysates prepared from cells treated with GT or AT for 24h. It was observed that intracellular uptake of GT was significantly higher than AT (Fig. 5A-B).

6. GT Did Not Induce Cytotoxic Effect in Human PBMCs, the Normal Counter Part of Jurkat Cells: Since selective toxic effect of GT on lymphoid tumor cells is highly desirable in the tumor therapy, we measured its cytotoxic effect on human PBMCs. Results showed that GT exposure to human PBMCs did not induce any significant cytotoxicity at the concentrations studied (Fig. 5C).

Discussion

The strong antioxidant, cardioprotective and antitumor properties of tocotrienols have generally attributed to their antioxidant properties. In this study, addition of GT to Jurkat cells was observed to significantly increase apoptosis at 25 µM. However, AT failed to induce cell death in lymphoma cells indicating that GT possess better antitumor activity than AT. Further, GT treatment resulted in elevated mitochondrial ROS production and induced calcium release, loss of mitochondrial membrane potential and cytochrome c release from the mitochondria. Our results showed that GT induced cell death in Jurkat cells via increased mitochondrial

ROS generation followed by activation of both extrinsic as well as intrinsic apoptotic pathways. Abrogation of GT mediated apoptosis by inhibitors of caspase-8 and caspase-9 also underscore the significance of these two apoptotic pathways in GT mediated cytotoxicity. Cellular uptake studies with AT and GT showed that intracellular accumulation of GT was higher as compared to AT which may be responsible for its better antitumor efficiency. In contrast GT was not toxic to normal human peripheral blood mononuclear cells (PBMCs) suggesting differential cytotoxicity towards normal lymphocytes and transformed lymphoma cells.

References

1. Wong RS, Radhakrishnan AK. Tocotrienol research: past into present. *Nutrition reviews* 2012;70:483-90.
2. Theriault A, Chao JT, Wang Q, Gapor A, Adeli K. Tocotrienol: a review of its therapeutic potential. *Clinical Biochemistry* 1999;32:309-19.
3. Colombo ML. An update on vitamin E, tocopherol and tocotrienol-perspectives. *Molecules* 2010;15:2103-13.
4. Aggarwal BB, Sundaram C, Prasad S, Kannappan R. Tocotrienols, the vitamin E of the 21st century: its potential against cancer and other chronic diseases. *Biochemical Pharmacology* 2010;80:1613-31.
5. Ling MT, Luk SU, Al-Ejeh F, Khanna KK. Tocotrienol as a potential anticancer agent. *Carcinogenesis* 2012;33:233-9.

CONTRIBUTION OF ERK & NRF-2-ARE PATHWAY TO CONSTITUTIVE AND INDUCIBLE RADIORESISTANCE OF TUMOR CELLS VIS A VIS NORMAL CELLS

**Raghavendra S. Patwardhan, Rahul Checker, Deepak Sharma,
Santosh Kumar Sandur and Krishna B. Sainis**
Radiation Biology & Health Sciences Division

This Paper received the Best Poster Award at the International Conference on Free Radicals, Antioxidants and Nutraceuticals in Health, Disease & Radiation Biology, held at Kolkata, from 12-14 January, 2012

Introduction

Radiation therapy is one of the main line treatment modalities for different types of solid tumors. Tumor cells possess inherent and/or exhibit acquired resistance to radiation induced cytotoxicity (1). Ionizing radiation (IR) mediates damage to cells by both direct and indirect processes. Reactive oxygen species (ROS) generated as a result of indirect effect cause damage to biomolecules resulting in cell death. Generation of ROS disturbs redox balance within the cells (2). Effective scavenging of ROS depends on how efficiently they are neutralized by antioxidants present inside cells so that ionizing radiation induced damage is not permanently fixed.

We have shown that intrinsic radioresistance of lymphoma cells vis-à-vis normal lymphocytes may be due to lower basal and inducible ROS levels. Further, lymphoma cells had higher GSH levels and antioxidant enzyme activities as compared to normal lymphocytes (3). The levels of intracellular antioxidants and antioxidant enzymes are regulated by redox sensitive transcription factor nuclear factor erythroid-2 related factor-2 (Nrf-2), that induces transcription of a battery of antioxidant enzymes viz. catalase, Mn-superoxide dismutase, glutathione peroxidase, glutathione-s-transferase, hemeoxygenase I etc.

It is important to identify newer targets to sensitize tumor cells to radiation without affecting normal

tissues. Recent reports indicate that ionizing radiation activates Nrf-2 pathway through oxidative stress and targeting this pathway may improve outcome of radiation therapy. Based on these reports, we hypothesized that Nrf-2-ARE pathway may contribute to the constitutive as well as inducible radioresistance in tumor cells. We compared murine splenic lymphocytes from C57/BL6 mice with syngenic murine T cell lymphoma cells (EL-4). The aim of this study is to determine the contribution of ERK/Nrf-2-ARE pathway in tumor radioresistance.

Results

EL-4 cells showed higher resistance to ionizing radiation induced cell death than normal murine splenic lymphocytes

Fig.1 shows IR induced apoptosis in mouse T lymphoma cell line EL-4 and mouse splenic lymphocytes (Fig. 1A). Ionizing radiation induced apoptosis in about 60% of murine splenic lymphocytes over control. However, EL-4 lymphoma cells showed significantly lower radiation induced apoptosis (~10%) as compared to murine lymphocytes. Basal levels of cellular ROS were significantly lower in tumor cells as compared to their normal counterpart as measured by different redox-sensitive fluorescent probes.

BARC NEWSLETTER

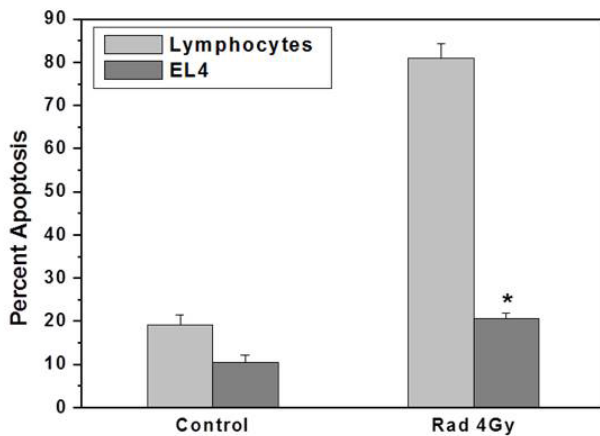


Fig. 1a: Basal and radiation induced cell death in normal and tumor cells

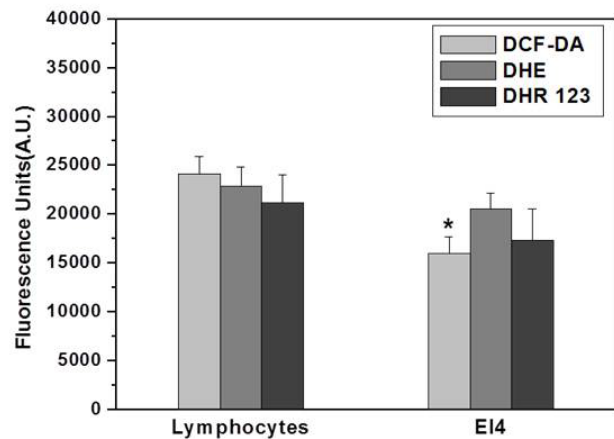


Fig. 1b: Basal ROS levels in normal and tumor cells

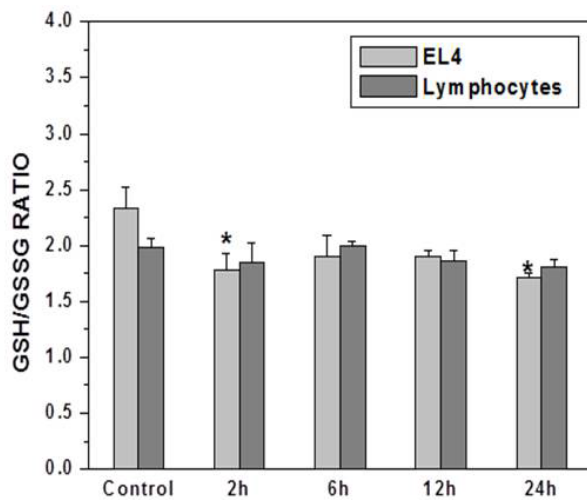


Fig. 2: Basal and radiation induced GSH/GSSG ratio in normal and tumor cells

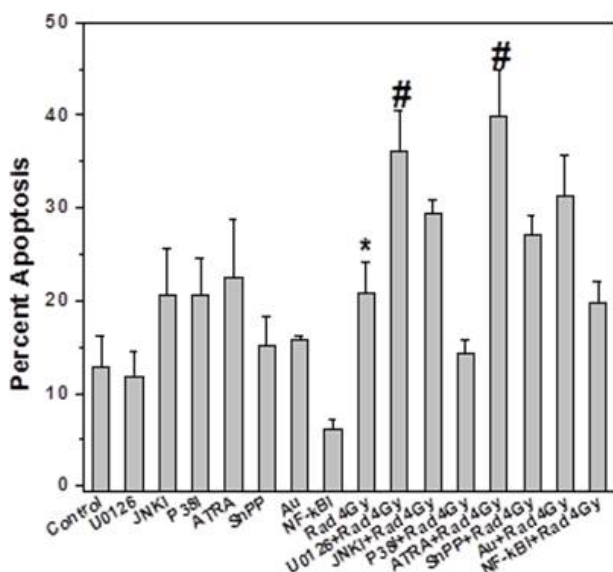


Fig. 3: Effect of pharmacological inhibitors on radiation induced cell death in EL-4 cells

Murine T cell lymphoma cells showed higher GSH to GSSG ratio

There was a significant decrease in GSH/GSSG ratio in tumor cells at 2h post-irradiation but stabilized at later time points (Fig. 2). However, in normal lymphocytes the change in ratio of GSH to GSSG was not significant post-irradiation.

ERK or Nrf-2 inhibitor significantly enhanced radiation induced cell death in tumor cells

Inhibitors of ERK, Nrf-2, HO-1 and thioredoxin reductase significantly enhanced radiation induced cell death in EL-4 cells suggesting their involvement in cellular radioresistance (Fig 3).

EL-4 cells showed upregulation of Nrf-2 and its dependent gene expression at different time points after radiation exposure

Murine splenic lymphocytes showed complete down regulation of Nrf-2 at 24hrs but, EL-4 cells showed upregulation in Nrf-2 mRNA levels at all the time points studied (Fig. 4a). There was also a significant increase in mRNA copy number of Nrf-2 dependent genes viz. Mn-SOD, catalase, thioredoxin reductase, GCLC and HO-1 in EL-4 cells (Fig. 4b).

Exposure of EL-4 cells to radiation increased nuclear levels of Nrf-2

Nuclear translocation of Nrf-2 was assessed by electrophoretic mobility shift assay. EL-4 cells exposed

BARC NEWSLETTER

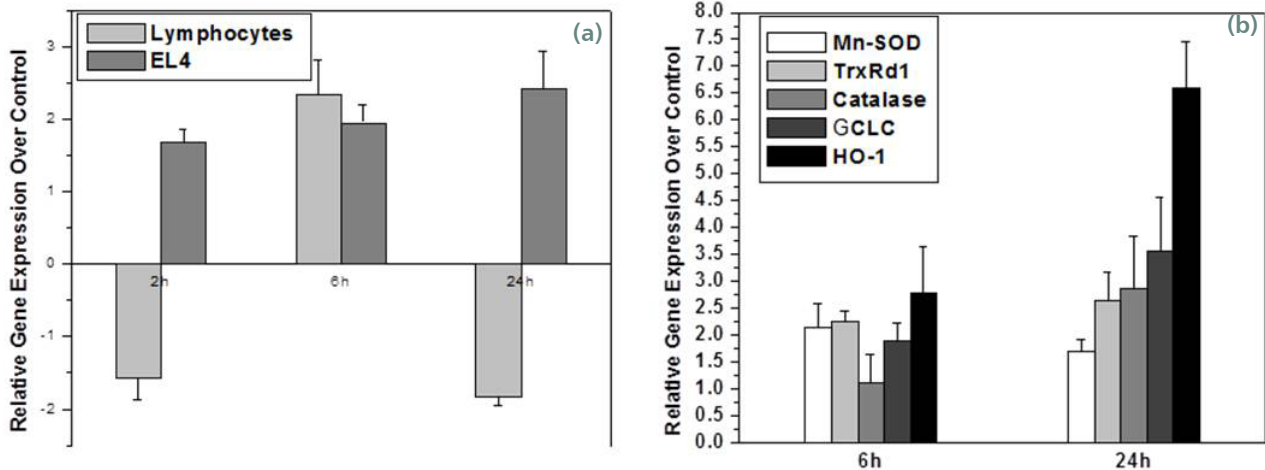


Fig. 4: Effect of radiation on mRNA levels of Nrf-2 and its dependent genes

to radiation showed increased levels of Nrf-2 in nuclear extracts at 6h but decreased at later time points (Fig. 5).

ERK or Nrf-2 knockdown EL-4 cells showed significantly higher radiosensitivity than wild type cells

Cells were transfected with scrambled shRNA plasmids or shRNA against ERK/Nrf-2 and then exposed to radiation. Cell death was measured by propidium iodide staining followed by flow cytometry (Fig. 6). ERK or Nrf-2 knockdown cells showed higher radiation induced

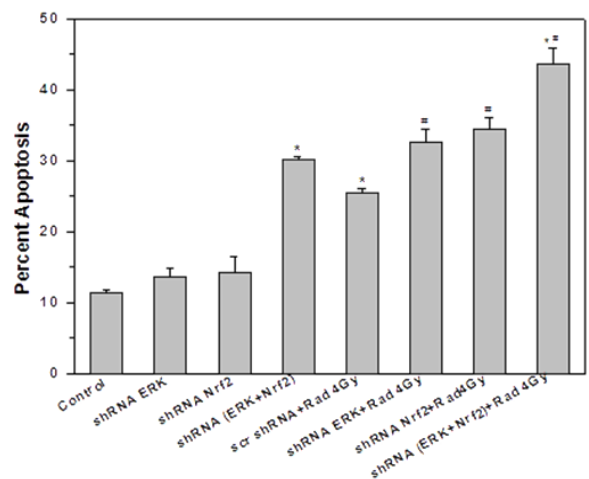


Fig. 6: Effect of ERK and Nrf-2 knockdown on radiation induced cell death in EL-4 cells

24	6	12	24	U+24	Time (h)
--	+	+	+	+	Rad 4Gy

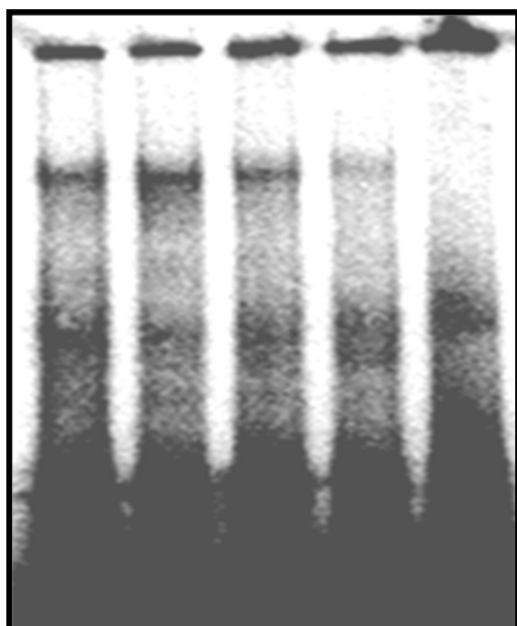


Fig. 5: Basal and radiation induced changes in nuclear Nrf-2 levels

apoptosis as compared to wild type cells. However, double knockdown ERK and Nrf-2 showed increased level of basal apoptosis.

Discussion

Our earlier report showed that decreased generation of radiation induced ROS in mouse lymphoma cells was associated with reduced extent of radiation induced apoptosis as compared to that in normal lymphocytes (2,4). The present studies also confirmed these observations and further probed the role of cellular redox signaling in murine lymphocytes and EL-4 lymphoma cells after exposure to ionizing radiation.

The ratio of GSH to GSSG and activity of thioredoxin in EL-4 cells (data not shown) was significantly higher in

BARC NEWSLETTER

EL-4 lymphoma cells as compared to normal lymphocytes under basal conditions (Fig 2). Cellular redox state can influence the pro-survival/pro-apoptotic signaling targets and thereby decide the fate of a cell [2]. Pharmacological inhibitors of MAPK, Nrf-2, HO-1 and thioredoxin reductase significantly enhanced radiosensitivity of EL-4 cells. Interestingly it was observed that, incubation of EL-4 cells with ERK or Nrf-2 inhibitor decreased their cell survival (Fig. 3) highlighting their importance in survival of these lymphoma cells.

To further confirm these findings, we examined the radiosensitivity of EL-4 cells after knocking down ERK and Nrf-2. It was observed that knockdown of ERK or Nrf-2 enhanced radiation induced apoptosis (Fig 5). Nrf-2 was found to be constitutively active in EL-4 cells which may help to express genes involved in scavenging

cellular ROS (Fig. 4). Our results show that constitutive and inducible activation of Nrf-2 and its upstream kinase ERK plays an important role in determining tumor radio-responsiveness.

References

1. Deorukhkar A, Krishnan S. Targeting inflammatory pathways for tumor radiosensitization. *Biochem Pharmacol.* 2010;80:1904-14.
2. D'Autreaux B, Toledano MB. ROS as signalling molecules: mechanisms that generate specificity in ROS homeostasis. *Nat Rev Mol Cell Biol.* 2007;8:813-24.
3. Shankar B, Kumar SS, Sainis KB. Generation of reactive oxygen species and radiation response in lymphocytes and tumor cells. *Radiat Res.* 2003;160:478-87.

SINTERING KINETICS STUDY OF THE NANO-CRYSTALLINE 3-MOL% YTTRIA-SAMARIA CODOPED TETRAGONAL ZIRCONIA POLYCRYSTAL CERAMICS

Soumyajit Koley, A.K. Sahu, A. Ghosh, S. Ramanathan & G.P. Kothiyal
Glass & Advanced Materials Division

This Paper received the Best Poster Award at the 18th DAE-BRNS International Symposium on Thermal Analysis, held at Mumbai from 31st January to 2nd February, 2012

Abstract

The sintering kinetics of the in-house synthesized nano-crystalline 3-mol% yttria-samaria codoped tetragonal zirconia polycrystal ceramics has been studied. The product of activation energy (Q) and sintering parameter (n) was calculated from the shrinkage data recorded under constant rate heating (CRH). The activation energy of sintering (Q) was calculated using Dorn method. The value of 'n' was found to be constant at ~0.42 for all samples indicating 'grain-boundary assisted volume diffusion' as the dominating sintering mechanism.

Introduction

Sintering of powder compact at high temperature is a combination of several intermediate processes/mechanisms which eventually results in to elimination of pores leading to densification. At elevated temperature, sintering takes place by various diffusion mechanisms which makes a study of kinetics of sintering difficult beyond initial stage of sintering. There are few already established models to calculate the product of two most important parameters of sintering kinetics i.e. activation energy of sintering (Q) and order (n) of the process that throws light on the mechanism of sintering) [1-3]. According to the model proposed by Young & Cutler[2] for the initial stage of sintering the rate of change of shrinkage with respect to absolute temperature is expressed as follows:

$$T \left(\frac{dY}{dT} \right) \cong A^n \exp \left(- \frac{nQ}{RT} \right) \quad (1)$$

Where, T is absolute temperature, Y is shrinkage, R is universal gas constant and A is a constant. The slope of the plot of $\ln \left[T \left(\frac{dY}{dT} \right) \right]$ vs $1/T$ is $\frac{nQ}{R}$ (by magnitude).

A similar model, as shown in Eq.2 was proposed by Woolfrey & Bannister[3] to calculate 'nQ'.

$$T^2 \left(\frac{dY}{dT} \right) = \frac{nQ}{R} Y \quad (2)$$

$\frac{nQ}{R}$ can be obtained from a plot of $T^2 \frac{dY}{dT}$ vs 'Y'.

Activation energy for initial stage of sintering in ceramic materials can be found out using modified Dorn method[4]. In this technique, the sample from one isothermal range (say T_1 K) is heated to next level (say T_2 K) with a rapid heating rate so that the microstructure remained unchanged. The rate of shrinkage ($\frac{dY}{dt}$) just before heating (say $(\frac{dY}{dt})_1$) and after temperature stabilization (say $(\frac{dY}{dt})_2$) are used to calculate 'Q' as shown in Eq. (3).

$$Q \cong \left(\frac{RT_1 T_2}{T_2 - T_1} \right) \ln \left[\frac{\left(\frac{dY}{dt} \right)_2}{\left(\frac{dY}{dt} \right)_1} \right] \quad (3)$$

In the present work, the 'nQ' value was determined with certainty by using two CRH models and

BARC NEWSLETTER

subsequently in combination with the 'Q' value obtained from the Dorn method, the predominating sintering mechanism was estimated.

Experimental

The powders having compositions $(Y_2O_3)_{3-x}-(Sm_2O_3)_x-(ZrO_2)_{97}$ (where, x takes the values of 0, 1, 2 and 3) were selected (nomenclature x=0: 3Y-TZP, x=1, 1S-2Y-TZP, x=2, 2S-1Y-TZP, x=3: 3S-TZP) for this study. Details of powder synthesis process and its characterization have been discussed elsewhere[5, 6]. Sintering behaviour of the iso-pressed powder compacts were studied in a horizontal dual push-rod type dilatometer (TD 5000S, MAC Science, Japan). CRH experiments were carried out from room temperature to 1200°C. For Dorn method, temperature was held at different levels in the range of 800-1000°C for 20 min followed by fast heating (15°C/min) to reach the next isothermal zone.

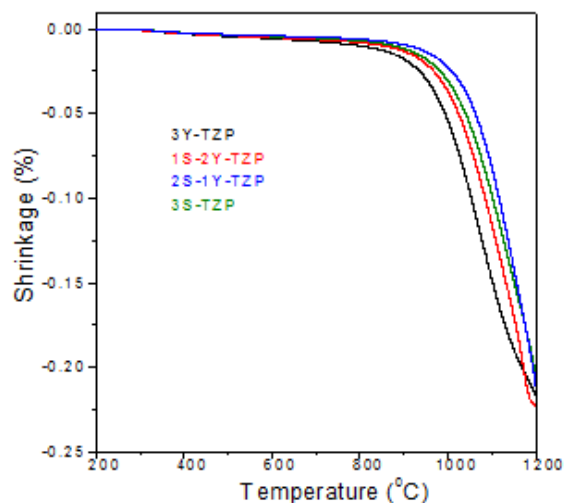


Fig. 1: Shrinkage profile of the four different iso-pressed powder compacts under linear heating profile

Results & Discussion

Fig 1 depicts the shrinkage as a function of temperature of the four different samples. It shows an increase in the onset temperature of shrinkage with continuous replacement of yttria with samaria. The Young Cutler and Bannister plot for all four samples are shown in the Fig 2(A) and 2(B) respectively. Presence of unbroken linear plots indicate only one shrinkage mechanism is operative for each of the four samples. The value of 'nQ' was calculated from the slope of the plots for each sample and they are tabulated in the Table 1.

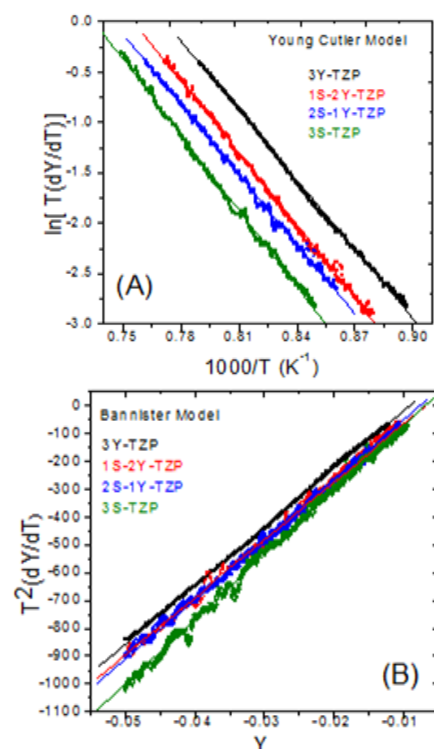


Fig. 2: Experimental shrinkage data are plotted following two different models (A) Young & Cutler and (B) Bannister. Linearity in the plots indicates presence of single operative sintering mechanism.

Table 1: The value of 'nQ', activation energy (Q) and sintering mechanism (n) are tabulated

Sample	'nQ'		'Q' From Dorn Method KJ/mol	'n' Value	
	From Young & Cutler Method KJ/mol	From Bannister Method KJ/mol		From Young & Cutler Method	From Bannister Method
3Y-TZP	191±0.4	174±0.1	412±27	0.46342	0.42226
1S-2Y-TZP	200±0.6	179±0.2	438±30	0.45548	0.40817
2S-1Y-TZP	193±0.6	172±0.1	450±50	0.42806	0.38205
3S-TZP	207±0.5	192±0.3	472±35	0.43902	0.40695

BARC NEWSLETTER

The activation energy of the four samples was calculated using Eq (3) are given in the Table 1. The activation energy of the samples were found to be in the range of 412-472 KJ/mol, which is in close proximity with the value reported by Matsui et al et al[7] for yttria doped zirconia for bulk diffusion controlled sintering. The value of 'n' was calculated and it was found to be around ~0.42 for all samples (tabulated in the Table 1). According to the models proposed by Young & Cutler[2] and Bannister[3], the value of 'n' in this range indicates grain-boundary assisted volume diffusion controlled sintering. Albeit, both grain boundary and volume diffusion controlled sintering mechanism for doped zirconia system can be found in the literature[3, 8].

Conclusions

The present investigation leads to the following conclusions:

1. Following different models e.g. CRH (Young & Cutler and Bannister) and Dorn method simultaneously it is possible to find out the activation energy of sintering and sintering parameters for a particular system.
2. The activation energy of the yttria-samarium co-doped zirconia powder was in the range of 412-472 KJ/mol.
3. The sintering parameters as estimated from this work was found to be constant at 0.42 for all samples indicating grain-boundary assisted volume diffusion as the dominating sintering mechanism.

Acknowledgements

The authors thank Dr. Madangopal Krishnan, Head, Glass & Advanced Materials Division for his support & interest in this work.

References

1. Johnson, D. L..New Method of Obtaining Volume, Grain-Boundary and Surface Diffusion Coefficients from Sintering Data..*J. Appl. Phys.* 40 (1969): 192-200.
2. Young, W. S. and Cutler, I. B..Initial Sintering with Constant Rates of Heating. . *J. Am. Ceram. Soc.* 53 (1970): 659-63.
3. Woolfrey, J. L. and Bannister, M. J.. Nonisothermal Techniques for Studying Initial-Stage Sintering.. *J. Am. Ceram. Soc.* 55 (1972): 390-94.
4. Bacmann, J. J. and Cizeron, G.. Dorn Method in the Study of Initial Phase of Uranium Dioxide Sintering.. *J. Am. Ceram. Soc.* 51 (1968): 209-12.
5. Koley, S. Ghosh, A. Sahu, A. K. and Suri, A. K.. Nano-Crystalline Yttria Samaria Codoped Zirconia: Comparison of Electrical Conductivity of Microwave & Conventionally Sintered Samples.. *Ceramic Engineering and Science Proceedings* 31 (2010): 113-26.
6. Ghosh, A. Suri, A. K., Rao, B. T., Ramamohan, T. R.. Synthesis of nanocrystalline sinteractive 3Y-TZP powder in presence of ammonium sulphate and poly ethylene glycol.. *Advances in Applied Ceramics.* 108 (2009) 183-188
7. Matsui, K., Tanaka, K., Yamakawa, T., Uehara, M., Enomoto, N., and Hojo, J.. Sintering kinetics at isothermal shrinkage: II, effect of Y_2O_3 concentration on the initial sintering stage of fine zirconia powder.. *J. Am. Ceram. Soc.* 90 (2007) 443-447
8. Jorgensen, P. J. Diffusion Controlled Sintering in Oxide. In: N A Hooter G C Kuczynski, C F Gibbon, editor. *Sintering and Related Phenomena.* New York, Gordon and Breach, 1967. p.401-422.

INFLUENCE OF A RAGI-SOYBEAN COMBINATION ON THE VIABILITY OF PROBIOTIC ORGANISMS DURING STORAGE AND UNDER SIMULATED GASTROINTESTINAL CONDITIONS

Minelly Rodrigues and Subhadra Mandalika

College of Home Science, Mumbai

and

Sahayog Jamdar and Arun Sharma

Food Technology Division

This Paper received the Best Poster Award at the International Conference and Exhibition on Food Processing and Technology, 2012, held at Hyderabad, from 22-24 November, 2012

Abstract

Synbiotic food products in matrices other than dairy foods are needed to address the problem of lactose intolerance in certain segments of the population. In this study an attempt was made to develop a synbiotic food based on cereals, millets and legumes which comprise dietary staples in India. A nutritious combination of ragi-soybean (7:3) was found to be very effective in supporting growth of probiotic microorganisms. A 10% slurry was inoculated with a mixed culture of approx. $5 \log \text{ cfu mL}^{-1}$ of *L. casei* (MTCC 1423), *L. plantarum* (MTCC 2621) and *L. fermentum* (MTCC 0903) and fermented at 37°C for 16 h. An increase in approx. $4 \log \text{ cfu mL}^{-1}$ was achieved at the end of the fermentation period with an increased production of lactic acid (0.393 g %) and a decrease in pH (4.8) and viscosity (240 cP). The mixture was lyophilised with trehalose (1%) added as a cryoprotectant. The viability of the organisms during storage was studied at 5, 10, 15, $25 \pm 2^\circ\text{C}$ for a period of 8 weeks. The results showed that the viability of the organisms was best at 5°C. At other temperatures the viability was reduced as temperature of storage increased. The efficacy of the formulation in maintaining stability of the organisms during exposure to simulated gastrointestinal juices was studied. The results showed for the first time that ragi-soybean combination could provide a good medium for enhanced survival of the probiotic organisms and potential for development of a synbiotic product.

Introduction

Synbiotic food products in matrices other than dairy foods are needed to address the problem of lactose intolerance in certain segments of the population. Cereal-legume combinations improve nutritional quality of the diet and may be used as fermentable substrates in synbiotic food formulations due to their specific nutrient composition that selectively stimulates probiotic growth and the probiotic organisms improve the nutritional and sensory quality of these commodities due to fermentation, thus exerting a 'sym'biotic or 'cobiotic' effect (Charalampopoulos et al, 2002;

Blandino et al, 2003; Leroy and De Vuyst, 2004). Probiotic strains have to maintain viability during product manufacture and storage to confer health benefits to the host when consumed (Sareela et al, 2000). These organisms delivered through food systems also have to survive during transit through the upper gastrointestinal tract and then colonise in the large intestine (Chou and Weimer, 1999). In our laboratory, different cereals, millets, legumes and their combinations were screened for their efficacy in supporting probiotic growth. Among these combination of finger millet- soybean could achieve the highest cell counts of LAB and also higher acid

BARC NEWSLETTER

production and lowering of pH. The present studies report the growth of a mixed culture of probiotic organisms- *L. casei* (MTCC 1423), *L. plantarum* (MTCC 2621) and *L. fermentum* (MTCC 0903) in a combination of ragi-soybean. Moreover, the survivability of the cells during the process of freeze drying, storage and exposure to simulated gastrointestinal conditions is also reported.

Materials And Methods

Growth profile of mixed culture in ragi-soybean

A 10 % slurry was prepared from Ragi and soybean flour (7:3), autoclaved, cooled and inoculated with ~ 5 Log cfu mL⁻¹ of *L. casei* MTCC 1423 (Microbial Type Culture Collection, Chandigarh, Haryana, India) and fermented at 37°C for 24 h. Cell counts were enumerated by pour plate technique using De Man, Rogosa, & Sharpe (MRS) Agar (HiMedia Laboratories, India). The plates were incubated at 37°C for 48 h. Viable counts were recorded as log cfu mL⁻¹ slurry. The pH of the samples was measured using a digital pH meter (ISFETCOM Co., Ltd, Japan). Total titratable acidity (TTA) was estimated as lactic acid (g%) using the standard method (AOAC, 2000). Viscosity was measured using a Brookfield Viscometer (DV-I + Viscometer, Brookfield Engineering Laboratories, MA, USA) using spindle No. 7 set at 50 rpm at ambient temperature (28±2°C).

Effect of lyophilization and storage on viability

The fermented slurry was freeze dried without and with Trehalose (1%) used as a cryoprotectant. Viable cell counts in the product after freeze drying as well as during storage at different temperatures (5°C, 10°C, 15°C & 25°C± 2°C) were analysed by pour plate technique.

Efficacy of the formulation in maintaining stability of the organisms during exposure to simulated gastrointestinal juices

The stability of the organisms in the formulation during exposure to simulated gastrointestinal juices was

studied according to the method of Charteris et al (1998). The free cell suspensions and the ragi-soybean synbiotic product were exposed to gastric juices (Pepsin 3g L⁻¹) at pH 2.0, 3.0 & 4.0 and to small intestinal juices (Pancreatin 1g L⁻¹) at pH 8.0 [without or with bile salts (0.45%)]. The viability was determined using the plate count method.

Statistical analysis

The data was statistically analyzed using SPSS, Version 16.0. (Chicago, SPSS Inc.). One-way ANOVA was used to compare the differences in mean between the samples. Level of significance was set to 0.05. For multiple comparisons Tukey's post hoc test was used.

Results & Discussion

Growth profile of LAB during fermentation

Ragi-soybean slurry proved effective as a substrate for probiotic growth with significant ($p < 0.05$) increase in cell counts upon fermentation (5.711 at 0 hours to 8.618 log cfu mL⁻¹ at the end of the 16 hour fermentation period). The desired cell counts of 7 Log cfu mL⁻¹ were achieved within 5 hours of fermentation (Fig.1). Growth pattern of the probiotic organisms in the ragi-soybean slurry was similar to that observed in MRS broth, the medium used for cultivation of lactobacilli (data not shown).

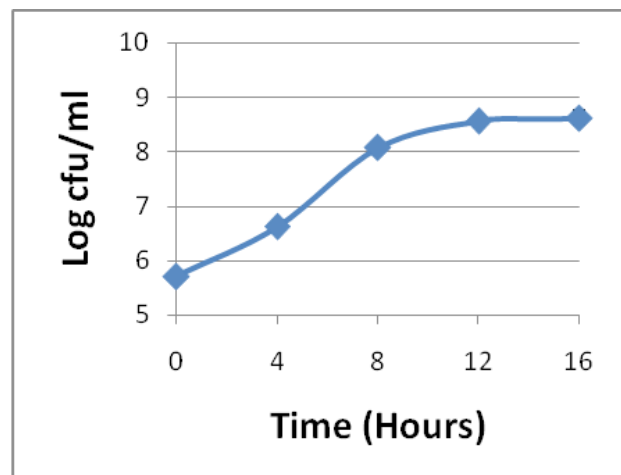


Fig. 1: Growth profile of mixed culture of LAB in ragi-soybean combination (7:3) media

BARC NEWSLETTER

Changes in pH and Lactic acid

A decline in pH is beneficial as it suppresses the development of contaminating microflora and improves the organoleptic properties of the product. High cell growth rates and acidification rates result in reduction of fermentation time and enhance viability of the strains by preventing growth of undesirable microorganisms (Marklinder and Lonner, 1992). Accumulation of lactic acid (0.4 g% at the end of the fermentation period) and thereby reduction in pH to 4.6 was observed in the ragi- soybean combination (Fig. 2A).

Viscosity changes

Probiotic organisms produce amylase that hydrolyses starch and thereby decrease the viscosity of cereal-legume based products (Songre-Ouattara, 2010). Viscosity of the ragi-soybean blend changed from 640 cP to 240 cP upon fermentation and may be attributed to the amylolytic activity exhibited by probiotic organisms (Fig. 2B).

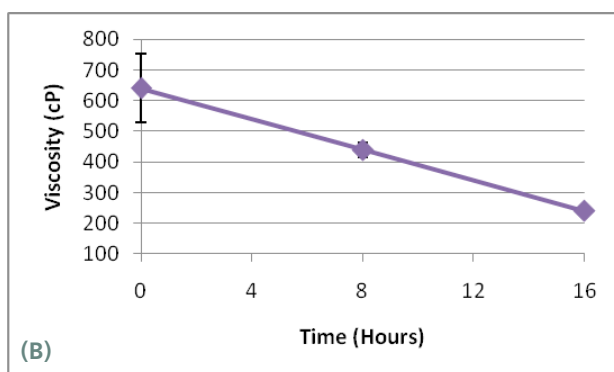
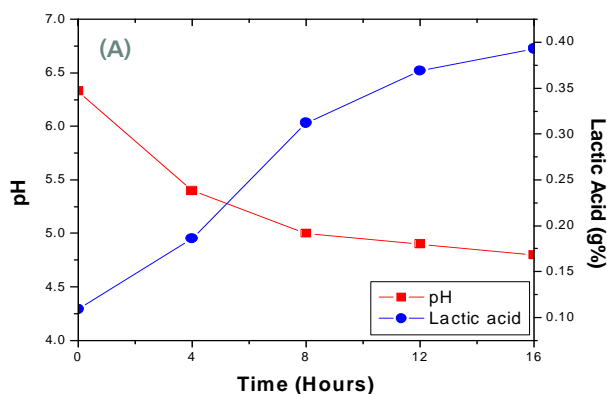


Fig. 2: Changes in pH and lactic acid (A) and viscosity (B) in ragi-soybean slurry during fermentation.

Effect of lyophilisation on viability of probiotic organisms

Maintenance of viability of probiotic organisms in foods is essential. Hence should be protected during product formulation and subsequent storage. Freeze drying affects cell viability- need for cryoprotectants to improve cell survival (Fig. 3). Trehalose significantly protected the viability of the cells during freeze drying ($p < 0.05$). Hence a synbiotic food product in a powdered form with the prescribed counts of probiotic organisms was obtained.

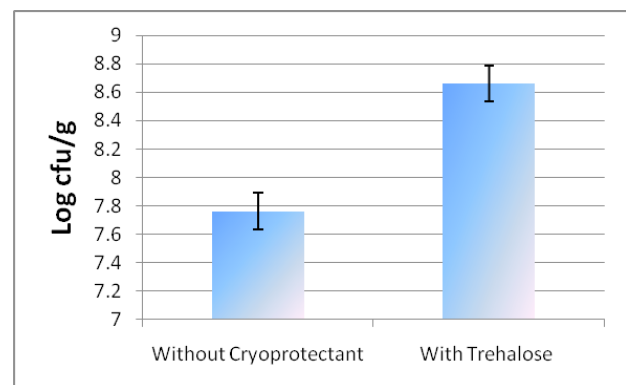


Fig. 3: Cell counts in lyophilized ragi-soybean slurry

Viability of the organisms in the lyophilized product during storage at different temperatures.

Cell counts above the recommended level of 7 Log cfu mL⁻¹ were maintained throughout the 8 week storage period only in the product stored at 5°C. At other storage temperatures (10, 15 and 25°C) the cell counts decreased rapidly with the increasing the storage period (Fig.4).

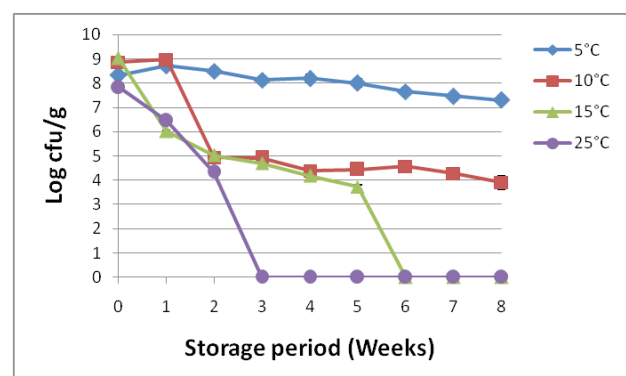


Fig. 4: Cell counts in lyophilized products during storage

BARC NEWSLETTER

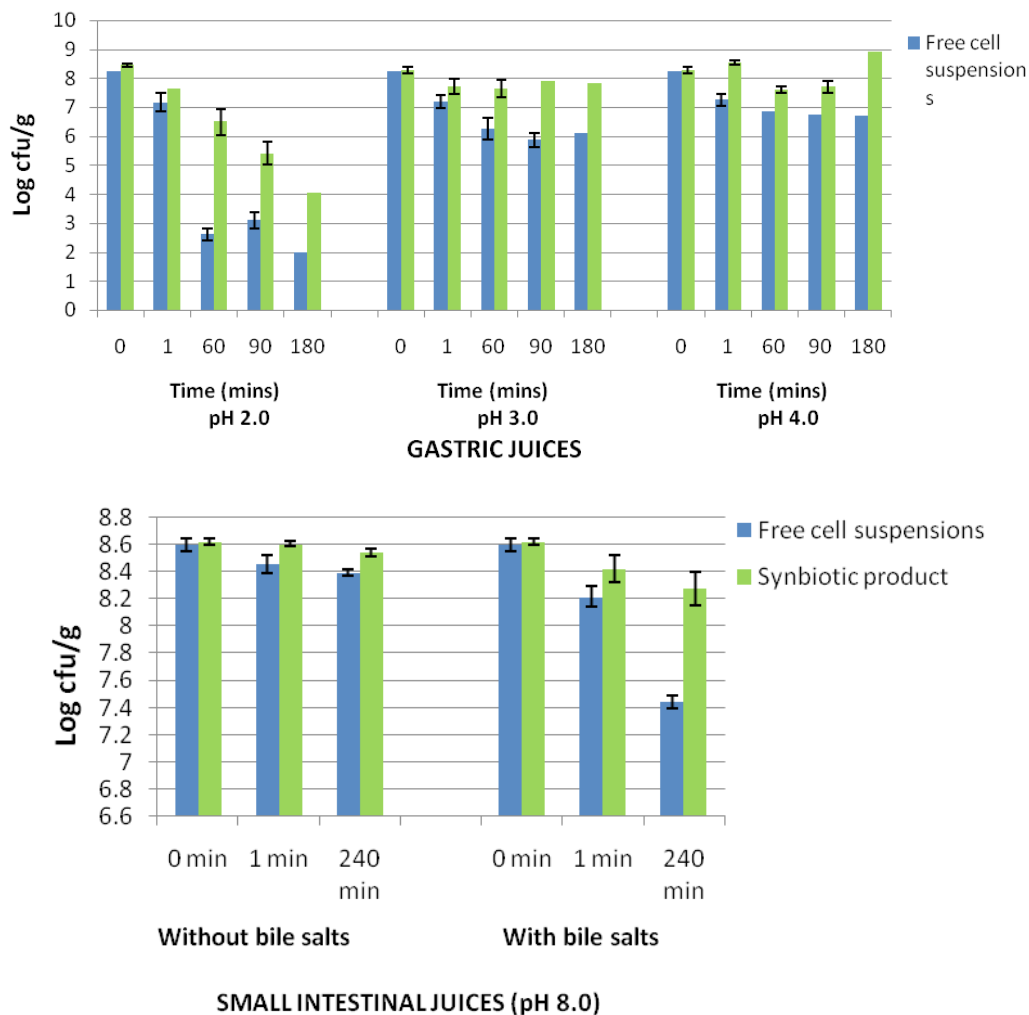


Fig. 5: Viability of probiotic organisms during exposure to simulated gastrointestinal juices

Efficacy of the formulation in maintaining stability of the organisms during exposure to simulated gastrointestinal conditions.

The presence of the organisms in the form of a synbiotic product in the ragi-soybean matrix greatly enhanced the tolerance of the organisms to simulated gastrointestinal transit as compared to free cell suspensions (Fig.5). The simulated gastric tolerance of the organisms in the synbiotic product was pH dependent. The organisms showed lower viability in simulated gastric juice at pH 2.0 than pH 3.0 or pH 4.0. The organisms retained their viability during 240 min of simulated small intestinal transit in the absence of bile salts. However slight reduction in viable counts was observed in the presence of bile salts.

Conclusion

The ragi-soybean combination was found to be an effective medium for enhancing the growth of the probiotic organisms. The freeze dried product retained its viability up to 8 weeks at 5°C. Viability during simulated GI transit was enhanced when the organisms were present in the form of a synbiotic product. Therefore it can effectively serve as a replacement for dairy based probiotic foods offering the consumer nutritional as well as health benefits.

References

1. AOAC, (2000). Official Methods of Analysis of the Association of Official Agricultural Chemists, Washington, DC: Association of Analytical Chemists, pp.125-139.

BARC NEWSLETTER

2. Blandino, A., Al-Aseeri, M.E., Pandiella, S.S., Cantero, D., & Webb, C. (2003). Cereal-based fermented foods and beverages. *Food Research International*, 36, 527-543.
3. Charalampopoulos, D., Wang, R., Pandiella, S.S., & Webb, C. (2002). Application of cereals and cereal components in functional foods: a review. *International Journal of Food Microbiology*, 79, 131-141.
4. Charteris, W.P., Kelly, P.M., Morelli, L., & Collins, J.K. (1998). Development and application of an in vitro methodology to determine the transit tolerance of potentially probiotic *Lactobacillus* and *Bifidobacterium* species in the upper human gastrointestinal tract. *Journal of applied microbiology*, 84, 759-768.
5. Chou, L., & Weimer, B. Isolation and characterization of acid and bile-tolerant isolates from strains of *Lactobacillus acidophilus*. *Journal of Dairy Science*, 82, 23-31.
6. Leroy, F., & De Vuyst, L. (2004). Lactic acid bacteria as functional starter cultures for the food fermentation industry. *Trends in Food, Science and Technology*, 15, 67-78.
7. Marklinder, I., & Lonner, C. (1992). Fermentation properties of intestinal strains of *Lactobacillus*, of a sour dough and of a yoghurt starter culture in an oat-based nutritive solution. *Food Microbiology*, 9, 197-205.
8. Saarela, M., Mogensen, G., Fonden, R., Matto, J., & Mattila-Sandholm, T. (2000). Probiotic bacteria: safety, functional and technological properties. *Journal of Biotechnology*, 84, 197-215.
9. Songre-Ouattara, L.T., Mouquet-Rivier, C., Humblot, C., Rochette, I., Diawara, B., & Guyot, J.-P. (2010). Ability of selected lactic acid bacteria to ferment a pearl millet-soybean slurry to produce gruels for complementary foods for young children. *Journal of Food Science*, 75, M261-M269.

BARC NEWSLETTER

SUPPRESSION OF RADIATION INDUCED DNA DAMAGE AND APOPTOSIS IN HAEMATOPOIETIC CELLS OF MICE BY UMBELLIFERONE

S. Jayakumar, Hari N. Bhilwade, Ramesh C. Chaubey

Radiation Biology and Health Sciences Division

This Paper received the Best Poster Award at the International Conference on Emerging Frontiers and Challenges in Radiation Biology, held at Bikaner, on 24th & 25th January, 2012

Abstract

In current scenario there is need to understand the mechanisms of radiation damage to human and its possible prevention by drugs such as radioprotectors. Radioprotectors are useful in increasing therapeutic efficiency as well as during nuclear emergency situations. In the present study, radioprotective effect of Umbelliferone (UMB) was investigated. In mouse splenic lymphocytes, it was observed that the pretreatment of UMB (6.5 μ M-50 μ M) reduced the radiation induced DNA damage and apoptosis to a significant extent in comparison to radiation control (6 Gy). Similarly, mice administered with UMB prior to the radiation exposure showed significant decrease in DNA damage, cell death and the frequency of micronucleated erythrocytes in bone marrow. Our study demonstrated the radioprotective potential of UMB *in vitro* and *in vivo*.

Introduction

Radiation is increasingly being used in human health through several diagnostic and therapeutic applications. Radiotherapy of cancer is one of the major applications of radiation. Sixty percent of all the tumor types are being treated with radiotherapy alone or in combination with surgery and chemotherapy. But the success of radiotherapy is limited by injury to the normal cells. Protection of the normal cells from radiation induced damage by radioprotectors can increase therapeutic efficiency. These radioprotectors can also be used during nuclear emergency situations. Radiation causes damage to living cells by producing reactive oxygen species (ROS) like hydroxyl radical, hydrogen peroxide and superoxide [1] which cause damage to biomolecules including DNA (indirect effect) or by directly causing damage to biomolecules (direct effect). The proportion of direct and indirect damage depends on the quality and type of radiation. Gamma radiation kills cells mainly by indirect damage. The most important biomolecule in the cell whose damage causes cell death is DNA. Because in contrary to the abundance of the

other molecule, only two copies of DNA is present in the cell most of the times. DNA is the crucial molecule in the cell which codes for the information necessary for coding proteins and also is the genetic material of the cell which needs to be passed on to the next generation of cells with high fidelity. When ionization happens involving DNA, which leads to the breakage of bonds in the DNA. If the phosphodiester bond which connects the nucleotides together gets broken, that leads to the single strand break. If the phosphodiester bond present in the opposite strands in the close vicinity gets broken that leads to double strand breaks. Apart from the strand breaks, many other damages like base damage, base modification, sugar modification also happens in the DNA molecule. Cells employ variety of defence mechanisms to overcome this oxidative stress and damage caused by radiation. Intracellular antioxidants like glutathione, thioredoxin, catalase and superoxide dismutase etc. form the first line of defence against oxidative stress in the cells. These antioxidants help cells in scavenging free radicals and salvaging biomolecules from oxidative damage. Apart from the antioxidants, radiation exposure also triggers variety of

BARC NEWSLETTER

signalling pathways which include, DNA damage recognition and repair, cell cycle arrest or cell death (apoptosis)[2]. To counter radiation induced apoptosis, cells need to activate prosurvival and cytoprotective pathways[3]. Any drug which helps in augmenting these response pathways in terms of increasing the free radical scavenging and enhancement of repair in cells can be a good radioprotector. From this perspective, extensive research is going on around the globe for development of good radioprotector[4]. However, there is no bonafide radioprotector available that can be used under clinical settings. Therefore, there is a need for the development of an effective radioprotector which can protect normal cells from radiation injury. Umbelliferone (UMB) is a wide spread natural product of the coumarin family. It occurs in many plants from the apiaceae family. UMB is reported to have antioxidant, anti-diabetic[5] and anti-tumor properties[6]. In this study, we have investigated the radioprotective potential of UMB under *in vitro* and *in vivo* conditions using comet assay and micronuclei assay. These two assays are the standard assays used in quantifying genotoxicity in mammals. Many regulatory authorities including IAEA, use these techniques to assess the effect of radiation at genetic level.

Materials and Methods

Chemicals and animals

Umbelliferone, High-, low-melting agarose, dimethylsulfoxide (DMSO), ethylenediaminetetraacetic acid (EDTA), Triton X-100, tris base and SYBR Green-II were procured from Sigma Chemical Co. (St. Louis, MO, USA). Fetal bovine serum (FBS) was obtained from Himedia (Mumbai, India). Sodium hydroxide and Sodium chloride were from Sisco fine chemicals (Mumbai, India). Female Swiss albino mice (6–8 weeks old, weighing 20–25 g) supplied by animal house facility (Bhabha Atomic Research Centre, Mumbai) were maintained under standard conditions of temperature (25 ± 2 °C) and humidity with 12 h light / dark cycle. Animal experiments were carried out according to the

ethical guidelines laid down by BARC Animal Ethics Committee.

Comet assay

To determine the magnitude of DNA damage, alkaline comet assay was performed[7]. Control and irradiated cells were suspended in 0.8 % low melting agarose and were layered on to frosted slides pre-coated with 1 % normal agarose. After solidification, slides were kept in the lysis buffer (2.5M NaCl, 10 mM Tris-HCl of pH 10.0, 100 mM Na₂-EDTA with freshly added 1% Triton X-100 and 10% DMSO) at 4 °C for 60 min. For equilibration, the slides were transferred to electrophoretic tank containing alkaline solution (300 mM NaOH, 1 mM EDTA, pH 13.0). Slides were electrophoresed in the same buffer for 30 min at 0.8 V/cm. After electrophoresis, slides were neutralised (0.4 M Tris-HCl), stained (SYBR Green II dye) and visualised at 40X magnifications using fluorescence microscope (Axioplan, Carl-Zeiss, Germany). For every treatment two slides were prepared and at least 50 images were grabbed per slide. The images were analysed using CASP software (www.casplab.com) to obtain tail moment, which has been used to represent extent of DNA damage.

Micronucleus assay

The animals were sacrificed by cervical dislocation, and the femurs of each animal were dissected out and the bone marrow was flushed out into fetal bovine serum[8]. The suspension was centrifuged at 1,000 rpm, and bone marrow smears were made from the cell button. The smears were stained (May-Grunwald & Giemsa) and mounted in DPX. For each animal, two slides were made. Coded slides were scored for the incidence of micronucleated polychromatic erythrocytes (mn-PCEs) and micronucleated normochromatic erythrocytes (mn-NCEs) at 100X magnification. A minimum of 4000 PCEs and the corresponding number of NCEs with or without micronucleus were counted from each group. Data regarding the PCEs/NCEs ratio were also collected.

BARC NEWSLETTER

Statistical analysis

The statistical analysis of the comet assay data was carried out using the one-way ANOVA and Student's t-test was applied for the micronucleus data. The values were considered significant at $p < 0.05$

Results and Discussion

Effect of Umbelliferone on radiation induced DNA damage of splenic lymphocytes in vitro

To establish the radioprotective role of Umbelliferone (UMB) *in vitro*, we have evaluated its anti-genotoxic property in mouse splenic lymphocytes. For estimation of DNA damage comet assay was used. Comet assay is a simple, sensitive, and versatile assay which can be used to detect and quantify DNA damage and repair. In comet assay the cells are layered on to the slide along with agarose gel matrix, lysed, and subjected to electrophoresis. After electrophoresis, when the DNA is visualised using fluorescent microscope, the damaged DNA will exhibit larger movement from the head region and appear like a comet (Fig.1). Based on the extent of DNA movement to the tail region (tail moment) DNA damage can be quantified.

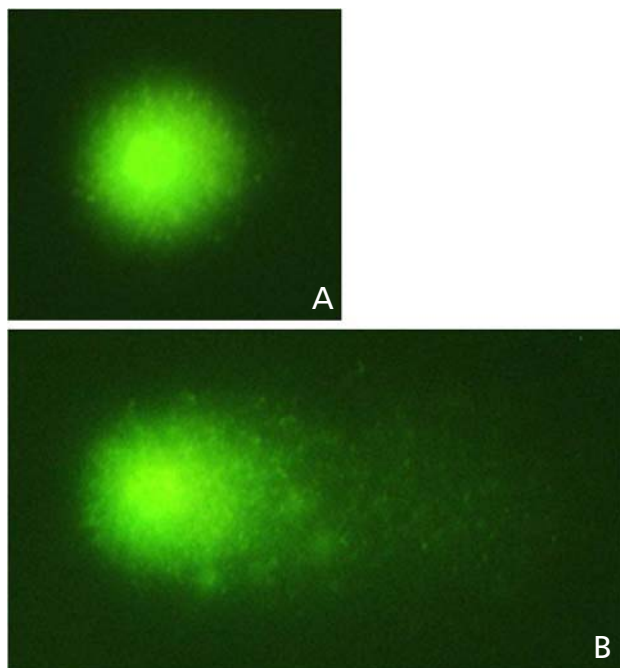


Fig. 1: (a) Representative images obtained from comet assay in control and (b) irradiated cells

For assessing the anti-genotoxic potential of UMB, splenic lymphocytes were isolated from mice and treated with different concentration of UMB (6.5, 12.5, 25 and 50 μM) and incubated for 1 h followed by gamma irradiation (6 Gy). After radiation treatment, the extent of DNA damage in the cells was assessed by comet assay at different time intervals (0 to 120 min). Radiation treatment alone showed significant increase in DNA damage as reflected by tail moment values in comet assay (Table.1). Pretreatment of cells with UMB prior to radiation exposure showed significant reduction in DNA damage observed immediately after radiation exposure, except at 6.5 μM . Maximum reduction of 48% in DNA damage was seen when the cells were treated with 25 μM UMB, followed by 34.2% reduction with 12.5 μM and 28.87% reduction with 50 μM UMB treatment prior to irradiation. This reduction in DNA damage in the presence of UMB might be due to its anti-oxidant activity and free radical scavenging activity.

We have also seen the effect of UMB pre-treatment on radiation induced DNA damage at 2 h after irradiation on mouse splenic lymphocytes. Cells treated with UMB showed significant reduction in DNA damage as compared to radiation control (Table 1). Percentage reduction in DNA strand breaks seen after 2 h of irradiation is 66, 35 and 30% respectively for 25 μM , 12.5 μM and 50 μM UMB treatment. Treatment concentration of 25 μM showed highest protection (66%) followed by 12.5 μM (35%) and 50 μM (30%). Further, UMB pretreatment enhanced the DNA damage repair in the cells in comparison to the radiation control. Cells pre-treated with 25 μM UMB prior to the radiation (6 Gy) showed maximum such enhancement in DNA repair (73%) in comparison to 58% repair observed with 6 Gy radiation group.

Effect of Umbelliferone pre-treatment on radiation induced apoptosis in splenic lymphocytes

Having seen the ability of UMB to reduce radiation induced DNA damage, we examined the effect of UMB on radiation induced apoptosis. Apoptosis is a mark of cell death and for this purpose, splenic lymphocytes were pre-treated with various concentrations of UMB

BARC NEWSLETTER

Table 1: Extent of radiation induced DNA damage (tail moment) observed in mouse splenic lymphocytes after UMB pre-treatment.

Treatment	Tail moment (immediately after irradiation)	SEM	Tail moment (120 min after irradiation)	SEM
Control	0.1	0.03	0.38	0.12
0.1% DMSO	0.24	0.22	1.19	1.03
6.5M UMB	0.07	0.02	0.79	0.24
12.5M UMB	0.09	0.03	0.37	0.21
25M UMB	0.12	0.06	0.38	0.12
50M UMB	1.36	0.49	1.00	0.55
6 Gy	15.76*	2.93	6.60*	1.16
6.5M UMB + 6 Gy	15.15	2.78	5.90	0.92
12.5M UMB + 6 Gy	10.37 [#]	2.35	4.30 [#]	0.86
25M UMB + 6 Gy	8.23 [#]	1.42	2.24 [#]	0.69
50M UMB + 6 Gy	11.21	2.05	4.62	1.10

Mean tail moment values and standard error of means (SEM) were obtained from two independent experiments. * $p < 0.05$ in comparison to control group. [#] $p < 0.05$ in comparison to 6 Gy radiation group

before radiation exposure. Extent of apoptosis was measured using flow cytometer after propidium iodide staining at 24 h after irradiation. Pretreatment of cells with 25 μ M UMB significantly reduced the radiation induced cell death. Apoptosis observed in cells pre-treated with 25 μ M UMB prior to 6 Gy radiation exposure was 47% as against 65% cell death observed with radiation control.

Effect of UMB on radiation induced DNA damage and micronuclei frequency *in vivo*

In order to understand the radio-modulative effect of UMB *in vivo*, mice were administered with either 20 mg/Kg or 40 mg/Kg UMB before irradiation (2 Gy) and their DNA damage and micronuclei frequency were analysed in peripheral leucocytes and bone marrow cells respectively. Irradiated mice showed significantly higher DNA damage in their peripheral blood leucocytes in comparison to control as reflected by tail moment values in comet assay (Table 2).

Animals which were administered with UMB showed significant reduction in DNA damage. UMB at 40 mg/Kg was found to be more effective than that of UMB at 20 mg/Kg.

Table 2: DNA damage observed in peripheral leukocytes obtained from mice treated with UMB and radiation.

Treatment	Tail moment	SEM
Control	1.28	0.13
0.1%DMSO	1.23	0.08
20mg/Kg UMB	1.77	0.13
40mg/Kg UMB	0.93	0.14
2 Gy	12.45*	0.65
20mg/Kg UMB + 2 Gy	8.34 [#]	0.54
40mg/Kg UMB + 2 Gy	7.33 [#]	0.49

Mean tail moment values and standard error of means (SEM) were obtained from two independent experiments. * $p < 0.05$ in comparison to control group. [#] $p < 0.05$ in comparison to 2 Gy radiation group

Apart from DNA damage, frequency of micronucleated erythrocytes were also analysed in bone marrow cells. Micronuclei are the remnants of the fragmented DNA observed in cells. These micronuclei can be easily scored in erythrocytes as erythrocytes undergo enucleation during their maturation process. During the enucleation process normal nucleus would be removed and if any DNA fragment is present, they are scored as micronuclei (Fig.2). The frequency of micronucleated erythrocytes observed in bone marrow cells are the one of the best indicators of genotoxicity.

BARC NEWSLETTER

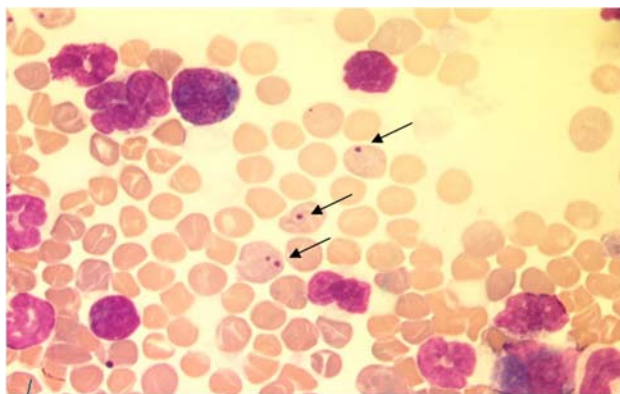


Fig. 2: Representative image obtained from micronuclei assay. Micronuclei present in the immature polychromatic erythrocytes are marked with arrows.

In our study, the group of mice which were exposed to radiation showed 2.5% micronucleated erythrocytes in their bone marrow. In groups treated with UMB at 20 and 40 mg/Kg this frequency came down to 1.6% and 1.1% respectively (Table 3). Ratio between PCEs/NCEs which represents the proliferation index, reduced upon irradiation. But on UMB pre-treatment this ratio got restored close to control levels.

Table 3: Frequency of polychromatic micronucleated erythrocytes (mn-PCE) observed in bone marrow cells obtained from mice treated with UMB and radiation.

Treatment	% of mn-PCEs	SEM	PCEs/NCEs Ratio
Control	0.14	0.04	1.04
0.1% DMSO	0.20	0.01	1.03
20mg/Kg UMB	0.44	0.05	0.95
40mg/Kg UMB	0.14	0.05	1.02
2 Gy	2.55	0.09*	0.74
20mg/Kg UMB + 2 Gy	1.63	0.07#	0.86
40mg/Kg UMBb + 2 Gy	1.07	0.21#	0.89

% of mn-PCEs values and standard error of means (SEM) were obtained from two independent experiments. * $p < 0.05$ in comparison to control group. # $p < 0.05$ in comparison to 2 Gy radiation group

These studies demonstrate the radioprotective potential of umbelliferone in mice. Our results indicated that radioprotective ability of UMB was through free radical scavenging and its ability to enhance the DNA repair capability in lymphocytes. Further studies are being carried out to understand the molecular mechanism of the radioprotective potential of UMB and also to evaluate the effect of UMB treatment on mortality and

morbidity of mice which were exposed to lethal doses of radiation.

Acknowledgements

The authors would like to thank Shri. B. A. Naidu for technical assistance. The authors also thank the Department of Atomic Energy, India, for funding this research.

References

1. P.A. Riley, Free radicals in biology: oxidative stress and the effects of ionizing radiation, *Int J Radiat Biol*, 65 (1994): 27-33.
2. G. Iliakis, Y. Wang, J. Guan, H. Wang, DNA damage checkpoint control in cells exposed to ionizing radiation, *Oncogene*, 22 (2003) 5834-5847.
3. K. Valerie, A. Yacoub, M.P. Hagan, D.T. Curiel, P.B. Fisher, S. Grant, P. Dent, Radiation-induced cell signaling: inside-out and outside-in, *Mol Cancer Ther*, 6 (2007): 789-801.
4. J.F. Weiss, M.R. Landauer, Protection against ionizing radiation by antioxidant nutrients and phytochemicals, *Toxicology*, 189 (2003): 1-20.
5. B. Ramesh, K.V. Pugalendi, Antihyperglycemic effect of umbelliferone in streptozotocin-diabetic rats, *Journal of medicinal food*, 9 (2006): 562-566.
6. C. Kofinas, L. Chinou, A. Loukis, C. Harvala, C. Roussakis, M. Maillard, K. Hostettmann, Cytotoxic coumarins from the aerial parts of *Tordylium apulum* and their effects on a non-small-cell bronchial carcinoma cell line, *Planta medica*, 64 (1998): 174-176.
7. S. Jayakumar, H.N. Bhilwade, P.S. Dange, H.D. Sarma, R.C. Chaubey, B.N. Pandey, Magnitude of radiation-induced DNA damage in peripheral blood leukocytes and its correlation with aggressiveness of thymic lymphoma in Swiss mice, *Int J Radiat Biol*, 87 (2011): 1113-1119.
8. A. Kunwar, S. Jayakumar, H.N. Bhilwade, P.P. Bag, H. Bhatt, R.C. Chaubey, K.I. Priyadarsini, Protective effects of selenocystine against gamma-radiation-induced genotoxicity in Swiss albino mice, *Radiat Environ Biophys*, 50 (2011): 271-280.

BARC NEWSLETTER

CHARACTERISATION OF THREE SINGLE STRANDED DNA BINDING (SSB)-LIKE PROTEINS FROM THE NITROGEN-FIXING CYANOBACTERIUM *ANABAENA* PCC7120

Anurag Kirti, Hema Rajaram and Shree Kumar Apte
Molecular Biology Division

This Paper received the Best Poster Presentation Award at the Indo-US Workshop on Cyanobacteria, held at Lonavala, from Dec. 16-20, 2012

Abstract

Anabaena sp. strain PCC 7120 is a filamentous, nitrogen-fixing radioresistant cyanobacterium with a robust DNA repair system. Of the several DNA repair proteins involved in maintaining the integrity of genome, single stranded DNA binding (SSB) protein plays a central role. Unlike most other bacteria, *Anabaena* 7120, has three genes possibly coding for SSB-like protein, namely *alr0088* and *alr7579* (both annotated as *ssb*) and *all4779* (annotated as a hypothetical protein), and designated as *ssb1*, *ssb2* and *ssb3* respectively. While the 13 kDa SSB1 and 14 kDa SSB2 proteins have only the N-terminal oligonucleotide binding (OB)-fold region corresponding to bacterial SSBs, All4779 possesses all three regions, namely N-terminal OB-fold, C-terminal acidic tail separated by a Proline/Glycine-rich linker, typical of bacterial SSBs. In fact the SSB1 and SSB2 proteins are the smallest reported SSB-like proteins among prokaryotes and eukaryotes. Owing to the OB-fold, all three *Anabaena* SSB proteins bind single-stranded DNA (ssDNA), but differ in their binding affinity and length of ssDNA bound. Expression of all three SSB proteins in *Anabaena* indicates that these are functional genes and possibly have distinct physiological roles.

Introduction

Single stranded DNA (ssDNA) binding proteins (SSBs) are essential for all DNA metabolic processes, such as DNA replication, recombination as well as repair for genome maintenance (Shereda et al, 2008), all of which require presence of ssDNA. This is achieved by the non-specific binding of SSB protein to ssDNA, thereby preventing them from forming secondary structures. These are ubiquitous proteins, present across all organisms from viruses to bacteria to humans, show significant degree of homology in the functional domains and are essential for cell survival. A typical bacterial SSB protein has three domains, the N-terminal oligonucleotide-binding (OB)-fold for interacting with ssDNA, a C-terminal acidic tail to interact with other proteins, and a proline/glycine (P/G)-rich linker separating the positively charged N-terminus from the negatively charged C-terminus (Lohman and Ferrari

1984). The P/G-rich region results in kinks in the ordered structure of protein allowing better spatial separation of oppositely charged ends (Belts and Russell, 2003). Though SSB protein is functionally, biochemically and structurally well studied in other organisms including the radioresistant *Deinococcus* (Eggington et al 2004; Basu and Apte 2012), very little is known about them in cyanobacteria. The photosynthetic nitrogen-fixing *Anabaena* 7120, exhibits high tolerance towards radiation stresses ($LD_{50} = 6$ kGy) (Singh et al, 2011). This offers an advantage over *Deinococcus*, since *Anabaena* can survive with minimal nutritional assistance, requiring mainly sunlight and air. Thus, as a first step in this direction the three SSB proteins of *Anabaena*, central to all DNA metabolism, were characterised. The presence of multiple SSB-like proteins, which is rare in bacteria, raises several questions, such as whether they are real or pseudo genes, whether they are expressed *in vivo* or not,

BARC NEWSLETTER

differences in their biochemical activities and role of each of these proteins in *Anabaena*.

Results and Discussion

Schematic representation of the domains of the three SSB proteins of *Anabaena* 7120 indicated termination of the protein sequence immediately after the N-terminal OB-fold in SSB1 and SSB2 (Fig. 1). The SSB3 protein, on the other hand, exhibited all three domains and was as large as *E. coli* SSB (Fig. 1). Thus, SSB1 and SSB2 are the smallest reported SSB proteins till date. The smallest prokaryotic SSB reported earlier was 140 amino acid long SSB from *Thermatoga* sp. (Olszewski et al, 2010) and the 130 amino acid long human mitochondrial SSB (Curth et al, 1994). The amino acid sequence of the three *Anabaena* SSB proteins bear low homology and thus could not have arisen by gene duplication.

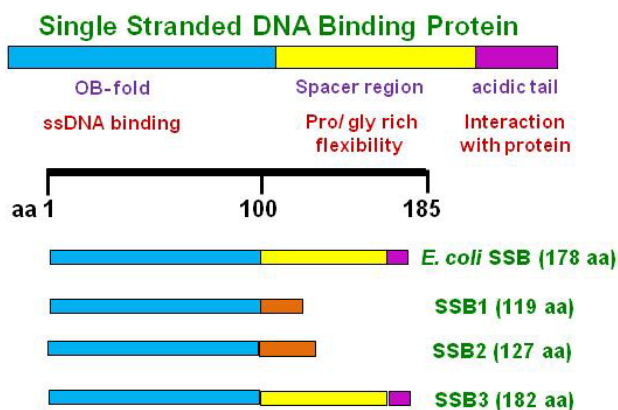
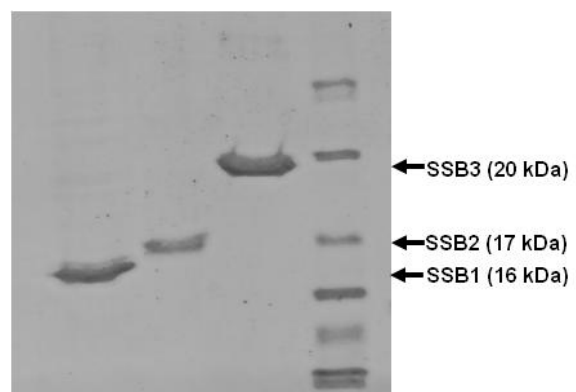


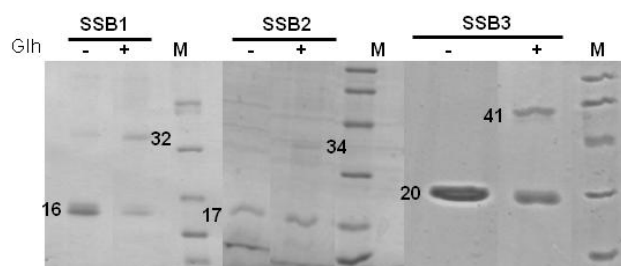
Fig. 1: Domain organization of *Anabaena* and *E. coli* SSB proteins. The Blue box indicates the OB-fold, the yellow box indicates the P/G-rich region and the magenta box indicates the acidic tail. The region in SSB1 and SSB2 beyond the OB-fold is indicated as an orange box.

Presence of OB-fold is indicative of the ability to bind to ssDNA. To validate this bioinformatically obtained information, the three *Anabaena* SSB proteins were characterised *in vitro* for their ability to bind ssDNA. To obtain pure proteins for biochemical analysis, the respective genes were obtained from the genomic DNA of *Anabaena* 7120 by Polymerase Chain Reaction-based amplification using gene specific primers. Design of such DNA primers was facilitated by the availability of the entire genome sequence of *Anabaena* 7120 (<http://genome.microbedb.or.jp/cyanobase>).

DNA sequencing of these fragments confirmed amplification of the desired genes and the DNA sequences were submitted to GENBANK (Accession Nos. GU225949, GU225950 and GU225951). These DNA fragments were cloned in an expression vector, pET16b, which provides a His₆-tag to the N-terminal of the overexpressed protein. This assists in affinity based purification of proteins. Overexpression of the protein coded by the cloned gene was achieved in *E. coli* using Isopropyl β-D-1-thiogalactopyranoside (IPTG) as an inducer. The overexpressed protein was purified from the recombinant *E. coli* cell lysate by Ni-NTA based affinity chromatography (Fig. 2A), and the purified protein was used to generate polyclonal antibodies. Analysis of *Anabaena* cell free extracts with these antibodies indicated that all three SSB proteins expressed in *Anabaena*, and thus are all functional genes.



(a)



(b)

Fig. 2: Purification and Glutaraldehyde cross-linking of *Anabaena* SSB proteins. (A) The three SSB proteins of *Anabaena* were purified by Ni-NTA chromatography. (B) Native SSB proteins were cross-linked with glutaraldehyde. The proteins were electrophoretically separated on SDS-polyacrylamide gel and stained with Coomassie brilliant blue G-250. Molecular mass of different molecular form is indicated.

BARC NEWSLETTER

Binding of SSB to ssDNA requires the availability of at least two OB-folds, while the wrapping around of the ssDNA by SSB requires simultaneous availability of four OB-folds. This is aided by the tetramerisation of bacterial SSB proteins (Lohman and Ferrari, 1984), or dimerisation of *Deinococcal* SSB protein, which has two OB-folds per monomer (Eggington et al, 2004). HPLC based size determination of the *Anabaena* SSB proteins in their native state indicated formation of a dimer of 26 and 27 kDa for SSB1 and SSB2 respectively, while the SSB3 was found to exist as a monomer of about 20 kDa. Further confirmation of the oligomeric status of *Anabaena* SSB proteins was achieved by allowing cross-linking of the individual purified *Anabaena* SSB proteins using glutaraldehyde followed by analysis by SDS-polyacrylamide gel electrophoresis. The existence of the dimeric forms in addition to the monomeric forms of SSB1 and SSB2 was further confirmed, while a dimeric form of about 41 kDa was also detected for SSB3 (Fig. 2B). Thus, *Anabaena* SSB proteins exhibit a unique feature in existing as a dimer.

The ability of the dimeric SSB proteins of *Anabaena* to bind ssDNA was evaluated by (i) Electrophoretic Mobility Shift Assay (EMSA) and (ii) Fluorescence Quenching techniques using ssDNA as substrate. In EMSA, binding of the SSB protein with ssDNA (digoxigenin-labeled 27 base long ssDNA) would result in retardation in the mobility of the ssDNA compared to the free DNA.

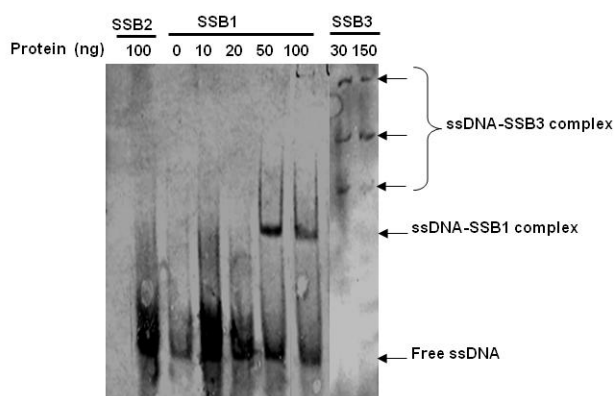
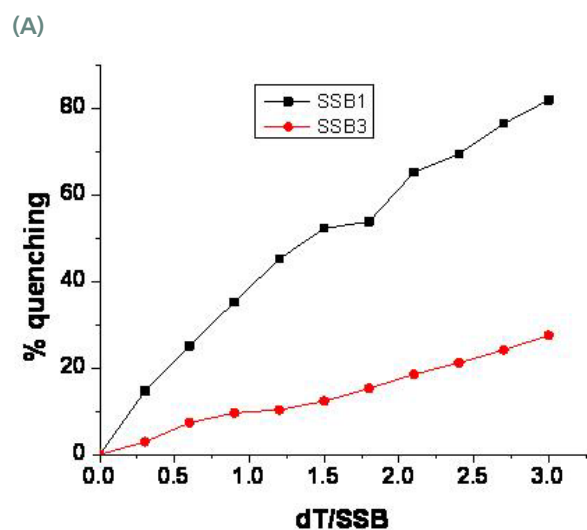


Fig. 3: Electrophoretic Mobility Shift Assay (EMSA). DIG-labelled 30-mer oligonucleotide (free ssDNA) was incubated in the presence of different concentrations of SSB proteins, followed by electrophoretic separation by 12% native PAGE in 1X TBE, blotting and development of autoradiogram. The free and bound ssDNA are indicated by arrows.

Decreased mobility of the 27-mer ssDNA was observed in the presence of SSB1 and SSB3, but not SSB2 even at high concentrations of the proteins (Fig. 3). This indicated that the OB-fold of SSB1 and SSB3 was active, but does not discount that of SSB2, since it may require different binding conditions.

To assess this further, a quantitative estimation of binding affinity was carried out using fluorescence quenching technique. The presence of aromatic amino acids, such as tyrosine, tryptophan and phenylalanine render a characteristic fluorescence pattern for each protein, when excited at a particular wavelength based on the spatial arrangement of these amino acids within the protein. And when the protein interacts with DNA, the changes in conformation are reflected by decrease in the intrinsic protein fluorescence, which is measured as fluorescence quenching. In this experiment, two kinds of substrate were used, poly(dT) or 7 kb long M13 ssDNA, as shown in Fig. 4.

The ability of the *Anabaena* SSB proteins to bind ssDNA was quantitatively analysed by determining the binding affinity using fluorescence quenching technique. Small oligonucleotides (30 -100 bases) and the 7 kDa M13 ssDNA were used as substrate. Quenching of fluorescence of SSB1 and SSB3 was achieved with short oligonucleotides (polydT) (Fig. 4A) as well as long M13 ssDNA (Fig. 4B), while that of SSB2 could be achieved with only M13 ssDNA (Fig. 4B).



(B)

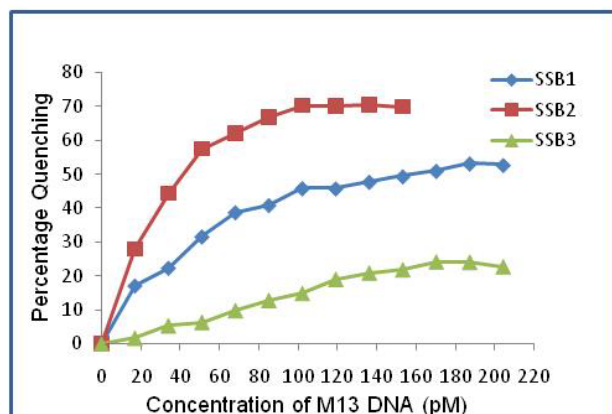


Fig. 4: Measurement of change in fluorescence of SSB proteins in the presence of ssDNA. Fluorescence of SSB proteins was measured in the presence of increasing concentration of (A) poly (dT) or (B) 7 kb M13 ssDNA.

The fluorescence quenching experiments showed that the SSB3 protein has maximum affinity to ssDNA. Due to the presence of the C-terminal acidic tail, which would allow it to interact with other DNA binding proteins, it may be the true or real functional SSB protein of *Anabaena*, instead of the other two annotated but truncated SSB proteins. Of the two naturally C-terminal truncated *Anabaena* SSB proteins, SSB1 binds short ssDNA preferably, while SSB2 prefers long ssDNA. This indicates different physiological roles for all three proteins in *Anabaena*. Instead of a single SSB protein catering to the various needs of SSB for replication, repair and recombination, the ancient organism *Anabaena*, synthesises three different proteins, possibly for each of these distinct roles. The *in vivo* functional roles of the three SSB proteins is currently under investigation.

References

1. Basu B, Apte SK (2012) Gamma radiation-induced proteome of *Deinococcus radiodurans* primarily targets DNA repair and oxidative stress alleviation. *PLoS One* 11: 1-15
2. Belts MJ, Russell RB (2003) Amino acid properties and consequences of substitutions. In *Bioinformatics for Geneticists*. Ed. Barnes MR and Gray IC. John Wiley and Sons, pp 289-316.
3. Curth U, Urbanke C, Greipel J, Gerberding H, Tiranti V, Zeviani M (1994) Single-stranded-DNA binding proteins from human mitochondria and *Escherichia coli* have analogous physicochemical properties. *Eur J Biochem* 221: 435-443.
4. Eggington JM, Haruta N, Wood EA, Cox MM (2004) The single-stranded DNA binding protein of *Deinococcus radiodurans*. *BMC Microbiol* 4: 2
5. Lohman TM, Ferrari ME (1994) *Escherichia coli* single-stranded DNA binding protein: multiple DNA-binding modes and co-operativities. *Annu Rev Biochem* 63: 527-570
6. Olszewski M, Grot A, Wojciechowski M, Novak M, Mickiewicz M, Kur J (2010) Characterization of exceptionally thermostable single-stranded DNA binding proteins from *Thermotoga maritima* and *Thermotoga neopolitana*. *BMC Microbiol* 10: 260-270.
7. Shereda RD, Kozlov AG, Lohman TM, Cox MM, Keck JL (2008) SSB as an organizer/mobilizer of genome maintenance complexes. *Critical Rev in Biochem and Mol Biol* 43:289-318
8. Singh H, Fernandes T, Apte SK (2010) Unusual radioresistance of nitrogen-fixing cultures of *Anabaena* strains. *J Biosci.* 35: 427-434

SYNTHESIS AND HYDROGEN ABSORPTION KINETICS OF V4Cr4Ti ALLOY

Sanjay Kumar, Sagar Sonak, Uttam Jain and Nagaiyar Krishnamurthy
Fusion Reactor Materials Section

This Paper received the Best Poster Award at the 18th DAE-BRNS International Symposium on Thermal Analysis, held at Mumbai from 31st January to 2nd February, 2012

Abstract

The hydrogen absorption kinetics of V4Cr4Ti alloy synthesized by aluminothermy process was investigated in the temperature range of 373-773 K. Three-dimensional diffusion process appears as the intrinsic rate limiting step of the hydrogen absorption reaction. The apparent activation energy was calculated using Arrhenius equation and was found to be 6.1 kJ/mol.

Introduction

In the search of alternative energy options, hydrogen looks promising, renewable and eco-friendly for transportation and domestic applications. Key issues related to the application of hydrogen as portable energy are safe storage system with good sorption kinetics. The storage of hydrogen in intermetallic system looks promising. In this regard vanadium-titanium-chromium (V-Ti-Cr) alloy with substantially varying composition of Ti and Cr is considered as a potential candidate for hydrogen storage due to its high volumetric hydrogen absorption, good cyclic properties and good absorption-desorption [1]. Storage capacity and hydrogen sorption kinetics of a gas-solid reaction depends upon various parameters. One of the essential parameters is the sample composition which is determined by the sample synthesis route. Vanadium and most of its alloys are generally produced via aluminothermy i.e. reduction of appropriate mixture of oxides. The process is highly cost-effective. However, the product retains several atom percent of aluminum even after purification. The kinetics study on V-Ti-Cr alloy prepared by aluminothermy process will be useful to implement aluminothermy process to produce V-Ti-Cr alloy for various applications where hydrogen solubility and kinetics are the key concerns. In the present investigation, the hydrogen absorption kinetics in V4Cr4Ti alloy, prepared by aluminothermy has been

studied at constant pressure employing variable mass technique. Hereafter in the text, V4Cr4Ti composition will be referred as "alloy".

Experimental

The alloy was prepared by aluminothermy and purified by electron beam melting. The resulting button was hot rolled into 0.3 mm thick strips. The hot rolled strip was cut into small pieces of an average weight of 400-500 mg and annealed at 1473K temperature under high vacuum condition (10^{-5} mbar). Before hydrogenation, the specimens were metallographically polished and kept in argon gas flushed vacuum desiccators. A thermobalance connected with Sieverts apparatus was used in the present investigation. Two types of hydrogen absorption experiments were conducted: Continuous and isothermal heating. The continuous heating was carried out to determine the starting temperature of the hydrogen absorption, while the isothermal heating was carried out to determine the kinetics parameters of hydrogen absorption. In the continuous heating, the sample was kept in a sample holder in the reaction chamber followed by evacuation to 10^{-5} mbar. The vacuum system was disconnected and hydrogen gas was slowly introduced in the reaction chamber to a predetermined level of 150 Torr hydrogen pressure. The reaction chamber was placed inside the furnace and heated at the rate of 5°C/min. The changes

BARC NEWSLETTER

in weight were recorded. In the isothermal experiment, samples were kept in the sample holder inside the reaction chamber followed by evacuation. The evacuated chamber was disconnected from the vacuum chamber and then hydrogen gas was introduced into the chamber to a predetermined level of 150 torr pressure. The sample was introduced into the furnace directly at the predetermined temperatures of 373,413,473,573,673 and 773K. The changes in weight were recorded.

The solid gas reaction's kinetic rate equation can be expressed as $\frac{d\alpha}{dt} = kf(\alpha)$. Where, α is the reacted fraction at time t , k is the rate constant, $f(\alpha)$ is function of the reaction mechanism, integral of $f(\alpha)$ is expressed as $g(\alpha)$:

$$g(\alpha) = \int \frac{d\alpha}{f(\alpha)} = kt$$

$g(\alpha)$ refers to the reaction mechanism function of the present study. Based on experimental data of hydrogen absorption curve, the reacted fraction α were calculated as $\alpha = (\omega_t - \omega_0) / (\omega_{eq} - \omega_0)$. Where, ω_0 is the initial weight; ω_t and ω_{eq} are the weight at time t and final equilibrium, respectively. The α - t kinetic curve gives the data for t and α for hydrogen absorption, which were fitted to various $g(\alpha)$ function listed in the literature. The mechanism of hydrogen absorption reaction in the alloy is indicated by the function $g(\alpha)$ giving the best linear fit. The kinetic parameter k was obtained from the slope of linear regression fitting of $g(\alpha)$. Based on the Arrhenius equation, the apparent activation energy of hydrogen absorption in the alloy was calculated.

Results and Discussion

The sample weight gain, due to hydrogen absorption, as a function of temperature during the continuous heating of sample is shown in the Fig 1. Marginal weight gain was recorded below 327K. Considerable weight gain was observed only above 327K which continued upto 800K.

Based on the continuous heating result, the isothermal hydrogenation was carried out in the temperature range of 373K to 773K, where kinetics is reasonably fast. An isothermal weight gain versus time curve is shown in the Fig. 2a The figure illustrates that the weight of the sample increased with time and finally reaches equilibrium. The reacted fractions ' α ' calculated as a function of time at different temperatures and presented in Fig. 2b. The experimental results were linearly fitted to various rate equation at different stages listed in the literature [1-2]. The fitting equations with large correlation coefficient and smallest standard

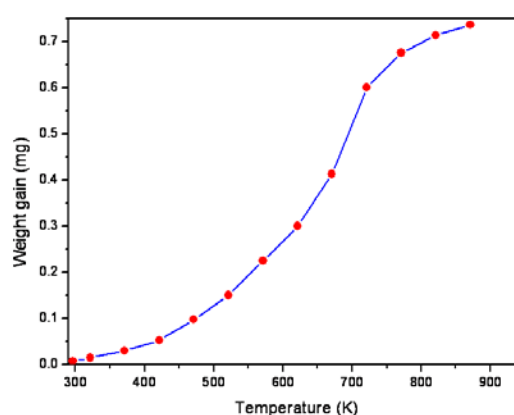


Fig. 1: Weight gain during the continuously heating process of the V4Cr4Ti sample.

deviation are considered as the best kinetics reaction mechanism to describe the hydrogen absorption process.

The best fitting equation of hydrogen absorption process at temperature 473K-773K is shown in the Fig 3a. The figure shows that the mechanism of three-

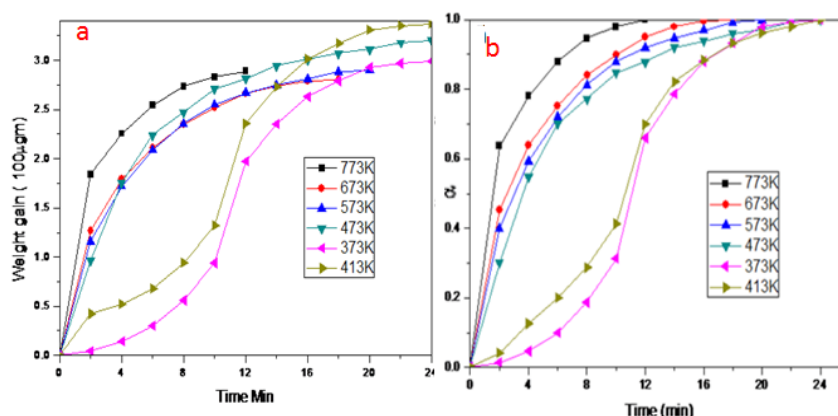


Fig. 2: (a) Isothermal weight gain curve of V4Cr4Ti alloy at different temperatures and (b) reacted fraction calculated with respect to time and temperature

dimensional diffusion only dominates the hydrogen absorption process at temperatures $\leq 473\text{K}$.

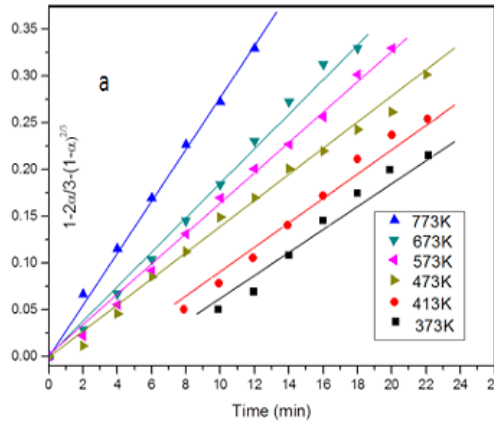


Fig. 3: Relation of common mechanism functions with time for hydrogen absorption in V4Cr4Ti between 373 K and 773 K

Assuming reaction mechanism is the same for all the temperature investigated, the rate constant can be obtained according to Arrhenius equation: $k = A \cdot \exp(-E_a/RT)$ Where, A is the pre-exponential factor, R is the molar gas constant (J/(molK)), T is hydrogenation temperature (K) and E_a is the apparent activation energy of the reaction (J/mol). The natural logarithm of Arrhenius equation is $\ln k = \ln A - E_a/RT$. The rate constants at different temperatures are extracted from slope of the linearly fitted hydrogen absorption mechanism function, the apparent activation energy E_a of the hydrogen absorption was obtained from the slope of $\ln k$ vs. $1/T$ curve.

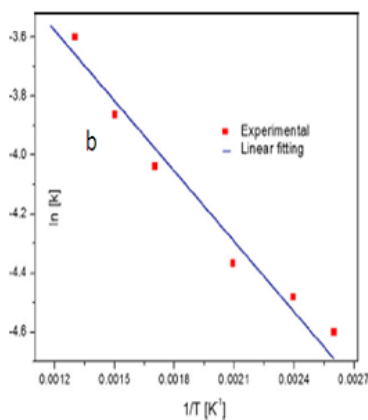


Fig. 4: Arrhenius plot of hydrogen absorption reaction rate in V4Cr4Ti alloy

As the hydrogen absorption process in the alloy is controlled by the same reaction mechanism in the temperature range of 473-773K, the Arrhenius plot is constructed and presented in Fig 4. The calculated apparent activation energy for absorption of hydrogen into V4Cr4Ti alloy is 6.1 kJ/mol.

Conclusion

V4Cr4Ti alloy prepared by aluminothermy process starts absorbing hydrogen right from the room temperature but the kinetics become reasonably high only above 327K. The initial hydrogen absorption rate constant increases with the increasing temperature. The mechanism of three dimensional diffusion processes is the intrinsic rate limiting step of hydrogen absorption above 473K temperature. The calculated apparent activation energy for the absorption of hydrogen into V4Cr4Ti alloy is 6.1 kJ/mol.

References

1. Sanjay Kumar, PhD Thesis, HBNI-2012
2. Sanjay Kumar and N Krishnamurthy. Vanadium based hydrogen storage materials: a review. Progress in Materials Science, (2013) Under review
3. Sanjay Kumar, M Taxak and N Krishnamurthy. Synthesis and hydrogen absorption in V-Ti-Cr alloy, J Thermal Analysis Calorimetry ; 112(1), (2013), 51-57
4. Sanjay Kumar, M. Taxak, N Krishnamurthy. Hydrogen absorption kinetics of V4Cr4Ti alloy prepared by aluminothermy process. Int J Hydrogen Energy 2012; 37(4) (2012): 3283-91.
5. Sanjay Kumar and N Krishnamurthy. Variation of activation energy of hydrogen absorption of vanadium as a function of Al. Int J Hydrogen Energy, 2012; 37(18) 13,429-36.

β -CYCLODEXTRIN FUNCTIONALIZED CDSE QUANTUM DOTS SYNTHESIZED VIA ELECTRON BEAM IRRADIATION

A. Guleria, S. Singh, M. C. Rath, A. K. Singh, S. Adhikari and S. K. Sarkar

Radiation & Photochemistry Division

This Paper received the Best Poster Award at the DAE-BRNS 11th Biennial Trombay Symposium on Radiation & Photochemistry (TSRP 2012), held at Mumbai, from 4th-7th January, 2012

Abstract

Herein, we report a simple, rapid and one step method for the synthesis of β -cyclodextrin (β -CD) functionalized CdSe quantum dots (QDs) in aqueous solution *via* electron beam irradiation technique. The QDs exhibited excitonic absorption in the range of 400-500 nm, depending on the experimental parameters (i.e. dose, dose rate and molar ratio of β -CD to precursors) and displayed broad photoluminescence (PL) with two emission peak regions at \sim 525 nm and \sim 600 nm, at room temperature. The observed PL peaks were assigned as band gap and trap state emissions respectively, which could be tuned by varying aforementioned parameters. The as grown QDs were water soluble and possessed fairly good colloidal stability therefore can have potential applications in sensing and bio-labeling.

Keywords: CdSe, Quantum dots, Cyclodextrin, Electron beam, Photoluminescence

Introduction

In this work, we have employed β -cyclodextrin (β -CD) to functionalize the CdSe quantum dots (QDs) grown by electron beam (EB) assisted technique. We have earlier reported the synthesis of bare CdSe nanoparticles (NPs) in aqueous solutions using EB irradiation [1]. Those NPs were found to be quite unstable in ambient conditions and did not exhibit any photoluminescence (PL). However, on functionalization accompanied by the optimization of various parameters (i.e. absorbed dose, dose rate (Grey (Gy) per pulse, GPP), molar concentrations of β -CD and the precursor), the as grown QDs showed good colloidal stability, size tunability and superior PL properties as compared from bare ones. Besides, the use of supramolecular assemblies i.e. CDs as stabilizing/capping agents and water as a solvent medium aligns with the increasing emphasis on the topic of green chemistry and simultaneously, enhancing the possibility of greater

functions with some unique and exciting applications of these NPs.

Experimental

Briefly, CdSe NPs were synthesized by irradiating the reaction mixture containing the precursors of Cd and Se along with CD as a capping agent at optimized concentration levels. Also, tertiary-butanol was added to this reaction mixture to scavenge the OH \cdot radicals generated during the radiolysis of aqueous solution. Precursor for Se (Sodium selenosulphate (Na₂SeSO₃) solution) and Cd (cadmium sulfate) were prepared by the earlier reported method [2]. Mean while, a 7 MeV EB (FWHM 2 μ s) sourced from a linear electron accelerator (LINAC) was used for irradiating the samples. On irradiation, the color of the solution turned to greenish-yellow or reddish-orange, depending on the experimental parameters, and this was the primary indication for the formation of the CdSe NPs.

Results and discussion

Morphology and Structural Characterization of as grown CdSe QDs

Fig. 1A shows the TEM image of β -CD capped CdSe NPs. In the absence of β -CD, the CdSe NPs agglomerated and formed a complex network with no well defined structure/pattern. While, β -CD coated NPs appear to form an array like network in which small beads are joined together to give a pearl necklace shape pattern. The size of the NPs observed from the TEM images was predominantly found to be in the range of 2-3 nm.

The XRD pattern of as grown NPs has been shown in Figure 1B. The diffraction pattern of the NPs has been found to be in good agreement with the standard JCPDS card no. 19-0191, corresponding to the cubic structure of CdSe.

FT-IR spectra gave the direct evidence of the *in situ* adsorption or functionalization of β -CD on the surface of the as grown CdSe QDs (Figure 1C). The sizes of NPs determined from the TEM and absorption (discussed later) measurements were much larger than the diameter of the β -CD cavity, therefore the possibility of formation of inclusion complexes has been ruled out. The strong resemblance between their IR spectra indicates a successful anchoring of β -CD onto the CdSe QDs surface. A doublet at $\sim 2356\text{ cm}^{-1}$ and 2333 cm^{-1} can be noticed in the IR spectra of β -CD coated CdSe NPs. These peaks have been ascribed to the presence of CO_2 in the sample chamber. Besides, there is a red

shift accompanied by broadening of the peak in the O-H stretching frequency of β -CD coated CdSe NPs ($\sim 3248\text{ cm}^{-1}$) compared with that of β -CD ($\sim 3300\text{ cm}^{-1}$), which indicates a sort of bond formation between -OH groups of β -CD and the CdSe QDs.

Optical studies: Effect of Molar ratio, absorbed dose and dose rate

The optical absorption measurements were carried out before and after the EB irradiation. As can be seen in Figure 2A, a red shift in the excitonic peak was observed on varying the molar ratio (CD: QD) to 2:1 ($\sim 420\text{ nm}$), 1:1 ($\sim 432\text{ nm}$) and 1:2 ($\sim 443\text{ nm}$) (Figure 2A). Mean while, the radiolytic decomposition of CD was found to be less than 10 % when irradiated to various doses up to $\sim 72\text{ kGy}$ [3]. Taking note of the radiation stability of CDs, the effect of absorbed dose on the absorption spectra of β -CD coated CdSe QDs was examined. The excitonic peak undergoes blue shift with the increase in dose. This indicates that the size of β -CD/ CdSe NPs decreases with the increase in dose. The observed trend can be explained on the basis that at higher radiation doses, the number of nucleation centers formed are much more and lead to the retardation of growth process. Similarly, the effect of dose rate was investigated and it was observed that excitonic absorption peak underwent gradual red shift with the decrease in the dose rate. It signifies that the size of as grown NPs increased with the decrease in the dose rate.

The estimated size values of the primary CdSe NPs functionalized with β -CD at various experimental parameters were calculated from the absorption spectra

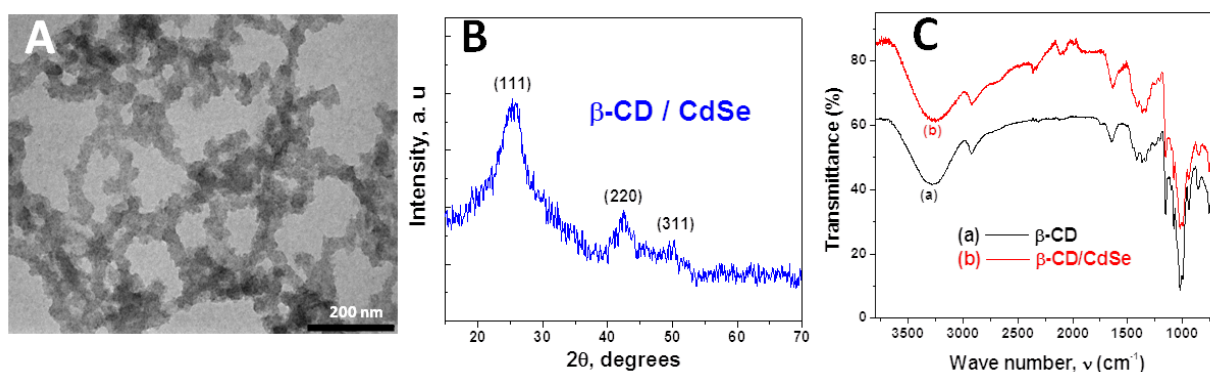


Fig.1: (A) TEM image, (B) XRD pattern of β -CD/CdSe QD, (C) FT-IR spectra of β -CD (a), β -CD/CdSe (b). Molar ratio (β -CD:QD) = 2:1, Absorbed Dose = 25 kGy @ 140 GPP.

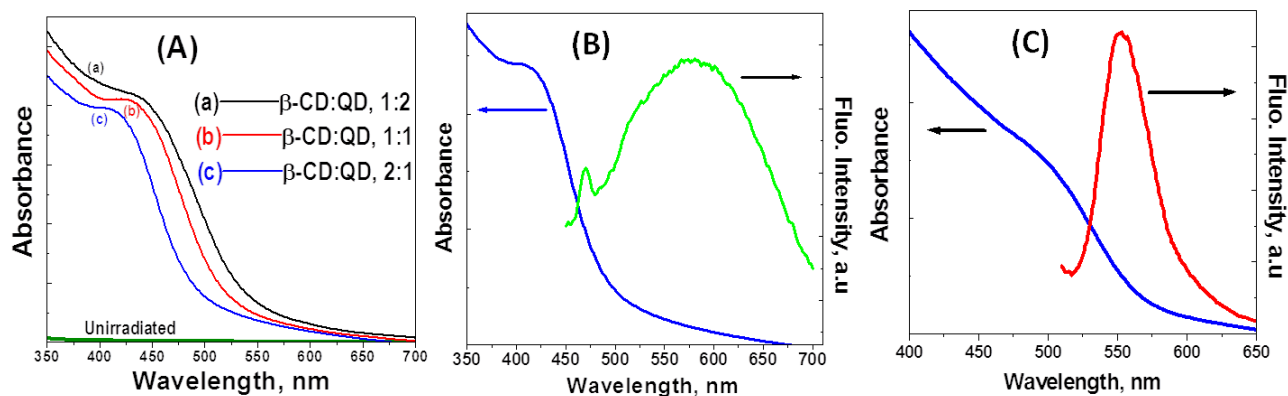


Fig.2: (A) UV-Vis absorption spectra of β -CD/CdSe QDs with different molar ratios (β -CD: QD); Absorbed Dose = 25 kGy @ 140 GPP; (B) PL spectra of β -CD/CdSe QDs with molar ratio (β -CD: QD) of 2:1, absorbed dose = 25 kGy @ 140 GPP; (C) PL spectra of β -CD/CdSe NPs with molar ratio (β -CD: QD) of 2:1, absorbed dose = 1 kGy @ 10 GPP.

Table 1: The energy band gap values (E_g , eV) and the size of the CdSe QDs (nm) synthesized *via* EB irradiation at different experimental parameters.

Molar ratio effect (25 kGy @ 140 GPP)			Absorbed dose effect (CD:QD = 2:1@140 GPP)			Dose rate effect (CD:QD = 2:1@25 kGy)		
Molar ratio (β -CD: QD)	E_g (eV)	Particle size	Dose, kGy	E_g (eV)	Particle size	Dose rate, GPP	E_g (eV)	Particle size
1:2	2.40	2.36	10	2.31	2.31	50	2.42	2.33
1:1	2.46	2.26	15	2.47	2.25	80	2.45	2.28
2:1	2.54	2.10	25	2.54	2.10	140	2.54	2.10

by using the modified Brus equation [2] and the same has been listed in Table 1.

The absorbed dose and the dose rate were found to have significant impact on the PL properties of these NPs (see Figure 2B & C). A evolution of band gap (BGE) and trap state (TSE) emission was observed in case of QDs synthesized with an absorbed dose of 25 kGy @ 140 GPP, withg dominant contribution from the later one (Figure 2B). While, the PL observed in case of β -CD/CdSe NPs grown with an absorbed dose of 1 kGy @ 10 GPP, can be ascribed to be originated from the intrinsic recombination (BGE) of charge carriers (Figure 2C). Thus, the fine tuning of the PL properties of as grown β -CD coated CdSe NPs could be achieved simply by varying the experimental parameters.

Conclusions

A simple, rapid, one step method assisted by EB irradiation technique has been demonstrated for the synthesis as well as *in situ* functionalization of CdSe

QDs with β -CD in aqueous solution. It was observed that the β -CD molecules cap the as grown NPs through the -OH groups and eventually forming a non-inclusion complex. A fine control and tuning the PL properties of as synthesized QDs was illustrated. The present methodology of EB assisted synthesis of nanomaterials in the host matrix of supramolecular assemblies is relatively new and may provide some unique and interesting aspects to control and fine tune the morphology *vis-à-vis*, the optical properties of nanomaterials.

References

1. Singh S, Rath MC, Singh AK, Mukherjee T, Jayakumar OD, Tyagi AK, Sarkar SK. Radiat Phys Chem. 80 (2011): 736-741.
2. Singh S, Guleria A, Rath MC, Singh AK, Adhikari S, Sarkar SK. J. Nanosci. Nanotechnol. 13 (2013): 5365-5373.
3. Phillips G O, Young M. J Chem. Soc. (A) 1966, 383-387.

BARC NEWSLETTER

HONEY: A NATURAL FUNCTIONAL FOOD HAVING BROAD-SPECTRUM ANTIMUTAGENIC AND ANTI-PROLIFERATIVE CHARACTERISTICS

S. Saxena, S. Gautam and A. Sharma

Food Technology Division

and

D. K. Maurya

Radiation Biology and Health Sciences Division

and

G. Maru

Advanced Centre for Treatment, Research and Education in Cancer, Kharghar, Navi Mumbai

This Paper received the Best Poster Award at the Innovations in Food Science and Technology to fuel the growth of the Indian food industry, (XXI ICFOST), held at Pune, on 20th & 21st January, 2012

Abstract

Commercial Indian honey was found to display broad spectrum antimutagenicity against various physical (UV, γ) and chemical (EMS) mutagens, evaluated through *rpoB/Rif^S→Rif^R* (*E. coli* based) and Ames (*Salmonella typhimurium* based) assays. To understand the molecular mechanism of antimutagenicity, the effect of honey was evaluated in radiation exposed *E. coli* cells for SOS response, a well known error prone repair pathway that is known to contribute significantly to mutagenicity by quantifying LexA repressor level, measuring cell filamentation frequency, and prophage induction by SIVET (Selectable *in-vivo* Expression Technology) assay. LexA was almost completely degraded, phenotypically long filamentous cells were formed, and SIVET induction frequency was increased in radiation exposed *E. coli*, however, these changes were significantly inhibited in the presence of honey confirming its strong antimutagenic nature, and efficiency to suppress the error-prone repair pathway. Honey showing strongest antimutagenicity was subjected to solid phase extraction that resulted in partial purification of the phenolic fraction that displayed significantly higher cytotoxicity against breast cancer (MCF-7) and myeloid leukemia (K562) cell lines as compared to normal (Mouse splenocytes and Int-407) cells as evidenced by microscopic observations and MTT assay. Besides, clonogenic assay also indicated anti-proliferative property of the bio active fraction of honey against MCF-7 cells. These findings establish honey as an effective natural antimutagen confirming its nutraceutical and therapeutic potential.

Introduction

Honey is known to have therapeutic and prophylactic action against neoplastic changes caused by environmental mutagens and carcinogens. It has been reported to inhibit growth of tumors and tumor cell lines *in vitro* including colon carcinoma cells (Samarghandian et al., 2011). In higher systems error-prone DNA repair such as nonhomologous end joining

and/or microhomology-mediated end joining are the important routes to mutagenesis that could eventually lead to oncogenesis. In lower system like *E. coli* SOS response is an established error-prone pathway leading to mutator phenotype (Patel et al., 2010). In a recent study honey has been reported as a good source of nutrients rich in antioxidants (Saxena et al., 2010; Bogdanov, 2011). However, very limited information is available on the antimutagenic property of honey.

BARC NEWSLETTER

The current study was undertaken to evaluate the efficacy of antimutagenicity of commercial honey and to understand the underlying molecular basis of antimutagenicity using *E. coli* as a model system. The findings from the current study could provide scientific basis for the use of honey as a health protective functional food.

Material and methods

Honey samples and bacterial strains

Seven (I-VII) different commercial Indian honey were purchased from a local market. The *Salmonella typhimurium* tester strains TA100 and TA102 were procured from Xenometrix, Inc. USA. *E. coli* strains MG1655 and SIVET strain SG104 were gifted by Prof. M.Z. Humayun, University of Medicine and Dentistry, NJ, USA. *E. coli* strains *recA*⁻; *umuC*⁻; *umuD*⁻) were procured from Keio collection, Japan.

Evaluation of diastase activity and pollen profile

The diastase activity (Diastase number, DN) was calculated following the method of the International Honey Commission (2002). The pollen analysis was performed as per the method of International Commission for Bee Botany at the Birbal Sahni Institute of Palaeobotany, Lucknow, India.

Antimutagenicity assay

The *rpoB*/Rif^S→Rif^R forward mutation assay was performed as per the method described earlier by Cupples and Miller (1989). In this assay control *E. coli* cells are unable to grow on rifampicin selective plate as rifampicin inhibits DNA dependent RNA polymerase (RNAP) and physically prevents the synthesis of RNA. However, mutations in the *rpoB* gene reduce the affinity of rifampicin binding to RNAP and thus confers rifampicin resistance (Rif^R) to *E. coli* cells. Therefore, induced mutagenesis leads to acquisition of rifampicin resistance by these cells which are thus able to grow on rifampicin selective plates. Physical [(Ultraviolet, (UV) and gamma radiation, (γ-ray)] and chemical (EMS) mutagens were employed in the assay.

Antimutagenicity was assayed by treating cell suspension with mutagens in the absence (control) as well as presence of honey solution. After treatments the *E. coli* culture was spread plated on LB-rifampicin plate for scoring Rif^R (rifampicin resistant) mutants and on LB plates for enumerating total viable cells. Mutation frequency was calculated as ratio of total no. of Rif^R mutants per ml to the total no. of viable cells per ml. Ames test, an auxotrophic reverse mutation detection system using *Salmonella Typhimurium* tester strains was performed as per the procedure described earlier (Maron and Ames, 1983). The antimutagenic effect (%) was calculated relative to controls as $[1-T/M] \times 100$; where T is the average number of revertants in the presence of mutagen plus extract - number of spontaneous revertants and M is the number of revertants in the presence of mutagen alone - number of spontaneous revertants.

Analysis of SOS response

The LexA level was quantitatively measured by Western blotting as per the procedure described earlier (Gautam and Sharma, 2002). The filamentation assay in *E. coli* was performed as per the method of Gottesman et al., 1981. Cells having length $\geq 3.0 \mu\text{m}$ were recorded to be filamentous. Filamentation frequency was calculated as percentage of filamented cells with respect to total cell population. Selectable-*in-vivo* Expression Technology (SIVET) assay was performed using *E. coli* strain SG104 as per the methods described earlier (Gautam et al., 2012). The frequency of Cm^R cells serves as a measure of prophage induction which in turn parallels SOS induction. SIVET induction frequency was indexed as ratio of SIVET induced cells to total viable cells.

Solid phase extraction

As phenolics from other food commodities have been reported earlier to show antimutagenicity, hence in the current study also the phenolics were extracted from honey using C-18 Sep-Pak column using methanol as an eluent as per the method of Khalil et al. (2011). This phenolics suspension was analyzed for antimutagenicity against UV induced mutagenesis

BARC NEWSLETTER

using *E. coli rpoB/Rif^S→Rif^R* assay as mentioned earlier. Besides, the phenolic extract was also evaluated for antiproliferative property against cancer cell lines through MTT and clonogenic assays.

Results and discussion

Antimutagenic property of honey

Of the seven honey brands honey brand III (showing highest antimutagenicity) and VII (displaying lowest antimutagenicity) were selected for further detailed studies. Honey of either brand was not found to affect the background Rif^R frequency and hence considered to be non-mutagenic in this assay system. In the presence of honey, the UV mutation frequency reduced by 97 and 94% by honey III and VII, respectively (Table 1). Similarly, reduction in gamma radiation induced mutagenesis was 87 and 82%, and EMS induced mutagenesis 80 and 32%, respectively with the two honey samples. In Ames test UV treatment resulted in almost ~7 fold increase in the reversion frequency in TA102, which was found to be reduced in presence of honey (Table 2). Antimutagenic effect of honey was found to be concentration dependent. Honey III reduced mutagenicity by 77 and 61% at 100

Table 1: Enhancement in *E. coli rpoB/Rif^R* mutation (Rif^S-Rif^R) frequency by different mutagens and its inhibition by honey.

Treatments	Number of Rif ^R mutants /100 million cells (Mean ± SD)
None	1.0 ± 0.2
Honey (III)	1.0 ± 0.6
Honey (VII)	1.0 ± 0.8
UV	1000 ± 42
UV + Honey (III)	33 ± 5
UV + Honey (VII)	66 ± 7
Gamma radiation	60 ± 8
Gamma radiation + honey (III)	7.0 ± 2
Gamma radiation + honey (VII)	10 ± 4
EMS	2200 ± 167
EMS + honey (III)	430 ± 43
EMS + honey (VII)	1500 ± 117

Table 2: Enhancement in his⁺ reversion frequency (Ames test) in *Salmonella typhimurium* tester strains TA100 and TA102 by mutagens and its inhibition by honey.

Treatments		Antimutagenic effect (%) w.r.t. control (without honey) mutagen exposed cells (TA 102)	Antimutagenic effect (%) w.r.t. control mutagen exposed cells (TA 100)
UV + Honey (III)	100 mg/ml	61	* (Not done)
	250 mg/ml	77	*
UV + Honey (VII)	100 mg/ml	60	*
	250 mg/ml	71	*
EMS + Honey (III)	10 mg/ml	9	37
	100 mg/ml	53	68
	250 mg/ml	59	74
EMS + Honey (VII)	10 mg/ml	6	36
	100 mg/ml	30	61
	250 mg/ml	42	68

and 250 mg/ml concentrations, respectively, whereas, honey VII reduced mutagenicity by 70 and 60% at these two concentrations. Even post UV exposure, immediate addition of honey was found to have a profound antimutagenic effect. The his⁺ reversion frequency in these populations was found to be inhibited by 35 and 25%, respectively at 250 and 100 mg/ml concentrations of honey of both these brands.

Pollen profile and diastase activity

Both these commercial honey (brand III and VII) were found to be floral (blossom) in nature by pollen analysis. In honey III (unifloral), *Syzygium cumini* was found to be dominating pollen flora, whereas, in honey VII (bifloral), the pollen assemblage was dominated by *Adhatoda vasica* and *Terminalia* having almost equal proportions. The diastase activity in honey III and VII was found to be 13 and 9 DN (Diastase number), respectively.

Evaluation of SOS hallmarks: LexA status, cell filamentation and prophage induction

Upon radiation (UV or gamma) exposure almost complete degradation of LexA, was observed in *E. coli* cells. Interestingly, significant (~98%) protection of LexA was noticed when cells were subjected to radiation in the presence of honey (Fig. 1). Morphology of *E. coli*

BARC NEWSLETTER

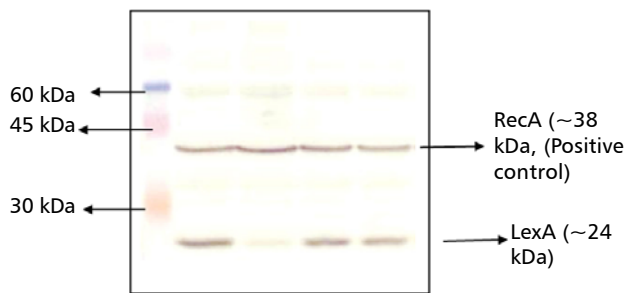


Fig. 1: Western blot showing the degradation of LexA repressor protein upon radiation (UV) exposure and its protection by honey.

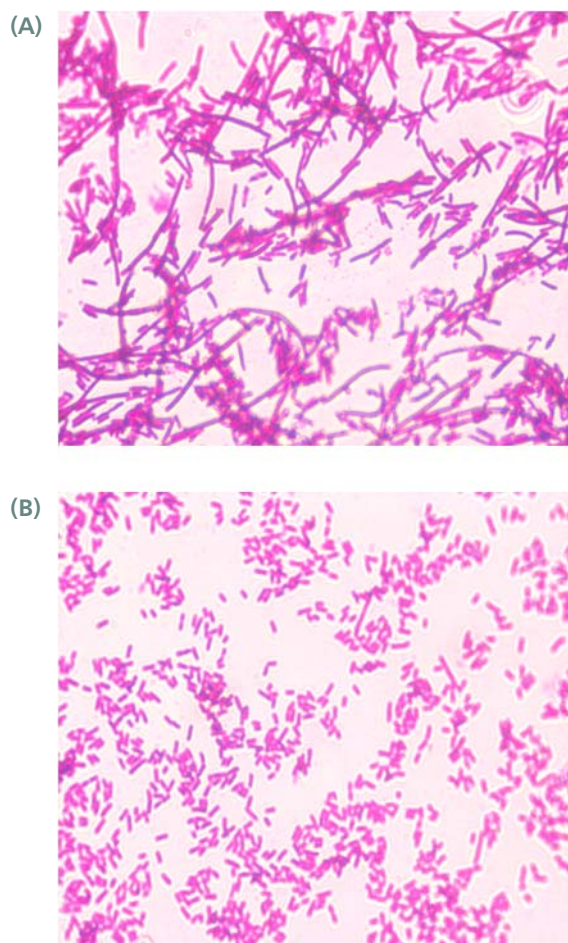


Fig. 2: Cell filamentation in radiation (UV or gamma) exposed *E. coli* and its inhibition by honey (III). A: Radiation treated cells; B: Radiation + honey treated cells

MG1655 cells after radiation exposure changed drastically to long filaments due to loss of post DNA replication cell partitioning activity (Fig. 2). Activation of *sulA* gene leads to inhibition of cell partitioning because of SulA-FtsZ association. It drastically increased to 65% upon UV exposure. Interestingly, the presence of honey reduced filamentation frequency to 1/9

compared to UV treated cells. In comparison to UV, the filamentation frequency upon gamma radiation exposure was observed to be comparatively lesser and it was almost equally inhibited by honey. The cells were found to be SIVET induced upon UV or gamma radiation treatment by 73 and 90%, respectively. In this prophage induction assay induction of defective lambdaoid prophage does not lead to cell lysis but instead makes *E. coli* cells chloramphenicol resistant. Interestingly, honey was found to be highly effective in reducing the extent of SIVET induction to 18 and 40%, respectively (Fig. 3).

UV induced Rif^R mutation frequency in single gene-knockout mutants of *E. coli*

In comparison to wild-type *E. coli* cells, the mutation frequency in knock-out strains was found to be

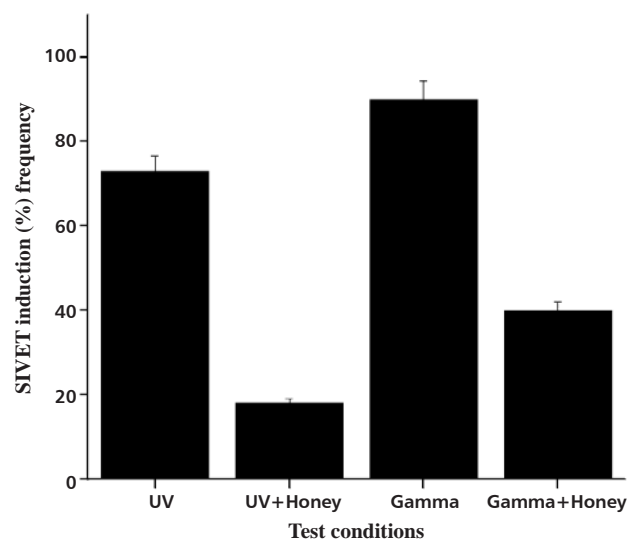


Fig. 3: SIVET induction frequency in radiation exposed *E. coli* (SG 104) cells and its inhibition by honey (III).

Table 3: Extent of cell filamentation in radiation exposed *E. coli* and its inhibition by honey

Treatments	Filamentation frequency (%) (Mean ± SD)
Control (No treatment)	0.2 ± 0.001
UV	65 ± 2.3
UV + honey (III)	3.0 ± 0.014
UV + honey (VII)	5.5 ± 0.04
Gamma radiation	45 ± 3.3
Gamma + honey (III)	2.0 ± 0.5
Gamma + honey (VII)	7.0 ± 0.4

BARC NEWSLETTER

drastically reduced. Mutation frequency in *recA* knockout strain was comparable to the spontaneous mutation frequency, whereas, the mutation frequency was marginally higher in *umuC* and *umuD* knockout strains. However, the presence of honey or its phenolic extract was not found to alter the respective mutation frequencies (Table 4).

Table 4: UV induced *rpoB*/Rif^R mutation (Rif^S-Rif^R) frequency in single gene-knockout *E. coli* mutants and effect of honey.

<i>E. coli</i> and treatment conditions	Number of Rif ^R mutants /100 million cells (Mean ± SD)
<i>E. coli</i> MG1655 (wild type)	1000 ± 42
<i>E. coli</i> (wild type) + Phenolic extract (1 mg/ml)	150 ± 11
<i>E. coli</i> (wild type) + Sugar solution	650 ± 44
<i>E. coli</i> (<i>recA</i>)	1 ± 0.2
<i>E. coli</i> (<i>recA</i>) + honey(III)	1 ± 0.3
<i>E. coli</i> (<i>recA</i>) + Phenolic extract (1 mg/ml)	1 ± 0.3
<i>E. coli</i> (<i>umuC</i>)	16 ± 3
<i>E. coli</i> (<i>umuC</i>) + honey(III)	13 ± 8
<i>E. coli</i> (<i>umuC</i>) + Phenolic extract (1 mg/ml)	13 ± 3
<i>E. coli</i> (<i>umuD</i>)	15 ± 3
<i>E. coli</i> (<i>umuD</i>) + honey(III)	13 ± 2
<i>E. coli</i> (<i>umuD</i>) + Phenolic extract (1 mg/ml)	17 ± 2

Biochemical composition of honey and its relevance to antimutagenicity and anticarcinogenicity

Honey is a complex mixture of different substances including sugars, proteins and phenolics as indicated in our earlier study (Saxena et al., 2010). To evaluate the role of sugar in observed antimutagenicity, a sugar solution (1.52 M) was prepared and analyzed for antimutagenicity. Surprisingly, contribution of sugar preparation to the antimutagenic property of honey was found to be significantly less than those observed with honey as such. Further one of the honey brands showing highest antimutagenicity (brand III) was subjected to solid phase extraction for the purification of phenolics and it was analyzed for antimutagenicity against UV induced mutagenesis using *E. coli rpoB*/Rif^S→Rif^R assay. Interestingly, the extract reduced the UV induced mutation frequency to 1/5th indicating its

significant contribution in the observed antimutagenic property of honey. Phenolic extract was also found to inhibit LexA degradation upon radiation exposure. It is interesting to mention that concentration of phenolics in honey is almost 760 fold less than that of sugar; still phenolics extract showed strong antimutagenicity than the sugars. The phenolic extract also displayed differential activity against normal cells and cancer cells. The phenolic extract was not found to affect the viability (~100 %) of normal cells (Int-407 as well mouse splenocytes) in MTT assay even at higher conc. (800 µg/ml). Interestingly, in cancer cell lines such as MCF-7 (breast cancer cell line) and K-562 (Myeloid leukemia cell line), phenolic extract exerted significant effect even at 100 µg/ml concentration. It also displayed antiproliferative activity against MCF-7 cells as ascertained by clonogenic assay (Fig. 4).

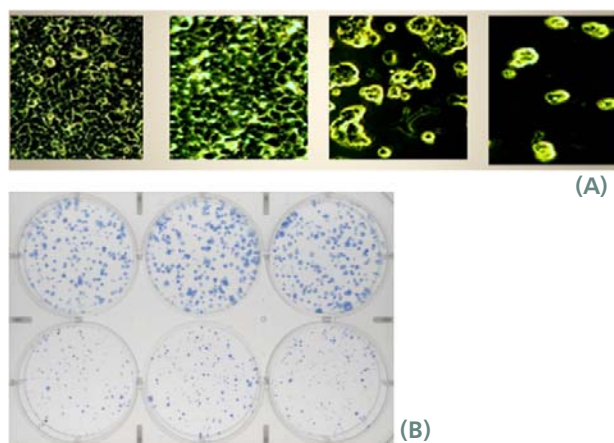


Fig. 4:(A). Microscopical examination indicating loss of adherence & viability in breast cancer cell line (MCF-7) treated with phenolic extract; (B) Antiproliferative property (using clonogenic assay) displayed by phenolic extract of honey.

Conclusion

This study reported the broad spectrum antimutagenic potential of honey against various physical and chemical mutagens, which was evaluated through Ames test, as well as *E. coli rpoB*/Rif^S→Rif^R assay. Antimutagenicity of honey was found to be due to its ability to suppress the error-prone repair pathway that is mainly executed as a result of SOS response in *E. coli*. The findings established honey as an effective natural antimutagen confirming its nutraceutical and therapeutic potentials.

BARC NEWSLETTER

References

1. Cupples, C.G., Miller, J.H. (1989). A set of *lacZ* mutations in *Escherichia coli* that allow rapid detection of each of the six base substitutions. *P Natl. Acad. Sci. USA*. 86, 5345-5349.
2. Gautam, S., and Sharma, A. (2002). Involvement of caspase-3 like protein in rapid cell death of *Xanthomonas*. *Mol. Microbiol.* 44(2), 393-401.
3. Gautam, S., Kalidindi, R., Humayun, M.Z. (2012). SOS induction and mutagenesis by *dnaQ* missense alleles in wild type cells. *Mutat. Res.* 735, 46-50.
4. Gottesman, S., Halpern, E., Trisler, P. (1981). Role of *sulA* and *sulB* in filamentation by *Lon* mutants of *Escherichia coli* K-12. *J. Bacteriol.* 148(1), 265-273.
5. International Honey Commission (2002). Harmonised methods of the International honey commission. http://www.apiculturacluj.com/ApiculturaCluj/italiano/Documents/IHCmethods_e.pdf.
6. Khalil, M.I., Alam, N., Moniruzzaman, M., Sulaiman, S.A., Gan, S.H. (2011). Phenolic acid composition and antioxidant properties of Malaysian honeys. *J. Food. Sci.* 76(6), C921-C928.
7. Maron, D.M., Ames, B.N. (1983). Revised methods of the *Salmonella* mutagenicity test. *Mutat. Res.* 113, 173-215.
8. Patel, M., Jiang, Q., Woodgate, R., Cox, M.M., Goodman, M.F. (2010). A new model for SOS-induced mutagenesis: how RecA protein activates DNA polymerase V. *Crit. Rev. Biochem. Mol.* 45(3), 171-184.
9. Samarghandian, S., Afshari, J.T., Davoodi, S. (2011). Honey induces apoptosis in renal cell carcinoma. *Pharmacogn. Mag.* 7(25), 46-52.
10. Saxena S., Gautam S., Sharma A. (2010). Physical, biochemical and antioxidant properties of some Indian honeys. *Food Chem.* 118(2), 391-397.

RADIATION INDUCED CELL DEATH IN BACTERIA IS PARTIALLY PROGRAMMED

S. Wadhawan, S. Gautam, and A. Sharma
Food Technology Division

This Paper received the Best Poster Award at the XXXVI All India Cell Biology Conference and International Symposium on Stress Adaptive Response and Genome Integrity (SARGI), held at Mumbai, from Oct. 17-19, 2012

Abstract

Radiation exposed *E.coli* cells die through a molecular mechanism involving caspase-3 activation and phosphatidylserine externalization, similar to that reported during eukaryotic programmed cell death (PCD) or apoptosis. The bacterial cell death was found to be suppressed upon pretreatment with sublethal concentrations of rifampicin or chloramphenicol indicating the requirement of *de novo* gene expression. The radiation induced cell death (RICD) was also found to be inhibited by cell permeable inhibitors of caspase-3 or poly (ADP-ribose) polymerase, indicating the involvement of PCD during RICD in *E.coli*. Radiation treatment resulted in induction of SOS response by DNA damage mediated autocatalytic cleavage of LexA repressor, which resulted in enhanced cell filamentation. However, this was inhibited in the presence of caspase-3 inhibitor. Further, the inhibitor mediated rescue was not observed in *E. coli* single gene knockouts of *umuC*, *umuD*, *recB* and *ruvA*. These genes are associated with SOS response. Thus the current findings imply a linkage between SOS response and PCD, the two molecular events in radiation exposed *E.coli* cells.

Introduction

Ionizing radiation (IR) can damage cell or its macromolecules, including DNA, either directly or indirectly through free radicals generated by radiolysis of water. It has been reported that low doses of IR initiate reversible cell growth arrest allowing repair to take place, whereas, higher doses of IR trigger cell death through necrotic or apoptotic mechanisms to eliminate irreparable injured cells (Elmore et al. 2007). PCD has been established to play vital role in bacterial developmental processes (Lewis 2000; Rice and Bayles 2003). Some of these include mother cell lysis during sporulation in *Bacillus* (Lewis 2000), vegetative cell lysis during myxobacterial fruiting body formation (Lewis 2000) and salt-stress-induced PCD in *Anabaena*, a cyanobacterium (Ning et al. 2002). PCD in bacteria plays an altruistic role by removing defective cells and allowing the nutrients to be accessible to the remaining healthy population. It also ensures that no defective genome is allowed to replicate. A metabolic-stress-

induced PCD, dependent on a caspase-3-like protein, has been demonstrated earlier in *Xanthomonas campestris* (Gautam and Sharma 2002a, b; Gautam and Sharma 2005; Gautam et al. 2005; Raju et al. 2006; Wadhawan et al. 2010). In a recent study, it was shown that *Streptococcus pneumoniae* and *Haemophilus influenzae* underwent apoptosis-like death and displayed its characteristic morphological as well as biochemical features when treated with a human milk complex of alpha lactalbumin and oleic acid (termed HAMLET) (Hakansson et al. 2011). In another recent study, antibiotic-induced cell death in *E. coli* has been shown to exhibit physiological and biochemical hallmarks of eukaryotic apoptosis including DNA fragmentation and phosphatidylserine externalization, and *E. coli* RecA was shown to bind a peptide sequence that serves as substrate for eukaryotic caspases (Dwyer et al. 2012). Gamma-radiation-exposed *E. coli* cells suffer DNA strand breaks in a dose-dependent manner that leads to induction of SOS response (Kuzminov 1999). Upon encountering ssDNA, RecA forms a

BARC NEWSLETTER

nucleoprotein complex which induces autocatalytic cleavage of LexA, a repressor of SOS genes. This results in the induction of around 40 SOS genes mainly involved in DNA repair and translesion DNA synthesis at the cost of mutagenesis. If the damage is too severe to mount SOS response, then the cell is destined to die. The present study was undertaken to ascertain whether PCD was involved in radiation-induced cell death (RICD) in *E. coli* and if this event was linked to SOS response. The findings will help in understanding the fundamentals of these two important molecular events occurring in stressed bacterial population.

Materials and methods

Bacterial strains and growth conditions

Escherichia coli MG1655 and the single-gene deletion mutants of a related strain, *E. coli* K-12 strain BW25113 [*recA* (Keio strain no. JW 2669), *recB* (JW 2788), *ruvA* (JW 1850), *sula* (JW 0941), *umuC* (JW 1173) and *umuD* (JW 1172)], were used in the current study (Baba et al. 2006). All these strains were grown in Luria-Bertani (LB) medium on a rotary shaker (150 rpm) at 37 ± 2 °C.

Radiation exposure and viable plate count

An aliquot of log-phase-grown bacterial culture was diluted to cell density of $\sim 10^6$ cfu/ml using saline and irradiated (0.1 to 1 kGy) in a Gamma Chamber (Cobalt-60 source (BRIT), dose rate 5 Gy/min), and plated on LB agar plates to score the number of viable cells. For studying the effect of inhibitors of proteins of PCD pathway such as caspase-3, poly (ADP-ribose) polymerase (PARP) and endonucleases which are inhibited by Ac-DEVD-CMK (a chloromethylketone tetrapeptide derivative), 3-amino benzamide (ABA) and aurintricarboxylic acid (ATA), respectively, or antibiotics affecting transcription (rifampicin) and translation (chloramphenicol), the cells were pre-incubated with the compound for 30 min before subjecting to irradiation. In case of antibiotics, the cells were washed twice with sterile saline before irradiation.

Analysis of PCD specific markers

Caspase3 activity was analysed as per the manufacturer's guidelines using synthetic fluorogenic substrate Ac-DEVD-AMC (BD Pharmingen, USA) as described earlier (Gautam and Sharma 2002). Phosphatidyl externalization was analysed using AnnexinVFITC labeling and DNA damage by TUNEL (Terminal deoxynucleotidyl transferase dUTP nick end labeling) assay using flow cytometry as described earlier (Gautam and Sharma 2002).

Immunoblotting

Protein equivalent to 100 μ g/ml was loaded in each lane and subjected to SDS-PAGE followed by Western blotting as described earlier (Gautam and Sharma 2002). The level of caspase-3 was determined using polyclonal rabbit anti-active human caspase-3 antibody (BD Pharmingen, affinity purified, biotin conjugated) and that of LexA with anti-LexA antibody (Abcam), respectively. Bacterial alkaline phosphatase was used as a positive control (Abcam).

Betagalactosidase assay

It was performed to normalize the total protein content by the method described by Miller (1972) using *o*-nitrophenyl- β -d-galactopyranoside substrate and measuring the absorbance of the product at 420 nm.

Cell filamentation assay

An aliquot of cell suspension was smeared on a glass slide, air dried, heat fixed, stained with crystal violet and examined under a microscope.

Results & Discussion

Activation of bacterial caspase 3like protein (BCLP) during radiationinduced cell death (RICD)

Caspase-3 works at the execution stage to induce cell death by activating DNase (Earnshaw et al. 1999). When the *E. coli* cells suspended in saline (0.85 %) at an initial cell density of $\sim 10^6$ cfu/ml were exposed to radiation

BARC NEWSLETTER

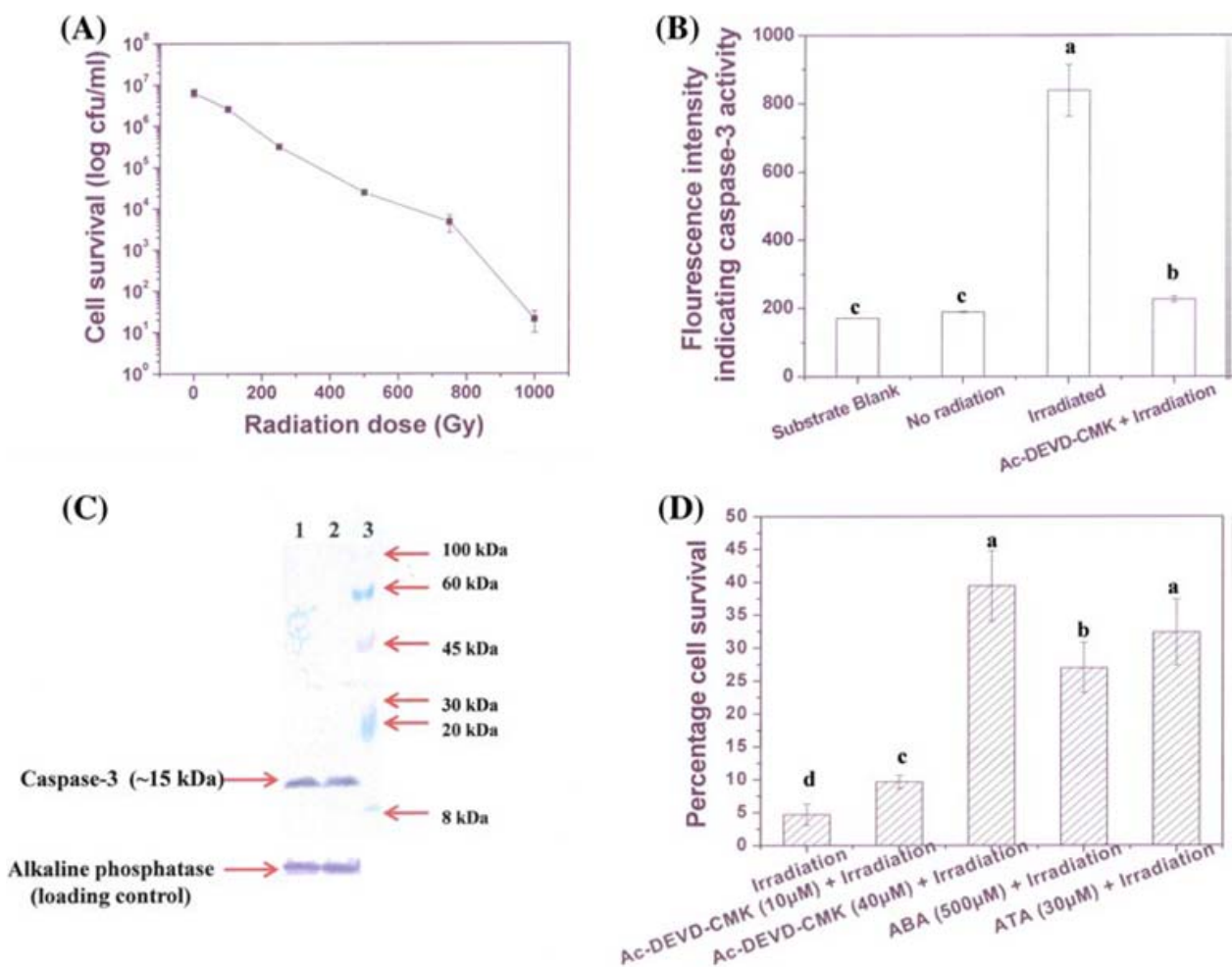


Fig. 1: Effect of gamma radiation on *E. coli* cells: A survival of *E. coli* cells exposed to different doses of gamma radiation; B level of bacterial-caspase-3-like protein (BCLP) activity in *E. coli* cells exposed to D10 dose (180 Gy) in absence or presence of caspase-3 inhibitor (40 μ M); C western hybridization using polyclonal rabbit anti-active human caspase-3 antibody [lane 1 non-irradiated (control) cells, lane 2 irradiated (180 Gy) cells, lane 3 colored protein molecular weight marker]. Alkaline phosphatase (loading control) was detected using anti-bacterial alkaline phosphatase antibody. D Rescue of cells from radiation-induced death by inhibitors of caspase-3, PARP (3-ABA) or endonuclease (aurintricarboxylic acid; ATA). Data is presented as mean \pm SD ($p < 0.05$); ($n = 9$). The mean values were compared using one-way ANOVA (analysis of variance) test for establishing the significance of observed variation among them ($p < 0.05$). The same letter on different bars indicates that the means are not significantly different at the specified p value ($p < 0.05$), whereas different letter on the bar indicates that the means are significantly different at $p < 0.05$.

in the dose range of 0.1–1 kGy, the D10 (decimal reduction dose) was found to be 180 Gy (Fig. 1A). Interestingly, caspase-3-like activity in *E. coli* cells was found to increase significantly (~fourfold) upon radiation exposure (Fig. 1B). However, immunoblotting using polyclonal antiactive caspase-3 antibody indicated no significant increase in BCLP level in radiation-exposed *E. coli* cells (Fig. 1C). Caspases are known to be synthesized as zymogens, which get activated by autocatalytic cleavage.

Inhibition of RICD by caspase3, PARP and endonuclease inhibitors

Authenticity of bacterial caspase-like protein (BCLP) was further confirmed by assaying its activity in cells pre-incubated with Ac-DEVD-CMK, water soluble, cell permeable and irreversible caspase-3 inhibitor. The presence of the inhibitor resulted in significant drop in caspase-3 activity in radiation-exposed *E. coli* cells and was found to be close to that in control (non-irradiated) cells (Fig. 1B). Interestingly, the cell survival increased

BARC NEWSLETTER

to 39 % when pre-treated with 40 μ M of caspase inhibitor for 30 min before radiation exposure of cells at one D10 dose (Fig. 1D). These findings imply that a significant part of the radiation-exposed bacterial population dies through the caspase-dependent mechanism. Further, preincubation with 3-aminobenzamide (3-ABA) (500 μ M), a poly (ADPribose) polymerase (PARP) inhibitor, also increased the *E. coli* cell survival by around fivefold from 5 to 27 % upon gamma radiation exposure at its one D10 dose (Fig. 1D). Also, pre-incubation with aurintricarboxylic acid (ATA), an endonuclease inhibitor (Chen et al. 2002), increased the cell survival to 32 % (around sixfold) in radiation-exposed cells, and the viability was close to that observed with caspase-3 inhibitor, Ac-DEVD-CMK (Fig. 1D).

Phosphatidylserine (PS) externalization in radiation treated cells

PS externalization in radiation (180 Gy)-treated cultures increased from 7 to 30 % (Fig. 2); however, it decreased to 17 % in cultures pre-incubated with caspase-3 inhibitor (Fig. 2). These findings endorse the assumption that PCD is one of the mechanisms leading to cell death in radiation-exposed bacterial culture.

Suppression of RICD in *E. coli* by transcription or translation inhibitors at sublethal doses

The effect of global inhibition of gene expression using sublethal concentrations of inhibitor of transcription or translation on PCD in radiation-exposed *E. coli* cells

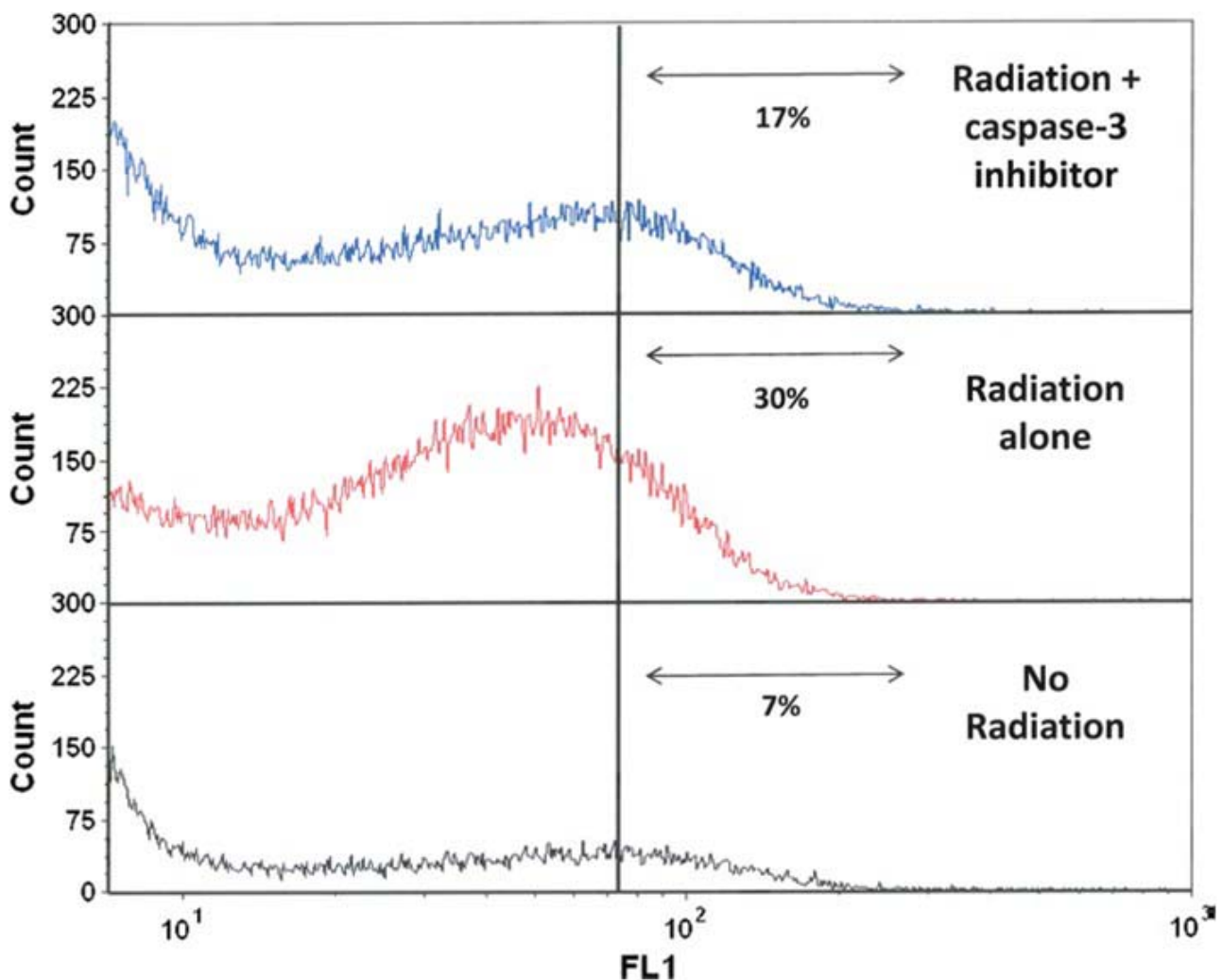


Fig. 2: Status of phosphatidylserine (PS) externalization in *E. coli* cells as determined by FACS analysis.

BARC NEWSLETTER

was investigated further. *E. coli* cells exposed to radiation at one D10 dose after pretreatment for 30 min with sublethal doses of inhibitor of transcription (rifampicin) or translation (chloramphenicol) showed significant increase in viability. Approximately threefold and fivefold increase in viability was observed when cells were irradiated after pretreatment with 2 and 6 $\mu\text{g/ml}$ rifampicin, respectively (Fig. 3A). Similarly, the cell survival was found to increase by sixfold and ninefold by pretreatment with 8 and 12 $\mu\text{g/ml}$ of chloramphenicol, respectively (Fig. 3B). Further higher concentrations of these antibiotics were found to be lethal to the cells. Interestingly, sublethal doses of rifampicin (6 $\mu\text{g/ml}$) or chloramphenicol (12 $\mu\text{g/ml}$)

were also found to inhibit caspase-3 enzyme activity by 50 and 30 %, respectively (Fig. 3C). These results indicated that RICD in *E. coli* was indeed genetically regulated and required de novo RNA and protein synthesis.

Effect of caspase-3 inhibitor on extent of radiation induced DNA damage

In TUNEL assay the proportion of dUTP-FITC-labeled cells after irradiating at 90 Gy increased from 12 to 36 % as compared to non-irradiated control cells (Fig. 4F). However, a 46 % decrease in DNA damage was observed in the cells irradiated in the presence of

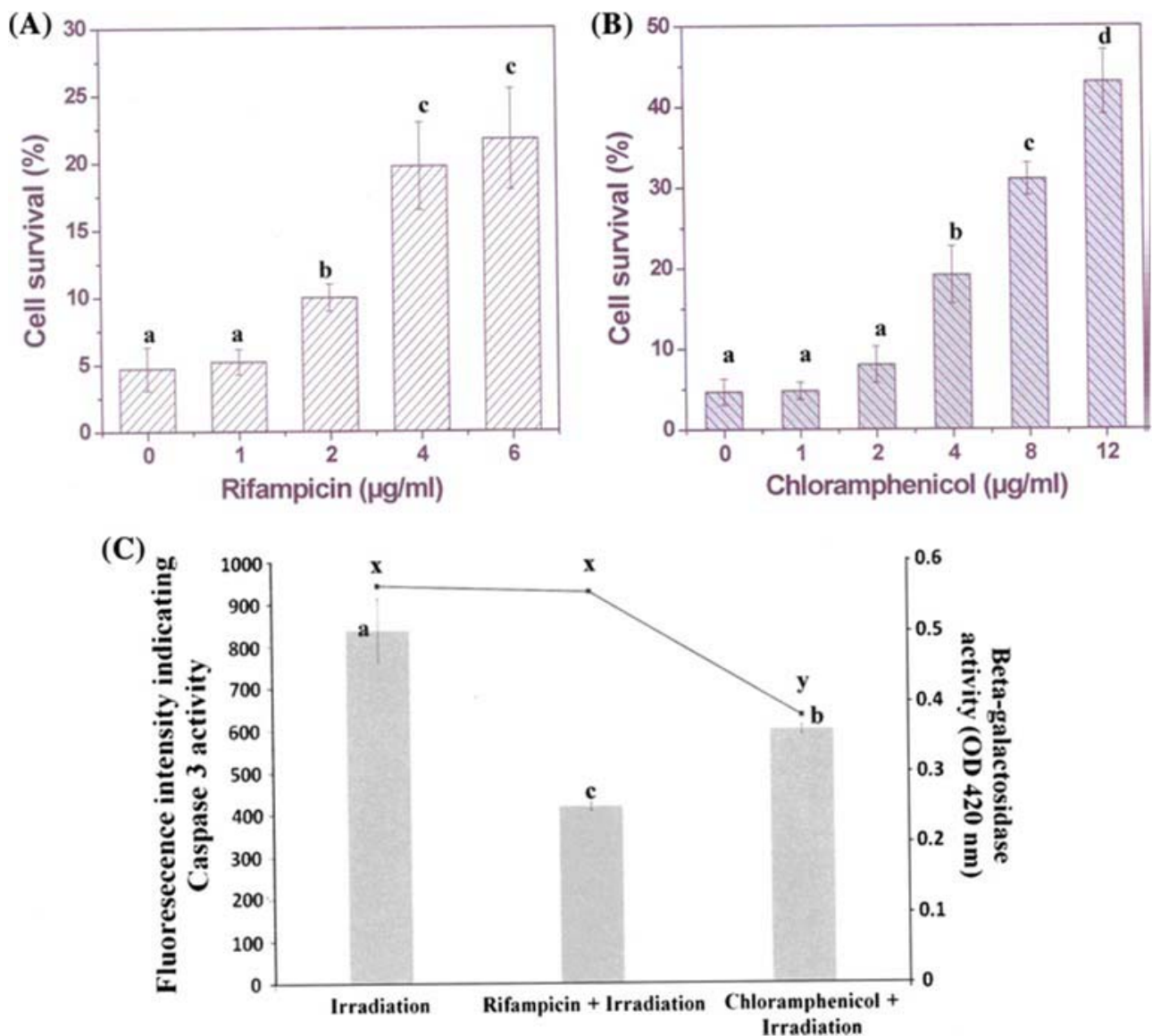


Fig. 3: Effect of transcription/ translation inhibitors on radiation-induced death in *E. coli* cell.

BARC NEWSLETTER

caspase-3 inhibitor as compared to those irradiated in its absence (Fig. 4F).

Inhibition of radiation-induced SOS response by caspase 3 inhibitor

Radiation is also known to induce SOS response, an errorprone DNA repair pathway in many bacteria

including *E. coli*. Radiation (90 Gy)-exposed *E. coli* cells were found to display SOS-specific phenotypic markers. These cells were found to undergo extensive cell filamentation due to induction of SOS regulon (Janion 2008) (Fig. 4A, B). Interestingly, the presence of caspase-3 or endonuclease inhibitor (aurintricarboxylic acid, ATA) significantly reduced this cell filamentation (Fig. 4C, D, respectively). The level of LexA, a constitutive

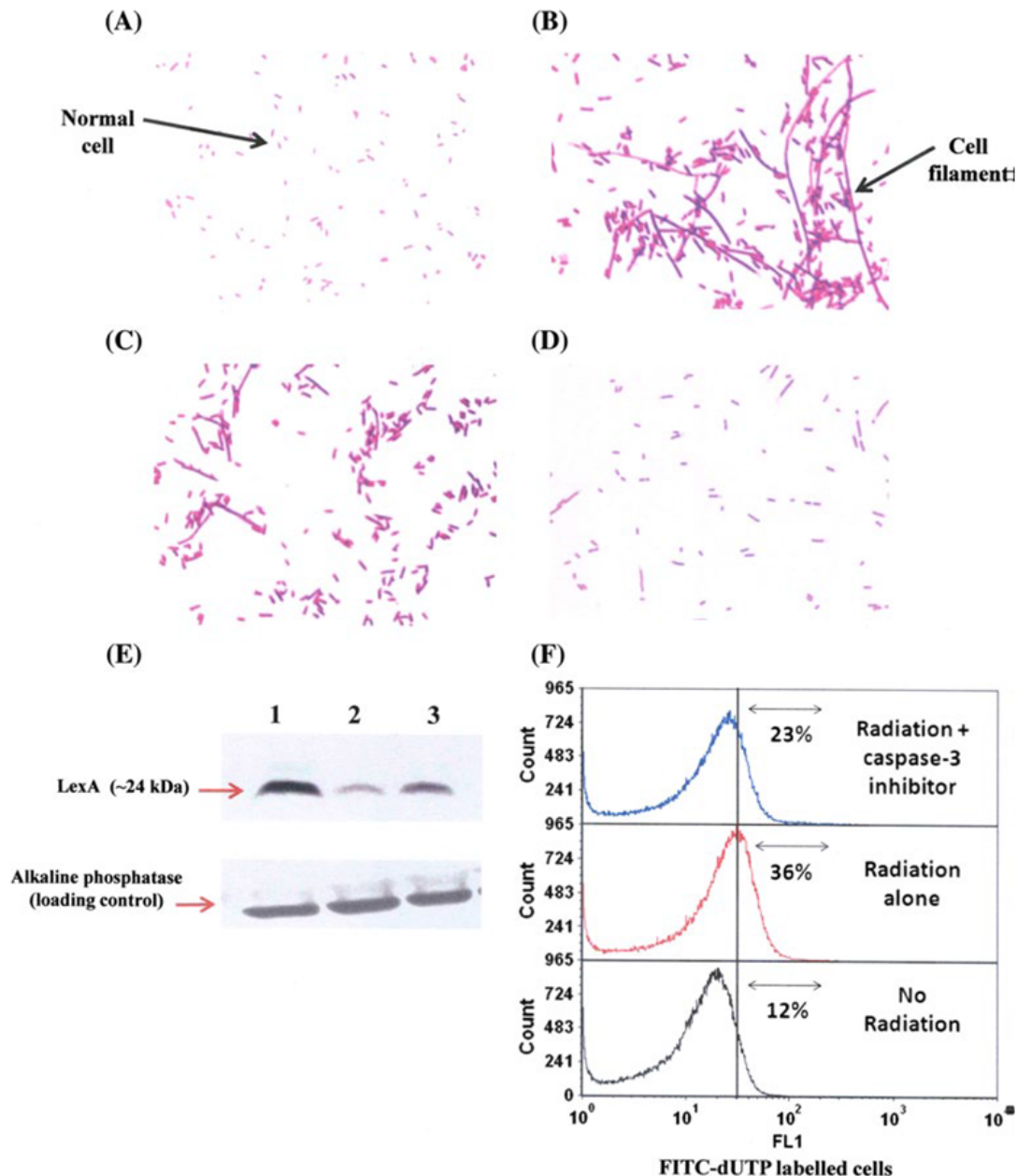


Fig. 4: Status of SOS induction in radiation-exposed cells: Cell filamentation in A non-irradiated cells; B cells irradiated at 90 Gy; C cells irradiated in presence of caspase-3 inhibitor (40 μ M); D cells irradiated in the presence of endonuclease inhibitor (aurintricarboxylic acid, 30 μ M); E immunoblot using anti-LexA antibody indicating inhibition of LexA degradation in radiationexposed (90 Gy) culture in the presence of caspase-3 inhibitor (40 μ M) [lane 1 non irradiated cells; lane 2 irradiated cells (90 Gy); lane 3 cells irradiated in the presence of caspase-3 inhibitor (40 μ M)]. Alkaline phosphatase served as loading control and was detected using anti-bacterial alkaline phosphatase antibody. F TUNEL assay indicating DNA damage

BARC NEWSLETTER

repressor of SOS regulon, was found to decrease transiently in radiation-exposed culture (Fig. 4E, lane 2), but its level was found to be significantly restored in the presence of caspase-3 inhibitor. The LexA band intensity compared to control (non irradiated culture) was 9 and 41 %, respectively, in the absence and presence of the caspase-3 inhibitor (Fig. 4E, lanes 2 and 3, respectively). These findings strongly established the existence of interplay between caspase-dependent cell death and SOS pathway in bacteria. Besides caspase-3 inhibitor, an endonuclease inhibitor, ATA, was also found to decrease both the filamentation frequency as well as the length of filaments in irradiated (90 Gy) *E. coli* culture (Fig. 4D). Further, to investigate the involvement of different SOS regulated proteins, single-gene knockouts of *E. coli* *recA*, *recB*, *ruvA*, *umuC*, *umuD* and *sulA* were used in the study. RecA, RecB and RuvA are involved in homologous recombination, whereas UmuC and UmuD are subunits of DNA Polymerase V (UmuD22C). This polymerase is responsible for translesion DNA synthesis (Kuzminov 1999). SulA is involved in the inhibition of cell division. The suppression of RICD by caspase-3 inhibitor was found to be *umuC*, *umuD*, *recB* and *ruvA* dependent but independent of *sulA* gene product. In conclusion, there was involvement of SOS and PCD during radiation-induced cell death in *E. coli*.

References

1. Baba T, Ara T, Hasegawa M, Takai Y, Okumura Y, Baba M, Datsenko KA, Tomita M, Wanner BL, Mori H (2006) Construction of *Escherichia coli* K-12 in-frame, single-gene knockout mutants: the Keio collection. *Mol Syst Biol* 2:1–11.
2. Dwyer DJ, Camacho DM, Kohanski MA, Callura JM, Collins JJ (2012) Antibiotic-induced bacterial cell death exhibits physiological and biochemical hallmarks of apoptosis. *Mol Cell* 46:561–572.
3. Earnshaw WC, Martins LM, Kaufmann SH (1999) Mammalian caspases: structure, activation, substrates, and functions during apoptosis. *Annu Rev Biochem* 68:383–424.
4. Elmore S (2007) Apoptosis: a review of programmed cell death. *Toxicol Pathol* 35:495–516.
5. Gautam S, Sharma A (2002a) Rapid cell death in *Xanthomonas campestris* pv. *glycines*. *J Gen Appl Microbiol* 48:67–76.
6. Gautam S, Sharma A (2002b) Involvement of caspase-3-like protein in rapid cell death of *Xanthomonas*. *Mol Microbiol* 44:393–401.
7. Gautam S, Sharma A (2005) Programmed cell death: an overview. In: Chakraborty C (ed) *Advances in biochemistry and biotechnology*. Daya Publishing House, India, pp 122–157.
8. Gautam S, Sharma A, Kobayashi I (2005) Programmed cell death in microorganisms. In: Yamada M (ed) *Survival and death in bacteria*. Research Sign Post, India, pp 1–39.
9. Hakansson AP, Roche-Hakansson H, Mossberg AK, Svanborg C (2011) Apoptosis-like death in bacteria induced by HAMLET, a human milk lipid-protein complex. *PLoS ONE* 6(3):e17717.
10. Kuzminov A (1999) Recombinational repair of DNA damage in *Escherichia coli* and bacteriophage ϕ . *Microbiol Mol Biol Rev* 63:751–813.
11. Lewis K (2000) Programmed death in bacteria. *Microbiol Mol Biol Rev* 64:503–514.
12. Miller JH (1972) *Experiments in molecular genetics*. Cold Spring Harbor Laboratory Press, Cold Spring Harbor.
13. Ning SB, Guo HL, Wang L, Song YC (2002) Salt stress induces programmed cell death in prokaryotic organism *Anabaena*. *J Appl Microbiol* 93:15–28.
14. Raju KK, Gautam S, Sharma A (2006) Molecules involved in the modulation of rapid cell death in *Xanthomonas*. *J Bacteriol* 188:5408–5416.
15. Raju KK, Misra HS, Sharma A (2007) *Xanthomonas* caspase displays an inherent PARP-like activity. *FEMS Microbiol Lett* 272:259–268.
16. Rice KC, Bayles KW (2003) Death's toolbox: examining the molecular components of bacterial programmed cell death. *Mol Microbiol* 50:729–738.
17. Wadhawan S, Gautam S, Sharma A (2010) Metabolic stress-induced programmed cell death in *Xanthomonas*. *FEMS Microbiol Lett* 312:176–183.

SILVER NANOPARTICLES BASED OPTICAL BIOSENSORS FOR ESTIMATION OF URIC ACID

Nilanjal Misra, Virendra Kumar, Lalit Varshney
Radiation Technology Development Division

This Paper received the Best Poster Presentation Award at the Interdisciplinary Symposium on Materials Chemistry (ISMC-2012), held at Mumbai, from 11th-15th December, 2012

Abstract

A simple colorimetric method for estimation of uric acid has been designed based on the localized surface plasmon resonance (LSPR) band of polyvinyl pyrrolidone (PVP)-capped-silver nanoparticles. PVP-Ag NPs were synthesized via gamma radiolytic route. These radiation synthesized spherical Ag nanoparticles, in turn, were investigated for their potential application as uric acid biosensor. The detection technique is based on the enzymatic oxidation of uric acid in presence of enzyme uricase to generate H₂O₂. The in situ generated H₂O₂ in turn causes partial oxidation of the silver nanoparticles, which is manifested by the decrease in LSPR band intensity of Ag NPs. A linear relationship between this decrease in LSPR band intensity and increase in uric acid concentration was established.

Introduction

Uric acid represents the major catabolite of purine breakdown in humans. The normal concentration of uric acid in blood samples is reported to be in the range 150–420 μM. Estimation of uric acid in blood can be used as a diagnostic tool for monitoring a large number of diseases. In view of this, numerous techniques have been developed over the years for detection and estimation of uric acid levels [1]. In recent years, the use of metal nanoparticles as analytical and bioanalytical sensors has been receiving significant attention because of their unusual optical, electronic, and chemical properties. Gamma radiolytic method has emerged as an efficient technique for fast and one step synthesis of uniformly dispersed metal nanoparticles. This method is unique because it is a room temperature process and the reaction system is devoid of any external chemical reducing agents [2]

The LSPR wavelength of noble metal nanoparticles is extremely sensitive to the local environment around the nanoparticles, which facilitates their use as sensing devices [3]. To the best of our knowledge, we report herein for the first time, gamma radiolytically synthesized PVP-Ag-NPs for the detection of uric acid

in biological samples. Spherical silver nanoparticles were synthesized via gamma irradiation of precursor silver ions in presence of PVP. The PVP-Ag NPs system was successfully employed for estimation of uric acid concentration in human serum samples.

Experimental

Preparation of PVP-Ag NPs

An aqueous solution containing 4×10⁻⁴ mol dm⁻³ Ag⁺, 1.0% PVP (w/v) and 0.2 mol dm⁻³ 2-propanol was purged with N₂ and subjected to gamma irradiation to a target absorbed dose at a dose rate of 2.47 kGy/hr. In this study, PVP with molecular weight of 40kD was used as the capping agent. The formation of Ag nanoparticles was indicated by development of bright yellow color and the saturation gamma radiation dose determined by spectroscopic monitoring of the LSPR band of Ag NPs.

Estimation of uric acid

For estimation of uric acid, 0.2mL of 0.137mg/mL of Uricase stock solution and different volumes of a known concentration of uric acid solution were taken in 25mL

conical flasks and diluted to 6.25mL. The resultant mixtures were allowed to stand for 20 minutes. Subsequently, 3.75 mL of 4×10^{-4} mol.dm⁻³ Ag nanoparticles solution (in terms of Ag^I, assuming complete reduction of the precursor ion) were added to each of the mixtures. The reaction mixtures were allowed to stand for another 60 minutes and the UV-visible spectra were recorded in the wavelength range 250-650 nm. A calibration curve was established by plotting the absorbance at λ_{max} as a function of uric acid concentration, from which the concentrations of uric acid in the unknown samples were estimated.

Results and discussions

Formation of Ag nanoparticles

When an aqueous solution containing Ag^I, PVP (Mol. Wt.=40kD) and 2-propyl alcohol is purged with N₂ and subjected to gamma radiation, radiolysis of water takes place. As a result, reactive transient species, namely, e_{aq}⁻, H[•], ·OH, etc., are generated. 2-propyl alcohol present in the reaction medium reacts with H[•] and OH[•] to give 2-propyl radical, a mild reducing agent. At the same time the oxidizing radical ·OH gets eliminated in the process. The reducing species present in the system viz. e_{aq}⁻ and 2-propyl radical reduce the metal ion to metal in zero valent state, i.e., Ag^I to Ag⁰. After formation of Ag⁰, coalescence step leads to formation of Ag nanoparticles in presence of PVP as a capping and stabilizing agent. PVP contains functional groups like >C=O and >N- groups, which facilitates

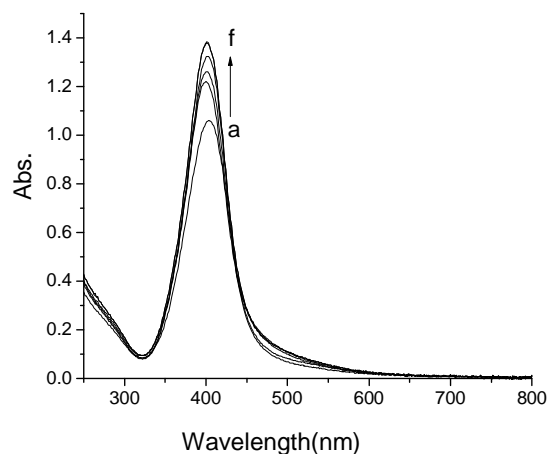


Fig.1: UV-Visible spectra of aqueous PVP-Ag-NPs solution obtained at different radiation doses: (a) 1.0kGy, (b) 1.3kGy, (c) 1.6kGy, (d) 2.0kGy, (e) 2.3kGy, (f) 2.5kGy

anchorage of metal nanoparticles onto their surface. The UV-visible spectra of Ag NPs show a characteristic LSPR band at 427nm. [Fig.1]

The PVP-Ag NPs were characterized using TEM, AFM and Zeta potential analyser. TEM analysis revealed spherical nanoparticles with an average particle size of 5.1 ± 1.6 nm. AFM images also supported the formation of uniformly dispersed spherical nanoparticles. Zeta potential measurements were carried out to determine the stability of the Ag colloids formed. For the PVP-Ag NPs control sample, zeta potential was found to be -29.6mV at pH=7.4, which indicated formation of stable PVP capped Ag colloids.

PVP-Ag NPs as LSPR-based uric acid sensor

Uric acid undergoes enzymatic oxidation in presence of enzyme Uricase under optimum assay conditions of 37°C and pH 7.4. Hydrogen peroxide is generated as one of the reaction products, which, in turn, causes oxidation of silver nanoparticles resulting in a decrease in intensity of the SPR band. [Fig.2]

For the evaluation of PVP-Ag NPs as a uric acid biosensor, different concentrations of uric acid were taken and a known concentration of Uricase stock solution was added to each of them. After incubation at 37°C for 20 minutes, a known concentration of Ag nanoparticle solution was added to each of the flasks and the mixtures allowed to stand at room temperature for another 60 minutes. The UV-visible spectra were recorded thereafter in the wavelength range

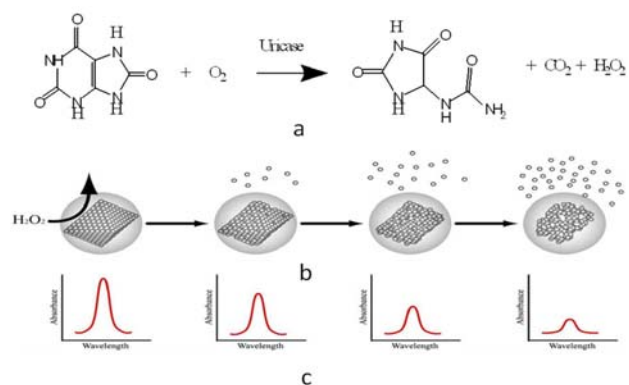


Fig.2: Schematic of detection principle (a) Oxidation of uric acid in presence of enzyme uricase (b) Partial oxidation of Ag NPs (c) Decrease in LSPR band intensity of Ag NPs

BARC NEWSLETTER

250-650nm. It was observed that intensity of the LSPR band decreases linearly with increase in uric acid concentration. The decrease was accompanied by a slight red shift in the absorption maxima of the band, which is attributed to the partial oxidation of nano-Ag, followed by aggregation. [Fig. 3] The response was found to be linear in the uric acid concentration range of 0-50 μM .

The resultant aggregation of the particles is evident from the TEM analysis. While the control (PVP-Ag-NPs) exhibited an average particle size of $5.1 \pm 1.6\text{nm}$, those in presence of uric acid-uricase system were found to have bigger particle size of $15.4 \pm 4.6\text{nm}$. [Fig. 4]

Uric acid estimation in human serum samples

The method described in section 3.2 was effectively applied for determination of uric acid concentration in serum samples. To minimize interference from proteins, the serum samples were first deproteinized using standard protocol before being subjected to the estimation technique as mentioned in section 3.2. The uric acid concentrations were estimated using the calibration plot (Fig. 3 inset).

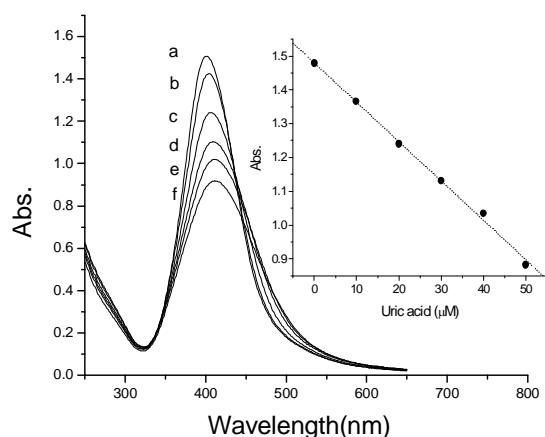


Fig. 3: Absorption spectra of PVP-Ag-NPs solution in presence of different concentrations of uric acid, after 60 min: (a) 0 μM , (b) 10 μM , (c) 20 μM , (d) 30 μM , (e) 40 μM , (f) 50 μM . [Inset: Linear plot of absorbance of PVP-Ag-NPs vs uric acid concentration ($R^2=0.9964$), uric acid concentration range= 0 to 5×10^{-5} mol.dm $^{-3}$.]

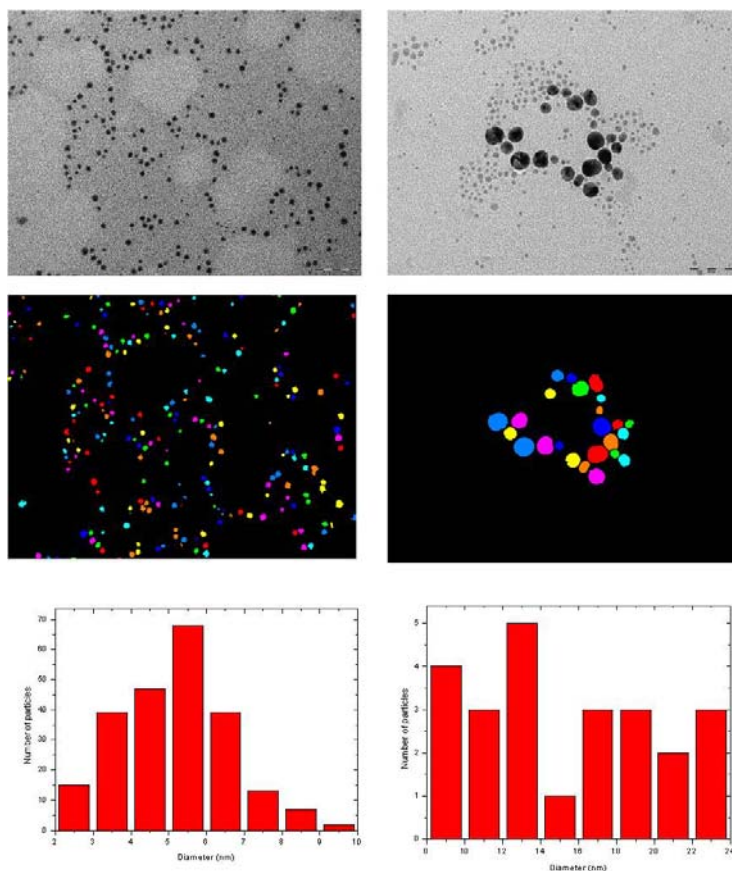


Fig. 4: TEM analysis of Ag nanoparticles prepared using PVP of molecular weight 40kD (a) TEM image before addition of uric acid (b) Visilog 6.3 image processing result of TEM image-a, (c) particle size distribution histogram of TEM image-a (d) TEM image after addition of uric acid, (e) Visilog 6.3 image processing result of TEM image-d, (f) particle size distribution histogram of TEM image-d.

Conclusion

A colorimetric method based on oxidation of Ag NPs by in situ generated hydrogen peroxide has been developed for estimation of uric acid. Linear range of detection of uric acid by this technique was found to be 0 to 5×10^{-5} mol.dm $^{-3}$ with minimum detection limit of 5×10^{-6} mol.dm $^{-3}$. Further, this method was also effectively employed to determine concentration of uric acid in actual biological fluids such as human serum samples.

References

1. J. Galbán, Y. Andreu, M. J. Almenara, S. de Marcos, J. R. Castillo, *Talanta*. 54 (2001) 847.
2. N. Misra, J. Biswal, A. Gupta, J.K. Sainis, S. Sabharwal, *Radiat. Phys. Chem.*, 81 (2012) 195.
3. P. Vasileva, B. Donkova, I. Karadjova, C. Dushkin, *Colloid. Surface A*. 382 (2011) 203.

THERMAL ANALYSIS OF POLYETHERSULFONE BASED COMPOSITE BEADS ENCAPSULATED WITH DI-2-ETHYL HEXYL PHOSPHORIC ACID

Kartikey Kumar Yadav, Dhruva Kumar Singh and Harvinderpal Singh

Rare Earths Development Section, Materials Group

and

S. Francis and L. Varshney

Radiation Technology Development Division

This Paper received the Best Poster Award (Third Prize) at the 18th DAE-BRNS International Symposium on Thermal Analysis, held at Mumbai from 31st January to 2nd February, 2012

Abstract

A novel polymeric composite bead encapsulating organophosphorus extractant D2EHPA has been developed and tested for rare earths separation. Analytical techniques such as TGA, SEM and IR were employed to characterize the physical and thermal behavior of the bead. Weight loss profile as a function of temperature revealed the extractant encapsulation capacity of the beads. Microscopic examination of the composite bead confirmed central coconut type cavity surrounded by porous polymer layer of the beads through which exchange of metal ions occurs. The composite beads have the potential for rare earths separation from aqueous solutions.

Introduction

There is a considerable interest in evaluating alternative methods for separation of metal ions from various types of aqueous streams. Solid-liquid extraction method, employing polymer based composite in the form of beads, encapsulating organic solvent, has emerged as an effective separation tool over conventional liquid-liquid extraction and ion exchange techniques [1]. The advantages of the use of polymeric beads over other processes extends due to large surface area, minimal use of organic solvents (extractant, diluent), reusability, stability and absence of phase separation phenomenon. A liquid cation exchange type of extractant, D2EHPA (di 2 ethyl hexyl phosphoric acid) has been widely used for the separation of rare earths by liquid-liquid extraction technique [2]. In the present study, we report preparation of polyethersulfone based composite beads (PBC) encapsulating D2EHPA under various experimental condition and their characterization by TGA, SEM and optical microscope. These beads were

also evaluated for their usability in the separation of rare earths from aqueous solution.

Experimental

Commercially available polyethersulfone (PES, Molecular weight ~30000), N-methyl pyrrolidone (NMP) and poly(vinyl alcohol) PVA (MW 31,000–50,000) were used for the preparation of beads. D2EHPA was procured from Albright and Wilson and used as received. Rare earths (such as Y(III), Sm(III) and La(III)) solutions were prepared by dissolving their oxides (>99% purity) in hydrochloric acid. Polymeric composite beads (PES/PVA/D2EHPA/NMP/water system) were prepared as per the procedure described elsewhere [3]. Morphology and internal structure of the composite beads were examined by optical microscope and scanning electron microscope (SEM). Thermo gravimetric analysis (TGA, Mettler) of all types of polymeric beads was carried out to evaluate the percentage of extractant, polymer, water and NMP content in the composite bead. ICP-

BARC NEWSLETTER

AES (JY-Ultima -II) was used to estimate rare earths in aqueous samples.

Results and Discussion

Microstructural examination of beads

Three types PBC viz. (a) PES bead without extractant (b) PES bead encapsulating D2EHPA and (c) PVA doped PES bead encapsulating D2EHPA were examined by SEM and optical microscope. Typical SEM micrographs of the PVA doped PES beads encapsulating D2EHPA are shown in Fig. 1(a-e). Figure 1(a) shows the overall image of solvent encapsulated sphere and Fig. 1 (b,c) depict the details of its surface structure at different levels of magnification. These images suggest that beads are almost spherical with uniformly distributed pores (i.d. = 1 μ m). The cross-sectional image of doped (Fig. 1d) and normal beads (Fig. 1f) lead to the distinguishing observations as: PBC without additives had relatively thin outer polymeric layer and shell within shell type of internal structure due to uneven distribution of polymer in comparison with doped beads. PBC having PVA as an additive had coconut type of internal structure with a central void (volume~10 mm³) filled with organic extractant (Fig 1d). The internal structure of these beads was found to be more porous (high surface area) in comparison to beads without additive and the porosity decreases from center to circumference of the spherical bead (Fig 1e, contains CNT as coadditive). NMP and PVA both are soluble in water. During phase inversion,

not only NMP diffuses out through PES, water also ingress into PES due to hydrophilicity of PVA. This results in more porous, thicker walled bead structure.

Thermal analysis of polymeric composite beads

PES/PVA/D2EHPA beads with different extractant to polymer solution ratio were prepared. Thermo gravimetric analysis of these polymeric beads was carried out to evaluate the percentage of extractant, PES, water and NMP content in the composite material. TGA (Fig. 2) representing change in the weight of sample (beads) with increase in temperature showed mainly three segments of 80-160°C, 230-260°C and 460-560°C. First segment represents evaporation of water and NMP in the range of 80 to 160°C, second zone of weight loss depicts the disintegration of D2EHPA and 460 to 560°C part of the profile shows the weight loss due to dissociation of PES and disintegrated parts of D2EHPA. Evaluation of thermograms revealed that increase in extractant to polymer ratio from 1:15 to 1:4 lead to increase in D2EHPA content from 9% to 25.5% in the beads, whereas polymer content in the beads was in the range of 10 to 16%. These results were in good agreement with the encapsulated amount of D2EHPA (7-25%) taken during preparation of beads. Comparison of TGA profiles of D2EHPA encapsulating beads with the profiles of D2EHPA and PES showed no shift in the mass loss vs. temperature profile of individual compound eliminating any possibility of chemical interaction

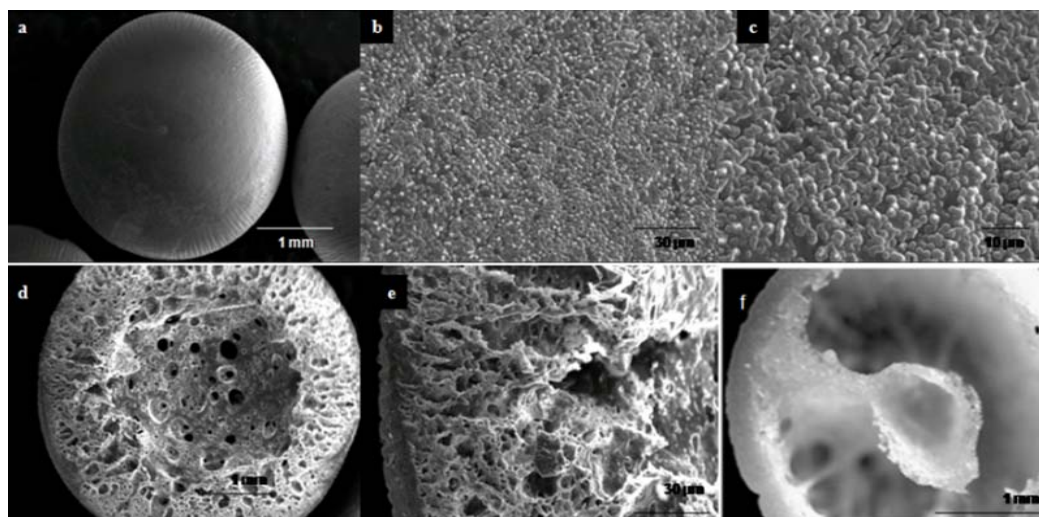


Fig. 1: SEM images of surface (a,b,c) and cross-section(d,e) of PES/PVA/D2EHPA, optical image of cross section (f) of PES/D2EHPA bead

among the main constituents of the extractant encapsulating beads. Further the TGA of PES/PVA/D2EHPA beads were performed to evaluate the extractant loading (L) calculated in grams of extractant per gram of PES. The value of L for PES based material was found to be 1.4 ± 0.2 gram of D2EHPA per gram of polymer.

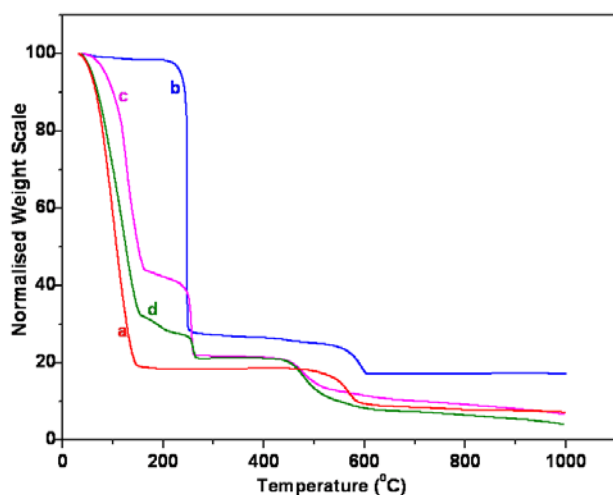


Fig.2: TGA of (a) Blank polymer bead (b) D2EHPA (3M) (c) PES/D2EHPA bead (polymer: extractant =4:1) (d) PES/D2EHPA bead (polymer: extractant = 15:1)

Application of the bead in rare earths separation

The feasibility of using PES/PVA/D2EHPA based polymeric composite beads for rare earths separation were tested by performing the extraction experiment with mixed rare earths solution containing 450 mg/L

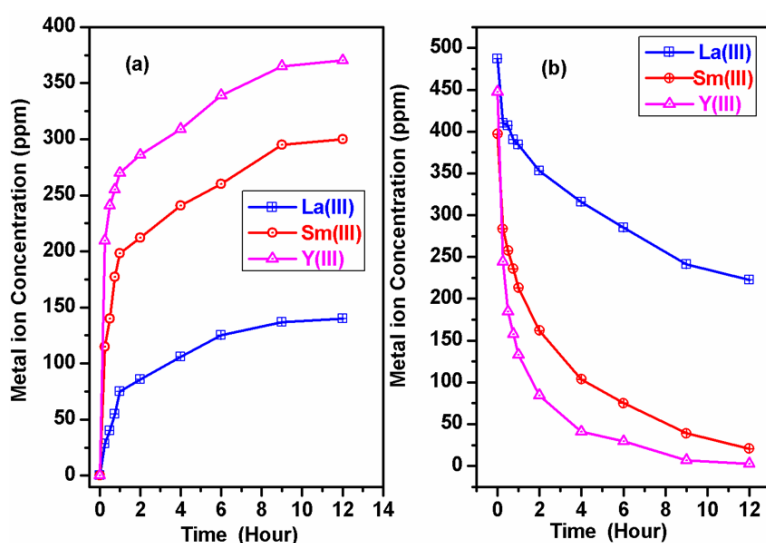


Fig. 3 (a) Extraction of mixed rare earths, (b) Stripping of mixed rare earths

of La(III), Sm(III), Y(III) each at 0.5N HCl. The extraction profiles of these rare earths are shown in Fig. 3(a), which clearly demonstrates the possible use of these beads for separation purposes. The order of extraction of rare earths was $La(III) < Sm(III) < Y(III)$; showing appreciable separation factor between them. Equilibration time of 6 hours was found to be sufficient for $>80\%$ extraction of rare earths. Later these beads were subjected for stripping of rare earths with 5NHCl(Fig.3b). It is evident that with 6 hours of contact time $>90\%$ rare earths were brought back to the aqueous phase. This study demonstrated that these beads can be used for separation of rare earths from aqueous solution.

Conclusions

TGA and microscopic examination of PES/PVA/D2EHPA PBC has been performed. D2EHPA encapsulation in PBC has been estimated using TGA. Thermal analysis results indicated no interaction between polymer and extractant and thus preserving extractant properties. Feasibility of employing PBC for the separation of rare earths from hydrochloric medium has been demonstrated.

Acknowledgements

The authors are grateful to Dr. M. Anitha of REDS for analysis of rare earths sample by ICP-AES and Mr. Kinshuk Dasgupta of REDS for his help in characterization of beads with SEM.

References

1. A. Warshawsky, *Talanta* 21 (1974) 962-965.
2. D.K.Singh, H. Singh, J.N. Mathur, *Hydrometallurgy* 81 (2006) 174-181.
3. X.C. Gong, G.S. Luo, W.W. Yang, F.Y. Wu, *Sep. Purif. Technol.* 48 (2006) 235-243.

STUDIES ON CNT DOPED D2EHPA IMPREGNATED POLYMERIC BEADS FOR YTTRIUM EXTRACTION

**Kartikey Kumar Yadav, Kinshuk Dasgupta, Dhruva Kumar Singh,
Mallavarapu Anitha and Harvinderpal Singh**

Rare Earths Development Section, Materials Group

and

Lalit Varshney

Radiation Technology Development Division, RC&I Group

This Paper received the Best Poster Award (Third Prize) at the Interdisciplinary Symposium on Materials Chemistry (ISMC-2012), held at Mumbai, from 11th-15th December, 2012

Abstract

Novel polyethersulfone based composite beads encapsulating di-(2-ethylhexyl)-phosphoric acid (D2EHPA) in combination with different additives, such as, PEG, PVA, LiCl and multiwalled-carbon nanotube (MWCNT) have been prepared by non-solvent phase inversion method. These beads were characterized by scanning electron microscopy, thermogravimetry and infra-red spectroscopy. Effect of additives on bead structure, encapsulation capacity, extractability and stability has been examined to compare their usability for extraction of yttrium from acidic medium. Microstructural investigation confirmed the role of additives in modifying the pore structures in beads, responsible for varied degree of yttrium extraction. PES/D2EHPA/MWCNT/PVA beads were found to be superior for Y extraction.

Introduction

Polymeric matrix based composite beads encapsulating organic extractants have recently been investigated for the extraction of metal ions from aqueous solution due to large surface area, minimal use of organic solvents (extractant, diluent), reusability, stability and absence of phase separation phenomenon [1]. Polymeric composites encapsulating organophosphorus type of extractants have been studied for metal ion extraction from aqueous solution [2]. There is not much information available for the extraction and separation of rare earths using polymeric beads. Rare earths are considered as important elements due to their importance in high tech materials such as superconductors, lasers and magnetic materials. Extraction of Y(III) by polymeric beads has been reported recently[3]. With the objective of extraction of rare earths from aqueous phase, different types of novel composite beads having PES as the base matrix

encapsulating D2EHPA with various additives like polyethylene glycol (PEG), polyvinyl alcohol (PVA), lithium chloride (LiCl) and multiwall carbon nanotubes (MWCNT) have been prepared and evaluated for yttrium extraction from chloride medium. Different analytical tools including SEM, TG/DTA and FTIR have been utilized to acquire information related to morphology, pore size distribution and encapsulation capacity. The analysis of the beads by these techniques provided the basis for the selection of multiwall carbon nanotubes containing PES/PVA/D2EHPA beads for extraction of yttrium.

Materials and methods

PES was obtained from local vendor and used without any further purification. Chemicals like N-methylpyrrolidone (NMP), PVA, PEG and LiCl were purchased from Merck India. Organic extractant D2EHPA (>95% diester), Albright & Wilson, USA was

BARC NEWSLETTER

used as received. MWCNT was prepared by chemical vapour deposition method from acetylene using ferrocene as a catalyst in our laboratory [4]. Different types of beads namely, PES/PVA /D2EHPA, PES/PEG / D2EHPA, PES/LiCl /D2EHPA, PES/PVA (as blank), PES/PVA/MWCNT/D2EHPA were prepared by non-solvent induced phase inversion method under optimized preparatory conditions [5]. Polymeric composite beads were characterized by SEM and FT-IR. ICP-AES (JY Ultima 2) was used to determine the yttrium concentration in aqueous solution. Y(III) extraction data was interpreted by evaluating weight distribution ratio (D_w), using following equation [6]

$$D_w = [(C_f - C_r)/C_r] \times (V/w) \quad (1)$$

Where C_f (mg/L) and C_r (mg/L) are the aqueous phase Y(III) ion concentrations before and after equilibration, respectively; w (g) is weight of dry polymer and V (mL) is the volume of aqueous phase.

Results and Discussion

Cross sectional SEM images of all types of composite beads are illustrated in Fig 1(a-f). Fig. 1a shows a blank bead based on PES matrix only. When D2EHPA is encapsulated, the bead becomes more porous with uneven distribution of polymer (Fig. 1 b). Additives were added in order to modify the structure. PVA doped bead (Fig. 1 c) has relatively thinner outer membrane layer whereas, PEG and LiCl doped beads (Fig. 1d and 1 e)

have thick outer polymeric shell with varying morphological structures. Polymeric bead containing PVA and CNT both as additives (Fig. 1 f) has more porosity and uniform distribution of pores and polymer matrix in comparison to PVA doped D2EHPA bead (Fig. 1 c). From the images it is evident that the additives not only act as the pore forming reagents, but also change the configuration of PES molecules and affect the dispersive state of D2EHPA in the polymeric system. The FTIR spectra of the liquid phase D2EHPA, blank PES/PVA bead and D2EHPA impregnated PES/PVA/CNT beads are depicted in Fig. 2(a, b & c). The D2EHPA spectrum in Fig.2(a) shows a doublet at 1460 and 1380 cm^{-1} due to the C-H deformation vibrations and peaks at the interval 2800–3000 cm^{-1} corresponding to the radical 2-ethylhexyl. In Fig. 2 b, three peaks between 1600 cm^{-1} to 1400 cm^{-1} were attributed to representative aromatic skeletal vibration of PES. In Fig. 2(c), the peaks at 1250-1210 cm^{-1} , which corresponds to P=O group and low intense band around 1680 cm^{-1} , along with characteristic peaks of PES demonstrated that D2EHPA exist in the bead independently within the polymer matrix without any chemical interaction with PES.

The composite beads were evaluated and compared for their extractability towards yttrium from chloride medium. Metal ion extraction by these polymeric matrix based composite membrane beads occurs via formation of metal ion complex and subsequent diffusion of the complex species through the pores inside the impregnated beads [7]. The values of D_w obtained with

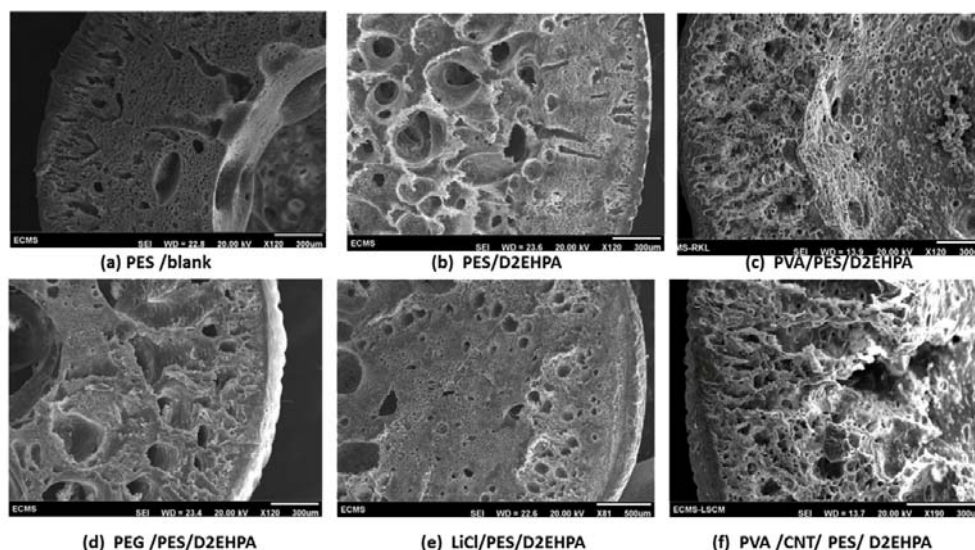


Fig. 1: Cross-sectional images of PES composite beads with different additives by SEM

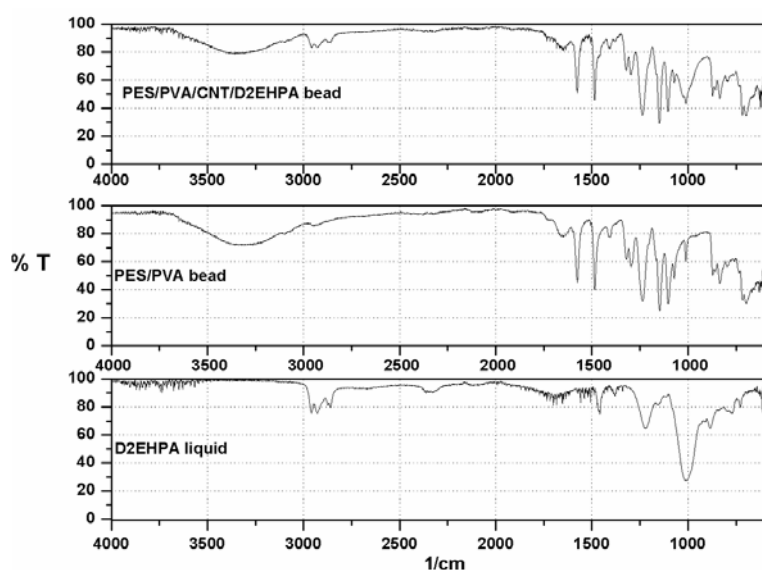


Fig.2: IR spectra of (a) D2EHPA liquid, (b) blank PES/PVA beads and (c) synthesized PES/PVA/CNT/D2EHPA beads.

different types of beads are shown in Fig. 3. The extraction of yttrium with additives follows the order: PES/PVA/MWCNT /D2EHPA > PES/PVA/D2EHPA > PES/D2EHPA > PES/LiCl/D2EHPA > PES/PEG/D2EHPA. PES/D2EHPA beads doped with PVA or PVA+ CNT resulted in an enhanced extraction of yttrium. The D_w value of Y(III) increased significantly from 14 (PES/D2EHPA) to 72 (PES/D2EHPA/PVA). The increase in D_w value in the case PVA doped composite beads can be attributed to the increased porosity and modified hydrophilicity causing better contact between aqueous and organic phases thereby facilitating the faster ion exchange mechanism [8]. The addition of MWCNT to PES/PVA/

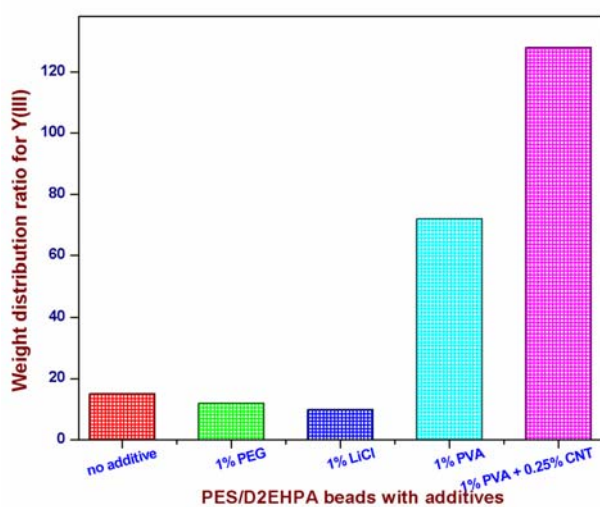


Fig.3: Effect of different additives in polymeric composite beads on weight distribution ratio for Y(III) extraction by PES beads.

D2EHPA beads significantly increased the D_w value from 72 to 128. This may presumably be due to functionalization of CNT by attaching additional D2EHPA molecules on its surface, which in turn gets distributed on the surface near peripherals of the beads resulting in ion exchange as well as adsorption phenomenon taking place simultaneously. MWCNT/PVA doped composite beads were evaluated for their reusability by repeated extraction and stripping operation and even after 10 cycles there was no sign of physical degradation or decrease in extraction capacity of the beads.

Conclusions

D2EHPA impregnated PES composite beads with different additives were successfully prepared and tested for Y(III) recovery from aqueous media. Morphology and encapsulation capacity of the beads could be controlled by suitably selecting the additives. Composite beads doped with PVA and CNT were found to be superior among the tested beads for the recovery of yttrium even at higher acidities. These beads were found to be stable even after 10 cycles of operations without loss of D2EHPA.

References

1. A. A. Zagorodni, Ion exchange materials: properties and applications, Elsevier, 2006.
2. S.Ozcan, A. Tor, M.E. Aydin, *Desalination* 259 (2010)179.
3. K.K. Yadav, D.K. Singh, M.Anitha, L. Varshaney, H. Singh, *Sep. Puri. Tec.* Doi 10.1016/j.seppur.2013.07.012
4. K. Dasgupta, R. Venugopalan, G.K. Dey, D. Sathiyamoorthy, *J. Nanopart. Res.* 10 (2008) 69.
5. K.K. Yadav, K. Dasgupta, D.K. Singh, M. Anitha, L. Varshney, H. Singh, ISMC-2012, Mumbai, DAE-BRNS, p.87.
6. E.P. Horwitz, D.R. Mcalister, A.H. Bond, R.E. Barrans, *Sol. Ex. Ion. Exc.* 23 (2005) 319.
7. E. Kamio, M. Matsumoto, K. Kondo, *Ind. Eng. Chem. Res.* 46 (2007) 255-265.
8. H. Susanto, M. Ulbricht, *J. Membr. Sci.* 327(2009)125-135.

COMPATIBILITY OF SILICON CARBIDE WITH LEAD-BISMUTH EUTECTIC - THE EFFECT OF OXYGEN INGRESS

P. Chakraborty, R.K. Fotedar and N. Krishnamurthy

Fusion Reactor Materials Section

and

P. K. Pradhan

Materials Processing Division

This Paper received the Best Poster Award at the National Symposium on Materials and Processing, (MAT 2012), held at Mumbai, from 10th-12th October, 2012

Abstract

In the Indian High Temperature Reactor Program, silicon carbide composites has been proposed as an oxidation and corrosion resistant coating over the graphite fuel tubes inside the Compact High Temperature Reactor (CHTR). The coating will be exposed to molten Lead-bismuth eutectic coolant at temperatures around 1173K to 1273K. The paper discusses the results of 1000 h compatibility study of a SiC pellet exposed to static lead-bismuth eutectic at 1173K and the effect of oxygen ingress into the system pertaining to certain accidental conditions.

Keywords: - Silicon Carbide, Lead-Bismuth Eutectic, CHTR, Oxygen

Introduction

In order to meet the growing energy demand and to mitigate the negative atmospheric effects of using fossil fuels; hydrogen has been proposed to serve as a clean and sustainable energy source. Industrially usable hydrogen can be efficiently and economically produced by the splitting of water, but the process requires comparatively higher temperatures. To achieve this objective, Bhabha Atomic Research Centre (BARC) is developing a prototype Compact High Temperature Reactor (CHTR) which will validate the technologies associated with High Temperature Reactors (HTRs) [1]. The objective of Indian HTRs is to supply the high grade heat required for possible hydrogen production. The CHTR uses U-233 and thorium-based carbide as fuel (TRISO coated particle) compacted in a graphite matrix where beryllium oxide is used both as the moderator and reflector. Cylindrical fuel compacts are packed in fuel bores located at the walls of graphite fuel tubes

[1, 2]. The core heat is removed by natural circulation of lead-bismuth eutectic alloy [44.5 wt.% Pb + 55.5 wt.% Bi], which enters the fuel tube at 1173K, and after taking the reactor heat, leaves the tube at 1273K towards the upper plenum. Lead-bismuth eutectic (LBE) is known to be corrosive towards various structural materials above 623K [3, 4]. Considering this aspect, a protective oxidation and corrosion resistant coating of Silicon carbide (SiC) composite material has been proposed over the graphite fuel tubes. Under some unforeseen accidental situations, this SiC coated graphite fuel tube may get exposed to oxygen. Thus, maintenance of long term integrity of the same in the presence of lead-bismuth eutectic under various reactor conditions will be an important criteria in deciding the feasibility of this process. To assess the compatibility of SiC with Pb-Bi eutectic in the presence of oxygen, an attempt was made to study the corrosion behavior of SiC exposed to static lead-bismuth eutectic at 1123K for 1000 h of exposure.

BARC NEWSLETTER

Experimental

The experiment was conducted in an inert gas furnace capable of providing temperatures upto 1673K. Initially, lead-bismuth eutectic chunks weighing 35 g in total, and a cylindrical SiC pellet weighing 1.86g were placed in an alumina boat. The furnace along with the unloaded alumina boat is shown in Fig. 1. The boat was covered with an alumina lid to avoid spillage of molten mass and was kept inside the vertical furnace. Subsequently, argon- 5% oxygen gas was introduced into the furnace at a nominal rate. The set up was maintained at 1173K for 1000 h. Later the furnace was cooled to room temperature and the boat along with the solidified lead-bismuth was taken out of it. Sample analysis was carried out through SEM-EDS and XRD.

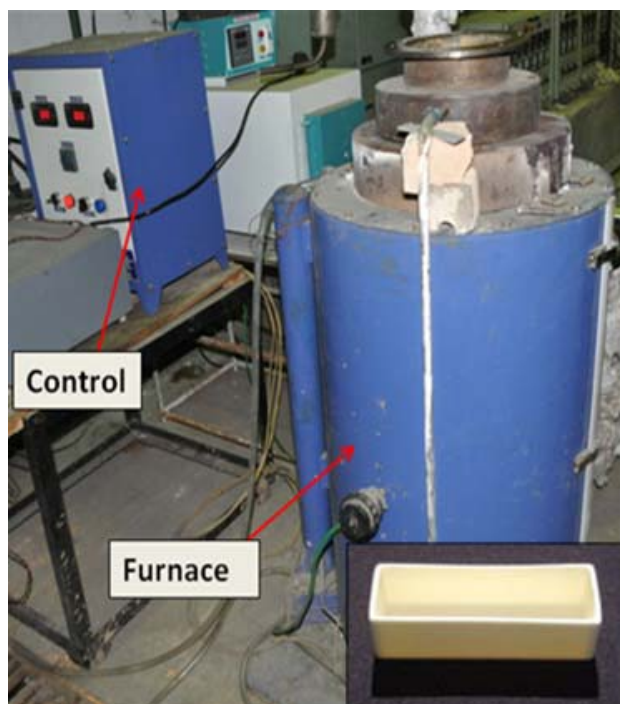


Fig. 1: Furnace used for conducting 1000 h static experiment; (Inset) Alumina boat used for holding SiC pellet and LBE chunks.

Results

Considerable degradation of the SiC pellet was noted after 1000 h of exposure to lead-bismuth eutectic under oxygen at 1173K. This predicts that under accidental conditions, SiC coating could deteriorate considerably inside high temperature reactors.

On the other hand, the walls of the alumina crucible along with the top surface of the solidified LBE were found covered with a yellowish glassy adherent coating. As shown in Fig. 2, XRD analysis revealed the presence of lead silicate along with lead and bismuth oxides individually, in the glassy coating. To investigate the composition of the exposed lead-bismuth eutectic, SEM-EDS were carried out on the LBE sample. Fig. 3 shows an SEM image of the solidified eutectic and the EDS analysis carried out at two different locations [1 and 2] over the same area could be observed in Table 1 and 2 respectively. Table 1 shows the association of lead with silicon and oxygen whereas Table 2 predicts the formation of bismuth oxide, thus confirming the XRD results.

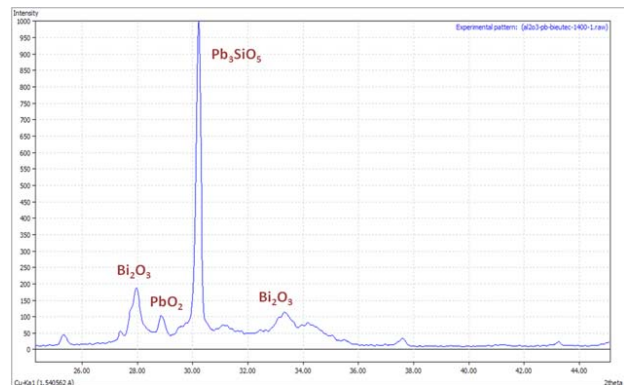


Fig. 2: XRD analysis of the adherent glassy layer present over the exposed LBE sample shows lead silicate and oxides of lead and bismuth.

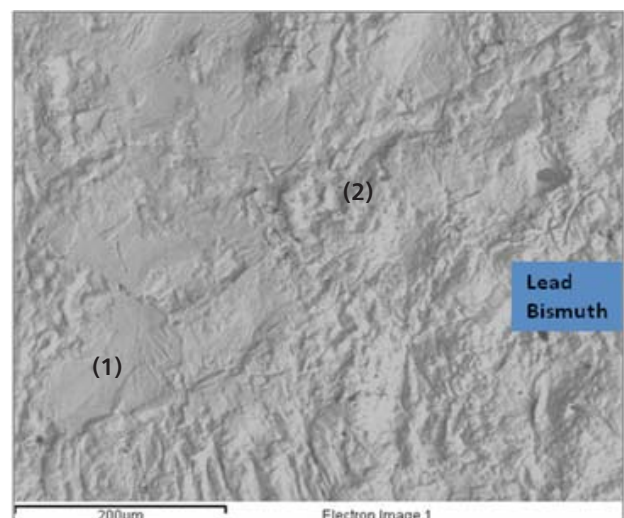


Fig. 3: SEM Image of the LBE sample exposed to SiC pellet at 1173K for 1000 h

BARC NEWSLETTER

Table 1: EDS analysis of the LBE sample exposed to SiC pellet at 1173K for 1000 h showing association of lead with silicon and oxygen

Element	Weight%
O K	16.46
Si K	11.56
Pb M	71.96

Table 2: EDS analysis of the LBE sample exposed to SiC pellet at 1173K for 1000 h showing association of bismuth and oxygen

Element	Weight%
O K	10.34
Bi M	89.66

Discussion

From the results discussed above, the degradation of SiC pellet seems to be possibly associated with a series of events. Due to oxygen exposure, lead-bismuth eutectic started converting into lead and bismuth oxides i.e. PbO_2 and Bi_2O_3 respectively. It is a well known fact that a silicon carbide pellet inherently contains a protective layer of Silica i.e. SiO_2 over its entire surface. In the presence of oxygen and Bi_2O_3 , this SiO_2 layer interacted with PbO_2 , thus forming lead silicate (Pb_3SiO_5) as obtained in XRD analysis. As a consequence, fresh silicon carbide surface got exposed and in the presence of oxygen, a second layer of SiO_2 was developed. This once again triggered the sequence of events discussed above. The process continued in a cyclic manner each time exposing of new SiC surfaces ready for interaction, thereby forming lead and bismuth silicates leading to formation of the glassy coating. This

might be the probable reason for degradation of the silicon carbide pellet.

Conclusion

1. Silicon Carbide was considerably degraded by lead-bismuth eutectic at 1273 K in the presence of oxygen.
2. The process was initiated by interaction of inherently present SiO_2 with lead and bismuth oxide formed in the presence of oxygen. This later continued in cyclic manner led to exposure of fresh SiC surface and to the formation of a yellowish glassy layer comprising of lead silicate.

Acknowledgements

We would like acknowledge the informative technical discussions with Dr. Abhijit Ghosh, G&ACD, BARC. We would also like to thank Shri A. Nagraj, L&PTD, BARC and Shri Bhaskar Paul, MPD, BARC for carrying out the XRD and SEM-EDS analysis respectively

References

1. R. K. Sinha, I. V. Dulera, Indian Journal of Engineering and Materials Sciences, 17(2010) 321-326.
2. R. K. Sinha, Asian Nuclear Prospects 2010, Energy Procedia, 7 (2011) 34–50.
3. L. Soler, F.J. Martin, F. Hernandez, D. Gomez - Briceno, Journal of Nuclear Materials 335 (2004) 174–179.
4. Eric P. Loewen George Bisanz, Materials Characterisation, 49, 5(2002) 463–470.

CHARACTERIZATION OF POLYPHENOL OXIDASE (PPO) FROM BRINJAL (EGGPLANT; *Solanum melongena*)

Bibhuti B. Mishra, Satyendra Gautam and Arun Sharma
Food Technology Division

This Paper received the Best Poster Award at the DAE-BRNS Life Sciences Symposium (LSS-2012) on Trends in Plant, Agriculture and Food Sciences, held at Mumbai, from 17th-19th December, 2012

Abstract

Brinjal is a rich source of polyphenol oxidase (PPO), which negatively affects its quality upon cutting and postharvest processing. PPO inhibitors from natural or synthetic sources are used to tackle this problem. With this aim, PPO enzyme purification from brinjal and its characterization including inhibitor studies were undertaken. Brinjal was found to contain two isoforms of PPO (PPO1 and PPO2) which were resolved during differential ammonium sulfate precipitation and native PAGE. PPO1 was precipitated at 30%, whereas, PPO2 was precipitated at 70% ammonium sulfate saturation. The PPO2 showed higher specific activity and was further purified to about 259 fold using ion exchange, hydrophobic interaction, and gel filtration chromatography. The molecular size of purified brinjal PPO2 was found to be a 112 kDa, a homodimer of 56 kDa each. This purified enzyme showed very low K_m (0.34 mM) and high catalytic efficiency (3.3×10^6) with 4-methyl catechol. The substrate specificity was found in the order 4-methyl catechol > tert-butylcatechol > dihydrocaffeic acid > pyrocatechol. Cysteine hydrochloride, potassium metabisulfite, ascorbic acid, erythorbic acid, resorcylic acid and kojic acid showed competitive inhibition, whereas, citric acid and sodium azide showed mixed inhibition of PPO activity. Cysteine hydrochloride was found to be an excellent inhibitor with K_i of 1.8 μM .

Key words: chromatography; enzyme; inhibitor; methyl catechol; polyphenol oxidase (PPO)

Introduction

The postharvest processing of brinjal (*Solanum melongena*) in ready-to-cook (RTC) form is one of the major problems for food industries dealing with vegetable processing (Madinez & Whitaker, 1995). Polyphenol oxidase has been reported to be one of the important factors contributing to its browning during postharvest processing. In brinjal the PPO and phenolics were reported to be present in chloroplast and vacuoles, respectively (Mayer & Harel, 1979). Disruption of cellular structures during cutting leads to release of PPO enzyme and its phenolic substrate. This has been demonstrated using electron and fluorescence microscopy (Mishra et

al., 2012a). In the presence of oxygen, this enzymatic reaction takes place leading to the formation of melanin like brown colored pigment (Madinez & Whitaker, 1995), resulting brownin of cut surface, and thereby, the original whitish appearance is lost. The inhibition of PPO enzyme and browning has remained a challenge for processed fruits and vegetable industry (Mayer, 2006). The purification and characterization of the enzyme in brinjal could help find suitable approach for controlling this problem. In the current study, PPO enzyme from brinjal was purified to homogeneity and the kinetic parameters were determined using natural and synthetic inhibitors.

BARC NEWSLETTER

Materials and methods

Assay Polyphenol oxidase (PPO) activity

The PPO enzyme activity was determined using 4-methyl catechol as substrate. The enzyme assay was carried out taking 0.88 ml of phosphate buffer (pH 6.8, 50 mM), 0.1 ml substrate (0.1M) and 0.02 ml of enzyme extract. The increase in absorbance at 420 nm was monitored at 30 sec interval for 3 min and the average change in absorbance per min was calculated. One unit of enzymatic activity caused a change of 0.1 in absorbance/min. The PPO activity was expressed as U/g of brinjal weight. The specific activity was determined as PPO activity/mg protein. Protein content of the brinjal extract was determined by the Bradford method (1976), using bovine serum albumin (BSA) as standard.

Purification of PPO

The popular brinjal (cv. 'Kalpatharu') variety (1 kg) was homogenized in 3 litre of extraction solution containing sodium phosphate buffer (pH 6.8, 0.05 M) having polyvinyl pyrrolidone (PVP) (1%), polyvinyl polypyrrolidone (PVPP) (2%), triton X-100 (1%) and ascorbic acid (30 mM). The extract was filtered and centrifuged (10000xg for 15 min at 4°C). The activity in supernatant was considered as 100%. The crude extract was further fractionated using ammonium sulfate precipitation and dialysis.

Chromatography

The DEAE (Diethylaminoethyl) Cl-6B Sepharose anion exchange chromatography was performed with dialyzed enzyme extract (Mishra et al., 2012b). The pH was adjusted to 8.0 and mixed with DEAE column material, kept at slow stirring for 30 min at 4°C. This slurry was then washed twice and loaded onto the column. The elution was carried out using increasing gradient of NaCl from 0 to 0.5 M in phosphate buffer (pH 8.0, 2 mM). The fractions having maximum activity were pooled and further purified by phenyl Sepharose hydrophobic interaction chromatography. The column material and enzyme extract were equilibrated with 18% ammonium sulfate, phosphate buffer (pH 6.8,

20 mM) and loaded on column, washed and eluted with decreasing gradient of ammonium sulfate from 18 to 0% in phosphate buffer (50 ml, pH 6.8, 20 mM). The fractions exhibiting PPO activity were pooled and further purified using Superdex gel filtration chromatography. The protein was loaded into HPLC column and the elution was carried out with phosphate buffer (pH 6.8, 20 mM) containing NaCl (150 mM). The molecular weight was determined using a calibration curve prepared from the retention time of proteins of known molecular weight. The native and SDS PAGE was performed to identify the PPO isoforms and determine their molecular weight.

Determination of kinetic parameters of PPO

The substrate specificity with different substrates (4-methyl catechol, tert-butylcatechol, pyrocatechol, chlorogenic acid, L-DOPA (dihydroxyphenylalanine), cresol, dihydrocaffeic acid, caffeic acid, dihydroxybenzaldehyde, pyrogallol, D-DOPA, and gallic acid) was determined and expressed as percentage relative activity with respect to 4-methyl catechol (Mishra et al., 2012b). The enzymatic activity was monitored with fixed purified enzyme concentration and increasing substrate [S] concentration. The reaction velocity [V] was determined by monitoring change in absorbance per min. The reciprocal plot of 1/[V] vs. 1/[S] was plotted and the Km and Vmax were determined from the slope and intercept of the line, respectively. The total enzyme molecule concentration was determined by dividing estimated total protein by molecular weight of PPO. The turnover number (kcat) was calculated by dividing total substrate molecules changed per min by total molecules of PPO enzyme in the reaction mix. The catalytic efficiency (kcat/Km) was calculated by dividing kcat by Km. The inhibitor studies were carried out with eight natural and synthetic compounds (Mishra et al., 2012b).

Results and Discussion

Optimization of process parameters for extraction of PPO

The crude buffer extract from brinjal showed extensive browning of enzyme extract during extraction process.

BARC NEWSLETTER

Addition of detergent (triton X-100, 1%), salt (NaCl, 0.5 M), or SDS (0.5%) during extraction did not increase PPO activity which indicated the absence of strongly membrane bound, weakly ionic bound, or latent forms of PPO in brinjal, respectively. In the current study, the ammonium sulfate fractionation was performed with gradual increase of 10-20% in each step. The high PPO activity was observed in two discrete fractions (20-30% and 50-70%) which could be due to the presence of two isoforms of PPO (Fig. 1a). These two fractions were tested with PPO

inhibitor potassium metabisulfite (PMS) for ruling out the enzyme activity by any other proteins including peroxidase. PPO activity was completely inhibited by PMS in both these fractions. This also indicated that PPO in these two fractions could be differing in its hydrophobic characteristics resulting in precipitation at two different ammonium sulfate concentrations. The specific activity in 50-70% fraction was found to be highest and was about 62% higher than that of 20-30% fraction and hence was further purified and characterized (Fig. 1a).

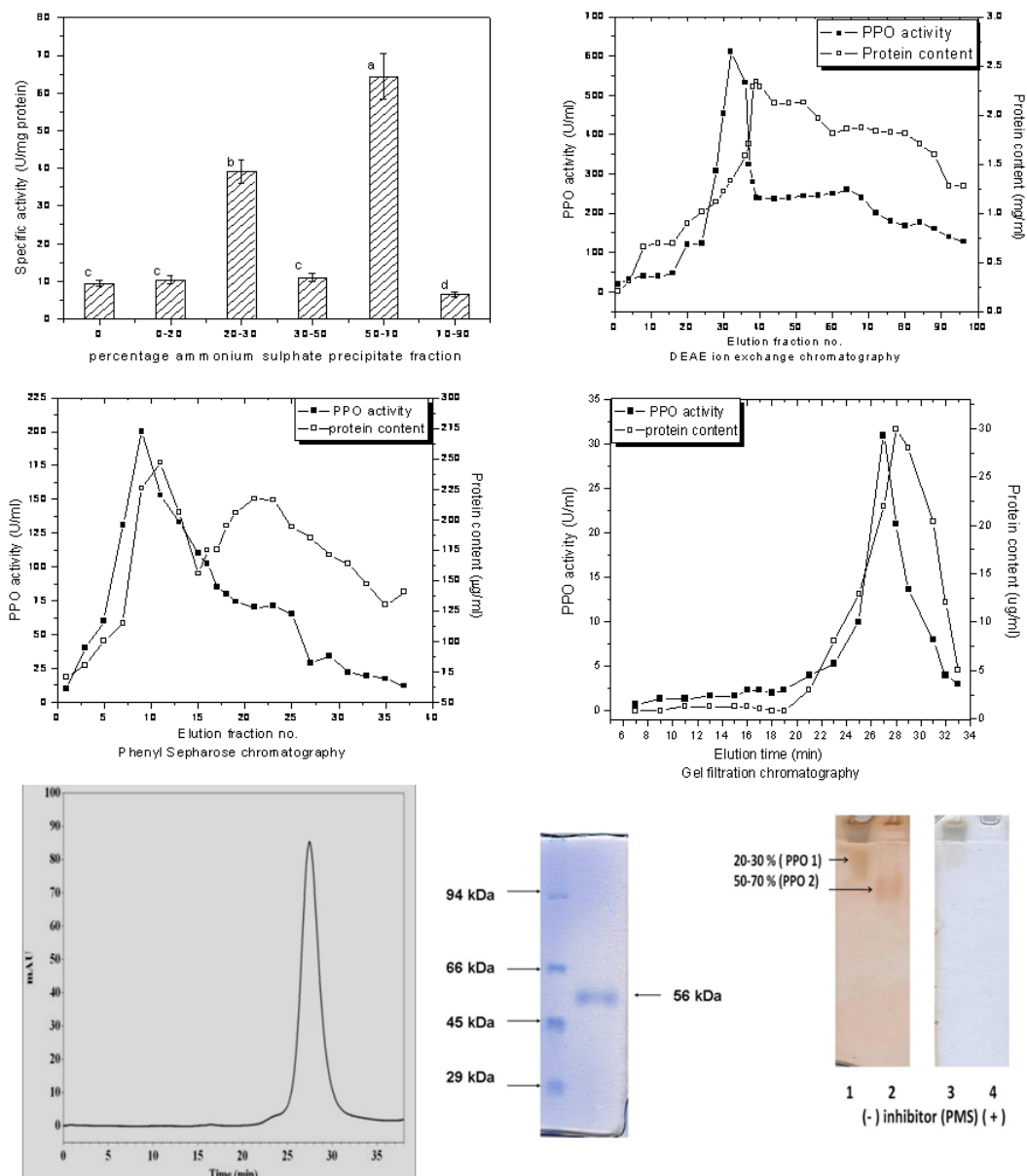


Fig. 1: The different steps of purification and profile of PPO from brinjal. (a) Ammonium sulfate precipitation (different letters in the superscript indicate significance of difference in the mean), (b) DEAE ion exchange chromatography, (c) Phenyl Sepharose hydrophobic interaction chromatography, (d) Superdex gel filtration chromatography, (e) HPLC profile indicating gel filtration purified PPO with molecular weight markers, (f) native PAGE indicating PPO1 (lane 1) and PPO 2 (lane 2) while incubated with buffer and substrate (4-methyl catechol) without (lane 3) and with (lane 4) potassium metabisulfite, a PPO inhibitor.

BARC NEWSLETTER

Molecular weight of brinjal PPO

During DEAE (Fig. 1b), phenyl Sepharose (Fig 1c), and gel filtration (Fig. 1d) chromatography, PPO activity/ml increased and the protein content decreased. This resulted in increase in specific activity to 259 fold after gel filtration chromatography (Table 1). However, at each step of purification loss in total activity was noticed because, only fractions displaying PPO activity was purposely collected. This significantly increased the specific activity and purification fold, but the total yield was significantly reduced to about 0.02%. From 1 kg of brinjal, the finally purified PPO fraction contained 0.37 mg of active protein (Table 1). The gel filtration revealed molecular weight of purified PPO to about 112 kDa, based on a calibration curve prepared using proteins of known molecular weight (Fig. 1e). The SDS-PAGE profile of the finally purified protein showed a single band of about 56 kDa (Fig. 1f). This indicated the active protein to be a homodimer of total weight 112 kDa.

Native PAGE showed presence of two isoforms of PPO

The 20-30 and 50-70% ammonium sulfate precipitated extracts were also analysed on a native PAGE. The results confirmed that PPO1 and PPO2 are indeed isoforms and hence displayed differential mobility on gel. In addition to this, the PPO activity of these two fractions was also tested by enzyme assay in the presence and absence of inhibitor.(Fig. 1g) The results also showed complete inhibition by PMS in both these fractions,

which again confirmed the existence of two isoforms of PPO in brinjal.

PPO substrate specificity showed higher catechol oxidase activity

The enzyme activity with 4-methyl catechol substrates was found to be maximum. Higher enzyme activity was observed with substrates having catechol ring structure and a smaller organic moiety (-R) at meta position with respect to -OH group. The presence of a smaller moiety (-CH₃) in 4-methyl catechol probably contributed its maximum activity. With increase in molecular mass of this group, the activity decreased, as was observed in case of tert-butylcatechol, chlorogenic acid, and DL-DOPA. On the contrary, the absence of this moiety also decreased activity by 30% as observed in case of pyrocatechol. These observations indicated the important role of the -CH₃ residue and its location in catechol structure in determining its specificity. Most of the substrates with catechol ring structure and a moiety at other position of the ring (-OH at *ortho* position as in pyrogallol, gallic acid, and -CH₃ at *para* position as in p-cresol) showed very less or absence of activity. The enzyme did not show any activity against monophenol like tyrosine.

Kinetic characteristics of PPO

The lowest Km (0.34 mM) and highest Vmax (212 μM) was observed in case of 4-methyl catechol. The Km value increased with less specific substrates. However,

Table 1. The purification of PPO from brinjal.

Purification step	Total activity (Units)	Protein (mg/ml)	Specific activity (U/ mg protein)	Yield (%)	Purification (fold)
Crude	(8.4±0.6) x10 ⁴	1.47±0.1	19±5	100±0*	1±0
50-70% Ammonium sulfate saturation	(3.8±0.3) x10 ⁴	2.05±0.2	65±5	45±5	3.42±0.3
Ion exchange (DEAE)	(1.1±0.2) x10 ⁴	1.5±0.1	170±16	13±1.1	8.94±0.7
Hydrophobic (Phenyl Sepharose)	2268±226	0.45±0.04	840±55	2.7±0.2	44±3
Gel filtration (Superdex)	1851±154	0.08±0.01	4925±460	0.02±0.002	259±23

* represents activity of extract prepared by homogenizing 1 kg of eggplant in 3 litre of extraction solution.

BARC NEWSLETTER

the V_{max} remained almost same. The tert-butyl catechol, dihydrocaffeic acid, and pyrocatechol showed 29, 41, and 58% higher K_m compared to 4-methyl catechol and the difference was found to be significant. The turnover number (k_{cat}) and catalytic efficiency (K_{cat}/K_m) were also found to be maximum for 4-methyl catechol and lesser for pyrocatechol.

Inhibitor studies

The eight different inhibitors namely ascorbic acid, α -resorcylic acid, erythorbic acid, cysteine hydrochloride, potassium metabisulfite, kojic acid, citric acid, and sodium azide were evaluated. Out of which, citric acid and sodium azide showed mixed inhibition and the rest six showed competitive inhibition. The competitive inhibitors showed the same V_{max} value with same Y-axis intercept, whereas, the mixed inhibitors had different V_{max} values. The most effective competitive inhibition was shown by cysteine hydrochloride with the lowest K_i of 1.8 μ M. The newly studied compound cysteine hydrochloride was structurally quite similar to the earlier studied inhibitor cysteine and showed significant inhibition of PPO activity at a concentration much below the permissible level. Cysteine hydrochloride is derived from amino acid cysteine and is highly soluble in water. It is a reducing agent and known to form adduct with intermediate quinones, which inhibits the PPO enzyme at much lower concentration. The next effective competitive inhibitor was potassium metabisulfite with K_i value of 9 μ M. It is known to inhibit PPO by the reaction of sulfite with intermediate quinones, resulting in the formation of sulphoquinones, which irreversibly inhibits PPO, resulting in its complete inactivation. The ascorbic and erythorbic acid showed similar competitive inhibition with K_i values of 15.2 and 19.6 μ M, respectively. The kojic acid and resorcylic acid showed K_i of 0.123 and 8.2 mM, respectively. The mixed inhibition was shown by sodium azide and citric acid with higher K_i values of 3.3 and 13.5 mM, respectively, and were observed to be less effective. The findings of this study provide valuable information with respect to control of browning in fruits and vegetables processing industry using a simple GRAS chemical such as cysteine hydrochloride.

Conclusions

A highly active PPO from brinjal which gets precipitated at 50-70% ammonium sulfate saturation was significantly purified (259 fold), and characterized to be a homodimer each of molecular weight 56 kDa. The substrate specificity indicated its nature as a catechol oxidase (EC 1.10.3.2) with maximum activity with 4-methyl catechol. The enzyme lacked cresolase and tyrosinase activity. Catechol ring structure and a smaller side chain moiety (4-methyl) at meta position with respect to -OH group were found to be the major determinants of its activity. It showed significant competitive inhibition by a GRAS compound cysteine hydrochloride which has higher efficiency compared to the conventionally used potassium metabisulfite.

References

1. Madinez, M. V., & Whitaker, J. R. (1995). The biochemistry and control of enzymatic browning. *Trends in Food Science and Technology*, 6, 195-200.
2. Marshall, M. R., Kim, J. & Cheng-I, W. (2000). Enzymatic browning in fruits, vegetables and seafoods. FAO. Available online at <http://www.fao.org/ag/ags/agsi/ENZYMEFINAL/>.
3. Mayer, A. M. (2006). Polyphenol oxidases in plants and fungi: Going places? A review. *Phytochemistry*, 67, 2318-2331.
4. Mayer, A. M., & Harel, E. (1979). Polyphenol oxidase in plants. *Phytochemistry*, 18, 193-215.
5. Mishra, B. B., Gautam, S., & Sharma, A. (2012a). Browning of fresh-cut eggplant: Impact of cutting and storage. *Postharvest Biology and Technology*, 67, 44-51.
6. Mishra, B. B., Gautam, S., & Sharma, A. (2012b). Purification and characterization of polyphenol oxidase (PPO) from eggplant (*Solanum melongena*). *Food Chemistry* 134 1855–1861.
6. Pérez-Gilabert, M., & Carmona, F. G. (2000). Characterization of catecholase and cresolase activities of eggplant polyphenol oxidase. *Journal of Agricultural and Food Chemistry*, 48, 695-700.

CHARACTERIZATION AND PROPERTY EVALUATION OF U-15WT%Pu ALLOY FOR FAST BREEDER REACTOR

Santu Kaity, Joydipta Banerjee, K. Ravi and Arun Kumar

Radiometallurgy Division

and

R. Keswani

Metallic Fuels Division

and

G.J. Prasad

Nuclear Fuels Group

This Paper received the Best Poster Award at the Interdisciplinary Symposium on Materials Chemistry (ISMC-2012), held at Mumbai, from 11th-15th December, 2012

Abstract

The characterization and high temperature behaviour of U-15wt%Pu alloy has been investigated in this study for the first time. U-15wt%Pu alloy sample for this study was prepared by following melting and casting route. Microstructural characterization of the alloy was carried out by XRD and optical microscopy. The thermophysical properties like phase transition temperatures, coefficient of thermal expansion and hot hardness were determined. Eutectic temperature between T91 and U-15wt%Pu was established. The fuel-cladding chemical compatibility of U-15wt%Pu alloy with T91 grade steel was studied by diffusion couple experiment.

Introduction

Metallic fuel is considered as a future fast reactor fuel since they have high fissile and fertile atom densities, which in turn offer relatively better breeding ratio. They are relatively easy to fabricate and have high thermal conductivity and lower heat capacity [1]. Metallic fuel has some disadvantages like low solidus temperature, relatively high swelling rate and fission gas release, and susceptibility to chemical and mechanical interaction with cladding materials. Primarily, two design concepts have been proposed for the metallic fuel development programme for fast breeder reactors in India [2]. These two concepts are: (a) Mechanically bonded pin with U-15wt%Pu alloy as fuel, and (b) Sodium bonded pin with U-15wt%Pu-6wt%Zr alloy as fuel. T91 grade steel (mod. 9Cr1Mo steel) has been used as the cladding material in these designs. In the case of the mechanically bonded binary alloy fuel, Zr liner is proposed to be used

inside the cladding to prevent the fuel-cladding chemical interaction. The mechanically bonded binary U-15wt%Pu (hereafter, referred to as U-15Pu) fuel is a new concept without much international experience. Hence, studies related to development of fast reactor fuels based on binary U-15Pu alloy has been initiated for building a data base on thermo-physical and thermodynamic properties, fuel-cladding compatibility etc. which are very useful to the fuel-designer to optimize design feature and to predict in-reactor fuel behaviour. The main objectives of present study are:

- i. investigation on the microstructures of as-cast alloy by XRD and optical microscope,
- ii. determination of phase transformation temperatures and coefficient of thermal expansion with the help of differential thermal analysis (DTA) and dilatometer, respectively,
- iii. evaluation of the hot-hardness data of the alloy from room temperature to 1000 K, and

iv. studies on the fuel-cladding chemical compatibility by diffusion couple experiments.

Experimental procedure

U-15Pu alloy was prepared by melting and casting route. The trace metallic constituents in the alloy were analyzed by DC-arc AES. The microstructural analysis was carried out using an optical microscope. The phase analysis of the fuel alloy was carried out using XRD with Cu-K α radiation. The distribution of plutonium in the alloy was evaluated by using alpha-autoradiography. The transformation temperature measurements were carried out using a differential thermal analyzer (DTA). The expansion behaviour of U-15Pu alloy was studied using a high temperature vertical dilatometer. Hot hardness measurements were carried out using a hot hardness tester with the help of a diamond Vickers pyramid indenter. The eutectic temperature between U15Pu and T91 was determined by using DTA. The fuel-clad chemical interaction between U-15Pu and T91 was investigated by carrying out diffusion couple experiment where U-15Pu/Zr/T91 couple (i.e. a 100 μm thick Zr foil sandwiched between U-15Pu and T91 discs) was heated at 973 K for 500 h under helium atmosphere. The interaction layers formed at the interfaces were examined under optical microscope.

Results and Discussion

The XRD analysis of U-15Pu alloy is presented in Fig. 1. The peaks in the XRD data correspond to α phase of uranium. The microstructure of as-cast U-15Pu alloy is shown in Fig. 2. The microstructure consists of a single phase structure with some inclusions. The average grain size was found to be around 30 μm . XRD data do not contain any peak corresponding to the ζ phase. Similarly, the formation of ζ phase is not evident in the microstructural analysis also. The homogeneous distribution of plutonium in fuel pellets is to be ensured for safe and satisfactory performance of fuel. Fig. 3 shows the alpha-autoradiograph of U-15Pu alloy. Alpha-radiograph showed a uniform distribution of Pu in U-matrix. It did not show any Pu-rich area. This

indicates that the alloy sample is fully homogeneous in nature.

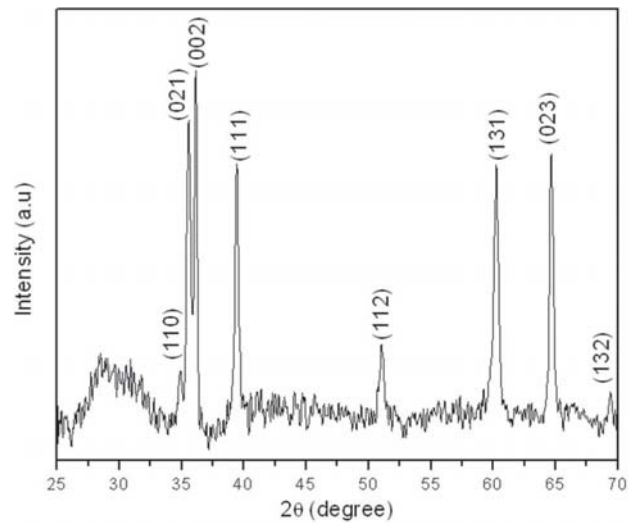


Fig. 1: XRD data of as-cast U-15Pu alloy. All the peaks correspond to α -U phase.



Fig. 2: Optical micrograph of U-15Pu alloy

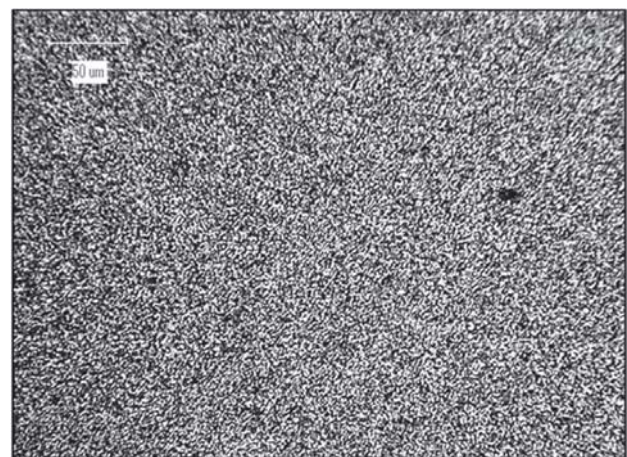


Fig. 3 Alpha-autoradiograph of U-15Pu alloy

BARC NEWSLETTER

The DTA curve of as-cast U-15Pu alloy on heating is shown in Fig. 4. The peak observed at 837 K corresponds to (α U) \leftrightarrow (β U) transition and that at 991 K is due to the (β U) \leftrightarrow (ϵ Pu, γ U) transition. The peak at 1248 K indicates the solidus temperature. The dilatometric curve of U-15Pu alloy presented in Fig. 5, shows two distinct phase transformations at 842 K and 992 K, respectively. The first transition starting at 842 K is due to (α U) \leftrightarrow (β U) transformation where a sharp change in length of the sample occurs. The second transformation at 992 K corresponds to the (β U) \leftrightarrow (ϵ Pu, γ U) transformation. The dilatometric curve of U-15Pu can be fitted by a second degree polynomial as:

$$\frac{\Delta L}{L_0} \times 100 = -0.431 + 1.000 \times 10^{-3} (T/K) + 8.609 \times 10^{-7} (T/K)^2$$

where, L_0 is the initial length (at 300 K) and ΔL is the difference between the instantaneous length (at any temperature T) and L_0 . The average coefficient of

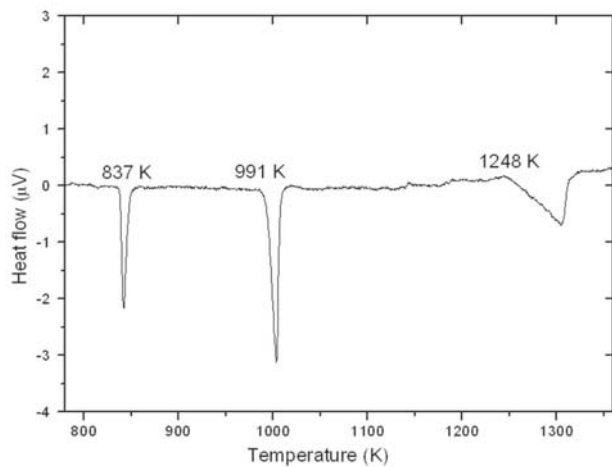


Fig. 4: DTA curve of U-15Pu alloy

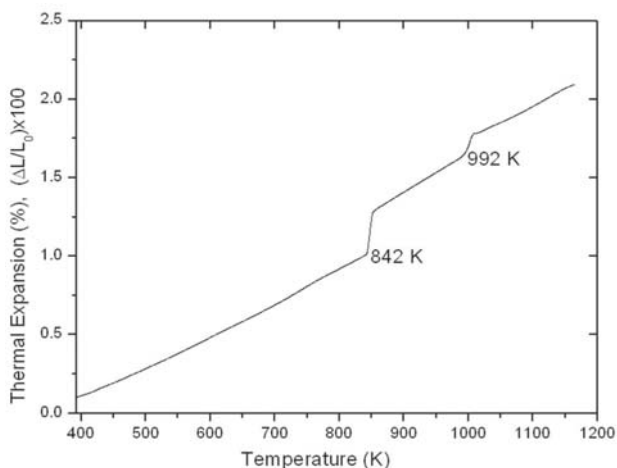


Fig. 5: Thermal expansion curve of U-15Pu alloy

thermal expansion of U-15Pu alloy was found to be $18.58 \times 10^{-6} \text{ K}^{-1}$ in the temperature range 300–823 K. The room temperature hardness of U-15Pu alloy was found to be $280 \pm 20 \text{ kg mm}^{-2}$. The hardness of this alloy gradually decreases with increasing in temperature. The hardness (H) vs. temperature (T) plot for U-15Pu alloy in the temperature range of 298–988 K as shown in Fig. 6, was fitted by a polynomial and the equation for the best fit is given below:

$$H = -544.52 + 7.23 (T/K) - 2.10 \times 10^{-2} (T/K)^2 + 2.32 \times 10^{-5} (T/K)^3 - 8.87 \times 10^{-9} (T/K)^4 \quad (5)$$

where, H is in kg mm^{-2} and T is in K. At 988 K, hardness falls steeply reaching a value as low as $\sim 0.43 \text{ kg mm}^{-2}$.

The fuel-cladding chemical interaction (FCCI) between U-15Pu alloy fuel and T91 grade steel cladding is of

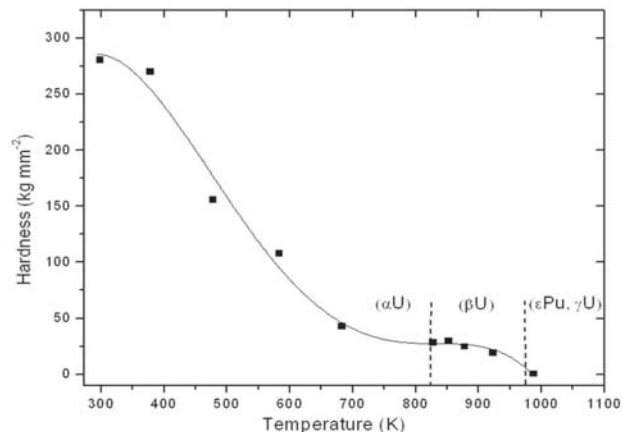


Fig. 6 Hardness vs temperature plot of U-15Pu

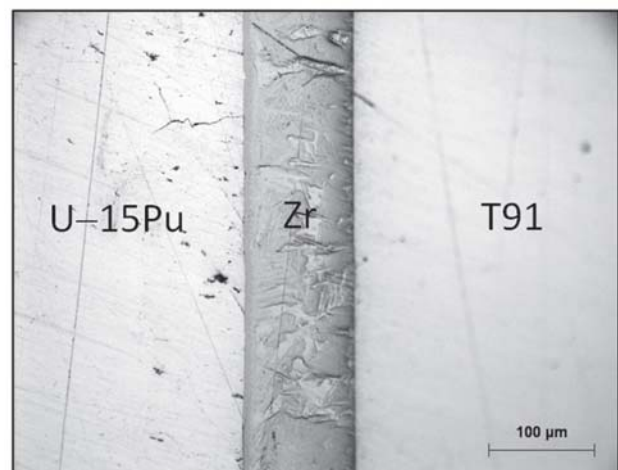


Fig. 7: Microstructure of U-15Pu/Zr/T91 diffusion couple heated at 973 K for 500 h

BARC NEWSLETTER

prime concern because of formation of low melting eutectic. The measured eutectic temperature between U-15Pu alloy and T91 was found to be 948 K. The microstructure of the U-15Pu/Zr/T91 diffusion couple annealed at 973 K for 500 h is shown in Fig. 7. The microstructural analysis of U-15Pu/Zr/T91 diffusion couples revealed an excellent bond formation at both the U-15Pu/Zr and Zr/T91 interfaces after annealing. Any evidence, related to formation of liquid phase was not observed in the U-15Pu/Zr/T91 diffusion couple even after annealing at 973 K for 500 h. The results of the U-15Pu/Zr/T91 diffusion couple indicate that the Zr liner was effective in preventing fuel-cladding chemical interaction at 973 K.

Conclusions

A detailed study on thermophysical properties of U-15Pu alloy at high temperatures have been conducted for the first time and the following conclusions are drawn:

- The XRD and microstructure of as-cast U-15Pu alloy showed only the presence of α -U phase. ζ phase could not be detected in this alloy.
- The solidus temperature was found to be around 1248 K.
- The average coefficient of thermal expansion was found to be $18.58 \times 10^{-6} \text{ K}^{-1}$ (300-823 K).
- γ phase region of U-15Pu was found to be very soft.
- The eutectic reaction temperature between U-15Pu alloy and T91 steel was found to be 948 K. The results of U-15Pu/Zr/T91 diffusion couple indicate that the Zr liner was effective in preventing fuel-cladding chemical interaction at 973 K for 500 h.

References

1. G.L. Hofman, L.C. Walters, Mater. Sci. Technol. 10A (1994) 3.
2. S. Kaity, T.R.G. Kutty, R. Agarwal, A. Laik, A. Kumar, Nucl. Eng. Des. 250 (2012) 267.

BARC NEWSLETTER

STUDIES ON *MUSAWRKY71*, A MULTIPLE STRESS INDUCIBLE TRANSCRIPTION FACTOR GENE FROM BANANA WHICH IS INVOLVED IN DIVERSE STRESS RESPONSES

Upendra K.S. Shekhawat and Thumballi R. Ganapathi
Plant Cell Culture Technology Section,
Nuclear Agriculture and Biotechnology Division

This Paper received the Best Poster Award at the DAE-BRNS Life Sciences Symposium (LSS-2012) on Trends in Plant, Agriculture and Food Sciences, held at Mumbai, from 17th-19th December, 2012

Abstract

WRKY transcription factor proteins play conspicuously important roles in diverse plant stress responses. We have identified and characterized a novel *WRKY* gene, *MusaWRKY71* from banana cultivar *Musa spp. cv Karibale Monthan* (ABB group). *MusaWRKY71* shares significant similarity with other monocot *WRKY* proteins and is translocated to nucleus. *MusaWRKY71* transcripts are induced in banana in response to exposure to cold, drought, salt, ABA, H₂O₂, ethylene, salicylic acid and methyl jasmonate. Transgenic banana plants overexpressing *MusaWRKY71* display better endurance to salt and oxidative stress. Overexpression of *MusaWRKY71* transcripts in these plants resulted in differential expression of several putative target genes of *WRKY* proteins like other *WRKY* genes, *pathogenesis-related (PR) protein genes*, *non-expressor of pathogenesis-related genes 1 (NPR1)* and *chitinase* genes. This study confirms that *MusaWRKY71* is an important player in the transcriptional reprogramming following the perception of diverse stress stimuli in banana plants.

Introduction

Plant growth and wellbeing are negatively influenced by various abiotic and biotic stress stimuli. To survive these challenges, plants possess functional capacity to perceive and react to these signals using sophisticated physiological and biochemical strategies Shinozaki and Shinozaki (2000). Typically once the incidence of stress is sensed, plants set upon a chain of cellular events wherein multiple parallel transduction pathways together modulate the activity of specific transcription factors leading to differential expression of genes responsible for synthesis of effector proteins and/ or metabolites which ultimately contribute to stress tolerance (Chen and Zhu et al., 2004). Important among these transcription factors are plant specific *WRKY* transcription factors which have been widely

studied in several plant species in context of both abiotic and biotic stress responses (Rushton et al., 2010). We have identified and characterized a multiple stress responsive *WRKY* transcription factor gene from banana, *MusaWRKY71*. Apart from its expression and localisation pattern in native banana plants (Shekhawat et al., 2010), we also undertook investigations on its role in stress tolerance by generating banana plants overexpressing this transcription factor.

***MusaWRKY71* is multiple stress inducible and nuclear localized**

MusaWRKY71 gene encodes a protein consisting of 280 amino acids and contains a characteristic *WRKY* domain in its C-terminal half. Semi-quantitative expression profiling indicated that low levels of

BARC NEWSLETTER

MusaWRKY71 transcripts are present in the unstressed leaves and roots of banana plants. In contrast, when banana plants are exposed to cold, dehydration, or oxidative stress or are treated with NaCl, ABA, ethylene, SA or MeJA, *MusaWRKY71* transcripts are substantially induced in both leaves and roots although the exact quantum of this induction varies between different stress stimuli. Transcript level induction in response to different stress stimuli indicate that *MusaWRKY71* is probably a part of the complex signaling networks controlling abiotic and biotic stress responses of banana plant. Being a transcription factor *MusaWRKY71* protein should localize to the nucleus of the banana cells and this was proved by transforming a expression cassette consisting of *MusaWRKY71*::GFP fusion cDNA into banana suspension cells. In these transiently transformed cells, GFP fluorescence was prominently noticed in the nuclei whereas in cells transformed with GFP alone, the fluorescence was present throughout the entire cell.

***MusaWRKY71* overexpressing plants are salt and oxidative stress tolerant**

Banana plants overexpressing *MusaWRKY71* were generated by *Agrobacterium* mediated genetic transformation of banana embryogenic cells (Fig. 1) using a binary vector wherein CaMV 35S promoter was used to express *MusaWRKY71* cDNA essentially as described previously (Ganapathi et al., 2001). Once the putatively transformed plants were confirmed to be transgenic using Southern blotting, these plants were subjected to oxidative and salt stress treatments. The detached leaf assays for enhanced salt and oxidative stress tolerance indicated that the *MusaWRKY71* overexpressing plants endured the stress conditions better than the equivalent control plants. This was further proved by better photosynthesis efficiency (Fv/Fm) and lower membrane damage of the assayed transgenic leaves.

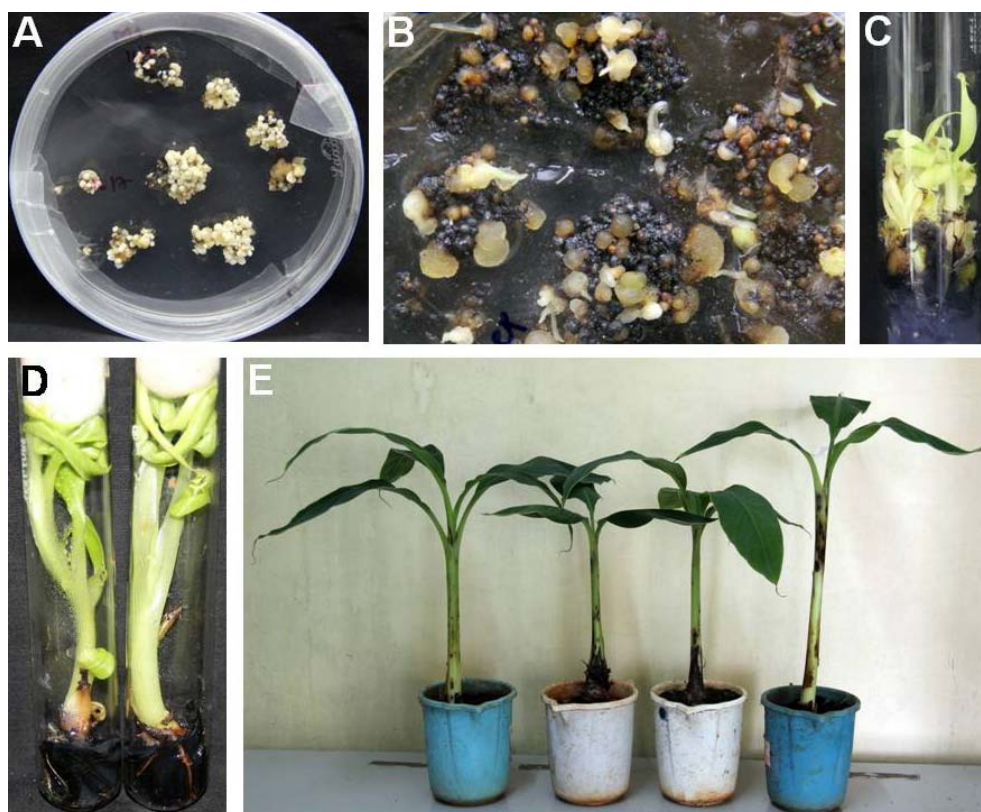


Fig. 1: *Agrobacterium*-mediated genetic transformation of banana embryogenic cells to overexpress *MusaWRKY71* in transgenic banana plants. (A) Putatively transformed banana embryos on banana embryo induction medium (B) Germinating embryos on embryo germination medium (C) Multiple shoot cultures derived from putatively transformed tissues (D) Rooted plantlets (E) Hardened transformed plants in greenhouse.

BARC NEWSLETTER

MusaWRKY71 influences the expression of several related genes

In order to understand the role of *MusaWRKY71* in biotic stress reception and regulation of banana plant, we identified several defense related genes whose expression was modulated by *MusaWRKY71* overexpression in the transgenic banana plants. Differential regulation of these putative targets of *MusaWRKY71* protein were studied using real-time RT-PCR expression analysis of genes from *WRKY*, *non-expressor of pathogenesis-related genes 1 (NPR1)*, *pathogenesis-related (PR) protein genes* and *chitinase* families. Out of a total of 122 genes tested belonging to these families (identified from banana genome database), 10 genes (6 *WRKY* genes, 3 *PR* genes and 1 *chitinase* gene) were found to display significant differential expression in *MusaWRKY71* overexpressing banana plants.

Discussion and conclusions

In the last decade there have been several reports detailing overexpression and downregulation of select specific *WRKY* genes in transgenic plants (Song et al., 2010; Ren et al., 2010). These studies have proved that *WRKY* proteins are involved in a multitude of processes in plants especially biotic and abiotic stress responses. *MusaWRKY71* is proposed to be one of the important members of the *WRKY* gene family in banana which is involved in both abiotic and biotic stress responses and possesses the capacity to regulate other *WRKY* genes as also other genes involved in biotic stress signaling pathways. Also, since overexpression of *MusaWRKY71* imparts the transgenic plants improved oxidative and salt stress tolerance, it is predicted to be a significant linkage in the interface between the various stress response pathways in banana plant.

References

1. Chen WJ, Zhu T (2004) Networks of transcription factors with roles in environmental stress response. *Trends Plant Sci* 9:591-596.
2. Ganapathi TR, Higgs NS, Balint-Kurti PJ, Arntzen CJ, May GD, Van Eck JM (2001) *Agrobacterium*-mediated transformation of embryogenic cell suspensions of banana cultivar Rasthali (AAB). *Plant Cell Rep* 20:157-162.
3. Ren X, Chen Z, Liu Y, Zhang H, Zhang M, Liu Q, Hong X, Zhu JK, Gong Z (2010) *ABO3*, a *WRKY* transcription factor, mediates plant responses to abscisic acid and drought tolerance in Arabidopsis. *Plant J* 63:417-429.
4. Rushton PJ, Somssich IE, Ringler P, Shen QJ (2010) *WRKY* transcription factors. *Trends Plant Sci* 15:247-258.
5. Shekhawat UKS, Ganapathi TR, Srinivas L (2011) Cloning and characterization of a novel stress-responsive *WRKY* transcription factor gene (*MusaWRKY71*) from *Musa* spp. cv. Karibale Monthan (ABB group) using transformed banana cells. *Mol Biol Rep* 38:4023-4035.
6. Shinozaki K, Yamaguchi-Shinozaki K (2000) Molecular responses to dehydration and low temperature: differences and cross-talk between two stress signaling pathways. *Curr Opin Plant Biol.* 3:217-223.
7. Song Y, Chen L, Zhang L, Yu D (2010) Overexpression of *OsWRKY72* gene interferes in the abscisic acid signal and auxin transport pathway of Arabidopsis. *J Biosci.* 35:459-471.

FUEL CELL FABRICATION AND CHARACTERIZATION OF SINGLE CELL OF PROTON CONDUCTING SOFC

Pooja Sawant, S. Varma, B.N. Wani, S.R. Bharadwaj

Chemistry Division

and

D. Prakash

Energy Conversion Materials Section, Materials Group

This Paper received the 3rd Best Poster Presentation Award at the Interdisciplinary Symposium on Materials Chemistry (ISMC-2012), held at Mumbai, from 11th-15th December, 2012

Abstract

BaCe_{0.8}Y_{0.2}O_{3-δ} (BCY) is well known electrolyte material for proton conducting solid oxide fuel cells (SOFCs). In this work, we have synthesized BCY by sol-gel route and also selected corresponding cathode and anode materials to prepare single cell. Hence, an attempt was made to fabricate anode supported single cell with Ba_{0.5}Sr_{0.5}Co_{0.2}Fe_{0.8}O_{3-δ} (BSCF) as cathode and BCY-Ni cermet as anode materials. Current-voltage characteristics of this single cell were measured at different temperatures.

Introduction

Fuel cells which is an alternative energy technology, have received growing attention in recent years since they have been a most promising energy production systems to reduce pollutant emissions. They are electrochemical devices that directly convert the chemical energy into electrical energy. Among the different types of fuel cells, the Solid Oxide Fuel Cell (SOFC) emerges as one of the most promising devices with regard to its fuel flexibility, high efficient power generation and also provides significant environmental benefits. Conventional SOFCs are based on oxygen ion-conducting electrolyte (SOFC-O), state of art the electrolyte, in which yttria-stabilized zirconia (YSZ) is used. However, their high temperature operation (800-1000 °C), creates problems associated with the lack of stability and compatibility with other cell components. SOFCs using ceramic proton conductors as a solid electrolyte (SOFC-H) have attracted more interests as compared to traditional oxide ion conductors due to their capability for low temperature operation [1-2]. In early 1980s, Iwahara et al found several perovskite-type

oxides exhibiting high proton conductivity at elevated temperatures, above 450 °C [1].

Among different proton conducting materials, perovskite based rare earth doped BaCeO₃ shows excellent proton conductivity at lower temperature [3,4]. Hence, BaCe_{0.8}Y_{0.2}O_{3-δ} (BCY) is selected as electrolyte material for cell fabrication. Suitable cathode and anode materials for BCY electrolyte are also synthesized in our laboratory. Ba_{0.5}Sr_{0.5}Co_{1-x}Fe_xO_{3-δ} (BSCF) is well known mixed conducting cathode material with low polarization resistance used in IT-SOFC [5,6]. Whereas, Ni-cermet is used as anode material in composite form with NiO and BCY. In present work, anode supported single cell is fabricated from above selected materials and their current-voltage characteristics are investigated.

Experimental

In this work, anode supported single cell for proton conducting SOFC, comprising of BSCF (Ba_{0.5}Sr_{0.5}Co_{0.2}Fe_{0.8}O_{3-δ}, cathode) | BCY (BaCe_{0.8}Y_{0.2}O_{3-δ},

BARC NEWSLETTER

electrolyte) | NiO-BCY (anode) has been fabricated. BCY powder synthesized in our laboratory by sol-gel route heated at 1200 °C was used for cell fabrication. Anode powder was prepared by mixing BCY and commercially available NiO powder in 50:50 wt% respectively and 10% starch was added as a pore former. BSCF cathode material was synthesized by glycine-nitrate gel-combustion route. X-ray diffraction (XRD) patterns of all materials were recorded prior to use them for cell fabrication. Also, chemical as well as mechanical compatibility of all three cell components was previously checked. To begin with, half cell of BCY | NiO-BCY was prepared by co-pressing and co-firing at 1400 °C for about 4 h. Over the electrolyte layer BSCF cathode layer was brush painted in the form of slurry with terpineol binder which was then sintered at 900 °C. The diameter of anode supported cell is ~12 mm where electrolyte, cathode and anode thickness are ~0.5 mm, ~0.2 mm and ~0.12 mm respectively. This single cell was tested using ProboStat (NorECs, Norway) set up. Anode chamber was exposed to humidified hydrogen (~3% H₂O) and the cathode was exposed to atmospheric air. Current-voltage (I-V) characteristics were recorded at 500 °C and 600 °C. Microscopic features of the cross section of single cell were examined after cell testing using scanning electron microscope, SEM (Seron Technology, Korea).

Results and discussion

XRD pattern recorded for BCY, BSCF and BCY-Ni showed that all three components are phase pure and also it was found that selected materials are well compatible with each other in working temperature range making

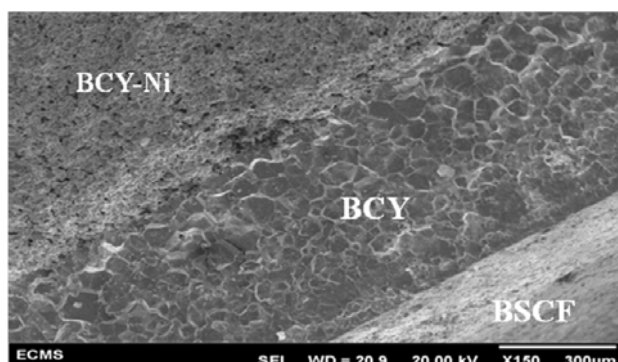


Fig. 1: SEM micrograph of cross section of anode supported single cell

them suitable for the fabrication of proton conducting single cells. Fig. 1 shows the SEM micrograph of cross section of anode supported single cell made up of above three components. The electrolyte layer was found to be quite dense and sandwiched by porous cathode and anode layer.

The current-voltage (I-V) characteristics were measured with the help of laboratory made testing system with humidified hydrogen (~3% H₂O) as a fuel and oxygen as oxidant at 500 °C and 600 °C. Electrical performance of the single cell at 500 °C and 600 °C are shown in Fig. 2. An open circuit voltage (OCV) of about 0.833 V was achieved at 500 °C, and 0.809 V at 600 °C, respectively. This suggests that proton conducting single cell was successfully fabricated where output of cell can be further improved by optimizing the thickness of electrolyte.

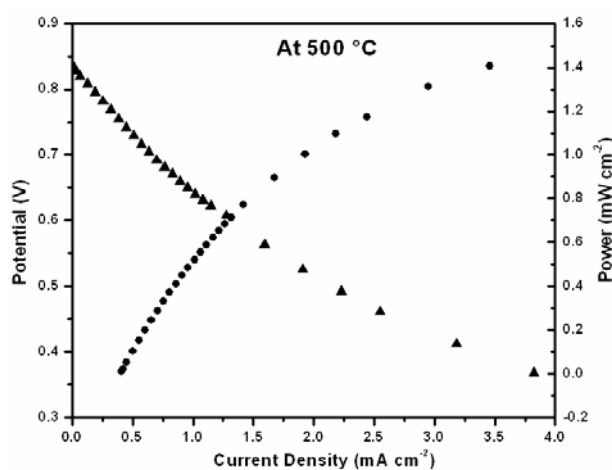
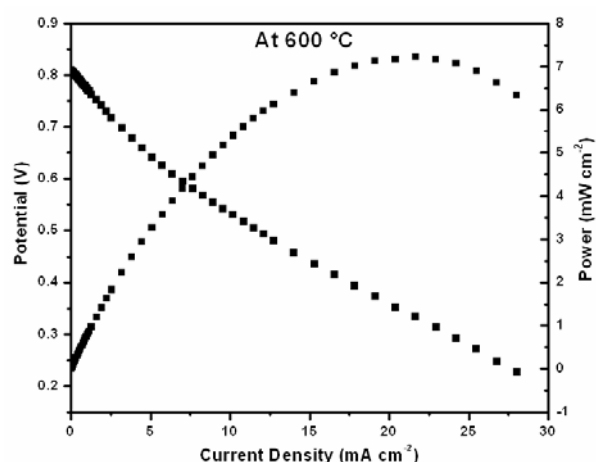


Fig. 2 : Cell voltage and power density as a function of current density for the single cell

BARC NEWSLETTER

Conclusions

Proton conducting anode supported single cell was successfully fabricated by co-sintering and co-firing technique. The cell fabricated generated an OCV of 0.833 V at 500 °C. All cell components are well compatible with each other. Higher current could not be drawn because of shortfall in sealing, poor current collection and high lead wire resistance. Performance can be improved by addressing these as well as by minimizing electrode polarization resistance through refining and optimizing the ceramic processing parameters. Overall, the present study establishes that co-sintering and co-firing approach can be a viable technique for fabrication of anode supported planer SOFC.

Acknowledgement

Author (P. Sawant) gratefully acknowledge Department of Atomic Energy (DAE) for providing financial support

during the research work and Dr. D. Das, Ex-Head Chemistry Division, Bhabha Atomic Research Centre for his keen interest in this work.

References

1. H. Iwahara, T. Esaka, H. Uchida, N. Maeda, *Solid State Ionics*, 3/4 (1981) 359.
2. A.K. Demin, P.E. Tsiakaras, V.A. Sobyenin, S.Y. Hramova, *Solid State Ionics*, 152–153(2002) 555.
3. W.G. Coors, D.W. Readey, *J. Am. Ceram. Soc.*, 85(11) (2002) 2637.
4. F. Giannici, A. Longo, F. Deganello, A. Balerna, A.S. Arico, A. Martorana, *Solid State Ionics*, 178 (2007) 587.
5. H. Zhao, W. Shen, Z. Zhu, X. Li, Z. Wang, *J. Power Sources*, 182 (2008) 503.
6. E. Magnone. *J. Fuel Cell Sci. Technol.*, 7 (2010) 064001-1-11.

BARC NEWSLETTER

AUTHOR INDEX

A

Abraham GJ	268
Achary SN	53
Acharya C	272
Adhikari S	339
Agarwal Renu	295
Agarwal Ritu	238
Almeida AJ	226
Ananthapadmanabhan PV	22
Anitha M	361
Anupama P	226
Apte SK	272, 332
Aswal DK	99, 258
Awale P	133

B

Badodkar DN	73
Bagul RK	198
Balasubramanian V	250
Bandyopadhyay N	245
Banerjee J	372
Banerjee P	256
Bharadhwai G	133, 150
Bharadwaj SR	379
Bharathan R	133
Bhatia MS	287
Bhatia RK	113
Bhattacharjee D	129
Bhattacharyya S	106
Bhavsar SS	250
Bhilwade HN	327
Biswas D	79

Bodile VP	106
Bose SK	110

C

Chakraborty P	213, 364
Chakraborty S	264
Chakravarthy DP	238
Chakravarthy Y	226
Chatterjee H	241
Chaturvedi S	117
Chaubey RC	327
Chavan RB	129
Chawla SP	307
Checker R	311, 315
Choudhury RK	124

D

Darbhe MD	150
Das AK	226
Das D	276
Dasgupta K	170, 361
Debnath AK	99, 258
Dehade SS	226
Devasagayam TPA	311
Dikshit B	287
Dinesh KP	233
Dixit KP	129
Dutta Choudhury S	176

E

Eswaramoorthy C	217
-----------------	-----

BARC NEWSLETTER

F

Fotedar RK	213,364
Francis S	358

G

Gadgil K	133
Gadre VM	73
Gaikwad SB	226
Ganapathi TR	376
Gantayet LM	129
Garg RK	250
Gautam S	245,342,348,367

Ghosh A	319
Goswami D	291
Gota V	311
Govindankutty TL	57
Govindwar SP	303
Guha S	124
Guleria A	339
Gulhane MM	113
Gupta GP	287
Gupta RK	57
Gupta SC	300
Gupta SK	99,113,258

H

Hajare SN	245
Hari Prasad M	142
Hazra P	207

I

Islam A	207
---------	-----

J

Jadhav NV	279
Jain A	261
Jain U	155, 336
Jamdar S	322
James Jacob M	217
Jat RA	295
Jawale SB	57,124
Jayakumar S	327
Jayarajan K	43
Joshi JB	162

K

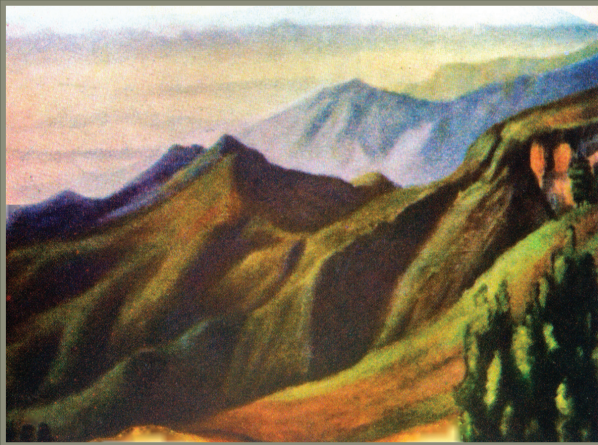
Kadam AA	303
Kadu A	250
Kain V	268
Kaity S	372
Kanatt SR	307
Kannan S	17
Kansal A	198
Kar DC	43
Kashyap YS	120
Kaushik CP	223
Keswani R	372
Khan NM	311
Kirti A	332
Kota S	179
Kolekar RV	300
Koley S	319
Kothiyal GP	250,319
Krishnamurthy N	155,213, 276, 336, 364
Kulkarni MP	241
Kulkarni S	207

BARC NEWSLETTER

Kulkarni SG	295	Mohanty J	49
Kumar Abhay	124	Mondal JA	194
Kumar Amit	190,279	More VS	245
Kumar Arun	372	Mukherjee A	155
Kumar Ashok	284	Mukherjee J	226
Kumar Ashwani	61	Mundada RS	110
Kumar J	185		
Kumar M	61	N	
Kumar P	303	Nagaraj A	226
Kumar R	124	Nagesh KV	238
Kumar S	245	Nataraju V	113
Kumar Sanjay	155,213,336	Nath S	57
Kumar V	355	Ningthoujam RS	279
		Niranjan R	300
L			
Laghate MM	110		
		P	
M		Padmanabhan PVA	226
Mahadeshwar VM	113	Palit DK	194
Maheshwari NK	198	Pandey BN	279
Malhotra S	213	Pant LM	88
Mandalika S	322	Parida SC	295
Manna S	162	Patel AS	238
Maru G	342	Patel RJ	106,137,241
Maurya DK	342	Patel T	146
Menon R	238	Patil AD	173
Mishra BB	245,367	Patil NV	226
Mishra R	276	Patwardhan RS	311,315
Misra HS	179	Paul B	213
Misra N	355	Paul J	303
Misra VK	203	Pilkhwal DS	198
Mitra S	238	Prabhala A	226
Mittal KC	129,238	Pradhan PK	213,364
Modak P	83	Prakash D	379
		Prasad CSR	203

BARC NEWSLETTER

Prasad GJ	372	Sahu R	43
Prasad TL	291	Sainis KB	315
Punekar P	159	Sakrikar RV	43,250
Puri RK	73	Samanta S	99,258
		Sandur SK	311,315
R		Sanjiva K	250
Rajan Babu V	250	Sanyasi Rao VVS	142
Rajan MGR	73,207	Sarkar S	203
Rajaram H	332	Sarkar SK	339
Rama Rao A	159	Sarode DM	110
Ramanathan S	319	Satpute RU	226
Ramakrishna P	137	Sawant P	379
Ramkumar N	150	Saxena S	245, 342
Ramprasad V	233	Sengar RS	73
Ranjon R	241	Sengupta C	133
Rao H	210	Senthil K	167,238
Rao SM	307	Seshadri R	207
Rao SVG	203	Sethi S	226
Rath MC	339	Shah J	137
Ravi K	372	Shah ML	287
Ravisankar E	113	Shanmugavelu P	217
Ray AK	238	Sharma Archana	31,238
Rodrigues M	322	Sharma Arun	245,307,322, 342,348,367
Rout RK	300	Sharma D	311, 315
Roy A	238	Sharma G	106
Roy K	150	Sharma VK	238
Roy SB	162	Shekhawat UKS	376
		Shenoy KT	223
S		Shete PP	110
Saha TK	113	Shiv Chandan	129
Sahoo DK	276	Shukla R	256
Sahoo NK	250	Shyam A	256
Sahu AK	319	Shyam TV	65



"A Painting of the Swiss Alps by Dr. Homi Bhabha"